LIPIDS IN CYANOBACTERIA, ALGAE, AND PLANTS - FROM BIOLOGY TO BIOTECHNOLOGY

EDITED BY: Eric Marechal, Koichiro Awai, Juliette Jouhet and Mie Shimojima

PUBLISHED IN: Frontiers in Plant Science

frontiers Research Topics

Frontiers eBook Copyright Statement

The copyright in the text of individual articles in this eBook is the property of their respective authors or their respective institutions or funders. The copyright in graphics and images within each article may be subject to copyright of other parties. In both cases this is subject to a license granted to Frontiers.

The compilation of articles constituting this eBook is the property of Frontiers.

Each article within this eBook, and the eBook itself, are published under the most recent version of the Creative Commons CC-BY licence. The version current at the date of publication of this eBook is CC-BY 4.0. If the CC-BY licence is updated, the licence granted by Frontiers is automatically updated to the new version.

When exercising any right under the CC-BY licence, Frontiers must be attributed as the original publisher of the article or eBook, as applicable.

Authors have the responsibility of ensuring that any graphics or other materials which are the property of others may be included in the CC-BY licence, but this should be checked before relying on the CC-BY licence to reproduce those materials. Any copyright notices relating to those materials must be complied with.

Copyright and source acknowledgement notices may not be removed and must be displayed in any copy, derivative work or partial copy which includes the elements in question.

All copyright, and all rights therein, are protected by national and international copyright laws. The above represents a summary only. For further information please read Frontiers' Conditions for Website Use and Copyright Statement, and the applicable CC-BY licence.

ISSN 1664-8714
ISBN 978-2-88974-417-6
DOI 10.3389/978-2-88974-417-6

About Frontiers

Frontiers is more than just an open-access publisher of scholarly articles: it is a pioneering approach to the world of academia, radically improving the way scholarly research is managed. The grand vision of Frontiers is a world where all people have an equal opportunity to seek, share and generate knowledge. Frontiers provides immediate and permanent online open access to all its publications, but this alone is not enough to realize our grand goals.

Frontiers Journal Series

The Frontiers Journal Series is a multi-tier and interdisciplinary set of open-access, online journals, promising a paradigm shift from the current review, selection and dissemination processes in academic publishing. All Frontiers journals are driven by researchers for researchers; therefore, they constitute a service to the scholarly community. At the same time, the Frontiers Journal Series operates on a revolutionary invention, the tiered publishing system, initially addressing specific communities of scholars, and gradually climbing up to broader public understanding, thus serving the interests of the lay society, too.

Dedication to Quality

Each Frontiers article is a landmark of the highest quality, thanks to genuinely collaborative interactions between authors and review editors, who include some of the world's best academicians. Research must be certified by peers before entering a stream of knowledge that may eventually reach the public - and shape society; therefore, Frontiers only applies the most rigorous and unbiased reviews.
Frontiers revolutionizes research publishing by freely delivering the most outstanding research, evaluated with no bias from both the academic and social point of view. By applying the most advanced information technologies, Frontiers is catapulting scholarly publishing into a new generation.

What are Frontiers Research Topics?

Frontiers Research Topics are very popular trademarks of the Frontiers Journals Series: they are collections of at least ten articles, all centered on a particular subject. With their unique mix of varied contributions from Original Research to Review Articles, Frontiers Research Topics unify the most influential researchers, the latest key findings and historical advances in a hot research area! Find out more on how to host your own Frontiers Research Topic or contribute to one as an author by contacting the Frontiers Editorial Office: frontiersin.org/about/contact

LIPIDS IN CYANOBACTERIA, ALGAE, AND PLANTS - FROM BIOLOGY TO BIOTECHNOLOGY

Topic Editors:
Eric Marechal, UMR5168 Laboratoire de Physiologie Cellulaire Vegetale (LPCV), France
Koichiro Awai, Shizuoka University, Japan
Juliette Jouhet, UMR5168 Laboratoire de Physiologie Cellulaire Vegetale (LPCV), France
Mie Shimojima, Tokyo Institute of Technology, Japan

Citation: Marechal, E., Awai, K., Jouhet, J., Shimojima, M., eds. (2022). Lipids in Cyanobacteria, Algae, and Plants - From Biology to Biotechnology. Lausanne: Frontiers Media SA. doi: 10.3389/978-2-88974-417-6

Table of Contents

05 ***Editorial: Lipids in Cyanobacteria, Algae, and Plants—From Biology to Biotechnology***
Juliette Jouhet, Mie Shimojima, Koichiro Awai and Eric Maréchal

07 ***Fumonisin B1: A Tool for Exploring the Multiple Functions of Sphingolipids in Plants***
Hong-Yun Zeng, Chun-Yu Li and Nan Yao

23 ***Lipidome Remodeling and Autophagic Respose in the Arachidonic-Acid-Rich Microalga* Lobosphaera incisa *Under Nitrogen and Phosphorous Deprivation***
Kamilya Kokabi, Olga Gorelova, Boris Zorin, Shoshana Didi-Cohen, Maxim Itkin, Sergey Malitsky, Alexei Solovchenko, Sammy Boussiba and Inna Khozin-Goldberg

44 ***Expression of a Bacterial Trehalose-6-phosphate Synthase otsA Increases Oil Accumulation in Plant Seeds and Vegetative Tissues***
Zhiyang Zhai, Jantana Keereetaweep, Hui Liu, Regina Feil, John E. Lunn and John Shanklin

52 ***Galactolipid and Phospholipid Profile and Proteome Alterations in Soybean Leaves at the Onset of Salt Stress***
Ailin Liu, Zhixia Xiao, Zhili Wang, Hon-Ming Lam and Mee-Len Chye

66 ***Temperature Acclimation of the Picoalga* Ostreococcus tauri Triggers *Early Fatty-Acid Variations and Involves a Plastidial ω3-Desaturase***
Charlotte Degraeve-Guilbault, Nattiwong Pankasem, Maurean Gueirrero, Cécile Lemoigne, Frédéric Domergue, Tomonori Kotajima, Iwane Suzuki, Jérôme Joubès and Florence Corellou

83 ***The Role of Sugar Signaling in Regulating Plant Fatty Acid Synthesis***
Zhiyang Zhai, Jantana Keereetaweep, Hui Liu, Changcheng Xu and John Shanklin

90 ***Dynamism of Metabolic Carbon Flow of Starch and Lipids in* Chlamydomonas debaryana**
Naoki Sato and Masakazu Toyoshima

108 ***Enhanced Lipid Production in* Chlamydomonas reinhardtii *Caused by Severe Iron Deficiency***
Elsinraju Devadasu and Rajagopal Subramanyam

120 **Arabidopsis thaliana *EARLY RESPONSIVE TO DEHYDRATION 7 Localizes to Lipid Droplets via Its Senescence Domain***
Nathan M. Doner, Damien Seay, Marina Mehling, Siqi Sun, Satinder K. Gidda, Kerstin Schmitt, Gerhard H. Braus, Till Ischebeck, Kent D. Chapman, John M. Dyer and Robert T. Mullen

139 **In silico *Analysis of Acyl-CoA-Binding Protein Expression in Soybean***
Nur Syifaq Azlan, Ze-Hua Guo, Wai-Shing Yung, Zhili Wang, Hon-Ming Lam, Shiu-Cheung Lung and Mee-Len Chye

157 ***CRISPR/Cas9-Induced* fad2 *and* rod1 *Mutations Stacked With* fae1 *Confer High Oleic Acid Seed Oil in Pennycress (*Thlaspi arvense *L.)***
Brice A. Jarvis, Trevor B. Romsdahl, Michaela G. McGinn, Tara J. Nazarenus, Edgar B. Cahoon, Kent D. Chapman and John C. Sedbrook

175 ***Lipid Droplets in Unicellular Photosynthetic Stramenopiles***
Nolwenn Guéguen, Damien Le Moigne, Alberto Amato, Juliette Salvaing and Eric Maréchal

197 ***Semi-Quantitative Targeted Gas Chromatography-Mass Spectrometry Profiling Supports a Late Side-Chain Reductase Cycloartenol-to-Cholesterol Biosynthesis Pathway in Brown Algae***
Jean Girard, Goulven Lanneau, Ludovic Delage, Cédric Leroux, Arnaud Belcour, Jeanne Got, Jonas Collén, Catherine Boyen, Anne Siegel, Simon M. Dittami, Catherine Leblanc and Gabriel V. Markov

207 ***Phytosterol Profiles, Genomes and Enzymes – An Overview***
Sylvain Darnet, Aurélien Blary, Quentin Chevalier and Hubert Schaller

225 ***Functional and Predictive Structural Characterization of WRINKLED2, A Unique Oil Biosynthesis Regulator in Avocado***
Jyoti R. Behera, Md. Mahbubur Rahman, Shina Bhatia, Jay Shockey and Aruna Kilaru

240 **Haematococcus pluvialis *Accumulated Lipid and Astaxanthin in a Moderate and Sustainable Way by the Self-Protection Mechanism of Salicylic Acid Under Sodium Acetate Stress***
Qunju Hu, Mingjian Song, Danqiong Huang, Zhangli Hu, Yan Wu and Chaogang Wang

frontiers in Plant Science

EDITORIAL
published: 11 January 2022
doi: 10.3389/fpls.2021.834384

Editorial: Lipids in Cyanobacteria, Algae, and Plants—From Biology to Biotechnology

Juliette Jouhet[1], *Mie Shimojima*[2], *Koichiro Awai*[3] *and Eric Maréchal*[1]*

[1] *Laboratoire de Physiologie Cellulaire et Végétale, CNRS, CEA, INRAE, Université Grenoble Alpes, IRIG, CEA Grenoble, Grenoble, France,* [2] *School of Life Science and Technology, Tokyo Institute of Technology, Tokyo, Japan,* [3] *Department of Biological Science, Faculty of Science, Shizuoka University, Shizuoka, Japan*

Keywords: alga lipid, plant lipid, fatty acid, glycerolipid, sphingolipid, sterol, triacylglycerol

Editorial on the Research Topic

Lipids in Cyanobacteria, Algae, and Plants—From Biology to Biotechnology

Lipids are small amphipathic molecules, harboring a hydrophobic moiety and more or less developed hydrophilic regions, with a broad diversity of chemical structures, ranging from fatty acids and acyl-lipids, like glycerolipids, sphingolipids, wax esters, etc, to isoprene-derived structures that include polycyclic forms like sterols. Lipids are therefore generated by a variety of distinct pathways within carbon metabolism but they converge to populate (and generate) specific cell structures, most notably cell membranes, lipid droplets and extracellular barriers. The composition of each of these compartments is not random, but finely controlled, regulated and tuned, reflecting important biological roles for each lipid class and the existence of mechanisms regulating the corresponding metabolic routes in a coherent manner. In addition to this contribution to cell architecture, and to a multitude of functions including cell signaling, lipids are energetically dense and store carbon and energy in the form of triacylglycerol, or oil. Photosynthetic cells contain the common lipids conserved from bacteria to eukaryotes including fungi and animals, as well as unique classes of lipids, which are absent or under-represented in non-photosynthetic systems. These lipids play specific roles in photosynthetic organism. Cyanobacteria, algae and plants have lifestyles marked by a strong exposure to environmental variations, which they need to acclimate and adapt to, strikingly at the level of their lipid composition. Eventually, photosynthetic organisms are established sources of lipids for humans, for food, health, green chemistry and energy sectors.

The multidisciplinary study of plant lipids in general sense, from basic to applied sciences, is achieved by a scientific community, who gather every 2 years at the International Symposium on Plant Lipids (ISPL). ISPL meetings were started in 1974 by an initiating Plant Acyl Lipid Symposium in Norwich, organized by Terry Galliard. In 1976, the Karlsruhe Symposium extended its scope to all other plant lipids, such as isoprenoid lipids (sterols, carotenoids and prenyl side chains of chlorophylls and prenylquinones) and lipid polymers. The 24th ISPL was organized in July 2020 as a web-based event in the context of the Covid-19 pandemic. The present Research Topic compiles key contributions in the scope of this meeting, addressing lipids in cyanobacteria, algae, and plants, from biology to biotechnology.

At the front of basic knowledge, whereas it is commonly considered that the components of some pathways have been elucidated in plants and algae, others remain puzzling. This is particularly the case in three areas. Firstly, sterols are marked by the existence of complex and sometimes diverging metabolic pathways in different photosynthetic lineages. Darnet et al. provide

OPEN ACCESS

Edited and reviewed by:
Samuel Cirés, Autonomous University of Madrid, Spain

***Correspondence:**
Eric Maréchal
eric.marechal@cea.fr

Specialty section:
This article was submitted to Marine and Freshwater Plants, a section of the journal Frontiers in Plant Science

Received: *13 December 2021*
Accepted: *20 December 2021*
Published: *11 January 2022*

Citation:
Jouhet J, Shimojima M, Awai K and Maréchal E (2022) Editorial: Lipids in Cyanobacteria, Algae, and Plants—From Biology to Biotechnology. Front. Plant Sci. 12:834384. doi: 10.3389/fpls.2021.834384

a comprehensive review on phytosterol in the evolution of photosynthetic eukaryotes, and Girard et al. address more particularly a possible cycloartenol-to-cholesterol route in brown algae. Secondly, our view of the biosynthesis and role of sphingolipids is incomplete. In this regard, the development of fumonisin B1 to disrupt sphingolipid biosynthesis can be considered as an interesting tool for functional studies in plants, as overviewed by Zeng et al. Thirdly, the determination of the composition of the cytosolic compartment loaded with triacylglycerol, i.e., the lipid droplet (LD), and the deciphering of its biogenesis, need also important efforts. Indeed the lack of conservation of LD associated proteins in the course of evolution limits knowledge transfers from non-plant models. Filling knowledge gap on LD is also critical for biotechnological and agronomical purposes detailed below. Doner et al. describe how EARLY RESPONSIVE TO DEHYDRATION 7 localizes to LD in *Arabidopsis* and Guéguen et al. review our current knowledge on LD architecture and dynamics in Stramenopiles, a group of complex algae.

In both plant and algal models, lipid remodeling proves to be one of the very first responses to abiotic stresses. Lipid metabolism and cell compartmentation are therefore critical for the acclimation and adaptation of photosynthetic organism to environmental changes. Liu et al. show how galacto- and phosphoglycerolipids respond to salt stress in the crop *Glycine max*. Degraeve-Guilbault et al. decipher the processes involved in the control of acyl desaturation level in the green alga *Ostreococcus tauri* in response to temperature variations. Kokabi et al. detail acyl-lipid remodeling in *Lobosphaera incisa* in response to nitrogen and phosphorus availability, whereas Devadasu and Subramanyam highlight an enhanced accumulation of triacylglycerol in *Chlamydomonas reinhardtii* upon iron deficiency. This later work illustrates how a natural response of an alga to a nutrient stress may be translated in an industrial process to enhance algal oil production. Likewise, triacylglycerol and astaxanthin accumulation in *Haematococcus pluvialis* upon acetate stress, detailed by Hu et al. could be useful for biotechnological applications.

Based on robust knowledge on fatty acid and acyl-lipid metabolism, it is possible to develop strategies to improve the quality and quantity of triacylglycerol (oil) in oleaginous algae and crops. Concerning acyl-lipid metabolism in the general scheme of carbon partitioning, Zhai, Keereetaweep, Liu, Xu, et al. analyze the impact of sugar signaling on fatty acid biosynthesis in plants, whereas Sato and Toyoshima provide a remarkable analysis of carbon flow in starch and lipids in *Chlamydomonas debaryana* based on isotopic labeling experiments. Azlan et al. analyze the expression of acyl-CoA binding proteins in soybean to provide useful information for future biotechnological improvements. Behera et al. evaluate the role of WRINKLED2 in triacylglycerol production in avocado, providing new targets to enhance oil biosynthesis. Based on the stabilization of WRINKLED1 by trehalose-6-phosphate, Zhai, Keereetaweep, Liu, Feil, et al. show that the heterologous expression of bacterial trehalose-6-phosphate synthase increases oil accumulation in seeds and vegetative tissues. Eventually, Jarvis et al. explore Crispr/CAS9-based edition of specific genes to increase oleic acid content in pennycress seed oil.

Altogether, the contributions to this Research Topic illustrate the dynamic international efforts to fill gaps in knowledge on lipid biology in algae and plants, as well as attempts to translate this knowledge into biotechnological applications. The role of lipids in the early response of photosynthetic organisms to abiotic stresses also highlight how lipids are critical in the context of climate change. There is no doubt this question will become central in the near future.

AUTHOR CONTRIBUTIONS

All authors have contributed to the writing of the editorial.

FUNDING

JJ and EM are supported by the National Research Agency (BLinK ANR-18-CE92-0015, Alpalga ANR-20-CE02-0020, GlycoAlps ANR-15-IDEX-02, GRAL Labex ANR-10-LABEX-04, and EUR CBS ANR-17-EURE-0003) and Institut Carnot 3BCAR. EM was supported by the Kilian Jornet Foundation. MS and KA are supported by the Japan Society for the Promotion of Science (JSPS) KAKENHI (JP18H03941). MS was supported by JSPS KAKENHI (21K05325). KA was supported by JSPS KAKENHI (20K06683).

Conflict of Interest: The authors declare that the research was conducted in the absence of any commercial or financial relationships that could be construed as a potential conflict of interest.

Publisher's Note: All claims expressed in this article are solely those of the authors and do not necessarily represent those of their affiliated organizations, or those of the publisher, the editors and the reviewers. Any product that may be evaluated in this article, or claim that may be made by its manufacturer, is not guaranteed or endorsed by the publisher.

Copyright © 2022 Jouhet, Shimojima, Awai and Maréchal. This is an open-access article distributed under the terms of the Creative Commons Attribution License (CC BY). The use, distribution or reproduction in other forums is permitted, provided the original author(s) and the copyright owner(s) are credited and that the original publication in this journal is cited, in accordance with accepted academic practice. No use, distribution or reproduction is permitted which does not comply with these terms.

frontiers in Plant Science

REVIEW
published: 27 October 2020
doi: 10.3389/fpls.2020.600458

Fumonisin B1: A Tool for Exploring the Multiple Functions of Sphingolipids in Plants

*Hong-Yun Zeng[1], Chun-Yu Li[2] and Nan Yao[1]**

[1] State Key Laboratory of Biocontrol and Guangdong Provincial Key Laboratory of Plant Resource, School of Life Sciences, Sun Yat-sen University, Guangzhou, China, [2] Institution of Fruit Tree Research, Guangdong Academy of Agricultural Sciences, Guangzhou, China

Fumonisin toxins are produced by *Fusarium* fungal pathogens. Fumonisins are structural analogs of sphingosine and potent inhibitors of ceramide synthases (CerSs); they disrupt sphingolipid metabolism and cause disease in plants and animals. Over the past three decades, researchers have used fumonisin B1 (FB1), the most common fumonisin, as a probe to investigate sphingolipid metabolism in yeast and animals. Although the physiological effects of FB1 in plants have yet to be investigated in detail, forward and reverse genetic approaches have revealed many genes involved in these processes. In this review, we discuss the intricate network of signaling pathways affected by FB1, including changes in sphingolipid metabolism and the effects of these changes, with a focus on our current understanding of the multiple effects of FB1 on plant cell death and plant growth. We analyze the major findings that highlight the connections between sphingolipid metabolism and FB1-induced signaling, and we point out where additional research is needed to fill the gaps in our understanding of FB1-induced signaling pathways in plants.

Keywords: fumonisin B1, sphingolipid, long chain bases, ceramides, cell death, plant growth

OPEN ACCESS

Edited by:
Eric Marechal, UMR5168 Laboratoire de Physiologie Cellulaire Vegetale (LPCV), France

Reviewed by:
Ivo Feussner, University of Göttingen, Germany
Chiara Dall'Asta, University of Parma, Italy

****Correspondence:***
Nan Yao
yaonan@mail.sysu.edu.cn

Specialty section:
This article was submitted to Plant Physiology, a section of the journal Frontiers in Plant Science

Received: *30 August 2020*
Accepted: *05 October 2020*
Published: *27 October 2020*

Citation:
Zeng H-Y, Li C-Y and Yao N (2020) Fumonisin B1: A Tool for Exploring the Multiple Functions of Sphingolipids in Plants. Front. Plant Sci. 11:600458. doi: 10.3389/fpls.2020.600458

INTRODUCTION

Fumonisins are produced by several species of *Fusarium* molds such as *Fusarium verticillioides* and *Fusarium moniliforme*, which infect many cereal crops such as maize (*Zea mays*), wheat (*Triticum aestivum*), and barley (*Hordeum vulgare*) (Rheeder et al., 2002). Fumonisins are required for the development of foliar disease symptoms in infected maize seedlings (Glenn et al., 2008). In the field, fumonisins are synthesized *in planta* by fungi and can be taken up by roots and disseminated inside seedlings, possibly affecting the fungus–host interaction prior to the first contact between the pathogen and seedling (Arias et al., 2016). Contaminated corn and corn-based products are frequently ingested in food or feed, causing diseases such as equine leukoencephalomalacia, porcine pulmonary edema, and possibly kidney and liver cancer (as revealed in rats in the laboratory) (Riley and Merrill, 2019).

In 1988, fumonisin B1 (FB1) and FB2 were isolated from *F. verticillioides* (*F. moniliforme*) MRC 826 cultures as novel mycotoxins with cancer-promoting activity in rat livers (Gelderblom et al., 1988). FB1 and FB2 are diesters of propane-1,2,3-tricarboxylic acid with similar long-chain aminopolyol backbones. These compounds are structurally similar to the sphingoid bases sphinganine and sphingosine, with tricarboxylic acid groups added at the C14 and C15 positions

(**Supplementary Figure S1**). However, the chain lengths of their backbones differ, with sphingosine mostly containing 18 carbons and FB1 containing 20 carbons (**Supplementary Figure S1**). Three years after the chemical structures of fumonisins were elucidated, these carcinogenic mycotoxins were found to disrupt the pathway for *de novo* sphingolipid biosynthesis (Wang et al., 1991). Accumulating evidence has confirmed that the wide spectrum of animal and plant diseases caused by fumonisins are due to changes in the levels of multiple bioactive lipids and related biological processes. Although the mode of action of these toxins has been studied in detail at the cellular level in animals, their role in plant diseases has not been thoroughly elucidated.

To explore how FB1 affects plants, it is important to understand the plant sphingolipid metabolism pathway (**Figure 1**). There are five major classes of plant sphingolipids: long-chain bases (LCBs), ceramides (Cers), hydroxyceramides (hCers), glucosylceramides (GluCers), and more complex glycosylated sphingolipids known as glycosyl inositol phosphoryl ceramides (GIPCs). The first four groups are produced in the endoplasmic reticulum (ER), whereas GIPC biosynthesis is initiated in the ER and completed in the Golgi apparatus (**Figure 1**). The serine palmitoyl-CoA transferase (SPT) protein complex catalyzes *de novo* biosynthesis of LCBs resulting from the condensation of serine and palmitoyl-CoA moieties (Kimberlin et al., 2013). The SPT product is subsequently reduced to form sphinganine, the precursor of the eight other LCBs found in plants.

Ceramide synthases (CerSs) are encoded by a multigenic family named after the yeast protein Lag One Homolog (LOH) and are responsible for the formation of the amide bond that links long-chain ($<$C20) fatty acids (LCFs) or very-long-chain ($\geq$C20) fatty acids (VLCFAs) to LCB, leading to Cer formation (Markham et al., 2011). Cers can then be phosphorylated to form ceramide 1-phosphate (ceramide-1P) (Liang et al., 2003), or α-hydroxylated at the fatty acid moiety to form hCers (Konig et al., 2012). Cers can also be used as backbones for the production of GluCer and GIPC by the addition of a glucose molecule or an inositolphosphoryl group, followed by one glycosylation step for GluCer or several glycosylations for GIPC (Markham et al., 2013).

Sphingolipid compounds have a multitude of functions. In addition to functioning as structural components of the plasma membrane and other endomembrane systems, sphingolipids serve as bioactive molecules and second messengers for an array of cellular signaling activities in plant cells, such development, biotic and abiotic stress responses, and programmed cell death (PCD). However, compared with animals, much less is known about sphingolipid metabolism and signaling in plants. For instance, the receptors, targets, and mediators involved in these processes are almost totally unclear (Ali et al., 2018), limiting our understanding of the FB1 signal transduction pathway in plants.

Schematic representation of the sphingolipid biosynthetic pathway in plants. 3-KSR, 3-ketosphinganine reductase; ACD11, accelerated cell death 11, Cer-1P transporter; ACD5, accelerated cell death 5, ceramide kinase; ACER, alkaline ceramidase; CoA, coenzyme A; d18:1$^{\Delta 4}$, sphingosine; d18:0, sphinganine; DPL1, dihydrosphingosine phosphate lyase; FAH1/2, fatty acid hydroxylase; GCS, glucosylceramide synthase; GINT1, glucosamine inositolphosphorylceramide transferase 1; GMT1, GIPC mannosyl-transferase 1; GONST1, Golgi localized nucleotide sugar transporter 1; IPC, inositol phosphorylceramide; IPUT1, inositol phosphorylceramide glucuronosyltransferase 1; LCB, long-chain-base; LCB1/2, subunit of serine palmitoyltransferase 1/2; LCBK1/2, long-chain base kinase 1/2; LCB-P, long-chain-base phosphate; LOH1/2/3, LAG1 Homolog 1/2/3, ceramide synthase; NCER, neutral ceramidase; ORM1/2, orosomucoid-like protein 1/2; SBH1/2, sphingoid base hydroxylase 1/2; DPL1, dihydrosphingosine phosphate lyase; SL, sphingolipid; SPHK1/2, sphingosine kinase 1/2; SPP1, sphingoid phosphate phosphatase; SPT, serine palmitoyl transferase; ssSPT, small subunit of serine palmitoyl transferase; t18:0, phytosphingosine; TOD1, turgor regulation defect 1.

FB1 DISRUPTS SPHINGOLIPID HOMEOSTASIS IN PLANTS

Inhibition of Ceramide Synthase Activity

In mammals, FB1 inhibits the activity of the six known CerSs, which differ in terms of tissue distribution and fatty acyl-CoA specificity (Cingolani et al., 2016). Tomato (*Solanum lycopersicum*) Alternaria stem canker resistance-1 (Asc-1) was the first CerS identified in plants (Brandwagt et al., 2000; Spassieva et al., 2002). A tBLASTn search of the complete *Arabidopsis thaliana* genome using the sequence of the CerS gene longevity assurance gene 1 (*LAG1*) from yeast and *Asc-1* as queries identified three Asc-1/LAG1 Homologs, *LOH1–3* (Markham et al., 2011). Phylogenetic analysis revealed that LOH1 and LOH3 are closely related and belong to a cluster with most other plant LAG1 homologs, but LOH2 appears to be evolutionarily distinct from LOH1 and LOH3 (Markham et al., 2011; Ternes et al., 2011).

The varied chemical compositions of Cers in Arabidopsis are determined by the specificity of three different isoforms of CerS for a range of LCBs and acyl-CoA substrates. LOH1 and LOH3 prefer very-long chain acyl-CoA and trihydroxy LCB as substrates, but LOH2 prefers palmitoyl-CoA and dihydroxy LCB as substrates (Markham et al., 2011; Ternes et al., 2011; Luttgeharm et al., 2015, 2016). The differences between the two groups of CerSs are reflected by the phylogenetic separation of the *LOHs*, which preceded the separation of mosses and vascular plants (Ternes et al., 2011). Consistent with their redundant biochemical functions, LOH1 and LOH3 share high sequence similarity and a more recent evolutionary origin (Ternes et al., 2011). Nevertheless, when the physiological functions of these CerSs were examined by mutant analysis, only *loh1* plants showed spontaneous cell death, perhaps due to the higher expression level of *LOH1* and the stronger contribution of LOH1 to Cer biosynthesis compared with LOH3 (Ternes et al., 2011). *In vitro* ceramide synthase assays showed that LOH1 was the most sensitive to inhibition by FB1 (Luttgeharm et al., 2016). Furthermore, overexpressing *LOH1* had no effect on FB1 resistance in Arabidopsis, whereas overexpressing *LOH2* or *LOH3* resulted in increased plant resistance to FB1 treatment, confirming the notion that LOH1 confers FB1 sensitivity to

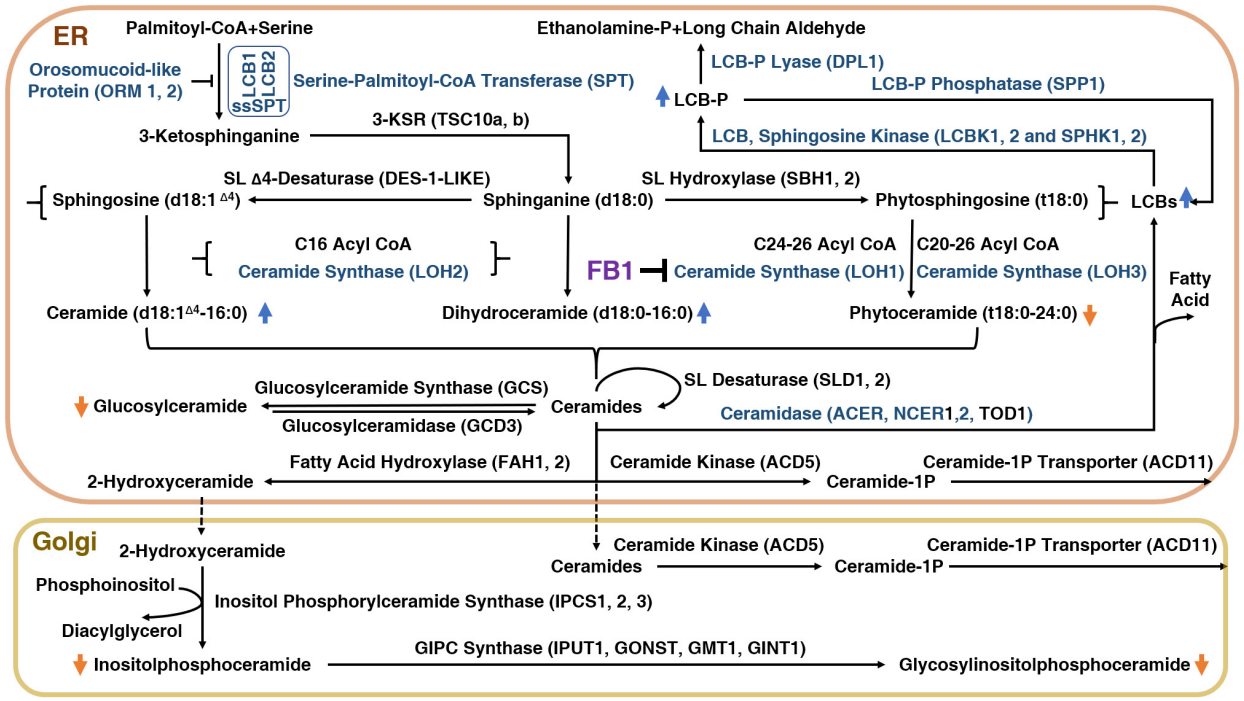

FIGURE 1 | The sphingolipid biosynthetic pathway in plants and the inhibition of this pathway by FB1.

plants (Luttgeharm et al., 2015). In line with these observations, *LOH2*- and *LOH3*-overexpressing plants had reduced levels of free LCBs and LCB-Ps in response to FB1 treatment (Luttgeharm et al., 2015).

It remains unknown why FB1 preferentially inhibits LOH1 rather than LOH3, which share similar properties, but have slightly different substrate binding pockets. Supporting the hypothesis that the difference in substrate binding pockets affects their inhibition by FB1, LOH1 prefers FB1-like saturated trihydroxy LCBs, but LOH3 prefers unsaturated trihydroxy LCB (Luttgeharm et al., 2016). It is unclear if LOH1 and LOH3 in other plant species show parallel differences in substrate preference. Notably, in tomato, the presence of Asc-1 relieves blocked sphingolipid synthesis caused by AAL toxin (a tomato-specific toxin produced by the fungus *Alternaria alternata* f.sp. *lycopersici*) (**Supplementary Figure S1**), which would otherwise lead to PCD (Spassieva et al., 2002), pointing to the presence of at least one more ceramide synthesis enzyme besides Asc-1. Notably, maize (*Z. mays*) likely contains at least two ceramide synthase isoforms with different substrate specificities, which may result in susceptibility/resistance to *F. verticillioides* (Arias et al., 2016).

FB1 Treatment Increases LCB and C16 Sphingolipid Levels and Reduces VLC Sphingolipid Levels

When applied to plants, FB1 triggers the accumulation of LCBs and LCB-Ps (Shi et al., 2007; Tsegaye et al., 2007; Saucedo-García et al., 2011b; Yanagawa et al., 2017; **Figure 1**). Indeed, 1 h of FB1 treatment altered the levels of LCBs in Arabidopsis (Shi et al., 2007). Interestingly, like treatment with FB1, infection with *Pseudomonas syringae* pv. *tomato* DC3000 also provoked a rapid increase in t18:0 (phytosphinganine) levels, implying that LCBs function in pathogen resistance (Peer et al., 2010).

Fumonisin B1 suppresses the activity of all six known mammalian CerSs and therefore, LC and VLC sphingolipid levels decreased in response to FB1 treatment. Moreover, FB1 treatment resulted in the specific inhibition of C16:0 Cer biosynthesis and cured *adipose triglyceride lipase* macrophages from mitochondrial dysfunction and PCD (Aflaki et al., 2012), suggesting that FB1 counters C16 ceramide-mediated cell death. However, the situation is quite different in plants, since FB1 significantly increases C16 ceramide levels in plants. FB1 treatment or depletion of LOH1 and LOH3 resulted in a reduction in VLCF Cer levels (Markham et al., 2011). The levels of Cers and hCer with very long fatty acid chains decreased slightly after 24 h of FB1 treatment (Markham et al., 2011). Significant increases in the levels of 16:0-containing Cer and GluCer were observed in Arabidopsis *loh1* null mutants (Ternes et al., 2011). Furthermore, a stronger depletion of VLC sphingolipids and enhanced accumulation of 16:0 sphingolipids were detected in FB1-treated *loh1-1 loh3-1* double mutants (Markham et al., 2011).

LCBs Primarily Contribute to the Cytotoxicity of FB1 in Plants

Long-chain bases serve as building blocks of sphingolipids and act as second messengers. These compounds are primarily

responsible for FB1-induced cell death (**Figure 2**). The regulation of LCB homeostasis is as essential in plants as it is in animal models. Although the exact molecular mechanism underlying how LCBs control cell fate in plants is far from clear, it is assumed that LCB accumulation would kill plant cells, as it does in animals. The observation that FB1 treatment leads to LCB accumulation and cell death could be tentatively explained by the disequilibrium of the tightly regulated intracellular balance between free LCBs and Cers.

Early insight into the relationship between FB1 and the sphingolipid pathway in plants came from genetic studies focused on identifying Arabidopsis FB1-resistant mutants. *FB1-resistant 11* was characterized as a deletion mutant in the gene encoding a long-chain base1 (LCB1) subunit of SPT. SPT mediates FB1-initiated PCD by catalyzing the first rate-limiting step of *de novo* sphingolipid biosynthesis (Shi et al., 2007; Saucedo-García et al., 2011b; Kimberlin et al., 2013, 2016; Li et al., 2016; Shao et al., 2019; **Table 1**). For example, increasing SPT activity by overexpressing small subunit of SPT (*ssSPTa*) resulted in the accumulation of LCBs and reduced tolerance to FB1, whereas *ssSPTa* suppression lines displayed lower levels of LCBs but enhanced tolerance to FB1 (Kimberlin et al., 2013). Notably, among all SPTs, only fumonisin b1 resistant 41 (FBR41) represses FB1-elicited cell death when overexpressed, consistent with its negative effect on SPT activity.

Orosomucoid proteins (ORMs) negatively regulate SPT activity to maintain sphingolipid levels in humans and yeast, and are required for sphingolipid homeostasis in plants, as well as FB1 resistance (Kimberlin et al., 2016; Li et al., 2016). The tolerance of Arabidopsis *ORM* overexpression plants to FB1 was accompanied by reduced levels of C16 Cers, LCBs, and their phosphorylated counterparts (Kimberlin et al., 2016). By contrast, *AtORM* RNA interference lines were more sensitive to FB1 treatment and contained more C16 Cers, LCBs, and LCB-Ps than the wild type (Kimberlin et al., 2016).

In addition to SPT, many enzymes related to LCB metabolism control plant responses to FB1. Overexpressing *AtLCBK1* (*A. thaliana* sphingoid LCB kinase) increased plant resistance to FB1 treatment, whereas *AtLCBK1* knockdown plants showed increased sensitivity to FB1 treatment (Yanagawa et al., 2017). Moreover, analysis of transgenic plants with altered levels of proteins including long-chain base kinase 1 (LCBK1), sphingoid phosphate phosphatase (SPP1), and dihydrosphingosine phosphate lyase (DPL1), which are involved in maintaining LCB/LCB-P homeostasis, revealed a positive correlation between the levels of free LCBs and the degree of FB1-induced cell death (Yanagawa et al., 2017). FB1-induced PCD is primarily due to the accumulation of free LCBs. Directly feeding plants with the free sphingoid bases dihydrosphingosine, phytosphingosine, and sphingosine efficiently induced cell death (Shi et al., 2007). Overexpressing *LCBK1* in Arabidopsis led to hyposensitivity to FB1, whereas knockdown of *LCBK1* conferred hypersensitivity to FB1 (Yanagawa et al., 2017).

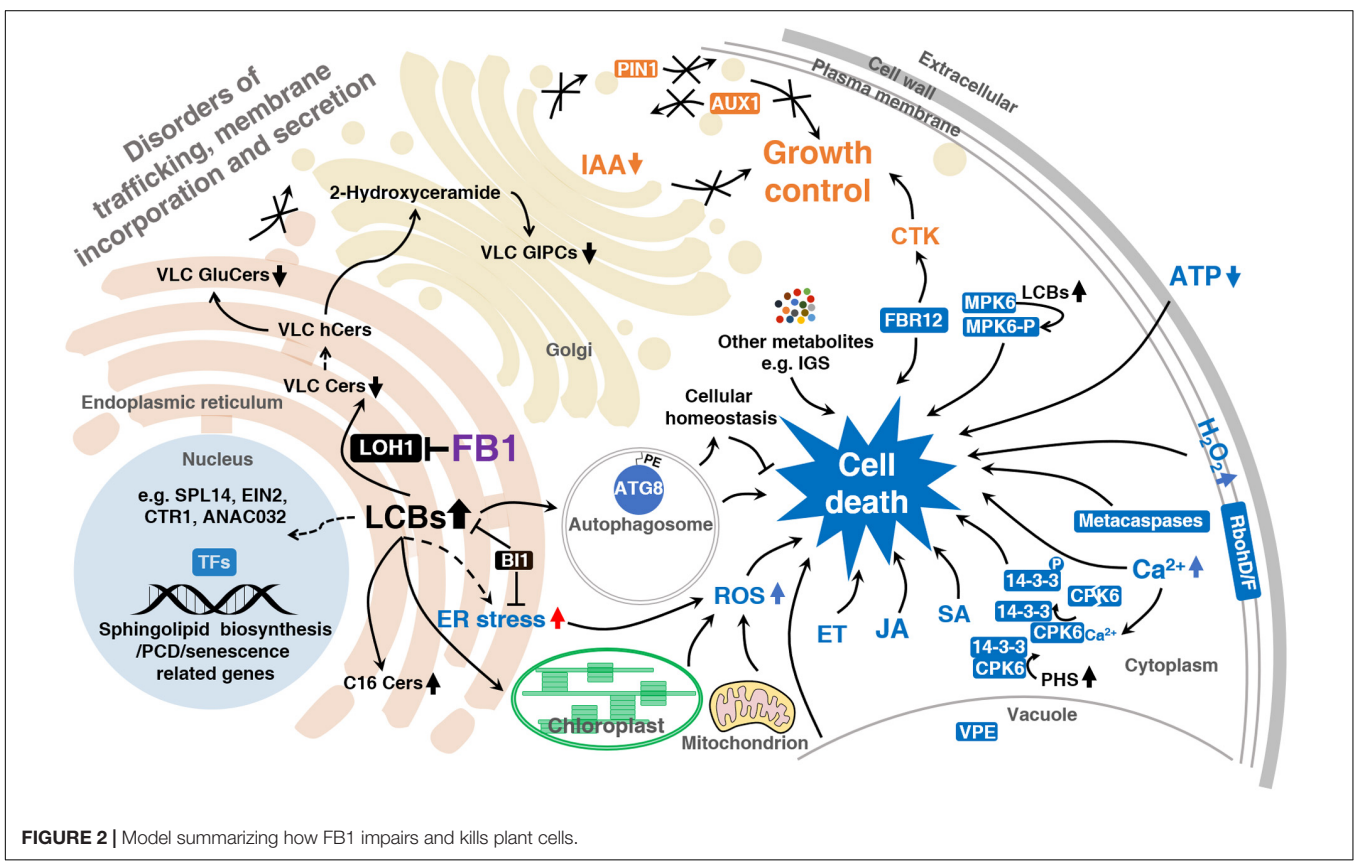

FIGURE 2 | Model summarizing how FB1 impairs and kills plant cells.

TABLE 1 | Sphingolipid metabolism genes involved in plant responses to FB1.

Gene name	Function	Species	Mutant/transgenic plants	FB1 response	System	References
LCB1/FBR11	Subunit of serine palmitoyltransferase	At	*fbr11-1*	Tolerant	Leaves, seedlings	Shi et al., 2007
LCB2a	Subunit of serine palmitoyltransferase	At	*lcb2a-1, -2, -3*	Tolerant	Seedlings	Saucedo-García et al., 2011a,b
LCB2b/	Subunit of serine	At	dominant mutant fbr41	Tolerant	Leaves, seedlings	Shao et al., 2019
FBR41	palmitoyltransferase	At	*FBR41 OE*	Tolerant	Leaves	Shao et al., 2019
ssSPTa	Small subunit of serine	At	ssSPTa RNAi	Tolerant	Seedlings	Kimberlin et al., 2013
	palmitoyltransferase	At	ssSPTa-OE	Sensitive	Seedlings	Kimberlin et al., 2013
ORM1	Orosomucoid-like protein	At	ORM1-OE	Tolerant	Seedlings	Kimberlin et al., 2016; Li et al., 2016
ORM2	Orosomucoid-like protein	At	ORM2-OE	Tolerant	Seedlings	Kimberlin et al., 2016; Li et al., 2016
ORM1/	Orosomucoid-like protein	At	*orm1 amiR-ORM2*	Sensitive	Seedlings	Li et al., 2016
ORM2			ORM RNAi			
LCBK1	Long-chain base kinase	At	LCBK1-KD	Sensitive	Leaves, seedlings	Yanagawa et al., 2017
		At	LCBK1-OE	Tolerant	Leaves, seedlings	Yanagawa et al., 2017
SPHK1	Sphingosine kinase 1	At	*SPHK1-KD, sphk1-1*	Tolerant	Leaves	Qin et al., 2017
		At	*SPHK1-KD*	Sensitive	Leaves	Glenz et al., 2019
		At	SPHK1 OE	Sensitive	Leaves	Qin et al., 2017; Glenz et al., 2019
SPHK2	Sphingosine kinase 2	At	*sphk2-1*	Tolerant	Leaves	Qin et al., 2017
		At	SPHK2 OE	Sensitive	Leaves	Qin et al., 2017
SPP1	Sphingoid phosphate	At	*Spp1*	Tolerant	Leaves	Yanagawa et al., 2017
	phosphatase	At	*SPPASE RNAi (SPHK1-OE)*	Sensitive	Leaves	Qin et al., 2017
		At	*SPP1*-OE	Sensitive	Leaves	Glenz et al., 2019
DPL1	Dihydrosphingosine-1-phosphate lyase	At	*dpl 1-1, -2, DPL1 RNAi (SPHK1-OE)*	Sensitive	Leaves	Tsegaye et al., 2007; Nakagawa et al., 2012; Qin et al., 2017; Yanagawa et al., 2017; Glenz et al., 2019
LOH2	Ceramide synthase	At	*loh2-1, -2*	Sensitive	Leaves	Mase et al., 2013
		At	LOH2-OE	Tolerant	Seedlings	Luttgeharm et al., 2015
LOH3	Ceramide synthase	At	LOH3-OE	Tolerant	Seedlings	Luttgeharm et al., 2015
ACER	Alkaline ceramidase	At	amiR-*ACER*-1, *acer-1*	Sensitive	Seedlings, Protoplasts	Wu et al., 2015a
		At	ACER-OX-1	Tolerant	Seedlings, Protoplasts	Wu et al., 2015a
NCER	Neutral ceramidase	At	*ncer2*	Sensitive	Seedlings	Zienkiewicz et al., 2019
BI1	Protein that interacts with sphingolipid-modifying enzymes	At	*atbi1-l, atbi1-2*	Sensitive	Leaves	Watanabe and Lam, 2006
PAS1	*PASTICCINO1*, required for VLCF synthesis	At	*Pas1*	Sensitive	Roots	Markham et al., 2011

KD, knockdown; OE or OX, overexpressing line. At, Arabidopsis thaliana.

Fumonisin B1-elicited cell death is mainly ascribed to the accumulation of dihydroxy-LCBs, but not trihydroxy-LCBs (Saucedo-García et al., 2011b). For instance, the *sbh1-1* mutant, which is deficient in one of the two LCB hydroxylase genes (*SBH1*), contains lower levels of trihydroxy-LCBs and higher levels of total LCBs than wild-type plants (Chen et al., 2008). However, these plants appeared similar to wild-type plants when exposed to FB1 (Saucedo-García et al., 2011b).

Phosphorylated LCB derivatives appear to block cell death induced by the corresponding LCB in a dose-dependent manner, implying that the maintenance of homeostasis between a free sphingoid base and its phosphorylated derivative determines cell fate (Shi et al., 2007). The application of S1P or inhibitors of sphingosine kinase reduced apoptotic-like PCD and promoted cell survival in Arabidopsis cell suspension cultures (Alden et al., 2011). However, the antagonistic effects of phosphorylated LCBs after simultaneous treatment with non-phosphorylated LCBs were due to the reduced uptake of non-phosphorylated LCBs into the tissue (Glenz et al., 2019). Increasing the *in vivo* levels of phosphorylated LCBs did not reduce FB1-induced cell death (Glenz et al., 2019). Analysis of FB1-treated Arabidopsis lines with perturbed levels of phosphorylated LCBs highlighted a positive correlation between non-phosphorylated LCB levels and FB1-elicited cell death, rather than a negative correlation between phosphorylated LCB levels and this process (Glenz et al., 2019).

FB1 as a Tool to Investigate Sphingolipid Metabolism

Deciphering the role of a putative LCB/Cer metabolic enzyme in FB1 resistance is an excellent first step in confirming its function (**Table 1**). Ceramidases such as ACER maintain the homeostasis between LCB and Cer. *ACER1*-silenced plants and *acer1* mutant plants were sensitive to FB1, and *ACER1*-overexpressing plants were relatively resistant to FB1 (Wu et al., 2015a). Disrupting neutral ceramidase 2 (NCER2), which likely functions as a ceramide synthase, increased sensitivity to FB1 in Arabidopsis (Zienkiewicz et al., 2019). Bax Inhibitor-1 (BI-1), an evolutionarily conserved cell death suppressor in mammals and plants (Kawai-Yamada et al., 2001; Mosblech et al., 2009; Christensen and Kolomiets, 2011), attenuates cell death progression triggered by FB1 in plants (Watanabe and Lam, 2006). Knockout mutants of *AtBI1* (*atbi1-1* and *atbi1-2*) exhibited increased sensitivity to FB1, whereas these phenotypes were rescued by the overexpression of *AtBI1* (Watanabe and Lam, 2006). Similar to its function in mammals (Chae et al., 2004; Bailly-Maitre et al., 2006), BI-1 helps protect plant cells from ER stress-induced apoptosis (Gao et al., 2007, 2009). The ER membrane-localized protein BI-1 modifies sphingolipids by interacting with FATTY ACID HYDROXYLASE 1 (FAH1) and FAH2 via the electron donor cytochrome b5 (Cb5) in plant cells. BI-1 contributes to sphingolipid biosynthesis during cold stress in Arabidopsis by interacting with ceramide-modifying enzymes (Nagano et al., 2014). Moreover, BI-1 regulates VLCF synthesis by forming a complex with VLCF-synthesizing enzymes (Nagano et al., 2019).

FB1 INDUCES CELL DEATH IN PLANTS

Fumonisin B1 induces cell death in a process involving multiple signaling pathways (**Table 2** and **Figure 2**).

Hormone Signaling

The link between ethylene and plant responses to FB1 is well known. Initially, it was reported that ethylene-dependent signaling pathways are required for FB1-induced cell death in Arabidopsis protoplasts (Asai et al., 2000). Arabidopsis ethylene receptors play distinct roles in FB1-induced cell death (Plett et al., 2009). Intriguingly, different reports describe different phenotypes of *ethylene response 1-1* (*etr1-1*) mutants, possibly due to different growth conditions such as photoperiod (Asai et al., 2000; Plett et al., 2009; Mase et al., 2013; Wu et al., 2015b). By investigating the responses of various ethylene mutants to FB1 and the corresponding sphingolipid profiles of the plants, as well as the effects of 1-aminocyclopropane-1-carboxylic acid on FB1-induced cell death and sphingolipid metabolism, our group demonstrated that ethylene signaling inhibits sphingolipid synthesis, thereby playing a negative role in FB1-induced cell death (Wu et al., 2015b). Despite the finding that ethylene signaling modulates sphingolipid metabolism, the possibility that ethylene signaling acts downstream of sphingolipids (such LCBs and Cers) cannot be excluded. Notably, C24:1-Cer interacts with constitutive triple response 1 (CTR1) and inhibits its kinase activity, thereby modulating CTR1-mediated ethylene signaling (Xie et al., 2015), supporting this hypothesis.

The role of the plant hormone jasmonate (JA) in plant resistance to fungi is well known (Pieterse et al., 2009). The role of JA in mediating FB1-induced PCD was first described by Asai et al. (2000). The authors found that Arabidopsis protoplasts isolated from jasmonate resistant 1-1 (*jar1-1*) plants, which are insensitive to JA, exhibited much lower susceptibility to cell death induced by FB1 than FB1-treated wild-type protoplasts (Asai et al., 2000). Similarly, the deletion of oxophytodienoate reductase 3 (*OPR3*), which is involved in JA biosynthesis, enhanced the resistance of protoplasts to FB1 upon a dark/light shift (Danon et al., 2004). However, these findings may need to be further explored, since OPR3 is only partially required for JA biosynthesis and data obtained with the *opr3* mutants are often unclear (Chini et al., 2018). FB1 hijacks the JA pathway to initiate PCD. FB1 induces JA-responsive defense genes but represses growth-related and JA biosynthesis-related genes, thereby reducing JA contents in plants (Zhang et al., 2015). Furthermore, the ubiquitin ligases ring domain ligase 3 (RGLG3) and RGLG4 coordinately and positively regulate FB1-triggered PCD by modulating the JA signaling pathway in a coronatine insensitive 1 (COI1)- and MYC2-dependent manner in Arabidopsis (Zhang et al., 2015).

In addition to ethylene and JA, plant susceptibility to FB1 appears to be associated with salicylic acid (SA) signaling, whereas FB1-induced PCD does not require the SA signal transmitter non-expresser of PR genes 1 (Asai et al., 2000). Indeed, SA promotes FB1-induced cell death (Smith et al., 2015). Moreover, FB1-induced SA likely suppresses the JA pathway to facilitate cell death, since exogenously applied SA inhibited JA signaling additively with FB1 treatment (Zhang et al., 2015).

Taken together, these findings indicate that FB1-elicited cell death requires ethylene, JA, and SA. Nevertheless, the molecular mechanisms underlying the roles of these hormone-signaling pathways in FB1-induced cell death remain to be investigated.

MPK6, Ca^{2+}, Reactive Oxygen Species, and ATP Signaling

Mitogen-activated protein kinases (MAPKs) were activated in FB1-treated monkey kidney samples, but the functional role of MAPKs in FB1-induced toxicity has not been addressed in this system (Yin et al., 2016). In Arabidopsis, MAP kinase 6 (MPK6) was described as a novel transducer in the pathway leading to LCB-induced PCD (Saucedo-García et al., 2011b). In addition to mediating PCD downstream of LCBs, MPK6 can be activated by phytosphingosine−1−phosphate (PHS−P), a response rapidly and transiently evoked by chilling (Dutilleul et al., 2012). Nevertheless, how MPK6 triggers FB1-induced cell death downstream of PCD signaling remains unknown.

Calcium signaling is also required for FB1-induced cell death. Upon exposure to FB1, intracellular Ca^{2+} levels increase via FB1-induced phytosphingosine (PHS) (Lachaud et al., 2013). Meanwhile, PHS activates calcium-dependent kinase 3 (CPK3), which phosphorylates its associated partners, the 14-3-3 proteins, thus leading to the disruption of the 14-3-3-CPK3 complex

TABLE 2 | Genes in various signaling pathways involved in plant responses to FB1.

Gene name	Function	Species	Mutant/transgenic plants	FB1 response	System	References
MPK6	SA, ET	At	*mpk6*	Tolerant	Seedlings	Saucedo-García et al., 2011b
ACD2	SA	At	*acd2-2*	Sensitive	Protoplasts	Asai et al., 2000
CPR1	SA	At	*cpr1-1*	Sensitive	Protoplasts	Asai et al., 2000
CPR6	SA	At	*cpr6-l*	Sensitive	Protoplasts	Asai et al., 2000
PAD4	SA	At	*pad4-l*	Tolerant	Protoplasts	Asai et al., 2000
ETR1	ET	At	*etr1-1*	Tolerant	Protoplasts	Asai et al., 2000
		At	*etr1-1*	Tolerant	Leaves	Mase et al., 2013
		At	*etr1-1*	Sensitive	Leaves	Plett et al., 2009
		At	*etr1-1*	Sensitive	Seedlings	Wu et al., 2015b
EIN2	ET	At	*ein2*	Sensitive	Leaves	Wu et al., 2015b
EIN3	ET	At	*ein3*	Tolerant	Leaves	Mase et al., 2013
EIN4	ET	At	*ein4-1*	Tolerant	Leaves	Plett et al., 2009
ETO1	ET	At	*eto1-1*	Tolerant	Seedlings	Wu et al., 2015b
CTR1	ET	At	*ctr1-1*	Tolerant	Seedlings	Wu et al., 2015b
ERF4/MACD1	ET	*Nu*	TRV:NuERF4	Tolerant	Leaves	Mase et al., 2013
		Nu	MACD1 OE	Sensitive	Leaves	Mase et al., 2013
ERF102	ET	At	*erf 102,*	Tolerant	Leaves	Mase et al., 2013
			erf 102 (loh2)	Tolerant	Leaves	Mase et al., 2013
ERF103	ET	At	*erf 103 (erf 102)*	Tolerant	Leaves	Mase et al., 2013
JAR1	JA	At	*jar1-1*	Tolerant	Protoplasts	Asai et al., 2000
RGLG3	JA	At	*rglg3*	Tolerant	Leaves	Zhang et al., 2015
		At	RGLG3OE	Sensitive	Leaves	Zhang et al., 2015
RGLG4	JA	At	*rglg4*	Tolerant	Leaves	Zhang et al., 2015
		At	RGLG4OE	Sensitive	Leaves	Zhang et al., 2015
RGLG3/4	JA	At	*rglg3 rglg4*	Tolerant	Leaves	Zhang et al., 2015
COI1	JA	At	*coi1-2*	Tolerant	Leaves	Zhang et al., 2015
MYC2	JA	At	*myc2-2*	Sensitive	Leaves	Zhang et al., 2015
CPK3	Ca^{2+}	At	*cpk3-1, cpk3-2*	Tolerant	Leaves	Lachaud et al., 2013
VPE	Vacuole	At	VPE-null mutant	Tolerant	Leaves	Kuroyanagi et al., 2005
ATG5	Autophagy	At	*atg5*	Sensitive	Leaves	Lenz et al., 2011
ATG10	Autophagy	At	*atg10*	Sensitive	Leaves	Lenz et al., 2011
ATG18	Autophagy	At	*atg18*	Sensitive	Leaves	Coll et al., 2014
			Atg18-1	Sensitive	Leaves	Lenz et al., 2011
ATG18 and *MC1*	Autophagy and Metacaspases		*atg18 mc1*	Sensitive	Leaves	Coll et al., 2014
MC1	Metacaspases	At	*Mc1*	Sensitive	Leaves	Coll et al., 2014
MC4/MCP2d	Metacaspases	At	*mcp2d-1, mc$_p$2d-3*	Tolerant	Seedlings	Watanabe and Lam, 2011
		At	AtMCP2d OE	Sensitive	Leaves	Watanabe and Lam, 2011
KTI1	Kunitz Trypsin Inhibitor	At	*kti1* RNAi	Sensitive	Leaves	Li et al., 2008
		At	KTI1 OE	Tolerant	Leaves	Li et al., 2008
RD21	Papain-like cysteine protease	At	*rd21-1, -4*	Sensitive	Root	Ormancey et al., 2019
LSD1	Zinc finger protein	*Os*	*OsLSD1*	Tolerant	Tobacco Seedlings	Wang et al., 2005
SPL14/FBR6	Transcription	At	*fbr6*	Tolerant	Seedlings	Stone et al., 2005
ANAC032	Transcription, senescence	*At*	ANAC032 SRDX lines	Tolerant	Seedlings	Mahmood et al., 2016
CYP79B2/CYP79B3	Glucosinolates	At	*cyp79B2 cyp79B3*	Sensitive	Leaves	Zhao et al., 2015
TGG1 TGG2	Glucosinolates	At	*tgg1 tgg2*	Sensitive	Leaves	Zhao et al., 2015
UGP1	UDP-glucose pyrophosphorylase	At	*SALK_020808 SALK_100183*	Tolerant	Leaves	Chivasa et al., 2013
ATP SYNTHASE β- SUBUNIT	ATP synthase	At	*SALK_024990 SALK_135351 SALK_005252*	Tolerant	Leaves	Chivasa et al., 2011
CYCLASE1	Cyclase-family protein, SA, ATP	At	*cyclase1-1, -2*	Sensitive	Leaves	Smith et al., 2015

(Continued)

TABLE 2 | Continued

Gene name	Function	Species	Mutant/transgenic plants	FB1 response	System	References
RING1	RING motif protein	At	amiR-R1^{159} #1-16, #39-1	Tolerant	Seedlings	Lin et al., 2008
		At	RING1-3HA #2-26, #4-1	Sensitive	Seedlings	Lin et al., 2008
DAL1	Ring finger protein		*dal1-1, -2*	Sensitive	Leaves	Basnayake et al., 2011
DAL2	Ring finger protein		*dal2-1, -2*	Sensitive	Leaves	Basnayake et al., 2011
BI1	ER stress	At	*atbi1-1/atbi1-2*	Sensitive	Leaves	Watanabe and Lam, 2006; Nagano et al., 2009
RabG3b	GTPase, ATG	At	constitutively active RabG3b (RabG3bCA) and RabG3b OE *sad2-2, -5*	Sensitive	Leaves	Kwon et al., 2009; Kwon et al., 2013
SAD2	Importin beta-like protein	At		Sensitive	Seedlings	Zheng et al., 2019
ILP	Inhibitor of apoptosis-like protein, ring finger protein	At	*ILP*	Tolerant	Seedlings	Kim et al., 2011
ATR1	Unknown	At	*Atr1*	Tolerant	Seedlings	Gechev et al., 2008

KD, knockdown; OE or OX, overexpressing line. At, Arabidopsis thaliana.

and CPK3 degradation, ultimately triggering PCD in plants (Lachaud et al., 2013).

Reactive oxygen species (ROS) have key roles in PCD; in fact, cell death is considered to be triggered by ROS (Mittler, 2017) and ROS production precedes LCB-induced PCD in many cases (Shi et al., 2007; Saucedo-García et al., 2011a). The cytosolic increase in Ca^{2+} levels and the accumulation of ROS are critical for inducing PCD. The disruption of Arabidopsis super sensitive to aba and drought 2 (*SAD2*) (an importin beta-like gene) enhanced H_2O_2 accumulation and cell death in the *sad2-5* mutant under FB1 treatment (Zheng et al., 2019). The FB1 sensitivity of *sad2-5* is partially dependent on Ca^{2+} signaling (Zheng et al., 2019). SAD2-mediated Ca^{2+} and ROS signaling appear to function downstream of LCB, since the *sad2-5 fbr11-1* double mutant exhibited the same FB1-insensitive phenotype as *fbr11-1* (Zheng et al., 2019). In fact, many signaling pathways involved in regulating FB1-induced cell death are associated with ROS. For instance, the breakdown products of indole glucosinolate (IGS), which function in innate immune responses (Clay et al., 2009), attenuate FB1-induced cell death through their ROS-scavenging activity and function independently of indole-3-acetic acid signaling (Zhao et al., 2015).

Fumonisin B1 triggers the rapid depletion of extracellular ATP in Arabidopsis, which initiates cell death; this process was rescued by exogenous ATP treatment (Chivasa et al., 2005). ADP, AMP, and inorganic phosphate had no effect on this process, indicating that intact ATP is required for the rescue of FB1-induced cell death. In line with this notion, Arabidopsis knockout mutants lacking the gene encoding the mitochondrial ATP synthase β-subunit are resistant to FB1 (Chivasa et al., 2011). ATP and SA antagonistically regulate the cell death process (Smith et al., 2015). Further study based on this hypothesis revealed that CYCLASE1, an extracellular matrix proteins whose response to SA is suppressed by ATP, is a negative regulator of FB1-induced cell death (Smith et al., 2015).

Autophagy, Disruption of the Vacuolar Membrane, and ER Stress

Autophagy, a mechanism used to degrade unwanted constituents in eukaryotic cells, is essential for maintaining cell homeostasis and nutrient recycling. We recently demonstrated that FB1 and LCBs induce autophagy in Arabidopsis (Zheng et al., 2018). The loss of Arabidopsis ACER, an ACER that hydrolyzes Cer to LCB, inhibited autophagy, and its overexpression promoted autophagy under various abiotic stress conditions (Zheng et al., 2018).

In animals, the induction of autophagy has either cytoprotective or cytotoxic effects in certain types of mycotoxin-mediated cytotoxicity, but how the role (pro-survival or pro-death) of autophagy in regulating cell death is determined remains elusive (Yin et al., 2018). In plants, autophagy has also been assigned pro-death and pro-survival functions in controlling cell death (Zeng et al., 2019). Treatment with FB1 caused spreading lesions to form in several *autophagy-related* (*atg*) mutants (Lenz et al., 2011; Coll et al., 2014), implying that autophagy constitutes a pro-survival mechanism that contains unrestricted cell death in the presence of FB1. Consistent with this finding, autophagy participates in controlling plant lipid metabolism and catabolism (Have et al., 2019). Cer and GIPC levels are significantly altered in *atg5* mutants in a SA-independent manner (Have et al., 2019). This observation suggests that autophagy modifies the composition of endomembrane lipids, especially plasma membrane lipids, thereby altering the outcome of FB1 treatment. Nevertheless, overexpressing or constitutively active Rab GTPase RabG3b, which contributes to cell death during the hypersensitive response (HR) in Arabidopsis by activating autophagy, led to unrestricted hypersensitive PCD in response to FB1 (Kwon et al., 2009, 2013), confirming another role of autophagy in FB1-associated cell death. In summary, autophagy functions in life and death of the cell through multiple pathways, but the underlying molecular mechanisms remain to be revealed.

The disruption of vacuolar membranes is one of the early events in FB1-induced cell death, followed by lesion formation (Kuroyanagi et al., 2005). The deletion of all four vacuolar processing enzyme (VPE) genes or treatment with VPE-specific inhibitors significantly suppressed FB1-induced cell death in Arabidopsis (Kuroyanagi et al., 2005). VPE exhibits caspase-1 activity and is required for the collapse of the tonoplast during FB1 treatment (Kuroyanagi et al., 2005). Treatment with caspase-1 inhibitors prevented the formation of FB1-induced

lesions, indicating that caspase activity is required during FB1-induced cell death (Kuroyanagi et al., 2005). Notably, a deficiency of the retromer complex leads to defects in late endocytic/lytic compartments and impairs autophagy-associated vacuolar processes (Munch et al., 2015). vacuolar protein sorting 35, part of the retromer complex, functions in endosomal protein sorting and vacuolar trafficking and is involved in *acd11*-associated cell death (Munch et al., 2015). It would be interesting to investigate whether this process is required for FB1 resistance.

In animals, ER stress is responsible for autophagy and autophagic cell death induced by FB1 (Yin et al., 2016). Although we lack direct evidence in plants, the accumulation of LCB appears to increase ER stress-related responses. We frequently observed irregular ER and vacuolization in *orm1* amiR-ORM2 cells, with many tiny membrane sacs located close to the plasma membrane and cell wall (Li et al., 2016). In line with this observation, the expression of ER stress marker genes significantly increased in *orm1* amiR-ORM2 plants compared to the wild type (Li et al., 2016). Apart from mediating sphingolipid metabolism, AtBI1 plays a pivotal role as a highly conserved survival factor during ER stress that acts in parallel with the unfolded protein response pathway. Compared to wild-type plants, *atbi1-1* and *atbi1-2* exhibit hypersensitivity to tunicamycin, an inducer of ER stress, whereas overexpressing *AtBI1* markedly reduced the sensitivity of Arabidopsis seedlings to tunicamycin (Watanabe and Lam, 2008). Whether the role of BI1 in the ER stress response is associated with its sphingolipid-modifying function remains to be investigated.

Other Participants in FB1-Induced PCD

Plant proteases, such as serine proteases and cysteine proteases, have been implicated in PCD (Rotari et al., 2005). The serine protease kunitz trypsin inhibitor 1 (KTI1) acts as a functional protease in Arabidopsis when produced in bacteria and *in planta*. RNAi silencing of *KTI1* resulted in enhanced lesion development in plants after FB1 treatment (Li et al., 2008). Conversely, overexpressing *AtKTI1* reduced lesion development in plants after FB1 treatment (Li et al., 2008). The cysteine protease metacaspase 2D (MCP2d)/MC4 also participates in FB1-induced PCD. The AtMCP2d mutants *mcp2d-1* and *mcp2d-3* show reduced sensitivity to FB1, whereas *AtMCP2d* overexpression lines are more sensitive to FB1 and display accelerated progression of cell death (Li et al., 2008). AtMCP2d exclusively localizes to the cytosol (Li et al., 2008). AtMCP2d is engaged in both oxidative stress-induced cell death and pathogen-induced cell death (Li et al., 2008). The type I metacaspase AtMC1 likely plays a positive role in the HR, methyl viologen-induced cell death, and FB1-induced cell death (Coll et al., 2014). Finally, the Arabidopsis papain-like cysteine protease responsive to desiccation 21 is a negative regulator of FB1-induced cell death (Ormancey et al., 2019). Together, these findings support the notion that the cell death triggered by FB1 requires general cell death factors, such as various proteases.

Membrane microdomains have also been implicated in PCD. RING1, a RING finger domain protein with E3 ligase activity, is localized to the lipid rafts of plasma membranes (Lin et al., 2008). Knockdown of *RING1* led to FB1 hyposensitivity, whereas overexpressing *RING1* conferred hypersensitivity to this treatment (Lin et al., 2008). RING1 acts as a signal from lipid rafts in the plasma membrane that trigger the FB1-induced plant PCD pathway (Lin et al., 2008). Transient expression of *Capsicum annuum RING1* induced cell death in pepper leaves (Lee et al., 2011). It would be interesting to further investigate how lipid rafts in the plasma membrane respond to FB1. Suppressor of PPI1 locus 1 (SP1) regulates chloroplast biosynthesis, and both SP1 and SP1-like 1 (SPL1) regulate peroxisome biosynthesis in Arabidopsis (Ling et al., 2012, 2019; Pan et al., 2016, 2018). These proteins negatively regulate FB1-induced PCD as well (Basnayake et al., 2011). The involvement of these two regulators of organelle biogenesis in FB1-induced cell death points to a possible link between organelles and FB1 resistance.

Various proteins involved in FB1-induced cell death, such FBR6 and FBR12, also regulate plant growth and development. Misexpression of *AtSPL14*, encoding a plant-specific SQUAMOSA promoter (SBP)-domain putative transcription factor, conferred FB1 resistance in *fbr6* plants (Stone et al., 2005). In addition to participating in FB1-associated cell death, AtSPL14 modifies normal plant development, as the *fbr6* mutant displays altered plant architecture in the absence of FB1, most notably elongated petioles and enhanced leaf margin serration (Stone et al., 2005). These findings point to a possible association between insensitivity to FB1-induced cell death and altered plant development. Similar observations were made for Arabidopsis *fbr12*, a mutant deficient in eukaryotic translation initiation factor 5A. FBR12 positively regulates PCD caused by infection with virulent *P. syringae* pv. *tomato* DC3000 (*Pst* DC3000), and transgenic plants constitutively overexpressing *FBR12* exhibited phenotypes consistent with precocious cell death (Hopkins et al., 2008).

FBR12 mediates processes beyond cell death, such as cell division and cell growth (Feng et al., 2007). The *fbr12* mutant is extremely dwarf, with substantially reduced sizes and numbers of all adult organs, and shows abnormal floral organ development and defective sporogenesis, leading to the abortion of both female and male germline cells during reproductive development (Feng et al., 2007). FBR12 also functions in cytokinin-mediated specification of the root protoxylem, as a mutation in *FBR12* led to defective protoxylem development and reduced sensitivity to cytokinin (CTK) (Ren et al., 2013). These findings point to a connection between PCD and inhibited development induced by FB1.

The solid arrows indicate established links and the dashed arrows indicate putative links. Reduced VLC sphingolipid levels lead to disordered trafficking, membrane incorporation, and secretion. LCBs produced in response to FB1 to trigger cell death signaling, such as ET, JA, SA, ROS, Ca^{2+}, ATP signaling, and so on. LCBs regulate the activities of cell death-associated proteins such as MPK6, CPK6, and 14-3-3 proteins. LCBs also induce autophagosome formation, which maintains cellular homeostasis, protecting the cell from unnecessary death. ER stress appears to be involved in this process. LCBs induce the expression of sphingolipid biosynthesis, PCD, and senescence-related genes through transcription factors such as EIN2, CTR1, SPL14, and ANAC032. 14-3-3, 14-3-3 family

protein; ANAC032, NAC domain containing protein 32; ATG8, autophagy 8; AUX1, auxin resistant 1; BI1, bax inhibitor 1; Cers, ceramides; CPK6, calcium dependent protein kinase 6; CTK, cytokinin; CTR1, constitutive triple response 1; EIN2, ethylene insensitive 2; ET, ethylene, ER stress, endoplasmic reticulum stress; FB1, fumonisin B1; FBR12, fumonisin B1 resistant 12; GluCers, glucosylceramides; GIPCs, glycosyl-inositolphosphoryl-ceramides; hCers, hydroxyceramides; IAA, indole-3-acetic acid; IGS, indole glucosinolate; JA, jasmonate; LCBs, long-chain bases; LOH1, LAG1 Homolog 1; MPK6, MAP kinase 6; MPK6-P, MPK6 phosphorylated form; PE, phosphatidylethanolamine; PHS, phytosphingosine; PIN1, PIN-FORMED 1; RbohD/F, respiratory burst oxidase homolog; ROS, reactive oxygen species; SA, salicylic acid; SPL14, squamosa promoter binding protein-like 14; TFs, transcription factors; VLC, very-long-chain; VPE, vacuolar processing enzyme.

FB1 IMPAIRS PLANT GROWTH AND AFFECTS PLANT DEVELOPMENT

Sphingolipids, particularly those containing VLCFAs, are essential for protein sorting and secretion in eukaryotes. The hydrophobicity, membrane-leaflet interdigitation, and transition of a membrane from a fluid to a gel phase, which are required for microdomain formation, are highly correlated with the presence of VLC sphingolipids (Markham et al., 2011). Several reports speculated that sphingolipids may represent the main reservoir of VLCFAs in leaves; since phosphatidylserine and phosphatidylethanolamine harbor VLCFAs as well in their backbone and no quantitative comparison with these lipid classes exist, this needs to be analyzed in more detail in the future (Pata et al., 2010; Maatta et al., 2012; Cacas et al., 2016; De Bigault Du Granrut and Cacas, 2016). Plants overexpressing *LOH1* and *LOH3* showed increased growth and cell division, with enhanced production of Cers with VLCFAs and trihydroxy LCBs (Luttgeharm et al., 2015). Interestingly, unlike *LOH2*, overexpressing *LOH1/3* had only a minor effect on the sphingolipid profiles of plants.

Fumonisin B1-mediated reductions in VLCFA levels remodel the membrane structure and influence numerous processes that require the foundation maintained by VLC sphingolipids (**Figure 2**). Upon FB1 application, tobacco (*Nicotiana tabacum*) BY2 cells showed severe effects on cell growth and cell shape and a delay in cell division (Aubert et al., 2011). These changes were accompanied by the formation of ER-derived tubular aggregates, as well as inhibited ER-to-Golgi cargo transport (Aubert et al., 2011). A change in the polar localization of the auxin transporter PIN-FORMED 1 (PIN1) was also observed, but there was little effect on endocytic processes. FB1 targets molecules distinct from those targeted by Brefeldin A, an ER-to-Golgi transport inhibitor (Ritzenthaler et al., 2002; Langhans and Robinson, 2007), as revealed by electron microscopy. These findings reflect the importance of sphingolipids in cell growth and the establishment of cell polarity in plant cells, especially their contribution to the functional organization of the ER or its differentiation into distinct compartments (Aubert et al., 2011).

The reduction in VLC sphingolipid levels leads to auxin-dependent inhibition of lateral root emergence, which is correlated with the selective aggregation of the plasma membrane auxin carriers auxin resistant 1 (AUX1) and PIN1 in the cytosol (Markham et al., 2011). Defective targeting of polar auxin carriers is characterized by the specific aggregation of Rab-A2a- and Rab-A1e-labeled early endosomes along the secretory pathway (Markham et al., 2011). The formation of these aggregates is associated with the accumulation of membrane structures and vesicle fragmentation in the cytosol (Markham et al., 2011), indicating that sphingolipids with very long acyl chains define a trafficking pathway with specific endomembrane compartments and polar auxin transport protein cargoes (Markham et al., 2011). Finally, VLC sphingolipids, particularly VLC glycosphingolipids, are essential structural determinants of vesicle dynamics and membrane fusion during cytokinesis (Molino et al., 2014). Inhibiting VLC sphingolipids biosynthesis by FB1 led to the formation of defective cell plates with persistent vesicular structures and large gaps (Molino et al., 2014).

Route 1 (Orange): FB1-induced decreases in VLCF levels strongly affect membrane properties, which are responsible for normal plant growth. Route 2 (Blue): FB1-induced increases in LCB and C16 Cer levels primarily affect hormone, Ca^{2+}, ROS, and ATP signaling, which ultimately contribute to cell death. However, this process is sufficiently complex such that interplay with other factors in each route and even across routes determines the final outcomes. Black, targeted by FB1 (purple), orange, inhibited or reduced by FB1; blue, promoted or elevated by FB1. CerS, ceramide synthase; ET, ethylene, FB1, fumonisin B1; IGS, indole glucosinolate; JA, jasmonate; LCBs, long-chain bases; ROS, reactive oxygen species; SA, salicylic acid; SLs, sphingolipids; VLCFA, very-long-chain fatty acid.

MAIZE–*F. verticillioides* INTERACTION

Fumonisin-producing pathogens are the major causal agents of fusarium ear rot, one of the most important diseases affecting maize production worldwide (Picot et al., 2010). FB1 is the predominant fumonisin in maize kernels (Bartók et al., 2006). The fungal genes required for fumonisin biosynthesis are organized in a cluster designated the fumonisin (FUM) gene cluster, which contains 22 genes with a length of 42 kb (Proctor et al., 1999, 2003). This cluster may be regulated by multiple environmental factors including pH, water availability or nutrient sources, and various fungal genes to favor or restrain fumonisin biosynthesis (Picot et al., 2010). Among the 22 genes, 15 are co-regulated, including the key gene *FUM1*, which encodes a polyketide synthase (PKS) (Proctor et al., 1999).

In the complex interaction between *F. verticillioides* and maize, investigation of the role of fumonisin production on disease development has yielded controversial results. Only strains of *F. verticillioides* that produce fumonisins cause foliar disease symptoms on seedlings of the sweet maize hybrid "Silver Queen" (Williams et al., 2006; Lanubile et al., 2012a,b). However, the *FUM1* deletion mutants, which do not produce fumonisin, still cause ear rot, implying that production of fumonisins is not

required for ear rot (Jardine and Leslie, 1999; Desjardins et al., 2002). Lanubile et al. (2013) found that *PKS* is a relevant gene, essential not only for the fumonisin biosynthetic pathway, but also for pathogen colonization (Lanubile et al., 2013).

Sarocladium zeae, a fungal endophyte of maize, can co-inhabit a seed with *F. verticillioides* due to its capability to produce pyrrocidines A and B, which inhibit the growth of *F. verticillioides* (Gao et al., 2020). *FvZBD1* (*FVEG_00314*) encodes a genetic repressor of fumonisin production, is directly adjacent to the *FUM* cluster, and was induced in response to pyrrocidines. This suggests that other microbes may manipulate the fumonisin biosynthetic program of *F. verticillioides* to control *F. verticillioides* growth in the host (Gao et al., 2020). Interestingly, a high dose of fumonisin induced necrosis and wilting in maize seedlings, but a low dose activated detoxification processes, indicating that maize has recovery mechanisms (Arias et al., 2012).

In maize, batteries of defense genes involved in pathogen-associated molecular pattern-triggered immunity and effector-triggered immunity, as well as multiple signaling, such as MAPK, Ca^{2+}, ROS, hormones (including SA, auxin, abscisic acid, ethylene, JA) signaling are activated in response to *F. verticillioides* infection (Lanubile et al., 2017). A complex network of metabolic pathways is required for resistance to *F. verticillioides* (Lanubile et al., 2017). *Lipoxygenase* (*LOX*) genes encode non-heme iron-containing dioxygenases that catalyze the oxygenation of polyunsaturated fatty acids (Vick and Zimmerman, 1983), which are processed into an estimated 400 metabolites including JA (Mosblech et al., 2009). In plants, LOXs are involved in host susceptibility to fungal invasion and mycotoxin production (Kock et al., 2003; Christensen and Kolomiets, 2011; Maschietto et al., 2015). Depending on which carbon on the fatty acid chain is oxygenated, LOXs are classified into two main functional groups, 9-LOXs and 13-LOXs. It seems that a specific plant 9-LOX isoform is required for fungal pathogenesis, including disease development and production of spores and mycotoxins (Gao et al., 2007, 2009; Christensen et al., 2014). In addition, many factors contribute to resistance to *F. verticillioides* and fumonisin contamination, including the biochemical composition of the endosperm, and fatty acid composition, as well as many other metabolites, such phenylpropanoid pathway-related metabolites (flavonoids, phenolic compounds, and phytoalexins), flavones, and 2-amino-3H-phenoxazin-3-one (Lanubile et al., 2017).

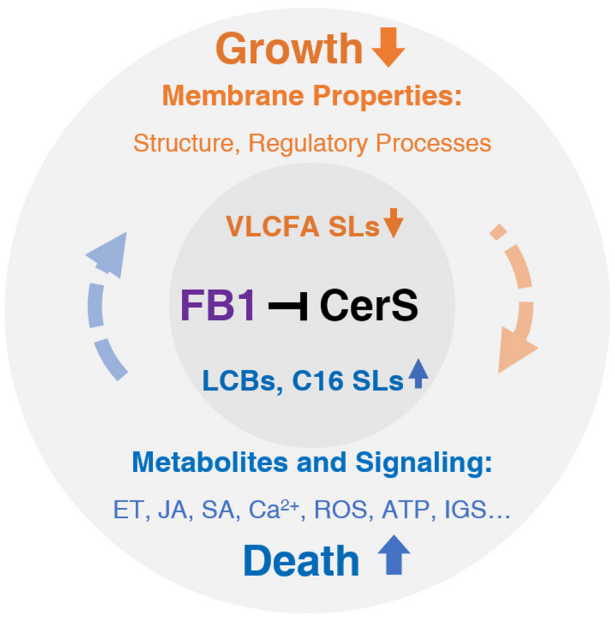

FIGURE 3 | The effects of FB1 treatment.

CONCLUDING REMARKS AND OUTLOOK

Inhibition of ceramide synthesis by FB1 disturbs the homeostasis of sphingolipid metabolism, resulting in changes in structural and signaling sphingolipids, including elevated LCB and LCF Cer levels and decreased formation of Cers and complex VLC sphingolipids, accounting for the broad spectrum of plant disease symptoms. LCBs, as well as LCF Cers, contribute to cell death by functioning as signals, while Cers and complex VLC sphingolipids are critical components of the plant plasma membrane and endomembrane system that are closely associated with the fluidity and biophysical order of the membrane. Thus, the perturbations caused by FB1 not only induce cell death signals, but they also damage the structural components of the cell and impair plant growth. Small molecules and metabolites such as certain hormones (ethylene, JA, SA), ROS, NO, ATP, and Ca^{2+} likely affect FB1-triggered PCD, highlighting the strong association between sphingolipids and cell death. Nevertheless, the molecular details of the underlying mechanism are largely unclear.

In addition to being used as a ceramide inhibitor or a fungal toxicant, FB1 represents a highly useful tool for revealing details about sphingolipid-controlled cell death and growth inhibition. These details would benefit agriculture by helping us overcome the subtle strategy of FB1-producing pathogens and others foes sharing similar mechanisms in plant–pathogen interactions.

Based on the complicated signaling network induced by FB1, we propose a model to classify the global effects of this compound into basic two routes (**Figure 3**). However, it should be noted that most of these events interact with each other in a complex manner. For example, FB1 manipulates the JA signaling pathway through SA signaling (Zhang et al., 2015). In general, the activation of cell death signaling represses plant growth, which in turn sometimes leads to cell death.

Sphingolipids remain an underexplored, large group of metabolites (Ali et al., 2018). The study of FB1, the best-characterized inhibitor of sphingolipid biosynthesis, provides a fascinating illustration of the remarkably sophisticated sphingolipid-signaling network that is established in plants and animals. However, our understanding of the mechanisms underlying FB1 toxicity in plants is still in its infancy in terms

of identifying the direct target(s) of FB1 and key elements in the responses to FB1.

Recent studies using molecular genetics and biochemical approaches have enhanced our understanding of this issue in plants and provided a deeper understanding of the roles of sphingolipids in plant life and death. Despite these important findings, our understanding of the importance of sphingolipids for the regulation of plant cell death and growth, and consequently crop yields remains limited and sphingolipids represent an exciting area for further study. Many efforts have been made to functionally characterize individual genes downstream of FB1. However, little is known about the FB1 signal transduction network. Therefore, apart from screening more participants involved in the FB1 response, studies should be designed to elaborate how the known participants operate simultaneously in a coordinated signaling network under FB1 treatment. In particular, it is crucial to investigate the connection between the regulators of FB1 resistance and sphingolipid metabolism. Specifically, sphingolipid profile analysis of FB1-resistant or -sensitive mutants with and without FB1 treatment should be performed to determine whether these proteins engage in sphingolipid metabolism. Furthermore, our lack of knowledge about the molecular targets of individual sphingolipid components, as well as their biological significance to plants, is still a major impediment to understanding FB1 signaling. Thus, there is a need for interactome association analysis between proteins downstream of FB1 and LCB, as well as sphingolipid enzymes, to untangle the interplay between these signals and sphingolipid metabolites or metabolism pathways. Recent studies have demonstrated the great potential of using the photoactivatable and clickable analog of sphingosine (pacSph) and azide-tagged sphingolipids to identify sphingolipid targets (Haberkant et al., 2016; Schulte-Zweckel et al., 2018). In addition to high-throughput screening of sphingolipid-interacting proteins, it will be important to gain deep insight into the roles of essential components of the HR, particularly enhanced disease susceptibility 1, activated disease resistance 1, and non-race-specific disease resistance 1, in FB1-triggered cell death, given that these HR signaling pathways are active in response to FB1.

Beside Arabidopsis, the FB1 signaling network should be elaborated in crop plants. Relatively little is known about the physiological effects of fumonisins from fungal pathogens in the natural environment on the development of plant diseases. The introduction and manipulation of parts of the FB1 signaling pathway in crop plants will have broad and overarching impacts on agriculture to help overcome the effects of FB1-producing pathogens. In view of the broad host range of FB1-producing pathogens, the eradication of plant diseases (as well as animal diseases) caused by FB1 appears to be elusive. However, better insight into the global effects of FB1 on plants will undoubtedly contribute to the development of a rational, effective approach to reducing the hazards of FB1 contamination.

AUTHOR CONTRIBUTIONS

H-YZ and NY designed the manuscript and wrote the manuscript. C-YL and NY contributed to the reagents and materials. All authors have discussed and approved the final manuscript.

FUNDING

This work was supported by the National Natural Science Foundation of China (31771357) and the Natural Science Foundation of Guangdong Province (2019B1515120088 and 2017A030311005).

SUPPLEMENTARY MATERIAL

The Supplementary Material for this article can be found online at: https://www.frontiersin.org/articles/10.3389/fpls.2020.600458/full#supplementary-material

REFERENCES

Aflaki, E., Doddapattar, P., Radovic, B., Povoden, S., Kolb, D., Vujic, N., et al. (2012). C16 ceramide is crucial for triacylglycerol-induced apoptosis in macrophages. *Cell Death Dis.* 3:e280. doi: 10.1038/cddis.2012.17

Alden, K. P., Dhondt-Cordelier, S., McDonald, K. L., Reape, T. J., Ng, C. K., McCabe, P. F., et al. (2011). Sphingolipid long chain base phosphates can regulate apoptotic-like programmed cell death in plants. *Biochem. Biophys. Res. Commun.* 410, 574–580. doi: 10.1016/j.bbrc.2011.06.028

Ali, U., Li, H., Wang, X., and Guo, L. (2018). Emerging roles of sphingolipid signaling in plant response to biotic and abiotic stresses. *Mol. Plant* 11, 1328–1343. doi: 10.1016/j.molp.2018.10.001

Arias, S. L., Mary, V. S., Otaiza, S. N., Wunderlin, D. A., Rubinstein, H. R., and Theumer, M. G. (2016). Toxin distribution and sphingoid base imbalances in Fusarium verticillioides-infected and fumonisin B1-watered maize seedlings. *Phytochemistry* 125, 54–64. doi: 10.1016/j.phytochem.2016.02.006

Arias, S. L., Theumer, M. G., Mary, V. S., and Rubinstein, H. R. (2012). Fumonisins: probable role as effectors in the complex interaction of susceptible and resistant maize hybrids and *Fusarium verticillioides*. *J. Agr. Food Chem.* 60, 5667–5675. doi: 10.1021/jf3016333

Asai, T., Stone, J. M., Heard, J. E., Kovtun, Y., Yorgey, P., Sheen, J., et al. (2000). Fumonisin B1–induced cell death in *Arabidopsis* protoplasts requires jasmonate-, ethylene-, and salicylate-dependent signaling pathways. *Plant Cell* 12, 1823–1835. doi: 10.2307/3871195

Aubert, A., Marion, J., Boulogne, C., Bourge, M., Abreu, S., Bellec, Y., et al. (2011). Sphingolipids involvement in plant endomembrane differentiation: the BY2 case. *Plant J.* 65, 958–971. doi: 10.1111/j.1365-313X.2011.04481.x

Bailly-Maitre, B., Fondevila, C., Kaldas, F., Droin, N., Luciano, F., Ricci, J. E., et al. (2006). Cytoprotective gene bi-1 is required for intrinsic protection from endoplasmic reticulum stress and ischemia-reperfusion injury. *Proc. Natl. Acad. Sci. U.S.A.* 103, 2809–2814. doi: 10.1073/pnas.0506854103

Bartók, T., Szécsi, Á, Szekeres, A., Mesterházy, Á, and Bartók, M. (2006). Detection of new fumonisin mycotoxins and fumonisin-like compounds by reversed-phase high-performance liquid chromatography/electrospray ionization ion trap mass spectrometry. *Rapid Commun. Mass. Sp.* 20, 2447–2462. doi: 10.1002/rcm.2607

Basnayake, B. M., Li, D., Zhang, H., Li, G., Virk, N., and Song, F. (2011). *Arabidopsis* DAL1 and DAL2, two RING finger proteins homologous to Drosophila DIAP1, are involved in regulation of programmed cell death. *Plant Cell Rep.* 30, 37–48. doi: 10.1007/s00299-010-0941-6

Brandwagt, B. F., Mesbah, L. A., Takken, F. L. W., Laurent, P. L., Kneppers, T. J. A., Hille, J., et al. (2000). A longevity assurance gene homolog of tomato mediates resistance to Alternaria alternata f. sp. lycopersici toxins and fumonisin B1. *Proc. Natl. Acad. Sci. U.S.A.* 97:4961. doi: https://doi.org/10.1073/pnas.97.9.4961

Cacas, J. L., Buré, C., Grosjean, K., Gerbeau-Pissot, P., Lherminier, J., Rombouts, Y., et al. (2016). Revisiting plant plasma membrane lipids in tobacco: a focus on sphingolipids. *Plant Physiol.* 170, 367–384. doi: 10.1104/pp.15.00564

Chae, H.-J., Ke, N., Kim, H.-R., Chen, S., Godzik, A., Dickman, M., et al. (2003). Evolutionarily conserved cytoprotection provided by Bax Inhibitor-1 homologs from animals, plants, and yeast. *Gene* 323, 101–113. doi: 10.1016/j.gene.2003.09.011

Chae, H.-J., Kim, H.-R., Xu, C., Bailly-Maitre, B., Krajewska, M., Krajewski, S., et al. (2004). BI-1 regulates an apoptosis pathway linked to endoplasmic reticulum stress. *Mol. Cell* 15, 355–366. doi: 10.1016/j.molcel.2004.06.038

Chen, M., Markham, J. E., Dietrich, C. R., Jaworski, J. G., and Cahoon, E. B. (2008). Sphingolipid long-chain base hydroxylation is important for growth and regulation of sphingolipid content and composition in *Arabidopsis*. *Plant Cell* 20, 1862–1878. doi: 10.1105/tpc.107.057851

Chini, A., Monte, I., Zamarreño, A. M., Hamberg, M., Lassueur, S., Reymond, P., et al. (2018). An OPR3-independent pathway uses 4,5-didehydrojasmonate for jasmonate synthesis. *Nat. Chem. Biol.* 14, 171–178. doi: 10.1038/nchembio.2540

Chivasa, S., Ndimba, B. K., Simon, W. J., Lindsey, K., and Slabas, A. R. (2005). Extracellular ATP functions as an endogenous external metabolite regulating plant cell viability. *Plant Cell* 17, 3019–3034. doi: 10.1105/tpc.105.036806

Chivasa, S., Tome, D. F., Hamilton, J. M., and Slabas, A. R. (2011). Proteomic analysis of extracellular ATP-regulated proteins identifies ATP synthase beta-subunit as a novel plant cell death regulator. *Mol. Cell Proteomics* 10:M110.003905. doi: 10.1074/mcp.M110.003905

Chivasa, S., Tomé, D. F. A., and Slabas, A. R. (2013). UDP-glucose pyrophosphorylase is a novel plant cell death regulator. *J. Plant Res.* 12, 1743–1753. doi: 10.1021/pr3010887

Christensen, S. A., and Kolomiets, M. V. (2011). The lipid language of plant-fungal interactions. *Fungal Genet. Biol.* 48, 4–14. doi: 10.1016/j.fgb.2010.05.005

Christensen, S. A., Nemchenko, A., Park, Y.-S., Borrego, E., Huang, P.-C., Schmelz, E. A., et al. (2014). The novel monocot-specific 9-lipoxygenase ZmLOX12 is required to mount an effective jasmonate-mediated defense against *Fusarium verticillioides* in Maize. *Mol. Plant Microbe Interact.* 27, 1263–1276. doi: 10.1094/MPMI-06-13-0184-R

Cingolani, F., Futerman, A. H., and Casas, J. (2016). Ceramide synthases in biomedical research. *Chem. Phys. Lipids* 197, 25–32. doi: 10.1016/j.chemphyslip.2015.07.026

Clay, N. K., Adio, A. M., Denoux, C., Jander, G., and Ausubel, F. M. (2009). Glucosinolate metabolites required for an *Arabidopsis* innate immune response. *Science* 323, 95–101. doi: 10.1126/science.1164627

Coll, N. S., Smidler, A., Puigvert, M., Popa, C., Valls, M., and Dangl, J. L. (2014). The plant metacaspase AtMC1 in pathogen-triggered programmed cell death and aging: functional linkage with autophagy. *Cell Death Differ.* 21, 1399–1408. doi: 10.1038/cdd.2014.50

Danon, A., Miersch, O., Felix, G., Camp, R. G. L., and Apel, K. (2004). Concurrent activation of cell death-regulating signaling pathways by singlet oxygen in *Arabidopsis thaliana*. *Plant J.* 41, 68–80. doi: 10.1111/j.1365-313X.2004.02276.x

De Bigault Du Granrut, A., and Cacas, J. L. (2016). How very-long-chain fatty acids could signal stressful conditions in plants? *Front Plant Sci.* 7:1490. doi: 10.3389/fpls.2016.01490

Desjardins, A. E., Munkvold, G., Plattner, R., and Proctor, R. (2002). FUM1 — A gene required for fumonisin biosynthesis but not for maize ear rot and ear infection by *Gibberella moniliformis* in field tests. *Mol. Plant Microbe Interact.* 15, 1157–1164. doi: 10.1094/MPMI.2002.15.11.1157

Dutilleul, C., Benhassaine-Kesri, G., Demandre, C., Reze, N., Launay, A., Pelletier, S., et al. (2012). Phytosphingosine-phosphate is a signal for AtMPK6 activation and *Arabidopsis* response to chilling. *New Phytol.* 194, 181–191. doi: 10.1111/j.1469-8137.2011.04017.x

Feng, H., Chen, Q., Feng, J., Zhang, J., Yang, X., and Zuo, J. (2007). Functional characterization of the *Arabidopsis* eukaryotic translation initiation factor 5A-2 that plays a crucial role in plant growth and development by regulating cell division, cell growth, and cell death. *Plant Physiol.* 144, 1531–1545. doi: 10.1104/pp.107.098079

Gao, M., Glenn, A. E., Gu, X., Mitchell, T. R., Satterlee, T., Duke, M. V., et al. (2020). Pyrrocidine, a molecular off switch for fumonisin biosynthesis. *PLoS Pathog.* 16:e1008595. doi: 10.1371/journal.ppat.1008595

Gao, X., Brodhagen, M., Isakeit, T., Brown, S. H., Gobel, C., Betran, J., et al. (2009). Inactivation of the lipoxygenase *ZmLOX3* increases susceptibility of Maize to *Aspergillus* spp. *Mol. Plant Microbe Interact.* 22, 222–231. doi: 10.1094/MPMI-22-2-0222

Gao, X., Shim, W. B., Göbel, C., Kunze, S., Feussner, I., Meeley, R., et al. (2007). Disruption of a maize 9-lipoxygenase results in increased resistance to fungal pathogens and reduced levels of contamination with mycotoxin fumonisin. *Mol. Plant Microbe Interact.* 20, 922–933.

Gechev, T. S., Ferwerda, M. A., Mehterov, N., Laloi, C., Qureshi, M. K., and Hille, J. (2008). *Arabidopsis* AAL-toxin-resistant mutant *atr1* shows enhanced tolerance to programmed cell death induced by reactive oxygen species. *Biochem. Biophys. Res. Commun.* 375, 639–644. doi: 10.1016/j.bbrc.2008.08.056

Gelderblom, W. C., Jaskiewicz, K., Marasas, W. F., Thiel, P. G., Horak, R. M., Vleggaar, R., et al. (1988). Fumonisins–novel mycotoxins with cancer-promoting activity produced by *Fusarium moniliforme*. *Appl. Environ. Microb.* 54, 1806–1811. doi: 10.1002/bit.260320218

Glenn, A., Zitomer, N., Zimeri, A., Williams, L., and Riley, R. (2008). Transformation-mediated complementation of a *FUM* gene cluster deletion in *Fusarium verticillioides* restores both fumonisin production and pathogenicity on maize seedlings. *Mol. Plant Microbe Interact.* 21, 87–97.

Glenz, R., Schmalhaus, D., Krischke, M., Mueller, M. J., and Waller, F. (2019). Elevated levels of phosphorylated sphingobases do not antagonize sphingobase- or fumonisin B1-induced plant cell death. *Plant Cell Physiol.* 60, 1109–1119. doi: 10.1093/pcp/pcz033

Haberkant, P., Stein, F., Hoglinger, D., Gerl, M. J., Brugger, B., Van Veldhoven, P. P., et al. (2016). Bifunctional sphingosine for cell-based analysis of protein-sphingolipid interactions. *ACS Chem. Biol.* 11, 222–230. doi: 10.1021/acschembio.5b00810

Have, M., Luo, J., Tellier, F., Balliau, T., Cueff, G., Chardon, F., et al. (2019). Proteomic and lipidomic analyses of the *Arabidopsis atg5* autophagy mutant reveal major changes in endoplasmic reticulum and peroxisome metabolisms and in lipid composition. *New Phytol.* 223, 1461–1477. doi: 10.1111/nph.15913

Hopkins, M. T., Lampi, Y., Wang, T. W., Liu, Z., and Thompson, J. E. (2008). Eukaryotic translation initiation factor 5A is involved in pathogen-induced cell death and development of disease symptoms in *Arabidopsis*. *Plant Physiol.* 148, 479–489. doi: 10.1104/pp.108.118869

Jardine, D., and Leslie, J. (1999). Aggressiveness to mature maize plants of *Fusarium* strains differing in ability to produce fumonisin. *Plant Dis.* 83, 690–693. doi: 10.1094/PDIS.1999.83.7.690

Kawai-Yamada, M., Jin, L., Yoshinaga, K., Hirata, A., and Uchimiya, H. (2001). Mammalian Bax-induced plant cell death can be down-regulated by overexpression of *Arabidopsis* Bax Inhibitor-1 (*AtBI-1*). *Proc. Natl. Acad. Sci. U.S.A.* 98, 12295–12300. doi: 10.1073/pnas.211423998

Kim, W. Y., Lee, S. Y., Jung, Y. J., Chae, H. B., Nawkar, G. M., Shin, M. R., et al. (2011). Inhibitor of apoptosis (IAP)-like protein lacks a Baculovirus IAP Repeat (BIR) domain and attenuates cell death in plant and animal systems. *J. Biol. Chem.* 286, 42670–42678. doi: 10.1074/jbc.M111.262204

Kimberlin, A. N., Han, G., Luttgeharm, K. D., Chen, M., Cahoon, R. E., Stone, J. M., et al. (2016). *ORM* expression alters sphingolipid homeostasis and differentially affects ceramide synthase activity. *Plant Physiol.* 172, 889–900. doi: 10.1104/pp.16.00965

Kimberlin, A. N., Majumder, S., Han, G., Chen, M., Cahoon, R. E., Stone, J. M., et al. (2013). *Arabidopsis* 56-amino acid serine palmitoyltransferase-interacting proteins stimulate sphingolipid synthesis, are essential, and affect mycotoxin sensitivity. *Plant Cell* 25, 4627–4639. doi: 10.2307/23598494

Kock, J. L. F., Strauss, C. J., Pohl, C. H., and Nigam, S. (2003). The distribution of 3-hydroxy oxylipins in fungi. *Prostag. Oth. Lipid M* 71, 85–96. doi: 10.1016/S1098-8823(03)00046-7

Konig, S., Feussner, K., Schwarz, M., Kaever, A., Iven, T., Landesfeind, M., et al. (2012). *Arabidopsis* mutants of sphingolipid fatty acid alpha-hydroxylases accumulate ceramides and salicylates. *New Phytol.* 196, 1086–1097. doi: 10.1111/j.1469-8137.2012.04351.x

Kuroyanagi, M., Yamada, K., Hatsugai, N., Kondo, M., Nishimura, M., and Hara-Nishimura, I. (2005). Vacuolar processing enzyme is essential for mycotoxin-induced cell death in *Arabidopsis thaliana*. *J. Biol. Chem.* 280, 32914–32920. doi: 10.1074/jbc.M504476200

Kwon, S. I., Cho, H. J., Bae, K., Jung, J. H., Jin, H. C., and Park, O. K. (2009). Role of an *Arabidopsis* Rab GTPase RabG3b in pathogen response and leaf senescence. *J. Plant Biol.* 52, 79–87. doi: 10.1007/s12374-009-9011-4

Kwon, S. I., Cho, H. J., Kim, S. R., and Park, O. K. (2013). The Rab GTPase RabG3b positively regulates autophagy and immunity-associated hypersensitive cell death in *Arabidopsis*. *Plant Physiol.* 161, 1722–1736. doi: 10.1104/pp.112.208108

Lachaud, C., Prigent, E., Thuleau, P., Grat, S., Da Silva, D., Briere, C., et al. (2013). 14-3-3-regulated Ca(2+)-dependent protein kinase CPK3 is required for sphingolipid-induced cell death in *Arabidopsis*. *Cell Death Differ.* 20, 209–217. doi: 10.1038/cdd.2012.114

Langhans, M., and Robinson, D. G. (2007). 1-Butanol targets the Golgi apparatus in tobacco BY-2 cells, but in a different way to Brefeldin A. *J. Exp. Bot.* 58, 3439–3447. doi: 10.1093/jxb/erm194

Lanubile, A., Bernardi, J., Battilani, P., Logrieco, A., and Marocco, A. (2012a). Resistant and susceptible maize genotypes activate different transcriptional responses against *Fusarium verticillioides*. *Physiol. Mol. Plant Pathol.* 77, 52–59. doi: 10.1016/j.pmpp.2011.12.002

Lanubile, A., Bernardi, J., Marocco, A., Logrieco, A., and Paciolla, C. (2012b). Differential activation of defense genes and enzymes in maize genotypes with contrasting levels of resistance to *Fusarium verticillioides*. *Environ. Exp. Bot.* 78, 39–46. doi: 10.1016/j.envexpbot.2011.12.006

Lanubile, A., Logrieco, A., Battilani, P., Proctor, R., and Marocco, A. (2013). Transcriptional changes in developing maize kernels in response to fumonisin-producing and nonproducing strains of *Fusarium verticillioides*. *Plant Sci.* 210, 183–192. doi: 10.1016/j.plantsci.2013.05.020

Lanubile, A., Maschietto, V., Borrelli, V. M., Stagnati, L., Logrieco, A. F., and Marocco, A. (2017). Molecular basis of resistance to Fusarium ear rot in Maize. *Front Plant Sci.* 8:1774. doi: 10.3389/fpls.2017.01774

Lee, D. H., Choi, H. W., and Hwang, B. K. (2011). The pepper E3 ubiquitin ligase RING1 gene, *CaRING1*, is required for cell death and the salicylic acid-dependent defense response. *Plant Physiol.* 156, 2011–2025. doi: 10.1104/pp.111.177568

Lenz, H. D., Haller, E., Melzer, E., Kober, K., Wurster, K., Stahl, M., et al. (2011). Autophagy differentially controls plant basal immunity to biotrophic and necrotrophic pathogens. *Plant J.* 66, 818–830. doi: 10.1111/j.1365-313X.2011.04546.x

Li, J., Brader, G., and Palva, E. T. (2008). Kunitz trypsin inhibitor: an antagonist of cell death triggered by phytopathogens and fumonisin B1 in *Arabidopsis*. *Mol. Plant* 1, 482–495. doi: 10.1093/mp/ssn013

Li, J., Yin, J., Rong, C., Li, K. E., Wu, J. X., Huang, L. Q., et al. (2016). Orosomucoid proteins interact with the small subunit of serine palmitoyltransferase and contribute to sphingolipid homeostasis and stress responses in *Arabidopsis*. *Plant Cell* 28, 3038–3051. doi: 10.1105/tpc.16.00574

Liang, H., Yao, N., Song, J. T., Luo, S., Lu, H., and Greenberg, J. T. (2003). Ceramides modulate programmed cell death in plants. *Genes Dev.* 17, 2636–2641. doi: 10.1101/gad.1140503

Lin, S. S., Martin, R., Mongrand, S., Vandenabeele, S., Chen, K. C., Jang, I. C., et al. (2008). RING1 E3 ligase localizes to plasma membrane lipid rafts to trigger FB1-induced programmed cell death in *Arabidopsis*. *Plant J.* 56, 550–561. doi: 10.1111/j.1365-313X.2008.03625.x

Ling, Q., Broad, W., Trösch, R., Töpel, M., Demiral Sert, T., Lymperopoulos, P., et al. (2019). Ubiquitin-dependent chloroplast-associated protein degradation in plants. *Science* 363:eaav4467. doi: 10.1126/science.aav4467

Ling, Q., Huang, W., Baldwin, A., and Jarvis, P. (2012). Chloroplast biogenesis is regulated by direct action of the ubiquitin-proteasome system. *Science* 338, 655–659. doi: 10.1126/science.1225053

Luttgeharm, K. D., Cahoon, E. B., and Markham, J. E. (2016). Substrate specificity, kinetic properties and inhibition by fumonisin B1 of ceramide synthase isoforms from *Arabidopsis*. *Biochem. J.* 473, 593–603. doi: 10.1042/BJ20150824

Luttgeharm, K. D., Chen, M., Mehra, A., Cahoon, R. E., Markham, J. E., and Cahoon, E. B. (2015). Overexpression of *Arabidopsis* ceramide synthases differentially affects growth, sphingolipid metabolism, programmed cell death, and mycotoxin resistance. *Plant Physiol.* 169, 1108–1117. doi: 10.1104/pp.15.00987

Maatta, S., Scheu, B., Roth, M. R., Tamura, P., Li, M., Williams, T. D., et al. (2012). Levels of *Arabidopsis thaliana* leaf phosphatidic acids, phosphatidylserines, and most trienoate-containing polar lipid molecular species increase during the dark period of the diurnal cycle. *Front. Plant Sci.* 3:49. doi: 10.3389/fpls.2012.00049

Mahmood, K., El-Kereamy, A., Kim, S. H., Nambara, E., and Rothstein, S. J. (2016). ANAC032 positively regulates age-dependent and stress-induced senescence in *Arabidopsis thaliana*. *Plant Cell Physiol.* 57, 2029–2046. doi: 10.1093/pcp/pcw120

Markham, J. E., Lynch, D. V., Napier, J. A., Dunn, T. M., and Cahoon, E. B. (2013). Plant sphingolipids: function follows form. *Curr. Opin. Plant Biol.* 16, 350–357. doi: 10.1016/j.pbi.2013.02.009

Markham, J. E., Molino, D., Gissot, L., Bellec, Y., Hématy, K., Marion, J., et al. (2011). Sphingolipids containing very-long-chain fatty acids define a secretory pathway for specific polar plasma membrane protein targeting in *Arabidopsis*. *Plant Cell* 23, 2362–2378. doi: 10.1105/tpc.110.080473

Maschietto, V., Marocco, A., Malachova, A., and Lanubile, A. (2015). Resistance to *Fusarium verticillioides* and fumonisin accumulation in maize inbred lines involves an earlier and enhanced expression of lipoxygenase (LOX) genes. *J. Plant Physiol.* 188, 9–18. doi: 10.1016/j.jplph.2015.09.003

Mase, K., Ishihama, N., Mori, H., Takahashi, H., Kaminaka, H., Kodama, M., et al. (2013). Ethylene-responsive AP2/ERF transcription factor MACD1 participates in phytotoxin-triggered programmed cell death. *Mol. Plant Microbe Interact.* 26, 868–879. doi: 10.1094/MPMI-10-12-0253-R

Mittler, R. (2017). ROS are good. *Trends Plant Sci.* 22, 11–19. doi: 10.1016/j.tplants.2016.08.002

Molino, D., Van der Giessen, E., Gissot, L., Hematy, K., Marion, J., Barthelemy, J., et al. (2014). Inhibition of very long acyl chain sphingolipid synthesis modifies membrane dynamics during plant cytokinesis. *Biochim. Biophys. Acta* 1842, 1422–1430. doi: 10.1016/j.bbalip.2014.06.014

Mosblech, A., Feussner, I., and Heilmann, I. (2009). Oxylipins: structurally diverse metabolites from fatty acid oxidation. *Plant Physiol. Bioch.* 47, 511–517. doi: 10.1016/j.plaphy.2008.12.011

Munch, D., Teh, O. K., Malinovsky, F. G., Liu, Q., Vetukuri, R. R., El Kasmi, F., et al. (2015). Retromer contributes to immunity-associated cell death in *Arabidopsis*. *Plant Cell* 27, 463–479. doi: 10.1105/tpc.114.132043

Nagano, M., Ihara-Ohori, Y., Imai, H., Inada, N., Fujimoto, M., Tsutsumi, N., et al. (2009). Functional association of cell death suppressor, *Arabidopsis* Bax inhibitor-1, with fatty acid 2-hydroxylation through cytochrome b (5). *Plant J.* 58, 122–134. doi: 10.1111/j.1365-313X.2008.03765.x

Nagano, M., Ishikawa, T., Ogawa, Y., Iwabuchi, M., Nakasone, A., Shimamoto, K., et al. (2014). *Arabidopsis* Bax inhibitor-1 promotes sphingolipid synthesis during cold stress by interacting with ceramide-modifying enzymes. *Planta* 240, 77–89. doi: 10.1007/s00425-014-2065-7

Nagano, M., Kakuta, C., Fukao, Y., Fujiwara, M., Uchimiya, H., and Kawai-Yamada, M. (2019). *Arabidopsis* Bax inhibitor-1 interacts with enzymes related to very-long-chain fatty acid synthesis. *J. Plant Res.* 132, 131–143. doi: 10.1007/s10265-018-01081-8

Nakagawa, N., Kato, M., Takahashi, Y., Shimazaki, K., Tamura, K., Tokuji, Y., et al. (2012). Degradation of long-chain base 1-phosphate (LCBP) in *Arabidopsis*: functional characterization of LCBP phosphatase involved in the dehydration stress response. *J. Plant Res.* 125, 439–449. doi: 10.1007/s10265-011-0451-9

Ormancey, M., Thuleau, P., van der Hoorn, R. A. L., Grat, S., Testard, A., Kamal, K. Y., et al. (2019). Sphingolipid-induced cell death in *Arabidopsis* is negatively regulated by the papain-like cysteine protease RD21. *Plant Sci.* 280, 12–17. doi: 10.1016/j.plantsci.2018.10.028

Pan, R., Satkovich, J., Chen, C., and Hu, J. (2018). The E3 ubiquitin ligase SP1-like 1 plays a positive role in peroxisome biogenesis in *Arabidopsis*. *Plant J.* 94, 836–846. doi: 10.1111/tpj.13900

Pan, R., Satkovich, J., and Hu, J. (2016). E3 ubiquitin ligase SP1 regulates peroxisome biogenesis in *Arabidopsis*. *Proc. Natl. Acad. Sci. U.S.A.* 113, E7307–E7316. doi: 10.1073/pnas.1613530113

Pata, M. O., Hannun, Y. A., and Ng, C. K. (2010). Plant sphingolipids: decoding the enigma of the Sphinx. *New Phytol.* 185, 611–630. doi: 10.1111/j.1469-8137.2009.03123.x

Peer, M., Stegmann, M., Mueller, M. J., and Waller, F. (2010). Pseudomonas syringae infection triggers de novo synthesis of phytosphingosine from sphinganine in *Arabidopsis thaliana*. *FEBS Lett.* 584, 4053–4056. doi: 10.1016/j.febslet.2010.08.027

Picot, A., Barreau, C., Pinson-Gadais, L., Caron, D., Lannou, C., and Richard-Forget, F. (2010). Factors of the *Fusarium verticillioides*-maize environment modulating fumonisin production. *Curr. Opin. Microbiol.* 36, 221–231. doi: 10.3109/10408411003720209

Pieterse, C. M. J., Leon-Reyes, A., Van der Ent, S., and Van Wees, S. C. M. (2009). Networking by small-molecule hormones in plant immunity. *Nat. Chem. Biol.* 5, 308–316. doi: 10.1038/nchembio.164

Proctor, R. H., Desjardins, A. E., Plattner, R. D., and Hohn, T. M. (1999). A polyketide synthase gene required for biosynthesis of fumonisin mycotoxins in Gibberella fujikuroi mating population A. *Fungal Genet. Biol.* 27, 100–112. doi: 10.1006/fgbi.1999.1141

Proctor, R. H., Brown, D. W., Plattner, R. D., and Desjardins, A. E. (2003). Co-expression of 15 contiguous genes delineates a fumonisin biosynthetic gene cluster in Gibberella moniliformis. *Fungal Genet. Biol.* 38, 237–249. doi: 10.1016/S1087-1845(02)00525-X

Plett, J. M., Cvetkovska, M., Makenson, P., Xing, T., and Regan, S. (2009). *Arabidopsis* ethylene receptors have different roles in fumonisin B1-induced cell death. *Physiol. Mol. Plant Pathol.* 74, 18–26. doi: 10.1016/j.pmpp.2009.08.004

Qin, X., Zhang, R. X., Ge, S., Zhou, T., and Liang, Y. K. (2017). Sphingosine kinase AtSPHK1 functions in fumonisin B1-triggered cell death in *Arabidopsis*. *Plant Physiol. Bioch.* 119, 70–80. doi: 10.1016/j.plaphy.2017.08.008

Ren, B., Chen, Q., Hong, S., Zhao, W., Feng, J., Feng, H., et al. (2013). The *Arabidopsis* eukaryotic translation initiation factor eIF5A-2 regulates root protoxylem development by modulating cytokinin signaling. *Plant Cell* 25, 3841–3857. doi: 10.1105/tpc.113.116236

Rheeder, J. P., Marasas, W. F. O., and Vismer, H. F. (2002). Production of fumonisin analogs by *Fusarium* Species. *Appl. Environ. Microb.* 68, 2101–2105. doi: 10.1128/AEM.68.5.2101-2105-2002

Riley, R. T., and Merrill, A. H. (2019). Ceramide synthase inhibition by fumonisins: a perfect storm of perturbed sphingolipid metabolism, signaling, and disease. *J. Lipid Res.* 60, 1183–1189. doi: 10.1194/jlr.S093815

Ritzenthaler, C., Nebenführ, A., Movafeghi, A., Stussi-Garaud, C., Behnia, L., Pimpl, P., et al. (2002). Reevaluation of the effects of Brefeldin A on plant cells using Tobacco Bright Yellow 2 cells expressing Golgi-targeted green fluorescent protein and COPI Antisera. *Plant Cell* 14, 237–261. doi: 10.1105/tpc.010237

Rotari, V. I., He, R., and Gallois, P. (2005). Death by proteases in plants: whodunit. *Physiol. Plantarum* 123, 376–385. doi: 10.1111/j.1399-3054.2005.00465.x

Saucedo-García, M., González-Solís, A., Rodríguez-Mejía, P., Olivera, M. T., Vazquez Santana, S., Cahoon, E., et al. (2011a). Reactive oxygen species as transducers of sphinganine-mediated cell death pathway. *Plant Signal Behav.* 6, 1616–1619. doi: 10.4161/psb.6.10.16981

Saucedo-García, M., Guevara-García, A., González-Solís, A., Cruz-García, F., Vázquez-Santana, S., Markham, J. E., et al. (2011b). MPK6, sphinganine and the LCB2a gene from serine palmitoyltransferase are required in the signaling pathway that mediates cell death induced by long chain bases in *Arabidopsis*. *New Phytol.* 191, 943–957. doi: 10.1111/j.1469-8137.2011.03727.x

Schulte-Zweckel, J., Schneidewind, T., Abad, J. L., Brockmeyer, A., Janning, P., and Triola, G. (2018). Azide-tagged sphingolipids for the proteome-wide identification of C16-ceramide-binding proteins. *Chem. Commun.* 54, 13742–13745. doi: 10.1039/C8CC05691A

Shao, Z., Zhao, Y., Liu, L., Chen, S., Li, C., Meng, F., et al. (2019). Overexpression of *FBR41* enhances resistance to sphinganine analog mycotoxin-induced cell death and *Alternaria* stem canker in tomato. *Plant Biotechnol. J.* 18, 141–154. doi: 10.1111/pbi.13182

Shi, L., Bielawski, J., Mu, J., Dong, H., Teng, C., Zhang, J., et al. (2007). Involvement of sphingoid bases in mediating reactive oxygen intermediate production and programmed cell death in *Arabidopsis*. *Cell Res.* 17, 1030–1040. doi: 10.1038/cr.2007.100

Smith, S., Kroon, J., Simon, W., Slabas, A., and Chivasa, S. (2015). A novel function for *Arabidopsis* CYCLASE1 in programmed cell death revealed by isobaric tags for relative and absolute quantitation (iTRAQ) analysis of extracellular matrix proteins. *Mol. Cell Proteomics* 14, 1556–1568. doi: 10.1074/mcp.M114.045054

Spassieva, S. D., Markham, J. E., and Hille, J. (2002). The plant disease resistance gene Asc-1 prevents disruption of sphingolipid metabolism during AAL-toxin-induced programmed cell death. *Plant J.* 32, 561–572. doi: 10.1046/j.1365-313X.2002.01444.x

Stone, J. M., Liang, X., Nekl, E. R., and Stiers, J. J. (2005). *Arabidopsis* AtSPL14, a plant-specific SBP-domain transcription factor, participates in plant development and sensitivity to fumonisin B1. *Plant J.* 41, 744–754. doi: 10.1111/j.1365-313X.2005.02334.x

Ternes, P., Feussner, K., Werner, S., Lerche, J., Iven, T., Heilmann, I., et al. (2011). Disruption of the ceramide synthase LOH1 causes spontaneous cell death in *Arabidopsis thaliana*. *New Phytol.* 192, 841–854. doi: 10.1111/j.1469-8137.2011.03852.x

Tsegaye, Y., Richardson, C. G., Bravo, J. E., Mulcahy, B. J., Lynch, D. V., Markham, J. E., et al. (2007). *Arabidopsis* mutants lacking long chain base phosphate lyase are fumonisin-sensitive and accumulate trihydroxy-18:1 long chain base phosphate. *J. Biol. Chem.* 282, 28195–28206. doi: 10.1074/jbc.M705074200

Vick, B. A., and Zimmerman, D. C. (1983). The biosynthesis of jasmonic acid: a physiological role for plant lipoxygenase. *Biochem. Biophys. Res. Commun.* 111, 470–477. doi: 10.1016/0006-291X(83)90330-3

Wang, E., Norred, W. P., Bacon, C. W., Riley, R. T., and Merrill, A. H. (1991). Inhibition of sphingolipid biosynthesis by fumonisins. Implications for diseases associated with *Fusarium moniliforme*. *J. Biol. Chem.* 266, 14486–14490. doi: 10.1016/0014-5793(91)80056-9

Wang, L., Pei, Z., Tian, Y., and He, C. (2005). OsLSD1, a rice zinc finger protein, regulates programmed cell death and callus differentiation. *Mol. Plant Microbe Interact.* 18, 375–384. doi: 10.1094/MPMI-18-0375

Watanabe, N., and Lam, E. (2006). *Arabidopsis* Bax inhibitor-1 functions as an attenuator of biotic and abiotic types of cell death. *Plant J.* 45, 884–894. doi: 10.1111/j.1365-313X.2006.02654.x

Watanabe, N., and Lam, E. (2008). BAX inhibitor-1 modulates endoplasmic reticulum stress-mediated programmed cell death in *Arabidopsis*. *J. Biol. Chem.* 283, 3200–3210. doi: 10.1074/jbc.M706659200

Watanabe, N., and Lam, E. (2011). *Arabidopsis* metacaspase 2d is a positive mediator of cell death induced during biotic and abiotic stresses. *Plant J.* 66, 969–982. doi: 10.1111/j.1365-313X.2011.04554.x

Williams, L. D., Glenn, A. E., Bacon, C. W., Smith, M. A., and Riley, R. T. (2006). Fumonisin production and bioavailability to maize seedlings grown from seeds inoculated with *Fusarium verticillioides* and grown in natural soils. *J. Agr. Food Chem.* 54, 5694–5700. doi: 10.1021/jf0610209

Wu, J. X., Li, J., Liu, Z., Yin, J., Chang, Z. Y., Rong, C., et al. (2015a). The *Arabidopsis* ceramidase AtACER functions in disease resistance and salt tolerance. *Plant J.* 81, 767–780. doi: 10.1111/tpj.12769

Wu, J.-X., Wu, J.-L., Yin, J., Zheng, P., and Yao, N. (2015b). Ethylene modulates sphingolipid synthesis in *Arabidopsis*. *Front. Plant Sci.* 6:1122. doi: 10.3389/fpls.2015.01122

Xie, L. J., Chen, Q. F., Chen, M. X., Yu, L. J., Huang, L., Chen, L., et al. (2015). Unsaturation of very-long-chain ceramides protects plant from hypoxia-induced damages by modulating ethylene signaling in *Arabidopsis*. *PLoS Genet.* 11:e1005143. doi: 10.1371/journal.pgen.1005143

Yanagawa, D., Ishikawa, T., and Imai, H. (2017). Synthesis and degradation of long-chain base phosphates affect fumonisin B1-induced cell death in *Arabidopsis thaliana*. *J. Plant Res.* 130, 571–585. doi: 10.1007/s10265-017-0923-7

Yin, S., Guo, X., Li, J., Fan, L., and Hu, H. (2016). Fumonisin B1 induces autophagic cell death via activation of ERN1-MAPK8/9/10 pathway in monkey kidney MARC-145 cells. *Arch. Toxicol.* 90, 985–996. doi: 10.1007/s00204-015-1514-9

Yin, S., Liu, X., Fan, L., and Hu, H. (2018). Mechanisms of cell death induction by food-borne mycotoxins. *Crit. Rev. Food Sci.* 58, 1406–1417. doi: 10.1080/10408398.2016.1260526

Zeng, H. Y., Zheng, P., Wang, L. Y., Bao, H. N., Sahu, S. K., and Yao, N. (2019). Autophagy in plant immunity. *Adv. Exp. Med. Biol.* 1209, 23–41. doi: 10.1007/978-981-15-0606-2_3

Zhang, X., Wu, Q., Cui, S., Ren, J., Qian, W., Yang, Y., et al. (2015). Hijacking of the jasmonate pathway by the mycotoxin fumonisin B1 (FB1) to initiate programmed cell death in *Arabidopsis* is modulated by RGLG3 and RGLG4. *J. Exp. Bot.* 66, 2709–2721. doi: 10.1093/jxb/erv068

Zhao, Y., Wang, J., Liu, Y., Miao, H., Cai, C., Shao, Z., et al. (2015). Classic myrosinase-dependent degradation of indole glucosinolate attenuates fumonisin B1-induced programmed cell death in *Arabidopsis*. *Plant J.* 81, 920–933. doi: 10.1111/tpj.12778

Zheng, P., Wu, J. X., Sahu, S. K., Zeng, H. Y., Huang, L. Q., Liu, Z., et al. (2018). Loss of alkaline ceramidase inhibits autophagy in *Arabidopsis* and plays an important role during environmental stress response. *Plant Cell Environ.* 41, 837–849. doi: 10.1111/pce.13148

Zheng, Y., Zhan, Q., Shi, T., Liu, J., Zhao, K., and Gao, Y. (2019). The nuclear transporter SAD2 plays a role in calcium- and H2O2 -mediated cell death in *Arabidopsis*. *Plant J.* 101, 324–333. doi: 10.1111/tpj.14544

Zienkiewicz, A., Gömann, J., König, S., Herrfurth, C., Liu, Y. T., Meldau, D., et al. (2019). Disruption of *Arabidopsis* neutral ceramidases 1 and 2 results in specific sphingolipid imbalances triggering different phytohormone-dependent plant cell death programs. *New Phytol.* 228, 170–188. doi: 10.1111/nph.16336

Conflict of Interest: The authors declare that the research was conducted in the absence of any commercial or financial relationships that could be construed as a potential conflict of interest.

Copyright © 2020 Zeng, Li and Yao. This is an open-access article distributed under the terms of the Creative Commons Attribution License (CC BY). The use, distribution or reproduction in other forums is permitted, provided the original author(s) and the copyright owner(s) are credited and that the original publication in this journal is cited, in accordance with accepted academic practice. No use, distribution or reproduction is permitted which does not comply with these terms.

frontiers in Plant Science

ORIGINAL RESEARCH
published: 27 November 2020
doi: 10.3389/fpls.2020.614846

Lipidome Remodeling and Autophagic Respose in the Arachidonic-Acid-Rich Microalga *Lobosphaera incisa* Under Nitrogen and Phosphorous Deprivation

*Kamilya Kokabi[1,2†], Olga Gorelova[3], Boris Zorin[2], Shoshana Didi-Cohen[2], Maxim Itkin[4], Sergey Malitsky[4], Alexei Solovchenko[3,5,6], Sammy Boussiba[2] and Inna Khozin-Goldberg[2]**

[1]The Albert Katz International School for Desert Studies, The Jacob Blaustein Institutes for Desert Research, Ben-Gurion University of the Negev, Midreshet Ben-Gurion, Israel, [2]Microalgal Biotechnology Laboratory, The French Associates Institute for Agriculture and Biotechnology of Drylands, The J. Blaustein Institutes for Desert Research, Ben-Gurion University of the Negev, Sede Boqer Campus, Midreshet Ben-Gurion, Israel, [3]Department of Bioengineering, Faculty of Biology, Moscow State University, GSP-1, Moscow, Russia, [4]Metabolic Profiling Unit, Life Science Core Facilities, Weizmann Institute of Science, Rehovot, Israel, [5]Institute of Natural Sciences, Derzhavin Tambov State University, Tambov, Russia, [6]Peoples Friendship University of Russia (RUDN University), Moscow, Russia

OPEN ACCESS

Edited by:
Eric Marechal,
UMR5168 Laboratoire de Physiologie Cellulaire Vegetale (LPCV), France

Reviewed by:
Alberto Amato,
CEA Grenoble, France
Krzysztof Zienkiewicz,
Nicolaus Copernicus University in Toruń, Poland

***Correspondence:**
Inna Khozin-Goldberg
khozin@bgu.ac.il

†Present address:
Kamilya Kokabi,
Weizmann Institute of Science, Rehovot, Israel

Specialty section:
This article was submitted to Marine and Freshwater Plants, a section of the journal Frontiers in Plant Science

Received: 07 October 2020
Accepted: 02 November 2020
Published: 27 November 2020

Citation:
Kokabi K, Gorelova O, Zorin B, Didi-Cohen S, Itkin M, Malitsky S, Solovchenko A, Boussiba S and Khozin-Goldberg I (2020) Lipidome Remodeling and Autophagic Respose in the Arachidonic-Acid-Rich Microalga Lobosphaera incisa Under Nitrogen and Phosphorous Deprivation. Front. Plant Sci. 11:614846. doi: 10.3389/fpls.2020.614846

The green microalga *Lobosphaera incisa* accumulates triacylglycerols (TAGs) with exceptionally high levels of long-chain polyunsaturated fatty acid (LC-PUFA) arachidonic acid (ARA) under nitrogen (N) deprivation. Phosphorous (P) deprivation induces milder changes in fatty acid composition, cell ultrastructure, and growth performance. We hypothesized that the resource-demanding biosynthesis and sequestration of ARA-rich TAG in lipid droplets (LDs) are associated with the enhancement of catabolic processes, including membrane lipid turnover and autophagic activity. Although this work focuses mainly on N deprivation, a comparative analysis of N and P deprivation responses is included. The results of lipidomic profiling showed a differential impact of N and P deprivation on the reorganization of glycerolipids. The formation of TAG under N deprivation was associated with the enhanced breakdown of chloroplast glycerolipids and the formation of lyso-lipids. N-deprived cells displayed a profound reorganization of cell ultrastructure, including internalization of cellular material into autophagic vacuoles, concomitant with the formation of LDs, while P-deprived cells showed better cellular ultrastructural integrity. The expression of the hallmark autophagy protein ATG8 and the major lipid droplet protein (MLDP) genes were coordinately upregulated, but to different extents under either N or P deprivation. The expression of the Δ5-desaturase gene, involved in the final step of ARA biosynthesis, was coordinated with *ATG8* and *MLDP*, exclusively under N deprivation. Concanamycin A, the inhibitor of vacuolar proteolysis and autophagic flux, suppressed growth and enhanced levels of ATG8 and TAG in N-replete cells. The proportions of ARA in TAG decreased with a concomitant increase in oleic acid under both N-replete and N-deprived conditions. The photosynthetic apparatus's recovery from N deprivation was impaired in the presence of the inhibitor,

along with the delayed LD degradation. The GFP-ATG8 processing assay showed the release of free GFP in N-replete and N-deprived cells, supporting the existence of autophagic flux. This study provides the first insight into the homeostatic role of autophagy in *L. incisa* and points to a possible metabolic link between autophagy and ARA-rich TAG biosynthesis.

Keywords: autophagy, LC-PUFA, lipid, microalgae, nutrient deprivation, triacylglycerol

INTRODUCTION

Microalgae constitute an extremely diverse group of predominantly photosynthetic and aquatic eukaryotic microorganisms with immense biotechnological potential and ecological significance. Dwelling in ever-changing, often harsh, environments, microalgae dynamically respond to variations in nutrient availability. To mitigate nutrient starvation conditions, microalgae arrest their growth, enter a quiescent state, and/or form resilient resting forms for long-term endurance while accumulating storage compounds (Boussiba, 2000; Hu et al., 2008; Dong et al., 2013; Takeuchi and Benning, 2019). Oleaginous species accumulate carbon- and energy-rich reserves in the form of triacylglycerols (TAGs). The production of TAG can be manipulated and enhanced by environmental cues and stress stimuli, such as light and nutrient availability, often by nitrogen (N) deprivation (Hu et al., 2008). Stress-induced TAG accumulation is associated with intensive transcriptional reprograming, metabolome reorganization, membrane lipid remodeling (Hockin et al., 2012; Valledor et al., 2014; Abida et al., 2015; Remmers et al., 2018), and an enhancement in the autophagic response (Martin et al., 1976; Davey et al., 2014; Schatz et al., 2014; Pérez-Pérez et al., 2017; Couso et al., 2018). Under N deprivation, self-cannibalization, scavenging, and recycling of cellular components fuel TAG formation with energy and nutrient requirements. The ultrastructural manifestations of chloroplast degradation, a reduction in cytoplasmic ribosome abundance, and the formation of autophagic vacuoles in the course of lipid droplet (LD) formation were observed in microalgae under various stresses (Zhao et al., 2014; Shebanova et al., 2017; Tsai et al., 2017; Gorelova et al., 2018). Phosphorous (P) deprivation is mitigated by an array of mechanisms, which include membrane lipid remodeling in favor of non-phosphorous lipids, reallocation of cellular C resources, P scavenging from endogenous reserves, and autophagy (Feng et al., 2015; Cañavate et al., 2017; Alipanah et al., 2018; Solovchenko et al., 2019).

Autophagy is a highly conserved and regulated recycling process by which undesired proteins and damaged organelles are degraded in lysosomes (animals) or vacuoles (yeast and plants) to maintain cell homeostasis, survival, and turnover of cellular constituents (see Feng et al., 2014), among others. Recent insights into the mechanisms of autophagy in land plants and photosynthetic microalgae have revealed some distinct features, compared with the process in mammals and yeast (Masclaux-Daubresse et al., 2020). Two major forms of autophagy, macro- and micro-autophagy, have so far been characterized in plants. The analysis of the mutants of the key autophagy-related genes (ATG) has revealed a number of physiological functions attributed to autophagy in the sensing and mobilization of nutrients in plants (Phillips et al., 2008; Avin-Wittenberg et al., 2015; Minina et al., 2018; Chen et al., 2019).

The stress-induced and autophagy-mediated effects in microalgae are of both fundamental and biotechnological importance (Couso et al., 2018; Yoshitake et al., 2019; Kajikawa and Fukuzawa, 2020). The dynamic nature of the micro-algal metabolism, as well as the ways to manipulate it for industrial applications, has attracted significant attention to the study of autophagy's role. Many tools to study autophagy and monitor autophagic flux have been developed and applied in the model microalga *Chlamydomonas reinhardtii*, illuminating the role of autophagy in cell homeostasis under various stresses, including N and P deprivation (Pérez-Pérez et al., 2016; Couso et al., 2018), among others. The isolation of the first *Chlamydomonas* autophagy mutants, lacking ATG8 and ATG3, marked an important milestone in assessing the function of autophagy in response to nutrient stress by genetic means (Kajikawa et al., 2019). Depleting a hallmark autophagy protein, ATG8, reduced cell viability under N deprivation, and, to a lesser extent, under P and S deprivation. Furthermore, autophagy appeared to be important in the early events of TAG mobilization (Kajikawa et al., 2019). Linking chloroplast quality control, autophagy, and lipid metabolism, the pharmaceutical inhibition of fatty acid synthesis promoted chloroplast damage and triggered autophagy (Heredia-Martínez et al., 2018). Further, administration of the vacuolar ATPase inhibitor concanamycin A, which blocks autophagic flux by repressing autophagy-mediated protein degradation, reduced TAG and LD formation in N-starved *C. reinhardtii* (Couso et al., 2018). Alternatively, the induction of autophagy by pharmaceutically inactivating the target of the rapamycin (TOR) kinase (Imamura et al., 2015; Prioretti et al., 2017), or by inhibiting III PI3K VPS34 that acts in autophagy (Zienkiewicz et al., 2020), induced LD formation and enhanced TAG production in the nutrient-replete Chlorophyte and Stramentopile microalgae.

The mechanisms involved in LD formation, mobilization, and degradation are still understudied in microalgae, in particular, the involvement of autophagy. The dual role of autophagy to reciprocally support LD formation and degradation in plants and microalgae has been proposed (Fan et al., 2019; Tran et al., 2019). The autophagic degradation of LDs under carbon starvation was observed in the unicellular charophyte *Micrasterias denticulata* (Schwarz et al., 2017). Autophagy inhibitors were shown to impair LD remobilization upon nutrient resupply to N-deprived microalgae (Nonoyama et al., 2019; Zienkiewicz et al., 2020). However, further studies in diverse species are obviously needed to clarify whether LDs

can be degraded by autophagy-dependent (lipophagy) or independent mechanisms (lipolysis), or both, as suggested in other systems (Schulze et al., 2017).

The present study emerged from our previous work, which reported differential physiological and metabolic responses of the green oleaginous microalga *Lobosphaera incisa* to N and P deprivation. This chlorophyte uniquely accumulates TAG with a high content of the omega-6 long-chain polyunsaturated fatty acid (LC-PUFA) arachidonic acid (ARA, 20:4*n*-6) in the cytoplasmic LDs, under N deprivation. The enhanced biosynthesis and sequestration of ARA in reserve lipids require intensive metabolic expenditures (Kokabi et al., 2019). Upon nutrient replenishment, N-starved cells of *L. incisa* degrade LDs, hydrolyze TAG and remobilize a fraction of ARA-rich TAG to rapidly restore the unsaturation level of chloroplast membrane lipids (Khozin-Goldberg et al., 2005). The assortment of TAG lipases (Siegler et al., 2017), associated with LDs in N-starved *L. incisa*, has recently been identified, presumably contributing differentially to TAG lipolysis under N deprivation or repletion. Although this work mainly focuses on N deprivation, we combined ultrastructural, lipidomics, and some biochemical analyses to comparatively assess some aspects of N and P deprivation responses. We suggested that ARA-rich TAG biosynthesis involves the concerted deployment of catabolic activities to support the metabolic costs associated with ARA biosynthesis and endogenous resource repurposing. Here, we provide several pieces of evidence on the involvement and importance of autophagy in cellular homeostasis and, in general, in ARA-rich TAG accumulation under N deprivation, in particular.

MATERIALS AND METHODS

Algal Strain and Experimental Conditions

Lobosphaera incisa (SAG 2468) was cultivated in a modified BG-11 medium in a semi-continuous mode in 250-ml glass flasks placed in an illuminated incubator shaker (New Brunswick G-25, Edison, NJ, United States) in a CO_2-enriched atmosphere at 25°C, as previously described (Kokabi et al., 2019). For nutrient-deprivation experiments, the cells from regularly diluted replete cultures were collected by centrifugation, washed twice with double-distilled water, and resuspended in mBG-11 lacking either a N source (sodium nitrate) or a P source (K_2HPO_4 and KH_2PO_4) to an initial chlorophyll content of 30 mg l^{-1} (approximately 1 mg l^{-1} dry weight). Control cultures were grown in complete mBG-11. For recovery from N and P deprivation, cells were collected by centrifugation after 10 days of cultivation, washed, and resuspended in nutrient-replete mBG-11 to an initial chlorophyll content of 15 mg l^{-1}. For nutrient deprivation experiments, cells were withdrawn at the logarithmic stage and resuspended in N-depleted or P-depleted mBG-11 media. When indicated, the cultures were supplemented with concanamycin A (Cayman) from a stock solution in DMSO (1 mM); an equal volume of DMSO was added to the control cultures serving as the vehicle control.

Determination of Fatty Acid Composition and Content

Fatty acid composition and content were determined following direct transmethylation of freeze-dried biomass and isolated TAG in dry methanol containing 2% (v/v) sulfuric acid at 80°C for 1.5 h under an argon atmosphere, using heptadecanoic acid 17:0 as an internal standard. Fatty acid methyl esters (FAME) were resolved by gas chromatography on a Trace GC ultra (Thermo Fisher Scientific, Milan, Italy) equipped with a flame-ionization detector (FID; Pal-Nath et al., 2017).

Lipid Extraction and TAG Analysis

Lipids were extracted from lyophilized biomass, and total lipid extracts were resolved by one-dimensional thin-layer chromatography TLC on silica-gel plates (Silica Gel 60, 10 × 10 cm, 0.25-mm thickness, Merck, Darmstadt, Germany) to isolate TAG. Extraction, analysis of TAG, and fatty acid quantification were performed by GC-FID (Zorin et al., 2017).

Lipidomics Profiling by LC-MS

Biomass samples were extracted with a methanol:methyl tert-butyl ether (MTBE) mixture as described by Malitsky et al. (2016), containing the following internal standards: 0.1 μg ml^{-1} phosphatidylcholine 34:0 (17:0/17:0), 0.1 μg ml^{-1} phosphoethanolamine 34:0 (17:0/17:0), 0.15 nmol ml^{-1} of LM6002, and LM6005 d5TG (Merck) standard mix. Post-extraction, the organic phase, containing lipids, was analyzed using a Waters ACQUITY UPLC system coupled to a Vion IMS QTof mass spectrometer (Waters Corp., MA, United States). Chromatographic conditions were as described by Malitsky et al. (2016) with small modifications. Briefly, the chromatographic separation was performed on an ACQUITY UPLC BEH C8 column (2.1 × 100 mm, i.d., 1.7 μm; Waters Corp., MA, United States). Mobile phase A consisted of 45% water (UPLC grade) with 1% 1 M NH_4Ac, 0.1% acetic acid, and 55% acetonitrile:isopropanol (7:3) with 1% 1 M NH_4Ac, 0.1% acetic acid (mobile phase B). The column was maintained at 40°C, and the mobile phase flow rate was 0.4 ml min^{-1}. Mobile phase A was run for 1 min at 100%; then, it was gradually reduced to 25% at 12 min, followed by a decrease to 0% at 16 min. Then, mobile phase B was run at 100% for 21 min, and mobile phase A was set to 100% at 21.5 min. Finally, a column was equilibrated at 100% of mobile phase A for 25 min. The MS parameters were as follows: the source and de-solvation temperatures were maintained at 120 and 450°C, respectively. The capillary voltage was set at 3.0 and 2 kV for the positive and negative ionization modes, respectively; cone voltage was set at 40 V. Nitrogen was used as a de-solvation gas and cone gas at the flow rates of 800 and 30 L h^{-1}, respectively. The mass spectrometer was operated in the full scan MS^E positive resolution mode over a mass range of 50–1800 Da. For the high energy scan function, a collision energy ramp of 20–60 eV was applied; for the low energy scan function, −4 eV was applied. Leucine-enkephalin was used as a lock-mass reference standard.

Lipid Species Identification and Relative Normalization

LC-MS data were analyzed and processed with UNIFI (Version 1.9.2, Waters Corp., MA, United States). The putative identification of the different lipid species was performed by a comparison of accurate mass, fragmentation pattern, and ion mobility (CCS) values with an in-house-made lipid database, in which several lipids were identified vs. standards, when available. Further annotation of the lipids was based on the correlation between the retention time (RT) and the carbon chain length and degree of unsaturation. Validation of the putative lipid identification was performed by a comparison with a home-made library, which contains lipids produced by various organisms. Relative lipid levels were normalized to the internal standards (see Lipid Species Identification and Relative Normalization) and the amount of tissue used for analysis.

Electron Microscopy

Cells for TEM were harvested from approximately 5-ml culture aliquots. The fixation, dehydration, embedding, and staining procedures were described by Kokabi et al. (2019). Ultra-thin sections (60–90 nm) were observed and imaged under an FEI Tecnai 12 (FEI, OR, United States) or a JEM-1011 (JEOL, Tokyo, Japan) transmission electron microscope (TEM) for the ultrastructural analysis.

The samples for nanoscale elemental analysis in analytical TEM using EDX were fixed, dehydrated, and embedded in araldite (Electron Microscopy Sciences, United States) as described above. Ultra-thin sections for energy-dispersive X-ray spectroscopy (EDX) analysis were examined under a JEM-2100 (JEOL, Tokyo, Japan) microscope equipped with a LaB_6 gun at the accelerating voltage of 200 kV. Point EDX spectra were recorded using a JEOL bright-field scanning TEM (STEM) module and an X-Max X-ray detector system with an ultra-thin window, capable of analyzing light elements, starting from boron (Oxford Instruments, High Wycombe, UK). The energy range of the recorded spectra was 0–10 keV with a resolution of 10 eV per channel. Spectra were background-corrected and further processed with INKA software (Oxford Instruments). Quantitative morphometric analysis of TEM micrographs was performed using Zen software (Carl Zeiss Microscopy GmbH).

Fluorescence and Immunofluorescence Microscopy

Nile Red (NR) staining (Sigma-Aldrich) and imaging of LDs was performed as described by Kokabi et al. (2019). For the immunofluorescence detection of *Li*ATG8, the cells were collected by centrifugation (3,000 rpm for 1 min) from approximately 2-ml aliquots of regularly diluted culture grown in the replete medium. The pellet was fixed with 4% paraformaldehyde in phosphate-buffered saline (PBS) for 20 min at room temperature (RT), and then rinsed three times with PBS. The cells were permeabilized with 1% Triton X-100 in PBS for 10 min at RT. After blocking with 2% bovine serum albumin in PBS for 30 min, cells were labeled at RT for 1 h with anti-ATG8 antibody diluted to 1:200 in a blocking solution. The cells were rinsed three times with PBS and incubated with secondary antibody Alexa Fluor 488 donkey anti-rabbit IgG (Jackson IR Laboratories) at a dilution of 1:500 for 40 min. After washing three times, cells were observed under a Zeiss LSM 880 Axio Observer laser scanning confocal microscope using an alpha Plan-Apochromat 63×/1.4 Oil DIC M27 objective. Images were analyzed by Zen Blue software (Zeiss).

RNA and DNA Isolation, cDNA Synthesis, and Quantitative Real-Time PCR

Total RNA was isolated from the cell pellets placed in 2-ml Eppendorf safe-lock tubes and snap-frozen in liquid N_2. Frozen cells were disrupted by using 2.5-mm iron beads in a Retsch MM400 tissue homogenizer in 7–8 cycles of 45 s at 25 Hz, and placing tubes in liquid N_2 between cycles. An SV Total RNA isolation kit (Promega, Madison, WI, United States) was used, according to the manufacturer's protocol. The genomic DNA isolation was performed as described by Zorin et al. (2014). cDNA was synthesized by a Verso cDNA synthesis kit (Thermo Fisher Scientific) on a 500-ng aliquot of total RNA pre-heated at 70°C for 5 min to eliminate secondary structures. The qRT-PCR was performed with iTaq Universal SYBR Green Supermix (Bio-Rad Laboratories, Hercules, CA, United States) on a CFX96 Touch Real-Time PCR Detection System (Bio-Rad, Hercules, CA, United States). Genes that were constitutively expressed under N starvation were used as reference genes after confirming their stable expression. The primers used in this study are listed in **Supplementary Table S1**. The primers used in qRT-PCR were tested for amplification efficiency (95–100%) by generating calibration curves. Gene expression was quantified by the ΔΔCq method in CFX Manager Software (Bio-Rad).

Plasmid Construction for GFP-ATG8 Tagging

To create the N-terminal fusion of GFP to the ATG8 gene, the entire genomic sequence of ATG8, including the promoter (269 bp) and terminator (508 bp) regions, was amplified by PCR using a Phusion High-Fidelity DNA-polymerase (BioLAbs New England, United States). The primers were designed to introduce *SpeI* restriction sites for further manipulation (**Supplementary Table S1**). The PCR product of expected size was purified from agarose using a Zymoclean Gel DNA Recovery Kit and inserted into the pJet-AHAS plasmid using isoschizomer *XbaI* and *SpeI* enzymes. The plasmid contained the mutated sequence of the *L. incisa* acetohydroxyacid synthase (AHAS) gene, conferring resistance to the herbicide sulfometuron methyl (SMM), as an endogenous selection marker (Grundman et al., 2012). The PCR-amplified codon-optimized eGFP (Genescript) without a stop codon and the linearized vector with the inserted *Li*ATG8 gene were obtained with 15-bp overlaps at their 5' and 3' ends. The fragments were ligated using an In-Fusion HD Cloning Kit (Takara Clontech, United State) according to the manufacturer's protocols. *Escherichia coli* strain Zymo 5α competent cells were used for cloning, and transformation procedures were performed with a Mix & Go Kit (Zymo Research, United States). Transformed colonies were selected

based on ampicillin resistance and examined for the presence of inserts using an on-colony PCR. Plasmids were purified from *E. coli* cultures using a Midi Plasmid Kit (Geneaid Biotech Ltd., Taiwan).

Nuclear Transformation of *L. incisa*

The nuclear transformation was performed by electroporation using a Gene Pulser XCell apparatus (Bio-Rad, CA, United States) as described by Zorin et al. (2014). Transformed cells were plated on modified LB agar plates, supplemented with 30 μM SMM and grown at 25°C and a light intensity of 35 μmol photons m^{-2} s^{-1}. After the second sub-culturing under selection pressure, transgene integration was verified by PCR.

Detection of the GFP-Tagged *Li*ATG8 Protein by Confocal Microscopy

Confocal microscopy was conducted using a Zeiss LSM 510 Meta confocal microscope equipped with AIM 4.2 software. In order to visualize the GFP signal in *L. incisa* cells, we used a Plan-Apochromat 63×/1.4 oil objective with an argon laser (488 nm). To diminish the background and chlorophyll autofluorescence, the signal was collected using a 505/50 emission filter. Image analysis was conducted using Zeiss LSM Image Examiner (Version 3.5.0.359) software.

Protein Preparation and Western Blot Analysis

The culture aliquots of WT *L. incisa* or transformants expressing GFP-ATG8 were collected by centrifugation at 3,000 rpm for 5 min. The pellet was washed twice with double-distilled water (DDW) and stored at −80°C for further use. The total protein extraction was performed from 2 to 5 mg of dry weight (DW) by grinding frozen biomass in liquid nitrogen with a mortar and pestle with a minimal amount of extraction buffer [1.25 mM EDTA, 250 mM Tris-HCl pH 7.5, 250 mM sucrose, 4 mM dithiothreitol (DTT), 14.3 mM glutathione (GSH), and 1 × protease inhibitor cocktail (P9599; all reagents were from Sigma-Aldrich]. The homogenate was centrifuged at 13,000 rpm for 15 min at 4°C, and the protein content in the supernatant was estimated by Bradford assay (Bio-Rad). Western blot analysis was performed on the protein extracts of the samples collected at the specified time points, using the primary anti-CrATG8 (Agrisera) or anti-GFP (Evrogen, Russia) antibodies. Either 2 or 5 μg of total proteins was loaded into each well and separated on a 15 or 10% SDS-PAGE gel for detection of ATG8 or GFP, respectively. The proteins were transferred from the gel onto a nitrocellulose 0.2-μm membrane (BioRad) for 45 min at 120 V. The membrane was incubated with 5% nonfat milk in 1 × phosphate-buffered saline (PBS) with 0.5% Tween-20 (PBS-T) for 1 h at room temperature (RT), and then incubated with either an anti-CrATG8 or anti-GFP antibody with 1:1,000 dilution at 4°C overnight. The membrane was washed three times with PBS-T and incubated with an anti-rabbit secondary (BioRad) antibody at 1:10,000 dilutions for 1 h at room temperature. The blot was washed three times and developed with the chemiluminescence detection kit for HRP (EZ-ECL Kit, Biological Industries, BI-20-500-120) according to the manufacturer's protocols.

Statistical Analysis

Student's *t*-test was used to determine statistically significant differences. Significance was determined at $p < 0.05$. The webserver MetaboAnalyst 4.0 (Chong et al., 2018) was used for statistical analysis of lipidomics data to compare changes in lipid species among treatments. The data were filtered by relative standard deviation (RSD = SD/mean), auto-scaled, log-transformed, and normalized. Significant differences were determined using ANOVA with a Tukey *post hoc* test. FDR adjusted $p < 0.05$ were used to account for multiple comparisons.

RESULTS

Ultrastructural Modifications in the Course of N and P Deprivation

In our prior work, some ultrastructural features of *L. incisa*, under nutrient-replete conditions and after 3 days of N and P deprivation have been described (Kokabi et al., 2019). Here, using TEM, we mainly focused on the dynamics of vacuoles and vacuole-like structures, including their inclusions and interactions with LDs under N deprivation and following nutrient resupply. The replete cells of *L. incisa* harbor a variety of acidic vacuoles and vacuole-like structures of diverse sizes and shapes, containing various inclusions, predominantly polyphosphate (polyP), and N-containing granules (Kokabi et al., 2019; **Figures 1A,B**). We assumed that the abundant organelles housing polyP granules may mirror the acidocalcisomes described in microorganisms and microalgae (Goodenough et al., 2019). We also observed vacuoles lacking polyP granules, for instance, sequestering the portions of the cytoplasm with ribosomes in young daughter cells (**Figure 1C**), harboring the multiple twisted-strand structures (**Figure 1D**), or including non-homogeneous electron density (**Figures 1E–H**). Notably, the small cytoplasmic LDs in N-replete cells were often located in close proximity to the vacuoles, and even seemed to be partially engulfed by them (**Figures 1A,B,E,G,H**).

The cell ultrastructure was drastically altered after exposure to N deprivation. The main changes, 12 h following the transfer to the N-deprived medium, included the fusion of vacuoles (**Figure 2A**), the partial degradation of granular bodies in vacuole interiors (**Figures 2A–D**), and the increased diversity of vacuolar inclusions (**Figures 2B–D**). Vacuoles with membranous debris visible as multi-lamellar structures were observed. Similarly, autophagic vacuoles, with various cargo material and debris have been described in N-starved *C. reinhardtii* (Goodenough et al., 2014), *Dunaliella salina* (Polle et al., 2020), and Cd^{2+}-stressed *Micrasterias denticulata* (Andosch et al., 2012). Autophagy-related vacuoles, containing membrane debris, can be distinguished from acidocalcisomes using advanced microscopic methods, such as quick-freeze deep-etch electron microscopy, and their appearance generally coincides with the expression of genes associated with autophagy (Goodenough et al., 2014, 2019).

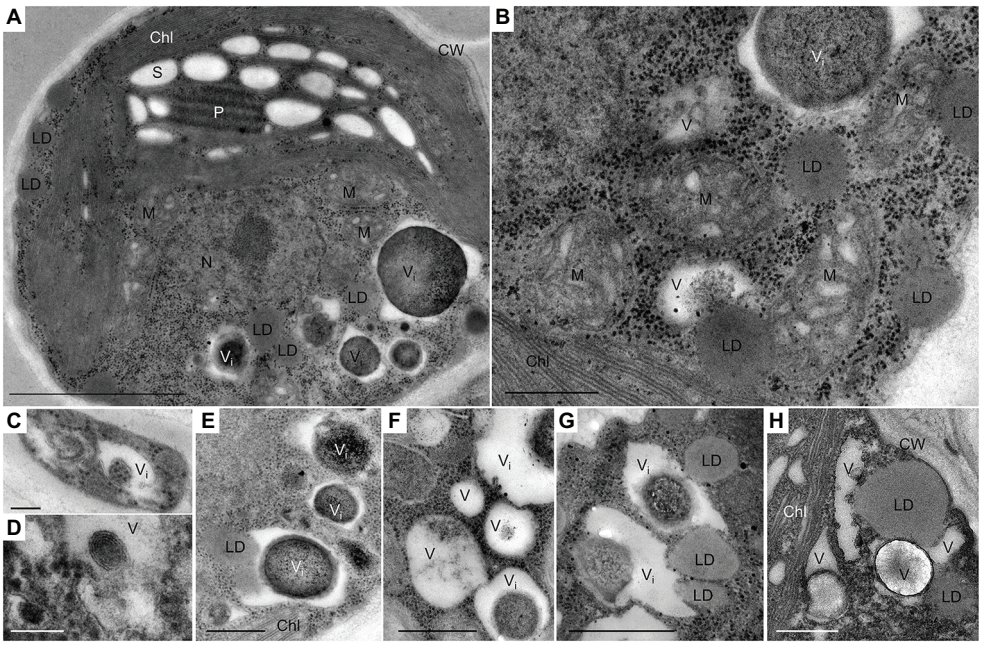

FIGURE 1 | Transmission electron micrographs of *L. incisa* cells in the logarithmic growth stage. **(A)** General cell ultrastructure and **(B)** different cytoplasmic components; **(C–H)** vacuoles and vacuole-like structures with different inclusions. LD-vacuole interactions, as indicated by their close special association **(E,G,H)**. Chl, chloroplast; S, starch granules; CW, cell wall; LD, lipid droplet; P, pyrenoid; M, mitochondria; N, nucleus; V, vacuole; Vi, vacuole with electron-dense inclusion. Scale bars in **(A)** = 1 μm, **(B,E–H)** = 0.5 μm, and **(C,D)** = 0.1 μm.

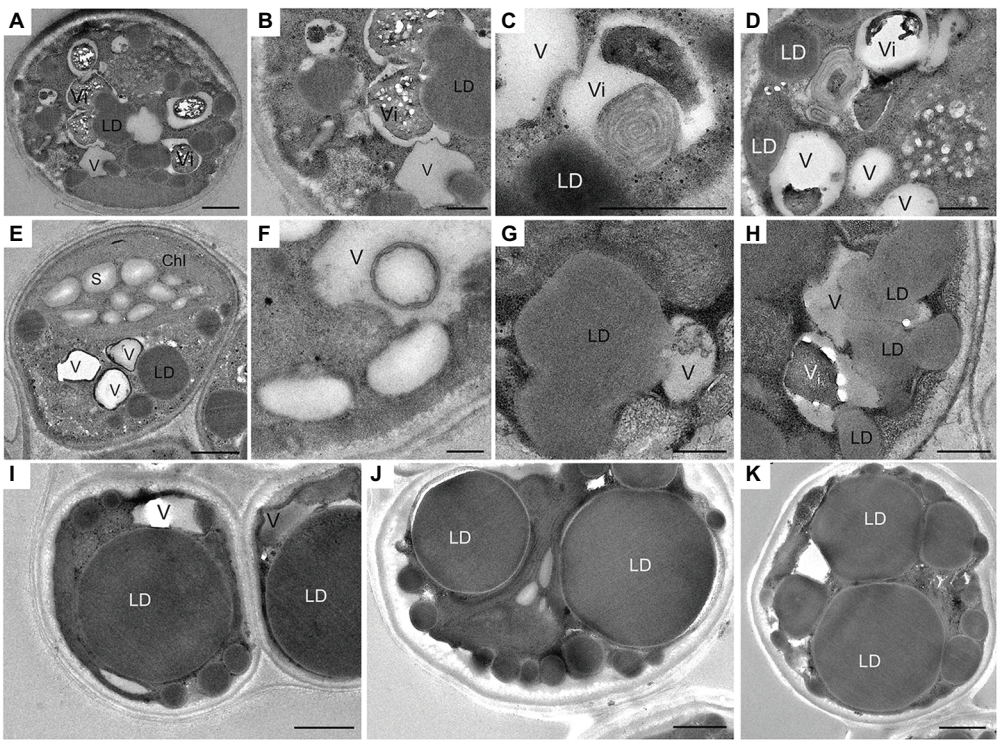

FIGURE 2 | Ultrastructural changes in *L. incisa* cells under N deprivation: **(A–D)** N-deprived cell after 12 h; **(E,F)** 24 h; **(G,H)** 48 h; **(I–K)** 10 days. LD, lipid droplet; V, vacuole; Vi, vacuole with electron-dense inclusion; Chl, chloroplast; S, starch granules. Scale bars in **(A,I,J,H)** = 1 μm and **(B–G,K)** = 0.5 μm.

Numerous cytoplasmic LDs were formed with the progression of N deprivation, while the vacuole abundance decreased (**Table 1**; all vacuole-like structures were considered). During their expansion and growth, LDs frequently showed a close special association with vacuoles and even seemed to appear inside the vacuolar lumen (**Figure 2**). After 10 days of N deprivation, LDs occupied over 50% of the cell volume; starch granules were observed near the partially lysed pyrenoid in the abridged chloroplast (not shown), while the vacuoles became fewer and empty, and the abundance of cytoplasmic components decreased (**Figure 2I**). N deprivation led to more severe growth retardation than P deprivation and was associated with a concomitant decline in the photosynthetic pigment content and chloroplast dismantling (Kokabi et al., 2019). Indeed, P-deprived cells (**Figure 3**) displayed fewer LDs and a far better integrity of the chloroplast and cytoplasmic components. A distinct feature of P-deprived cells was the structure of vacuolar inclusions, showing multiple twisted strands connected to the tonoplast (**Figure 3**), presumably consisting of polyP chains combined with N-containing material (**Figure 3M**).

After 10 days of N deprivation, nutrients were replenished by resuspending the cells in the replete medium, and cells were observed at TEM. After 24 h, a fraction of LDs fragmented into smaller ones (**Figure 4**). The partial enclosure of LDs with vacuole-like structures and degradation at LD-vacuole contact sites resembled a macroautophagy-like process observed in the oleaginous microalga *Nannochloropsis oceanica* and *Arabidopsis thaliana* leaves (Tsai et al., 2014; Fan et al., 2019). Notably, the core of degrading LDs displayed an inhomogeneous electron density, suggesting compositional transitions in the TAG. Along with an increase in their number, the emerging and initially visibly empty vacuoles filled up with electron-dense material. N and P peaks in the point spectra of vacuolar inclusions were detected by EDX in a STEM mode (**Figure 4E**), suggesting an acquisition of N and P by vacuoles after nutrient replenishment. Given certain limitations of the EDX analysis on the resin-embedded samples, it was used to distinguish inclusions containing both N and P from those containing only P (in addition to O and C; Ismagulova et al., 2018). EDX did not detect Ca in the vacuoles of replenished cells (as in replete cells), but interestingly, Ca and Na signals were also found to be associated with degrading LDs, regardless of the LD-core osmophilicity (**Figure 4F**). We speculate that the Ca signal may be due to the LD-associated Ca-binding protein caleosin identified in the *L. incisa* LD proteome (Siegler et al., 2017), and whose possible function in LD degradation will be discussed later. The chloroplast and chlorophyll production recovered by day 2–3, following nutrient resupply (Kokabi et al., 2019; section Pharmaceutical Treatment with Concanamycin A Impairs ARA Biosynthesis).

TABLE 1 | Morphometric analysis of vacuoles and lipid droplets in nutrient-replete and N-deprived (2 days-N) *L. incisa* cells.

Time point	Vacuole per cell		LD per cell	
	Number	Diameter (μm)	Number	Diameter (μm)
Time 0	4.6 (±0.28)	0.80 (±0.04)	2.5 (±0.36)	0.31 (±0.05)
2d-N	3.05 (±0.23)	0.82 (±0.08)	10.7 (±0.31)	0.78 (±0.06)

Quantification analysis was carried out from 20 TEM images at each time point.

Comparative Lipidomics Profiling Under N and P Deprivation

Lobosphaera incisa's fatty acid and glycerolipid composition responded differently to N and P deprivation (Kokabi et al., 2019). In this report, the LC-MS-based lipidomics profiling in a semi-quantitative mode was performed to depict additional features pertaining to the differential impacts of P and N deprivation on the TAG biosynthesis and membrane lipid remodeling. The relative abundance of lipid molecular species was determined using internal standards and normalization to dry weight after 3 days of P and N deprivation, as compared with time 0 and 3 days of nutrient-replete conditions (+N+P). The results showed extensive rearrangements in the profile of structural and storage glycerolipids. The lipidome of N-deprived cells (3d-N) differed significantly from P-deprived (3d−P) and control (3d+N+P) cells. A principal component analysis (PCA), performed on all lipids detected in a negative mode, demonstrated that a high level of variation in the lipidome (58.5%) among conditions can be explained by the first component (PC1; **Supplementary Figure S1**). To enable comparison among lipid species and conditions, the relative abundance of significantly different species was normalized and visualized using heatmaps (**Figures 5, 6**).

Similarities and specific nutrient-deprivation differences in the relative abundance of polar and neutral glycerolipids were examined. A distinct pattern of the polar lipidome remodeling under P deprivation, compared with N deprivation, was reflected in the far lesser extent of reorganization (**Figure 5**). The abundance of most of the detected chloroplast MGDG and SQDG species significantly decreased, while an increase in the number of DGDG species, and in particular, the accumulation of lyso-MGDGs and lyso-DGDGs, constituted a distinctive response to N deprivation. As expected, the chloroplast lipids were less altered under P deprivation. An increase in several PC and DGDG species under P deprivation may suggest the re-assembly of DGDG from PC. Indeed, PC may transiently increase under P deprivation for their reuse in DGDG biosynthesis (Jouhet et al., 2003). Concomitantly with the intensive degradation of chloroplast lipids under N deprivation, a number of lyso-PC species with 16:0, 18:2, 18:3, and 20:4 acyl groups exhibited a marked increase in their abundance. In addition, C20/C18 (38:3, 38:4; 38:5, and 38:7) and C20/C20 (40:7 and 40:8) PE species increased, in agreement with the proposed role of PE in the terminal step of ARA biosynthesis, followed by its shuffling to TAG (Bigogno et al., 2002). PE 36:3, DGTS 36:6, and PC 32:4, 38:7, 40:8 were also more represented in N-deprived cells.

The patterns of changes in the significantly altered TAG species under four experimental conditions are shown in **Supplementary Figure S2**. The lipidome of N-deprived cells displayed a set of strongly increased TAG species, with only a few of them shared with P-deprived cells. Approximately half of the detected TAG species either increased in a coordinated manner or decreased under N deprivation (**Supplementary Figure S2**). Among detected TAGs, several mono-, di-, and tri-ARA-containing

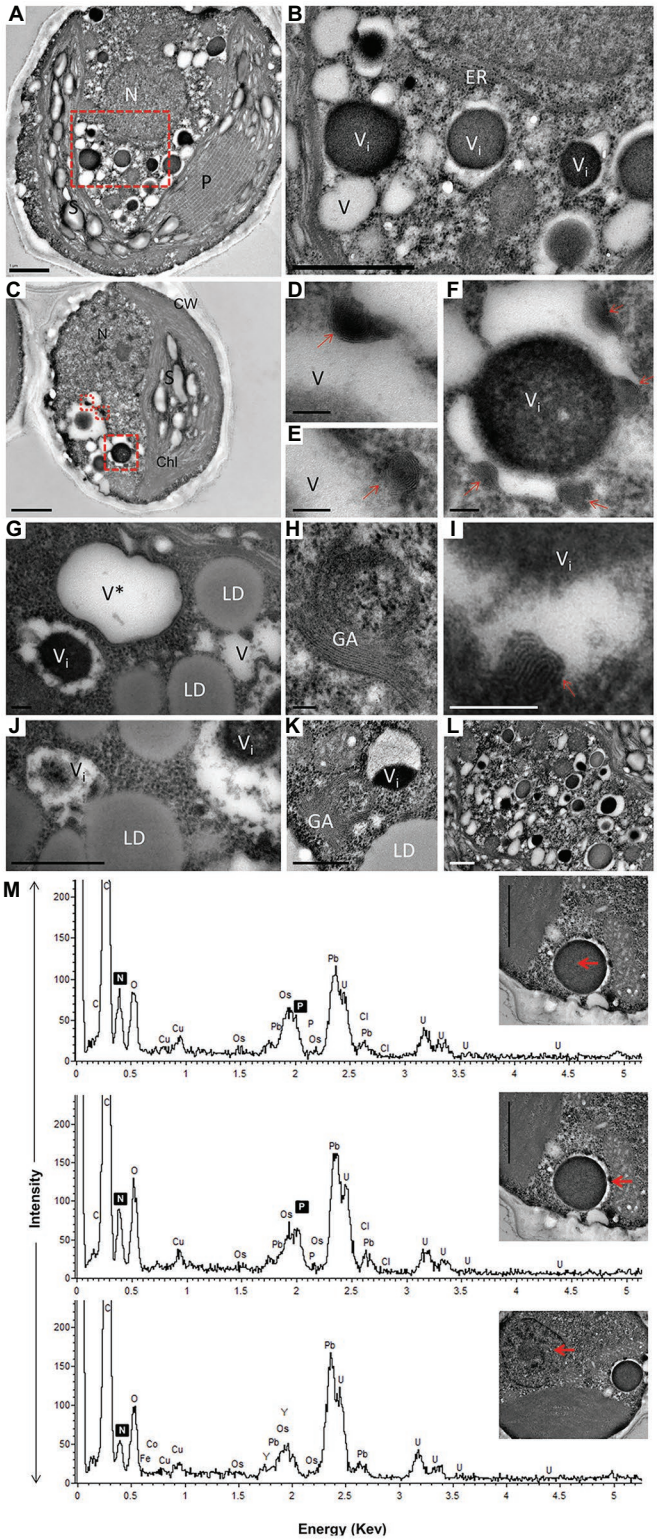

FIGURE 3 | TEM image **(A–L)** with elemental EDX analysis **(M)** of P-deprived cells for 3 days. The squares with red broken lines in **(A,C)** demark an area shown at higher magnification in **(B,D–F)**, respectively. Elemental EDX point spectra on vacuolar inclusions and nucleus **(M)** recorded in a STEM-mode on ultra-thin sections. Chl, chloroplast; S, starch granules; LD, lipid droplets; P, pyrenoid; N, nucleus; GA, Golgi apparatus; ER, rough endoplasmic reticulum; V, vacuole; V*, vacuole with a double membrane; **(D–F,I)** multiple twisted strands connected to the tonoplast (red arrow) in the vacuole; **(G,J)** close contact of LD with vacuole. Scale bars in **(A–C)** = 1 μm, **(J–L)** = 0.5 μm and **(D–I)** = 0.1 μm.

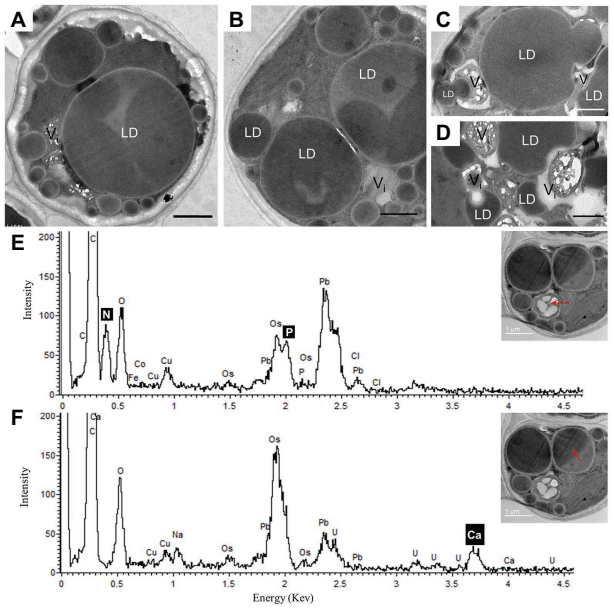

FIGURE 4 | Ultrastructural changes in *L. incisa* after nutrient replenishment to N-deprived cells (24 h) **(A–D)**. Elemental EDX point spectra on degrading lipid bodies and vacuolar inclusions **(E,F)** recorded in a STEM-mode on ultra-thin sections. LD, lipid droplet; V, vacuole. Scale bars in **(A–F)** = 1 μm.

species (C56, C58, and C60 TAGs) showed a significant increase in their relative abundance under N deprivation compared with P deprivation (**Figure 6**). Several C18-containing TAG species C56 (18/18/20) and C54 (18/18/18) were more presented in P-deprived cells (as 52:7 and 54:7). Noticeably, the very long-chain and highly unsaturated TAGs (C62 and 64) were detected in this study in *L. incisa*, and several C64 TAG species showed an increasing pattern in P-deprived cells as compared to four conditions examined (**Supplementary Figure S2**).

Taken together, the results of lipid profiling showed a coordinated but distinct reorganization of polar and neutral lipidomes under P and N deprivation. A stronger decline in membrane glycerolipids and an increase in the ARA-TAG species under N deprivation, compared to P deprivation, were in agreement with the greater extent of chloroplast dismantling, LD formation, and autophagic-like response.

Identification of Autophagy-Related (ATG) Genes in *L. incisa* and Their Expression in the Transciptome of N-Deprived Cells

Taking into account indications of the autophagic response observed in this and our previous work (Kokabi et al., 2019), we next searched the genome of *L. incisa* (deposited in NCBI under BioProject PRJNA262782 and PRJNA283614; Tourasse et al., in preparation) for the orthologs of autophagy-related proteins (ATG). Details on genomic and transcriptomic sequencing are reported in Siegler et al. (2017).

The putative ATG genes are present in the *L. incisa* genome in a single copy (**Supplementary Table S2**), and have their closest homologs in Trebouxiophyceae – the major class of green algae (Chlorophyta). Some deduced *L. incisa* ATG-proteins differed in their amino acid length and domain architecture from homologous proteins in other taxa (yeast, mammals, and higher plants) and showed similarity predominantly in the N terminal portion (**Supplementary Table S2**). WD domains with functions in various cellular processes, such as signaling and vesicle transport, were present in several ATG proteins (**Supplementary Table S2**). Interestingly, the majority of *ATG* genes are located relatively close to each other in the genome context, for example, *ATG13* (g9857), *ATG5* (g10190), *ATG1* (g10441), *ATG2* (g11309), and *ATG18* (g11431). The genes for *ATG4* (g4008), *ATG3* (g4126), *ATG8* (g4496), and *ATG7* (g5114), involved in the ubiquitin-like conjugation system of the autophagy machinery, are also located nearby in the genome. The function of identified *L. incisa* ATG-proteins in autophagy is hypothetical and requires further study.

The hallmark autophagy protein ATG8 showed high conservation and similarity to ATG8 proteins of other organisms. For instance, it is 83% identical to ATG8 from the model green alga *C. reinhardii*, while sharing 78 and 85% identity with *A. thaliana* ATG8A and ATG8D isoforms, respectively. It shares 74% similarity with the ATG8 of *S. cerevisiae* and is the most similar (98% identity) to a putative ATG8 of *Coccomyxa subellipsoidea* C-169, which belongs to the same class Trebouxiophyceae. The C-terminal cleavage site that is required for ATG8 lipidation is located at G119 (**Supplementary Figure S3**).

A transcriptomic study of *L. incisa* subjected to N deprivation for 12 and 72 h has been previously performed (Siegler et al., 2017). Among annotated *ATG*-related genes, the expression levels of *ATG1*, *ATG8, ATG14, ATG101*, and *VMP1* (vacuolar membrane protein 1) significantly increased after 72 h of N starvation (**Table 2**). Remarkably, *ATG8* displayed the highest FPKM values in nutrient-replete cells (day 0), compared with other *ATG*-related genes, and was strongly upregulated in response to N deprivation. In line with the *ATG8* gene expression in replete cells, the immunolocalization of ATG8 in nutrient-replete *L. incisa* revealed several spots per cell in the cytoplasm (**Figure 7**).

Expression of Selected Target Genes During N and P Deprivation Followed by Nutrient Replenishment

To determine whether differences in the gene expression of several relevant pathways (**Supplementary Table S3**) could be involved in *L. incisa* responses to N and P deprivation, we monitored the expression levels of selected genes, related to ARA biosynthesis, LD biogenesis, polyP metabolism, fatty acid β-oxidation, and autophagy (**Figure 8**). The results of a quantitative RT-PCR were normalized to the geometric mean of two reference genes (cytochrome-c oxidase COX3, and small nuclear ribonucleoprotein SNRP), which were stably expressed under experimental conditions.

The Δ5 desaturase mediates the terminal step in the biosynthesis of ARA (Iskandarov et al., 2010). *DesD5* expression displayed a large increase in the initial stages of N deprivation (**Figure 8**), consistent with previous studies (Iskandarov et al., 2010) and the transcriptomic data (**Supplementary Table S3**), but remained almost unaltered under P deprivation and in

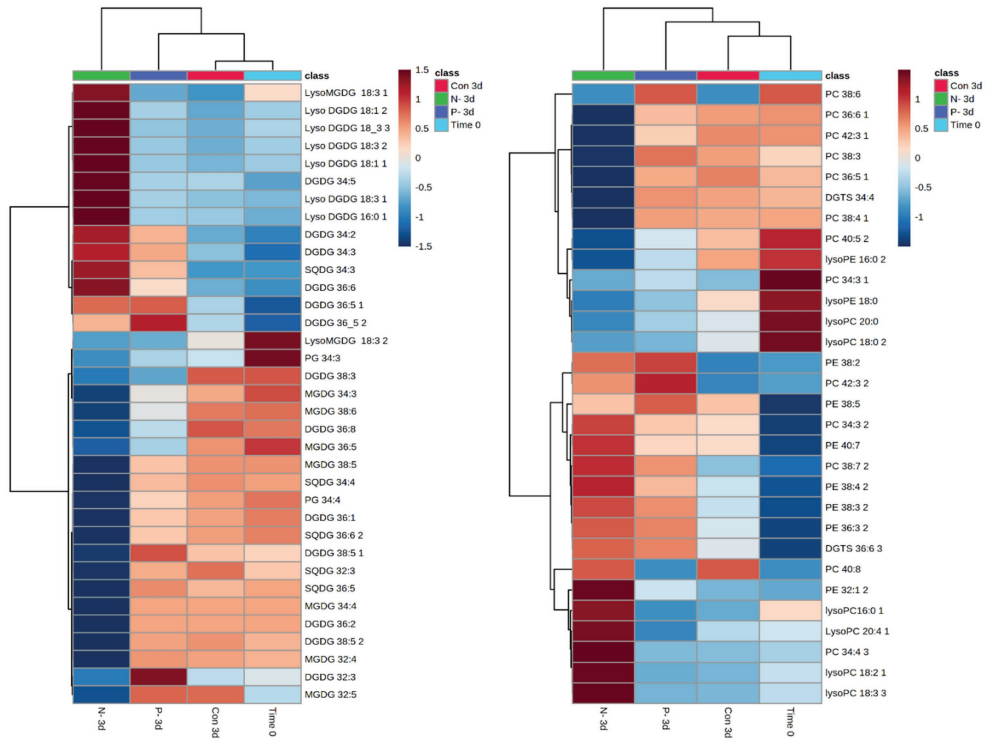

FIGURE 5 | Patterns in chloroplast and extraplastidial glycerolipid changes after 3 days of N and P deprivation compared with time 0 (at the onset of the experiment) and 3 days of nutrient-repletion (Con 3d). The results are shown for the top significantly different species among four conditions ranked by ANOVA, according to the adjusted value of *p* (FDR) cutoff 0.05. Statistical analysis, hierarchical clustering, and heatmaps were performed at https://www.metaboanalyst.ca (Chong et al., 2018). The original data (relative intensities of detected lipid species from four conditions) were quantile-normalized and log-transformed; distance was measured using Pearson's correlation. Lipid species are designated as C:N, where C is the total number of carbons in acyl chains, and N is the total number of double bonds. MGDG, monogalactosyldiacylglycerol; DGDG, digalactosyldiacylglycerol; DGTS, diacylglyceryl-N,N,N-trimethylhomoserine; PC, phosphatidylcholine; PE, phosphatidylethanolamine; PG, phosphatidylglycerol; SQDG, sulfoquinovosyldiacylglycerol. Positional analysis of acyl group distribution was not performed.

the +N+P control. *DesD5* expression exhibited a drop 24 h after nutrient replenishment under all conditions. The transcripts of the gene encoding the major LD protein (*MLDP*) were substantially and progressively upregulated under N and P deprivation, and in the late stationary phase, in the control culture. *MLDP* and *ATG8* were expressed in concert, in the course of N deprivation: with an over 5-fold increase in the later stages, and a strong decline after nutrient resupply. Under P deprivation, and in the replete cells, *ATG8* and *MLDP* were upregulated, but to a lesser extent, while *DesD5* expression was not altered, in line with the lower ARA production under P deprivation (Kokabi et al., 2019). Given the coordinated expression patterns of the ATG8 and MLDP genes, we searched for ATG8-interacting motifs in the MLDP sequence, using three bioinformatics resources trained on plant and non-plant organisms: iLIR[1]; hfAIM[2]; and ELM.[3] In *Nannochloropsis oceanica*, the major LD protein LDSP was predicted to possess an ATG8-interacting iLIR motif in silico and was shown to interact with ATG8 *in vivo* (Zienkiewicz et al., 2020). In the MLDP of *L. incisa*, the propensity for MLDP-ATG8 interactions was predicted only by ELM.

Since vacuolar polyP is an important depot of intracellular PO_4, we monitored the expression of two genes potentially associated with the metabolism of vacuolar polyP. The gene encoding the putative acid phosphatase PAPase was chosen from among other candidate acid phosphatases, based on its upregulation under N deprivation in the transcriptomics study. Its expression increased progressively under all conditions, but most noticeably under N deprivation. The *PAPase* transcript levels dropped sharply after nutrient replenishment, suggesting that this isoform may be involved in polyP hydrolysis under N deprivation and in the control culture, in the stationary phase. *VTC4* putatively encodes a polyP polymerase subunit of the vacuolar transporter chaperone complex (VTC). VTC4 is involved in polyP synthesis in acidocalcisomes, and microautophagy in yeast (Livermore et al., 2016), but its function has not yet been studied genetically in photosynthetic organisms (Sanz-Luque et al., 2020). *VTC4* showed a different expression pattern under P and N deprivation, attaining maximal levels after 2 and 5 days, respectively. Notably, in *C. reinhardtii*, *VTC4* expression also attained its maximum by day 5 of N deprivation and then decreased, supposedly associated with polyP synthesis

[1]repeat.biol.ucy.ac.cy/iLIR
[2]bioinformatics.psb.ugent.be/hfAIM
[3]elm.eu.org

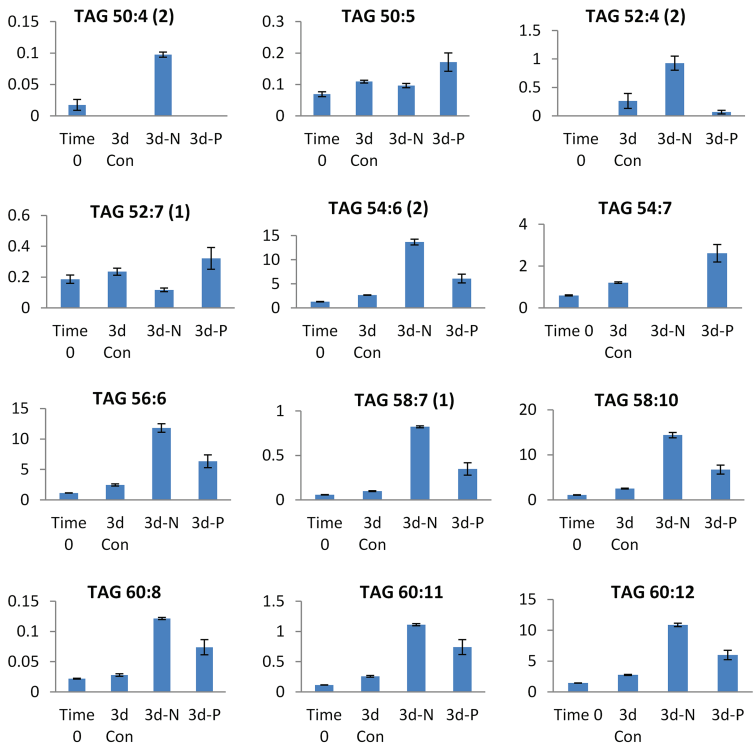

FIGURE 6 | Selected TAG species showing significant differences in their relative abundance (presented in Y-axis) between N and P deprivation conditions. Student's *t*-test (<0.05) test was applied.

TABLE 2 | Significantly upregulated ATG-related genes after 3 days of N deprivation in the transcriptomics study.

Gene ID	Gene symbol	FPKM		Fold change to time 0	*p* adjusted
		0 d	3d-N		
g10441	ATG1	6.96	17.66	2.46	0.001
g4496	ATG8	264.77	827.23	3.53	8e-0.5
g5843	ATG14	10.95	24.30	2.32	0.005
g4696	ATG101	11.11	32.25	3.25	0.0001
g8948	VMP1	13.81	25.93	2.04	0.04

The significance of fold-change is indicated by the p value adjusted for multiple testing at a false discovery rate of 0.05. FPKM: Fragments Per Kilobase Million. The L. incisa gene expression data have been deposited in NCBI GEO under accession GSE94666. Conditions and methods of the transcriptomics analysis are described in (Siegler et al., 2017). 0 day, nutrient replete culture; 3d-N, 3 days of N deprivation.

under N starvation (Goodenough et al., 2019). *VTC4* expression increased only after nutrient resupply to P-deprived cells, likely to circumvent the consequences of P deficiency through polyP re-synthesis. It is worth noting that the transient peak of expression of both *VTC4* and *PAP* was recorded after 12 h of N deprivation, which may indicate a compensatory effect under stress challenge.

The expression of the three genes involved in fatty acid catabolism by beta-oxidation (ABC-transporter D family member, ABC; multifunctional protein, MFP; and 3-ketoacyl-CoA thiolase, KAT) was monitored. The expression patterns of *KAT* and *MFP* – the homologs of plant and algal peroxisomal counterparts – were similar to those of *MLDP* and *ATG8*, although they were expressed at a lower level. Three genes showed a different expression pattern upon nutrient replenishment: the abundance of *MFP* and *KAT* transcripts increased only after nutrient resupply to the P-starved and control cells. Consistent with the cessation of the transcriptional activation of ARA and TAG biosynthesis after nutrient resupply, *DesD5*, *MLDP*, and *ATG8* showed a similar drop in expression after nutrient resupply. At the same time, the transcriptional regulation of the examined β-oxidation genes was not apparent, as indicated by the increase in *KAT* expression only.

ATG8 Protein Levels Under Nutrient Deprivation and After Nutrient Resupply

The *ATG8* gene showed a prominent upregulation during nutrient deprivation. The changes in ATG8 protein production during N and P deprivation were investigated using immunoblotting with the anti-CrAtg8 antibody (**Figure 9**). The ATG8 protein was detected in N-replete cells at the experiment onset (Time-0 for all conditions), and attained the maximal level after 5 days of replete conditions, consistent with the depletion of the N source (Kokabi et al., 2019). We notice a technical issue with ATG8 detection at Time-0 in the control (+N+P lane), since the same loading for Time-0 was done for N- and P-deprived samples. Under N deprivation, the ATG8 abundance increased, attaining a maximal level at day 3, followed

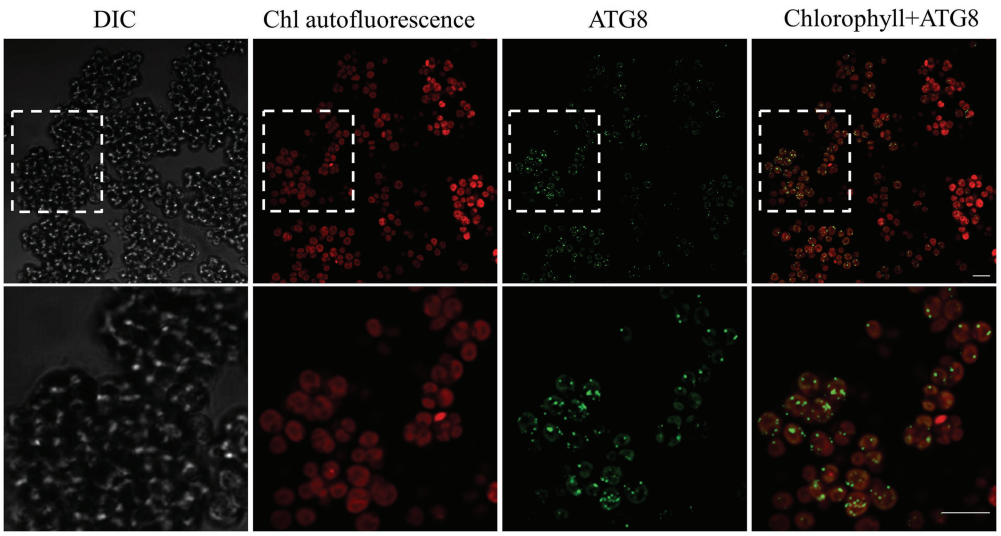

FIGURE 7 | Confocal immunofluorescence micrographs of *L. incisa* cells grown in a replete nutrient medium, displaying the *Li*ATG8 localization as bright green spots in the cytoplasm. Scale bar 10 μm. Cells were processed for immunofluorescence microscopy with an anti-ATG8 primary antibody and Alexa Fluor 488 donkey anti-rabbit IgG secondary antibody. DIC, Differential interference contrast; Chl, (Chlorophyll) autofluorescence; Chlorophyll+ATG8, merge image.

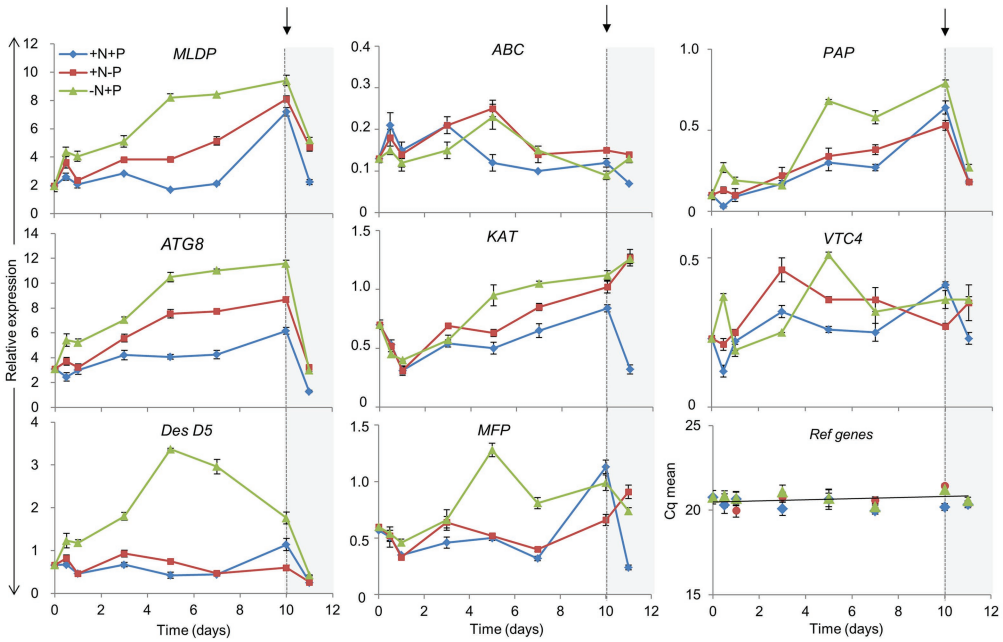

FIGURE 8 | Impact of N and P deprivation on the expression of selected genes related to lipid droplet formation, ARA biosynthesis, fatty acid β-oxidation, polyP metabolism, and autophagy. Control, replete culture (+N+P), blue lines; P deprivation (+N–P), red lines; N deprivation (–N+P), green lines. After 10 days of the indicated conditions, cells were harvested and nutrients replenished by resuspension of the cells in a replete medium: arrows indicate the time of nutrient resupply. Data are presented as means ± SD of the pooled RNA of three biological repetitions (n = 3), reverse-transcribed, and analyzed in three technical replicates. For gene abbreviations, refer to the text.

by a gradual decline. In contrast to N deprivation, ATG8 remained literally unaltered under P deprivation. ATG8 production increased after nutrient resupply to N-starved cells, but not in other treatments. A weak cross-reactive band below the main ATG8 band was observed under N deprivation and after nutrient replenishment. To test whether this may represent a conjugated ATG-PE form, which is more hydrophobic than free ATG8, the phospholipase D (PLD) treatment was carried

out on a concentrated protein sample of the nutrient-deprived (−N+P) cells 2 days after nutrient resupply (**Figure 9B**). The band with the faster electrophoretic mobility became less prominent after the PLD treatment, suggesting that it may represent the PE-conjugated form.

Pharmaceutical Treatment With Concanamycin A Impairs ARA Biosynthesis

Autophagy inhibitors are a valuable tool to experimentally link lipid metabolism and autophagy. Concanamycin A (CA) inhibits the activity of vacuolar H^+-ATPases, thereby inactivating vacuolar protein hydrolases and disrupting autophagic flux (Yoshimoto et al., 2004; Thompson et al., 2005). As a result of suppressing autophagic degradation, both ATG8 and its ATG8-PE lipidated form accumulate. CA was applied in N-replete cultures at a concentration range that had proved effective in *C. reinhardtii* (Couso et al., 2018). The ATG8 protein accumulated in a dose-dependent manner with the CA treatment (**Figure 10A**), suggesting suppression of autophagic flux. However, we did not detect a faster-moving band that could have been attributed to lipidated ATG8-PE, despite applying a 6 M Urea-15% SDS-gel, which allows separation of the free and PE-conjugated ATG8 forms. Hence, ATG8 lipidation in *L. incisa* remains enigmatic and needs further detailed investigation, beyond the scope of this work.

We next asked whether CA treatment would affect the dynamics of photosynthetic pigments, and TAG accumulation and composition. In N-replete flask-cultures, 0.1 µM of CA caused strong growth inhibition, which was observed as the cessation of Chl production and bleaching of the cultures (**Figure 10A**). It should be noted that cell counting to record growth curves is not feasible in *L. incisa*, because it forms clusters of multiple attached daughter cells. Microscopic observation revealed LD formation in replete cells under CA treatment (**Figure 10B**). In contrast, 0.1 µM of CA applied to N-deprived cultures did not exhibit a noticeable effect on culture performance and cell morphology (**Figure 10C**). Photosynthetic pigments degraded to a similar extent, accompanied by visually undisturbed LD formation. Importantly, total FA and TAG analysis showed that CA caused a strong increase in 18:1*n*9, the early precursor of ARA in the omega-6 pathway of LC-PUFA biosynthesis (Bigogno et al., 2002), with a concomitant decrease in ARA proportion (**Figures 10D,E**). While the proportion of ARA declined, the content of TAG in the biomass slightly increased, indicating that autophagic flux is important for ARA accumulation in TAG.

To test whether CA affects TAG remobilization and growth recovery after nutrient resupply to N-deprived cells, we applied the inhibitor to cells transferred to an N-replete complete medium after 10 days of N deprivation. At 0.1 µM, CA did not affect culture recovery (not shown), but when applied at 0.5 µM, it strongly inhibited re-growth and the restoration of Chl production (**Figure 11A**). The impaired build-up of the photosynthetic apparatus under CA treatment was consistent with the results of microscopy and cellular fatty acid analysis, showing a higher total fatty acid content, a higher proportion of 18:1*n*9, and a decreased proportion of 18:3*n*3, 3 days after nutrient replenishment (**Figure 11B**). The latter fatty acid is associated with the major chloroplast glycerolipids and, thus, its decreased proportion indicates a lesser extent of photosynthesis system recovery. Consistent with the results of previous studies, the proportion of ARA in TAG did not swiftly decline following nutrient replenishment (Kokabi et al., 2019). Microscopic observation (**Figures 11C,D**) revealed that CA treatment repressed cell enlargement, division and proliferation, and recovery of the photosynthetic apparatus,

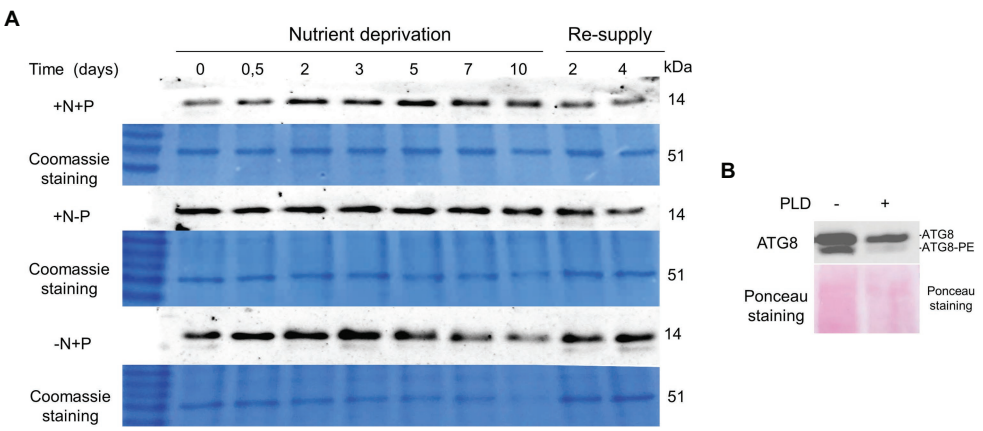

FIGURE 9 | ATG8 levels in the replete control (+N+P), during P (+N−P), N (−N+P) deprivation and following nutrient resupply. **(A)** Time-course of ATG8 production in the control culture (+N+P), during P (+N−P) and N (−N+P) deprivation detected by western blot analysis. Re-supply: on day 10, cells from all treatments were harvested and resuspended in a complete nutrient-replete medium for growth recovery. Then, 2 µg of total protein was resolved on 15% SDS-PAGE gel. A section of the gel stained with Coomassie brilliant blue is shown as a loading control. **(B)** Phospholipase D treatment of protein sample 2 days after nutrient re-supply to N-starved cells (shown in **A**). Approximately 20 µg of protein was treated with 100 units of cabbage phospholipase D (PLD; Sigma) for 1 h at 30°C, and resolved on the 15% SDS-PAGE gel with 6 M urea. The loading control is the nitrocellulose membrane stained with Ponceau S, Red.

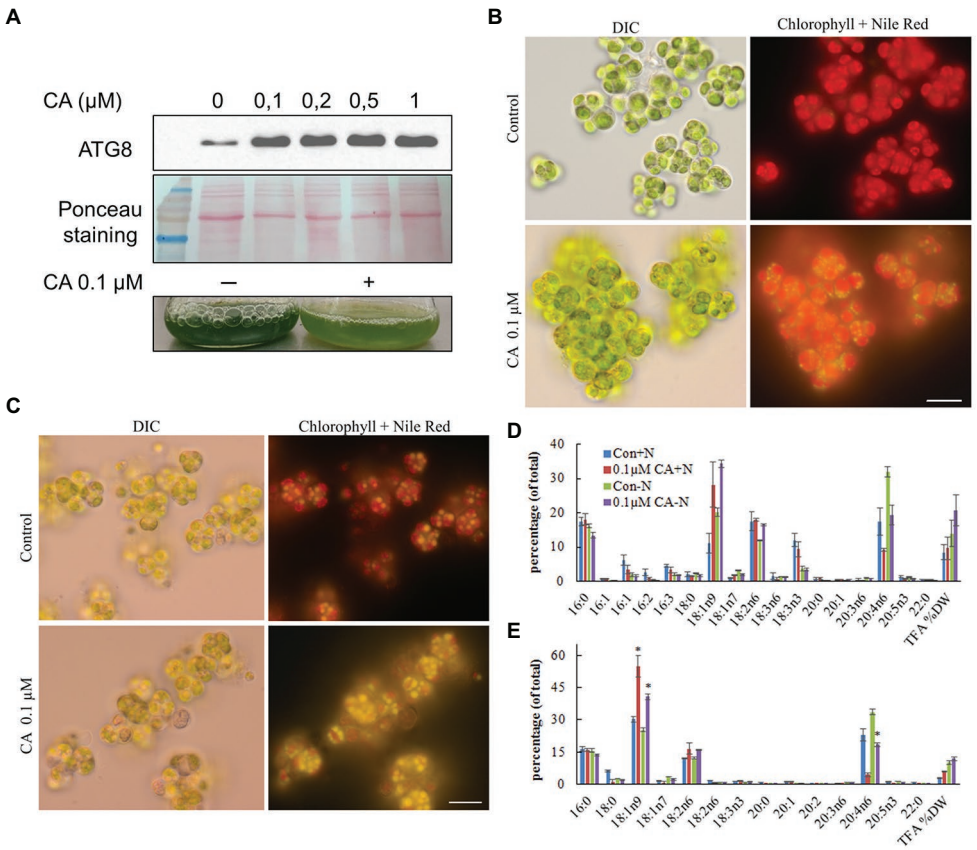

FIGURE 10 | Effect of Concamycin A (CA) on the growth and accumulation of arachidonic acid in *L. incisa*. **(A)** CA treatment promotes ATG8 accumulation in N-replete cells. CA was applied to N-replete cells in a 12-well plate for 12 h at the indicated concentration range; 2 μg of total protein extract was resolved on a 15% SDS-Urea gel. Micrographs of *L. incisa* cells 3 days after treatment of nutrient-replete **(B)** and N-deplete **(C)** cultures with 0.1 μM Concamycin A, compared to respective controls. DIC: Differential interference contrast; Lipid droplets stained with Nile Red are seen in bright yellow; Chloroplast area is seen as a red fluorescent area; Scale bars 10 μm. **(D)** Quantification of total fatty acids in cell biomass, and **(E)** TAG in *L. incisa* treated with 0.1 μM CA under nutrient repletion and N deprivation, compared with the respective controls. Cells were sampled after 3 days of indicated conditions. The data represent a mean ± SD from two biological replicates, each analyzed with three analytical repeats. Statistical analysis was carried out using Student's *t*-test (* denotes a significant difference from untreated control, $p < 0.05$).

and delayed LD degradation. These results suggest that autophagic flux may be involved in photosynthetic apparatus recovery and TAG mobilization.

Expression of GFP-ATG8 Fusion in *L. incisa* to Monitor Autophagic Flux

Suppression of the vacuolar proteolytic function by CA caused accumulation of the marker autophagy protein ATG8 in replete cells (**Figure 10A**) and inhibition of ARA accumulation in TAG (**Figure 10E**), suggesting the involvement of autophagic flux. A plasmid construct carrying the GFP-ATG8 fusion was generated to assess the proteolytic cleavage of N-terminal GFP, a key assay for the detection of autophagic flux. The *LiATG8* genomic sequence was amplified with its promotor and terminator sequences (1,570 bp), fused at the N terminus with *eGFP*, and expressed in *L. incisa* by electroporation (**Figure 12A**). Transgenic lines were selected based on resistance to the herbicide SMM (**Supplementary Figure S4A**), conferred by the expression of the mutated form of the *AHAS* gene (Grundman et al., 2012; see Materials and Methods). Integration of *GFP* was verified by PCR in several transformants (**Figure 12B**); GFP-ATG8 protein expression was confirmed by western blotting with anti-GFP antibody (**Figure 12C**) and confocal microscopy (**Figure 12F**). Two out of the four selected transformants displayed stronger ATG8 accumulation after 2 and 4 days of N deprivation, detected by western blotting with anti-ATG8 antibody (**Figure 12E**). Using the GFP-antibody, the production of GFP-ATG8 fusion (the predicted molecular weight about 42 kDa), and the release of free GFP were detected in replete cells, suggesting its proteolytic cleavage. The release of GFP from the GFP-ATG8 fusion was also detected under N deprivation in the selected transformant (**Figure 12D**). The fluorescent signal of GFP was observed predominantly as circular structures dispersed in the cytoplasm of the transformed cells, which is consistent with the distribution of vacuoles in replete cells, suggesting that GFP may be delivered to the

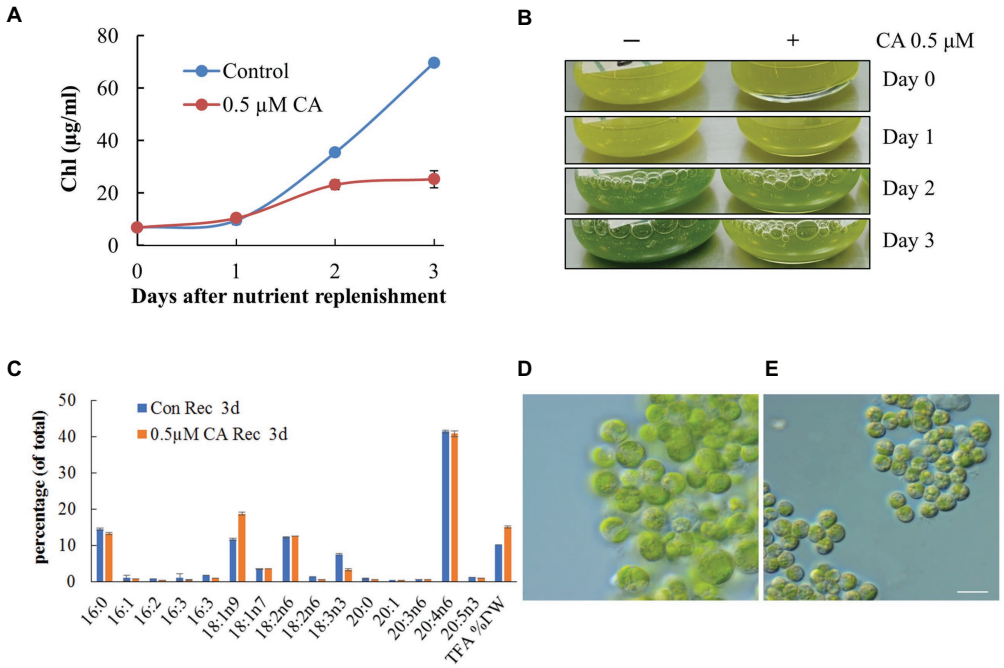

FIGURE 11 | Concamycin A (0.5 µM) inhibits culture recovery after a shift from an N-deprived to an N-replete medium. Chlorophyll production **(A,B)**, total fatty acid composition and content **(C)**, and micrographs of control untreated **(D)** and treated cells **(E)** 3 days after nutrient replenishment to N-deprived cells with and without 0.5 µM CA. The data shown represent a mean ± SD from two biological replicates analyzed in three analytical repeats. Scale bars 10 µm.

vacuoles. The transformant OE4 was subjected to different treatments to visualize the cellular localization of the GFP signal, 12 h after exposure to adverse conditions (P and N deprivation, and H_2O_2 treatment; **Supplementary Figure S4B**). However, the GFP signal stayed unvaried regardless the stress treatment applied. Furthermore, the substantial GFP signal observed in the untreated nutrient-replete cells of the transformants limited this approach for studying the enhancement of autophagy. Further in-detail characterization of the transformants is important, but it was beyond the scope of this study.

DISCUSSION

Different scenarios of transcriptome, proteome, and metabolome reorganization are associated with the differential rearrangement of lipid metabolism under N and P deprivation (López García de Lomana et al., 2015; Alipanah et al., 2018; Wördenweber et al., 2018; Kokabi et al., 2019). In this study, we aimed to provide a more detailed picture of *L. incisa* responses to N and P deprivation. It was hypothesized that the metabolic and energetic costs associated with enhanced ARA biosynthesis, in *L. incisa* under N deprivation, require increased catabolic activity and autophagy.

The observed changes in the TAG profile under N deprivation were consistent with the enhanced formation of ARA-containing species (Bigogno et al., 2002). In contrast, C18-containing TAGs were enhanced under P deprivation. The results of comparative lipid profiling of *L. incisa* indicated intensive membrane lipid breakdown under N deprivation compared with P deprivation. Under N deprivation, membrane lipid turnover and breakdown and neo-synthesis supply fatty acids for TAG assembly (Li et al., 2012; Rismani-Yazdi et al., 2012). Under P deprivation, membrane lipids are remodeled, whereby DAG, liberated from phospholipids, is used for non-phosphorous glycerolipid synthesis, while the deacylated G-3-P can be reused for TAG biosynthesis (Mühlroth et al., 2017). The increased ratio of two major galactolipids, DGDG to MGDG, is central for chloroplast membrane homeostasis under stress (Kobayashi, 2016). Accordingly, under N deprivation, the abundance of DGDG species decreased less than MGDG, while the abundance of lyso-DGDG species increased. The N-deprivation-induced release of acyl groups from the plastidial galactolipids, with the concomitant increase in the lyso-lipids, may be mediated by galactolipase/s (Li et al., 2012; Du et al., 2018) or the phospholipid: diacylglycerol acyltransferase (PDAT), which may act on different membrane lipids (Yoon et al., 2012; Liu et al., 2016). The liberation of chloroplast-derived fatty acids (linoleic and linolenic) and their volatile derivatives (fatty alcohols, fatty aldehydes, etc.), which could limit their integration into TAG, has recently been documented as an early response of *L. incisa* to N deprivation, consistent with the enhanced degradation of chloroplast glycerolipids and the transcriptional upregulation of putative galactolipid lipases (Kumari et al., 2020). Chloroplast dismantling is a characteristic consequence of N deprivation

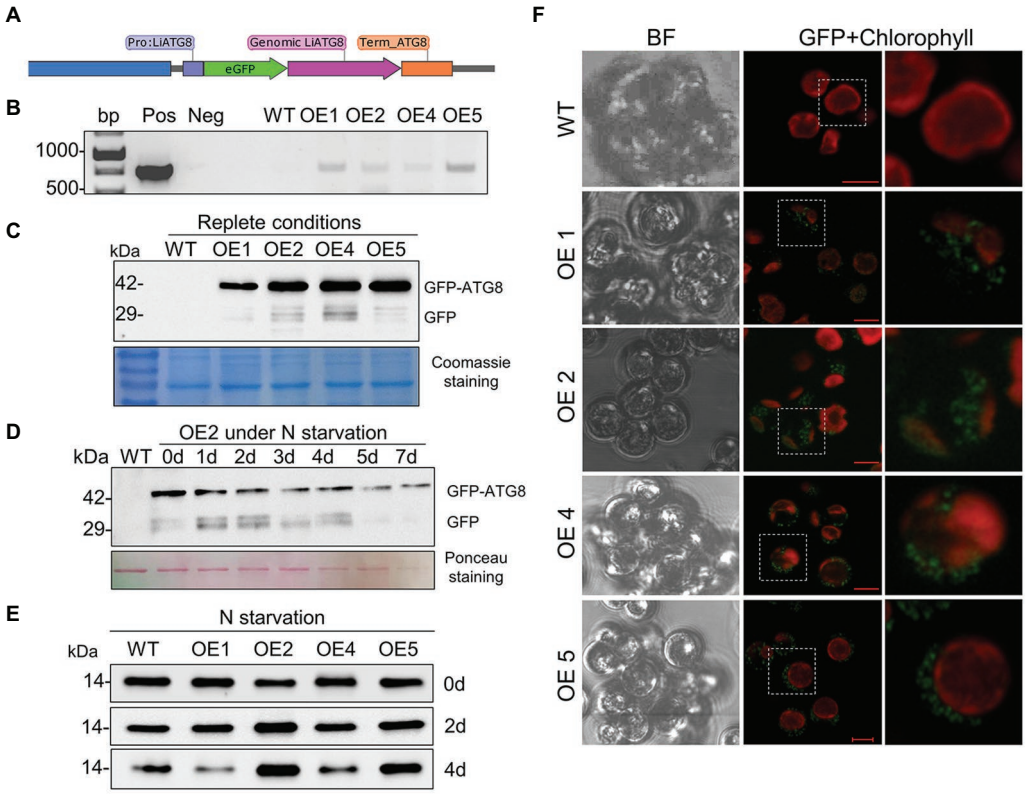

FIGURE 12 | The establishment of the GFP-ATG8 autophagy marker in *L. incisa*. **(A)** Schematics of the plasmid construct pLiATG8::GFP-ATG8; **(B)** PCR validation of transgene integration using GFP-specific primers; **(C)** detection of GFP-ATG8 fusion protein and free GFP in OE lines under nutrient-replete conditions, using western blot analysis with the anti-GFP antibody. Coomassie blue-stained SDS-PAGE is shown below the blots as a loading control. **(D)** Detection of GFP-ATG8 and free GFP in OE2 line under N deprivation (–N+P) by immunoblotting with anti-GFP antibodies. Ponceau staining of the membrane of total proteins is shown as a loading control. **(E)** Immunoblotting with anti-ATG8 antibody for ATG8 detection in WT and transformant OE lines under N deprivation. **(F)** Visualization of the GFP signal in selected transformants using confocal microscopy. Scale bars = 5 μm.

in microalgae whereby autophagy-mediated degradation of chloroplast components may play important roles in N scavenging, and the supply of amino acids and building blocks for enhanced FA and TAG biosynthesis.

Numerous acidic vacuoles with various inclusions are found in *L. incisa* cells (Watanabe et al., 1996; Merzlyak et al., 2007; Kokabi et al., 2019). We asked whether these organelles could be involved in the autophagic degradation and recycling of cellular components under nutrient deprivation. Double-membrane autophagosomes and autophagic vacuoles with a variety of cargo material were observed in microalgae (Ramundo et al., 2014; Schatz et al., 2014; Lütz-Meindl, 2016). Although we did not observe canonical autophagosomes in *L. incisa*, we observed some manifestations of autophagic activity in both nutrient-replete and deprived cells in this and a previous study (Kokabi et al., 2019). Autophagic vacuoles were observed under N deprivation, as well as the production of the key autophagy protein ATG8 in replete cells and under N and P deprivation.

The membrane-bounded acidic organelles, acidocalcisomes, play a key role in autophagy in eukaryotic microbial parasites (Li and He, 2014; Docampo, 2016). The role of acidocalcisomes in autophagy in microalgae remains to be investigated. In microalgae, acidocalcisomes are involved in the sequestration of nitrogenous compounds and polyP in close association with the uptake of inorganic cations (Ca^{2+}, Fe^{2+}, Mn^{2+}, Mg^{2+}, and others; Pick et al., 1990; Ruiz et al., 2001; Goodson et al., 2011; Moudříková et al., 2017; Shebanova et al., 2017; Tsednee et al., 2019). Although polyP and nitrogenous compounds were detected in *L. incisa*, in the acidic vacuoles with granular bodies (Kokabi et al., 2019), Ca^{2+} was not detected by the EDX analysis, applied in this and our prior study. In *C. reinhardtii*, acidocalsomes appeared to be restricted to stationary and N-starved cells, and can be distinguished from lytic vacuoles based on the membrane fracture-face morphology (Goodenough et al., 2019). In *L. incisa*, however, the organelles with distinct granular bodies were more abundant in nutrient-replete cells (Watanabe et al., 1996; Merzlyak et al., 2007; Kokabi et al., 2019). To ascertain their composition and structure in *L. incisa*, advanced microscopic methods have to be applied.

The genome of *L. incisa* contains a set of putative ATG-related genes consistent with bioinformatics studies in other microalgae (Jiang et al., 2012; Shemi et al., 2015; Zienkiewicz et al., 2020). Some of the *L. incisa* ATG proteins displayed additional structural features compared to their counterparts outside of Chlorophyta.

WD40 repeats, which have been reported in some algal ATGs (Shemi et al., 2015), were found at the carboxyl terminus of ATG16 and VPS15 in several tandem copies. This suggests that WD40 domains with the ability to scaffold and interact with a variety of cellular components (Smith, 2008) may endow these proteins with additional functions, which warrant further investigation.

Autophagy-related genes are upregulated by different stresses in microalgae, specifically under TAG-inducing conditions (Perez-Perez et al., 2012; Goodenough et al., 2014; Ramundo and Rochaix, 2014; Zienkiewicz et al., 2020). In *L. incisa*, among several ATG genes that were upregulated under N deprivation, *ATG8* was upregulated particularly strongly. The key autophagy protein was produced and the gene expressed in replete cells, consistent with the notion of basal autophagy activity. The expression patterns of *ATG8*, *MLDP*, and *DesD5* under N deprivation closely mirrored each other, pointing to the relationship between autophagy, LD biogenesis, and ARA sequestration in LDs in N-deprived *L. incisa*. Under P deprivation, the *DesD5* transcript and ATG8 protein displayed stable levels, but an increasing pattern was determined in the *ATG8* transcript level. This may suggest a different mechanism involved in P-deprivation-mediated signaling in autophagy-related genes. It has recently been shown that P limitation signaling and autophagy in *C. reinhardtii* are regulated by the TORC1's component LST8 and the upstream transcription factor PSR1 (Couso et al., 2019). The enhancement of autophagy under N deprivation allows for the degradation, recycling, and reutilization of cellular components and reserves, consistent with the results on the dynamics of ATG8 protein and gene expression and TEM of N-deprived *L. incisa* cells.

When LD mobilization was induced by nutrient resupply to N-deprived cells, the ATG8 protein's production was inconsistent with the *ATG8* gene expression. The observed discrepancy can be explained by the sufficient amount of transcript at the early stages of recovery. It is also possible that the turnover rate of the transcripts exceeded the rate of synthesis and/or post-transcriptional modifications were involved. It is also plausible that transcripts are present but sequestrated or frozen by proteins that keep them stable and hinder translation. Alternatively, LD degradation may be mediated by ATG8-independent mechanisms, such as microautophagy and lipolysis, in agreement with the identification of TAG lipases in the LD proteome of *L. incisa* (Siegler et al., 2017) and the previous study on remobilization of TAGs in *L. incisa* (Khozin-Goldberg et al., 2005).

Despite significant progress, relatively little is yet known about the molecular mechanisms underlying autophagy and its interaction with LD formation and remobilization in microalgae. The induction of autophagy by inhibition of the major nutrient sensor kinase TOR triggers autophagy in microalgae and LD accumulation without applying stress stimuli (Imamura et al., 2015; Mukaida et al., 2016; Prioretti et al., 2017). Class III PI3K plays a major role in regulating lipid metabolism and autophagosome formation, and its inhibition or knockdown enhances lipid content and TAG formation (Ramanan et al., 2018; Zienkiewicz et al., 2020). However, there are claims that TOR activation can regulate TAG biogenesis without activating the autophagic pathway (Kajikawa and Fukuzawa, 2020). Further, LDs are frequently found in proximity to, or even inside, the vacuoles (Gorelova et al., 2014; Tsai et al., 2017; Zienkiewicz et al., 2020), which is consistent with the TEM observations of this work. However, LD formation did not appear impaired in the *atg* mutants of *Chlamydomonas*, which displayed compromised recycling of various cytoplasmic components (Kajikawa et al., 2019), suggesting alternative ways of interacting.

The pharmaceutical inhibition of the lytic vacuolar function arrested growth and induced LD formation in replete cells of *L. incisa*; the effect is similar to the inhibition of the earlier steps of autophagy in other studies. In *Chlamydomonas*, CA suppressed formation of LDs and TAG accumulation under N and P deprivation (Couso et al., 2018). In *L. incisa*, CA did not enhance deleterious effects on the photosynthetic pigment degradation and LD formation under N deprivation. However, it led to a significant decrease in the ARA level in TAG. These findings suggest that autophagic flux may be particularly important for sustaining ARA biosynthesis under N deprivation. Since, ARA biosynthesis from 18:1 involves three energy-requiring desaturation and one elongation steps, the plausible explanation is that autophagy-mediated degradation of cellular components supports expenditures associated with the enhanced ARA biosynthesis.

LD mobilization after nutrient resupply provides fatty acids for restoring and rebuilding photosynthetic machinery and cellular membranes (Khozin-Goldberg et al., 2005), as well as a source of energy to fuel growth recovery. We observed changes in the osmophilicity of the LD-core during TAG remobilization, possibly attributed to the consumption of certain TAG species. LDs may indeed exhibit different internal organizations, as well as organelle associations, depending on cellular states (Mahamid et al., 2019). The EDX analysis pointing to LDs showed a high Ca^{2+} signal associated with the degrading LDs. Caleosin is a Ca-binding oil body/LD surface protein, whose role in seed oil-body degradation and interaction with vacuoles during seed germination is well-established (Poxleitner et al., 2006). We can speculate that LD-associated caleosins may play a role in LD degradation during growth recovery, mediating the degradation of fatty acids released from LDs. It is also plausible that caleosin may function in the maintenance of LDs under deprivation (Siegler et al., 2017).

To conclude, we provide several pieces of evidence that highlight the homeostatic role of autophagy in proliferating *L. incisa* cells and the role played by autophagy under N deprivation. We suggest that the ARA-rich TAG biosynthesis, as an energy- and resource-demanding challenge for N-deprived cells, has to be supported by numerous metabolic changes to meet these demands, including increased catabolic activity and autophagy. Although this microalga is difficult to transform, we managed to obtain the GFP-ATG8 expressing lines. Pharmaceutical inhibition of the late stages of autophagy halted nutrient-replete growth and reduced ARA accumulation in TAG under N deprivation, as well as impaired the buildup of photosynthetic membranes and delayed LD degradation after nutrient replenishment. Further investigation is obviously needed to elucidate the molecular basis of autophagy and LD degradation machinery, and LD-autophagy interaction in *L. incisa*.

DATA AVAILABILITY STATEMENT

The raw data supporting the conclusions of this article will be made available by the authors, without undue reservation.

AUTHOR CONTRIBUTIONS

KK and IK-G conceived the study and analyzed the data and wrote the manuscript. KK performed the experimental work. BZ designed the expression vectors and conceived the transformation of *L. incisa*. OG and AS performed the TEM and elemental analysis with TEM-EDX at the User Facilities Center of M.V. Lomonosov Moscow State University. SD-C performed TAG and fatty acid analysis. MI and SM performed the lipidomics analysis. IK-G and SB were involved in funding acquisition. All authors read, reviewed, and approved the manuscript.

FUNDING

This work was supported by a grant from the Israel Ministry of Science, Technology and Space (grant number 3-12422). AS has been supported in part by the RUDN University Strategic Academic Leadership Program.

ACKNOWLEDGMENTS

KK acknowledges PhD and short-term postdoctoral fellowships granted by the Kreitman School of Advanced Graduate Studies at Ben-Gurion University of the Negev, Israel. We thank A. Upcher and R. Jeger (BGU) for their help with the TEM imaging at Ben-Gurion University of the Negev and T. Pugacheva (MGU) for her help in the TEM-EDX analysis at the User Facilities Center of M.V. Lomonosov Moscow State University. We are indebted to O. Vallon (CNRS) for his help in the curation and annotation of ATG-related and FKBP12 genes, A. Batushansky for valuable suggestions on statistical analysis, and to S. Bel for English language editing and proofreading.

SUPPLEMENTARY MATERIAL

The Supplementary Material for this article can be found online at: https://www.frontiersin.org/articless/10.3389/fpls.2020.614846/full#supplementary-material

REFERENCES

Abida, H., Dolch, L. -J., Meï, C., Villanova, V., Conte, M., Block, M. A., et al. (2015). Membrane glycerolipid remodeling triggered by nitrogen and phosphorus starvation in *Phaeodactylum tricornutum*. *Plant Physiol.* 167, 118–136. doi: 10.1104/pp.114.252395

Alipanah, L., Winge, P., Rohloff, J., Najafi, J., Brembu, T., and Bones, A. M. (2018). Molecular adaptations to phosphorus deprivation and comparison with nitrogen deprivation responses in the diatom *Phaeodactylum tricornutum*. *PLoS One* 13:e0193335. doi: 10.1371/journal.pone.0193335

Andosch, A., Affenzeller, M. J., Lütz, C., and Lütz-Meindl, U. (2012). A freshwater green alga under cadmium stress: ameliorating calcium effects on ultrastructure and photosynthesis in the unicellular model *Micrasterias*. *J. Plant Physiol.* 169, 1489–1500. doi: 10.1016/j.jplph.2012.06.002

Avin-Wittenberg, T., Bajdzienko, K., Wittenberg, G., Alseekh, S., Tohge, T., Bock, R., et al. (2015). Global analysis of the role of autophagy in cellular metabolism and energy homeostasis in Arabidopsis seedlings under carbon starvation. *Plant Cell* 27, 306–322. doi: 10.1105/tpc.114.134205

Bigogno, C., Khozin-Goldberg, I., Adlerstein, D., and Cohen, Z. (2002). Biosynthesis of arachidonic acid in the oleaginous microalga *Parietochloris incisa* (Chlorophyceae): Radiolabeling studies. *Lipids* 37, 209–216. doi: 10.1007/s11745-002-0882-6

Boussiba, S. (2000). Carotenogenesis in the green alga *Haematococcus pluvialis*: cellular physiology and stress response. *Physiol. Plant.* 108, 111–117. doi: 10.1034/j.1399-3054.2000.108002111.x

Cañavate, J. P., Armada, I., and Hachero-Cruzado, I. (2017). Common and species-specific effects of phosphate on marine microalgae fatty acids shape their function in phytoplankton trophic ecology. *Microb. Ecol.* 74, 623–639. doi: 10.1007/s00248-017-0983-1

Chen, Q., Soulay, F., Saudemont, B., Elmayan, T., Marmagne, A., and Masclaux-Daubresse, C. (2019). Overexpression of ATG8 in Arabidopsis stimulates autophagic activity and increases nitrogen remobilization efficiency and grain filling. *Plant Cell Physiol.* 60, 343–352. doi: 10.1093/pcp/pcy214

Chong, J., Soufan, O., Li, C., Caraus, I., Li, S., Bourque, G., et al. (2018). MetaboAnalyst 4.0: towards more transparent and integrative metabolomics analysis. *Nucleic Acids Res.* 46, W486–W494. doi: 10.1093/nar/gky310

Couso, I., Esther Pérez-Pérez, M., Ford, M. M., Martínez-Force, E., Hicks, L. M., Umen, J. G., et al. (2019). Phosphorus availability regulates TORC1 Signaling via LST8 in Chlamydomonas. *Plant Cell* 32, 69–80. doi: 10.1105/tpc.19.00179

Couso, I., Pérez-Pérez, M. E., Martínez-Force, E., Kim, H. S., He, Y., Umen, J. G., et al. (2018). Autophagic flux is required for the synthesis of triacylglycerols and ribosomal protein turnover in Chlamydomonas. *J. Exp. Bot.* 69, 1355–1367. doi: 10.1093/jxb/erx372

Davey, M. P., Horst, I., Duong, G. -H., Tomsett, E. V., Litvinenko, A. C. P., Howe, C. J., et al. (2014). Triacylglyceride production and autophagous responses in *Chlamydomonas reinhardtii* depend on resource allocation and carbon source. *Eukaryot. Cell* 13, 392–400. doi: 10.1128/EC.00178-13

Docampo, R. (2016). The origin and evolution of the acidocalcisome and its interactions with other organelles. *Mol. Biochem. Parasitol.* 209, 3–9. doi: 10.1016/j.molbiopara.2015.10.003

Dong, H. P., Williams, E., Wang, D. Z., Xie, Z. X., Hsia, R. C., Jenck, A., et al. (2013). Responses of *Nannochloropsis oceanica* IMET1 to long-term nitrogen starvation and recovery. *Plant Physiol.* 162, 1110–1126. doi: 10.1104/pp.113.214320

Du, Z. Y., Lucker, B. F., Zienkiewicz, K., Miller, T. E., Zienkiewicz, A., Sears, B. B., et al. (2018). Galactoglycerolipid lipase PGD1 is involved in thylakoid membrane remodeling in response to adverse environmental conditions in Chlamydomonas. *Plant Cell* 30, 447–465. doi: 10.1105/tpc.17.00446

Fan, J., Yu, L., and Xu, C. (2019). Dual role for autophagy in lipid metabolism in Arabidopsis. *Plant Cell* 31, 1598–1613. doi: 10.1105/tpc.19.00170

Feng, Y., He, D., Yao, Z., and Klionsky, D. J. (2014). The machinery of macroautophagy. *Cell Res.* 24, 24–41. doi: 10.1038/cr.2013.168

Feng, T. -Y., Yang, Z. -K., Zheng, J. -W., Xie, Y., Li, D. -W., Murugan, S. B., et al. (2015). Examination of metabolic responses to phosphorus limitation via proteomic analyses in the marine diatom *Phaeodactylum tricornutum*. *Sci. Rep.* 5:10373. doi: 10.1038/srep10373

Goodenough, U., Blaby, I., Casero, D., Gallaher, S. D., Goodson, C., Johnson, S., et al. (2014). The path to triacylglyceride obesity in the sta6 strain of *Chlamydomonas reinhardtii*. *Eukaryot. Cell* 13, 591–613. doi: 10.1128/EC.00013-14

Goodenough, U., Heiss, A. A., Roth, R., Rusch, J., and Lee, J. H. (2019). Acidocalcisomes: ultrastructure, biogenesis, and distribution in microbial eukaryotes. *Protist* 170, 287–313. doi: 10.1016/j.protis.2019.05.001

Goodson, C., Roth, R., Wang, Z. T., and Goodenough, U. (2011). Structural correlates of cytoplasmic and chloroplast lipid body synthesis in *Chlamydomonas reinhardtii* and stimulation of lipid body production with acetate boost. *Eukaryot. Cell* 10, 1592–1606. doi: 10.1128/EC.05242-11

Gorelova, O., Baulina, O., Ismagulova, T., Kokabi, K., Lobakova, E., Selyakh, I., et al. (2018). Stress-induced changes in the ultrastructure of the photosynthetic apparatus of green microalgae. *Protoplasma* 256, 261–277. doi: 10.1007/s00709-018-1294-1

Gorelova, O., Baulina, O., Solovchenko, A., Selyakh, I., Chivkunova, O., Semenova, L., et al. (2014). Coordinated rearrangements of assimilatory and storage cell compartments in a nitrogen-starving symbiotic chlorophyte cultivated under high light. *Arch. Microbiol.* 197, 181–195. doi: 10.1007/s00203-014-1036-5

Grundman, O., Khozin-Goldberg, I., Raveh, D., Cohen, Z., Vyazmensky, M., Boussiba, S., et al. (2012). Cloning, mutagenesis, and characterization of the microalga *Parietochloris incisa* acetohydroxyacid synthase, and its possible use as an endogenous selection marker. *Biotechnol. Bioeng.* 109, 2340–2348. doi: 10.1002/bit.24515

Heredia-Martínez, L. G., Andrés-Garrido, A., Martínez-Force, E., Pérez-Pérez, M. E., and Crespo, J. L. (2018). Chloroplast damage induced by the inhibition of fatty acid synthesis triggers autophagy in Chlamydomonas. *Plant Physiol.* 178, 1112–1129. doi: 10.1104/PP.18.00630

Hockin, N. L., Mock, T., Mulholland, F., Kopriva, S., and Malin, G. (2012). The response of diatom central carbon metabolism to nitrogen starvation is different from that of green algae and higher plants. *Plant Physiol.* 158, 299–312. doi: 10.1104/pp.111.184333

Hu, Q., Sommerfeld, M., Jarvis, E., Ghirardi, M., Posewitz, M., Seibert, M., et al. (2008). Microalgal triacylglycerols as feedstocks for biofuel production: perspectives and advances. *Plant J.* 54, 621–639. doi: 10.1111/j.1365-313X.2008.03492.x

Imamura, S., Kawase, Y., Kobayashi, I., Sone, T., Era, A., Miyagishima, S. -Y., et al. (2015). Target of rapamycin (TOR) plays a critical role in triacylglycerol accumulation in microalgae. *Plant Mol. Biol.* 89, 309–318. doi: 10.1007/s11103-015-0370-6

Iskandarov, U., Khozin-Goldberg, I., and Cohen, Z. (2010). Identification and characterization of Δ12, Δ6, and Δ5 desaturases from the green microalga *Parietochloris incisa*. *Lipids* 45, 519–530. doi: 10.1007/s11745-010-3421-4

Ismagulova, T., Shebanova, A., Gorelova, O., Baulina, O., and Solovchenko, A. (2018). A new simple method for quantification and locating P and N reserves in microalgal cells based on energy-filtered transmission electron microscopy (EFTEM) elemental maps. *PLoS One* 13:e0208830. doi: 10.1371/journal.pone.0208830

Jiang, Q., Zhao, L., Dai, J., and Wu, Q. (2012). Analysis of autophagy genes in microalgae: Chlorella as a potential model to study mechanism of autophagy. *PLoS One* 7:e41826. doi: 10.1371/journal.pone.0041826

Jouhet, J., Maréchal, E., Bligny, R., Joyard, J., and Block, M. A. (2003). Transient increase of phosphatidylcholine in plant cells in response to phosphate deprivation. *FEBS Lett.* 544, 63–68. doi: 10.1016/S0014-5793(03)00477-0

Kajikawa, M., and Fukuzawa, H. (2020). Algal autophagy is necessary for the regulation of carbon metabolism under nutrient deficiency. *Front. Plant Sci.* 11:36. doi: 10.3389/fpls.2020.00036

Kajikawa, M., Yamauchi, M., Shinkawa, H., Tanaka, M., Hatano, K., Nishimura, Y., et al. (2019). Isolation and characterization of Chlamydomonas autophagy-related mutants in nutrient-deficient conditions. *Plant Cell Physiol.* 60, 126–138. doi: 10.1093/pcp/pcy193

Khozin-Goldberg, I., Shrestha, P., and Cohen, Z. (2005). Mobilization of arachidonyl moieties from triacylglycerols into chloroplastic lipids following recovery from nitrogen starvation of the microalga *Parietochloris incisa*. *Biochim. Biophys. Acta Mol. Cell Biol. Lipids* 1738, 63–71. doi: 10.1016/j.bbalip.2005.09.005

Kobayashi, K. (2016). Role of membrane glycerolipids in photosynthesis, thylakoid biogenesis and chloroplast development. *J. Plant Res.* 129, 565–580. doi: 10.1007/s10265-016-0827-y

Kokabi, K., Gorelova, O., Ismagulova, T., Itkin, M., Malitsky, S., Boussiba, S., et al. (2019). Metabolomic foundation for differential responses of lipid metabolism to nitrogen and phosphorus deprivation in an arachidonic acid-producing green microalga. *Plant Sci.* 283, 95–115. doi: 10.1016/j.plantsci.2019.02.008

Kumari, P., Cna'ni, A., Didi-Cohen, S., Tzin, V., and Khozin-Goldberg, I. (2020). Nitrogen deprivation-induced production of volatile organic compounds in the microalga *Lobosphaera incisa* underpins their role as ROS scavengers and chemical messengers. *Front. Mar. Sci.* 7:410. doi: 10.3389/fmars.2020.00410

Li, F. -J., and He, C. Y. (2014). Acidocalcisome is required for autophagy in *Trypanosoma brucei*. *Autophagy* 10, 1978–1988. doi: 10.4161/auto.36183

Li, X., Moellering, E. R., Liu, B., Johnny, C., Fedewa, M., Sears, B. B., et al. (2012). A galactoglycerolipid lipase is required for triacylglycerol accumulation and survival following nitrogen deprivation in *Chlamydomonas reinhardtii*. *Plant Cell* 24, 4670–4686. doi: 10.1105/tpc.112.105106

Liu, X. -Y., Ouyang, L. -L., and Zhou, Z. -G. (2016). Phospholipid: diacylglycerol acyltransferase contributes to the conversion of membrane lipids into triacylglycerol in *Myrmecia incisa* during the nitrogen starvation stress. *Sci. Rep.* 6:26610. doi: 10.1038/srep26610

Livermore, T. M., Chubb, J. R., and Saiardi, A. (2016). Developmental accumulation of inorganic polyphosphate affects germination and energetic metabolism in Dictyostelium discoideum. *Proc. Natl. Acad. Sci. U. S. A.* 113, 996–1001. doi: 10.1073/pnas.1519440113

López García de Lomana, A., Schäuble, S., Valenzuela, J., Imam, S., Carter, W., Bilgin, D. D., et al. (2015). Transcriptional program for nitrogen starvation-induced lipid accumulation in *Chlamydomonas reinhardtii*. *Biotechnol. Biofuels* 8:207. doi: 10.1186/s13068-015-0391-z

Lütz-Meindl, U. (2016). *Micrasterias* as a model system in plant cell biology. *Front. Plant Sci.* 7:999. doi: 10.3389/fpls.2016.00999

Mahamid, J., Tegunov, D., Maiser, A., Arnold, J., Leonhardt, H., Plitzko, J. M., et al. (2019). Liquid-crystalline phase transitions in lipid droplets are related to cellular states and specific organelle association. *Proc. Natl. Acad. Sci.* 116, 16866–16871. doi: 10.1073/pnas.1903642116

Malitsky, S., Ziv, C., Rosenwasser, S., Zheng, S., Schatz, D., Porat, Z., et al. (2016). Viral infection of the marine alga *Emiliania huxleyi* triggers lipidome remodeling and induces the production of highly saturated triacylglycerol. *New Phytol.* 210, 88–96. doi: 10.1111/nph.13852

Martin, N. C., Chiang, K. S., and Goodenough, U. W. (1976). Turnover of chloroplast and cytoplasmic ribosomes during gametogenesis in *Chlamydomonas reinhardii*. *Dev. Biol.* 51, 190–201. doi: 10.1016/0012-1606(76)90137-8

Masclaux-Daubresse, C., D'andrea, S., Bouchez, I., Cacas, J. L., and Raines, C. (2020). Reserve lipids and plant autophagy. *J. Exp. Bot.* 71, 2854–2861. doi: 10.1093/jxb/eraa082

Merzlyak, M. N., Chivkunova, O. B., Gorelova, O. A., Reshetnikova, I. V., Solovchenko, A. E., Khozin-Goldberg, I., et al. (2007). Effect of nitrogen starvation on optical properties, pigments, and arachidonic acid content of the unicellular green alga *Parietochloris incisa* (Trebouxiophyceae, Chlorophyta). *J. Phycol.* 43, 833–843. doi: 10.1111/j.1529-8817.2007.00375.x

Minina, E. A., Moschou, P. N., Vetukuri, R. R., Sanchez-Vera, V., Cardoso, C., Liu, Q., et al. (2018). Transcriptional stimulation of rate-limiting components of the autophagic pathway improves plant fitness. *J. Exp. Bot.* 69, 1415–1432. doi: 10.1093/jxb/ery010

Moudříková, Š., Nedbal, L., Solovchenko, A., and Mojzeš, P. (2017). Raman microscopy shows that nitrogen-rich cellular inclusions in microalgae are microcrystalline guanine. *Algal Res.* 23, 216–222. doi: 10.1016/j.algal.2017.02.009

Mühlroth, A., Winge, P., El Assimi, A., Jouhet, J., Maréchal, E., Hohmann-Marriott, M. F., et al. (2017). Mechanisms of phosphorus acquisition and lipid class remodeling under P limitation in a marine microalga. *Plant Physiol.* 175, 1543–1559. doi: 10.1104/pp.17.00621

Mukaida, S., Ogawa, T., Ohishi, K., and Tanizawa, Y. (2016). The effect of rapamycin on biodiesel-producing protist *Euglena gracilis*. *Biosci. Biotechnol. Biochem.* 80, 1223–1229. doi: 10.1080/09168451.2016.1141040

Nonoyama, T., Nojima, D., Maeda, Y., Noda, M., Yoshino, T., Matsumoto, M., et al. (2019). Proteomics analysis of lipid droplets indicates involvement of membrane trafficking proteins in lipid droplet breakdown in the oleaginous diatom *Fistulifera solaris*. *Algal Res.* 44:101660. doi: 10.1016/j.algal.2019.101660

Pal-Nath, D., Didi-Cohen, S., Shtaida, N., Nath, P. R., Samani, T., Boussiba, S., et al. (2017). Improved productivity and oxidative stress tolerance under nitrogen starvation is associated with the ablated Δ5 desaturation in the green microalga *Lobosphaera incisa*. *Algal Res.* 26, 25–38. doi: 10.1016/j.algal.2017.06.026

Pérez-Pérez, M., Couso, I., and Crespo, J. (2017). The TOR Signaling network in the model unicellular green alga *Chlamydomonas reinhardtii*. *Biomol. Ther.* 7:54. doi: 10.3390/biom7030054

Perez-Perez, M. E., Lemaire, S. D., and Crespo, J. L. (2012). Reactive oxygen species and autophagy in plants and algae. *Plant Physiol.* 160, 156–164. doi: 10.1104/pp.112.199992

Pérez-Pérez, M. E., Lemaire, S. D., and Crespo, J. L. (2016). Control of autophagy in Chlamydomonas is mediated through redox-dependent inactivation of the ATG4 protease. *Plant Physiol.* 172, 2219–2234. doi: 10.1104/pp.16.01582

Phillips, A. R., Suttangkakul, A., and Vierstra, R. D. (2008). The ATG12-conjugating enzyme ATG10 is essential for autophagic vesicle formation in *Arabidopsis thaliana*. *Genetics* 178, 1339–1353. doi: 10.1534/genetics.107.086199

Pick, U., Rental, M., Chitlaru, E., and Weiss, M. (1990). Polyphosphate-hydrolysis - a protective mechanism against alkaline stress? *FEBS Lett.* 274, 15–18. doi: 10.1016/0014-5793(90)81318-I

Polle, J. E. W., Roth, R., Ben-amotz, A., and Goodenough, U. (2020). Ultrastructure of the green alga *Dunaliella salina* strain CCAP19/18 (Chlorophyta) as investigated by quick-freeze deep-etch electron microscopy. *Algal Res.* 49:101953. doi: 10.1016/j.algal.2020.101953

Poxleitner, M., Rogers, S. W., Lacey Samuels, A., Browse, J., and Rogers, J. C. (2006). A role for caleosin in degradation of oil-body storage lipid during seed germination. *Plant J.* 47, 917–933. doi: 10.1111/j.1365-313X.2006.02845.x

Prioretti, L., Avilan, L., Carrière, F., Montané, M. H., Field, B., Grégori, G., et al. (2017). The inhibition of TOR in the model diatom *Phaeodactylum tricornutum* promotes a get-fat growth regime. *Algal Res.* 26, 265–274. doi: 10.1016/j.algal.2017.08.009

Ramanan, R., Tran, Q. -G., Cho, D. -H., Jung, J. -E., Kim, B. -H., Shin, S. -Y., et al. (2018). The ancient phosphatidylinositol 3-kinase Signaling system is a master regulator of energy and carbon metabolism in algae. *Plant Physiol.* 177, 1050–1065. doi: 10.1104/pp.17.01780

Ramundo, S., Casero, D., Mühlhaus, T., Hemme, D., Sommer, F., Crèvecoeur, M., et al. (2014). Conditional depletion of the Chlamydomonas chloroplast ClpP protease activates nuclear genes involved in autophagy and plastid protein quality control. *Plant Cell* 26, 2201–2222. doi: 10.1105/tpc.114.124842

Ramundo, S., and Rochaix, J. D. (2014). Loss of chloroplast ClpP elicits an autophagy-like response in Chlamydomonas. *Autophagy* 10, 1685–1686. doi: 10.4161/auto.29960

Remmers, I. M., D'Adamo, S., Martens, D. E., de Vos, R. C. H., Mumm, R., America, A. H. P., et al. (2018). Orchestration of transcriptome, proteome and metabolome in the diatom *Phaeodactylum tricornutum* during nitrogen limitation. *Algal Res.* 35, 33–49. doi: 10.1016/j.algal.2018.08.012

Rismani-Yazdi, H., Haznedaroglu, B. Z., Hsin, C., and Peccia, J. (2012). Transcriptomic analysis of the oleaginous microalga *Neochloris oleoabundans* reveals metabolic insights into triacylglyceride accumulation. *Biotechnol. Biofuels* 5:74. doi: 10.1186/1754-6834-5-74

Ruiz, F. A., Marchesini, N., Seufferheld, M., Govindjee, and Docampo, R. (2001). The polyphosphate bodies of *Chlamydomonas reinhardtii* possess a proton-pumping pyrophosphatase and are similar to Acidocalcisomes. *J. Biol. Chem.* 276, 46196–46203. doi: 10.1074/jbc.M105268200

Sanz-Luque, E., Bhaya, D., and Grossman, A. R. (2020). Polyphosphate: a multifunctional metabolite in cyanobacteria and algae. *Front. Plant Sci.* 11:938. doi: 10.3389/fpls.2020.00938

Schatz, D., Shemi, A., Rosenwasser, S., Sabanay, H., Wolf, S. G., Ben-Dor, S., et al. (2014). Hijacking of an autophagy-like process is critical for the life cycle of a DNA virus infecting oceanic algal blooms. *New Phytol.* 204, 854–863. doi: 10.1111/nph.13008

Schulze, R. J., Sathyanarayan, A., and Mashek, D. G. (2017). Breaking fat: the regulation and mechanisms of lipophagy. *Biochim. Biophys. Acta Mol. Cell Biol. Lipids* 1862, 1178–1187. doi: 10.1016/j.bbalip.2017.06.008

Schwarz, V., Andosch, A., Geretschläger, A., Affenzeller, M., and Lütz-Meindl, U. (2017). Carbon starvation induces lipid degradation via autophagy in the model alga Micrasterias. *J. Plant Physiol.* 208, 115–127. doi: 10.1016/J.JPLPH.2016.11.008

Shebanova, A., Ismagulova, T., Solovchenko, A., Baulina, O., Lobakova, E., Ivanova, A., et al. (2017). Versatility of the green microalga cell vacuole function as revealed by analytical transmission electron microscopy. *Protoplasma* 254, 1323–1340. doi: 10.1007/s00709-016-1024-5

Shemi, A., Ben-Dor, S., and Vardi, A. (2015). Elucidating the composition and conservation of the autophagy pathway in photosynthetic eukaryotes. *Autophagy* 11, 701–715. doi: 10.1080/15548627.2015.1034407

Siegler, H., Valerius, O., Ischebeck, T., Popko, J., Tourasse, N. J., Vallon, O., et al. (2017). Analysis of the lipid body proteome of the oleaginous alga *Lobosphaera incisa*. *BMC Plant Biol.* 17:98. doi: 10.1186/s12870-017-1042-2

Smith, T. F. (2008). Diversity of WD-repeat proteins. *Subcell. Biochem.* 48, 20–30. doi: 10.1007/978-0-387-09595-0_3

Solovchenko, A., Khozin-Goldberg, I., Selyakh, I., Semenova, L., Ismagulova, T., Lukyanov, A., et al. (2019). Phosphorus starvation and luxury uptake in green microalgae revisited. *Algal Res.* 43:101651. doi: 10.1016/j.algal.2019.101651

Takeuchi, T., and Benning, C. (2019). Nitrogen-dependent coordination of cell cycle, quiescence and TAG accumulation in Chlamydomonas. *Biotechnol. Biofuels* 12:292. doi: 10.1186/s13068-019-1635-0

Thompson, A. R., Doelling, J. H., Suttangkakul, A., and Vierstra, R. D. (2005). Autophagic nutrient recycling in Arabidopsis directed by the ATG8 and ATG12 conjugation pathways. *Plant Physiol.* 138, 2097–2110. doi: 10.1104/pp.105.060673

Tran, Q. -G., Yoon, H. R., Cho, K., Lee, S. -J., Crespo, J. L., Ramanan, R., et al. (2019). Dynamic interactions between Autophagosomes and lipid droplets in *Chlamydomonas reinhardtii*. *Cell* 8:992. doi: 10.3390/cells8090992

Tsai, C. -H. H., Uygun, S., Roston, R., Shiu, S. -H., and Benning, C. (2017). Recovery from N deprivation is a transcriptionally and functionally distinct state in Chlamydomonas. *Plant Physiol.* 176, 2007–2023. doi: 10.1104/pp.17.01546

Tsai, C. H., Warakanontb, J., Takeuchic, T., Sears, B. B., Moellering, E. R., and Benningc, C. (2014). The protein compromised hydrolysis of triacylglycerols 7 (cht7) acts as a repressor of cellular quiescence in Chlamydomonas. *Proc. Natl. Acad. Sci. U. S. A.* 111, 15833–15838. doi: 10.1073/pnas.1414567111

Tsednee, M., Castruita, M., Salomé, P. A., Sharma, A., Lewis, B. E., Schmollinger, S. R., et al. (2019). Manganese co-localizes with calcium and phosphorus in Chlamydomonas acidocalcisomes and is mobilized in manganese-deficient conditions. *J. Biol. Chem.* 294, 17626–17641. doi: 10.1074/jbc.RA119.009130

Valledor, L., Furuhashi, T., Recuenco-Muñoz, L., Wienkoop, S., and Weckwerth, W. (2014). System-level network analysis of nitrogen starvation and recovery in *Chlamydomonas reinhardtii* reveals potential new targets for increased lipid accumulation. *Biotechnol. Biofuels* 7:171. doi: 10.1186/s13068-014-0171-1

Watanabe, S., Hirabayashi, S., Boussiba, S., Cohen, Z., Vonshak, A., and Richmond, A. (1996). *Parietochloris incisa* comb. nov. (Trebouxiophyceae, Chlorophyta). *Phycol. Res.* 44, 107–108. doi: 10.1111/j.1440-1835.1996.tb00383.x

Wördenweber, R., Rokitta, S. D., Heidenreich, E., Corona, K., Kirschhöfer, F., Fahl, K., et al. (2018). Phosphorus and nitrogen starvation reveal life-cycle specific responses in the metabolome of *Emiliania huxleyi* (Haptophyta). *Limnol. Oceanogr.* 63, 203–226. doi: 10.1002/lno.10624

Yoon, K., Han, D., Li, Y., Sommerfeld, M., and Hu, Q. (2012). Phospholipid:diacylglycerol acyltransferase is a multifunctional enzyme involved in membrane lipid turnover and degradation while synthesizing triacylglycerol in the unicellular green microalga *Chlamydomonas reinhardtii*. *Plant Cell* 24, 3708–3724. doi: 10.1105/tpc.112.100701

Yoshimoto, K., Hanaoka, H., Sato, S., Kato, T., and Tabata, S. (2004). Processing of ATG8s, ubiquitin-like proteins, and their deconjugation by ATG4s are essential for plant autophagy. *Plant Cell* 16, 2967–2983. doi: 10.1105/tpc.104.025395.et

Yoshitake, Y., Ohta, H., and Shimojima, M. (2019). Autophagy-mediated regulation of lipid metabolism and its impact on the growth in algae and seed plants. *Front. Plant Sci.* 10:709. doi: 10.3389/fpls.2019.00709

Zhao, L., Dai, J., and Wu, Q. (2014). Autophagy-like processes are involved in lipid droplet degradation in *Auxenochlorella protothecoides* during the heterotrophy-autotrophy transition. *Front. Plant Sci.* 5:400. doi: 10.3389/fpls.2014.00400

Zienkiewicz, A., Zienkiewicz, K., Poliner, E., Pulman, J. A., Du, Z. Y., Stefano, G., et al. (2020). The microalga *Nannochloropsis* during transition from quiescence to autotrophy in response to nitrogen availability. *Plant Physiol.* 182, 819–839. doi: 10.1104/pp.19.00854

Zorin, B., Grundman, O., Khozin-Goldberg, I., Leu, S., Shapira, M., Kaye, Y., et al. (2014). Development of a nuclear transformation system for oleaginous green alga *Lobosphaera* (*Parietochloris*) *incisa* and genetic complementation of a mutant strain, deficient in arachidonic acid biosynthesis. *PLoS One* 9:e105223. doi: 10.1371/journal.pone.0105223

Zorin, B., Pal-Nath, D., Lukyanov, A., Smolskaya, S., Kolusheva, S., Didi-Cohen, S., et al. (2017). Arachidonic acid is important for efficient

use of light by the microalga *Lobosphaera incisa* under chilling stress. *Biochim. Biophys. Acta Mol. Cell Biol. Lipids* 1862, 853–868. doi: 10.1016/j.bbalip.2017.04.008

Conflict of Interest: The authors declare that the research was conducted in the absence of any commercial or financial relationships that could be construed as a potential conflict of interest.

Copyright © 2020 Kokabi, Gorelova, Zorin, Didi-Cohen, Itkin, Malitsky, Solovchenko, Boussiba and Khozin-Goldberg. This is an open-access article distributed under the terms of the Creative Commons Attribution License (CC BY). The use, distribution or reproduction in other forums is permitted, provided the original author(s) and the copyright owner(s) are credited and that the original publication in this journal is cited, in accordance with accepted academic practice. No use, distribution or reproduction is permitted which does not comply with these terms.

frontiers in Plant Science

ORIGINAL RESEARCH
published: 10 March 2021
doi: 10.3389/fpls.2021.656962

Expression of a Bacterial Trehalose-6-phosphate Synthase otsA Increases Oil Accumulation in Plant Seeds and Vegetative Tissues

Zhiyang Zhai[1†], Jantana Keereetaweep[1†], Hui Liu[1†], Regina Feil[2†], John E. Lunn[2†] and John Shanklin[1†]*

[1]Department of Biology, Brookhaven National Laboratory, Upton, NY, United States, [2]Max Planck Institute of Molecular Plant Physiology, Potsdam-Golm, Germany

We previously demonstrated that exogenous trehalose 6-phosphate (T6P) treatment stabilized WRINKLED1 (WRI1), a master transcriptional regulator of fatty acid (FA) synthesis and increased total FA content in *Brassica napus* (*B. napus*) embryo suspension cell culture. Here, we explore *Arabidopsis* lines heterologously expressing the *Escherichia coli* T6P synthase (otsA) or T6P phosphatase (otsB) to refine our understanding regarding the role of T6P in regulating fatty acid synthesis both in seeds and vegetative tissues. *Arabidopsis* 35S:*otsA* transgenic seeds showed an increase of 13% in fatty acid content compared to those of wild type (WT), while seeds of 35:*otsB* transgenic seeds showed a reduction of 12% in fatty acid content compared to WT. Expression of otsB significantly reduced the level of WRI1 and expression of its target genes in developing seeds. Like *Arabidopsis* seeds constitutively expressing otsA, transient expression of otsA in *Nicotiana benthamiana* leaves resulted in strongly elevated levels of T6P. This was accompanied by an increase of 29% in *de novo* fatty acid synthesis rate, a 2.3-fold increase in triacylglycerol (TAG) and a 20% increase in total fatty acid content relative to empty vector (EV) controls. Taken together, these data support the heterologous expression of otsA as an approach to increasing TAG accumulation in plant seeds and vegetative tissues.

Keywords: trehalose 6 phosphate, triacylglycerol, fatty acid synthesis, oil accumulation, sugar signaling

OPEN ACCESS

Edited by:
Mie Shimojima,
Tokyo Institute of Technology, Japan

Reviewed by:
Frederik Börnke,
Leibniz Institute of Vegetable and Ornamental Crops, Germany
Jin-Song Zhang,
Institute of Genetics and Developmental Biology (CAS), China

****Correspondence:***
John Shanklin
shanklin@bnl.gov

[†]ORCID:
Zhiyang Zhai
orcid.org/0000-0003-3181-1773
Jantana Keereetaweep
orcid.org/0000-0001-8314-9289
Hui Liu
orcid.org/0000-0001-8524-1759
Regina Feil
orcid.org/0000-0002-9936-1337
John E. Lunn
orcid.org/0000-0001-8533-3004
John Shanklin
orcid.org/0000-0002-6774-8043

Specialty section:
This article was submitted to Plant Physiology, a section of the journal Frontiers in Plant Science

Received: *22 January 2021*
Accepted: *18 February 2021*
Published: *10 March 2021*

Citation:
Zhai Z, Keereetaweep J, Liu H, Feil R, Lunn JE and Shanklin J (2021) Expression of a Bacterial Trehalose-6-phosphate Synthase otsA Increases Oil Accumulation in Plant Seeds and Vegetative Tissues. Front. Plant Sci. 12:656962. doi: 10.3389/fpls.2021.656962

INTRODUCTION

Lipids play key roles as structural components of cell membranes, energy-dense storage compounds, and cell signaling molecules. Fatty acids (FA) are major components of triacylglycerols (TAG), which occur in all tissues but accumulate to very high levels within lipid droplets in plant seeds (Li-Beisson et al., 2013). *De novo* synthesis of FA occurs in the plastid *via* the action of two multi-component enzyme systems: acetyl-CoA carboxylase (ACCase) and fatty acid synthase (Ohlrogge and Browse, 1995; Rawsthorne, 2002). In *Arabidopsis*, WRINKLED1 (WRI1), an APETALA2 (AP2)-type transcription factor, is a master transcriptional activator of FA synthesis. To date, more than 20 *WRI1* target genes coding for various steps in glycolysis

and fatty acid synthesis have been identified (Ruuska et al., 2002; Baud et al., 2007; Maeo et al., 2009; Fukuda et al., 2013; Li et al., 2015; Liu et al., 2019).

Fatty acids are synthesized *de novo* from acetyl-CoA, which is ultimately derived from photosynthetically derived sugars. Previous studies have demonstrated that sugars can potentiate fatty acid synthesis. For example, *Arabidopsis* leaves in which *ADG1* (encoding the small subunit of ADP-glucose pyrophosphorylase) was reduced by RNAi contained 3-fold more sucrose along with a 30% increase in TAG relative to wild type (WT; Sanjaya et al., 2011). In another study, it was shown that *Arabidopsis* roots accumulated 4-fold more TAG in the presence of one-half-strength MS medium supplemented with 5% sucrose compared to controls lacking sucrose (Kelly et al., 2013). To test the influence of endogenous sugar content on FA and TAG accumulation, we generated a high-leaf-sugar line by reducing sugar phloem loading along with starch synthesis by crossing the *suc2* (encoding a sucrose/H+ symporter that loads Sucrose into the phloem) mutant (Srivastava et al., 2009) with the *adg1* mutant. The sugar content (combined glucose and sucrose) in *adg1suc2* leaves is 80-fold higher than that of WT. Leaf TAG accumulation in *adg1suc2* increased by more than 10-fold relative to WT reaching approximately 1% of dry weight (DW; Zhai et al., 2017b). Besides the effects of sugars as direct precursors that supply carbon skeletons for FA synthesis, progress has also been made toward elucidating the effects of sugar signaling on FA synthesis. In one example, pyruvate and the tricarboxylic acid cycle intermediates: 2-oxoglutarate and oxaloacetate were shown to completely reverse the PII-dependent inhibition of ACCase (Bourrellier et al., 2010). PII is an evolutionarily conserved signal integrator involved in the regulation of nitrogen/carbon homeostasis in bacteria and plants that binds to the biotin carboxyl carrier protein (BCCP) subunit of the plastidial ACCase inhibiting its activity by up to 50% (Bourrellier et al., 2010). A second link between the availability of sugar and FA synthesis involves the snf1-related protein kinase1 (SnRK1), a major plant carbon/energy sensor (Baena-González et al., 2007). Under low sugar conditions, KIN10, the catalytic subunit of SnRK1 phosphorylates WRI1 predisposing it to proteasomal degradation. However, in the presence of higher sugar levels, KIN10 phosphorylation of WRI1 is inhibited and WRI1 is stabilized, increasing the transcription of WRI1 target genes involved in FA synthesis (Zhai et al., 2017a). This regulatory mechanism, couples FA synthesis to the availability of cellular carbon and energy.

In plants, the phosphorylated disaccharide trehalose 6-phosphate (T6P) acts as a signal of sucrose availability connecting its intracellular metabolic status with plant growth and development (Schluepmann et al., 2003; Lunn et al., 2006; Yadav et al., 2014; Figueroa and Lunn, 2016; Fichtner and Lunn, 2021). T6P is synthesized by the action of T6P synthase (TPS) with UDP-Glc (UDPG) and Glc 6-phosphate (G6P), both of which are central to plant metabolism (Cabib and Leloir, 1958). SnRK1 activity in crude extracts from developing *Arabidopsis* tissues is strongly inhibited by T6P, and the inhibition was reported to depend on unknown protein factor(s) principally expressed in young tissues (Zhang et al., 2009; Martínez-Barajas et al., 2011; Griffiths et al., 2016). KIN10 is activated by GEMINIVIRUS REP-INTERACTING KINASE1 (GRIK1; also known as SnRK1 ACTIVATING KINASE1, SnAK1) and GRIK2 (SnAK2), which phosphorylate T175 in KIN10's activation loop (Shen et al., 2009; Glab et al., 2017).

We recently demonstrated that T6P can bind directly to KIN10 at physiological concentrations and weaken its association with GRIK, thereby lowering its activation status and inhibiting SnRK1 phosphorylation of WRI1. This was confirmed by *in vivo* experiments in which a *Brassica napus* suspension cell culture was fed T6P in the medium, and WRI1 accumulated, resulting in the activation of FA synthesis (Zhai et al., 2018).

An alternative to feeding cell cultures with T6P is the use of *Arabidopsis* lines heterologously expressing the *Escherichia coli* T6P synthase (otsA), which have well documented elevation in T6P levels, and lines expressing T6P phosphatase (otsB) to increase T6P dephosphorylation to trehalose, which has been reported to lower T6P levels (Schluepmann et al., 2003; Wingler et al., 2012) or lead to the accumulation of sucrose and a reduction in the T6P:sucrose ratio (Yadav et al., 2014). Here, we make use of these previously reported stably transformed *Arabidopsis* otsA/otsB-overexpressing lines (Schluepmann et al., 2003; Wingler et al., 2012) along with transient expression of otsA and otsB in *Nicotiana benthamiana* leaves to investigate the effects of T6P on the regulation of FA synthesis in seeds and vegetative tissues, respectively. *Arabidopsis* otsA transgenics accumulate more seed oil and tobacco leaves transiently expressing otsA also show increased TAG accumulation, demonstrating that otsA overexpression is a viable approach for increasing lipid accumulation in both source and sink tissues.

MATERIALS AND METHODS

Plant Materials and Growth Conditions

Arabidopsis 35S:otsA and *35S:otsB* lines were obtained from Astrid Wingler (University of Cork, Ireland; Schluepmann et al., 2003; Wingler et al., 2012). *Arabidopsis* seeds were surface-sterilized and selected on agar plates containing half-strength Murashige and Skoog salts. After 1 week, seedlings were transplanted to moist soil (seed BM2 mix, Berger, Saint-Modeste, Canada). All plants (*Arabidopsis* and *N. benthamiana*) were grown with a 16 h-light/8 h-dark photoperiod (combination of cool white, fluorescent lamps, and incandescent lamps, at a photosynthetic photon flux density of 250 μmol m^{-2} s^{-1}) with a 23°/19°C day/night, 16/8 h temperature regime and approximately 75% relative humidity.

Genetic Constructs

The *otsA* and *otsB* coding regions were amplified by PCR from *E. coli* genomic DNA using primer pairs listed in supplementary Table S1. The PCR products were then cloned into the Invitrogen GATEWAY^{M} pDONR/Zeo vector (Thermo Fisher Scientific, Waltham, MA)[1] using the BP reaction and

[1]www.thermofisher.com

sub-cloned (LR reaction) into the plant GATEWAY™ binary vector: pGWB414 (Nakagawa et al., 2007) for transient expression in *N. benthamiana*.

Agroinfiltration of *Nicotiana benthamiana*

Transient gene expression in *N. benthamiana* by agroinfiltration was accomplished using a previously described procedure (Ohad and Yalovsky, 2010). Infiltrated leaves were harvested 3 days after infiltration with different constructs and analyzed for T6P and lipid contents and for SnRK1 kinase activity and *in vivo* [1-^{14}C] acetate labeling.

T6P Quantification

Water-soluble metabolites were extracted from aliquots (10–20 mg) of frozen tissue powder using chloroform-methanol (Lunn et al., 2006) and evaporated to dryness using a centrifugal vacuum drier. The dried extract was dissolved in 350 µl purified H_2O and filtered through MultiScreen PCR-96 Filter Plate membranes (Merck Millipore)[2] to remove high molecular weight compounds. T6P, phosphorylated intermediates, and organic acids were measured by high performance anion-exchange chromatography coupled to tandem mass spectrometry as described by Lunn et al. (2006), with modifications as described by Figueroa et al. (2016).

Triacylglycerol and Total Fatty Acid Quantification

Total lipids (TAG plus polar lipids) were isolated from 100 mg of freshly harvested leaf tissue by the addition of 700 µl of methanol:chloroform:formic acid (2:1:0.1, by volume) by vigorous shaking for 30 min, after which 1 ml of 1 M KCl, 0.2 M H_3PO_4 was added. After mixing, the samples were centrifuged at 1,500 × *g* (4°C) for 5 min, and total lipids were collected in the lower phase (chloroform). For TAG quantification, 60 µl of total lipid were separated by Silica Gel 60 (Merck Millipore, Billerica, MA)[3] TLC developed with hexane:diethyl ether:acetic acid (70,30:1, by volume) and visualized by spraying with 0.05% (w/v) primuline [in 80% (v/v) acetone]. TAG fractions identified under UV light were scraped from the plate and transmethylated to FA methyl esters (FAMEs) by incubation in 1 ml 12% (w/v) boron trichloride in methanol at 85°C for 40 min. For total FA quantification, 10 µl of total lipids were directly transmethylated with boron trichloride-methanol as described above. For both assays, 5 µg heptadecanoic acid (C17:0) was added as internal standard prior to transmethylation. FAMEs were extracted into hexane and dried under a nitrogen stream before being dissolved in 100 µl hexane and analyzed by GC-MS with an Agilent Technologies (Santa Clara, CA)[4] 7890A GC System equipped with an Agilent 60 m DB23 capillary column (ID 250-µm) and a 5975C mass selective detector.

In vivo [1-^{14}C] Acetate Labeling

Labeling experiments were performed essentially as described by Koo et al. (2004). *Nicotiana benthamiana* leaves were incubated in 25 mM MES-NaOH, pH 5.7 buffer containing 0.01% (w/v) Tween-20 as wetting agent under illumination (180 µmol m^{-2} s^{-1}) at 25°C. Labeling was initiated by the addition of 370 kBq of sodium [1-^{14}C] acetate solution (2.15 GBq/mmol, American Radiolabeled Chemicals, St Louis, MO).[5] Labeling was terminated by removal of the medium from the leaf, and the sample was washed three times with water. Total lipids were extracted and separated as described above. Radioactivity associated with total lipids was determined by liquid scintillation counting using a Tri-carb instrument (PerkinElmer).

Antibodies and Immunoblotting

Anti-WRI1 polyclonal antibodies were described by Zhai et al. (2017a). Anti-histone H3 polyclonal antibodies were purchased from Agrisera (Catalog No. AS10710, Vännäs, Sweden).[6] Proteins were resolved by SDS-PAGE (5–15% acrylamide gels) and transferred to PVDF membrane for immunoblot analysis. During primary antibody probe, WRI1 antibody with 1:5,000 dilution or H3 antibody (1:2,000) was incubated at 4°C overnight. Immunoblots of targeted proteins were visualized using alkaline phosphatase-conjugated secondary antibodies with colorimetric detection using 5-bromo-4-chloro-3-indolylphosphate/nitro-blue tetrazolium (BCIP/NBT; Bio-Rad). Immunoblot signals were digitalized with Image Quant LAS4000 and quantified with GelAnalyzer2010a.

RNA Isolation and Quantitative PCR (RT-qPCR)

To quantify gene expression, total RNA was extracted using an RNeasy Plant Mini Kit (Qiaqen, Gaithersburg, MD)[7] following the manufacturer's instructions. cDNA was prepared using SuperScript III First-Strand Synthesis SuperMix (Invitrogen). Quantitative PCR (qPCR) was performed using the CFX96 qPCR Detection System (Bio-Rad) and gene-specific primers for *BCCP2* (At5g15530), *KAS1* (At5g46290), and *PKPβ1* (At5g52920), with *F-box* (At5g15710) for *Arabidopsis*; Ctg24993647 for *N. benthamiana* as a reference gene, using oligonucleotide primers as described in Supplementary Table S1. Statistical analysis of RT-qPCR data was performed using the REST2009 algorithm (Pfaffl et al., 2002).

Accession Numbers

Sequence data from this article can be found in The *Arabidopsis* Information Resource or UniProtKB under the following accession numbers: *WRI1* (At3g54320), *F-box* (At5g15710), *BCCP2* (At5g15530), *KAS1* (At5g46290), *PKPβ1* (At5g52920), *otsA* (P31677), and *otsB* (C1KFX6).

[2]www.merckmillipore.com
[3]www.emdmillipore.com
[4]www.agilent.com
[5]www.arcincusa.com
[6]www.agrisera.com
[7]www.qiagen.com

RESULTS

Overexpression of otsA Increases Fatty Acid Content in *Arabidopsis* Seeds

In previous work, we showed that exogenous T6P can be taken up by *B. napus* suspension cells and cause a significant increase in total FA content relative to sucrose- or sorbitol-treated (Zhai et al., 2018). These experiments implicated T6P in the regulation of lipid accumulation, but its role in lipid synthesis *in planta* remained to be explored. Thus, to test whether elevated levels of T6P resulting from the expression of otsA also positively regulates FA accumulation in seeds, we obtained previously characterized transgenic *Arabidopsis* lines that constitutively express otsA with elevated T6P content, and otsB with reduced T6P content relative to WT (Schluepmann et al., 2003; Wingler et al., 2012). While 35S:*otsA* transgenic seeds appear visibly similar to those of wild type, 35S:*otsB* transgenic seeds frequently appear less symmetrical (**Figure 1A**). Quantification of FA showed significant differences between wild type seeds and those overexpressing either *otsA* or *otsB* (**Figures 1B,C**). The 35S:*otsA* transgenic seeds have 13% more FA on a DW basis than wild type seeds. Conversely, 35:*otsB* transgenic seed accumulated 12% lower levels of total FA than those of wild type (**Figure 1B**). Quantification of total FA as a proportion of seed dry weight

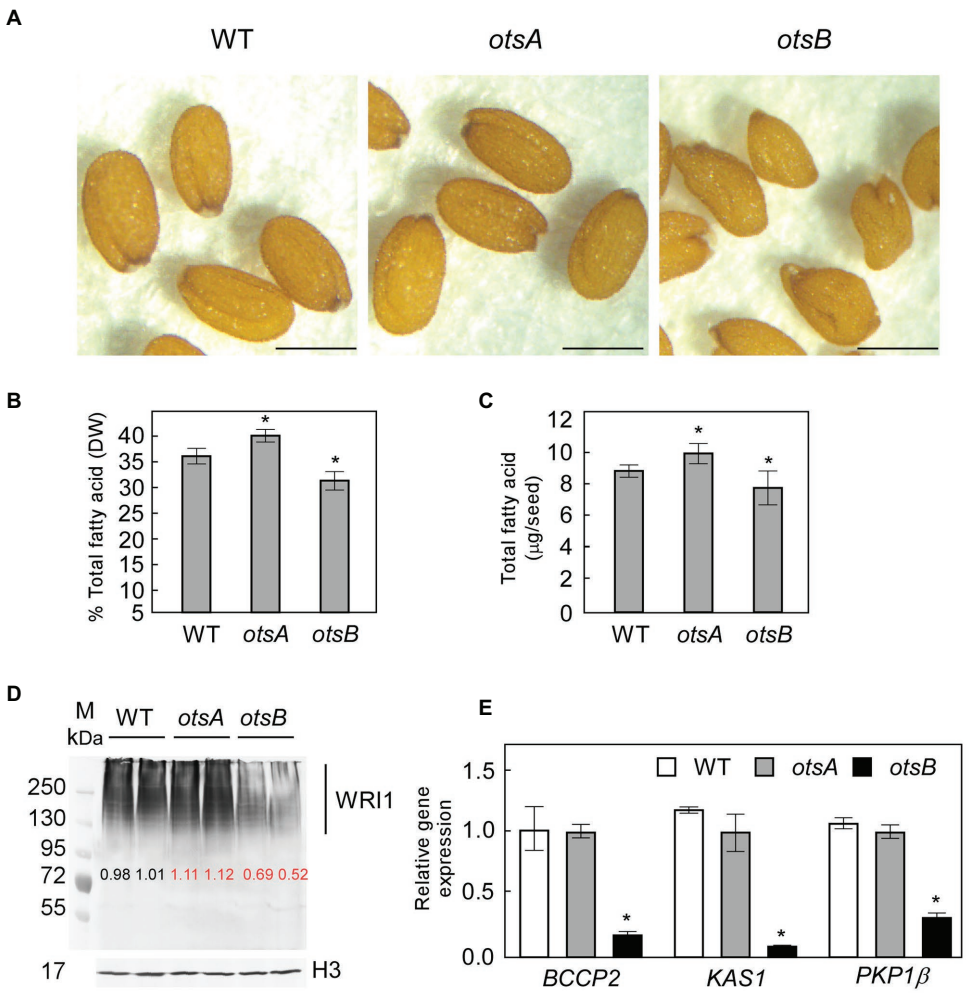

FIGURE 1 | Expression of a bacterial trehalose 6-phosphate (T6P) synthase (TPS) otsA in *Arabidopsis* increases seed fatty acid content by stabilizing WRINKLED1 (WRI1). **(A)** Representative phenotype of seeds of wild type (WT) *Arabidopsis* and of *35S:otsA*- and *35S:otsB*-expressing transgenic lines. Bar = 0.2 mm. Seed total fatty acid contents are presented on percentage dry weight (DW; **B**) and per seed **(C)** basis. Values represent mean ± SD, $n = 5$ for each sample of 30 seeds. Asterisks denote statistically significant difference from WT (Student's *t*-test, $^*p < 0.05$). **(D)** Levels of WRI1 in developing siliques [10 days after flowering (DAF)] were quantified from four biological replicates with GelAnalyzer2010 and normalized to the level of histone H3 (H3) in respective samples. A representative immunoblot is shown. Numbers in red indicate significant differences in mean levels from those of WT (Student's *t*-test, $p < 0.05$). **(E)** Expression levels of three of the gene targets of WRI1: *BCCP2*, *KAS1*, and *PKP-1*b. Values are means ± SD ($n = 3$) from three independent experiments. Transcript abundance is expressed relative to WT. For each experiment, total RNA was isolated from siliques (10 DAF) from WT, *35S:otsA*, and *35S:otsB* transgenic plants. Asterisks denote statistically significant differences from WT [using mean crossing point deviation analysis computed by the relative expression (REST) software algorithm, $^*p < 0.05$].

showed a similar trend (**Figure 1C**). To detect the WRI1 polypeptide in seeds, protein was extracted from siliques 10 days after flowering (DAF) and subjected to western blotting using anti-WRI1 antibodies. Consistent with our previous analysis of *Arabidopsis* seed extracts (Zhai et al., 2017a), we detected no unmodified WRI1 (49.3 kDa), but rather an ensemble of modified WRI1 species of higher molecular masses, which were previously identified as ubiquitin-WRI1 conjugates (**Figure 1D**). The levels of WRI1 polypeptide in extracts of 35:*otsA* transgenic seed were approximately 10% higher than these of corresponding wild type extracts. Conversely, WRI1 polypeptide levels in 35:*otsB* transgenic seed were reduced by 40% relative to wild type. Expression levels of *BCCP2*, *KAS1*, and *PKP-β1*, three target genes of WRI1 were measured by quantitative PCR of mRNA derived from siliques 10 DAF. While significant changes were not observed in *otsA*-overexpressing transgenics at 10 DAF, all three target genes showed significantly reduced levels of expression in 35S:*otsB* transgenics compared to wild type and 35S:*otsA* transgenics at this timepoint (**Figure 1E**).

Transient Expression of otsA Increases *de novo* Fatty Acid Biosynthesis in *Nicotiana benthamiana* Leaves

Transient expression in *N. benthamiana* leaves has emerged as a standard model system for exploring the effects of expressing lipogenic factors in plant vegetative tissues (Wood et al., 2009; Grimberg et al., 2015). We therefore used this system to assess whether elevated levels of T6P could positively regulate FA synthesis in plant vegetative tissues. The T6P level in *N. benthamiana* leaves expressing otsA (*35S:otsA*) for 3 days significantly increased intracellular T6P by several orders of magnitude relative to empty vector (EV) controls, while T6P levels in otsB overexpressing leaves were not significantly different from those of EV controls at 3 days (**Figure 2A**). Extractable SnRK1 activity in leaves expressing otsA was significantly lower than EV controls, SnRK1 activity in leaves expressing otsB was significantly higher than that EV controls (**Figure 2B**). The otsA expressing leaves also accumulated significant 2.3-fold increases in TAG and 20% higher total FA than EV controls (**Figures 2C,D**). To test whether higher TAG accumulation in otsA expressing leaves resulted from *de novo* fatty acid biosynthesis, we performed [1-^{14}C] acetate labeling studies in *N. benthamiana* leaves. The rate of FA synthesis in leaves expressing otsA was 29% higher than that of control leaves transformed with EV (**Figure 2E**).

DISCUSSION

The high cost of metabolic energy for lipid synthesis places an imperative on cells to proceed only when their intracellular carbon/energy levels are sufficient to support it. SnRK1, which evolved from an ancient family of energy sensors (Broeckx et al., 2016) that include mammalian AMP-dependent kinase and the fungal sucrose non-fermenting 1 (SNF1) kinase evolved to sense carbon/energy and post translationally regulate WRI1 and a host of other protein targets by phosphorylation under low carbon conditions (Zhai et al., 2017a). Such phosphorylation of WRI1 predisposes it to ubiquitination by a yet-to-be identified ubiquitin ligase leading to proteasomal degradation (Zhai et al., 2017a). Under conditions of high sugar, the levels of T6P become elevated (Lunn et al., 2006). T6P binds to KIN10, interfering with its activation by GRIK, thereby disrupting activation of SnRK1 activity limiting WRI1 phosphorylation and degradation (Zhai et al., 2018). Consequently, stabilized WRI1 accumulates and activates expression of its target genes leading to increased FA synthesis.

Optimizing TAG accumulation in plants is a central agronomic and biotechnological goal. The mechanism of WRI1 regulation detailed above offers several opportunities for intervention for optimizing TAG accumulation. One approach would be to minimize the activities of SnRK1 or its activating kinase GRIK. However, lines with strongly reduced expression of SnRK1 and GRIK activity display dwarf phenotypes that would result in unacceptable yield losses (Baena-González et al., 2007; Glab et al., 2017; Baena-González and Lunn, 2020). Another potential approach would be to interfere in other ways with the activation of KIN10 by GRIK1. In plants, a complex regulatory network maintains a proportionate relationship between the levels of T6P and the major photosynthetic sugar, sucrose (Yadav et al., 2014). While the overexpression of otsA or otsB in *Arabidopsis* does not break the correlation between sucrose and T6P, its effects can be attributed to a change in the slope of their relationship (Yadav et al., 2014). Our previous work linking T6P to the regulation of lipid synthesis was based on a combination of exogenous feeding of T6P to cultured *B. napus* cells along with biochemical and biophysical analysis. Here, we test our hypothesis that otsA-overexpressing lines containing elevated T6P (Schluepmann et al., 2003; Wingler et al., 2012) should also contain elevated levels of WRI1, FA synthesis and lipid accumulation. Conversely, the *E. coli* otsB-overexpressing lines should show reduced accumulation of WRI1, FA synthesis and lipid accumulation. That otsA overexpressing lines contained 13% more lipid and otsB overexpressing lines had 12% less lipid. Quantification of WRI1 showed that otsA-overexpressing lines had higher levels of WRI1, while otsB-overexpressing lines had lower levels of WRI1 than WT. We noted that in **Figure 1E**, higher levels of WRI1 did not result in higher levels of WRI1 target genes (BCCP, *KAS1*, and *PKP*). One possible explanation is that endogenous WRI1 expression peaks in seeds 10 DAF, which saturates the target gene promoters. Under such a scenario extra WRI1 resulting from its stabilization by otsA-mediated T6Pincrease would not be expected to result in an additional increase in WRI1 targets gene transcription. Taken together, these results are consistent with our hypothesis and validate the approach of using otsA overexpression to boost seed oil accumulation. However, in addition to the inhibition of SnRK1 activation by T6P, we note that constitutive otsA overexpression has been reported to result in pleiotropic effects involving changes in sucrose metabolism and its transport that could also contribute to the observed lipid phenotype (Yadav et al., 2014; Fichtner et al., 2020).

Several other approaches involving WRI1 have been explored to increase TAG accumulation. Mutations Thr70Ala and Ser166Ala, in the SnRK1 target sites within the conserved AP2 DNA-binding domains of WRI1 led to increased

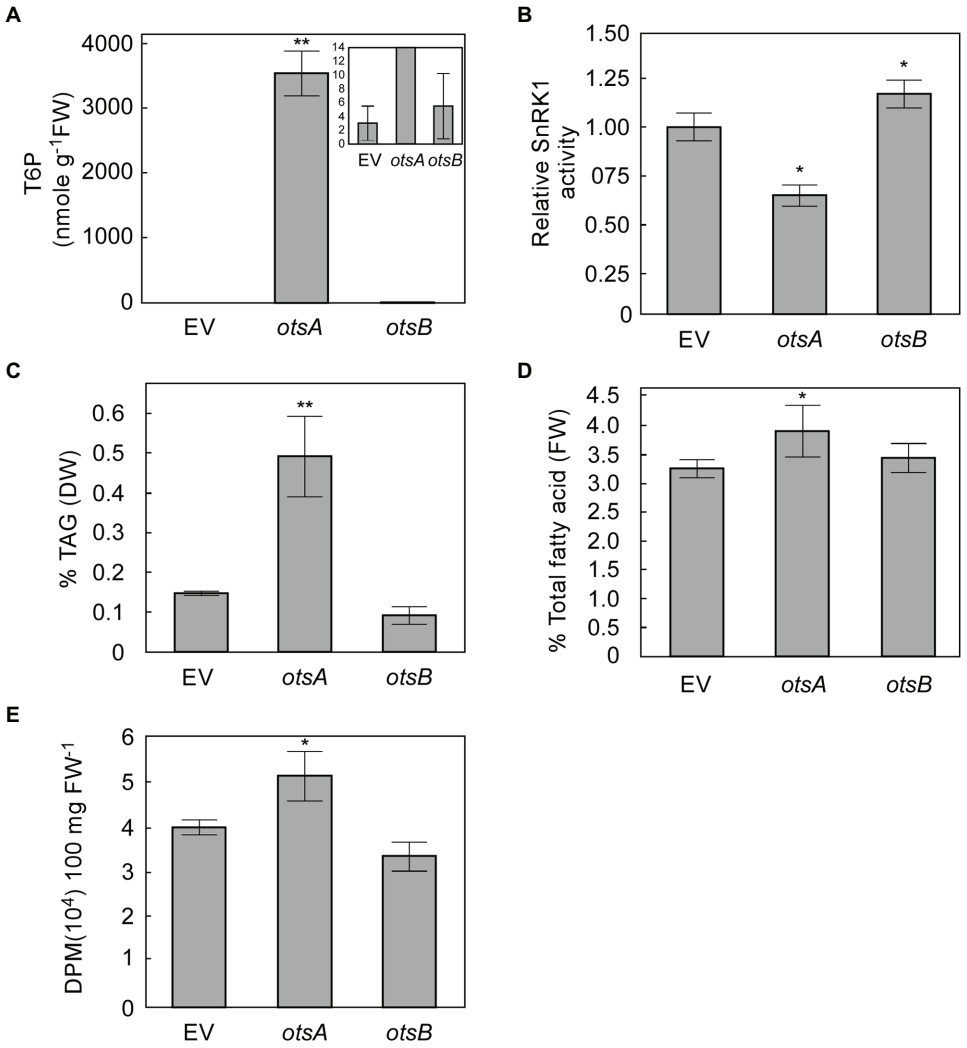

FIGURE 2 | Transient expression of TPS (otsA) increases biosynthesis of both triacylglycerol (TAG) and total fatty acid in *Nicotiana benthamiana* leaves. **(A)** T6P contents in 5-week-old *N. benthamiana* leaves transformed with empty vector (EV) or expressing *otsA* or *otsB* for 3 days. Values represent mean ± SD, $n = 5$ biological replicates (Student's *t*-test, $^{*}p < 0.05$; $^{**}p < 0.01$). **(B)** SnRK1 activity in crude extracts of infiltrated *N. benthamiana* leaves described in **(A)**. TAG **(C)** and total fatty **(D)** were quantified in the samples described in **(A)**. **(E)** [1-^{14}C] acetate incorporation into fatty acyl products by strips of *N. benthamiana* leaves transiently expressing genes as indicated. Values represent mean incorporation ± SD ($n = 5$) after 30 min of labeling. Asterisks denote statistically significant differences from the EV control material (Student's *t*-test, $^{*}p < 0.05$; $^{**}p < 0.01$).

accumulation of theWRI1 polypeptide. However, this did not boost TAG accumulation, likely due to changes in the ability of the mutated WRI1 to bind to DNA (Zhai et al., 2017a). WRI1 was stabilized upon the expression of a 14–3-3 protein, which resulted in increased TAG accumulation, presumably through its binding to phosphorylated WRI1, blocking its recognition by the ubiquitin-conjugation complex (Ma et al., 2016). In another approach, putative N-terminal ubiquitin conjugation sites at Lys2 and Lys3 in the *Arabidopsis* WRI1 amino acid sequence were converted to Ala, resulting in both stabilization of the WRI1 polypeptide and increased TAG accumulation (Zhai et al., 2017a).

While optimizing oil accumulation in sink tissues such as seeds is desirable to maximize TAG yield per acre for conventional oilseed crops, optimizing TAG yield in vegetative source tissues of many fast-growing biomass plants, specifically in leaves (Vanhercke et al., 2017) and stems (Zale et al., 2016; Parajuli et al., 2020) has garnered much interest in recent years. Consistent with seed FA, we also observed higher total fatty acid content in leaves of *Arabidopsis* otsA-overexpressing lines than that in WT leaves (**Supplementary Figure S1**). However, the very low TAG contents in *Arabidopsis* leaves, makes quantifying the variation of TAG levels challenging. Because tobacco (*Nicotiana tabacum*) has been shown to tolerate leaf TAG accumulation, and *N. benthamiana* has been extensively used as a model system to study vegetative oil accumulation using transient gene expression (Wood et al., 2009; Grimberg et al., 2015), we used it to explore the effects

of T6P manipulation on oil accumulation in vegetative tissues. OtsA-overexpression resulted in T6P accumulation levels several orders of magnitude higher than the reported *K*d of T6P binding to KIN10, ensuring the saturation of KIN10 by T6P, and thereby minimizing its activation by GRIK (Zhai et al., 2018). Under these conditions TAG accumulation increased by 2.3-fold, validating the otsA-overexpression approach for boosting vegetative TAG accumulation.

In summary, we show the overexpression of a bacterial T6P-synthesizing enzyme otsA has similar effects with respect to increasing TAG accumulation as we previously reported for the exogenous feeding of T6P to cultured *B. napus* cells (Zhai et al., 2018). Further, we show that otsA overexpression results in increased TAG accumulation in both sink, i.e., seed tissues, and source, i.e., leaf tissues. Deployment of otsA expression in a tissue and/or developmentally specific manner, either alone or along with other lipogenic factors (Xu and Shanklin, 2016; Vanhercke et al., 2019) may contribute to optimizing TAG accumulation in food and biofuel crops of the future.

DATA AVAILABILITY STATEMENT

The raw data supporting the conclusions of this article will be made available by the authors, without undue reservation.

AUTHOR CONTRIBUTIONS

JS, ZZ, and JK conceived the study. ZZ, JK, HL, RF, and JL performed experiments. ZZ, JK, RF, JL, and JS analyzed data. ZZ and JS wrote the manuscript. All authors contributed to the article and approved the submitted version.

FUNDING

This work was supported by the United States Department of Energy, Office of Science, and Office of Basic Energy Sciences under contract number DE-SC0012704, specifically through the Physical Biosciences program of the Chemical Sciences, Geosciences, and Biosciences Division (ZZ, JK, HL, and JS). T6P analysis was supported by the Max Planck Society (RF and JL).

SUPPLEMENTARY MATERIAL

The Supplementary Material for this article can be found online at: https://www.frontiersin.org/articles/10.3389/fpls.2021.656962/full#supplementary-material

Supplementary Table S1 | Oligonucleotide primer sequence pairs.

REFERENCES

Baena-González, E., and Lunn, J. E. (2020). SnRK1 and trehalose 6-phosphate–two ancient pathways converge to regulate plant metabolism and growth. *Curr. Opin. Plant Biol.* 55, 52–59. doi: 10.1016/j.pbi.2020.01.010

Baena-González, E., Rolland, F., Thevelein, J. M., and Sheen, J. (2007). A central integrator of transcription networks in plant stress and energy signalling. *Nature* 448, 938–942. doi: 10.1038/nature06069

Baud, S., Mendoza, M. S., To, A., Harscoët, E., Lepiniec, L., and Dubreucq, B. (2007). WRINKLED1 specifies the regulatory action of LEAFY COTYLEDON2 towards fatty acid metabolism during seed maturation in *Arabidopsis*. *Plant J.* 50, 825–838. doi: 10.1111/j.1365-313X.2007.03092.x

Bourrellier, A. B. F., Valot, B., Guillot, A., Ambard-Bretteville, F., Vidal, J., and Hodges, M. (2010). Chloroplast acetyl-CoA carboxylase activity is 2-oxoglutarate–regulated by interaction of PII with the biotin carboxyl carrier subunit. *Proc. Natl. Acad. Sci. U. S. A.* 107, 502–507. doi: 10.1073/pnas.0910097107

Broeckx, T., Hulsmans, S., and Rolland, F. (2016). The plant energy sensor: evolutionary conservation and divergence of SnRK1 structure, regulation, and function. *J. Exp. Bot.* 67, 6215–6252. doi: 10.1093/jxb/erw416

Cabib, E., and Leloir, L. F. (1958). The biosynthesis of trehalose phosphate. *J. Biol. Chem.* 231, 259–275. doi: 10.1016/S0021-9258(19)77303-7

Fichtner, F., Barbier, F. F., Annunziata, M. G., Feil, R., Olas, J. J., Mueller-Roeber, B., et al. (2020). Regulation of shoot branching in *Arabidopsis* by trehalose 6-phosphate. *New Phytol.* 229, 2135–2151. doi: 10.1111/nph.17006

Fichtner, F., and Lunn, J. E. (2021). The role of trehalose 6-phosphate (Tre6P) in plant metabolism and development. *Annu. Rev. Plant Biol.* 72, 3.1–3.24. doi: 10.1146/annurev-arplant-050718-095929

Figueroa, C. M., Feil, R., Ishihara, H., Watanabe, M., Kölling, K., Krause, U., et al. (2016). Trehalose 6–phosphate coordinates organic and amino acid metabolism with carbon availability. *Plant J.* 85, 410–423. doi: 10.1111/tpj.13114

Figueroa, C. M., and Lunn, J. E. (2016). A tale of two sugars: trehalose 6-phosphate and sucrose. *Plant Physiol.* 172, 7–27. doi: 10.1104/pp.16.00417

Fukuda, N., Ikawa, Y., Aoyagi, T., and Kozaki, A. (2013). Expression of the genes coding for plastidic acetyl-CoA carboxylase subunits is regulated by a location-sensitive transcription factor binding site. *Plant Mol. Biol.* 82, 473–483. doi: 10.1007/s11103-013-0075-7

Glab, N., Oury, C., Guerinier, T., Domenichini, S., Crozet, P., Thomas, M., et al. (2017). The impact of *Arabidopsis thaliana* SNF1-related-kinase 1 (SnRK1)-activating kinase 1 (SnAK1) and SnAK2 on SnRK1 phosphorylation status: characterization of a SnAK double mutant. *Plant J.* 89, 1031–1041. doi: 10.1111/tpj.13445

Griffiths, C. A., Sagar, R., Geng, Y., Primavesi, L. F., Patel, M. K., Passarelli, M. K., et al. (2016). Chemical intervention in plant sugar signalling increases yield and resilience. *Nature* 540, 574–578. doi: 10.1038/nature20591

Grimberg, Å., Carlsson, A. S., Marttila, S., Bhalerao, R., and Hofvander, P. (2015). Transcriptional transitions in Nicotiana benthamiana leaves upon induction of oil synthesis by WRINKLED1 homologs from diverse species and tissues. *BMC Plant Biol.* 15:192. doi: 10.1186/s12870-015-0579-1

Kelly, A. A., Van Erp, H., Quettier, A. -L., Shaw, E., Menard, G., Kurup, S., et al. (2013). The SUGAR-DEPENDENT1 lipase limits triacylglycerol accumulation in vegetative tissues of *Arabidopsis*. *Plant Physiol.* 162, 1282–1289. doi: 10.1104/pp.113.219840

Koo, A. J., Ohlrogge, J. B., and Pollard, M. (2004). On the export of fatty acids from the chloroplast. *J. Biol. Chem.* 279, 16101–16110. doi: 10.1074/jbc.M311305200

Li, Q., Shao, J., Tang, S., Shen, Q., Wang, T., Chen, W., et al. (2015). Wrinkled1 accelerates flowering and regulates lipid homeostasis between oil accumulation and membrane lipid anabolism in *Brassica napus*. *Front. Plant Sci.* 6:1015. doi: 10.3389/fpls.2015.01015

Li-Beisson, Y., Shorrosh, B., Beisson, F., Andersson, M. X., Arondel, V., Bates, P. D., et al. (2013). Acyl-lipid metabolism. *Arabidopsis Book* 11:e0161. doi: 10.1199/tab.0161

Liu, H., Zhai, Z., Kuczynski, K., Keereetaweep, J., Schwender, J., and Shanklin, J. (2019). WRINKLED1 regulates biotin attachment domain-containing proteins that inhibit fatty acid synthesis. *Plant Physiol.* 181, 55–62. doi: 10.1104/pp.19.00587

Lunn, J. E., Feil, R., Hendriks, J. H., Gibon, Y., Morcuende, R., Osuna, D., et al. (2006). Sugar-induced increases in trehalose 6-phosphate are correlated with redox activation of ADPglucose pyrophosphorylase and higher rates

of starch synthesis in *Arabidopsis thaliana*. *Biochem. J.* 397, 139–148. doi: 10.1042/BJ20060083

Ma, W., Kong, Q., Mantyla, J. J., Yang, Y., Ohlrogge, J. B., and Benning, C. (2016). 14-3-3 protein mediates plant seed oil biosynthesis through interaction with AtWRI1. *Plant J.* 88, 228–235. doi: 10.1111/tpj.13244

Maeo, K., Tokuda, T., Ayame, A., Mitsui, N., Kawai, T., Tsukagoshi, H., et al. (2009). An AP2-type transcription factor, WRINKLED1, of *Arabidopsis thaliana* binds to the AW-box sequence conserved among proximal upstream regions of genes involved in fatty acid synthesis. *Plant J.* 60, 476–487. doi: 10.1111/j.1365-313X.2009.03967.x

Martínez-Barajas, E., Delatte, T., Schluepmann, H., De Jong, G. J., Somsen, G. W., Nunes, C., et al. (2011). Wheat grain development is characterized by remarkable trehalose 6-phosphate accumulation pregrain filling: tissue distribution and relationship to SNF1-related protein kinase1 activity. *Plant Physiol.* 156, 373–381. doi: 10.1104/pp.111.174524

Nakagawa, T., Suzuki, T., Murata, S., Nakamura, S., Hino, T., Maeo, K., et al. (2007). Improved gateway binary vectors: high-performance vectors for creation of fusion constructs in transgenic analysis of plants. *Biosci. Biotechnol. Biochem.* 71, 2095–2100. doi: 10.1271/bbb.70216

Ohad, N., and Yalovsky, S. (2010). "Utilizing bimolecular fluorescence complementation (BiFC) to assay protein–protein interaction in plants" in *Plant developmental biology. Methods in molecular biology (Methods and Protocols). Vol 655*. eds. L. Hennig and C. Köhler (Totowa, NJ: Humana Press), 347–358.

Ohlrogge, J., and Browse, J. (1995). Lipid biosynthesis. *Plant Cell* 7, 957–970. doi: 10.1105/tpc.7.7.957

Parajuli, S., Kannan, B., Karan, R., Sanahuja, G., Liu, H., Garcia-Ruiz, E., et al. (2020). Towards oilcane: engineering hyperaccumulation of triacylglycerol into sugarcane stems. *Glob. Change Biol. Bioenergy* 12, 476–490. doi: 10.1111/gcbb.12684

Pfaffl, M. W., Horgan, G. W., and Dempfle, L. (2002). Relative expression software tool (REST©) for group-wise comparison and statistical analysis of relative expression results in real-time PCR. *Nucleic Acids Res.* 30:e36. doi: 10.1093/nar/30.9.e36

Rawsthorne, S. (2002). Carbon flux and fatty acid synthesis in plants. *Prog. Lipid Res.* 41, 182–196. doi: 10.1016/S0163-7827(01)00023-6

Ruuska, S. A., Girke, T., Benning, C., and Ohlrogge, J. B. (2002). Contrapuntal networks of gene expression during *Arabidopsis* seed filling. *Plant Cell* 14, 1191–1206. doi: 10.1105/tpc.000877

Sanjaya, Durrett, T. P., Weise, S. E., and Benning, C. (2011). Increasing the energy density of vegetative tissues by diverting carbon from starch to oil biosynthesis in transgenic *Arabidopsis*. *Plant Biotechnol. J.* 9, 874–883. doi: 10.1111/j.1467-7652.2011.00599.x

Schluepmann, H., Pellny, T., Van Dijken, A., Smeekens, S., and Paul, M. (2003). Trehalose 6-phosphate is indispensable for carbohydrate utilization and growth in *Arabidopsis thaliana*. *Proc. Natl. Acad. Sci. U. S. A.* 100, 6849–6854. doi: 10.1073/pnas.1132018100

Shen, W., Reyes, M. I., and Hanley-Bowdoin, L. (2009). *Arabidopsis* protein kinases GRIK1 and GRIK2 specifically activate SnRK1 by phosphorylating its activation loop. *Plant Physiol.* 150, 996–1005. doi: 10.1104/pp.108.132787

Srivastava, A. C., Dasgupta, K., Ajieren, E., Costilla, G., Mcgarry, R. C., and Ayre, B. G. (2009). *Arabidopsis* plants harbouring a mutation in AtSUC2, encoding the predominant sucrose/proton symporter necessary for efficient phloem transport, are able to complete their life cycle and produce viable seed. *Ann. Bot.* 104, 1121–1128. doi: 10.1093/aob/mcp215

Vanhercke, T., Divi, U. K., El Tahchy, A., Liu, Q., Mitchell, M., Taylor, M. C., et al. (2017). Step changes in leaf oil accumulation via iterative metabolic engineering. *Metab. Eng.* 39, 237–246. doi: 10.1016/j.ymben.2016.12.007

Vanhercke, T., Dyer, J. M., Mullen, R. T., Kilaru, A., Rahman, M. M., Petrie, J. R., et al. (2019). Metabolic engineering for enhanced oil in biomass. *Prog. Lipid Res.* 74, 103–129. doi: 10.1016/j.plipres.2019.02.002

Wingler, A., Delatte, T. L., O'hara, L. E., Primavesi, L. F., Jhurreea, D., Paul, M. J., et al. (2012). Trehalose 6-phosphate is required for the onset of leaf senescence associated with high carbon availability. *Plant Physiol.* 158, 1241–1251. doi: 10.1104/pp.111.191908

Wood, C. C., Petrie, J. R., Shrestha, P., Mansour, M. P., Nichols, P. D., Green, A. G., et al. (2009). A leaf-based assay using interchangeable design principles to rapidly assemble multistep recombinant pathways. *Plant Biotechnol. J.* 7, 914–924. doi: 10.1111/j.1467-7652.2009.00453.x

Xu, C., and Shanklin, J. (2016). Triacylglycerol metabolism, function, and accumulation in plant vegetative tissues. *Annu. Rev. Plant Biol.* 67, 179–206. doi: 10.1146/annurev-arplant-043015-111641

Yadav, U. P., Ivakov, A., Feil, R., Duan, G. Y., Walther, D., Giavalisco, P., et al. (2014). The sucrose–trehalose 6-phosphate (Tre6P) nexus: specificity and mechanisms of sucrose signalling by Tre6P. *J. Exp. Bot.* 65, 1051–1068. doi: 10.1093/jxb/ert457

Zale, J., Jung, J. H., Kim, J. Y., Pathak, B., Karan, R., Liu, H., et al. (2016). Metabolic engineering of sugarcane to accumulate energy-dense triacylglycerols in vegetative biomass. *Plant Biotechnol. J.* 14, 661–669. doi: 10.1111/pbi.12411

Zhai, Z., Keereetaweep, J., Liu, H., Feil, R., Lunn, J. E., and Shanklin, J. (2018). Trehalose 6-phosphate positively regulates fatty acid synthesis by stabilizing WRINKLED1. *Plant Cell* 30, 2616–2627. doi: 10.1105/tpc.18.00521

Zhai, Z., Liu, H., and Shanklin, J. (2017a). Phosphorylation of WRINKLED1 by KIN10 results in its proteasomal degradation, providing a link between energy homeostasis and lipid biosynthesis. *Plant Cell* 29, 871–889. doi: 10.1105/tpc.17.00019

Zhai, Z., Liu, H., Xu, C., and Shanklin, J. (2017b). Sugar potentiation of fatty acid and triacylglycerol accumulation. *Plant Physiol.* 175, 696–707. doi: 10.1104/pp.17.00828

Zhang, Y., Primavesi, L. F., Jhurreea, D., Andralojc, P. J., Mitchell, R. A., Powers, S. J., et al. (2009). Inhibition of SNF1-related protein kinase1 activity and regulation of metabolic pathways by trehalose-6-phosphate. *Plant Physiol.* 149, 1860–1871. doi: 10.1104/pp.108.133934

Conflict of Interest: The authors declare that the research was conducted in the absence of any commercial or financial relationships that could be construed as a potential conflict of interest.

Copyright © 2021 Zhai, Keereetaweep, Liu, Feil, Lunn and Shanklin. This is an open-access article distributed under the terms of the Creative Commons Attribution License (CC BY). The use, distribution or reproduction in other forums is permitted, provided the original author(s) and the copyright owner(s) are credited and that the original publication in this journal is cited, in accordance with accepted academic practice. No use, distribution or reproduction is permitted which does not comply with these terms.

frontiers in Plant Science

ORIGINAL RESEARCH
published: 17 March 2021
doi: 10.3389/fpls.2021.644408

Galactolipid and Phospholipid Profile and Proteome Alterations in Soybean Leaves at the Onset of Salt Stress

Ailin Liu[1,2†], Zhixia Xiao[2†], Zhili Wang[2], Hon-Ming Lam[2] and Mee-Len Chye[1*]*

[1] School of Biological Sciences, The University of Hong Kong, Pokfulam, China, [2] Centre for Soybean Research of the State Key Laboratory of Agrobiotechnology and School of Life Sciences, The Chinese University of Hong Kong, Shatin, China

Salinity is a major environmental factor that constrains soybean yield and grain quality. Given our past observations using the salt-sensitive soybean (*Glycine max* [L.] Merr.) accession C08 on its early responses to salinity and salt-induced transcriptomic modifications, the aim of this study was to assess the lipid profile changes in this cultivar before and after short-term salt stress, and to explore the adaptive mechanisms underpinning lipid homeostasis. To this end, lipid profiling and proteomic analyses were performed on the leaves of soybean seedlings subjected to salt treatment for 0, 0.5, 1, and 2 h. Our results revealed that short-term salt stress caused dynamic lipid alterations resulting in recycling for both galactolipids and phospholipids. A comprehensive understanding of membrane lipid adaption following salt treatment was achieved by combining time-dependent lipidomic and proteomic data. Proteins involved in phosphoinositide synthesis and turnover were upregulated at the onset of salt treatment. Salinity-induced lipid recycling was shown to enhance jasmonic acid and phosphatidylinositol biosyntheses. Our study demonstrated that salt stress resulted in a remodeling of membrane lipid composition and an alteration in membrane lipids associated with lipid signaling and metabolism in C08 leaves.

Keywords: *Glycine max*, lipid profiling, lipid signaling, membrane lipids, metabolism, salinity

OPEN ACCESS

Edited by:
Eric Marechal, UMR 5168 Laboratoire de Physiologie Cellulaire Vegetale (LPCV), France

Reviewed by:
Mie Shimojima, Tokyo Institute of Technology, Japan
Till Peter Ischebeck, University of Göttingen, Germany

***Correspondence:**
Hon-Ming Lam
honming@cuhk.edu.hk
Mee-Len Chye
mlchye@hku.hk

[†] *These authors have contributed equally to this work*

Specialty section:
This article was submitted to Plant Physiology, a section of the journal Frontiers in Plant Science

Received: *21 December 2020*
Accepted: *18 February 2021*
Published: *17 March 2021*

Citation:
Liu A, Xiao Z, Wang Z, Lam H-M and Chye M-L (2021) Galactolipid and Phospholipid Profile and Proteome Alterations in Soybean Leaves at the Onset of Salt Stress. Front. Plant Sci. 12:644408. doi: 10.3389/fpls.2021.644408

INTRODUCTION

Soybean (*Glycine max* [L.] Merr.) is one of the most important legume crops used as food and feed (Hasanuzzaman et al., 2016). As a major environmental constraint on crop yield, salinity triggers osmotic stress in roots followed by whole-plant ionic toxicity arising from Na^+ and Cl^- ion accumulation (Munns and Tester, 2008). Plants have evolved to adapt to high salt by salt-responsive signaling, balancing osmotic pressure in organic osmolyte formation, Na^+ compartmentalization, enhanced scavenging of reactive oxygen species (ROS), phytohormone regulation, and cell structure modulation (Parvaiz and Satyawati, 2008; Phang et al., 2008). As modifying in membrane lipid composition provides an effective strategy in maintaining cell membrane integrity to confront stress (Elkahoui et al., 2004), the characterization of membrane lipids following salt treatment is crucial in formulating strategies to overcome salinity. Qualitative and quantitative lipid profiling following abiotic stresses such as drought (Gigon et al., 2004), cold (Barrero-Sicilia et al., 2017), or heat (Higashi et al., 2015) have been studied in Arabidopsis. Furthermore, salt-induced membrane lipid alterations documented in salt-sensitive varieties of

Arabidopsis thaliana and *Triticum sativum*, and salt-tolerant varieties of *Brassica napus* and *Zea mays* indicated that adaptation to salinity stress relied on total membrane lipid composition (Guo et al., 2019). Other reports revealed a reduction in membrane lipids in the salt-sensitive barley after salinity stress (*Hordeum vulgare* L. cv. Manel) while no changes were evident in the salt-tolerant *Hordeum maritimum* and the halophyte *Suaeda altissima* (Chalbi et al., 2013; Tsydendambaev et al., 2013). Greater lipid accumulation and mobilization during seedling development occurred in the salt-sensitive variety of sunflower (*Helianthus annuus* L.) DRSH 1 than the salt-tolerant variety PSH 1962 (Gogna and Bhatla, 2020). However, lipid profiling to address membrane lipid compositional changes in salt-sensitive soybean leaves following salt treatment has not been reported.

The majority of membrane lipids in leaves are structural lipids including galactolipids (GLs) and phospholipids (PLs) (Guschina et al., 2014). Chloroplast membranes consist mainly of GLs including monogalactosyldiacylglycerol (MGDG) and digalactosyldiacylglycerol (DGDG) followed by anionic lipids comprising sulfoquinovosyldiacylglycerol (SQDG) and phosphatidylglycerol (PG) (Douce, 1974; Block et al., 1983). As the major components of photosystem II on the thylakoid membranes, MGDG and DGDG form an indispensable matrix for photosynthesis (Mizusawa and Wada, 2012), and their ratio is important in maintaining chloroplast membrane stability (Dörmann and Benning, 2002). The amounts of chloroplast lipids (MGDG, DGDG, SQDG, and PG) drastically decreased in *B. napus* leaves after cadmium stress (Nouairi et al., 2006). During drought stress, the ratio of DGDG/MGDG was elevated, mainly attributed by a fall in MGDG (Gigon et al., 2004; Torres-Franklin et al., 2007). Sodium chloride (NaCl)-induced decline in MGDG and DGDG was reported in leaves of *Thellungiella halophila*, *Sulla carnosa*, and *Sulla coronaria* (Sui and Han, 2014; Bejaoui et al., 2016).

Among the main PL classes, phosphatidic acid (PA) plays an important role in signal transduction and serves as a key intermediate in lipid metabolism (Athenstaedt and Daum, 1999). PA accumulation can be induced by biotic and abiotic stresses caused by salt, drought, cold, plant pathogens, and wounding (Tuteja and Sopory, 2008). Under duress, PA is produced through hydrolysis of the main structural PLs such as phosphatidylcholine (PC) and phosphatidylethanolamine (PE) by phospholipase D (PLD) (Pappan et al., 1998). It can also be generated by phosphorylation of diacylglycerol (DAG), which is the product of phospholipase C (PLC) hydrolysis on phosphatidylinositol (PI) (Arisz et al., 2009). PC also acts as a resource for lipid second messengers such as lysophosphatidylcholine (lysoPC), PA, and DAG (Exton, 1990). High salt and osmotic stress caused a rapid rise in PC turnover in Arabidopsis suspension−cultured cells along with an increase in phosphatidylinositol 4, 5-bisphosphate [$PI(4,5)P_2$] and DAG pyrophosphate (Pical et al., 1999). Moreover, PC turnover facilitates substrates for production of chloroplast GLs (Karki et al., 2019). The chloroplast is the site of *de novo* fatty acid synthesis (FAS) with the conversion of pyruvate to acetyl-CoA and generation of carbon (C) chains 16:0, 18:0 and 18:1-acyl-carrier protein (ACP) for the assembly of PA (Hölzl and Dörmann, 2019), which can be further utilized for building chloroplast structural membranes (PG, MGDG, and DGDG) *via* the prokaryotic pathway (Boudière et al., 2014). This pathway is distinguished from the eukaryotic (Kennedy) pathway by the presence of a C chain 16 at the *sn*-2 position of the glycerol backbone (Boudière et al., 2014). For the eukaryotic pathway, 18:1-CoA esters bound to acyl-CoA binding proteins are imported into the endoplasmic reticulum (ER) and integrated to PC (Karki et al., 2019), which then undergoes desaturation to 18:2 and 18:3-CoA by acyl chain editing, dependent on the dynamic interconversion between PC and lysoPC (Bates et al., 2012). After PC desaturation, a proportion could be incorporated in the chloroplasts as DAG during GL biosynthesis (Hölzl and Dörmann, 2019; He et al., 2020).

Given the complexities in protein function upon stress treatment, proteomics represents a powerful approach to evaluate the proteome. Such analysis related to stresses such as drought, salinity, and extreme temperatures has been reported in several major crops (Ahmad et al., 2016). Furthermore, the integration of proteomics data with others from genomics, transcriptomics, or metabolomics provides wider scope in understanding biological processes (Zhang and Kuster, 2019). In soybean, proteome studies on abiotic stress have been reported on flood, drought, heat, and salinity (Das et al., 2016; Ji et al., 2016; Yin and Komatsu, 2017; Katam et al., 2020). A case in point is the integration of metabolome and proteome studies of the maize *atg12* mutant which revealed a role for ATG12 in autophagic recycling by proteome remodeling and lipid turnover (McLoughlin et al., 2018).

To explore the adaptive mechanisms of soybean in lipid signaling and remodeling of metabolism following salt stress, lipid profiling was performed on leaves of seedlings from cultivar C08 (Lam et al., 2010; Qi et al., 2014) which is a salt-sensitive variety. In our previous study, C08 seedlings showed leaf drooping at 0.5 h under high salt stress followed by recovery (Liu et al., 2019). To study if this phenomenon could be closely linked to the dynamic changes in membrane lipid composition, integrated proteomic and lipidomic analyses were conducted. To address protein function in response to salt, label-free quantitative (LFQ) proteomic analysis on salt-treated soybean seedling leaves was conducted. Our study identified putative enzymes or protein components involved in lipid regulation and provide a comprehensive understanding of lipid remodeling following salt treatment in soybean.

MATERIALS AND METHODS

Plant Materials and Growth Conditions

Soybean *G. max* [L.] Merr., accession C08 (Lam et al., 2010) seeds were germinated in vermiculite in a greenhouse. Seedlings were transferred to 1/2 strength Hoagland nutrient solution (Hoagland and Arnon, 1950) when the primary leaves were fully expanded. Detailed growth conditions have been previously described (Liu et al., 2019). For salt treatment, 14-day-old seedlings were transferred to 1/2 strength Hoagland solution supplemented with 0.9% (w/v) NaCl. NaCl was omitted in the control. Primary leaves were harvested at 0, 0.5, 1, and 2 h after treatment.

Lipid Extraction and Profiling

Total lipids were extracted following the protocol of Shiva et al. (2018) with minor modifications. Around six leaf punches from the primary leaf were sampled using a liquid nitrogen (N_2) pre-cooled leaf puncher. The leaf punches were immediately immersed in 2 ml of isopropanol containing 0.01% butylated hydroxytoluene in a 20-ml vial at 75°C. The samples were heated at 75°C for 30 min to deactivate phospholipid-hydrolyzing enzymes. After cooling the samples to room temperature, 6 ml chloroform/methanol/water (30:41.5:3.5) were added, and the mixture was shaken at 100 rpm on an orbital shaker at room temperature for 24 h. To determine the dry weight after lipid extraction, the leaf punches were dried in an oven at 80°C for 72 h, cooled in an airtight desiccator, and weighed with a precision balance. The lipid content was estimated and normalized to the dry weight of the leaf punches. Five independent replicates of leaves from soybean seedlings were analyzed. Individual lipid species were denoted by the lipid class, followed by the total number of acyl Cs and the total number of C-C double bonds in the acyl chains, e.g., MGDG (34:6). The profile of membrane lipids was measured using an automated electrospray ionization-tandem mass spectrometry (Devaiah et al., 2006) at the Kansas Lipidomics Research Center.

Protein Extraction, Digestion and Peptide Preparation

Total leaf protein was extracted following the method of Lv et al. (2013) with minor modifications. Harvested primary leaves were ground in liquid N_2 with a mortar and pestle. The powdered sample was suspended in 2 ml of sodium dodecyl sulfate (SDS) buffer (2% [w/v] SDS, 100 mM Tris–HCl, pH 8.0, 50 mM ethylenediaminetetraacetic acid disodium salt [EDTA-Na_2], 20 mM dithiothreitol [DTT]) with 1 mM phenylmethanesulfonyl fluoride (Sigma) and 1× protease inhibitor cocktail (Sigma). The samples were heated at 95°C for 30 min. After clarification by centrifugation at 14,000 × *g*, the protein was precipitated with three volumes of acetone at −80°C for 1 h. The protein was pelleted by centrifugation at 14,000 × *g* and then resuspended in 8 M urea 50 mM Tris–HCl, pH 8.0. The precipitation procedure was repeated once. The air-dried protein pellet was further dissolved in 8 M urea 50 mM Tris–HCl, pH 8.0 at 37°C for over 3 h. Ten microgram protein per sample was reduced with 5 mM DTT at 37°C for 1 h and trypsin-digested at 37°C overnight using Trypsin Gold, Mass Spectrometry Grade (Promega) in a trypsin:protein ratio of 1:20 (w/w). The peptide mixture was desalted using a Pierce™ C-18 spin column (Thermo Fisher Scientific™) and then dissolved in 0.1% (v/v) formic acid. Three biological replicates were performed.

Orbitrap Liquid Chromatography-Tandem Mass Spectrometry (LC-MS/MS) and Quantitative Analysis

Eight hundred nanogram digested peptides from each sample was injected and analyzed using an Orbitrap Fusion™ Lumos™ Tribrid™ Mass Spectrometer (Thermo Fisher Scientific™). Nano-liquid chromatography (LC) separation of digested peptides was carried out using a LC Ultimate 3000 RSLCnano system equipped with a C-18 5 μm-pre-column (300 μm i.d. × 5 mm) and an Acclaim Pepmap RSLC nanoViper C-18 column (75 μm i.d. × 25 cm). Mobile phase A (1.9% acetonitrile and 0.1% formic acid) and mobile phase B (98% acetonitrile and 0.1% formic acid) were used in LC. The LC mobile phase gradient profile was set as follows: 50°C chamber with 3 μL min^{-1} flow rate, beginning with 100% mobile phase A for 5 min, increasing mobile phase B from 0 to 6% in 3 min, to 18% in 40 min, to 30% in 10 min, then to 80% in 7 min, and finally re-equilibrating with 100% mobile phase A for 10 min. Raw data was acquired with Xcalibur software and analyzed using the Proteome Discoverer v2.3 software (Thermo Fisher Scientific™). The resulted MS/MS spectra were searched against the *G. max* reference protein database (Williams 82 a2v1) downloaded from the Phytozome portal[1] with Proteome Discoverer internal engine SEQUEST HT. The false discovery rate (FDR) was calculated and assigned to matched peptides by Percolator (Käll et al., 2007). Peptides with an FDR-value ≤ 0.01 were selected for subsequent analysis. LFQ was performed using Proteome Discoverer comprehensive LFQ consensus workflow. Briefly, unique peptides were used for quantification, MS1 precursor abundance was estimated based on its intensity. Peptide abundance was normalized by total peptide amount and summed into protein abundances. Each time point has three biological replicates. Protein fold changes were calculated based on protein abundance using salt-treated against untreated samples, and imputation was performed with replicate based resampling. An ANOVA test was employed to test differentially expressed proteins (DEPs), *p*-value was corrected by BH method (Benjamini and Hochberg, 1995). Proteins detected in all replicates of any one of the two samples with an adjusted *p*-value ≤ 0.05 were selected as DEPs. Common and specific sets of identified proteins as well as DEPs were visualized by Venny 2.1 (Oliveros, 2007). The protein abundance identified in all three replicates was used to conduct principal component analysis (PCA), and batch effects were removed by the removeBatchEffect function of limma package (Smyth and Speed, 2003).

Gene Ontology (GO) enrichment was performed on AgriGO v2.0[2] using GO slim annotation (Tian et al., 2017). The reference William 82 a2v1 was set as background. The Fisher exact test was employed and the *p*-value was corrected by the Yekutieli method (Yekutieli and Benjamini, 2001). GO terms were selected using a cut-off of the adjusted *p*-value ≤ 0.05 and the minimum number of mapping entries ≥5. Annotation from the Kyoto encyclopedia genes and genomes (KEGG) database was used for pathway enrichment analysis with KOBAS v2.0 (Xie et al., 2011). Protein sequences of input genes were searched against KEGG *G. max* terms by BLASTP software (Camacho et al., 2009). The hypergeometric test was further conducted to test enrichment. The matched hits were filtered by coverage ≥80% and identity ≥99%. The prediction of protein subcellular localisation was performed on ProtComp9.0[3].

[1]https://phytozome.jgi.doe.gov/pz/portal.html

[2]http://systemsbiology.cau.edu.cn/agriGOv2/

[3]http://www.softberry.com/berry.phtml?topic=protcomppl&group=programs&subgroup=proloc

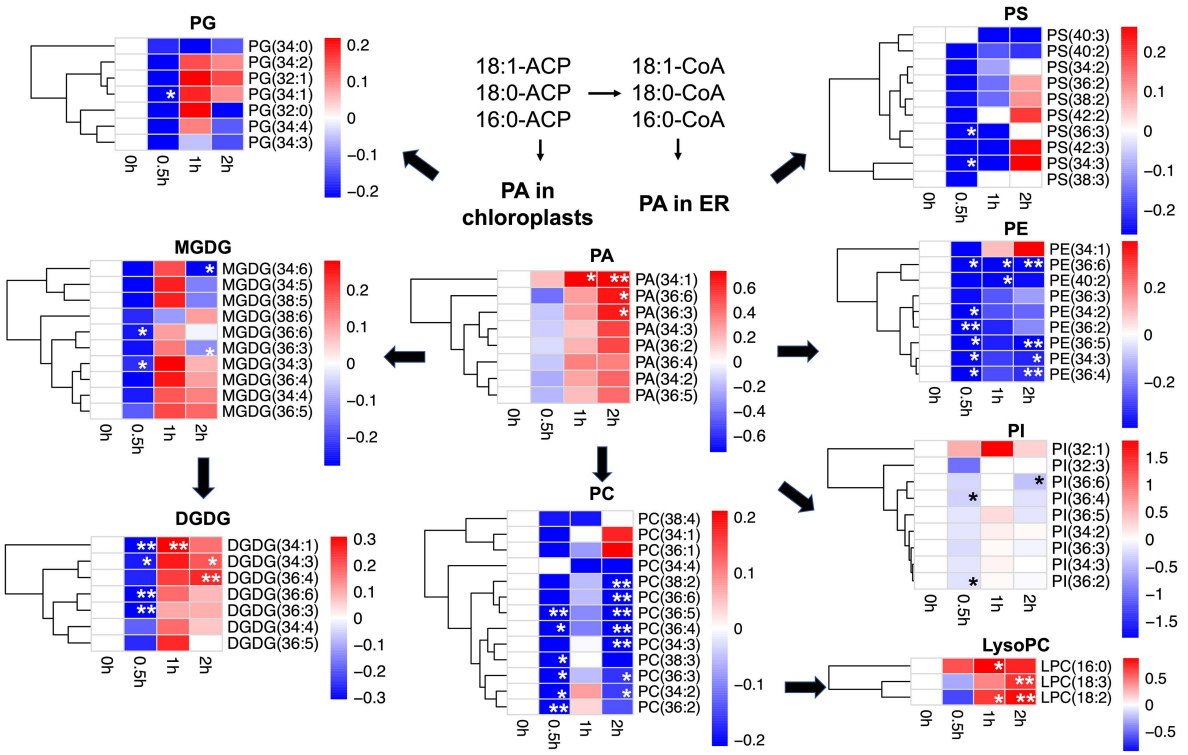

FIGURE 1 | Changes in lipid acyl species under salt stress in leaves of soybean (*Glycine max* [L.] Merr.) accession C08. Heatmaps showing the $\log_2$-fold changes in each affected lipid acyl species at 0.5, 1, and 2 h of salt treatment. PA as lipid metabolic intermediates in the endoplasmic reticulum (ER) are derived from 16:0, 18:0-ACP, and 18:1-ACP plastidial *de novo* fatty acid synthesis. Total lipids were extracted from leaves of 14-day-old C08 seedlings grown in 1/2 strength Hoagland solution and treated with or without 0.9% (w/v) NaCl. The lipid molecular species were quantified by tandem mass spectrometry. Scale bar represents $\log_2$-fold changes. *, significant difference at $p \leq 0.05$; **, significant difference at $p \leq 0.01$ using the Student's *t*-test. The raw data is provided in **Supplementary Table 1**. ACP, acyl carrier protein; DGDG, digalactosyldiacylglycerol; LysoPC, lysophosphatidylcholine; MGDG, monogalactosyldiacylglycerol; PA, phosphatidic acid; PC, phosphatidylcholine; PE, phosphatidylethanolamine; PG, phosphatidylglycerol; PI, phosphatidylinositol; PS, phosphatidylserine.

RESULTS

Salt-Induced GL and PL Changes in Soybean Leaves

On tandem mass spectrometry (**Table 1**), lipid species including GLs (MGDG and DGDG), PLs (PC, PE, PG, PI, PA, and PS), and lysoPLs (lysoPC, lysoPE, and lysoPG) were identified in soybean leaf samples, and the five species most abundant in soybean leaves includes MGDG (50.0–52.8%), DGDG (16.0–18.2%), PG (11.5–12.0%), PE (7.8–8.2%), and PC (3.7–6.2%) (**Supplementary Figure 1**). The total content as well as several membrane lipid classes (DGDG, MGDG, PG, PC, and PE) in soybean leaves showed a rapid reduction (0.8-fold) at 0.5 h of salt treatment, which reverted to normal at 1 h (**Table 1**). LysoPC increased by 1.4-fold at 1 h and 1.7-fold at 2 h of salt treatment (**Table 1**). For PA, a critical intermediate in lipid biosynthesis in both the chloroplasts and the ER, PA (34:1) accumulated at 1 and 2 h, and PA (36:3) and PA (36:6) were elevated at 2 h (**Figure 1** and **Supplementary Table 1**). For MGDG, DGDG, and PG, forming major components of chloroplast membranes primarily derived from PA in the plastids, abundant acyl species were MGDG (36:6), DGDG (34:3), DGDG (36:6), PG (32:1), and PG (34:2) (**Supplementary Table 1**). After salt treatment, MGDG (36:6), DGDG (36:6), and DGDG (34:3) significantly dipped at 0.5 h, but reverted to normal at 1 h (**Figure 1** and **Supplementary Table 1**). Of the three, only DGDG (34:3) rose markedly at 2 h after salt treatment (**Figure 1** and **Supplementary Table 1**). Moreover, the ratio of DGDG/MGDG, important in maintaining chloroplast membrane stability, increased at 1 and 2 h (**Supplementary Figure 2**). Amongst the PG acyl species, only PG (34:1) showed significant decrease at 0.5 h of salt treatment (**Figure 1** and **Supplementary Table 1**).

When PC and PE, the major PLs in the cell membranes formed from PA in the ER were analyzed, it was observed that PC acyl species including PC (36:3), PC (36:4), PC (36:5), and PC (34:2) were lower at 0.5 h after salt treatment, recovered at 1 h, and dropped again at 2 h (**Figure 1** and **Supplementary Table 1**). In contrast, all detected molecular species of lysoPC, including lysoPC (16:0), lysoPC (18:2), and lysoPC (18:3) were elevated only at 1 or 2 h (**Figure 1** and **Supplementary Table 1**). Similar to PC, most molecular species of PE declined after 0.5 h and again at 2 h, with PE (36:6) reduced at all the time points (**Figure 1** and **Supplementary Table 1**). The ratio of PC/PE for 34:3, 34:2, 36:6, 36:5, and 36:2 increased at 1 h (**Supplementary Table 2**). Also, the PI species 36:2 and

TABLE 1 | Changes in major lipid classes of soybean C08 leaves under salt treatment.

Lipid class	Untreated control				Salt treatment			Fold change (stress vs. control)		
	0 h	0.5 h	1 h	2 h	0.5 h	1 h	2 h	0.5 h	1 h	2 h
DGDG	7.24 ± 0.55	7.10 ± 0.35	6.49 ± 0.68	6.92 ± 0.52	**5.72 ± 0.75****	7.44 ± 1.49	7.49 ± 0.40	**0.81**	1.15	1.08
MGDG	21.40 ± 1.77	21.19 ± 1.44	20.45 ± 2.50	21.47 ± 1.67	**17.81 ± 2.38***	22.16 ± 4.76	21.41 ± 0.94	**0.84**	1.08	1.00
PG	5.14 ± 0.59	4.71 ± 0.36	4.63 ± 0.49	4.66 ± 0.43	**3.90 ± 0.59***	5.16 ± 0.99	4.84 ± 0.21	**0.83**	1.11	1.04
PC	3.49 ± 0.29	3.18 ± 0.23	3.52 ± 0.18	3.31 ± 0.25	**2.650 ± 0.31***	3.49 ± 0.92	2.89 ± 0.10	**0.83**	0.99	0.87
PE	2.11 ± 0.22	1.96 ± 0.33	2.49 ± 0.28	1.86 ± 0.26	**1.47 ± 0.20***	2.03 ± 0.51	1.53 ± 0.22	**0.75**	0.82	0.83
PI	1.14 ± 0.17	0.99 ± 0.09	1.01 ± 0.02	0.96 ± 0.05	0.86 ± 0.14	1.07 ± 0.23	0.97 ± 0.07	0.87	1.06	1.01
PS	0.22 ± 0.03	0.18 ± 0.06	0.20 ± 0.02	0.16 ± 0.03	0.14 ± 0.02	0.18 ± 0.04	0.17 ± 0.03	0.75	0.92	1.03
PA	2.00 ± 0.55	1.64 ± 0.49	1.57 ± 0.24	1.22 ± 0.26	1.44 ± 0.40	1.88 ± 0.50	1.71 ± 0.44	0.88	1.20	1.40
LysoPC	0.05 ± 0.01	0.04 ± 0.01	0.04 ± 0.01	0.03 ± 0.01	0.03 ± 0.01	**0.06 ± 0.01***	**0.05 ± 0.01****	0.81	**1.42**	**1.74**
LysoPG	0.03 ± 0.01	0.02 ± 0.01	0.04 ± 0.02	0.03 ± 0.02	0.02 ± 0.01	0.03 ± 0.01	0.05 ± 0.01	0.97	0.80	1.73
LysoPE	0.01 ± 0.01	0.02 ± 0.01	0.01 ± 0.00	0.01 ± 0.01	0.01 ± 0.01	0.02 ± 0.01	0.01 ± 0.01	0.59	1.68	1.01
In total	42.81 ± 3.56	41.02 ± 2.68	40.44 ± 3.91	40.63 ± 3.91	**34.00 ± 4.21***	43.51 ± 9.03	41.13 ± 1.77	0.83	1.08	1.01

Values are means ± SD (nmol/mg dry weight; n = 5).
Significant differences between control and salt treatment are bolded.
**, Significant difference at $p \leq 0.05$.*
***, Significant difference at $p \leq 0.01$ using the Student's t-test.*

36:4 were lower at 0.5 h and 36:6 declined after 2 h of salt treatment (**Figure 1** and **Supplementary Table 1**). Moreover, the unsaturation levels of certain lipid species decreased, primarily in MGDG, PC, PE, PS, and PA at 1 and 2 h after salt treatment (**Supplementary Table 3**). These changes in various membrane lipid molecular species indicate that salt stress altered membrane lipids dynamically in C08 leaves.

Proteomic Analysis of C08 Leaves Under Salt Stress

Given that lipid turnover in soybean leaves is facilitated by a series of metabolic enzymes, regulatory proteins and their related transporters, to identify the molecular mechanisms in lipid modulation, proteome profiling was performed in parallel to lipid profiling. In total, 2,399, 2,563, 2,499, and 2,049 master proteins were detected at 0, 0.5, 1, and 2 h, respectively, after salt treatment (**Table 2**). When the entire proteome was analyzed by PCA, clear differences among time points were observed with three biological replicates of each time point tending to cluster together (**Figure 2A**). Venn diagram analysis of identified proteins from all time points showed that 1,640 master proteins were common, and 148, 117, 95, and 81 unique proteins exist at 0, 0.5, 1, and 2 h, respectively (**Figure 2B**).

Pathway enrichment analysis was conducted by identifying KEGG pathways with all identified proteins with or without salt treatment. In comparison to 0 h, 11 and 7 metabolic or signaling pathways were enriched at 0.5 and 1 h, including pathways associated with amino acid (aa) biosynthesis and degradation, starch and sucrose metabolism, fatty acid (FA) metabolism and secondary metabolite biosynthesis pathways (**Figure 2C** and **Supplementary Table 4**). Furthermore, protein export was specially enriched at 0 h. The number of proteins enriched in biotin metabolism and FA biosynthesis increased after salt stress, while those associated with nucleotide excision repair and RNA degradation pathway declined (**Figure 2C** and **Supplementary Table 4**).

TABLE 2 | Summary of soybean C08 leaf proteome before and after salt treatment.

Salt treatment (h)	Samples (bioreplicates)	PSM*	Peptide groups	Identified master proteins
Untreated control	1	13,173	7,229	
	2	19,980	14,419	2,399
	3	19,885	14,155	
0.5	1	19,732	14,406	
	2	20,013	14,224	2,563
	3	13,517	8,620	
1.0	1	14,382	10,691	
	2	19,755	13,990	2,499
	3	14,326	8,494	
2.0	1	14,125	8,095	
	2	12,131	7,907	2,049
	3	11,194	6,628	

**PSM, peptide spectrum matches.*

To identify differential protein abundance at each time point in C08 leaves under salt stress, LFQ analysis was carried out and the fold changes of protein abundance under stress vs. the control (i.e., 0.5/0, 1/0, and 2/0 h) calculated. The results revealed that 120 (81 upregulated), 181 (78 upregulated), and 206 (91 upregulated) DEPs were identified after 0.5, 1, and 2 h, respectively, of salt treatment in comparison to the untreated sample (**Figure 3A** and **Supplementary Table 5**). GO analysis of DEPs from 0.5, 1, and 2 h is shown in **Figure 3B** and **Supplementary Table 6**. In the biological process category, for enrichment at 1 h DEPs were associated mainly with amino acid metabolism, nitrogen compound biosynthesis, while DEPs at 2 h clustered more in

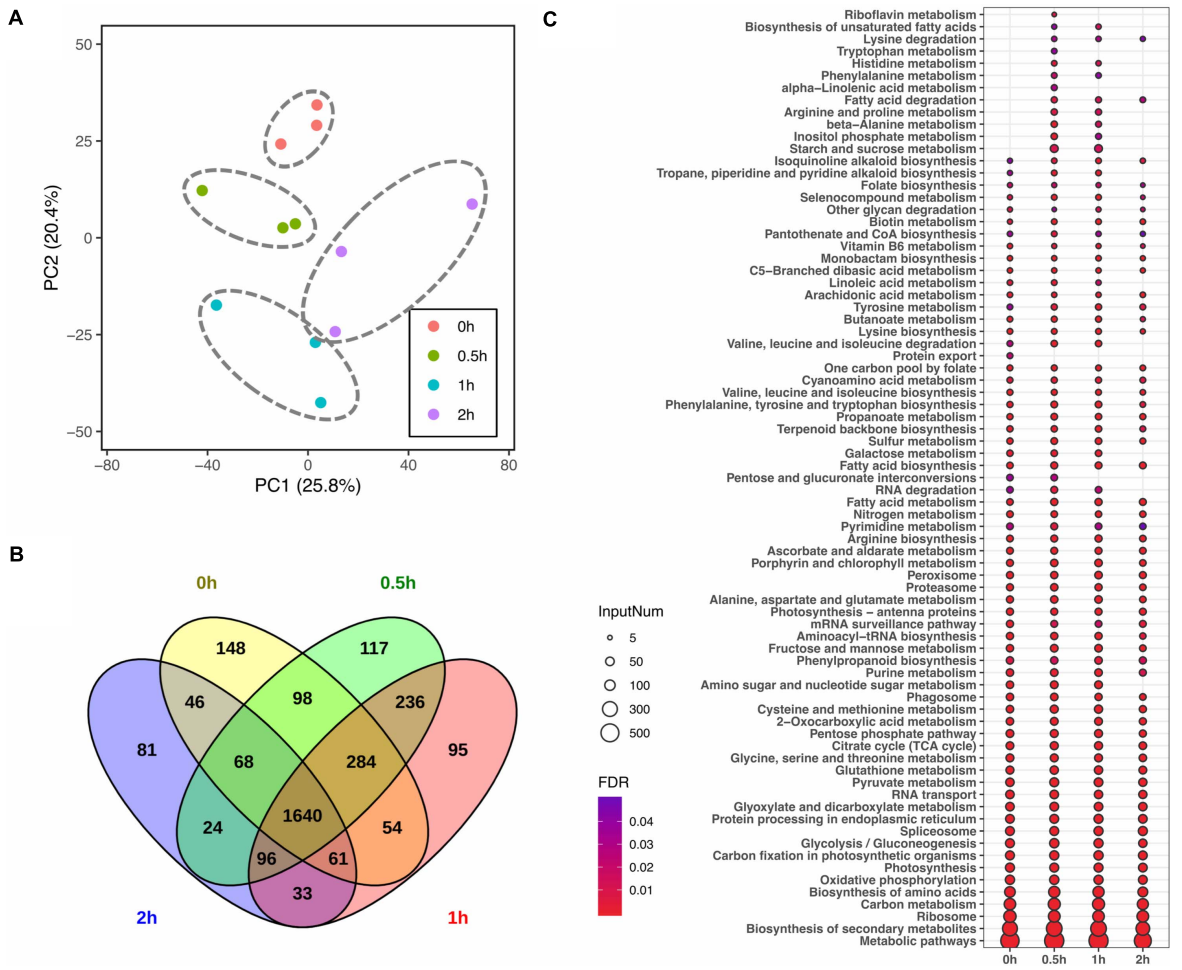

FIGURE 2 | Impact of salt treatment for 0, 0.5, 1, and 2 h on leaf proteome of soybean (*Glycine max* [L.] Merr.) accession C08. Total leaf protein was extracted and analyzed by tandem mass spectrometry from 14-day-old C08 seedlings grown in 1/2 strength Hoagland solution and treated with or without 0.9% (w/v) NaCl. **(A)** PCA of proteome profiles. Normalized protein abundance was Log_2 transformed and used as input data, centring and scaling was performed prior than calculating principle components. The first and second principal components were visualized in dot plot, and the variation was labeled in the brackets. **(B)** Venn diagram of identified proteins in each time point. **(C)** Kyoto Encyclopedia of Genes and Genomes (KEGG) analysis of identified proteins from each time point. The color gradient represents the value of a false discovery rate, with a cut-off ≤0.05. The size of each circle represents the input number of proteins in the enriched pathway. The protein lists of enriched pathways are provided in **Supplementary Table 4**.

steroid metabolism, lipid biosynthesis, oxidation reduction, and translation process (**Figure 3B**). Some stress responsive proteins including dehydrin and ROS scavenging enzyme glutathione S-transferase (GST) and heat shock proteins (HSPs) which accumulated after salt treatment corresponded with their induced transcription (**Supplementary Table 7**). Moreover, a major proportion DEPs was predicted to localize in the chloroplasts, mitochondria, nucleus, and cytoplasm after salt treatment (**Supplementary Figure 3**).

Alteration of *de novo* FA and JA Biosynthetic Enzymes in the Chloroplasts During Salt Stress

To further explore the possible mechanisms underlining redistribution of membrane lipids at the early stages of salt treatment, various proteins from the chloroplasts associated with FA and jasmonic acid (JA) biosyntheses were analyzed. Major enzymes related to *de novo* FAS were detected with no obvious changes, including the rate-limiting enzyme acetyl-CoA carboxylase (ACC), 3-oxoacyl-ACP synthase I, II, III, 3-hydroxyacyl-ACP dehydratase, enoyl-ACP reductase, oleoyl-ACP thioesterase, and stearoyl-ACP desaturase (**Figure 4** and **Supplementary Table 8**).

The enzymes related to the biosynthesis of JA, a fatty acid-derived phytohormone regulating abiotic stress responses in plants, were investigated (**Figure 4** and **Supplementary Table 8**). Most key enzymes chloroplast-localized 13S-lipoxygenase (13-LOX), allene oxide cyclase (AOC), allene oxide synthase (AOS), 12-oxophytodienoate reductase 3 (OPR3) as well as the peroxisome-localized β-ketothiolase were identified with no obvious changes in our results

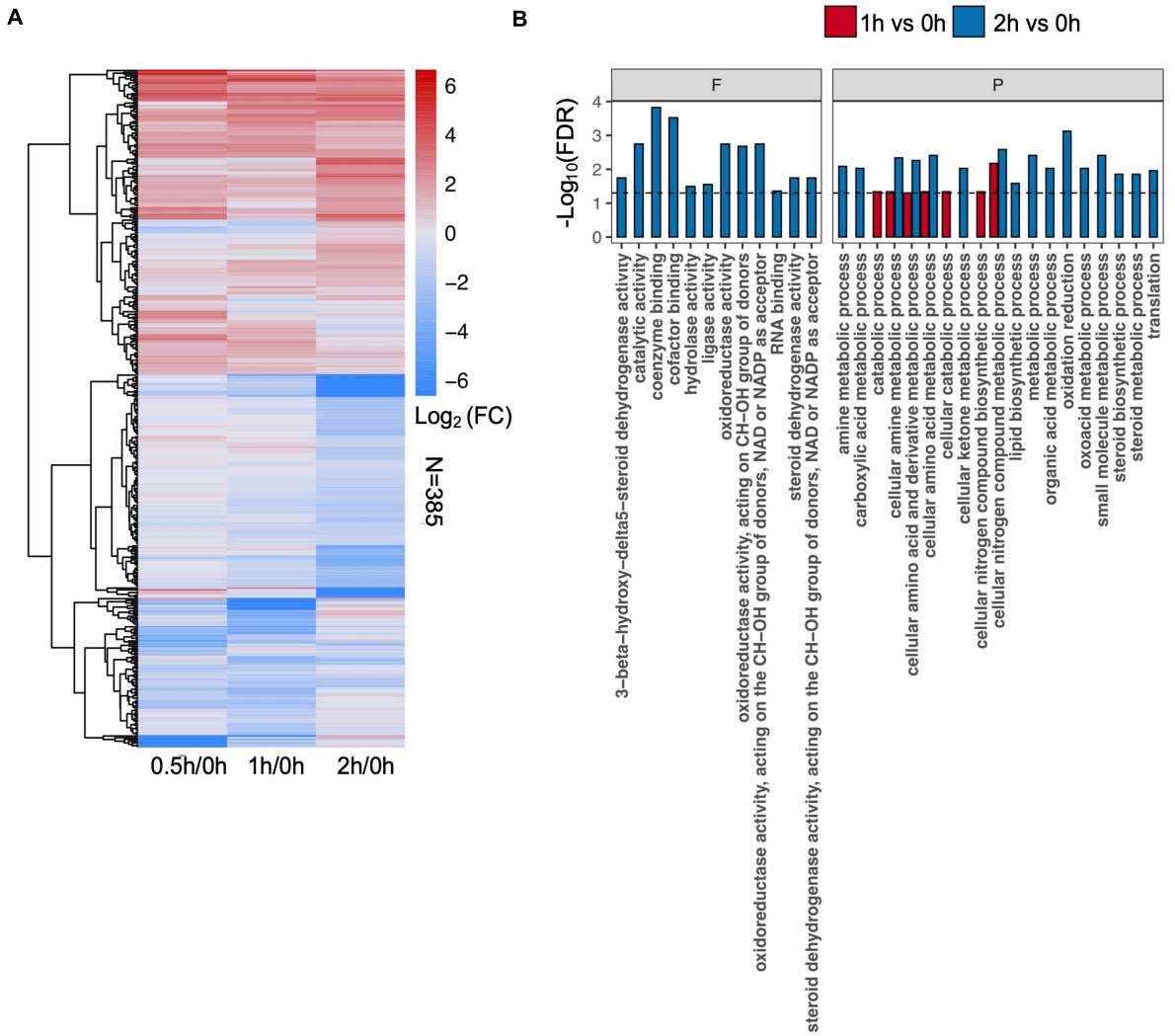

FIGURE 3 | Effect of salt treatment on the soybean (*Glycine max* [L.] Merr.) accession C08 leaf proteome. **(A)** Heatmap displays the $\log_2$-fold changes in abundance of significant differentially expressed proteins (DEPs) (stress vs. normal control), adjusted *p*-value ≤ 0.05. The union set was used to generate the plot. **(B)** Gene ontology (GO) enrichment of DEPs at each time point compared to 0 h sample. Three categories of GO terms including "cellular component," "biological process" (P), and "molecular function" (F) were used, only items in the last two were found enriched. Dashed line indicates FDR = 0.05. The protein lists of enriched items are provided in **Supplementary Table 6**.

(**Figure 4** and **Supplementary Table 8**). Only one AOC (Glyma.13G047300.1.p) was detected only after salt treatment (**Figure 4** and **Supplementary Table 8**).

As stress triggers membrane lipid degradation and the resultant polyunsaturated fatty acids (PUFAs) can be stored as triacylglycerol (TAG) in the plastoglobules (lipid bodies in the chloroplasts), it was not surprising that plastoglobule structural proteins, fibrillin and plastid-lipid-associated protein (PAP) (homologs of the fibrillin family) increased at 0.5, 1 and 2 h of salt treatment (**Figure 4** and **Supplementary Table 8**). Fibrillin (Glyma.09G111700.1.p) and PAP (Glyma.15G112500.1.p) were induced continuously from 0.5 to 2 h of salt treatment (**Figure 4** and **Supplementary Table 8**). Moreover, other plastidial proteins were also identified. The enzymatic antioxidant dehydroascorbate reductase 3 (DHR3) was elevated by three-fold at 2 h. The K^+ efflux antiporter, which facilitates endosomal pH homeostasis and salt tolerance, increased at 0.5 h (**Figure 4** and **Supplementary Table 8**).

Mitochondrial TCA Cycle and Cytosolic Glycolysis Enhanced During Salt Stress

Given that energy production processes such as glycolysis and TCA cycle are known to respond to early salt exposure, analysis on proteins related to these two pathways were conducted. The major enzymes of the TCA cycle including citrate synthase, malate dehydrogenase, succinate dehydrogenase, succinate synthetase, α-ketoglutarate, and isocitrate dehydrogenase were detected (**Figure 5** and **Supplementary Table 8**). An isocitrate dehydrogenase (Glyma.10G058100.1.p) was upregulated at least 7.8-fold during salt treatment

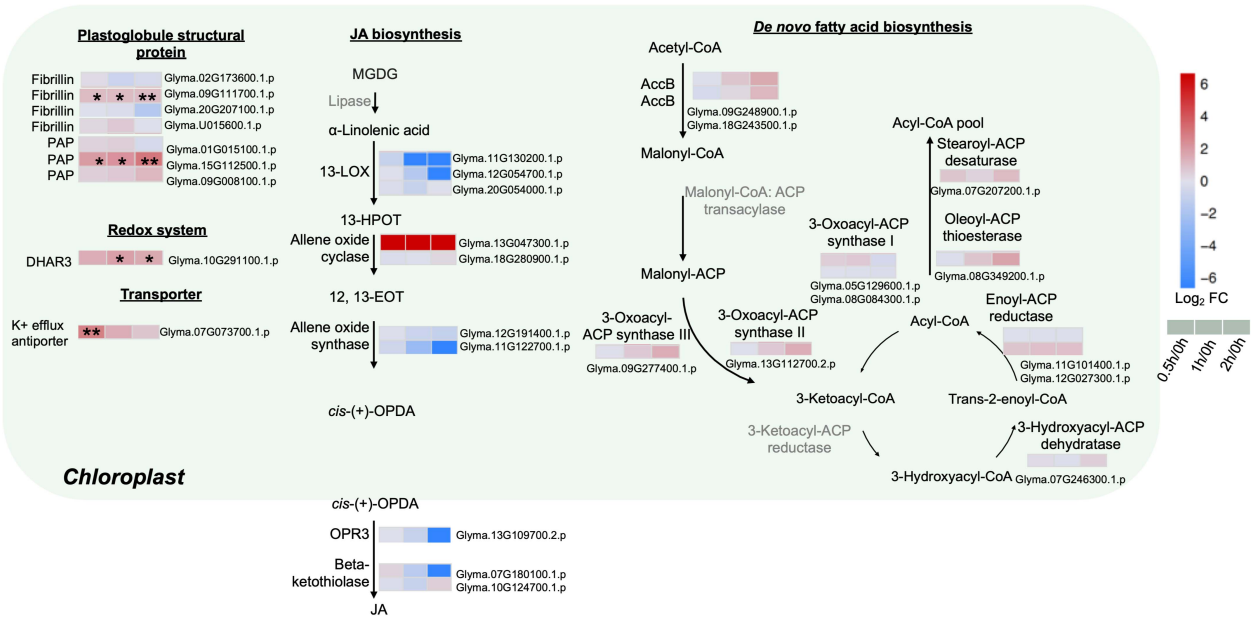

FIGURE 4 | Proteins with differential abundance related to various metabolic pathways in the chloroplasts and peroxisomes during salt stress in leaves of soybean (*Glycine max* [L.] Merr.) accession C08. Each significant differentially expressed protein is presented as heatmaps with shades of red or blue according to the scale bar. Scale bar indicates $\log_2$-fold changes of protein abundance (stress vs. control) with an adjusted *p*-value ≤ 0.05. *, significant difference at $p \leq 0.05$; **, significant difference at $p \leq 0.01$ using ANOVA test. For tandem mass spectrometry, the total leaf protein was extracted from leaves of 14-day-old C08 seedlings grown in 1/2 strength Hoagland solution and treated with or without 0.9% (w/v) NaCl. Differential protein abundances were calculated by label-free quantification of MS peptide signals. AccB, biotin carboxyl carrier protein of acetyl-CoA carboxylase; ACP, acyl carrier protein; DHAR3, dehydroascorbate reductase 3; 12, 13-EOT, 12, 13-epoxyoctadeca-9, 11, 15-trienoic acid; 13-HPOT, 13 hydroperoxyoctadeca-9, 11, 15-trienoic acid; JA, jasmonic acid; 13-LOX, 13-lipoxygenases; OPR3, 12-oxophytodienoate reductase 3; PAP, plastid lipid-associated protein.

(**Figure 5** and **Supplementary Table 8**). Some enzymes of the cytoplasmic glycolysis pathway also increased. A hexokinase (Glyma.07G124500.1.p) rose five-fold at 0.5 h, while an enolase (Glyma.16G204600.1.p) increased four-fold at 0.5 and 2 h after salt treatment (**Figure 5** and **Supplementary Table 8**). Proteome data indicated a three-fold increase in pyruvate dehydrogenase (PDH) complex E1 (Glyma.14G186900.2.p) at 0.5 h of salt treatment (**Figure 5** and **Supplementary Table 8**). PDH is a vital metabolic enzyme that links glycolysis to the TCA cycle by converting pyruvate to acetyl-CoA, and increasing the influx of acetyl-CoA from glycolysis into the TCA cycle. These results indicate that in C08 leaves, the TCA cycle and the glycolysis pathway were enhanced by salt treatment.

PI Signaling and PL Metabolism in the ER Are Affected by Salt Treatment

Our proteome data detected three phosphatidylinositol-4-phosphate 5-kinases (PI4P5Ks), of which one (Glyma.13G062700.1.p) was elevated continuously from 0.5 to 2 h (**Figure 6** and **Supplementary Table 8**). Phosphatidylinositol phospholipase C (PI-PLC), responsible for converting PI (4,5)P_2 to inositol 1,4,5-trisphosphate (IP_3) and DAG, was detected but not altered in our dataset (**Figure 6** and **Supplementary Table 8**).

Furthermore, the key enzymes related to PI biosynthesis accumulated after salt treatment. The ER-localized PI synthase (PIS) decreased by 0.3-fold at 1 h and increased by 2.3-fold at 2 h (**Figure 6** and **Supplementary Table 8**). The *myo*-inositol-3-phosphate synthase (MIPS, Glyma.08G138200.2.p) was induced 4.4-fold at 2 h and inositol monophosphatase (IMP) (Glyma.04G009800.1.p) was upregulated from 0.5 to 2 h salt treatment (**Figure 6** and **Supplementary Table 8**). Moreover, when other enzymes related membrane PL biosynthesis in the ER were examined, the results revealed that choline-phosphate cytidylyltransferase (CTP) essential in PC formation was not altered after salt treatment (**Figure 6** and **Supplementary Table 8**). PS decarboxylase (PSD) (Glyma.15G051100.1.p) that converts PS to PE, was only identified after salt treatment (**Figure 6** and **Supplementary Table 8**). The very-long-chain 3-oxoacyl-CoA reductase (KCR), required for the elongation of fatty acids, had decreased at 2 h of salt treatment (**Figure 6** and **Supplementary Table 8**).

DISCUSSION

Salt Stress Affects Membrane Lipid Composition

Earlier studies have shown the repercussion of salt stress on metabolites (Li et al., 2017), carbohydrate pool rebalancing aa metabolism (Zhang et al., 2017) and protein turnover (Kosová et al., 2013) as well as the maintenance of primary N homeostasis in various crops (Wang et al., 2012). Here we report on how

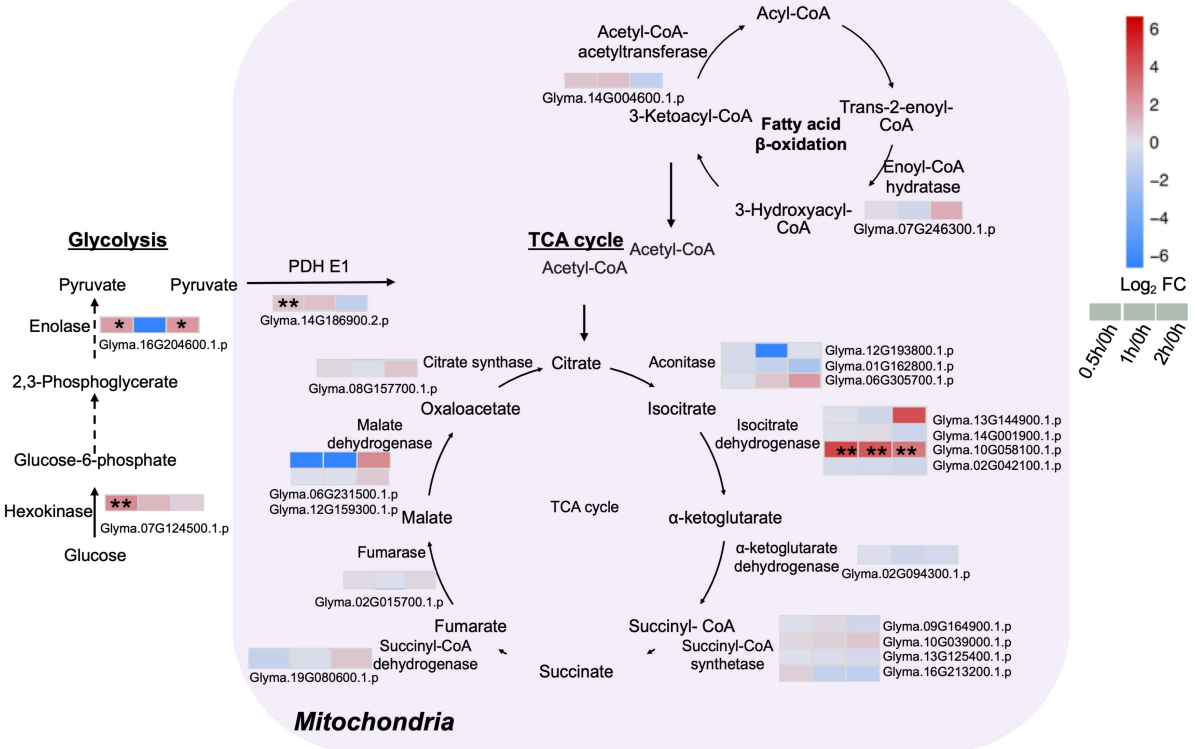

FIGURE 5 | Proteins with differential abundance involved in the tricarboxylic acid (TCA) cycle, glycolysis and fatty acid β-oxidation pathway during salt stress in leaves of soybean (*Glycine max* [L.] Merr.) accession C08. Each significant differentially expressed protein is presented as heatmaps with shades of red or blue according to the scale bar. Scale bar indicates $\log_2$-fold changes of protein abundance (stress vs. control) with an adjusted p-value ≤ 0.05. *, significant difference at $p \leq 0.05$; **, significant difference at $p \leq 0.01$ using ANOVA test. Black arrow, reaction between two intermediates; dashed arrow, several steps in the reaction. For tandem mass spectrometry, the total leaf protein was extracted from leaves of 14-day-old C08 seedlings grown in 1/2 strength Hoagland solution and treated with or without 0.9% (w/v) NaCl. Differential protein abundances were calculated by label-free quantification of MS peptide signals. PDH E1, pyruvate dehydrogenase E1 component.

high salt impacted membrane lipid composition and reveal a correlation in lipid metabolism with the remodulation of C and N pools upon salt treatment. Integration of lipidome and proteome data in a time series better facilitated an understanding on lipid turnover and protein alteration under salt stress. Salinity causes cell membrane breakdown and electrolyte leakage in soybean (Phang et al., 2008) and affects lipid composition (Shoemaker and Vanderlick, 2002). Leaf drooping was observed upon 30 min exposure to 0.9% salt solution, and recovery was evident at 1 h (Liu et al., 2019). Consistent with this, our lipid profiling of salt-treated soybean leaves showed a sharp decrease in total lipid content at 0.5 h of salt treatment which returned to normal at 1 h. The reduction and recovery of total lipids indicate that lipid composition could be rebalanced within a short period of time upon salt treatment of C08 leaves.

Our results showed a reduction in the major MGDG acyl species and most DGDG acyl species at 0.5 h of salt stress (**Figure 1** and **Supplementary Table 1**), consistent with salt-triggering GL reduction in leaves of rice, *Cucumis sativus* and *Vigna unguiculata* (De Paula et al., 1990; Yamane et al., 2004; Shu et al., 2012). Decreases in DGDG and MGDG are known to adversely affect photosynthetic membranes and membrane protein activity in the thylakoids (Simidjiev et al., 2000), and reduction of MGDG is a typical response to osmotic stress arising from salinity, drought or freezing in Arabidopsis (Welti et al., 2002; Gigon et al., 2004). Besides, an increased ratio in DGDG/MGDG at 1 and 2 h of salt treatment (**Supplementary Figure 1**) is consistent with a higher ratio in DGDG/MGDG in cowpea leaves after drought stress enhanced thylakoid stability and maintained the bilayer structure through the synthesis of stabilizing DGDG lipid species (Torres-Franklin et al., 2007). Therefore, a reduction in the major species of DGDG and MGDG and an increase in the DGDG/MGDG ratio of salt treatment may be a consequence of the disruption in chloroplast membrane stability and photosystem function at the onset of salt treatment.

Most PC and PE species declined at 0.5 h and again at 2 h after salt treatment (**Figure 1** and **Supplementary Table 1**), consistent with a degradation in major acyl species of PC and PE under drought stress in Arabidopsis leaves and winter wheat seedlings (Gigon et al., 2004; Wang et al., 2020). PC and PE are the major PLs in the structural membranes, and PC is known to be involved in the adaption to abiotic stresses (Tasseva et al., 2004). Increase in PC species following salt stress has been reported in salt-tolerant plants including *Catharanthus roseus* and *Mesembryanthemum crystallinum* (Elkahoui et al., 2004; Barkla et al., 2018) while a decrease in PC species occurs in

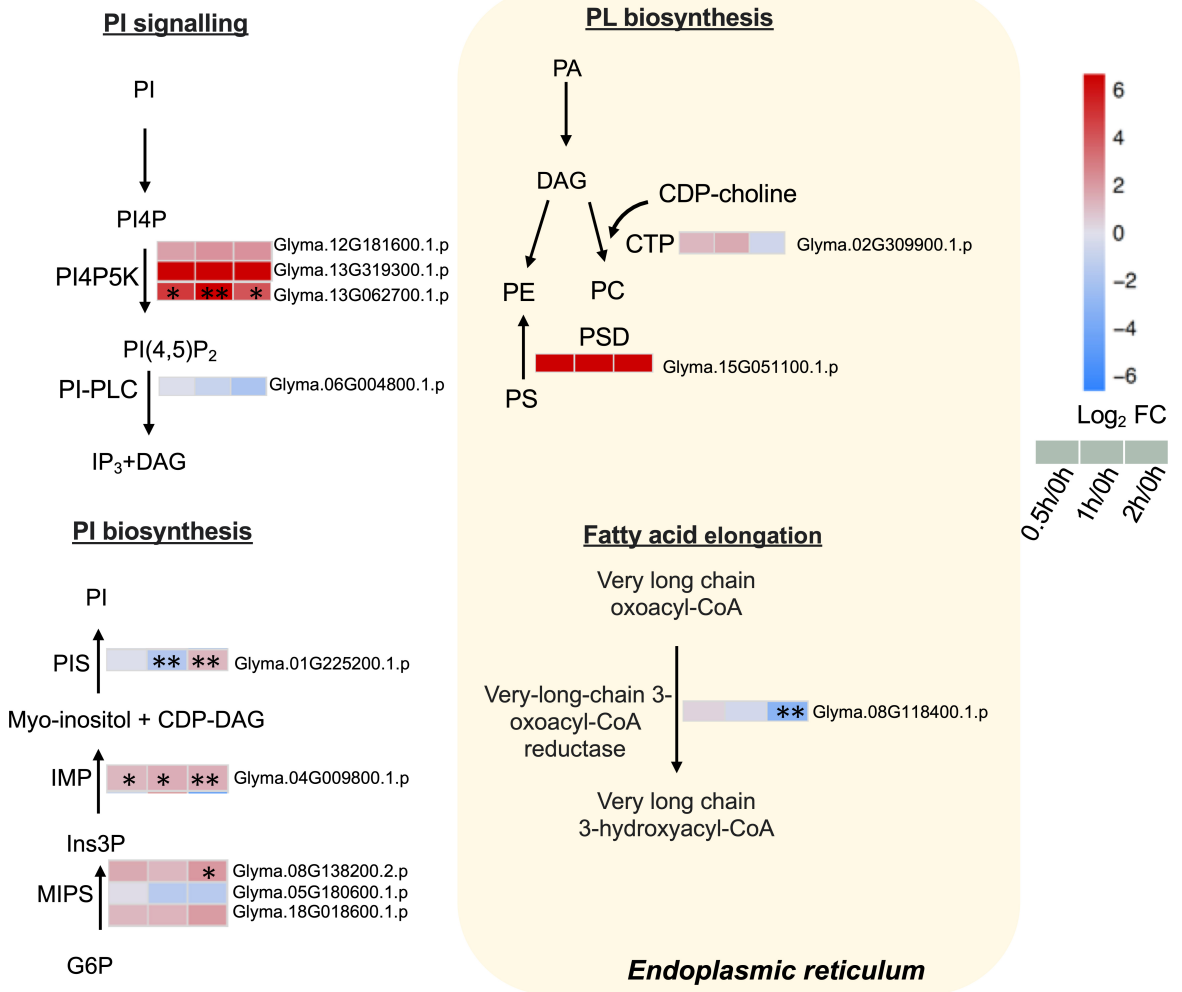

FIGURE 6 | Proteins with differential abundance involved in phospholipid metabolic pathways during salt stress in leaves of soybean (*Glycine max* [L.] Merr.) accession C08. Each significant differentially expressed protein is presented as heatmaps with shades of red or blue according to the scale bar. Scale bar indicates log_2-fold changes of protein abundance (stress vs. control) with an adjusted *p*-value ≤ 0.05. *, significant difference at $p \leq 0.05$; **, significant difference at $p \leq 0.01$ using ANOVA test. For tandem mass spectrometry, the total leaf protein was extracted from leaves of 14-day-old C08 seedlings grown in 1/2 strength Hoagland solution and treated with or without 0.9% (w/v) NaCl. Differential protein abundances were calculated by label-free quantification of MS peptide signals. CDP-choline, cytidine diphosphate choline; CDP-DAG, cytidine diphosphate diacylglycerol; PA, phosphatidic; CTP, choline-phosphate cytidylyltransferase; DAG, diacylglycerol; G6P, glucose 6-phosphate; Ins3P, *myo*–inositol–3–phosphate; IMP, inositol monophosphatase; MIPS, *myo*-inositol-1-phosphate synthase; PA, phosphatidic acid; PC, phosphatidylcholine; PE, phosphatidylethanolamine; PI, phosphatidylinositol; $PI(4,5)P_2$, phosphatidylinositol 4, 5-bisphosphate; PI4P, phosphatidylinositol 4-phosphate; PI4PK5, phosphatidylinositol-4-phosphate 5-kinase; PI-PLC, phosphoinositide phospholipase C; PIS, phosphatidylinositol synthase; PS, phosphatidylserine; PS decarboxylase, phosphatidylserine decarboxylase.

the salt-sensitive plants such as oats and wheat (Norberg and Liljenberg, 1991; Magdy et al., 1994).

Salt Stress Elevated Plastidial Proteins Related to Plastoglobules and JA Biosynthesis

Our results showed that AOC, a key enzyme in JA production, accumulated at 0.5, 1, and 2 h after salt treatment (**Figure 4** and **Supplementary Table 8**). JA, a major phytohormone regulating abiotic stress responses, is important in early responses to osmotic and salt stress (Fujita et al., 2006; Chen et al., 2017) and its biosynthesis was triggered by salt in Arabidopsis (Ishiguro et al., 2001; Wang et al., 2015, 2018). AOC affects the rate of flux through the JA biosynthetic pathway (Yoeun et al., 2018). Overexpression of *TaAOC1* conferred salt tolerance in wheat (Zhao et al., 2014). Using 2-DE and MALDI-TOF-MS/MS, higher AOC was reported in *Medicago sativa* following early salt stress (Xiong et al., 2017) while upregulated AtAOC2 protein abundance was reported in Arabidopsis under salt stress using 2-DE and iTRAQ LC-MS/MS (Pang et al., 2010). Our results lead support to lead support to an enhancement of JA production following salt treatment.

The upregulation of plastoglobule structural proteins was evident at the early stages of salt treatment (**Figure 4** and

Supplementary Table 8). Plastoglobules are known to play an essential role in lipid remodeling of the thylakoids (Rottet et al., 2015) and increase in size and number following FA accumulation under stress conditions (Bréhélin and Kessler, 2008; Rottet et al., 2015). They have been reported to be the site for the initiation of chloroplast stress-related JA biosynthesis (Hölzl and Dörmann, 2019). The accumulation of fibrillin FBN1-2 was found to affect JA biosynthesis under photosynthetic stress (Youssef et al., 2010). In Arabidopsis, FIBRILLIN2 protects photosystem II against abiotic stress by interacting with AOS and LOX of JA biosynthesis (Torres-Romero et al., 2020). Our results suggest that the breakdown of chloroplast membrane lipids (MGDG and DGDG) would lead to the production of PUFAs (Boudière et al., 2014), which act as substrates for JA biosynthesis at the onset of salt stress (**Figure 4** and **Supplementary Table 8**).

Enhanced Mitochondrial TCA Cycle and Cytosolic Glycolysis at the Onset of Salt Treatment

Some enzymes involved in the TCA cycle and glycolysis pathway increased after salt treatment (**Figure 5** and **Supplementary Table 8**), consistent with other proteome studies reported that major metabolic pathways in plants involved in energy generation (glycolysis, pyruvate decarboxylation and TCA cycle) induced by salt (Hossain et al., 2013). The TCA cycle is a crucial component of respiratory metabolism and an increased respiration after salinity exposure represents a short-term adjustment in demand for energy consumption (Bloom and Epstein, 1984). When salt-sensitive and salt-tolerant barley cultivars were subjected to short-term salinity exposure, both accumulated TCA cycle intermediates in the root elongation zone due to increased energy demand for cell division (Shelden et al., 2016). Pyruvate accumulated in both salt-sensitive and salt-tolerant soybean varieties under salt stress (Zhang et al., 2016). Pyruvate, the final product of the glycolysis pathway, can be converted to acetyl-CoA by the PDH complex and enter into the TCA cycle (Schertl and Braun, 2014). A higher level of certain enzymes in the glycolysis pathway and the TCA cycle during salt treatment (**Figure 5** and **Supplementary Table 8**) enables accelerated respiration (Bloom and Epstein, 1984), to accommodate increased FAS and salt stress adaption in C08 leaves.

PI Signaling and Biosynthesis Triggered at the Onset of Salt Stress

Phosphoinositides, vital lipid signaling molecules in response to salt, are derived from PI by the action of lipid kinases and phosphatases (Heilmann and Heilmann, 2015). PI4P5K catalyzes phosphatidylinositol 4-phosphate (PI4P) and generate $PI(4,5)P_2$ (Delage et al., 2013). Our data revealed an accumulation of PI4P5K at the initiation of salt treatment (**Figure 6** and **Supplementary Table 8**). $PI(4,5)P_2$ is a secondary messenger that functions in recruitment of signaling complexes to specific membrane locations (Martin, 1998). $PI(4,5)P_2$ is synthesized by PI4P5K which is the flux-limiting step in plant phosphoinositide metabolism (Yang et al., 2007). PI4P5K could interact with $PI(4,5)P_2$ and channel them toward different targets (Heilmann and Heilmann, 2015). While in response to salt stress, $PI(4,5)P_2$ levels rapidly (<30 min) rose in rice leaves (Darwish et al., 2009). In Arabidopsis, the expression of PI4P5K was induced by salt stress within 1 h (Mikami et al., 1998). Our results also support the early response of PI4P5K following salt stress. Increase in PI4P5K will supply $PI(4,5)P_2$ as substrates for phospholipases (Stenzel et al., 2008).

Enzymes involved in PI biosynthesis including IMP, MIPS, and PIS accumulated during salt treatment (**Figure 6** and **Supplementary Table 8**). MIPS, the first step of *myo*-inositol generation, coverts glucose 6-phosphate (G6P) to *myo*−inositol−3−phosphate (Ins3P), which further forms free *myo*-inositol by IMP (Loewus and Murthy, 2000). MIPS−produced *myo*−inositol plays a pivotal role in protective mechanisms in salt−tolerant plant species in *M. crystallinum* (Nelson et al., 1998). *PcINO1* encoding MIPS has been reported as a salt response protein in halophytic wild rice *Porteresia coarctata* Tateoka (Dastidar et al., 2006).

The overexpression of maize *ZmPIS* enhanced drought tolerance by elevating DGDG and MGDG contents and ABA synthesis in maize (Liu et al., 2013). Our results suggest that the increase of PI biosynthesis may subsequently accelerate the formation of products such as $PI(4,5)P_2$, DAG, $InsP_3$, and PA, boosting PI signaling cascades at the onset of salt stress.

CONCLUSION

In conclusion, our study shows the impact of short-term salt stress on lipid metabolism in a salt-sensitive soybean germplasm. Lipid remodeling was found to occur as early as 0.5 h of salt treatment coincident with the triggering of the PI signaling pathway. Membrane lipid recycling was observed to be related to an acceleration of plastidial JA biosynthesis and PI production. The TCA cycle and glycolysis pathways were activated for energy metabolism. In summary, salt stress caused an alteration in lipid composition and rapidly activated related protein responses in C08 leaves.

DATA AVAILABILITY STATEMENT

The raw values obtained from the lipidomic data sets are available in **Supplementary Table 1** (associated with **Table 1** and **Figure 1**). Gene expression in **Supplementary Table 7** was based on data retrieved from our previous study (Liu et al., 2019; NCBI SRA database with accession number SRP132150). The raw data and msf files for mass spectrometry proteomics data have been deposited to the ProteomeXchange Consortium via the PRIDE (https://www.ebi.ac.uk/pride/) partner repository with the dataset identifier PXD023092. The proteomics raw data are available in **Supplementary Table 9**. If any data sets are unavailable through the links stated above, they can be obtained from the corresponding author on the request.

AUTHOR CONTRIBUTIONS

M-LC and H-ML planned and designed the research. AL and ZW performed the experiments. ZX analyzed the data. AL, ZX and M-LC wrote the manuscript. All authors have read and approved the manuscript.

FUNDING

This work was supported by the Wilson and Amelia Wong Endowment Fund to M-LC, Hong Kong Research Grants Council Area of Excellence Scheme (AoE/M-403/16), and the Innovation and Technology Fund (funding support to State Key Laboratory of Agrobiotechnology) of the HKSAR, China to H-ML and M-LC, and Lo Kwee-Seong Biomedical Research Fund awarded to H-ML. Any opinions, findings, conclusions or recommendations expressed in this event/publication do not reflect the views of the Government of the Hong Kong Special Administrative Region or the Innovation and Technology Commission.

ACKNOWLEDGMENTS

We thank Mary Roth and Ruth Welti (Kansas Lipidomics Research Center) for lipid profiling and data analysis as well as Hafiz Mamoon Rehman and Chun-Ning Leung for advice on proteomics data generation and analysis.

SUPPLEMENTARY MATERIAL

The Supplementary Material for this article can be found online at: https://www.frontiersin.org/articles/10.3389/fpls.2021.644408/full#supplementary-material

REFERENCES

Ahmad, P., Abdel Latef, A. A. H., Rasool, S., Akram, N. A., Ashraf, M., and Gucel, S. (2016). Role of proteomics in crop stress tolerance. *Front. Plant Sci.* 7:1336. doi: 10.3389/fpls.2016.01336

Arisz, S. A., Testerink, C., and Munnik, T. (2009). Plant PA signaling via diacylglycerol kinase. *Biochim. Biophys. Acta Mol. Cell Biol. Lipids* 1791, 869–875. doi: 10.1016/j.bbalip.2009.04.006

Athenstaedt, K., and Daum, G. (1999). Phosphatidic acid, a key intermediate in lipid metabolism. *Eur. J. Biochem.* 266, 1–16. doi: 10.1046/j.1432-1327.1999.00822.x

Barkla, B. J., Garibay-Hernández, A., Melzer, M., Rupasinghe, T. W. T., and Roessner, U. (2018). Single cell-type analysis of cellular lipid remodelling in response to salinity in the epidermal bladder cells of the model halophyte *Mesembryanthemum crystallinum*. *Plant. Cell. Environ.* 41, 2390–2403. doi: 10.1111/pce.13352

Barrero-Sicilia, C., Silvestre, S., Haslam, R. P., and Michaelson, L. V. (2017). Lipid remodelling: unravelling the response to cold stress in arabidopsis and its extremophile relative *Eutrema salsugineum*. *Plant Sci.* 263, 194–200. doi: 10.1016/j.plantsci.2017.07.017

Bates, P. D., Fatihi, A., Snapp, A. R., Carlsson, A. S., Browse, J., and Lu, C. (2012). Acyl editing and headgroup exchange are the major mechanisms that direct polyunsaturated fatty acid flux into triacylglycerols. *Plant Physiol.* 160, 1530–1539. doi: 10.1104/pp.112.204438

Bejaoui, F., Salas, J. J., Nouairi, I., Smaoui, A., Abdelly, C., Martínez-Force, E., et al. (2016). Changes in chloroplast lipid contents and chloroplast ultrastructure in *Sulla carnosa* and *Sulla coronaria* leaves under salt stress. *J. Plant Physiol.* 198, 32–38. doi: 10.1016/j.jplph.2016.03.018

Benjamini, Y., and Hochberg, Y. (1995). Controlling the false discovery rate: a practical and powerful approach to multiple testing. *J. R. Stat. Soc. Ser. B.* 57, 289–300. doi: 10.1111/j.2517-6161.1995.tb02031.x

Block, M. A., Dorne, A. J., Joyard, J., and Douce, R. (1983). Preparation and characterization of membrane fractions enriched in outer and inner envelope membranes from spinach chloroplasts. *II. Biochemical characterization. J. Biol. Chem.* 258, 13281–13286.

Bloom, A., and Epstein, E. (1984). Varietal differences in salt-induced respiration in barley. *Plant Sci. Lett.* 35, 1–3. doi: 10.1016/0304-4211(84)90149-4

Boudière, L., Michaud, M., Petroutsos, D., Rébeillé, F., Falconet, D., Bastien, O., et al. (2014). Glycerolipids in photosynthesis: composition, synthesis and trafficking. *Biochim. Biophys. Acta Bioenerg.* 1837, 470–480. doi: 10.1016/j.bbabio.2013.09.007

Bréhélin, C., and Kessler, F. (2008). The plastoglobule: a bag full of lipid biochemistry tricks. *Photochem. Photobiol.* 84, 1388–1394. doi: 10.1111/j.1751-1097.2008.00459.x

Camacho, C., Coulouris, G., Avagyan, V., Ma, N., Papadopoulos, J., Bealer, K., et al. (2009). BLAST+: architecture and applications. *BMC Bioinformatics* 10, 1–9. doi: 10.1186/1471-2105-10-421

Chalbi, N., Hessini, K., Gandour, M., Mohamed, S., Smaoui, A., Abdelly, C., et al. (2013). Are changes in membrane lipids and fatty acid composition related to salt-stress resistance in wild and cultivated barley? *J. Plant Nutr. Soil Sci.* 176, 138–147. doi: 10.1002/jpln.201100413

Chen, J., Zhang, J., Hu, J., Xiong, W., Du, C., and Lu, M. (2017). Integrated regulatory network reveals the early salt tolerance mechanism of *Populus euphratica*. *Sci. Rep.* 7:6769. doi: 10.1038/s41598-017-05240-0

Darwish, E., Testerink, C., Khalil, M., El-Shihy, O., and Munnik, T. (2009). Phospholipid signaling responses in salt-stressed rice leaves. *Plant Cell. Physiol.* 50, 986–997. doi: 10.1093/pcp/pcp051

Das, A., Eldakak, M., Paudel, B., Kim, D. W., Hemmati, H., Basu, C., et al. (2016). Leaf proteome analysis reveals prospective drought and heat stress response mechanisms in soybean. *Biomed. Res. Int.* 2016:6021047. doi: 10.1155/2016/6021047

Dastidar, K. G., Maitra, S., Goswami, L., Roy, D., Das, K. P., and Majumder, A. L. (2006). An insight into the molecular basis of salt tolerance of L-*myo*-inositol 1-P synthase (PcINO1) from *Porteresia coarctata* (Roxb.) Tateoka, a halophytic wild rice. *Plant Physiol.* 140, 1279–1296. doi: 10.1104/pp.105.075150

De Paula, F. M., Thi, A. T. P., De Silva, J. V., Justin, A. M., Demandre, C., and Mazliak, P. (1990). Effects of water stress on the molecular species composition of polar lipids from *Vigna unguiculata* L. leaves. *Plant Sci.* 66, 185–193. doi: 10.1016/0168-9452(90)90203-Z

Delage, E., Puyaubert, J., Zachowski, A., and Ruelland, E. (2013). Signal transduction pathways involving phosphatidylinositol 4-phosphate and phosphatidylinositol 4,5-bisphosphate: convergences and divergences among eukaryotic kingdoms. *Prog. Lipid Res.* 52, 1–14. doi: 10.1016/j.plipres.2012.08.003

Devaiah, S. P., Roth, M. R., Baughman, E., Li, M., Tamura, P., Jeannotte, R., et al. (2006). Quantitative profiling of polar glycerolipid species from organs of wild-type arabidopsis and a *PHOSPHOLIPASE Dα1* knockout mutant. *Phytochemistry* 67, 1907–1924. doi: 10.1016/j.phytochem.2006.06.005

Dörmann, P., and Benning, C. (2002). Galactolipids rule in seed plants. *Trends Plant Sci.* 7, 112–118.

Douce, R. (1974). Site of biosynthesis of galactolipids in spinach chloroplasts. *Science* 183, 852–853. doi: 10.1126/science.183.4127.852

Elkahoui, S., Smaoui, A., Zarrouk, M., Ghrir, R., and Limam, F. (2004). Salt-induced lipid changes in *Catharanthus roseus* cultured cell suspensions. *Phytochemistry* 65, 1911–1917. doi: 10.1016/j.phytochem.2004.06.021

Exton, J. H. (1990). Signaling through phosphatidylcholine breakdown. *J. Biol. Chem.* 265, 1–4.

Fujita, M., Fujita, Y., Noutoshi, Y., Takahashi, F., Narusaka, Y., Yamaguchi-Shinozaki, K., et al. (2006). Crosstalk between abiotic and biotic stress

responses: a current view from the points of convergence in the stress signaling networks. *Curr. Opin. Plant Biol.* 9, 436–442. doi: 10.1016/j.pbi.2006.05.014

Gigon, A., Matos, A.-R., Laffray, D., Zuily-Fodil, Y., and Pham-Thi, A.-T. (2004). Effect of drought stress on lipid metabolism in the leaves of *Arabidopsis thaliana* (Ecotype Columbia). *Ann. Bot.* 94, 345–351. doi: 10.1093/aob/mch150

Gogna, M., and Bhatla, S. C. (2020). Salt-tolerant and -sensitive seedlings exhibit noteworthy differences in lipolytic events in response to salt stress. *Plant Signal. Behav.* 15:1737451. doi: 10.1080/15592324.2020.1737451

Guo, Q., Liu, L., and Barkla, B. J. (2019). Membrane lipid remodeling in response to salinity. *Int. J. Mol. Sci.* 20:4264. doi: 10.3390/ijms20174264

Guschina, I. A., Everard, J. D., Kinney, A. J., Quant, P. A., and Harwood, J. L. (2014). Studies on the regulation of lipid biosynthesis in plants: application of control analysis to soybean. *Biochim. Biophys. Acta Biomembr.* 1838, 1488–1500. doi: 10.1016/j.bbamem.2014.02.008

Hasanuzzaman, M., Nahar, K., Rahman, A., Mahmud, J. A., Hossain, M. S., and Fujita, M. (2016). *"Soybean production and environmental stresses," in Environmental stresses in soybean production*. Amsterdam, Netherlands: Elsevier, 61–102. doi: 10.1016/B978-0-12-801535-3.00004-8

He, M., Qin, C.-X., Wang, X., and Ding, N.-Z. (2020). Plant unsaturated fatty acids: biosynthesis and regulation. *Front. Plant Sci.* 11:390. doi: 10.3389/fpls.2020.00390

Heilmann, M., and Heilmann, I. (2015). Plant phosphoinositides complex networks controlling growth and adaptation. *Biochim. Biophys. Acta* 1851, 759–769. doi: 10.1016/j.bbalip.2014.09.018

Higashi, Y., Okazaki, Y., Myouga, F., Shinozaki, K., and Saito, K. (2015). Landscape of the lipidome and transcriptome under heat stress in *Arabidopsis thaliana*. *Sci. Rep.* 5:10533. doi: 10.1038/srep10533

Hoagland, D. R., and Arnon, D. I. (1950). The water-culture method for growing plants without soil. *Circular. California Agric. Exp. Station* 347:32.

Hölzl, G., and Dörmann, P. (2019). Chloroplast lipids and their biosynthesis. *Annu. Rev. Plant Biol.* 70, 51–81. doi: 10.1146/annurev-arplant-050718-100202

Hossain, Z., Khatoon, A., and Komatsu, S. (2013). Soybean proteomics for unraveling abiotic stress response mechanism. *J. Proteome Res.* 12, 4670–4684. doi: 10.1021/pr400604b

Ishiguro, S., Kawai-Oda, A., Ueda, J., Nishida, I., and Okada, K. (2001). The *DEFECTIVE IN ANTHER DEHISCENCE1* gene encodes a novel phospholipase A1 catalyzing the initial step of jasmonic acid biosynthesis, which synchronizes pollen maturation, anther dehiscence, and flower opening in Arabidopsis. *Plant Cell.* 13, 2191–2209. doi: 10.1105/tpc.13.10.2191

Ji, W., Cong, R., Li, S., Li, R., Qin, Z., Li, Y., et al. (2016). Comparative proteomic analysis of soybean leaves and roots by iTRAQ provides insights into response mechanisms to short-term salt stress. *Front. Plant Sci.* 7:573. doi: 10.3389/fpls.2016.00573

Käll, L., Canterbury, J. D., Weston, J., Noble, W. S., and MacCoss, M. J. (2007). Semi-supervised learning for peptide identification from shotgun proteomics datasets. *Nat. Methods* 4, 923–925. doi: 10.1038/nmeth1113

Karki, N., Johnson, B. S., and Bates, P. D. (2019). Metabolically distinct pools of phosphatidylcholine are involved in trafficking of fatty acids out of and into the chloroplast for membrane production. *Plant Cell.* 31, 2768–2788. doi: 10.1105/tpc.19.00121

Katam, R., Shokri, S., Murthy, N., Singh, S. K., Suravajhala, P., Khan, M. N., et al. (2020). Proteomics, physiological, and biochemical analysis of cross tolerance mechanisms in response to heat and water stresses in soybean. *PLoS One* 15:e0233905. doi: 10.1371/journal.pone.0233905

Kosová, K., Prášil, I., and Vítámvás, P. (2013). Protein contribution to plant salinity response and tolerance acquisition. *Int. J. Mol. Sci.* 14, 6757–6789. doi: 10.3390/ijms14046757

Lam, H.-M., Xu, X., Liu, X., Chen, W., Yang, G., Wong, F.-L., et al. (2010). Resequencing of 31 wild and cultivated soybean genomes identifies patterns of genetic diversity and selection. *Nat. Genet.* 42, 1053–1059. doi: 10.1038/ng.715

Li, M., Guo, R., Jiao, Y., Jin, X., Zhang, H., and Shi, L. (2017). Comparison of salt tolerance in soja based on metabolomics of seedling roots. *Front. Plant Sci.* 8:1101. doi: 10.3389/fpls.2017.01101

Liu, A., Xiao, Z., Li, M.-W., Wong, F.-L., Yung, W.-S., Ku, Y.-S., et al. (2019). Transcriptomic reprogramming in soybean seedlings under salt stress. *Plant. Cell. Environ.* 42, 98–114. doi: 10.1111/pce.13186

Liu, X., Zhai, S., Zhao, Y., Sun, B., Liu, C., Yang, A., et al. (2013). Overexpression of the phosphatidylinositol synthase gene (*ZmPIS*) conferring drought stress tolerance by altering membrane lipid composition and increasing ABA synthesis in maize. *Plant Cell. Environ.* 36, 1037–1055. doi: 10.1111/pce.12040

Loewus, F. A., and Murthy, P. P. N. (2000). *myo*-Inositol metabolism in plants. *Plant Sci.* 150, 1–19. doi: 10.1016/S0168-9452(99)00150-8

Lv, D.-W., Subburaj, S., Cao, M., Yan, X., Li, X., Appels, R., et al. (2013). Proteome and phosphoproteome characterization reveals new response and defense mechanisms of *Brachypodium distachyon* leaves under salt stress. *Mol. Cell. Proteomics* 13, 632–652. doi: 10.1074/mcp.m113.030171

Magdy, M., Mansour, F., Hasselt, P. R., and Kuiper, P. J. C. (1994). Plasma membrane lipid alterations induced by NaCl in winter wheat roots. *Physiol. Plant.* 92, 473–478. doi: 10.1111/j.1399-3054.1994.tb08838.x

Martin, T. F. J. (1998). Phosphoinositide lipids as signaling molecules: common themes for signal transduction, cytoskeletal regulation, and membrane trafficking. *Annu. Rev. Cell. Dev. Biol.* 14, 231–264. doi: 10.1146/annurev.cellbio.14.1.231

McLoughlin, F., Augustine, R. C., Marshall, R. S., Li, F., Kirkpatrick, L. D., Otegui, M. S., et al. (2018). Maize multi-omics reveal roles for autophagic recycling in proteome remodelling and lipid turnover. *Nat. Plants* 4, 1056–1070. doi: 10.1038/s41477-018-0299-2

Mikami, K., Katagiri, T., Luchi, S., Yamaguchi-Shinozaki, K., and Shinozaki, K. (1998). A gene encoding phosphatidylinositol-4-phosphate 5-kinase is induced by water stress and abscisic acid in *Arabidopsis thaliana*. *Plant J.* 15, 563–568. doi: 10.1046/j.1365-313X.1998.00227.x

Mizusawa, N., and Wada, H. (2012). The role of lipids in photosystem II. *Biochim. Biophys. Acta Bioenerg.* 1817, 194–208. doi: 10.1016/j.bbabio.2011.04.008

Munns, R., and Tester, M. (2008). Mechanisms of salinity tolerance. *Annu. Rev. Plant Biol.* 59, 651–681. doi: 10.1146/annurev.arplant.59.032607.092911

Nelson, D. E., Rammesmayer, G., and Bohnert, H. J. (1998). Regulation of cell-specific inositol metabolism and transport in plant salinity tolerance. *Plant Cell.* 10, 753–764. doi: 10.2307/3870662

Norberg, P., and Liljenberg, C. (1991). Lipids of plasma membranes prepared from oat root cells. *Plant Physiol.* 96, 1136–1141. doi: 10.1104/pp.96.4.1136

Nouairi, I., Ammar, W. B., Youssef, N. B., Daoud, D. B., Ghorbal, M. H., Zarrouk, M., et al. (2006). Comparative study of cadmium effects on membrane lipid composition of *Brassica juncea* and *Brassica napus* leaves. *Plant Sci.* 170, 511–519. doi: 10.1016/j.plantsci.2005.10.003

Oliveros, J. C. (2007). *VENNY. An interactive tool for comparing lists with Venn Diagrams*. Available Online at: http://bioinfogp.cnb.csic.es/tools/venny/index.html.bioinfogp.cnb.csic.es/tools/venny/index.html

Pang, Q., Chen, S., Dai, S., Chen, Y., Wang, Y., and Yan, X. (2010). Comparative proteomics of salt tolerance in *Arabidopsis thaliana* and *Thellungiella halophila*. *J. Proteome Res.* 9, 2584–2599. doi: 10.1021/pr100034f

Pappan, K., Austin-Brown, S., Chapman, K. D., and Wang, X. (1998). Substrate selectivities and lipid modulation of plant phospholipase Dα, -β, and -γ. *Arch. Biochem. Biophys.* 353, 131–140. doi: 10.1006/abbi.1998.0640

Parvaiz, A., and Satyawati, S. (2008). Salt stress and phyto-biochemical responses of plants – a review. *Plant Soil Environ.* 54, 89–99. doi: 10.17221/2774-PSE

Phang, T.-H., Shao, G., and Lam, H.-M. (2008). Salt tolerance in soybean. *J. Integr. Plant Biol.* 50, 1196–1212. doi: 10.1111/j.1744-7909.2008.00760.x

Pical, C., Westergren, T., Dove, S. K., Larsson, C., and Sommarin, M. (1999). Salinity and hyperosmotic stress induce rapid increases in phosphatidylinositol 4, 5-bisphosphate, diacylglycerol pyrophosphate, and phosphatidylcholine in *Arabidopsis thaliana* cells. *J. Biol. Chem.* 274, 38232–38240. doi: 10.1074/jbc.274.53.38232

Qi, X., Li, M.-W., Xie, M., Liu, X., Ni, M., Shao, G., et al. (2014). Identification of a novel salt tolerance gene in wild soybean by whole-genome sequencing. *Nat. Commun.* 5:4340. doi: 10.1038/ncomms5340

Rottet, S., Besagni, C., and Kessler, F. (2015). The role of plastoglobules in thylakoid lipid remodeling during plant development. *Biochim. Biophys. Acta Bioenerg.* 1847, 889–899. doi: 10.1016/j.bbabio.2015.02.002

Schertl, P., and Braun, H.-P. (2014). Respiratory electron transfer pathways in plant mitochondria. *Front. Plant Sci.* 5:163. doi: 10.3389/fpls.2014.00163

Shelden, M. C., Dias, D. A., Jayasinghe, N. S., Bacic, A., and Roessner, U. (2016). Root spatial metabolite profiling of two genotypes of barley (Hordeum vulgare L.) reveals differences in response to short-term salt stress. *J. Exp. Bot.* 67, 3731–3745. doi: 10.1093/jxb/erw059

Shiva, S., Enninful, R., Roth, M. R., Tamura, P., Jagadish, K., and Welti, R. (2018). An efficient modified method for plant leaf lipid extraction results in improved recovery of phosphatidic acid. *Plant Methods* 14:14. doi: 10.1186/s13007-018-0282-y

Shoemaker, S. D., and Vanderlick, T. K. (2002). Stress-induced leakage from phospholipid vesicles: effect of membrane composition. *Ind. Eng. Chem. Res.* 41, 324–329. doi: 10.1021/ie010049t

Shu, S., Guo, S.-R., Sun, J., and Yuan, L.-Y. (2012). Effects of salt stress on the structure and function of the photosynthetic apparatus in *Cucumis sativus* and its protection by exogenous putrescine. *Physiol. Plant.* 146, 285–296. doi: 10.1111/j.1399-3054.2012.01623.x

Simidjiev, I., Stoylova, S., Amenitsch, H., Javorfi, T., Mustardy, L., Laggner, P., et al. (2000). Self-assembly of large, ordered lamellae from non-bilayer lipids and integral membrane proteins in vitro. *Proc. Natl. Acad. Sci.* 97, 1473–1476. doi: 10.1073/pnas.97.4.1473

Smyth, G. K., and Speed, T. (2003). Normalization of cDNA microarray data. *Methods*. 31, 265–273. doi: 10.1016/S1046-2023(03)00155-5

Stenzel, I., Ischebeck, T., König, S., Hołubowska, A., Sporysz, M., Hause, B., et al. (2008). The type B phosphatidylinositol-4-phosphate 5-kinase 3 is essential for root hair formation in *Arabidopsis thaliana*. *Plant Cell* 20, 124–141. doi: 10.1105/tpc.107.052852

Sui, N., and Han, G. (2014). Salt-induced photoinhibition of PSII is alleviated in halophyte *Thellungiella halophila* by increases of unsaturated fatty acids in membrane lipids. *Acta Physiol. Plant.* 36, 983–992. doi: 10.1007/s11738-013-1477-5

Tasseva, G., Richard, L., and Zachowski, A. (2004). Regulation of phosphatidylcholine biosynthesis under salt stress involves choline kinases in *Arabidopsis thaliana*. *FEBS Lett.* 566, 115–120. doi: 10.1016/j.febslet.2004.04.015

Tian, T., Liu, Y., Yan, H., You, Q., Yi, X., Du, Z., et al. (2017). AgriGO v2.0: A GO analysis toolkit for the agricultural community, 2017 update. *Nucleic Acids Res.* 45, W122–W129. doi: 10.1093/nar/gkx382

Torres-Franklin, M.-L., Gigon, A., de Melo, D. F., Zuily-Fodil, Y., and Pham-Thi, A.-T. (2007). Drought stress and rehydration affect the balance between MGDG and DGDG synthesis in cowpea leaves. *Physiol. Plant* 131, 201–210. doi: 10.1111/j.1399-3054.2007.00943.x

Torres-Romero, D., Gomez-Zambrano, A., Serrato, A. J., Sahrawy, M., and Merida, A. (2020). Fibrillin 2 interacts with other proteins to protect photosystem II against abiotic stress in *Arabidopsis thaliana*. *bioRxiv*. doi: 10.1101/2020.10.07.329979

Tsydendambaev, V. D., Ivanova, T. V., Khalilova, L. A., Kurkova, E. B., Myasoedov, N. A., and Balnokin, Y. V. (2013). Fatty acid composition of lipids in vegetative organs of the halophyte *Suaeda altissima* under different levels of salinity. *Russ. J. Plant Physiol.* 60, 661–671. doi: 10.1134/S1021443713050142

Tuteja, N., and Sopory, S. K. (2008). Chemical signaling under abiotic stress environment in plants. *Plant Signal. Behav.* 3, 525–536. doi: 10.4161/psb.3.8.6186

Wang, H., Zhang, M., Guo, R., Shi, D., Liu, B., Lin, X., et al. (2012). Effects of salt stress on ion balance and nitrogen metabolism of old and young leaves in rice (*Oryza sativa* L.). *BMC Plant Biol.* 12:194. doi: 10.1186/1471-2229-12-194

Wang, K., Guo, Q., Froehlich, J. E., Hersh, H. L., Zienkiewicz, A., Howe, G. A., et al. (2018). Two abscisic acid-responsive plastid lipase genes involved in jasmonic acid biosynthesis in *Arabidopsis thaliana*. *Plant Cell.* 30, 1006–1022. doi: 10.1105/tpc.18.00250

Wang, T., Tohge, T., Ivakov, A., Mueller-Roeber, B., Fernie, A. R., Mutwil, M., et al. (2015). Salt-related *MYB1* coordinates abscisic acid biosynthesis and signaling during salt stress in arabidopsis. *Plant Physiol.* 169, 1027–1041. doi: 10.1104/pp.15.00962

Wang, Y., Zhang, X., Huang, G., Feng, F., Liu, X., Guo, R., et al. (2020). Dynamic changes in membrane lipid composition of leaves of winter wheat seedlings in response to PEG-induced water stress. *BMC Plant Biol.* 20:84. doi: 10.1186/s12870-020-2257-1

Welti, R., Li, W., Li, M., Sang, Y., Biesiada, H., Zhou, H.-E., et al. (2002). Profiling membrane lipids in plant stress responses. *J. Biol. Chem.* 277, 31994–32002. doi: 10.1074/jbc.M205375200

Xie, C., Mao, X., Huang, J., Ding, Y., Wu, J., Dong, S., et al. (2011). KOBAS 2.0: a web server for annotation and identification of enriched pathways and diseases. *Nucleic Acids Res.* 39, W316–W322. doi: 10.1093/nar/gkr483

Xiong, J., Sun, Y., Yang, Q., Tian, H., Zhang, H., Liu, Y., et al. (2017). Proteomic analysis of early salt stress responsive proteins in alfalfa roots and shoots. *Proteome Sci.* 15, 1–19. doi: 10.1186/s12953-017-0127-z

Yamane, K., Rahman, S., Kawasaki, M., Taniguchi, M., and Miyake, H. (2004). Pretreatment with a low concentration of methyl viologen decreases the effects of salt stress on chloroplast ultrastructure in rice leaves (*Oryza sativa* L.). *Plant Prod. Sci.* 7, 435–441. doi: 10.1626/pps.7.435

Yang, J. I., Perera, I. Y., Brglez, I., Davis, A. J., Stevenson-Paulik, J., Phillippy, B. Q., et al. (2007). Increasing plasma membrane phosphatidylinositol(4,5)bisphosphate biosynthesis increases phosphoinositide metabolism in *Nicotiana tabacum*. *Plant Cell.* 19, 1603–1616. doi: 10.1105/tpc.107.051367

Yekutieli, D., and Benjamini, Y. (2001). The control of the false discovery rate in multiple testing under dependency. *Ann. Stat.* 29, 1165–1188. doi: 10.1214/aos/1013699998

Yin, X., and Komatsu, S. (2017). Comprehensive analysis of response and tolerant mechanisms in early-stage soybean at initial-flooding stress. *J. Proteomics.* 169, 225–232. doi: 10.1016/j.jprot.2017.01.014

Yoeun, S., Cho, K., and Han, O. (2018). Structural evidence for the substrate channeling of rice allene oxide cyclase in biologically analogous nazarov reaction. *Front. Chem.* 6:500. doi: 10.3389/fchem.2018.00500

Youssef, A., Laizet, Y., Block, M. A., Maréchal, E., Alcaraz, J. P., Larson, T. R., et al. (2010). Plant lipid-associated fibrillin proteins condition jasmonate production under photosynthetic stress. *Plant J.* 61, 436–445. doi: 10.1111/j.1365-313X.2009.04067.x

Zhang, B., and Kuster, B. (2019). Proteomics is not an island: multi-omics integration is the key to understanding biological systems. *Mol. Cell. Proteomics* 18, S1–S4. doi: 10.1074/mcp.E119.001693

Zhang, J., Yang, D., Li, M., and Shi, L. (2016). Metabolic profiles reveal changes in wild and cultivated soybean seedling leaves under salt stress. *PLoS One* 11:e0159622. doi: 10.1371/journal.pone.0159622

Zhang, Z., Mao, C., Shi, Z., and Kou, X. (2017). The amino acid metabolic and carbohydrate metabolic pathway play important roles during salt-stress response in tomato. *Front. Plant Sci.* 8:1231. doi: 10.3389/fpls.2017.01231

Zhao, Y., Dong, W., Zhang, N., Ai, X., Wang, M., Huang, Z., et al. (2014). A wheat allene oxide cyclase gene enhances salinity tolerance via jasmonate signaling. *Plant Physiol.* 164, 1068–1076. doi: 10.1104/pp.113.227595

Conflict of Interest: The authors declare that the research was conducted in the absence of any commercial or financial relationships that could be construed as a potential conflict of interest.

Copyright © 2021 Liu, Xiao, Wang, Lam and Chye. This is an open-access article distributed under the terms of the Creative Commons Attribution License (CC BY). The use, distribution or reproduction in other forums is permitted, provided the original author(s) and the copyright owner(s) are credited and that the original publication in this journal is cited, in accordance with accepted academic practice. No use, distribution or reproduction is permitted which does not comply with these terms.

frontiers in Plant Science

ORIGINAL RESEARCH
published: 19 March 2021
doi: 10.3389/fpls.2021.639330

Temperature Acclimation of the Picoalga *Ostreococcus tauri* Triggers Early Fatty-Acid Variations and Involves a Plastidial ω3-Desaturase

*Charlotte Degraeve-Guilbault[1], Nattiwong Pankasem[2†], Maurean Gueirrero[1†], Cécile Lemoigne[1], Frédéric Domergue[1], Tomonori Kotajima[3], Iwane Suzuki[4], Jérôme Joubès[1] and Florence Corellou[1]**

[1] Univ. Bordeaux, CNRS, Laboratoire de Biogenèse membranaire, UMR 5200, Villenave d'Ornon, France, [2] School of Life and Environmental Sciences, University of Tsukuba, Tsukuba, Japan, [3] Graduate School of Life and Environmental Sciences, University of Tsukuba, Tsukuba, Japan, [4] Faculty of Life and Environmental Sciences, University of Tsukuba, Tsukuba, Japan

OPEN ACCESS

Edited by:
Eric Marechal,
UMR 5168 Laboratoire de Physiologie Cellulaire Vegetale (LPCV), France

Reviewed by:
Christophe Six,
Université Pierre et Marie Curie, France
Frederic Beaudoin,
Rothamsted Research, United Kingdom

***Correspondence:**
Florence Corellou
florence.corellou@u-bordeaux.fr

[†] These authors have contributed equally to this work

Specialty section:
This article was submitted to Marine and Freshwater Plants, a section of the journal Frontiers in Plant Science

Received: 08 December 2020
Accepted: 19 February 2021
Published: 19 March 2021

Citation:
Degraeve-Guilbault C, Pankasem N, Gueirrero M, Lemoigne C, Domergue F, Kotajima T, Suzuki I, Joubès J and Corellou F (2021) Temperature Acclimation of the Picoalga Ostreococcus tauri Triggers Early Fatty-Acid Variations and Involves a Plastidial ω3-Desaturase. Front. Plant Sci. 12:639330. doi: 10.3389/fpls.2021.639330

Alteration of fatty-acid unsaturation is a universal response to temperature changes. Marine microalgae display the largest diversity of polyunsaturated fatty-acid (PUFA) whose content notably varies according to temperature. The physiological relevance and the molecular mechanisms underlying these changes are however, still poorly understood. The ancestral green picoalga *Ostreococcus tauri* displays original lipidic features that combines PUFAs from two distinctive microalgal lineages (Chlorophyceae, Chromista kingdom). In this study, optimized conditions were implemented to unveil early fatty-acid and desaturase transcriptional variations upon chilling and warming. We further functionally characterized the *O. tauri* ω3-desaturase which is closely related to ω3-desaturases from Chromista species. Our results show that the overall omega-3 to omega-6 ratio is swiftly and reversibly regulated by temperature variations. The proportion of the peculiar 18:5 fatty-acid and temperature are highly and inversely correlated pinpointing the importance of 18:5 temperature-dependent variations across kingdoms. Chilling rapidly and sustainably up-regulated most desaturase genes. Desaturases involved in the regulation of the C18-PUFA pool as well as the Δ5-desaturase appear to be major transcriptional targets. The only ω3-desaturase candidate, related to ω3-desaturases from Chromista species, is localized at chloroplasts in *Nicotiana benthamiana* and efficiently performs ω3-desaturation of C18-PUFAs in *Synechocystis* sp. PCC6803. Overexpression in the native host further unveils a broad impact on plastidial and non-plastidial glycerolipids illustrated by the alteration of omega-3/omega-6 ratio in C16-PUFA and VLC-PUFA pools. Global glycerolipid features of the overexpressor recall those of chilling acclimated cells.

Keywords: temperature, microalgae (Mamiellophyceae), polyunsatutared-fatty-acid, octapentadecaenoic acid, desaturase, omega-3, transcription, *Ostreococcus tauri*

MATERIALS AND METHODS

All chemicals were purchased from Sigma Chemical (St. Louis, MO, United States), when not stated otherwise.

Biological Material and Cultures

Ostreococcus tauri (clonal isolate from OtH95) wild-type and transgenics were grown and monitored by flow cytometry as previously described (Degraeve-Guilbault et al., 2017). Vancomycin (1 mg/ml) was used to reduce bacterial contamination to less than 1% before experiments. Artificial sea-water base contained either 5 μM NaH_2PO_4 (phosphate limitation) or 35 μM. Cultures were grown in incubator-shaker (New Brunswick Innova 42R) with constant agitation (80 RPM) under white light (75 mmol photons m-2 s-1, 6 × T8 fluorescent bulbs 15 Watt each (Sylvania Gro-Lux). For screening of FA of *O. tauri* transgenics, cells were grown in T25 aerated culture flasks (Sartstedt, Nümbrecht, Germany) at 20°C. For *O. tauri* lipid analysis cells were grown in 200 mL of medium in 500 mL Erlenmeyer flasks. For temperature shift experiments cells were grown in either Erlenmeyer flasks or aerated T75 vertical flasks (100 mL medium in 250 mL flasks). *O. tauri* were acclimated at least for 10 generations (sub-cultivated twice) at a given temperature. *Synechocystis* sp. PCC6803 was grown accordingly to Kotajima et al. (2014). *Nicotiana benthamiana* plants were cultivated in a greenhouse under controlled conditions (16–8 h photoperiod, 25°C). *Agrobacterium tumefaciens* strain GV3101 was grown in Luria Broth medium at 30°C as previously described (Degraeve-Guilbault et al., 2020).

Sequences Analyses

Sequences of putative ω3-desaturases were retrieved from genomic and transcriptomic data from NCBI and those from Mamiellophyceae species were manually checked for completion of Nt sequences; cTP were predicted from PredAlgo; alignment was performed using Snapgene trial version (Clustal omega). A codon-optimized sequences without the cTP (sequence start MTYNET) was used for expression *Synechocystis* sp. PCC6803 (Genewiz, Europe).

Cloning Strategy

The *O. tauri* ω3-desaturase full-length sequence was amplified by PCR cycles from cDNA matrix using Q5® Polymerase by two-step PCR (5′-ATGCGCGCCGCGACGTC-3′ and 5′-CTAGTCGCCCCGCTCCCAGAC-3′), cloned in pGEM®-T Easy (Promega, Madison, WI, United States) and sequenced (Genwiz, Leipzig, Germany). Amplification from plasmid DNA was achieved with adapted primers to allow further cloning in pOtox-Luc (Moulager et al., 2010) (Restriction sites *Apa*I, *Avr*II) and using Gateway® system according to manufacturer instruction (pDONR 221, pVT102-U-GW for *Saccharomyces cerevisiae* and pK7W2G2D or pK7YWG2 for *N. benthamiana*). Primers are provided in **Supplementary Tables.**

Overexpression in *Synechocystis* sp. PCC6803 was performed using the pTHT2031S vector after ligation to introduce the synthetic gene using the In-Fusion® HD cloning kit (Takara Bio, Kusatsu, Japan). Primers are available from the **Supplementary Data File.**

RNA and cDNA Preparation and Quantitative RT-PCR Analysis

For every RNA extraction FAs were analyzed in parallel. RNeasy-Plus Mini kit (Qiagen, Hilden, Germany) was used for RNA purification; DNase I was used to remove contaminating DNA (DNA-free kit, Invitrogen, Carlsbad, CA, United States) and cDNA obtained using the reverse transcription iScript™ supermix kit (Bio-Rad, Hercules, CA, United States). Real-time RT quantitative PCR reactions were performed in a CFX96™ Real-Time System (Bio-Rad) using the GoTaq® qPCR Master mix (Promega, Madison, WI, United States). Bio-Rad CFX Manager software was used for data acquisition and analysis (version 3.1, Bio-Rad). Ct method was used to normalized transcript abundance with the references mRNA *EF1α* (elongation factor), *CAL* (calmodulin), and *ACTprot2* (Actin protein-related 2). PCR efficiency ranged from 95 to 105%. Primers are available from the **Supplementary Data File.**

Genetic Transformation

Ostreococcus tauri transformation was achieved using the pOtOXLuc vector and electroporation and transgenics were pre-screened accordingly to their luminescent level as previously described (Degraeve-Guilbault et al., 2020). Control lines are transgenics of empty vectors.

Nicotiana benthamiana were transformed by agroinfiltration of leaves from five-week old plants as previously described (Degraeve-Guilbault et al., 2020). Co-infiltration of RNA-silencing inhibitor P19 (equal volume of a bacterial suspension harboring pBin61-P19), was used in all experiments (Shah et al., 2013). DNA constructs were transferred by electroporation into the *Agrobacterium tumefaciens* GV3101 strain. Briefly, *A. tumefaciens* transformants were selected with antibiotics (gentamycin 25 μg/mL with spectinomycin 100 μg/mL or kanamycin 50 μg/mL). *A. tumefaciens* transformants were grown overnight, diluted to an optical density at 660 nm of 0.1, and grown up to 0.6–0.8. Cells were re-suspended in 5 mL sterilized H_2O for a final OD of 0.4 and 0.2 for overexpression and subcellular localization experiments, respectively. and 1 mL was agroinfiltrated using a synringe without needle. Plants were analyzed 2 and 5 days after *A. tumefaciens* infiltration for subcellular localization experiments and for overexpression, respectively.

Synechocystis sp. PCC6803 transformation was achieved by homologous recombination. Briefly, the plasmid was transformed into ten-time concentrated cells collected at mid-log phase. Subsequently, the cell was incubated at 30°C under white fluorescent lamps for 16–18 h and selected by 25 μg/mL chloramphenicol and 5 μg/mL spectinomycin on BG-11 solid media (1.5% w/v Bacto-agar).

Lipid Analysis

For all organisms, fatty acid analyses and for *O. tauri* further lipid analysis were achieved accordingly to Degraeve-Guilbault

et al. (2017). Organic solvents all contained butylhydroytoluene as an antioxidant (0.001%) and glassware was used. To gain resolution on *O. tauri* FA analysis, a minimum of 50 mL culture (approx. 1.5×10^9 cells) was pelleted and extracted (glass beads beating and 1 h at 80°C) in 1 mL acidic methanol (2% v/v H_2SO_4) containing heptadecanoic acid (2 or 10 μg/ml) as internal standard; phase separation was achieved using 1 mL of NaCl 2.5% (or water for *O. tauri*) and 1 mL of hexane. The upper phase was collected in a new tube and concentrated to 100 μL under nitrogen stream. Four μL were injected for GG-FID analysis (Hewlett-Packard 5,890 series II, Agilent, Waldbronn, Germany) on a15 m × 0.53 mm × 1.2 μ Carbowax column (Altech, Deerfield, IL, United States). This procedure allowed for increasing the resolution of minor FA detection without any column saturation with major FA. Lipid extraction was performed as previously described (Degraeve-Guilbault et al., 2020). Briefly, the material was extracted using glass beads in chloroform:methanol (2:1 v/v), pelleted and extracted again until no pigment could be extracted. Phase separation was performed adding 0.5 v of NaCl 0.9%. Lipid developments were achieved by HP-TCL under 33% humidity in the ADC2-chamber system, (CAMAG). For *O. tauri* polar lipid were separated using methyl acetate/isopropanol/chloroform/methanol/KCl 0.25% (25:25:25:10:4 v/v/v/v) and neutral lipid using hexane/diethyl-ether/glacial-acetic-acid (60:10:1.22 v/v/v). For *Synechocystis* sp. PCC6803, polar lipids were separated using chloroform/methanol/glacial acetic acid/water (85:12:12:1 v/v/v/v). Lipids were stained with a solution of 0.02% primuline in 80:20 acetone/water (deeping for 1 min, air dried for 20 min).

Confocal Microscopy

Live cell imaging was performed using a Leica SP5 confocal laser scanning microscopy system (Leica, Wetzlar, Germany) equipped with Argon, DPSS, He-Ne lasers, hybrid detectors, and 63x oil-immersion objective. *N. benthamiana* leave samples were transferred between a glass slide and coverslip in a drop of water. Fluorescence was collected using excitation/emission wavelengths of 488/490–540 nm for chlorophyll, 488/575-610 nm for YFP, and 561/710- 740 nm for m-cherry. Co-localization images were taken using sequential scanning between frames. Experiments were performed using strictly identical confocal acquisition parameters (e.g., laser power, gain, zoom factor, resolution, and emission wavelengths reception), with detector settings optimized for low background and no pixel saturation.

Statistical Analyses

GraphPad Prism version 9.0.0 for Windows (GraphPad Software, San Diego, CA, United States[1]), was used to compute statistical analysis following the recommendation of the user guide. PCA analyses was performed using the standardize method with parallel analysis option. The unpaired *t*-test with Welch correction (no assumption made about the variance of each group) was used when normality could be assessed otherwise the non-parametric Mann–Whitney test was used. Note that only the Shapiro–Wilk test for normality provided results when $n = 3$.

[1]www.graphpad.com

INTRODUCTION

Microalgae are key primary producers of polyunsaturated fatty-acids (PUFAs) including very-long chain PUFAs (VLC-PUFAs) commonly found in marine species (Khozin-Goldberg et al., 2016; Jonasdottir, 2019). Omega-3 PUFAs (ω3) largely predominate over omega-6 PUFA (ω6). Transfer and accumulation of PUFAs through the food-web is essential to support fundamental processes including fertility, development immunity at many trophic levels (Kainz et al., 2004). The synthesis of PUFAs in glycerolipids highly relies on desaturases (Des) that sequentially add *cis*-double bond at specific locations (stereospecificity and regiospecificity) (Shanklin et al., 2009). Des are called after their regiospecificity; for instance, Δ6-Des introduce a double bond in the acyl chain at the sixth carbon from the carboxyl-end (Δ-end) while ω-3-Des convert ω3 to ω6 (methyl end). Desaturases specificity also relies on the acyl-carrier, which can be soluble (Co-enzymeA and acyl-carrier-protein, ACP) or membranous (lipid). Exception made of the stearoyl-CoA Des, primitive eukaryotes (plants, worms. . .) displays acyl-lipid desaturases. In contrast to "higher" eukaryotes, they retained the ability to convert ω6 to ω3. The interplay of desaturases activity within and between the ω3 and ω6 pathways is assumed to be key for PUFA composition of microalgae and consequently for the well balance of ω6/ω3 in upper trophic levels (Galloway and Winder, 2015; Sun et al., 2019).

Phylogenetic markers could be identified despite the important variation of FA composition, including across species from a same taxa (Lang et al., 2011; Jonasdottir, 2019). The ω3 16:4$^{\Delta 4,7,10,13}$ (16:4n3) is the signature of Chlorophyta (Archaeplastida kingdom, "green lineage") while VLC-PUFAs such as 20:5$^{\Delta 5,8,11,14,17}$ (20:5n3) and 22:6 $^{\Delta 4,7,10,13,16,19}$ (22:6n3) are hallmarks of the Chromista kingdom. The peculiar 18:5$^{\Delta 3,6,9,12,15}$ (18:5n3), initially characterized from dinoflagellates (Dinophyta), is widespread in Chromista species including haptophytes and some raphidophytes (Ochrophyta) (Jonasdottir, 2019). 18:5n3 is only found in some classes of Chlorophyta that emerged early in the green lineage such as Pyramimonadphyceae and Mamiellophyceae. This highly unsaturated C18 has been reported to be rapidly metabolized in fish and give rise to 20:5n3 (Ghioni et al., 2001).

Abiotic stresses have major impact on microalgae FA composition (Los et al., 2013; Khozin-Goldberg et al., 2016; Kugler et al., 2019). In the context of climate change, it is all the more important to understand how temperature influences the fatty acid composition of key marine phytoplankton species. Temperature is recognized as a major cue for the regulation of PUFA composition of all organisms including cyanobacteria and microalgae (Nishida and Murata, 1996; Boelen et al., 2013; Kotajima et al., 2014; Aussant et al., 2018). Increasing unsaturation degree are usually inversely correlated with temperature. However, for microalgae the impact of

temperature on FA-profile appears highly dependent on the species. Important studies using *Bacillus subtilis* and *S. cerevisiae*, demonstrated that changes in the membrane state regulate FA desaturase expression allowing for the acclimation of membrane fluidity to occur (homeoviscous response) (Mansilla et al., 2008; Ernst et al., 2016). However, only desaturases introducing monounsaturation and monounsaturated FAs have been clearly demonstrated to be involved in both responses to membrane state and membrane fluidity changes. In contrast, the role of PUFAs for membrane organization appears much subtle. In plants, temperature regulation of desaturase has also been shown to occur at post-transcriptional levels (Gibson et al., 1994; Matsuda et al., 2005; Los et al., 2013).

Ostreococcus tauri is a representative species of the class Mamiellophyceae (Chlorophyta) (Chrétiennot-Dinet et al., 1995). Mamiellophyceae usually predominate marine picophytoeukaryote communities which have a fundamental role in coastal ecosystems (Massana, 2011; Rii et al., 2016). *O. tauri* and related species display a unique FA composition gathering features from the Archaeplastida and Chromista kingdoms. Together with the saturated FAs (SFA) 14:0 and 16:0, the ω3 16:4, 18:3, 18:4, 18:5, and 22:6 are the main FAs (Degraeve-Guilbault et al., 2017). The distribution of these PUFAs is strikingly clear-cut: C18-PUFAs prevail in plastidic lipids, 18:5n3 being restricted to galactolipids, and VLC-PUFAs are exclusively found in the extraplastidic lipids. Non-plastidic lipids are the betain lipid diacylglyceryl-hydroxymethyl-trimethyl-β-alanine (DGTA) and phosphatidyldimethylpropanethiol (PDPT), which are usually reported in Chromista species. We previously showed that nutrient availability importantly impacted the ratio of Δ6-Des substrates/products in plastidial C18-PUFAs and identified the two first plastidic Δ6-Des, one of which was transcriptionally repressed under phosphate starvation (Degraeve-Guilbault et al., 2017, 2020).

In the present work we studied the impact of temperature changes on *O. tauri* FA profile and glycerolipids content. Early changes in Des expression upon thermal shift were investigated. The ω3-Des from *O. tauri* was functionally characterized by overexpression in *N. benthamiana*, *Synechocystis* sp. PCC6803 (*Synechocystis* thereafter) and *O. tauri* giving insight into its involvement in temperature responses.

RESULTS

Temperature Impact on Glycerolipid FA Composition

We previously showed that during *O. tauri* batch-growth the proportion of 18:3n3 was readily increased at the expense of 18:4n3 and therefore might mask some specific impact of temperature on these FAs (Degraeve-Guilbault et al., 2017). Consequently, preliminary experiments were conducted to determine high and low temperatures for which minimal differences were observed with regards to the growth rate between temperatures and maximal differences for FA. Temperatures tested corresponded to those were *O. tauri* has been detected in the environment (**Supplementary Figure 1**; Limardo et al., 2017). In our conditions, cell-growth and/or viability appeared to be impaired at 10 and 32°C. Growth did not appear to be impacted at 15 and 25°C and monitoring growth in more details at 14°C and 24°C confirmed that acclimated cells displayed a similar daily growth rate with a μmax (14°C 0.91 ± 0.1 d^{-1} and 24°C 0.99 ± 0.146 d^{-1}) that was comparable to the one previously observed at 20°C (0.99 ± 0.006) (Degraeve-Guilbault et al., 2017; **Supplementary Figure 1A** and **Figure 1A**). Principal component analysis of FA and temperature values from preliminary experiment unveiled an inversed correlation of 18:5n3 and temperature, and a direct correlation of most ω6 FAs and 18:3n3 (**Supplementary Figures 1C,D**). To gain further insight into FA variations, the glycerolipid FA profile of cells acclimated at 14 and 24°C collected in mid-exponential growth (3.5×10^7 cell mL^{-1}) was analyzed (**Figure 1**). The proportion of most ω3-PUFAs was overall increased at the expense of ω6-PUFAs at 14°C. The proportion of 14:0 was also reduced. It was particularly noteworthy that 18:3n3 and 18:5n3 varied in a reverse way while 18:4n3 remained overall stable (**Figure 1B**). the most statistically relevant differences were detected for the ω3 18:3, 18:5, 20:4, 20:5, 22:5, and for the ω6 16:2, 18:3 as well as for the monounsaturated FA 18:1n9; an obvious drop occurred for the ω6 18:2 and 20:4 though computed *P* values were higher (**Figure 1C**).

Glycerolipid analysis from acclimated cells showed that the proportion of 18:5n3 was increased at low temperature in both MGDG and DGDG (**Figures 1D,E**). For MGDG this seemed to occur at the expense of both 18:3n3 and 18:4n3 while only at the expense of 18:3n3 in DGDG. The 18:4n3 proportion was higher in both SQDG and PG which are lacking 18:5n3, and this increase appeared to occur at the expense of 18:3n3 in SQDG (**Figures 1F,G**). A higher proportion of 22:6n3 was observed in DGTA but neither in PDPT/PS nor in TAG (**Figures 1I,H,J**). On the other hand, variations of other minor VLC-PUFAs such as 20:4n6, 20:5n3, and 22:5n3 were reverberated into TAG, in which 20:4n3 was also detected only at low temperature (**Figure 1J**). These changes translated into a higher unsaturation degree of the bulk of glycerolipids, including TAG, as well as a higher ω3/ω6 ratio in most glycerolipids, that was the highest for PG (**Supplementary Figures 2A,B**).

The glycerolipid composition was also impacted (**Figure 1K** and **Supplementary Figure 1C**). Considering the cellular amount, DGDG was increased at the expense of MGDG at 14°C (**Figure 1K**). This feature has been reported decades ago in both higher plants and algae grown at low temperature and is assumed to be related to the stabilization of plastid membranes in response to various stresses including phosphate deprivation (Lynch and Thompson, 1982; Kuiper, 1985; Li and Yu, 2018). More surprisingly, the amount of SQDG was significantly reduced while that of phospholipids increased, a feature recalling increased phosphate availability, though not coherent with the variation observed in galactolipids (Van Mooy et al., 2009). Noteworthy TAG were twice as abundant at low temperature.

Altogether, our results indicate that low temperature acclimation correlates with an overall increase of ω3-PUFAs and a concomitant decrease of ω6-PUFAs in all structural glycerolipids. A drop of 18:3n3 occurred in all plastidial lipids and was concomitant of a rise of 18:5n3 in galactolipids whereas 18:4n3 was increased only in PG and SQDG.

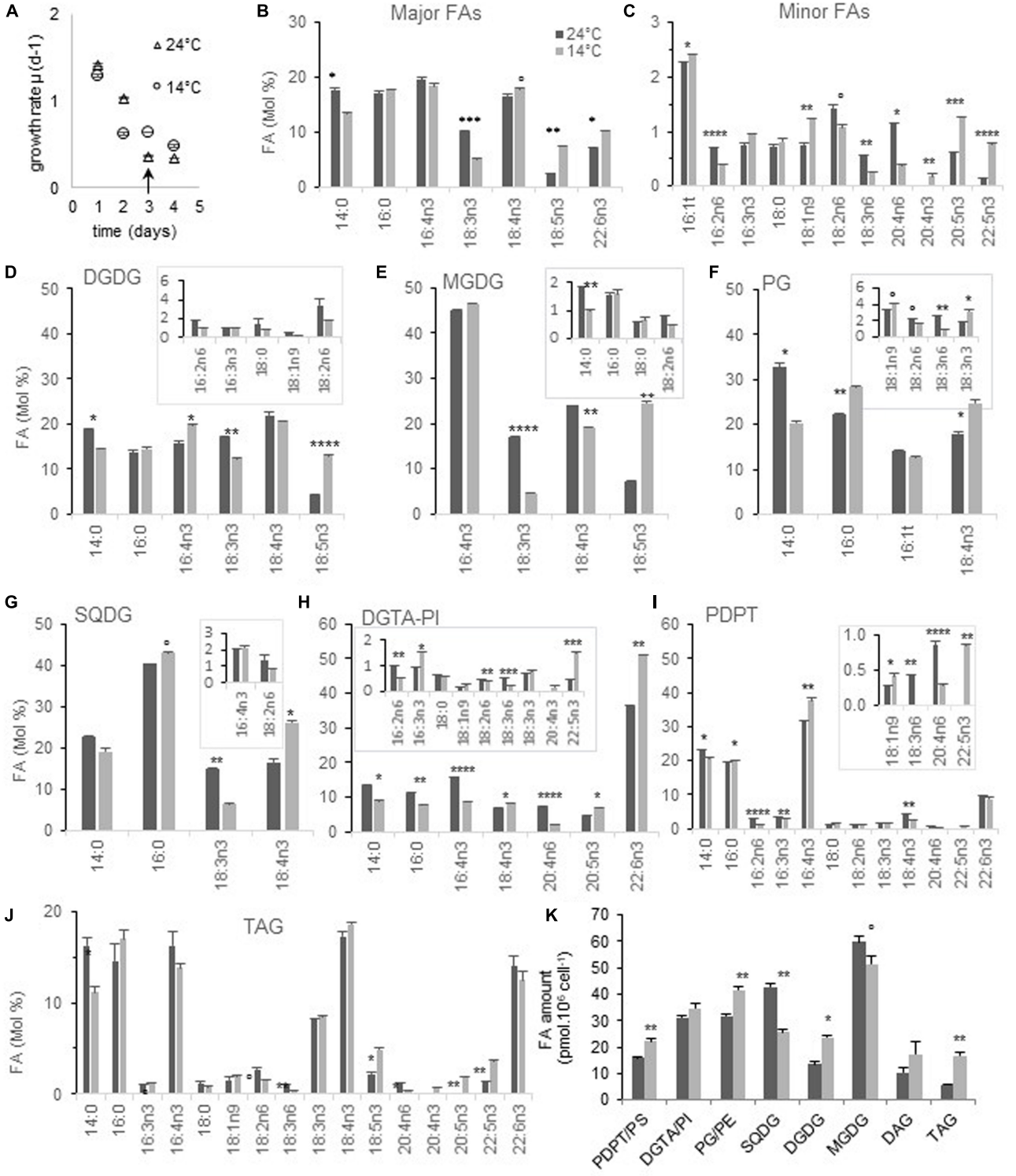

FIGURE 1 | FA and glycerolipid profiles from cells acclimated to 24 and 14°C. Cells were grown under continuous light and acclimated at each temperature before sampling. FAs ≤ 0.5% at both temperatures are not plotted except for 20:4n3 and PDPT. **(A,B)** Global FA profiles from glycerolipid analysis. **(C)** Growth rate of corresponding cultures; arrows indicate the sampling time. **(D–K)** Glycerolipid FA composition. Minor FAs are highlighted in framed inserts. Means and standard errors to the mean (SEM) from biological triplicate are shown. Marks correspond to statistical significant differences by unpaired *t*-test (°$P < 0.02$, *$P < 0.01$, **$P < 0.001$, ***$P < 0.0001$, and ****$P \leq 0.00001$).

Kinetics of FA Desaturation Upon Temperature-Shift

From experience we know that *O. tauri* rhythms are readily synchronized by external cues (Moulager et al., 2007; Monnier et al., 2010). In order to gain the most accurate insight into the kinetics of changes upon temperature shift, the cultures were synchronized by light-dark cycles (L/D) of 18–6 h. This experimental design aimed to restrain time resetting and cell re-synchronization by temperature shift. Indeed, continuous light does not abolish circadian rhythms but merely result in progressive desynchronization of rhythms between individual cell (Bieniawska et al., 2008). As temperature is a strong cue for time resetting, the cells switched to a novel temperature are most likely resynchronized while the control cell are not (McClung and Davis, 2010). This results in comparing different internal times. In contrast, under diurnal cycles internal rhythms and entrained, i.e., synchronized and set on the external time; temperature changes do not change the phase of the rhythms. Because temperature responses were reported to be augmented in the morning and since in *O. tauri* desaturase expression is known to peak from late night to mid-day, temperature-shifts were achieved [4.5 h after light on (T0)] (**Supplementary Figure 3**).

Cells acclimated at 14 and 24°C and collected at the time of the temperature shift displayed FA differences that were closely related to those observed under continuous light, though the *P* varied, with the further variation of 16:4n3 that was lower at 14°C (**Figures 2A,B**). Principal component analysis was used to test the relationship between FA variations and temperature in this homogeneous data set; it unveiled that minor ω3 PUFAs as well as 18:5n3, 16:0, 18:1, and were related and negatively correlated to temperature. In contrast, 20:4n6, 18:3n6 as well as 16:4n3 displayed correlation scores that were close to the temperature variable while 18:2, 16:2 as well as 18:3n3 variations were also explained by the second principal component (**Figure 2C**).

The swiftness of FA-variations upon chilling (24–14°C) and warming (14–24°C) was investigated achieving early sampling times after the temperature and following variations up to 36 h (**Figure 3**). The data were averaged from independent experiments. As the proportion of 18:3n3 and 18:4n3 were slightly different between experiments (due to the nutrient state), an individual kinetics is further provided as **Supplementary Data**, in order to better highlight the most earlier changes (**Supplementary Figure 4**).

Fatty-Acid Variations

Acclimated Cells

Over the 36 h sampling period the proportion of major FAs remained in average stable while that of the ω6 18:2, 18:3, and 20:4 progressively increased at 24°C (**Figures 3A,C**). The proportion 18:2n6 was further increased at dark transitions (T12, T36) (see also **Supplementary Figure 4**).

Temperature Shifts

Variations upon chilling were detected as early as 3 h, in particular for the minor FAs 18:2n6 and 18:3n6 and the major FA 18:5n3 (**Figure 3B**). It was striking that under chilling, the proportion of 18:3n3 was gradually decreased over time which contrasted to all other conditions. The proportion of 18:4n3 remained rather stable. Chilling also resulted in the gradual increase of 16:3n3 and was concomitant of a decrease of 16:2n6. For VLC-PUFAs, the proportion of 20:4n6 was progressively lowered while the increase of either 20:5n3 and/or 22:5n3 were not obvious from the pool of all data but detected in individual experiments (**Supplementary Figure 4**). Noteworthy, 22:6n3 was poorly/not increased over the sampling period and the minor FA 20:4n3 was detected only in cells acclimated to low temperature (**Figure 3** and **Supplementary Figure 4**). Conversely, warming triggered changes that were unambiguously detected after 6 h and were reversed compared to chilling; those included the increase of 18:3n3 that paralleled the decrease of both 18:4n3 and 18:5n3 as well as the increase of the ω6 (16:2,18:2, 18:3, and 20:4) that were concomitant with the decrease of minor ω3 (**Figure 3D**). Note that the 20:4n3 was still detected 36 h after transfer to high temperature.

In summary, chilling and warming triggered FA changes detected as early as 3–6 h after the shift, respectively. The patterns were reversed between chilling and warming and impacted the overall ω3/ω6 ratio. The earliest and most obvious variations were observed for ω6-C18-PUFAs and 18:5n3. Progressive variations further occurred in minor FAs including 16:2n6, 16:3n3, 20:4n6, and 20:5n3 and/or 22:5n3. The variations of 18:3n3 mirror the changes observed in 18:5n3 whereas the proportion 18:4n3 was rather stable. Finally, accumulation of 22:6n3 and 20:4n3 occurred at long term. These observations strongly suggested the involvement of ω3-desaturation in early temperature responses.

Desaturase Transcript Variations

In order to gain insight into early transcriptional control possibly involved in the dynamics of FA-changes, the expression of desaturases most relevant to the changes observed at the FA level were monitored (**Figure 4** and **Supplementary Figure 5**). Since FA variations upon chilling were detected as early as 3 h, desaturase expression upon chilling was monitored as earlier as 1 h after chilling.

Except for the ER and plastidial Δ4-Des, all desaturase transcripts were higher in cells acclimated or transferred to 14°C (**Figures 4A,B** and **Supplementary Figure 5A**). Values were unambiguously increased as early as 1 h after the shift. The highest differences were observed for the putative *ω3-Des* and the *plastidial*Δ*6-Des-2* (previously referred to as Ot10) whereas *p*Δ*6-Des-1* (previously Ot05) was moderately upregulated though its expression was definitely higher in cells acclimated to low temperature. Let us recall here, that pΔ6-Des2 has been recently shown to preferentially impact ω6-C18PUFAs, PG as well as highly unsaturated ω3-galactolipid species while the overexpression of *p*Δ*6-Des-1* had a much broader impact and was highly active on ω3-substrates (Degraeve-Guilbault et al., 2020). Early up-regulation was also unambiguous for the *Acyl-CoA*Δ*6-Des* and Δ*5-Des*, coding both for ER Des, as well as for the *MGDG*Δ*7-Des* and the *stearoyl-ACP*

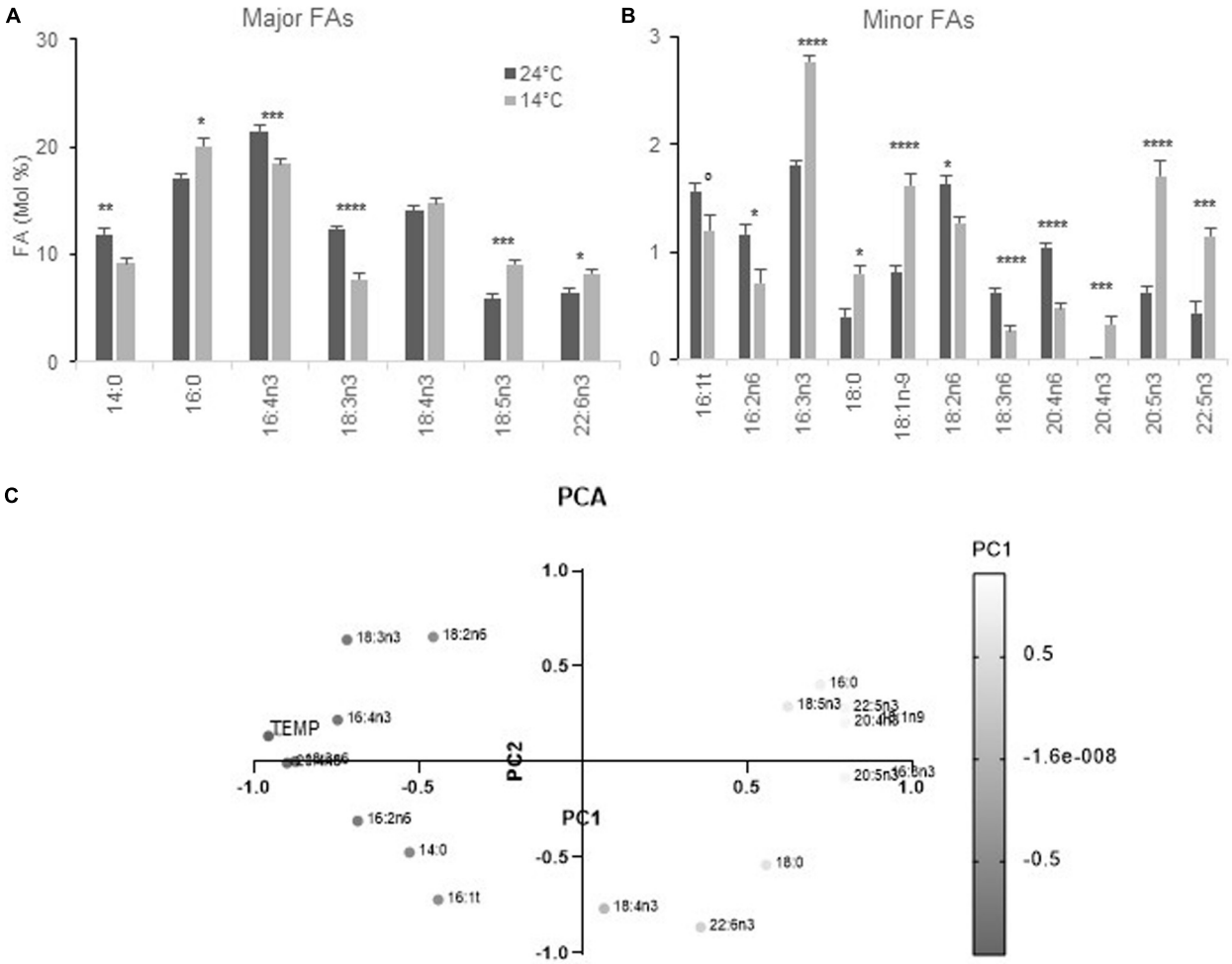

FIGURE 2 | FA profiles from cells acclimated to 24 and 14°C under diurnal conditions. Cells were grown under light-dark cycles (16–8 h). **(A,B)** FA-profile from cells collected at 4–4.5 h after light on. Means and standard errors to the means of 15 samples (extracted from four independent experiments) are shown. Marks correspond to statistical significant differences by unpaired *t*-test (°$P < 0.05$, *$P < 0.01$, **$P < 0.001$, ***$P < 0.0001$, and ****$P < 0.00001$). **(C)** Principal component analysis (PCA) of FAs and temperatures from the same data set. PC1 corresponds to 50.27% of the variance and PC2 to 19.96% (cumulative proportion of the variance 70.23%). The gray gradient applies for the value on PC1 the lightest being the lowest.

desaturase putative ortholog (*SAD*). Note that, similar trends were monitored under continuous light though both *Acyl-CoAΔ6-Des* and *pΔ6-Des1* underwent higher activation; this suggested that, under L/D, the full activation of these genes in the morning could be limited by a circadian control (circadian gating) (**Supplementary Figure 6**). Conversely, warming resulted in an overall reduction of desaturase transcript levels especially at 3 h after the temperature-shift, with the notable exception of the putative *MGDGΔ7-Des* whose expression appeared transiently increased (**Figure 4C**). Overtime, desaturase gene downregulation was more conspicuous for the *Acyl-CoAΔ6-Des*, as well as for *Δ5-Des, pΔ6-Des-1*, and the putative *pω3-Des* whose expressions were reduced by more than half.

Overall, our results indicate a tight and inverse control of the expression of most desaturase genes by temperature. The *Acyl-CoA Δ6-Des*, the putative *ω3-Des* and the *Δ5-Des* expressions appeared to be importantly regulated in both cases. Interestingly for the plastidial Δ6-desaturases, the expression of the *pΔ6-Des2* was importantly increased upon chilling whereas for warming, *pΔ6-Des1* transcript level was reduced to a greater extent compared to *pΔ6-Des2*.

Functional Characterization of the Putative ω-3-Des

As both FA and transcriptional variations strongly suggested the involvement of the ω3-Des in the temperature acclimation process, we next focused on the only ω3-Des candidate found in *O. tauri* (Otpω3-Des) and related species (Degraeve-Guilbault et al., 2020). These putative ω3-Des have been reported to be orthologous of the Δ15-Des of *Emiliania huxleyi* (EhΔ15-Des) and cluster apart from previously characterized Δ15-Des. The authors

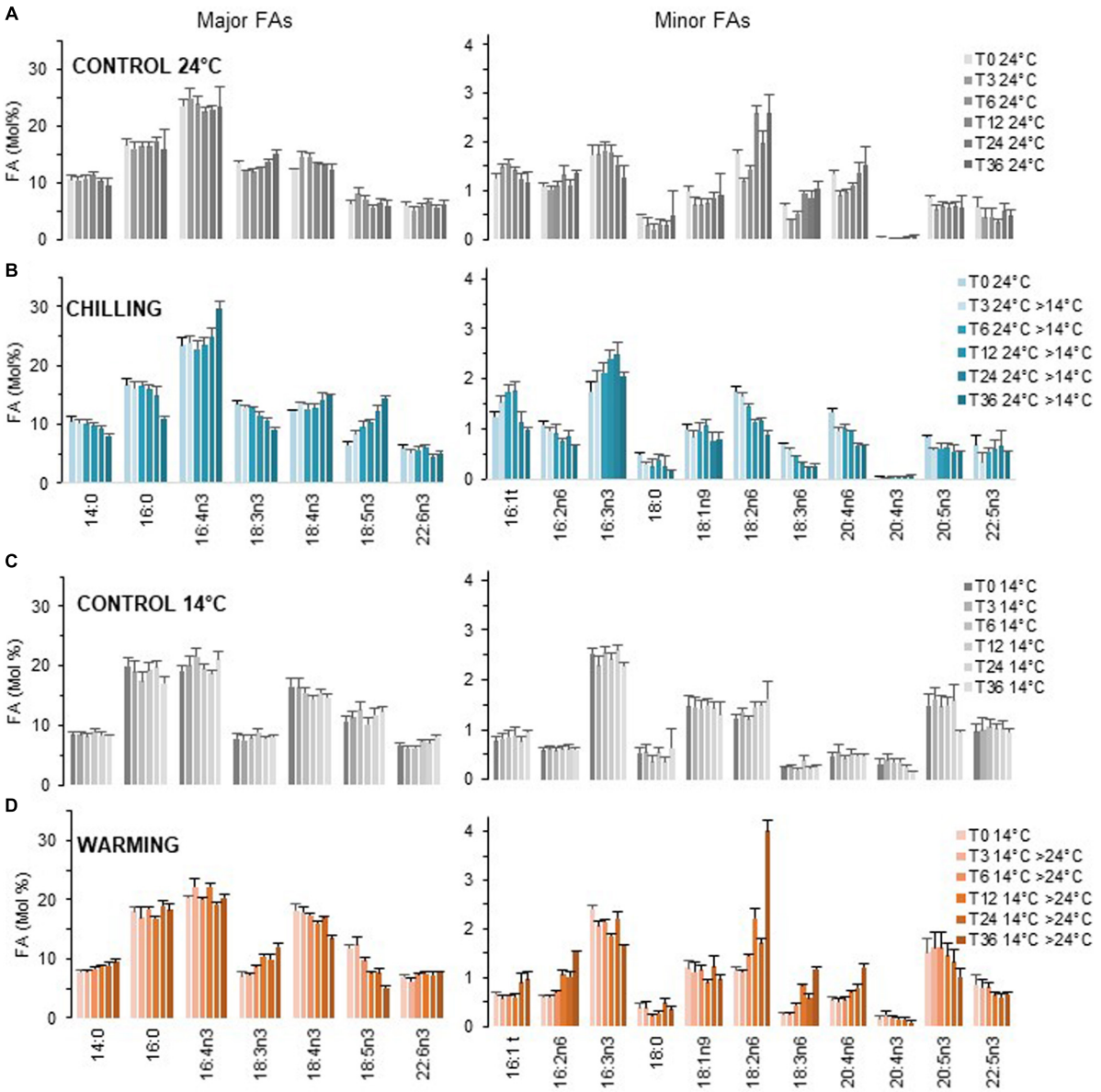

FIGURE 3 | Kinetics of FA profile variations upon chilling and warming. Major and minor FAs are represented on separate panels. Cultures grown under light/dark cycles (16/8 h) at 24°C **(A)** and 14°C **(C)** were transferred at 4.5 h after light on (T0) to 14°C [chilling, **(B)**] and 24°C [warming, **(D)**] respectively. Means and standard errors of biological replicate from at least two independent experiments (T36 chilling triplicate from one experiment).

hypothesized that EhΔ15-Des was involved in the accumulation of 18:5n3 that occurs in *E. huxleyii* at low temperature (Kotajima et al., 2014).

Sequence Features

We used sequences of functionally characterized ω3-Des from the green lineage and sequences with homology to the Otpω3-Des in different lineages to construct a phylogenetic tree (**Supplementary Figure 7A**). Our analysis confirmed that ω3-Des sequences from Mamiellophyceae were unrelated to green ω3-Des and clustered with desaturase sequences from the Chromista kingdom including the ω-3-Des from *Thraustochytrium* sp. shown to accept C20-FAs as substrates (Meesapyodsuk and Qiu, 2016). Sequence alignment of putative ω-3 Des from Mamiellophyceae species highlighted three typical His-boxes encompassing the motifs HHTCH, HNHLHH, and YQIEHH conserved in orthologs from haptophytes, diatoms, dinoflagellates, and labyrinthulomycetes and divergent form the motifs HXXXH, HXXHH, and HXXHH considered as hallmarks of eukaryotic ω-3 Des (**Supplementary Figure 7B**; Wang et al., 2013; Kabeya et al., 2018). In addition, all ω3-Des sequences from Mamiellophyceae encompassed a predicted chloroplastidic targeting peptide (cTP) upstream of highly conserved sequence starting with a methionine

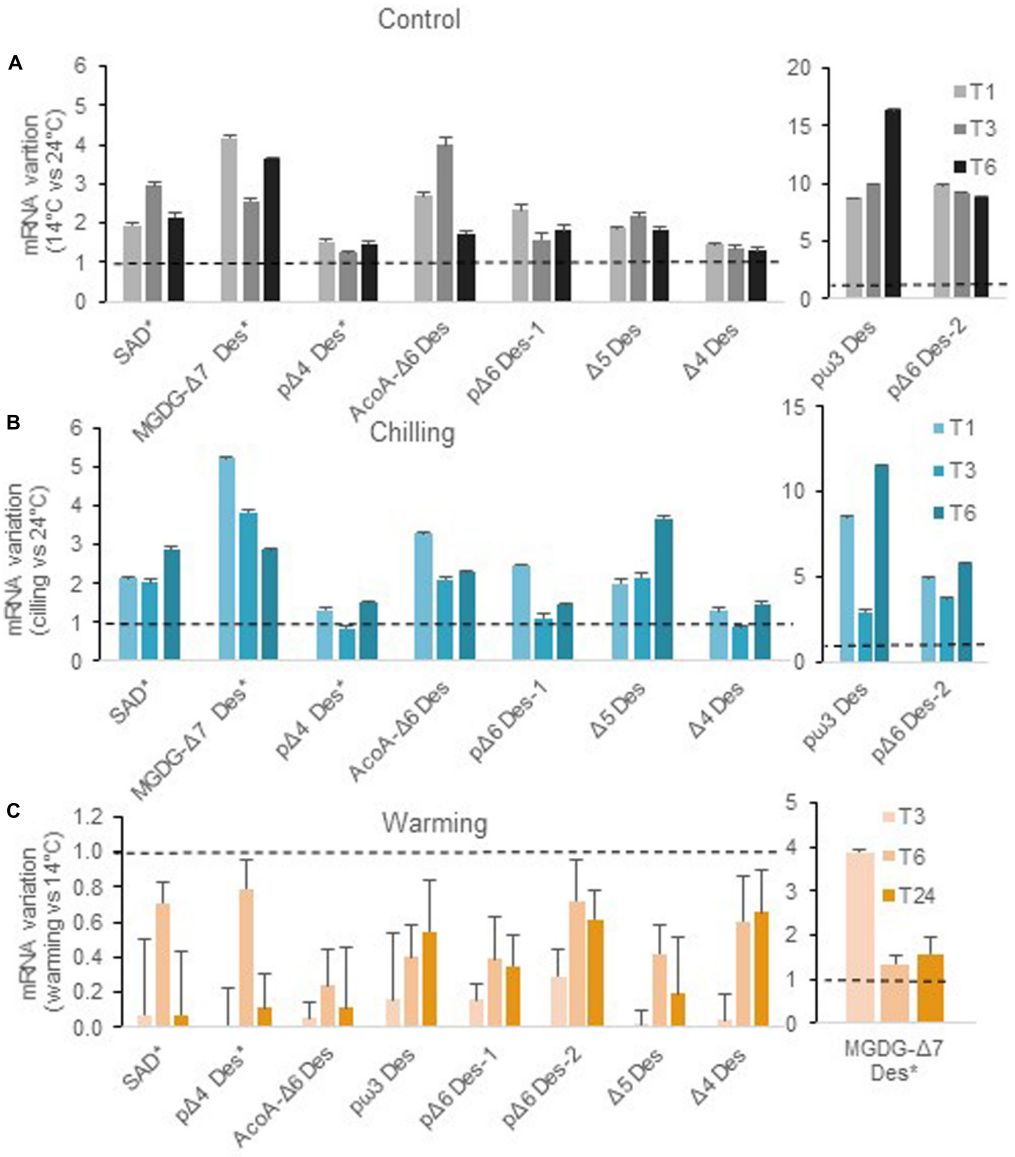

FIGURE 4 | Variations of desaturase transcript abundance upon chilling and warming relative to control cultures. Culture conditions were the same as in **Figure 2**. Plotted values correspond to the ratio of transcript abundance at 14°C relative to 24°C for controls **(A)**, and ratio of transcript abundance in cells shifted to either low **(B)** or high **(C)** temperature relative to cells at the initial temperature. Errors bars are standard deviations calculated following the error propagation rules using the formula $SD_{x/y} = \sqrt{(SD_x/x)^2 + (SD_y/y)^2}$. Relative transcript abundance is available from **Supplementary Figure 5**.

(**Supplementary Figure 8**). According to the PredAlgo prediction software the cTP score of Otpω3-Des was the highest among all desaturases (4.53/5) (Tardif et al., 2012; Degraeve-Guilbault et al., 2020).

Overexpression of the Putative ω3-Des in Heterologous Hosts

Transient expression of the *Otpω3* fused to YFP in *N. Benthamiana* resulted in a clear labeling of chloroplasts (**Figure 5A**). Overexpression of the label free *Otpω3-Des* had no detectable impact on the overall FA-profile (**Figure 5B**). We reasoned that the endogenous ω3-Des activity (FAD3/FAD7/FAD8) may mask the activity of the *Otpω3-Des*. To possibly unmask this activity, the *O. tauri pΔ6-Des2 (OtpΔ6-Des2)* was used. We previously showed that pΔ6-Des2 displays a preference for ω6-C18-PUFA; it was assumed to compete for the 18:2n6 the natural substrate of plant ω3-Des, thereby reducing the amount of 18:3n3 but allowing 18:4n3 production through 18:3n6 ω-3 desaturation (Degraeve-Guilbault et al., 2020). As expected, *OtpΔ6-Des2* overexpression in *N. benthamiana* resulted in the production of 18:3n6 and 18:4n3 while 18:3n3 was in average concomitantly decreased compared to the control lines, though the difference was estimated to be poorly relevant (*t*-test, $P = 0{,}021$); co-expression

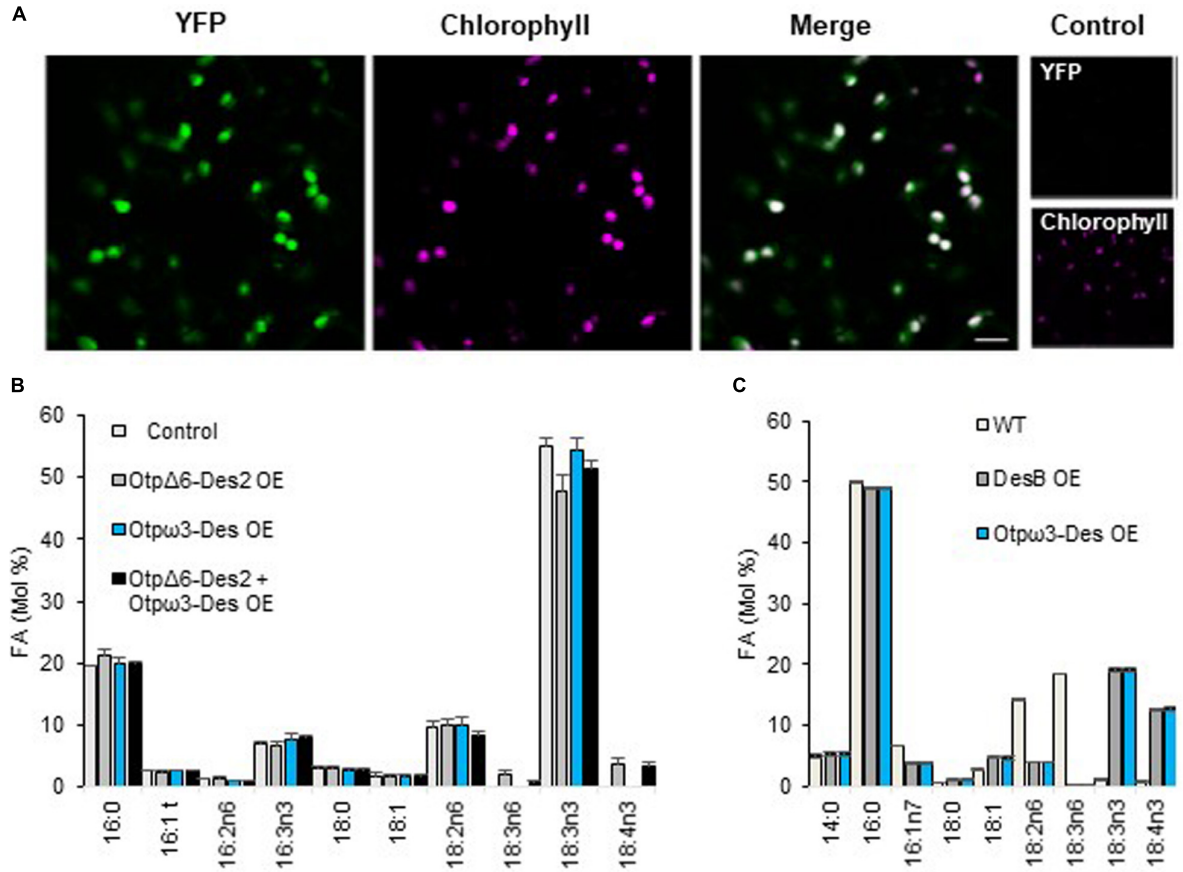

FIGURE 5 | Localization and activity of the *O. tauri* putative ω3-Des in heterologous hosts. **(A)** Confocal Microscopy of *N. benthamiana* transient overexpressing the putative ω3-Des C-terminal fused to YFP (YFP) (100% for 23 cells). Fluorescence from YFP, chlorophyll and cross bleeding with identical parameter (control). **(B)** Overexpression of the label-free putative ω3-Des (pω3-Des) in *N. benthamiana.* The overexpression of the plastidial *O. tauri pΔ6-Des2 (*pΔ6-Des2) is used to highlight the ω3-activity by competing for their common substrate 18:2n6. Means and standard errors of n replicate from two independent experiments are shown; P19 transgenics (control $n = 5$), pΔ6-Des2 OE ($n = 7$), pω3-Des OE ($n = 6$), pΔ6-Des2 + pω3-Des OE ($n = 17$). **(C)** Overexpression of the putative ω3-Des truncated for the cTP in *Synechocystis* PCC6803. A line overexpressing the native ω3-Des (DesB OE) was used as positive control. Cells were grown at 32°C, temperature at which the expression of *desB* is repressed in the wild-type. 14:0, 16:1n7, and 18:1 that represent each about 5% and did not varied are not represented. Means and standard errors of three independent experiments are shown.

of *OtpΔ6-Des2* OE and *Otp*ω3-Des lowered the proportion of 18:3n6 (*t*-test $P = 0{,}035$) and that of 18:3n3 was in average increased though it did not appear to be statistically relevant. These subtle FA-variations were coherent with *Otp*ω3-Des triggering the desaturation of 18:3n6 and/or competing with *OtpΔ6-Des2* for 18:2n6, thereby indirectly reducing the proportion of 18:3n6. The absence of clear variations of ω3-end-products 18:3n3 and 18:4n3 might result from compensatory regulations of the endogenous ω3-Des activities. In order to circumvent interference of endogenous ω3-Des activities, *Synechocystsis* sp. PCC6803 (*Synechocystis* thereafter) was chosen to overexpress *Otpω3-Des*. *Synechocystsis* displays one ω3-Des (DesB) whose expression is strongly inhibited at 32°C, precluding the production of 18:3n3 and 18:4n3 from 18:2n6-PG/SQDG species and 18:3n6-galactolipid-species, respectively (**Figure 5C**; Sakamoto et al., 1994). Heterologous gene expression in *Synechocystis* has the further advantage of being driven from the same insertion site (homologous recombination) (Williams, 1988). At 32°C, the *desB* and *Otpω3-Des* overexpressors (OE) produced 18:3n3 and 18:4n3 in a similar way. Both OE accumulated 18:4n3 in galactolipids and 18:3n3 in PG and SQDG indicating that *Otpω3-Des* accepted equally well galactolipids, PG and SQDG as substrates (**Supplementary Figure 9**). Altogether these results demonstrated that *Otp*ω3-Des is a plastid located desaturase which efficiently converts ω6-C18-PUFAs to ω3-C18-PUFAs in galactolipids, SQDG and PG.

Impact of Overexpressing the Plastidial pω3-Des in the Native Host

FAs and Glycerolipids

Ostreococcus tauri lines overexpressing *pω3-Des* (*pω3-Des* OE) were created using the pOtOXLuc vector where the high affinity phosphate transporter promoter (PromHAPT) is driving transgene expression. The full activity of promHAPT requires phosphate limited conditions (Djouani-Tahri el

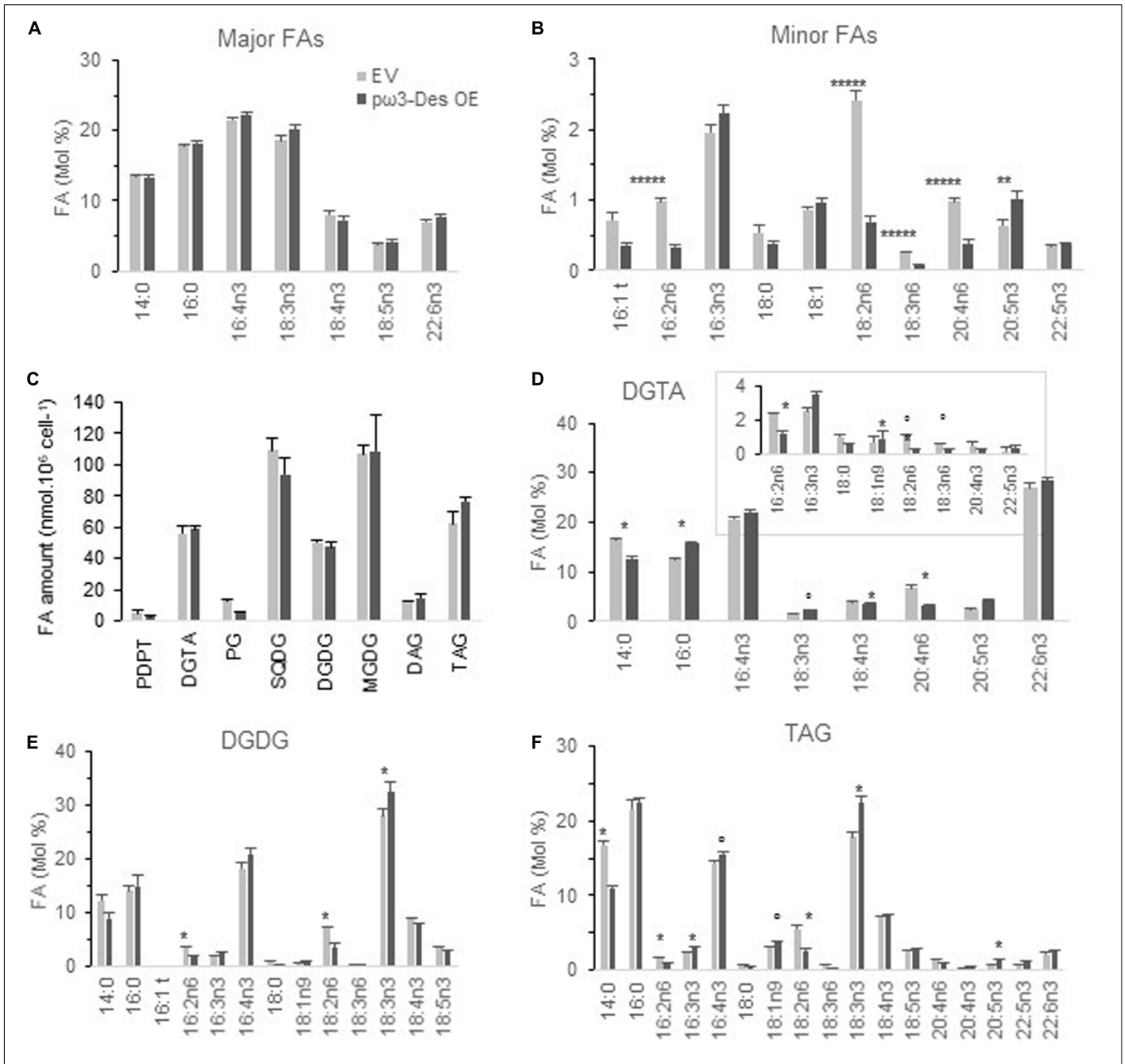

FIGURE 6 | Glycerolipid profiles of *O. tauri* pω3-Des OE. **(A,B)** FA profiles of transgenics at stationary phase, 20°C. Means and standard errors are shown (n = 12 from three independent experiments and five pω3-Des OE different lines). Asterisks indicate statistically significant differences by Wilcoxon–Mann–Whitney test (**P < 0.005; *****P < 0.000001). Expression and luminescence levels of transgenics are available from **Supplementary Figure 10**. **(C)** Glycerolipid content of one pω3-Des OE line in mid-exponential growth. **(D–E)** FA profile of glycerolipids, DGTA **(D)**, DGDG **(E)**, and TAG **(F)**. Marks indicate statistically significant differences by t-test (°P < 0.02 and *P < 0.01). MGDG, SQDG are shown in **Supplementary Figure 11**. Means and standard errors from three independent experiments are shown.

et al., 2011). It should be recalled that phosphate deprivation triggers the increase of 18:2n6 and 18:3n3 at the expense 18:3n6 and 18:4n3 in plastidial lipids, most probably though the inhibition of the plastidial Δ6-desaturation (Degraeve-Guilbault et al., 2017, 2020).

From the five selected *pω3-Des* OE subtle changes were detected under phosphate limitation at stationary phase (**Figures 6A,B** and **Supplementary Figure 10**). Proportions of all ω6-PUFAs were lower displaying relevant differences compared to control lines. As regards to minor ω3, 16:3n3 and 18:3n3 were slightly increased though only 20:5n3 appeared significantly higher. Variations in major ω3-PUFAs could, however, be detected from glycerolipids analysis (see below).

One of the transgenics was chosen for further detailed lipid analysis in mid-exponential growth (**Figures 6C–F** and **Supplementary Figure 11**). Glycerolipid composition of the *pω3-Des* OE was not significantly altered. Conspicuous differences were observed in individual glycerolipids. A lower proportion of 14:0 and a higher proportion of 18:3n3 were more obvious in TAG, but also significant in DGTA (**Figures 6D–F**). The ω6 C16- and C18-PUFAs, especially 18:2n6, were reduced in plastidic and extraplastidic lipids including TAG, while both 16:3n3 and 16:4n3 were increased, though with poor significance. In DGTA 20:4n6 was reduced while all VLC-PUFAs downstream in the pathway were all slightly increased; this trend was also detectable in TAG. Altogether these changes are coherent with an increased ω3-desaturation activity in *pω3-Des* OE that obviously impact all glycerolipids.

In summary, the overexpression the plastidial ω3-*Des* in the native host impacted the ω3/ω6 ratio at the level of minor FAs. These changes appeared to result from changes in all glycerolipid classes.

Growth at Different Temperature

FA remodeling of lipids is thought to be crucial for membrane acclimation to temperature changes. We therefore expected the growth of *pω3-Des* OE to display some distinctive patterns when transferred to either lower or higher temperature (**Supplementary Figure 12**). The growth of *pω3-Des* OE was, however, not consistently impacted neither by chilling nor by warming at limit high temperature (30–32°C).

DISCUSSION

In the present study, we achieved the functional characterization of the unique ω3-Des candidate from Mamiellophyceae species. Sequence analyses highlighted a predicted cTP, included in an ORF upstream of the conserved desaturase CDS, as well as His-Box motifs conserved in putative or established ω3-Des of protists belonging to the Chromista kingdom and highly distinctive from ω3-Des from cyanobacteria, fungi, plant, and animals. The Otpω3-Des localized to plastids in *N. benthamiana* and was shown to perform ω3-desaturation of all *Synechocystis* glycerolipid classes, which correspond to plastid lipids in eukaryotes. Moreover, *Otpω3-Des* overexpression in the native host, though it poorly impacted the C18-PUFA pool, unambiguously affected the ratio ω6/ω3 of C16-PUFAs in DGDG, DGTA, and TAG and of VLC-PUFAs in extraplastidic lipids. These results are strongly recalling of features reported for the plastidial CrFAD7 which is the only ω3-Des in *Chlamydomonas*. Knocking-out or overexpressing *CrFAD7* impacted both plastidic and extraplastidic lipids suggesting that CrFAD7, located at the plastid envelope, may have access to extraplastidic substrates. This hypothesis applies for *O. tauri*. It is also possible that alternative translation occurs from the second methionine in the native host to produce an extraplastidic isoform (Kochetov, 2008). On the other hand, the overall weak phenotype of pω3-Des OE might be related to post-transcriptional control, at least in the native host, and/or to the importance of Δ6-Des activities for the fine-tuning of C18-PUFAs and thereof of downstream products. Post-transcriptional regulations of ω3-Des have been reported from cyanobacteria and plant and showed to even occur in heterologous systems (Sakamoto and Bryant, 1997; Matsuda et al., 2005; O'Quin et al., 2010).

PUFAs and Temperature: Facts and Physiological Relevance

All organisms combined, the inverse correlation of FA unsaturation with temperature appears to be a universal trend. According to the homeoviscous hypothesis, the increase of FA unsaturation and thereby the decrease of the FA melting point, is necessary to maintain the fluid state of biological membranes at low temperature (Ernst et al., 2016). However, it should be emphasized that the addition of just one double-bound to saturated acyl-chain has the most drastic impact on the FA melting temperature and that the involvement of PUFAs for adjusting biomembrane physical properties has not been demonstrated; on the contrary omega-3 PUFAs failed to exhibit any peculiar fluidifying potency compared to oleic acid (De Santis et al., 2018). Although photosynthesis defects have been reported for mutants with altered UFAs content in plants and microalgae, it seems much more difficult to establish a causal link between these defects and impaired membrane fluidity (Vijayan and Browse, 2002; Falcone et al., 2004; Kugler et al., 2019). In cyanobacteria, ω3-PUFAs are only produced at chilling temperature and a direct link between membrane fluidity and *DesB* transcription has been demonstrated (Tasaka et al., 1996; Los et al., 2013; Mironov et al., 2018). However, neither membrane physical properties nor growth nor photosynthesis were significantly impacted in mutants lacking trienoic FAs. In contrast, plant mutants lacking trienoic FAs were reported to display distinct patterns of symptoms including sever thylakoid loss for cold temperature but also lower growth at high temperature (Routaboul et al., 2000). As trienoic PUFAs are the precursors of plant oxylipins and Nitro-FAs, it might be that these patterns are the result of impaired temperature signaling in plants (Mata-Perez et al., 2018; He and Ding, 2020; Yu et al., 2020). Though, establishing a relationship between PUFA membrane precursors and signaling down-products is a challenging issue, it should be kept in mind that oxylipins are also occurring in microalgae (Lauritano et al., 2016; Lupette et al., 2018).

As regards microalgae, temperature has been shown to impact FA profile in a species-dependent manner and it appears most difficult to discern a general trend from literature (Renaud et al., 1995; Boelen et al., 2013; Aussant et al., 2018; Gill et al., 2018; Balakrishnan and Shanmugam, 2020). Though it cannot be viewed as a general rule, the increase of ω3-PUFAs has been reported in response to chilling in various species of green microalgae while the increase of 18:5n3 and/or 20:5n3

was reported in Chromista species (see below) (Leblond et al., 2010; Kotajima et al., 2014; Aussant et al., 2018). The higher proportion of ω3 was in some case concomitant of a decline of the corresponding ω6-precursor (Nguyen et al., 2013; Zorin et al., 2017). The physiological relevance of PUFA variations have been only sporadically tackled. Works studying microalgal mutants with altered PUFA content at different temperature are scarce and overall provide mild evidences that mutations affect growth and/or photosynthetic processes (Sukenik et al., 1998; Nguyen et al., 2013; Zorin et al., 2017). For instance, the growth of *CrFAD7* knock-out mutant was not impaired at low temperature; extreme high temperature (45°C) was necessary to highlight that the mutation was associated with a reduced impairment of PSII activity. In these studies, early variations have not been investigated.

In the present work, experimental conditions were optimized for the identification of early temperature-specific FA variations. *O. tauri* growing temperature is commonly fixed at 20°C. In our conditions, *O. tauri* readily acclimated to 14°C and grew equally well at 24°C, in coherence with the range of temperature at which *Ostreococcus* species were identified in the environment (Limardo et al., 2017). Therefore, we can assume that temperature shifts between 14 and 24°C and reciprocally are moderate as regards to the thermoacclimation capacity of *O. tauri*. Finally, L/D entrainment was used to restrain internal time resetting by temperature reducing the chance that the differences observed are indirectly resulting from circadian rhythms shifts. It should be emphasized that early changes are more likely to be related to direct response to temperature whereas late variations may rather be related to indirect general metabolism adjustment. Chilling and warming triggered a swift and reverse adjustment of the ω6/ω3 PUFA ratio in all glycerolipids; the earliest variations occurred in C18-PUFAs (known to predominate in plastidic lipids), including 18:5n3, which is exclusively located in galactolipids (Degraeve-Guilbault et al., 2017). The progressive decrease of 20:4n6 upon chilling was also a robust trend. As evoked, compared to monounsaturated FA, the fluidizing potency of PUFAs have not been demonstrated to be better (De Santis et al., 2018). Though, the proportion of 18:1 is very low in *O. tauri* and even if it is increased in 14°C acclimated cells, other FAs, sterols and/or pigments might participate for acclimatizing membrane fluidity PUFAs are also known precursors of oxylipins and of Nitro-FAs in various organism ranging from microalgae to animals and their production could, to some extent, be related to the variation of membrane PUFAs and be involved in the signaling of temperature changes (Lupette et al., 2018; Wasternack and Feussner, 2018).

In the present work, the FA-phenotype of *pω3-Des* OE was weak and it was therefore not surprising that no growth defect could be detected. We assume that either compensatory mechanisms are taking place in *pω3-Des* OE and/or that our conditions are not appropriate and/or stringent enough to unveil any defects. Nevertheless, the fact that *pω3-Des* OE displayed lipid features closely related to those of low temperature acclimated cells was obvious and coherent with the involvement of *pω3-Des* in temperature acclimation. The reduction of 14:0 at low temperature might possibly be part of the homeoviscous process required at low temperature but in this case, would not be expected in the *pω3-Des* OE.

18:5n3: An Enigmatic Marker of Temperature

Most interestingly, the 18:5n3 variations observed in *O. tauri* were reported in evolutionary distant microalgae (Renaud et al., 1995; Kotajima et al., 2014). As evoked, prasinophyta (including Mamiellophyceae) are the only primary endosymbiotic organisms that encompass 18:5n3, which is commonly found in microalgae emerging from secondary endosymbiosis. In the haptophytes, *E. huxleyi* and *Isochrysis* species 18:5n3 was reported to increase at low temperature while it was found at higher percentage (together with 18:4n-3) in cold-adapted dinoflagellates (Leblond et al., 2006). We show here that the content of 18:5n3 is tightly regulated by temperature in a species from the green lineage and varies as early as 6 h after temperature-shift. This result points out the involvement of this peculiar FA in temperature responses may be an ancient feature. Since 18:5n3 is predominantly located in glycerolipids across all species, this regulation might be related to the fine-tuning of photosynthesis. The increase of 20:5n3 upon chilling has been reported for several species for which 20:5n3 is a major component of galactolipids and further evidences suggested that it could be involved in photosynthesis, in particular in non-photochemical quenching in *Nannochloropsis gaditana CCMP526* (Renaud et al., 1995; Camacho-Rodriguez et al., 2013; Dolch et al., 2017; Gill et al., 2018). On the other hand, 20:5 derived isoprostanes were characterized from *Phaeodactylum tricornutum* (Lupette et al., 2018). Interestingly their content was inversely correlated to that of 20:5 FA. It is therefore possible that non-enzymatic oxylipin derived from pentaenoic FAs might be involved in a retrograde signaling for temperature stress.

Biosynthesis of 18:5n3 is an enigmatic issue; several hypotheses have been proposed including a yet not identified Δ3-Des or the shortening of 20:5n3 (Joseph, 1975). Though no Δ3-Des have been identified to date, a positional isomer of stearidonic acid encompassing a double bond at position three ($18{:}4^{\Delta 3,6,9,12}$) in a thermophilic cyanobacterium has been described; as this species, like the bulk of cynaobacteria, do not produce VLC-PUFAs, this result is in favor of Δ3-Des activity in cyanobacteria (Rezanka et al., 2012). In *O. tauri*, the recent discovery of plastidial Δ6-desturases showed that the plastidic C18-PUFA-pool is regulated independently of ER-Des and therefore supports the existence of a yet not identified plastidial Δ3-Des in this species. This activity could be carried by either one of the plastidial Δ6-Des, as previously discussed elsewhere or by the Δ5-Des whose expression is tightly regulated by the temperature (Degraeve-Guilbault et al., 2020). It should be recalled here that *Bathycoccus prasinos* lacks both the *pΔ6-Des2* and 18:5 (Degraeve-Guilbault et al., 2017). On the other hand, several Δ5-Des from animals were reported to display extended Δ6 and Δ4 regiospecificities and plant Des regiospecificity was shown to switch with sub-cellular localization (Heilmann et al., 2004; Li et al., 2010). Noteworthy, a cTP is predicted for the

Δ5-Des and the recent genomic sequence assembly from the *O. tauri* strain RCC1115 further pinpointed an additional ORF opening the possibility that alternative translation might be used to produce two differentially located isoforms of Δ5-Des (Hoffmann et al., 2008).

The 20:5 shortening hypothesis cannot be excluded and is supported for *O. tauri* by: (1) the existence of *sn-1/sn-2* 20:5/16:4 DGTA, (2) the occurrence of high level of 20:5 in the acyl-CoA pool and the detection of 18:5n3, and (3) the occurrence of 18:5 in DAGs (Degraeve-Guilbault et al., 2017). From these observations, it can be speculated that either 18:5-CoA is transferred to the plastid after 20:5-CoA shortening in the cytosol and specifically esterified to lyso-16:4 galactolipids, or that 18:5-DAG arising from remodeled DGTA 20:5/16:4 DGTA serve as precursors for 18:5-galactolipid synthesis. Until a Δ3-activity can be demonstrated the two hypotheses remain equally speculative.

Temperature Control of Desaturase Expression

Ostreococcus tauri biological processes have been previously shown to highly rely on orchestrated transcriptional regulation (Monnier et al., 2010). Clustering of genes according to their temporal waveforms suggested that master transcriptional regulations are at work to coordinate lipid metabolism with chloroplast and carotenoids biogenesis at late night and with photosynthesis, oxidative stress, and DNA repair at mid-day. Transcriptional rewiring in response to temperature, especially chilling, has been extensively studied in freshwater cyanobacteria and plants and are beginning to be studied in marine cyanobacteria (Sinetova and Los, 2016; Shi et al., 2018; Breton et al., 2020; Guyet et al., 2020). However, there is a large gap of knowledge with regards to microalgae. Desaturase transcriptional induction in response to temperature and/or membrane fluidity has been demonstrated in freshwater cyanobacteria (Los et al., 1997). In *Arabidopsis*, the up-regulation of plastidial ω3-Des FAD8 upon cold/chilling was shown to involve both transcriptional and post-transcriptional regulations (Gibson et al., 1994; Matsuda et al., 2005). Higher transcript level of *ω3-Des* occurred in *Chlorella vulgaris* and *C. reinhardtii* at chilling temperature and early transcriptional activation of *Δ6-Des* has been reported for *Isochrysis sp*. (Suga et al., 2002; Nguyen et al., 2013; Wang et al., 2016). Part of our aim was to identify whether desaturases expression was regulated by temperature and how far these regulations were coherent with FA variations. Chilling was shown to swiftly and sustainably up-regulated most desaturase gene under both L/D and continuous light conditions while warming had an overall reverse impact. Under L/D, the plastidial desaturase genes *pΔ6-Des2* and *pω3-Des* as well as *Δ5-Des* were the most up-regulated genes. Conversely, warming repressed *pω3-Des, pΔ6-Des1*, *and Δ5-Des* and to a greater extent *Acyl-CoA-Δ6-Des.* These regulations are overall coherent with the activation of the ω3 pathway upon chilling and its repression upon warming. Since we previously showed that overexpression *Acyl-CoAΔ6-Des* in *O. tauri* mostly impacted TAG-FA profile, the temperature dependent regulation of *Acyl-CoA-Δ6-Des* expression might possibly be related to the accumulation of highly unsaturated TAG at low temperature. The differential transcriptional regulation of the plastidial Δ6-desaturases *pΔ6-Des1* and *pΔ6-Des2*, demonstrated to have different specificity for ω6 and ω3 might be required for proper adjustment of the ω3/ω6 ratio in response to temperature (Degraeve-Guilbault et al., 2020).

CONCLUSION

The peculiar pentaenoic FA 18:5n3 and 20:5n3, that are dominating plastid FAs in microalgae, may be early and conserved marker of temperature acclimation. The involvement of ω3-Des in temperature acclimation, though clearly demonstrated in cyanobacteria and plants have been poorly illustrated in microalgae. Our result support that in *O. tauri*, the plastidial ω3-Des is involved in temperature acclimation and that Δ6-Des are further involved in fine-tuning C18-PUFAs. Only a few studies provided clues about the implication of these changes in cell physiology, mostly indicating a relationship between photosynthesis and PUFA. The selective pressure that ensured the maintenance of peculiar PUFAs in microalgae, most likely relies on multiple environmental cues making difficult to unveil defects in PUFA mutants using conditions limited to one or two parameters. An alternative, is to directly search for the molecular function of PUFAs in structuring and/or signaling.

DATA AVAILABILITY STATEMENT

The original contributions presented in the study are included in the article/**Supplementary Material**, further inquiries can be directed to the corresponding author/s.

AUTHOR CONTRIBUTIONS

CD-G performed most of the experimental work related to chilling and the associated (cloning, transgenic screening, HP-TCL, GC-FID, and RT-qPCR). NP created the *Synechocystis* DesB OE and Otpω3-Des OE (transformation and screening). MG performed the experimental work mostly related to warming including FAMES and transcriptional analyses as well as analyses of lipids from *Synechocystis* (HP-TLC, GC-FID, and RT-qPCR). CL performed the lipid analysis of the *O. tauri* Otpω3-Des overexpressor. FD performed the work and analyses on *N. benthamiana* (cloning, agro-transformation, and FAMES analysis). JJ performed the work on DES localization and RT-qPCR for chilling experiments. TK initially assessed the ω3-Des activity of *O. tauri* ortholog. IS supervised the work on *Synechocystis*. FC designed, supervised, and performed the research, analyzed the data (*O. tauri, N. benthamiana*, and *Synechocystis*), and wrote the manuscript. All authors contributed to the article and approved the submitted version.

FUNDING

Université de Bordeaux- grant SB2: 2017–2019, project acronym PICO-FADO, Université de Bordeaux grant Emergence 2019, project acronym TOTOX.

ACKNOWLEDGMENTS

Routine lipid analyses were performed at the Metabolome Facility of Bordeaux-MetaboHUB (ANR-11-INBS-0010). Imaging was performed at the Bordeaux Imaging Center, member of the national infrastructure France BioImaging. We would like to thank Josselin Lupette for his kind advices for performing statistical analyses with GraphPad PRISM.

SUPPLEMENTARY MATERIAL

The Supplementary Material for this article can be found online at: https://www.frontiersin.org/articles/10.3389/fpls.2021.639330/full#supplementary-material

REFERENCES

Aussant, J., Guiheneuf, F., and Stengel, D. B. (2018). Impact of temperature on fatty acid composition and nutritional value in eight species of microalgae. *Appl. Microbiol. Biotechnol.* 102, 5279–5297. doi: 10.1007/s00253-018-9001-x

Balakrishnan, J., and Shanmugam, K. (2020). Lowering the culture medium temperature improves the omega-3 fatty acid production in marine microalga Isochrysis sp. CASA CC 101. *Prep. Biochem. Biotechnol.* 2020, 1–8. doi: 10.1080/10826068.2020.1833345

Bieniawska, Z., Espinoza, C., Schlereth, A., Sulpice, R., Hincha, D. K., and Hannah, M. A. (2008). Disruption of the Arabidopsis circadian clock is responsible for extensive variation in the cold-responsive transcriptome. *Plant Physiol.* 147, 263–279. doi: 10.1104/pp.108.118059

Boelen, P., Van Dijk, R., Sinninghe Damsté, J. S., Rijpstra, W. I., and Buma, A. G. (2013). On the potential application of polar and temperate marine microalgae for EPA and DHA production. *AMB Express* 3:26. doi: 10.1186/2191-0855-3-26

Breton, S., Jouhet, J., Guyet, U., Gros, V., Pittera, J., Demory, D., et al. (2020). Unveiling membrane thermoregulation strategies in marine picocyanobacteria. *N. Phytol.* 225, 2396–2410. doi: 10.1111/nph.16239

Camacho-Rodriguez, J., Gonzalez-Cespedes, A. M., Cerón-García, M. C., Fernandez-Sevilla, J. M., Acien, G., and Molina-Grima, E. (2013). A quantitative study of eicosapentaenoic acid (EPA) production by Nannochloropsis gaditana for aquaculture as a function of dilution rate, temperature and average irradiance. *Appl. Microbiol. Biotechnol.* 98, 2429–2440. doi: 10.1007/s00253-013-5413-9

Chrétiennot-Dinet, M.-J., Courties, C., Vaquer, A., Neveux, J., Claustre, H., Lautier, J., et al. (1995). A new marine picoeucaryote: Ostreococcus tauri gen. et sp. nov. (Chlorophyta, Prasinophyceae). *Phycologia* 34, 285–292. doi: 10.2216/i0031-8884-34-4-285.1

De Santis, A., Varela, Y., Sot, J., D'errico, G., Goñi, F. M., and Alonso, A. (2018). Omega-3 polyunsaturated fatty acids do not fluidify bilayers in the liquid-crystalline state. *Sci. Rep.* 8:16240. doi: 10.1038/s41598-018-34264-3

Degraeve-Guilbault, C., Bréhélin, C., Haslam, R., Sayanova, O., Marie-Luce, G., Jouhet, J., et al. (2017). Glycerolipid Characterization and Nutrient Deprivation-Associated Changes in the Green Picoalga Ostreococcus tauri. *Plant Physiol.* 173, 2060–2080. doi: 10.1104/pp.16.01467

Degraeve-Guilbault, C., Gomez, R. E., Lemoigne, C., Pankansem, N., Morin, S., Tuphile, K., et al. (2020). Plastidic Δ6 Fatty-Acid Desaturases with Distinctive Substrate Specificity Regulate the Pool of C18-PUFAs in the Ancestral Picoalga Ostreococcus tauri. *Plant Physiol.* 184, 82–96. doi: 10.1104/pp.20.00281

Djouani-Tahri el, B., Sanchez, F., Lozano, J. C., and Bouget, F. Y. (2011). A phosphate-regulated promoter for fine-tuned and reversible overexpression in Ostreococcus: application to circadian clock functional analysis. *PLoS One* 6:e28471. doi: 10.1371/journal.pone.0028471

Dolch, L.-J., Rak, C., Perin, G., Tourcier, G., Broughton, R., Leterrier, M., et al. (2017). A Palmitic Acid Elongase Affects Eicosapentaenoic Acid and Plastidial Monogalactosyldiacylglycerol Levels in Nannochloropsis. *Plant Physiol.* 173, 742–759. doi: 10.1104/pp.16.01420

Ernst, R., Ejsing, C. S., and Antonny, B. (2016). Homeoviscous Adaptation and the Regulation of Membrane Lipids. *J. Mol. Biol.* 428, 4776–4791. doi: 10.1016/j.jmb.2016.08.013

Falcone, D. L., Ogas, J. P., and Somerville, C. R. (2004). Regulation of membrane fatty acid composition by temperature in mutants of Arabidopsis with alterations in membrane lipid composition. *BMC Plant Biol.* 4:17. doi: 10.1186/1471-2229-4-17

Galloway, A. W., and Winder, M. (2015). Partitioning the Relative Importance of Phylogeny and Environmental Conditions on Phytoplankton Fatty Acids. *PLoS One* 10:e0130053. doi: 10.1371/journal.pone.0130053

Ghioni, C., Porter, A. E., Sadler, I. H., Tocher, D. R., and Sargent, J. R. (2001). Cultured fish cells metabolize octadecapentaenoic acid (all-cis delta3,6,9,12,15-18:5) to octadecatetraenoic acid (all-cis delta6,9,12,15-18:4) via its 2-trans intermediate (trans delta2, all-cis delta6,9,12,15-18:5). *Lipids* 36, 145–152. doi: 10.1007/s11745-001-0701-0

Gibson, S., Arondel, V., Iba, K., and Somerville, C. (1994). Cloning of a temperature-regulated gene encoding a chloroplast omega-3 desaturase from Arabidopsis thaliana. *Plant Physiol.* 106, 1615–1621. doi: 10.1104/pp.106.4.1615

Gill, S. S., Willette, S., Dungan, B., Jarvis, J. M., Schaub, T., Vanleeuwen, D. M., et al. (2018). Suboptimal Temperature Acclimation Affects Kennedy Pathway Gene Expression, Lipidome and Metabolite Profile of Nannochloropsis salina during PUFA Enriched TAG Synthesis. *Mar. Drugs* 16:425. doi: 10.3390/md16110425

Guyet, U., Nguyen, N. A., Doré, H., Haguait, J., Pittera, J., Conan, M., et al. (2020). Synergic Effects of Temperature and Irradiance on the Physiology of the Marine Synechococcus Strain WH7803. *Front. Microbiol.* 11:1707. doi: 10.3389/fmicb.2020.01707

He, M., and Ding, N. Z. (2020). Plant Unsaturated Fatty Acids: Multiple Roles in Stress Response. *Front. Plant Sci.* 11:562785. doi: 10.3389/fpls.2020.562785

Heilmann, I., Pidkowich, M. S., Girke, T., and Shanklin, J. (2004). Switching desaturase enzyme specificity by alternate subcellular targeting. *Proc. Natl. Acad. Sci. U S A.* 101, 10266–10271. doi: 10.1073/pnas.0402200101

Hoffmann, M., Wagner, M., Abbadi, A., Fulda, M., and Feussner, I. (2008). Metabolic engineering of omega3-very long chain polyunsaturated fatty acid production by an exclusively acyl-CoA-dependent pathway. *J. Biol. Chem.* 283, 22352–22362. doi: 10.1074/jbc.M802377200

Jonasdottir, S. H. (2019). Fatty Acid Profiles and Production in Marine Phytoplankton. *Mar. Drugs* 17:151. doi: 10.3390/md17030151

Joseph, A. D. (1975). Identification of 3, 6, 9, 12, 15-octadecapentaenoic acid in laboratory-cultured photosynthetic dinoflagellates. *Lipids* 10, 395–403.doi: 10.1007/BF02532443

Kabeya, N., Fonseca, M. M., Ferrier, D. E. K., Navarro, J. C., Bay, L. K., Francis, D. S., et al. (2018). Genes for de novo biosynthesis of omega-3 polyunsaturated fatty acids are widespread in animals. *Sci. Adv.* 4:eaar6849. doi: 10.1126/sciadv.aar6849

Kainz, M., Arts, M. T., and Mazumder, A. (2004). Essential fatty acids in the planktonic food web and their ecological role for higher trophic levels. *Limnol. Oceanogr.* 49, 1784–1793. doi: 10.4319/lo.2004.49.5.1784

Khozin-Goldberg, I., Leu, S., and Boussiba, S. (2016). Microalgae as a Source for VLC-PUFA Production. *Subcell Biochem.* 86, 471–510. doi: 10.1007/978-3-319-25979-6_19

Kochetov, A. V. (2008). Alternative translation start sites and hidden coding potential of eukaryotic mRNAs. *Bioessays* 30, 683–691. doi: 10.1002/bies.20771

Kotajima, T., Shiraiwa, Y., and Suzuki, I. (2014). Functional screening of a novel Delta15 fatty acid desaturase from the coccolithophorid Emiliania huxleyi. *Biochim. Biophys. Acta* 1842, 1451–1458. doi: 10.1016/j.bbalip.2014.07.010

Kugler, A., Zorin, B., Didi-Cohen, S., Sibiryak, M., Gorelova, O., Ismagulova, T., et al. (2019). Long-Chain Polyunsaturated Fatty Acids in the Green Microalga

Lobosphaera incisa Contribute to Tolerance to Abiotic Stresses. *Plant Cell Physiol.* 60, 1205–1223. doi: 10.1093/pcp/pcz013

Kuiper, P. J. C. (1985). Environmental changes and lipid metabolism of higher plants. *Physiol. Plant.* 64, 118–122. doi: 10.1111/j.1399-3054.1985.tb01221.x

Lang, I., Hodac, L., Friedl, T., and Feussner, I. (2011). Fatty acid profiles and their distribution patterns in microalgae: a comprehensive analysis of more than 2000 strains from the SAG culture collection. *BMC Plant Biol.* 11:124. doi: 10.1186/1471-2229-11-124

Lauritano, C., Romano, G., Roncalli, V., Amoresano, A., Fontanarosa, C., Bastianini, M., et al. (2016). New oxylipins produced at the end of a diatom bloom and their effects on copepod reproductive success and gene expression levels. *Harmful Algae* 55, 221–229. doi: 10.1016/j.hal.2016.03.015

Leblond, J. D., Anderson, B., Kofink, D., Logares, R., Rengefors, K., and Kremp, A. (2006). Fatty acid and sterol composition of two evolutionarily closely related dinoflagellate morphospecies from cold Scandinavian brackish and freshwaters. *Eur. J. Phycol.* 41, 303–311. doi: 10.1080/09670260600804843

Leblond, J. D., Dahmen, J. L., and Evens, T. J. (2010). Mono- and digalactosyldiacylglycerol composition of dinoflagellates. IV. Temperature-induced modulation of fatty acid regiochemistry as observed by electrospray ionization/mass spectrometry. *Eur. J. Phycol.* 45, 13–18. doi: 10.1080/09670260903171650

Li, H. M., and Yu, C. W. (2018). Chloroplast Galactolipids: The Link Between Photosynthesis, Chloroplast Shape, Jasmonates, Phosphate Starvation and Freezing Tolerance. *Plant Cell Physiol.* 59, 1128–1134. doi: 10.1093/pcp/pcy088

Li, Y., Monroig, O., Zhang, L., Wang, S., Zheng, X., Dick, J. R., et al. (2010). Vertebrate fatty acyl desaturase with Delta4 activity. *Proc. Natl. Acad. Sci. U S A.* 107, 16840–16845. doi: 10.1073/pnas.1008429107

Limardo, A. J., Sudek, S., Choi, C. J., Poirier, C., Rii, Y. M., Blum, M., et al. (2017). Quantitative biogeography of picoprasinophytes establishes ecotype distributions and significant contributions to marine phytoplankton. *Environ. Microbiol.* 19, 3219–3234. doi: 10.1111/1462-2920.13812

Los, D. A., Mironov, K. S., and Allakhverdiev, S. I. (2013). Regulatory role of membrane fluidity in gene expression and physiological functions. *Photosynth. Res.* 116, 489–509. doi: 10.1007/s11120-013-9823-4

Los, D. A., Ray, M. K., and Murata, N. (1997). Differences in the control of the temperature-dependent expression of four genes for desaturases in Synechocystis sp. PCC 6803. *Mol. Microbiol.* 25, 1167–1175.doi: 10.1046/j.1365-2958.1997.5641912.x

Lupette, J., Jaussaud, A., Vigor, C., Oger, C., Galano, J. M., Reversat, G., et al. (2018). Non-Enzymatic Synthesis of Bioactive Isoprostanoids in the Diatom Phaeodactylum following Oxidative Stress. *Plant Physiol.* 178, 1344–1357. doi: 10.1104/pp.18.00925

Lynch, D. V., and Thompson, G. A. (1982). Low Temperature-Induced Alterations in the Chloroplast and Microsomal Membranes of Dunaliella salina. *Plant Physiol.* 69, 1369–1375. doi: 10.1104/pp.69.6.1369

Mansilla, M. C., Banchio, C. E., and De Mendoza, D. (2008). Signalling pathways controlling fatty acid desaturation. *Subcell Biochem.* 49, 71–99. doi: 10.1007/978-1-4020-8831-5_3

Massana, R. (2011). Eukaryotic picoplankton in surface oceans. *Annu. Rev. Microbiol.* 65, 91–110. doi: 10.1146/annurev-micro-090110-102903

Mata-Perez, C., Padilla, M. N., Sanchez-Calvo, B., Begara-Morales, J. C., Valderrama, R., Chaki, M., et al. (2018). Biological properties of nitro-fatty acids in plants. *Nitric Oxide* Preprint. doi: 10.1016/j.niox.2018.03.011

Matsuda, O., Sakamoto, H., Hashimoto, T., and Iba, K. (2005). A temperature-sensitive mechanism that regulates post-translational stability of a plastidial omega-3 fatty acid desaturase (FAD8) in Arabidopsis leaf tissues. *J. Biol. Chem.* 280, 3597–3604. doi: 10.1074/jbc.M407226200

McClung, C. R., and Davis, S. J. (2010). Ambient thermometers in plants: from physiological outputs towards mechanisms of thermal sensing. *Curr. Biol.* 20, R1086–R1092. doi: 10.1016/j.cub.2010.10.035

Meesapyodsuk, D., and Qiu, X. (2016). Biosynthetic mechanism of very long chain polyunsaturated fatty acids in Thraustochytrium sp. 26185. *J. Lipid Res.* 57, 1854–1864. doi: 10.1194/jlr.M070136

Mironov, K. S., Shumskaya, M., Sidorov, R. A., Trofimova, M. S., and Los, D. A. (2018). Membrane physical state and stress regulation in Synechocystis: fluidizing alcohols repress fatty acid desaturation. *Plant J.* 96, 1007–1017. doi: 10.1111/tpj.14086

Monnier, A., Liverani, S., Bouvet, R., Jesson, B., Smith, J. Q., Mosser, J., et al. (2010). Orchestrated transcription of biological processes in the marine picoeukaryote Ostreococcus exposed to light/dark cycles. *BMC Genomics* 11:192. doi: 10.1186/1471-2164-11-192

Moulager, M., Corellou, F., Vergé, V., Escande, M. L., and Bouget, F. Y. (2010). Integration of Light Signals by the Retinoblastoma Pathway in the Control of S phase Entry in the Picophytoplanktonic Cell Ostreococcus. *PLoS Genet.* 6:e1000957. doi: 10.1371/journal.pgen.1000957

Moulager, M., Monnier, A., Jesson, B., Bouvet, R., Mosser, J., Schwartz, C., et al. (2007). Light-dependent regulation of cell division in Ostreococcus: evidence for a major transcriptional input. *Plant Physiol.* 144, 1360–1369. doi: 10.1104/pp.107.096149

Nguyen, H. M., Cuine, S., Beyly-Adriano, A., Legeret, B., Billon, E., Auroy, P., et al. (2013). The green microalga Chlamydomonas reinhardtii has a single omega-3 fatty acid desaturase that localizes to the chloroplast and impacts both plastidic and extraplastidic membrane lipids. *Plant Physiol.* 163, 914–928. doi: 10.1104/pp.113.223941

Nishida, I., and Murata, N. (1996). CHILLING SENSITIVITY IN PLANTS AND CYANOBACTERIA: The Crucial Contribution of Membrane Lipids. *Annu. Rev. Plant Physiol. Plant Mol. Biol.* 47, 541–568. doi: 10.1146/annurev.arplant.47.1.541

O'Quin, J. B., Bourassa, L., Zhang, D., Shockey, J. M., Gidda, S. K., Fosnot, S., et al. (2010). Temperature-sensitive post-translational regulation of plant omega-3 fatty-acid desaturases is mediated by the endoplasmic reticulum-associated degradation pathway. *J. Biol. Chem.* 285, 21781–21796. doi: 10.1074/jbc.M110.135236

Renaud, S. M., Zhou, H. C., Parry, D. L., Thinh, L.-V., and Woo, K. C. (1995). Effect of temperature on the growth, total lipid content and fatty acid composition of recently isolated tropical microalgae Isochrysis sp., Nitzschia closterium, Nitzschia paleacea, and commercial species Isochrysis sp. (clone T.ISO). *J. Appl. Phycol.* 7, 595–602. doi: 10.1007/BF00003948

Rezanka, T., Lukavsky, J., Siristova, L., and Sigler, K. (2012). Regioisomer separation and identification of triacylglycerols containing vaccenic and oleic acids, and alpha- and gamma-linolenic acids, in thermophilic cyanobacteria Mastigocladus laminosus and Tolypothrix sp. *Phytochemistry* 78, 147–155. doi: 10.1016/j.phytochem.2012.02.028

Rii, Y. M., Duhamel, S., Bidigare, R. R., Karl, D. M., Repeta, D. J., and Church, M. J. (2016). Diversity and productivity of photosynthetic picoeukaryotes in biogeochemically distinct regions of the South East Pacific Ocean. *Limnol. Oceanogr.* 61, 806–824. doi: 10.1002/lno.10255

Routaboul, J. M., Fischer, S. F., and Browse, J. (2000). Trienoic fatty acids are required to maintain chloroplast function at low temperatures. *Plant Physiol.* 124, 1697–1705. doi: 10.1104/pp.124.4.1697

Sakamoto, T., and Bryant, D. A. (1997). Temperature-regulated mRNA accumulation and stabilization for fatty acid desaturase genes in the cyanobacterium Synechococcus sp. strain PCC 7002. *Mol. Microbiol.* 23, 1281–1292. doi: 10.1046/j.1365-2958.1997.3071676.x

Sakamoto, T., Los, D. A., Higashi, S., Wada, H., Nishida, I., Ohmori, M., et al. (1994). Cloning of omega 3 desaturase from cyanobacteria and its use in altering the degree of membrane-lipid unsaturation. *Plant Mol. Biol.* 26, 249–263. doi: 10.1007/BF00039536

Shah, K. H., Almaghrabi, B., and Bohlmann, H. (2013). Comparison of Expression Vectors for Transient Expression of Recombinant Proteins in Plants. *Plant Mol. Biol. Rep.* 31, 1529–1538. doi: 10.1007/s11105-013-0614-z

Shanklin, J., Guy, J. E., Mishra, G., and Lindqvist, Y. (2009). Desaturases: emerging models for understanding functional diversification of diiron-containing enzymes. *J. Biol. Chem.* 284, 18559–18563. doi: 10.1074/jbc.R900009200

Shi, Y., Ding, Y., and Yang, S. (2018). Molecular Regulation of CBF Signaling in Cold Acclimation. *Trends Plant Sci.* 23, 623–637. doi: 10.1016/j.tplants.2018.04.002

Sinetova, M. A., and Los, D. A. (2016). New insights in cyanobacterial cold stress responses: Genes, sensors, and molecular triggers. *Biochim. Biophys. Acta* 1860, 2391–2403. doi: 10.1016/j.bbagen.2016.07.006

Suga, K., Honjoh, K.-I., Furuya, N., Shimizu, H., Nishi, K., Shinohara, F., et al. (2002). Two Low-temperature-inducible Chlorella Genes for Δ12 and ω-3 Fatty Acid Desaturase (FAD): Isolation of Δ12 and ω-3 fad cDNA Clones. *Biosci. Biotechnol. Biochem.* 66, 1314–1327. doi: 10.1271/bbb.66.1314

Sukenik, A., Zbigniew, K., and Prasil, O. (1998). Photosynthetic charcaterization of a mutant of Nannochloropsis deficient in the synthesis of eicosapentenoic acid. *Israel J. Plant Sci.* 46, 101–108. doi: 10.1080/07929978.1998.10676716

Sun, X. M., Ren, L. J., Zhao, Q. Y., Ji, X. J., and Huang, H. (2019). Enhancement of lipid accumulation in microalgae by metabolic engineering. *Biochim. Biophys. Acta Mol. Cell Biol. Lipids* 1864, 552–566. doi: 10.1016/j.bbalip.2018.10.004

Tardif, M., Atteia, A., Specht, M., Cogne, G., Rolland, N., Brugiere, S., et al. (2012). PredAlgo: a new subcellular localization prediction tool dedicated to green algae. *Mol. Biol. Evol.* 29, 3625–3639. doi: 10.1093/molbev/mss178

Tasaka, Y., Gombos, Z., Nishiyama, Y., Mohanty, P., Ohba, T., Ohki, K., et al. (1996). Targeted mutagenesis of acyl-lipid desaturases in Synechocystis: evidence for the important roles of polyunsaturated membrane lipids in growth, respiration and photosynthesis. *EMBO J.* 15, 6416–6425. doi: 10.1002/j.1460-2075.1996.tb01033.x

Van Mooy, B. A., Fredricks, H. F., Pedler, B. E., Dyhrman, S. T., Karl, D. M., Koblizek, M., et al. (2009). Phytoplankton in the ocean use non-phosphorus lipids in response to phosphorus scarcity. *Nature* 458, 69–72. doi: 10.1038/nature07659

Vijayan, P., and Browse, J. (2002). Photoinhibition in mutants of Arabidopsis deficient in thylakoid unsaturation. *Plant Physiol.* 129, 876–885. doi: 10.1104/pp.004341

Wang, M., Chen, H., Gu, Z., Zhang, H., Chen, W., and Chen, Y. Q. (2013). omega3 fatty acid desaturases from microorganisms: structure, function, evolution, and biotechnological use. *Appl. Microbiol. Biotechnol.* 97, 10255–10262. doi: 10.1007/s00253-013-5336-5

Wang, S., Zheng, L., Cui, Z., Chen, J., Yang, B., Han, X., et al. (2016). Cloning and molecular characterization of a delta-6 fatty acid desaturase gene from Isochrysis sp. CCMM5001. *J. Appl. Phycol.* 28, 921–929. doi: 10.1007/s10811-015-0623-4

Wasternack, C., and Feussner, I. (2018). The Oxylipin Pathways: Biochemistry and Function. *Annu. Rev. Plant Biol.* 69, 363–386. doi: 10.1146/annurev-arplant-042817-040440

Williams, J. G. K. (1988). "[85] Construction of specific mutations in photosystem II photosynthetic reaction center by genetic engineering methods in Synechocystis 6803," in *Methods in Enzymology*, eds J. Abelson, M. Simon, G. Verdine, and A. Pyle (Cambridge: Academic Press), 766–778. doi: 10.1016/0076-6879(88)67088-1

Yu, C.-W., Lin, Y.-T., and Li, H.-M. (2020). Increased ratio of galactolipid MGDG : DGDG induces jasmonic acid overproduction and changes chloroplast shape. *N. Phytol.* 228, 1327–1335. doi: 10.1111/nph.16766

Zorin, B., Pal-Nath, D., Lukyanov, A., Smolskaya, S., Kolusheva, S., Didi-Cohen, S., et al. (2017). Arachidonic acid is important for efficient use of light by the microalga Lobosphaera incisa under chilling stress. *Biochim. Biophys. Acta* 1862, 853–868. doi: 10.1016/j.bbalip.2017.04.008

Conflict of Interest: The authors declare that the research was conducted in the absence of any commercial or financial relationships that could be construed as a potential conflict of interest.

Copyright © 2021 Degraeve-Guilbault, Pankasem, Gueirrero, Lemoigne, Domergue, Kotajima, Suzuki, Joubès and Corellou. This is an open-access article distributed under the terms of the Creative Commons Attribution License (CC BY). The use, distribution or reproduction in other forums is permitted, provided the original author(s) and the copyright owner(s) are credited and that the original publication in this journal is cited, in accordance with accepted academic practice. No use, distribution or reproduction is permitted which does not comply with these terms.

frontiers in Plant Science

MINI REVIEW
published: 22 March 2021
doi: 10.3389/fpls.2021.643843

The Role of Sugar Signaling in Regulating Plant Fatty Acid Synthesis

*Zhiyang Zhai†, Jantana Keereetaweep†, Hui Liu†, Changcheng Xu and John Shanklin**

Biology Department, Brookhaven National Laboratory, Upton, NY, United States

Photosynthates such as glucose, sucrose, and some of their derivatives play dual roles as metabolic intermediates and signaling molecules that influence plant cell metabolism. Such sugars provide substrates for *de novo* fatty acid (FA) biosynthesis. However, compared with the well-defined examples of sugar signaling in starch and anthocyanin synthesis, until recently relatively little was known about the role of signaling in regulating FA and lipid biosynthesis. Recent research progress shows that trehalose 6-phosphate and 2-oxoglutarate (2-OG) play direct signaling roles in the regulation of FA biosynthesis by modulating transcription factor stability and enzymatic activities involved in FA biosynthesis. Specifically, mechanistic links between sucrose non-fermenting−1–related protein kinase 1 (SnRK1)–mediated trehalose 6-phosphate (T6P) sensing and its regulation by phosphorylation of WRI1 stability, diacylglycerol acyltransferase 1 (DGAT1) enzyme activity, and of 2-OG–mediated relief of inhibition of acetyl-CoA carboxylase (ACCase) activity by protein PII are exemplified in detail in this review.

Keywords: sugar signaling, fatty acid synthesis, metabolic regulation, SnRK1 kinase, WRINKLED1

OPEN ACCESS

Edited by:
Juliette Jouhet, UMR 5168 Laboratoire de Physiologie Cellulaire Vegetale (LPCV), France

Reviewed by:
Tore Brembu, Norwegian University of Science and Technology, Norway
Christoph Benning, Michigan State University, United States

***Correspondence:**
John Shanklin
shanklin@bnl.gov

†These authors have contributed equally to this work

Specialty section:
This article was submitted to Marine and Freshwater Plants, a section of the journal Frontiers in Plant Science

Received: *18 December 2020*
Accepted: *17 February 2021*
Published: *22 March 2021*

Citation:
Zhai Z, Keereetaweep J, Liu H, Xu C and Shanklin J (2021) The Role of Sugar Signaling in Regulating Plant Fatty Acid Synthesis. Front. Plant Sci. 12:643843. doi: 10.3389/fpls.2021.643843

INTRODUCTION

Sugars occupy a central role in plant metabolism, acting as both metabolic substrates and signaling molecules. Well-studied cases of sugar signaling in metabolism include sucrose (Suc) promotion of fructan synthesis in grasses by the induction of fructan-synthesizing enzymes (Nagaraj et al., 2001; Noël et al., 2001). Suc also appears to act as a signaling molecule that activates starch synthesis by upregulating the expression of multiple genes involved in starch synthesis, such as the large subunit of ADP-Glc pyrophosphorylase (AGPase), granule bound starch synthase 1 (GBSS1), and β-amylase (Nakamura et al., 1991; Harn et al., 2000; Wang et al., 2001; Nagata et al., 2012) and activating the AGPase enzyme by posttranslational redox modification (Tiessen et al., 2002). Another well-known case of Suc regulation is the induction of the biosynthesis of anthocyanins. Solfanelli et al. (2006) demonstrated in experiments with *Arabidopsis* that most of the genes coding for enzymes related to anthocyanins and flavonoid syntheses are induced by Suc feeding. Emerging evidence also supports a role for trehalose 6-phosphate (T6P) as both a signal (Lunn et al., 2006) and regulator of sucrose availability (Yadav et al., 2014; Figueroa and Lunn, 2016), providing a crucial link between energy (carbon) status and the processes of growth and development (Schluepmann et al., 2003). *In vivo* T6P levels have been reported to vary over a substantial range of between approximately 7 μM in *Arabidopsis* rosettes (Martins et al., 2013) to approximately 47 μM in maize floret tissue (Nuccio et al., 2015). T6P synthase catalyzes the synthesis of T6P from UDP-glucose and glucose 6-phosphate (G6P), two activated forms of glucose (Cabib and Leloir, 1958). At the molecular level, T6P affects starch synthesis *via* posttranslational redox activation of ADP pyrophosphorylase (Kolbe et al., 2005). It was also shown that sucrose non-fermenting−1–related

protein kinase 1 (SnRK1) activity in crude extracts from developing *Arabidopsis thaliana* tissues is inhibited by T6P, and this inhibition appears to depend on unknown protein factor(s) that are present only in young tissues (Zhang et al., 2009; Martínez-Barajas et al., 2011). Subsequent work showed that at much higher concentrations, G6P and glucose-1-phosphate can also inhibit SnRK1 (Nunes et al., 2013).

As an important sensor of low-carbon/low-energy status in the cell, SnRK1 is the plant ortholog of the evolutionarily conserved protein kinase family that includes the yeast sucrose non-fermenting kinase 1 (SNF1) and mammalian AMP-activated protein kinase (AMPK) (Broeckx et al., 2016). In response to cellular energy and/or carbon deficits, SNF1/AMPK phosphorylates multiple target proteins, leading to activation of catabolic processes and inhibition of anabolic processes, thereby rebalancing the energy and/or carbon status of the cell. At the molecular level, SnRK1 has been shown to phosphorylate and inactivate hydroxymethylglutaryl-CoA reductase, nitrate reductase, sucrose-phosphate synthase, and 6-phosphofructo-2-kinase/fructose-2,6-bisphosphate 2-phosphatase, which catalyze regulated steps in isoprenoid biosynthesis, nitrogen assimilation, sucrose biosynthesis, and the regulation of photosynthetic carbon partitioning, respectively (Sugden et al., 1999b; Kulma et al., 2004; Robertlee et al., 2017). SnRK1 also phosphorylates transcription factors, especially members of the bZIP family, including bZIP63, which is a key regulator of the energy/carbon starvation response in plants. The phosphorylation of bZIP63 by SnRK1 increases its ability to bind to other bZIP proteins and leads to changes in gene expression (Mair et al., 2015). SnRK1 was shown to phosphorylate B3-domain transcription factor FUSCA3 (FUS3) and increase its stability (Tsai and Gazzarrini, 2012). Accumulated evidence supports the crucial roles for SnRK1 in both normal development and responses to a wide variety of stresses that limit carbon supply, including sugar depletion, salt and osmotic stress, hypoxia, herbivory, and viral infection (Baena-González and Sheen, 2008). Structurally, both SNF1 and AMPK function as heterotrimers comprising a catalytic α-subunit together with regulatory β and γ subunits (Hardie, 2007). Although plants possess canonical α, β, and γ subunits, some of their β and γ subunits have domain architectures that are unique to plants, and a chimeric βγ subunit is the predominant γ-type subunit in SnRK1 heterotrimers (Ramon et al., 2013), suggesting that SnRK1 is a somewhat atypical member of the AMPK/SNF1/SnRK1 family (Emanuelle et al., 2015). The catalytic kinase activity of this family resides in the α subunits (i.e., KIN10, KIN11, and SnRK1.3 in *Arabidopsis*) and is strongly influenced by reversible phosphorylation of a specific threonine residue in the T-loop (also known as the activation loop) of these subunits (Estruch et al., 1992; Hawley et al., 1996; Shen et al., 2009). The degree of T-loop phosphorylation is inversely related to the energy or carbon status of the cell, because it is activated by phosphorylation under low-energy or low-carbon conditions and inactivated by dephosphorylation when energy or carbon levels increase. In mammals, the Ca^{2+}/calmodulin-dependent protein kinase kinase and the serine-threonine liver kinase B1 phosphorylate T172, whereas the PP2C and PP1 protein phosphophatases are responsible for its dephosphorylation (Davies et al., 1995; Woods et al., 2005; Garcia-Haro et al., 2010). In plants, geminivirus Rep-interacting kinases GRIK1 and GRIK2 phosphorylate T175 in the T-loop of KIN10 (Shen et al., 2009; Glab et al., 2017), whereas protein phosphatases abscisic acid insensitive 1 (type 2C protein phosphatase) and type 2C protein phosphatase A mediate its dephosphorylation (Rodrigues et al., 2013). In plants, activated SnRK1 can phosphorylate and moderate the activity of GRIK, providing potential feedback control over SnRK1 activation (Crozet et al., 2010). In mammals, the binding of AMP to the AMPK γ subunit induces conformational changes that promote the phosphorylation of T172 and inhibit its dephosphorylation (Sanders et al., 2007; Oakhill et al., 2011; Xiao et al., 2011; Gowans et al., 2013). In plants, there have been fragmentary reports of AMP inhibition of SnRK1, e.g., Sugden et al. (1999a). However, a more recent study disputed these findings, based on evidence that AMP neither directly activates recombinant SnRK1 heterotrimers nor inhibits their dephosphorylation by PP2C, indicating that plant SnRK1 is not directly affected by AMP (Emanuelle et al., 2015).

Lipids are primary metabolites in cells, playing important roles as structural components of cell membranes, storing energy in the form of triacylglycerols (TAGs) and in cell signaling. Fatty acids (FAs) are major components of lipids. TAGs are mostly sequestered in lipid droplets, also known as oil bodies. Catalyzed by FA synthase, the sugar-derived substrate acetyl-CoA, along with ATP and reductant in the form of NADPH, is required for *de novo* FA synthesis. Diacylglycerol acyltransferase 1 (DGAT1) is responsible for the final step of TAG synthesis by catalyzing the conversion of diacylglycerol and fatty acyl CoAs to TAG (Bhatt-Wessel et al., 2018). Although some studies showed Suc potentiates FA synthesis, knowledge of its precise role in this process has lagged behind our understanding of the role of sugar signaling in anthocyanin and starch syntheses. Recent studies have begun to elucidate the roles of sugar signaling in regulating lipid metabolism.

SUGAR STABILIZES WRI1 AND POTENTIATES FATTY ACID AND TAG ACCUMULATION

Lipids are derived from sugar (photosynthates), so it would be expected that higher sugar level would favor increased lipid synthesis. Sanjaya et al. (2011) observed both a 3-fold increase in Suc and 30% more TAG accumulation in leaves of AGPase-deficient plants in which *ADG1* (the small subunit of AGPase) expression was reduced by RNAi. It was also shown that *Arabidopsis* accumulated a 4-fold increase in TAG in roots when cultured on half-strength MS medium supplemented with 5% Suc than when cultured in the absence of exogenous Suc (Kelly et al., 2013). To test the influence of endogenous sugar content on FA and TAG accumulation, a high-leaf-sugar mutant was generated by reducing sugar phloem loading and starch synthesis by crossing the *suc2* (encoding a Suc/H^+ symporter that loads Suc into phloem) mutant (Srivastava et al., 2009) with the *adg1* mutant. The sugar content (combined Glc and

Suc) in *adg1suc2* leaves is 80-fold higher than that of wild-type (WT). Leaf total FA content in *adg1suc2* was 8.3% of dry weight (DW), i.e., 1.8-fold higher than WT. Leaf TAG of *adg1suc2* accumulated to 1% (DW), which is more than 10-fold higher than that of WT plants (Zhai et al., 2017b). Together, these studies confirmed that sugar potentiates TAG accumulation, lending support to the notion that sugars play roles beyond providing carbon skeletons for FA synthesis. Previous studies suggested that sugars regulate the expression of *WRI1*, an APETALA2 (AP2) transcriptional factor that induces the expression of more than 20 genes involved in glycolysis and FA synthesis (Cernac and Benning, 2004; Maeo et al., 2009). For instance, it was shown that glucose and fructose are necessary for elevated TAG accumulation in seedlings ectopically overexpressing *WRI1* (Cernac and Benning, 2004) and that the expression of *WRI1* is enhanced by Suc in *Arabidopsis* leaves (Masaki et al., 2005). Sanjaya et al. (2011) also observed that the expression of *WRI1* in seedling of AGP-deficient lines was increased compared to WT. However, later reports did not observe a significant increase in *WRI1* expression in *suc2adg1*, but a significant increase in the accumulation of WRI1 polypeptide in *suc2adg1* was observed relative to WT (Zhai et al., 2017b). Sugar-dependent regulation of gene expression and increased stability of the WRI1 polypeptide are consistent with the previously reported involvement of sugar signaling in regulating FA and TAG synthesis (Sanjaya et al., 2011).

KIN10 DIRECTLY PHOSPHORYLATES WRI1 AND RESULTS IN ITS PROTEASOMAL DEGRADATION

While screening for genes that can increase TAG accumulation in plant vegetative tissues, transient co-expression of WRI1 and KIN10, the catalytic subunit SnRK1 in tobacco, was found to strongly suppress the level or WRI1 polypeptide and abolish its stimulation of TAG accumulation (Zhai et al., 2017a). Further studies showed that KIN10 directly phosphorylates WRI1 at sites within its two AP2 DNA-binding domains, predisposing it to proteasomal degradation (Zhai et al., 2017a). This finding is consistent with previous observations showing high sugar levels in *adg1suc2* posttranscriptionally stabilizing WRI1. KIN10-dependent degradation of WRI1 provides a homeostatic mechanism that favors FA synthesis when intracellular sugar levels are elevated, and KIN10 is inhibited; conversely, FA synthesis is curtailed as sugar levels decrease, and sugar-dependent inhibition of KIN10 abates.

DGAT1 IS A TARGET OF KIN10

SnRK1 recognition motifs were first identified in *A. thaliana* DGAT1 (Zou et al., 1999) and subsequently in other plant DGAT1 sequences. Xu et al. (2008) demonstrated that substitution of Ser197 for Ala, within a SnRK1 recognition site in the *Tropaeolum majus* DGAT1, resulted in an increase in activity between 38 and 80%. More recently, *Brassica napus* DGAT1 was shown to be a direct substrate of SnRK1, which catalyzed its phosphorylation and converted it to a less active form (Caldo et al., 2018). SnRK1 (KIN10)–mediated modulation of DGAT1, the activity of which can limit TAG assembly (Sharma et al., 2008), provides another direct connection between cellular carbon (energy) status, sugar signaling, and TAG accumulation.

TREHALOSE-6-PHOSPHATE INHIBITS THE PLANT CARBON/ENERGY SENSOR SnRK1 POSITIVELY REGULATING FATTY ACID SYNTHESIS

That WRI1 is a target of KIN10 that suggested T6P, a potent inhibitor of KIN10 (Zhang et al., 2009), might stabilize WRI1 and positively regulate FA and synthesis and TAG assembly. In a recent study employing microscale thermophoresis, a technique for directly measuring dissociation constants (K*d*s), T6P was demonstrated to directly bind to KIN10 at physiologically relevant concentrations. The same approach was used to demonstrate that T6P binding weakens the KIN10-GRIK1 association, thereby reducing the activation of KIN10 and thus SnRK1 activity (**Figure 1**). T6P inhibition of KIN10 activity was shown to be strictly GRIK-dependent, in experiments using either purified recombinant proteins or crude *Arabidopsis* leaf extracts. Extracts from young leaves of *grik1*, *grik2*, and *grik1grik2* mutants showed reduced inhibition of KIN10 relative to those derived from WT leaves, confirming the dependency of T6P-mediated inhibition of KIN10 on GRIK1 (Zhai et al., 2018).

2-OXOGLUTARATE BINDING TO PII REGULATES ACETYL-CoA CARBOXYLASE

Another example of sugar signaling directly involved in regulating FA synthesis is through the PII protein. The PII protein is a signal integrator involved in the regulation of nitrogen/carbon homeostasis in bacteria (Gerhardt et al., 2015) and plants (Uhrig et al., 2009). PII binds ATP and 2-oxoglutarate (2-OG), and depending on the degree of ligand binding, it interacts with a constellation of enzymes, transcription factors, and transporters, modifying their activities (Arcondéguy et al., 2001; Ninfa and Jiang, 2005; Osanai and Tanaka, 2007; Forchhammer, 2008; Uhrig et al., 2009). In plant plastids, PII binds to biotin carboxyl carrier protein of acetyl-CoA carboxylase (BCCP), a subunit of the plastidial heteromeric acetyl-CoA carboxylase (ACCase), and inhibits ACCase activity in chloroplast extracts by up to 50%. The tricarboxylic acid (TCA) cycle intermediates 2-OG, pyruvate and oxaloacetate (OAA) were shown to completely reverse this PII-dependent inhibition of ACCase (Bourrellier et al., 2010) (**Figure 1**). The sugar derivatives OAA and pyruvate are not only involved in acetyl-CoA synthesis but are also closely related to the cellular carbon/energy status. It was shown by Nukarinen et al. (2016) that sugars are lower, whereas TCA intermediates including 2-OG, OAA, and pyruvate

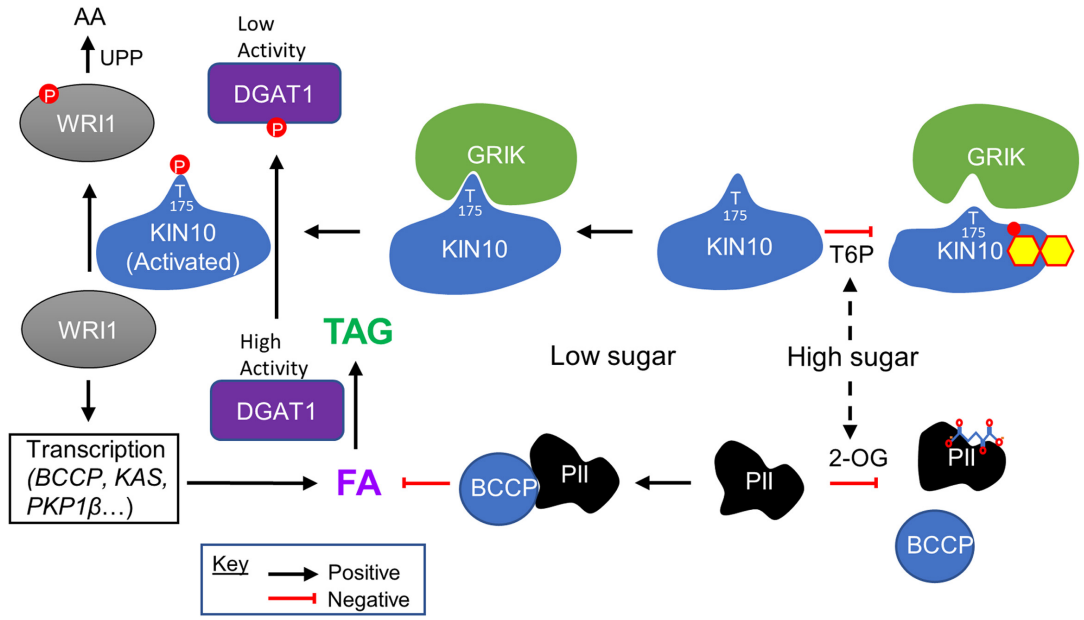

FIGURE 1 | Sugar signaling in regulating plant fatty acid and TAG biosynthesis. High levels of cellular sugars (carbon) are associated with the accumulation of trehalose 6-phosphate (T6P), which binds to KIN10 (shown as small molecule superimposed on KIN10), the catalytic subunit of SnRK1, weakening its affinity for GRIK. This results in decreased phosphorylation of the KIN10 activation loop, thereby reducing the proportion of activated KIN10. Under low KIN10 activity, WRI1 is more stable and activates the transcription of genes involved in glycolysis and fatty acid (FA) synthesis such as *BCCP*, *KAS* (*3-ketoacyl-acyl carrier protein synthase*), and *PKP1β* (*plastidial pyruvate kinase 1 beta*), promoting FA biosynthesis. DGAT1 is also more active and catalyzes the conversion of diacylglycerol and fatty acyl CoA to triacylglycerol (TAG). Conversely, when the cellular sugar levels are low, levels of T6P decrease, and GRIK binds tightly to KIN10, phosphorylating its activation loop and increasing SnRK1 activity. Activated KIN10 phosphorylates WRI1 and causes its degradation *via* the ubiquitin-proteasomal pathway (UPP) to amino acids (AA), thereby reducing FA synthesis. Activated KIN10 also phosphorylates DGAT1, inhibiting its enzyme activity, reducing TAG synthesis. High levels of cellular sugars are also associated with the accumulation of TCA cycle intermediates including 2-OG, which binds to PII protein (shown as small molecule superimposed on PII), disrupting its interaction with BCCP. This blocks the ability of PII to inhibit ACCase activity, thereby promoting FA biosynthesis. Conversely, when the cellular carbon level is low, the level of 2-OG decreases, and PII binds tightly to BCCP inhibiting ACCase activity and consequently FA biosynthesis.

are elevated, in the *snrk1α1/α2* mutant under extended dark conditions. By binding with TCA intermediates, PII conveys the signal of cellular carbon status directly to ACCase, thereby regulating FA synthesis.

SUMMARY AND FUTURE PERSPECTIVES

Recent reports elucidating the mechanisms by which 2-OG suppresses PII-mediated ACCase inhibition and T6P disrupts SnRK1-mediated turnover of WRI1 along with modulation of DGAT1 activity are revealing the critical roles of sugar signaling in lipid synthesis. It is interesting to note that while PII and KIN10 are unrelated evolutionarily, both mechanistically act as metabolic sensors that bind 2-OG and T6P, respectively. Further, the metabolite binding reduces their affinity for their respective protein binding partners, in both cases making FA synthesis contingent upon the availability of sufficient metabolic resources to support the process. While the research summarized herein has begun to fill a key knowledge gap in metabolic regulation by establishing clear mechanistic connections between sugar signaling and lipid synthesis and accumulation, it is anticipated that many additional connections will be discovered in the near future. Potential connections are included but not limited to the yet-to-be identified E3 ubiquitin ligase of WRI1 or other key enzymes of lipid metabolism that may be involved in sugar signaling, unknown regulators of WRI1 or LEC2 transcription that may also be a part of the carbon sensing network. Sugar signaling may also play roles in oil body stability and regulation of fatty acid degradation in peroxisomes from the perspective of carbon(energy) demand.

AUTHOR CONTRIBUTIONS

ZZ drafted and edited text and figure. JK and HL drafted and edited text. JS conceived the work, contributed to draft, and edited both text and figure. CX edited text. All authors contributed to the article and approved the submitted version.

FUNDING

This work was supported by Division of Chemical Sciences, Geosciences, and Biosciences, Office of Basic Energy Sciences, United States Department of Energy Grant DOE KC0304000.

REFERENCES

Arcondéguy, T., Jack, R., and Merrick, M. (2001). PII signal transduction proteins, pivotal players in microbial nitrogen control. *Microbiol. Mol. Biol. Rev.* 65, 80–105. doi: 10.1128/mmbr.65.1.80-105.2001

Baena-González, E., and Sheen, J. (2008). Convergent energy and stress signaling. *Trends Plant Sci.* 13, 474–482. doi: 10.1016/j.tplants.2008.06.006

Bhatt-Wessel, B., Jordan, T. W., Miller, J. H., and Peng, L. (2018). Role of DGAT enzymes in triacylglycerol metabolism. *Arch. Biochem. Biophys.* 655, 1–11. doi: 10.1016/j.abb.2018.08.001

Bourrellier, A. B. F., Valot, B., Guillot, A., Ambard-Bretteville, F., Vidal, J., and Hodges, M. (2010). Chloroplast acetyl-CoA carboxylase activity is 2-oxoglutarate–regulated by interaction of PII with the biotin carboxyl carrier subunit. *Proc. Natl. Acad. Sci. U.S.A.* 107, 502–507. doi: 10.1073/pnas.0910097107

Broeckx, T., Hulsmans, S., and Rolland, F. (2016). The plant energy sensor: evolutionary conservation and divergence of SnRK1 structure, regulation, and function. *J. Exp. Bot.* 67, 6215–6252. doi: 10.1093/jxb/erw416

Cabib, E., and Leloir, L. F. (1958). The biosynthesis of trehalose phosphate. *J. Biol. Chem.* 231, 259–275. doi: 10.1016/s0021-9258(19)77303-7

Caldo, K. M. P., Shen, W., Xu, Y., Hanley-Bowdoin, L., Chen, G., Weselake, R. J., et al. (2018). Diacylglycerol acyltransferase 1 is activated by phosphatidate and inhibited by SnRK1-catalyzed phosphorylation. *Plant J.* 96, 287–299. doi: 10.1111/tpj.14029

Cernac, A., and Benning, C. (2004). WRINKLED1 encodes an AP2/EREB domain protein involved in the control of storage compound biosynthesis in *Arabidopsis*. *Plant J.* 40, 575–585. doi: 10.1111/j.1365-313x.2004.02235.x

Crozet, P., Jammes, F., Valot, B., Ambard-Bretteville, F., Nessler, S., Hodges, M., et al. (2010). Cross-phosphorylation between *Arabidopsis thaliana* sucrose nonfermenting 1-related protein kinase 1 (AtSnRK1) and its activating kinase (AtSnAK) determines their catalytic activities. *J. Biol. Chem.* 285, 12071–12077. doi: 10.1074/jbc.m109.079194

Davies, S. P., Helps, N. R., Cohen, P. T., and Hardie, D. G. (1995). 5'-AMP inhibits dephosphorylation, as well as promoting phosphorylation, of the AMP-activated protein kinase. Studies using bacterially expressed human protein phosphatase-2C alpha and native bovine protein phosphatase-2AC. *FEBS Lett.* 377, 421–425. doi: 10.1016/0014-5793(95)01368-7

Emanuelle, S., Hossain, M. I., Moller, I. E., Pedersen, H. L., Meene, A. M., Doblin, M. S., et al. (2015). SnRK1 from *Arabidopsis thaliana* is an atypical AMPK. *Plant J.* 82, 183–192.

Estruch, F., Treitel, M. A., Yang, X., and Carlson, M. (1992). N-terminal mutations modulate yeast SNF1 protein kinase function. *Genetics* 132, 639–650. doi: 10.1093/genetics/132.3.639

Figueroa, C. M., and Lunn, J. E. (2016). A tale of two sugars: trehalose 6-phosphate and sucrose. *Plant Physiol.* 172, 7–27. doi: 10.1104/pp.16.00417

Forchhammer, K. (2008). PII signal transducers: novel functional and structural insights. *Trends Microbiol.* 16, 65–72. doi: 10.1016/j.tim.2007.11.004

Garcia-Haro, L., Garcia-Gimeno, M. A., Neumann, D., Beullens, M., Bollen, M., and Sanz, P. (2010). The PP1-R6 protein phosphatase holoenzyme is involved in the glucose-induced dephosphorylation and inactivation of AMP-activated protein kinase, a key regulator of insulin secretion, in MIN6 β cells. *FASEB J.* 24, 5080–5091. doi: 10.1096/fj.10-166306

Gerhardt, E. C., Rodrigues, T. E., Müller-Santos, M., Pedrosa, F. O., Souza, E. M., Forchhammer, K., et al. (2015). The bacterial signal transduction protein GlnB regulates the committed step in fatty acid biosynthesis by acting as a dissociable regulatory subunit of acetyl-CoA carboxylase. *Mol. Microbiol.* 95, 1025–1035. doi: 10.1111/mmi.12912

Glab, N., Oury, C., Guerinier, T., Domenichini, S., Crozet, P., Thomas, M., et al. (2017). The impact of *Arabidopsis thaliana* SNF1-related-kinase 1 (SnRK1)-activating kinase 1 (SnAK1) and SnAK2 on SnRK1 phosphorylation status: characterization of a SnAK double mutant. *Plant J.* 89, 1031–1041. doi: 10.1111/tpj.13445

Gowans, G. J., Hawley, S. A., Ross, F. A., and Hardie, D. G. (2013). AMP is a true physiological regulator of AMP-activated protein kinase by both allosteric activation and enhancing net phosphorylation. *Cell Metab.* 18, 556–566. doi: 10.1016/j.cmet.2013.08.019

Hardie, D. G. (2007). AMP-activated/SNF1 protein kinases: conserved guardians of cellular energy. *Nat. Rev. Mol. Cell Biol.* 8, 774–785. doi: 10.1038/nrm2249

Harn, C. H., Bae, J. M., Lee, S. S., Min, S. R., and Liu, J. R. (2000). Presence of multiple cDNAs encoding an isoform of ADP-glucose pyrophosphorylase large subunit from sweet potato and characterization of expression levels. *Plant Cell Physiol.* 41, 1235–1242. doi: 10.1093/pcp/pcd049

Hawley, S. A., Davison, M., Woods, A., Davies, S. P., Beri, R. K., Carling, D., et al. (1996). Characterization of the AMP-activated protein kinase kinase from rat liver and identification of threonine 172 as the major site at which it phosphorylates AMP-activated protein kinase. *J. Biol. Chem.* 271, 27879–27887. doi: 10.1074/jbc.271.44.27879

Kelly, A. A., Van Erp, H., Quettier, A.-L., Shaw, E., Menard, G., Kurup, S., et al. (2013). The SUGAR-DEPENDENT1 Lipase limits Triacylglycerol accumulation in vegetative tissues of *Arabidopsis*. *Plant Physiol.* 162, 1282–1289. doi: 10.1104/pp.113.219840

Kolbe, A., Tiessen, A., Schluepmann, H., Paul, M., Ulrich, S., and Geigenberger, P. (2005). Trehalose 6-phosphate regulates starch synthesis via posttranslational redox activation of ADP-glucose pyrophosphorylase. *Proc. Natl. Acad. Sci. U.S.A.* 102, 11118–11123. doi: 10.1073/pnas.0503410102

Kulma, A., Villadsen, D., Campbell, D. G., Meek, S. E., Harthill, J. E., Nielsen, T. H., et al. (2004). Phosphorylation and 14-3-3 binding of *Arabidopsis* 6-phosphofructo-2-kinase/fructose-2,6-bisphosphatase. *Plant J.* 37, 654–667. doi: 10.1111/j.1365-313x.2003.01992.x

Lunn, J. E., Feil, R., Hendriks, J. H., Gibon, Y., Morcuende, R., Osuna, D., et al. (2006). Sugar-induced increases in trehalose 6-phosphate are correlated with redox activation of ADPglucose pyrophosphorylase and higher rates of starch synthesis in *Arabidopsis thaliana*. *Biochem. J.* 397, 139–148. doi: 10.1042/bj20060083

Maeo, K., Tokuda, T., Ayame, A., Mitsui, N., Kawai, T., Tsukagoshi, H., et al. (2009). An AP2-type transcription factor, WRINKLED1, of *Arabidopsis thaliana* binds to the AW-box sequence conserved among proximal upstream regions of genes involved in fatty acid synthesis. *Plant J.* 60, 476–487. doi: 10.1111/j.1365-313x.2009.03967.x

Mair, A., Pedrotti, L., Wurzinger, B., Anrather, D., Simeunovic, A., Weiste, C., et al. (2015). SnRK1-triggered switch of bZIP63 dimerization mediates the low-energy response in plants. *eLife* 4:e05828.

Martínez-Barajas, E., Delatte, T., Schluepmann, H., De Jong, G. J., Somsen, G. W., Nunes, C., et al. (2011). Wheat grain development is characterized by remarkable trehalose 6-phosphate accumulation pregrain filling: tissue distribution and relationship to SNF1-related protein kinase1 activity. *Plant Physiol.* 156, 373–381. doi: 10.1104/pp.111.174524

Martins, M. C. M., Hejazi, M., Fettke, J., Steup, M., Feil, R., Krause, U., et al. (2013). Feedback inhibition of starch degradation in *Arabidopsis* leaves mediated by trehalose 6-phosphate. *Plant Physiol.* 163, 1142–1163. doi: 10.1104/pp.113.226787

Masaki, T., Mitsui, N., Tsukagoshi, H., Nishii, T., Morikami, A., and Nakamura, K. (2005). Activator of Spomin:: LUC1/WRINKLED1 of *Arabidopsis thaliana* transactivates sugar-inducible promoters. *Plant Cell Physiol.* 46, 547–556. doi: 10.1093/pcp/pci072

Nagaraj, V. J., Riedl, R., Boller, T., Wiemken, A., and Meyer, A. D. (2001). Light and sugar regulation of the barley sucrose: fructan 6-fructosyltransferase promoter. *J. Plant Physiol.* 158, 1601–1607. doi: 10.1078/0176-1617-00592

Nagata, T., Hara, H., Saitou, K., Kobashi, A., Kojima, K., Yuasa, T., et al. (2012). Activation of ADP-glucose pyrophosphorylase gene promoters by a WRKY transcription factor, AtWRKY20, in *Arabidopsis thaliana* L. and sweet potato (*Ipomoea batatas* Lam.). *Plant Prod. Sci.* 15, 10–18. doi: 10.1626/pps.15.10

Nakamura, K., Ohto, M.-A., Yoshida, N., and Nakamura, K. (1991). Sucrose-induced accumulation of β-amylase occurs concomitant with the accumulation of starch and sporamin in leaf-petiole cuttings of sweet potato. *Plant Physiol.* 96, 902–909. doi: 10.1104/pp.96.3.902

Ninfa, A. J., and Jiang, P. (2005). PII signal transduction proteins: sensors of α-ketoglutarate that regulate nitrogen metabolism. *Curr. Opin. Microbiol.* 8, 168–173. doi: 10.1016/j.mib.2005.02.011

Noël, G., Tognetti, J. A., and Pontis, H. G. (2001). Protein kinase and phosphatase activities are involved in fructan synthesis initiation mediated by sugars. *Planta* 213, 640–646. doi: 10.1007/s004250100550

Nuccio, M. L., Wu, J., Mowers, R., Zhou, H. P., Meghji, M., Primavesi, L. F., et al. (2015). Expression of trehalose-6-phosphate phosphatase in maize ears improves yield in well-watered and drought conditions. *Nat. Biotechnol.* 33, 862–869. doi: 10.1038/nbt.3277

Nukarinen, E., Nägele, T., Pedrotti, L., Wurzinger, B., Mair, A., Landgraf, R., et al. (2016). Quantitative phosphoproteomics reveals the role of the AMPK plant ortholog SnRK1 as a metabolic master regulator under energy deprivation. *Sci. Rep.* 6:31697.

Nunes, C., Primavesi, L. F., Patel, M. K., Martinez-Barajas, E., Powers, S. J., Sagar, R., et al. (2013). Inhibition of SnRK1 by metabolites: tissue-dependent effects and cooperative inhibition by glucose 1-phosphate in combination with trehalose 6-phosphate. *Plant Physiol. Biochem.* 63, 89–98. doi: 10.1016/j.plaphy.2012.11.011

Oakhill, J. S., Steel, R., Chen, Z.-P., Scott, J. W., Ling, N., Tam, S., et al. (2011). AMPK is a direct adenylate charge-regulated protein kinase. *Science* 332, 1433–1435. doi: 10.1126/science.1200094

Osanai, T., and Tanaka, K. (2007). Keeping in touch with PII: PII-interacting proteins in unicellular cyanobacteria. *Plant Cell Physiol.* 48, 908–914. doi: 10.1093/pcp/pcm072

Ramon, M., Ruelens, P., Li, Y., Sheen, J., Geuten, K., and Rolland, F. (2013). The hybrid four-CBS-domain KINbetagamma subunit functions as the canonical gamma subunit of the plant energy sensor SnRK1. *Plant J.* 75, 11–25. doi: 10.1111/tpj.12192

Robertlee, J., Kobayashi, K., Suzuki, M., and Muranaka, T. (2017). AKIN10, a representative *Arabidopsis* SNF1-related protein kinase 1 (SnRK1), phosphorylates and downregulates plant HMG-CoA reductase. *FEBS Lett.* 591, 1159–1166. doi: 10.1002/1873-3468.12618

Rodrigues, A., Adamo, M., Crozet, P., Margalha, L., Confraria, A., Martinho, C., et al. (2013). ABI1 and PP2CA phosphatases are negative regulators of Snf1-related protein kinase1 signaling in *Arabidopsis*. *Plant Cell* 25, 3871–3884. doi: 10.1105/tpc.113.114066

Sanders, M. J., Grondin, P. O., Hegarty, B. D., Snowden, M. A., and Carling, D. (2007). Investigating the mechanism for AMP activation of the AMP-activated protein kinase cascade. *Biochem. J.* 403, 139–148. doi: 10.1042/bj20061520

Sanjaya, T. P., Weise, S. E., and Benning, C. (2011). Increasing the energy density of vegetative tissues by diverting carbon from starch to oil biosynthesis in transgenic *Arabidopsis*. *Plant Biotechnol. J.* 9, 874–883. doi: 10.1111/j.1467-7652.2011.00599.x

Schluepmann, H., Pellny, T., Van Dijken, A., Smeekens, S., and Paul, M. (2003). Trehalose 6-phosphate is indispensable for carbohydrate utilization and growth in *Arabidopsis thaliana*. *Proc. Natl. Acad. Sci. U.S.A.* 100, 6849–6854. doi: 10.1073/pnas.1132018100

Sharma, N., Anderson, M., Kumar, A., Zhang, Y., Giblin, E. M., Abrams, S. R., et al. (2008). Transgenic increases in seed oil content are associated with the differential expression of novel Brassica-specific transcripts. *BMC Genomics* 9:619. doi: 10.1186/1471-2164-9-619

Shen, W., Reyes, M. I., and Hanley-Bowdoin, L. (2009). *Arabidopsis* protein kinases GRIK1 and GRIK2 specifically activate SnRK1 by phosphorylating its activation loop. *Plant Physiol.* 150, 996–1005. doi: 10.1104/pp.108.132787

Solfanelli, C., Poggi, A., Loreti, E., Alpi, A., and Perata, P. (2006). Sucrose-specific induction of the anthocyanin biosynthetic pathway in *Arabidopsis*. *Plant Physiol.* 140, 637–646. doi: 10.1104/pp.105.072579

Srivastava, A. C., Dasgupta, K., Ajieren, E., Costilla, G., Mcgarry, R.C., and Ayre, B. G. (2009). *Arabidopsis* plants harbouring a mutation in *AtSUC2*, encoding the predominant sucrose/proton symporter necessary for efficient phloem transport, are able to complete their life cycle and produce viable seed. *Ann. Bot.* 104, 1121–1128. doi: 10.1093/aob/mcp215

Sugden, C., Crawford, R. M., Halford, N. G., and Hardie, D. G. (1999a). Regulation of spinach SNF1-related (SnRK1) kinases by protein kinases and phosphatases is associated with phosphorylation of the T loop and is regulated by 5'-AMP. *Plant J.* 19, 433–439. doi: 10.1046/j.1365-313x.1999.00532.x

Sugden, C., Donaghy, P. G., Halford, N. G., and Hardie, D. G. (1999b). Two SNF1-related protein kinases from spinach leaf phosphorylate and inactivate 3-hydroxy-3-methylglutaryl-coenzyme A reductase, nitrate reductase, and sucrose phosphate synthase in vitro. *Plant Physiol.* 120, 257–274. doi: 10.1104/pp.120.1.257

Tiessen, A., Hendriks, J. H., Stitt, M., Branscheid, A., Gibon, Y., Farré, E. M., et al. (2002). Starch synthesis in potato tubers is regulated by post-translational redox modification of ADP-glucose pyrophosphorylase a novel regulatory mechanism linking starch synthesis to the sucrose supply. *Plant Cell* 14, 2191–2213. doi: 10.1105/tpc.003640

Tsai, A. Y. L., and Gazzarrini, S. (2012). AKIN10 and FUSCA3 interact to control lateral organ development and phase transitions in *Arabidopsis*. *Plant J.* 69, 809–821. doi: 10.1111/j.1365-313x.2011.04832.x

Uhrig, R. G., Ng, K. K., and Moorhead, G. B. (2009). PII in higher plants: a modern role for an ancient protein. *Trends Plant Sci.* 14, 505–511. doi: 10.1016/j.tplants.2009.07.003

Wang, S.-J., Yeh, K.-W., and Tsai, C.-Y. (2001). Regulation of starch granule-bound starch synthase I gene expression by circadian clock and sucrose in the source tissue of sweet potato. *Plant Sci.* 161, 635–644. doi: 10.1016/s0168-9452(01)00449-6

Woods, A., Dickerson, K., Heath, R., Hong, S.-P., Momcilovic, M., Johnstone, S. R., et al. (2005). Ca 2+/calmodulin-dependent protein kinase kinase-β acts upstream of AMP-activated protein kinase in mammalian cells. *Cell Metab.* 2, 21–33. doi: 10.1016/j.cmet.2005.06.005

Xiao, B., Sanders, M. J., Underwood, E., Heath, R., Mayer, F. V., Carmena, D., et al. (2011). Structure of mammalian AMPK and its regulation by ADP. *Nature* 472, 230–233. doi: 10.1038/nature09932

Xu, J., Francis, T., Mietkiewska, E., Giblin, E. M., Barton, D. L., Zhang, Y., et al. (2008). Cloning and characterization of an acyl-CoA-dependent diacylglycerol acyltransferase 1 (DGAT1) gene from Tropaeolum majus, and a study of the functional motifs of the DGAT protein using site-directed mutagenesis to modify enzyme activity and oil content. *Plant Biotechnol. J.* 6, 799–818. doi: 10.1111/j.1467-7652.2008.00358.x

Yadav, U. P., Ivakov, A., Feil, R., Duan, G. Y., Walther, D., Giavalisco, P., et al. (2014). The sucrose–trehalose 6-phosphate (Tre6P) nexus: specificity and mechanisms of sucrose signalling by Tre6P. *J. Exp. Bot.* 65, 1051–1068. doi: 10.1093/jxb/ert457

Zhai, Z., Keereetaweep, J., Liu, H., Feil, R., Lunn, J. E., and Shanklin, J. (2018). Trehalose 6-phosphate positively regulates fatty acid synthesis by stabilizing WRINKLED1. *Plant Cell* 30, 2616–2627. doi: 10.1105/tpc.18.00521

Zhai, Z., Liu, H., and Shanklin, J. (2017a). Phosphorylation of WRINKLED1 by KIN10 results in its proteasomal degradation, providing a link between energy homeostasis and Lipid biosynthesis. *Plant Cell* 29, 871–889. doi: 10.1105/tpc.17.00019

Zhai, Z., Liu, H., Xu, C., and Shanklin, J. (2017b). Sugar potentiation of fatty acid and triacylglycerol accumulation. *Plant Physiol.* 175, 696–707. doi: 10.1104/pp.17.00828

Zhang, Y., Primavesi, L. F., Jhurreea, D., Andralojc, P. J., Mitchell, R. A., Powers, S. J., et al. (2009). Inhibition of SNF1-related protein kinase1 activity and regulation of metabolic pathways by trehalose-6-phosphate. *Plant Physiol.* 149, 1860–1871. doi: 10.1104/pp.108.133934

Zou, J., Wei, Y., Jako, C., Kumar, A., Selvaraj, G., and Taylor, D. C. (1999). The *Arabidopsis thaliana* TAG1 mutant has a mutation in a diacylglycerol acyltransferase gene. *Plant J.* 19, 645–653. doi: 10.1046/j.1365-313x.1999.00555.x

Conflict of Interest: The authors declare that the research was conducted in the absence of any commercial or financial relationships that could be construed as a potential conflict of interest.

Copyright © 2021 Zhai, Keereetaweep, Liu, Xu and Shanklin. This is an open-access article distributed under the terms of the Creative Commons Attribution License (CC BY). The use, distribution or reproduction in other forums is permitted, provided the original author(s) and the copyright owner(s) are credited and that the original publication in this journal is cited, in accordance with accepted academic practice. No use, distribution or reproduction is permitted which does not comply with these terms.

GLOSSARY

T6P	Trehalose 6-phosphate
2-OG	2-Oxoglutarate
SNF1	Non-fermenting kinase 1
AMPK	AMP-activated protein kinase
SnRK1	Sucrose non-fermenting-1–related protein kinase1
GRIK	Geminivirus Rep-interacting kinase
TAG	Triacylglycerol
DGAT1	Diacylglycerol acyltransferase
ADG1	Small subunit of ADP-Glc pyrophosphorylase
ACCase	Acetyl-CoA carboxylase
BCCP	Biotin carboxyl carrier protein of acetyl-CoA carboxylase
KAS	3-Ketoacyl-acyl carrier protein synthase
PKP1β	Plastidial pyruvate kinase 1 beta

frontiers in Plant Science

ORIGINAL RESEARCH
published: 30 March 2021
doi: 10.3389/fpls.2021.646498

Dynamism of Metabolic Carbon Flow of Starch and Lipids in *Chlamydomonas debaryana*

Naoki Sato[*†] *and Masakazu Toyoshima*[†‡]

Department of Life Sciences, Graduate School of Arts and Science, University of Tokyo, Meguro, Japan

OPEN ACCESS

Edited by:
Mie Shimojima, Tokyo Institute of Technology, Japan

Reviewed by:
Alexei E. Solovchenko, Lomonosov Moscow State University, Russia
Masataka Kajikawa, Kindai University, Japan

***Correspondence:**
Naoki Sato
naokisat@bio.c.u-tokyo.ac.jp

[†]*These authors have contributed equally to this work*

[‡]***Present address:***
Masakazu Toyoshima, Department of Bioinformatic Engineering, Graduate School of Information Science and Technology, Osaka University, Osaka, Japan

Specialty section:
This article was submitted to Marine and Freshwater Plants, a section of the journal Frontiers in Plant Science

Received: *27 December 2020*
Accepted: *08 March 2021*
Published: *30 March 2021*

Citation:
Sato N and Toyoshima M (2021) Dynamism of Metabolic Carbon Flow of Starch and Lipids in Chlamydomonas debaryana. Front. Plant Sci. 12:646498. doi: 10.3389/fpls.2021.646498

Microalgae have the potential to recycle CO_2 as starch and triacylglycerol (TAG), which provide alternative source of biofuel and high added-value chemicals. Starch accumulates in the chloroplast, whereas TAG accumulates in the cytoplasmic lipid droplets (LD). Preferential accumulation of starch or TAG may be achieved by switching intracellular metabolic carbon flow, but our knowledge on this control remains limited. Are these two products mutually exclusive? Or, does starch act as a precursor to TAG synthesis, or vice versa? To answer these questions, we analyzed carbon flow in starch and lipids using a stable isotope ^{13}C in *Chlamydomonas debaryana* NIES-2212, which accumulates, without nutrient limitation, starch in the exponential growth phase and TAG in the stationary phase. Pulse labeling experiments as well as pulse labeling and chase experiments were conducted, and then, gas chromatography-mass spectrometry (GC-MS) analysis was performed on starch-derived glucose and lipid-bound fatty acids. We exploited the previously developed method of isotopomer analysis to estimate the proportion of various pools with different isotopic abundance. Starch turned over rapidly to provide carbon for the synthesis of fatty acids in the exponential phase cells. Most fatty acids showed rapid and slow components of metabolism, whereas oleic acid decayed according to a single exponential curve. Highly labeled population of fatty acids that accumulated during the initial labeling decreased rapidly, and replaced by low abundance population during the chase time, indicating that highly labeled fatty acids were degraded and the resulting carbons were re-used in the re-synthesis with about 9-fold unlabeled, newly fixed carbons. Elongation of C16–C18 acids *in vivo* was indicated by partially labeled C18 acids. The accumulation of TAG in the stationary growth phase was accounted for by both *de novo* synthesis and remodeling of membrane lipids. These results suggest that *de novo* synthesis of starch and TAG was rapid and transient, and also almost independent to each other, but there is a pool of starch quickly turning over for the synthesis of fatty acids. Fatty acids were also subject to re-synthesis. Evidence was also provided for remodeling of lipids, namely, re-use of acyl groups in polar lipids for TAG synthesis.

Keywords: biofuel production, green alga, isotopomer analysis, lipid biosynthesis, metabolic analysis, stable isotope

INTRODUCTION

Photosynthetic organisms, such as plants, algae, cyanobacteria and anoxygenic bacteria, recycle CO_2 under the sunlight to provide organic matters for the biosphere and human life. Currently, industrial production of biofuels such as bioethanol and biodiesel from the microalgal products, oil and starch, are extensively studied (Siaut et al., 2011; Aikawa et al., 2013; Bhowmick et al., 2016; Sato et al., 2017). Plant and microalgal oil is mainly triacylglycerol (TAG) consisting of long chain fatty acids. The overall picture of the complex metabolic pathway leading to TAG synthesis was elucidated in plants (Lung and Weselake, 2006; Li-Beisson et al., 2013; Bates, 2016), but this might not be simply adapted to microalgae, because microalgae are unicellular organisms that accumulate both starch and TAG within a single cell, whereas the sink and source organs are separated in plants. The metabolic pathways in microalgae have to be established using information of comparative genomics that links orthologs in algae, bacteria, protists and plants (Riekhof et al., 2005; Sato and Moriyama, 2007; Misra et al., 2012; Sato and Obayashi, 2021).

In plants, TAG is synthesized by two major pathways (Li-Beisson et al., 2013): namely, the acylation of glycerol-3-phosphate with acyl-CoA in the *de novo* pathway called Kennedy pathway, and the remodeling pathway in which phosphatidylcholine (PC) acts as an intermediate that provides fatty acids and/or diacylglycerol (DAG) for the synthesis of TAG (Bates et al., 2013). In plants, TAG is typically accumulated as lipid droplets (LD) in the cytosol of developing seeds, although LD is supposed to emerge by budding from the endoplasmic reticulum (ER). LD is typically a spherical globule of 0.1–1 μm in diameter, mainly consisting of TAG and surrounded by a half unit membrane containing oleosin and other specific proteins (Chapman et al., 2012). LD is also present in the cytosol of microalgae (Moriyama et al., 2018), but the proteins in the LD membrane are not related to oleosin. A major LD protein is called MLDP in *Chlamydomonas reinhardtii* (Moellering and Benning, 2010). TAG is also known to be present as a minor component of plastoglobules, which are small lipid droplets present in chloroplasts, consisting of plastoquinone, tocopherol, and phytyl esters (Bréhélin et al., 2007; Lohscheider and Bártulos, 2016).

Chlamydomonas reinhardtii has been used as a model organism for the production of TAG (Li et al., 2012; Merchant et al., 2012; Sakurai et al., 2014; Li-Beisson et al., 2015; Juergens et al., 2016) and starch (Van den Koornhuyse et al., 1996; Hicks et al., 2001) under nutrient-limited conditions such as nitrogen deficiency, which is also known to increase accumulation of TAG in various algae (Tornabene et al., 1983; Yusuf, 2007; Hu et al., 2008; Aikawa et al., 2012; Msanne et al., 2012; Iwai et al., 2014). In these cases, membrane lipids are remodeled to form TAG under limitation of *de novo* synthesis of lipids. Some algae are known to accumulate TAG or other lipid materials without severe limitation of nutrients. *Nannochloropsis* sp., *Botryococcus braunii*, *Dunaliella primolecta*, and *Nitzschia* sp. are representatives of many oil-accumulating microalgae known to date (for a review, see Menetrez, 2012). Different strains of *Chlamydomonas debaryana* also accumulate large amount of TAG in the stationary growth phase, but this is not caused by nutrient deficiency (Zhang et al., 2014; Toyoshima and Sato, 2015). In this respect, *C. debaryana* is different from *C. reinhardtii*, which does not accumulate TAG in the stationary growth phase without nutrient limitation (Sakurai et al., 2014). A recent research using gel encapsulation showed that increased cell density promoted cell growth and TAG accumulation in *C. debaryana* but not *C. reinhardtii* (Yoshitomi et al., 2020). In another study (Toyoshima and Sato, 2018), we tried to optimize TAG production in this alga, and found that initial starch accumulation was followed by TAG accumulation that accompanied degradation of starch. We suspected a close relationship between starch metabolism and TAG synthesis. However, no clear correlation was detected between maximum levels of starch and TAG accumulation under nitrogen limitation in various strains and mutants of *C. reinhardtii* (Siaut et al., 2011). This necessitates labeling studies on the carbon flow in starch and TAG. An NMR study using [^{13}C] acetate and bicarbonate was reported in *C. reinhardtii* and suggested the importance of autotrophic nutrition in starch and TAG accumulation (Singh et al., 2014). In this context, we found *C. debaryana* a good model system to study biosynthesis and carbon flow in starch and TAG under photoautotrophic condition without nutrient limitation.

Labeling study using ^{13}C is potentially useful and powerful. Mass spectral analysis of incorporated ^{13}C in various different parts of molecules will provide detailed information on the carbon flow in labeling-and-chase experiments. We developed a new method of ^{13}C isotopomer analysis, which is implemented in the C13dist program (Sato et al., 2016), focusing on the isotopic abundance (p), to trace differently labeled carbon pools in the cell. An isotopomer is a molecule containing a defined number of ^{13}C. A single value of p defines a binomial distribution of isotopomers. The C13dist program is intended to estimate the distribution of p from the observed isotopomer distribution. Carbon pools with different p values can be analyzed as separate pools. In this respect, a single isotope ^{13}C can be used as multiple tracers. In the present study, we exploited this ^{13}C isotopomer analysis to study synthesis of starch and lipids, potential conversion of starch to lipids, as well as remodeling of membrane lipids to TAG.

MATERIALS AND METHODS

Growth of Organism

Cells of *C. debaryana* NIES-2212 (Yumoto et al., 2013) were grown under continuous light (about 50 μmol m^{-2} s^{-1}) in the Modified Bristol's Medium (MBM; Watanabe, 1960) under aeration with 1.0% (v/v) CO_2 at 25°C. The actual constituents of the MBM that we use were described previously (Sakurai et al., 2014).

Photosynthetic Labeling With Sodium [^{13}C]bicarbonate

The cells (200-ml culture) grown under the photoautotrophic conditions at 48, 96, and 144 h after inoculation (**Figure 1A**) were collected by centrifugation (600 × g, 5 min, 4°C) and

then resuspended in 200 ml of fresh medium containing 13 mM sodium [^{13}C]bicarbonate (99% ^{13}C, Cambridge Isotope Laboratories, Inc., Tewksbury, MA, United States). The cells were allowed to grow for 2 h in the light with gentle stirring in a tightly closed flask. Cells were harvested by centrifugation. Total lipids were extracted according to the method of Bligh and Dyer (1959) as described in Toyoshima and Sato (2015). After partitioning, the interface fluff containing proteins, starch and other insoluble materials was recovered as a starch source, and stored at −80°C until analysis. The chloroform phase (lipids) was evaporated under reduced pressure. The lipids were dissolved in 0.2 ml of chloroform/methanol (2:1, by volume) plus 0.2 ml of ethanol, and stored at −20°C until use. The experiments were performed in triplicates.

Labeling and Chase Experiments With [^{13}C]bicarbonate and [2-^{13}C]acetate

The cells (300-ml culture) grown under the photoautotrophic conditions for 72 h after inoculation (**Figure 1B**) were collected by centrifugation (600 × *g*, 5 min, 4°C) and then resuspended in 300 ml of fresh medium containing 20 mM sodium [^{13}C] bicarbonate or sodium [2-^{13}C]acetate (99% ^{13}C, Cambridge Isotope Laboratories, Inc.). They were allowed to grow for 5 h in the light with gentle stirring in a tightly closed flask. A 50-ml aliquot was harvested by centrifugation, and subjected to Bligh-Dyer partitioning. Lipids and starch (as part of insoluble materials) were recovered as described above. The remaining part of the culture was washed by 2 cycles of centrifugation and resuspension in fresh medium, and finally resuspended in 250 ml of fresh medium. The cells were allowed to grow under the photoautotrophic conditions for 4 days (**Figure 1B**). A 50-ml aliquot was harvested each day, and lipids and starch were recovered and stored as described. The experiments were performed in triplicates.

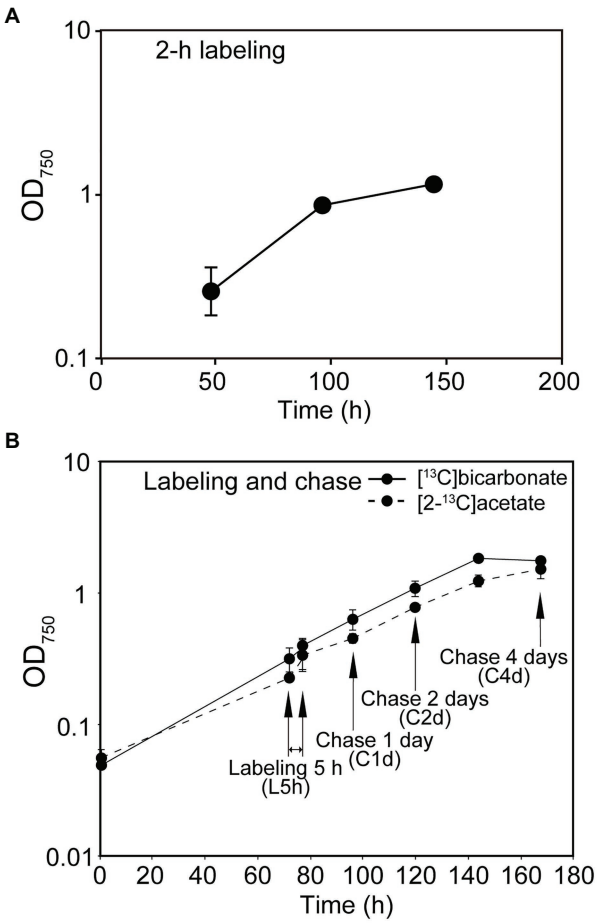

FIGURE 1 | Growth of cells used in the experiments. Turbidity at 750 nm is shown at each sampling point. **(A)** Labeling for 2 h. **(B)** Labeling for 5 h and chase.

Analysis of Lipids and Fatty Acids

All analytical methods (except ^{13}C analysis) were essentially identical to those described previously (Sakurai et al., 2014; Toyoshima and Sato, 2015). Briefly, lipid classes were separated by two-dimensional thin-layer chromatography (2D-TLC). Each spot of lipid class was scraped off the plate, and subjected to methanolysis in 2.5% HCl in anhydrous methanol (Kanto Kagaku, Ltd., Tokyo, Japan) at 85°C for 2.5 h. Pentadecanoic acid (15:0) was added before methanolysis as an internal standard for quantitation of fatty acid methyl esters (FAMEs). After the reaction, FAMEs were extracted with *n*-hexane. Lipids were quantified as the amount of fatty acids analyzed as methyl esters by gas chromatography-mass spectrometry (GC-MS; model GCMS-QP2010 Ultra; Shimadzu, Kyoto, Japan) using a BPX70 column (length, 60 m; internal diameter, 0.22 mm; SGE Analytical Science, Victoria, Australia). Analytical conditions were described in a previous report (Sato et al., 2016). Mass spectra were used in two ways in the following analyses: First, total ion intensity was used to quantify the amounts of fatty acids using the internal standard. Second, mass distribution of molecular ion (M^+) of FAME was obtained as a text file for the analysis of isotopomer distribution. For monoenoic fatty acids, the cluster of signals representing $(M-31)^+$ and $(M-32)^+$ was used for isotopomer analysis, while less intense peaks of M^+ were used to check unrelated or contaminant fragments.

Analysis of Starch

The insoluble fraction recovered from the fluff, containing starch, cell wall, among others, was dried under vacuum and then subjected to methanolysis in 2.5% HCl in anhydrous methanol to yield 1-methyl glucoside. Mannitol was added before methanolysis as an internal standard for quantitation. Hydrophobic materials were removed by extraction with *n*-hexane. After drying, 1-methyl glucoside was mixed with 20 µl of a trimethylsililation reagent, TMS-HT kit (Tokyo Chemical Industry CO., Ltd., Tokyo, Japan), and heated at 95°C for 10 min. The resulting tetrakis(TMS) 1-methyl glucoside was analyzed by GC-MS using an Rtx-5MS column (length, 30 m; internal diameter, 0.25 mm; Restek, Bellefonte, PA, United States). Analytical conditions were described in a previous

report (Sato, 2015). Amount of glucose was quantified by the total ion intensities of two major peaks of tetrakis (TMS) 1-methyl glucoside using the internal standard. Mass distribution of the ion retaining all six carbons with four TMS groups (the mass of monoisotopic ion is 361) was obtained as a text file, and used for isotopomer analysis. As the mass distribution was essentially identical in the two peaks, the data of both peaks were averaged and used for the subsequent calculation.

As the cell wall of *Chlamydomonas* does not contain cellulose, but consists of glycoproteins with arabinose, mannose, galactose and glucose (Harris, 2009), we checked a possible interference by cell wall materials in the starch analysis by finding non-glucose sugars in the GC-MS chromatogram, but we did not detect notable levels of pentoses and hexoses other than glucose. Accordingly, we can safely consider that the glucose that we analyzed was derived from starch, but not from other materials.

Isotopomer Analysis

Isotopomer analysis of glucose and fatty acids was performed essentially according to our original method using the C13dist software[1] (Sato et al., 2016). For technical details, see the Appendix of Sato et al. (2016). Actual procedure that was adapted for this study is explained in Results (section "Overall Design of Labeling Experiments") for readers unfamiliar with isotopomer analysis.

RESULTS

Overall Design of Labeling Experiments

We performed two types of labeling experiments: in the first series of experiments (**Figure 1A**), the cells of *C. debaryana* were grown under the standard autotrophic conditions, and the cells at 48, 96, and 144 h were photosynthetically labeled with [^{13}C]bicarbonate for 2 h, respectively. In the second series of experiments (**Figure 1B**), the cells grown for 72 h after inoculation was labeled with [^{13}C]bicarbonate for 5 h under standard growth conditions. The sample at this point was called "L5h." After washing, the cells were resuspended in fresh medium and then allowed to grow for further 4 days. Samples were taken at 1, 2, and 4 days, and named "C1d," "C2d," and "C4d," respectively. Similar labeling and chase experiments were performed with [2-^{13}C]acetate.

Starch was transmethylated to 1-methyl glucose, which was then analyzed by GC/MS as trimethylsilyl ether. Individual classes of lipids were isolated by 2D-TLC, and then the component fatty acids were analyzed by GC-MS as FAMEs. Two types of data were obtained from these analyses: first, the amounts of glucose or fatty acids were quantified using internal standard. Second, mass distribution of molecular or high-intensity ion was determined for isotopomer analysis (see **Figure 2** as examples). Methyl glucoside was analyzed as TMS derivatives, and the fragment m/z = 361 retaining all six carbons with four TMS groups was used for isotopomer analysis (**Figure 2A**). Two isomeric peaks were found in the GC/MS analysis, but both peaks were used for the calculation because they gave similar mass spectra with respect to the fragment that we focused on. For FAMEs, molecular ion was used for isotopomer analysis (**Figure 2D**), except for monoenoic FAMEs, in which the pair of fragments $(M-31)^+$ and $(M-32)^+$ were used for the analysis, because their intensities were higher than that of the molecular ion. In all cases, isotopomer distribution was estimated from the raw mass spectrum by the C13dist software (**Figure 2**, panels B and E). For the technical details of the program, see Appendix in Sato et al. (2016). We also calculated isotopic abundance (p) distribution using the band model (the model 4 in the mode 5 in the C13dist software), namely, we created a step-wise model of p-distribution that best simulates the actual isotopomer distribution. We used four steps plus unlabeled population (five variables in total) for the analysis of glucose, and 14 steps plus unlabeled population (15 variables in total) for the analysis of C16 and C18 fatty acids. The selection of number of steps depended on the number of carbon atoms (n). The degree of freedom of the isotopomer data was $n + 1$. Least square fitting requires that the number of variables should be less than $n + 1$. This was the reason why the number of steps was different in glucose and fatty acids.

In this way, we were able to distinguish high-p population and unlabeled (p = 0.0108, natural abundance or *NA*) population in glucose (**Figure 2C**). Likewise, in fatty acids, we identified high-p population (purple in **Figure 2F**), as well as low-p population (gray) and very-low-p population (light gray) within the labeled pool of molecules. Mid-p population (red) was also found in particular cases (see below). The isotopomers 0, 1, and 2 in **Figure 2E** seemed to be a part of unlabeled molecules (with natural abundance) at a glance, but the amounts of isotopomers 1, 2, and 3 were higher than in the authentic unlabeled molecules. This gives the gray peaks (with low p values) in **Figure 2F** after fitting with the band model.

The p value is an intrinsic value of average ^{13}C abundance in the respective pool of molecules. Namely, the pools with different values of p represent different pools. Such distinction is an advantage of using a stable isotope, which is not possible in radiolabeling experiments. Note, however, not all levels in the p-distribution graph represent different pools. The 5 or 15 levels were used to maximize the resolution of p. Metabolically meaningful pools were identified by the dynamics of individual populations assigned to the levels.

Lipid Profile in Exponential and Stationary Growth Phases

The amounts of starch and lipids in exponentially growing cells (48 h), and early (96 h) and late (144 h) stationary phase cells are shown in **Figures 3A,B**, respectively. Note that the starch data also include labeling results, which will be a topic in later sections. The cellular contents of both starch and lipids increased in the stationary phase. Proportion of individual lipid classes did not change markedly, except extensive accumulation of TAG in the late stationary phase. Other major

[1]http://nsato4.sakura.ne.jp/old/C13dist.html

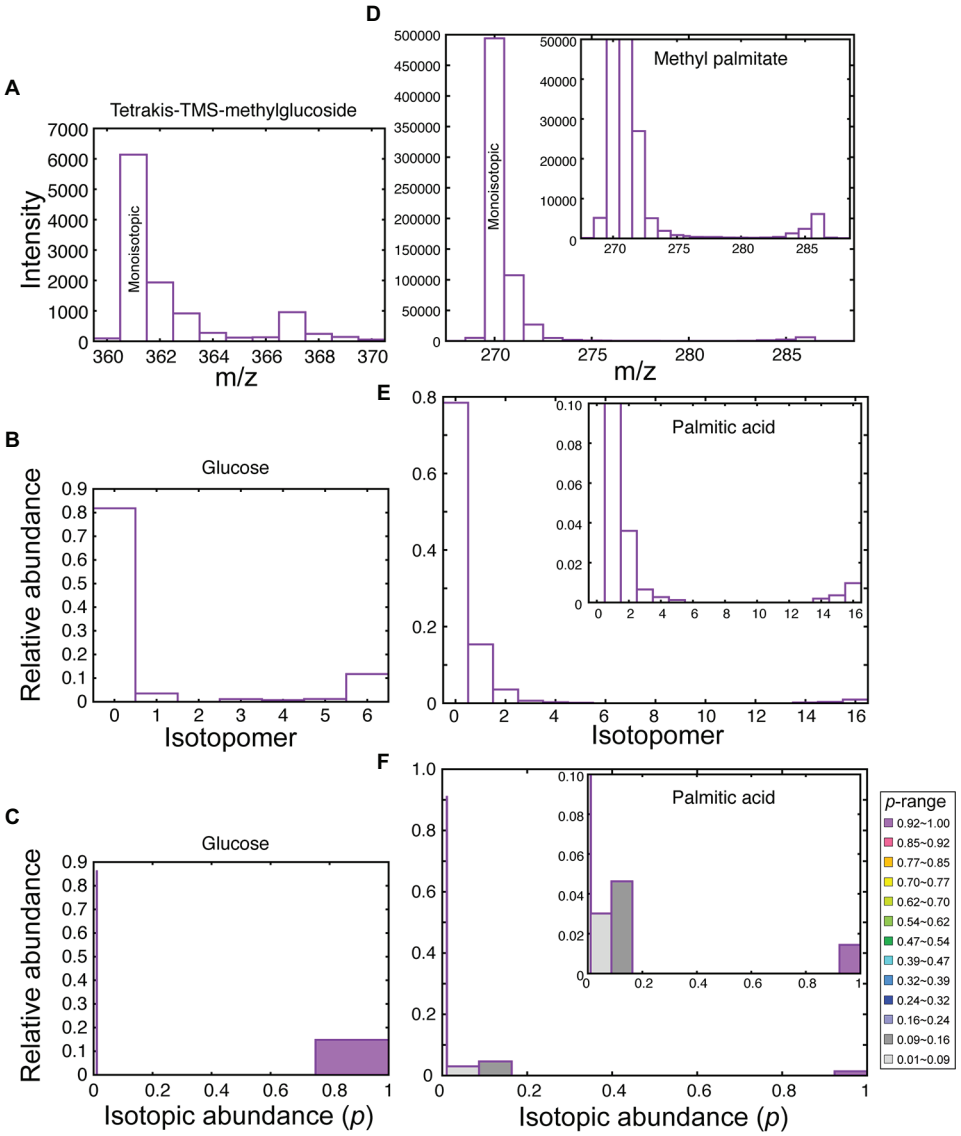

FIGURE 2 | Data processing in isotopomer analysis. **(A)** Mass spectrum of the fragment ion having the monoisotopic *m/z* = 361 from tetrakis (TMS) methylglucoside (from starch after 2-h labeling with [^{13}C]bicarbonate at the exponential growth phase, 48 h after innoculation). **(B)** Isotopomer distribution of glucose. **(C)** Distribution of isotopic abundance, estimated according to the band model of C13dist software, using four steps having the width of 0.247 plus the natural abundance (p = 0.0108) population. **(D)** Mass spectrum of the molecular ion of methyl palmitate (from TAG after 5-h labeling with [^{13}C]bicarbonate followed by 4 days chase). **(E)** Isotopomer distribution of palmitate. **(F)** Distribution of isotopic abundance, estimated according to the band model, using 14 steps having the width of 0.0707 plus the natural abundance population. Inset in **(D–F)** shows an enlargement.

lipid classes were: monogalactosyl diacylglycerol (MGDG), sulfoquinovosyl diacylglycerol (SQDG), digalactosyl diacylglycerol (DGDG), phosphatidylglycerol (PG), phosphatidylinositol (PI), phosphatidylethanolamine (PE), diacylglyceryl-*N,N,N*-trimethylhomoserine (DGTS), and PC.

Figure 4 shows a heat-map representation of a concise overview of fatty acid composition in individual lipid classes in exponential (panel A: 48 h after inoculation) and stationary (panel B: 144 h after inoculation) growth phases. Major fatty acids were myristic (14:0), palmitic (16:0), hexadecenoic (16:1), oleic [18:1(9)], linoleic [18:2(9,12)], and α-linolenic [18:3(9,12,15)] acids in most lipid classes. MGDG also contained unsaturated C16 acids, such as 16:2, 16:3, and 16:4. Pinolenic [18:3(5,9,12)] acid was enriched in DGTS and PE. In the stationary phase, highly accumulated TAG contained 16:0, 16:1, 18:1(9) and 18:2, as well as various minor fatty acids found in polar lipids. Fatty acid profiles of other lipid classes were more or less similar in the exponential and stationary phases.

The analytical results of the lipid and fatty acid compositions were consistent with the results presented earlier in *C. debaryana* (Toyoshima and Sato, 2015, 2018; Yoshitomi et al., 2020).

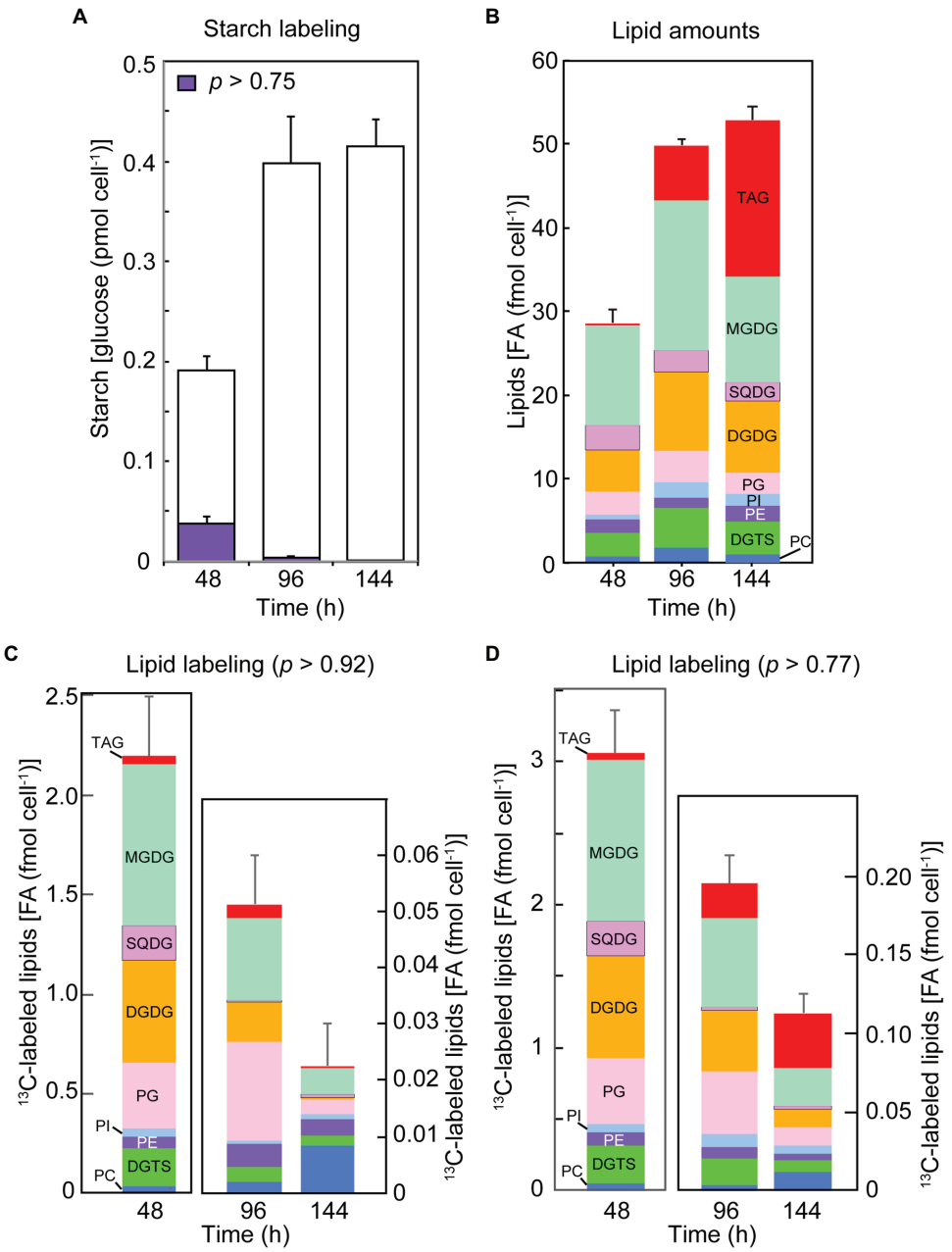

FIGURE 3 | The contents of total and labeled fractions of starch and lipids after the labeling for 2 h with sodium [^{13}C]bicarbonate at different growth stages. **(A)** The amounts of total and labeled ($p > 0.75$) fraction of starch. White bars show unlabeled glucose, while purple bars show labeled glucose. **(B)** The amounts of lipid classes. **(C)** The amounts of labeled lipids ($p > 0.92$). **(D)** The amounts of labeled lipids ($p > 0.77$). Lipid classes are color-coded. Each value represents the mean ± SE of three independent experiments.

De novo Synthesis of Starch and Lipids

To measure the rate of *de novo* synthesis of starch and lipids, the cells of *C. debaryana* at different times of growth were allowed to incorporate ^{13}C photosynthetically from sodium [^{13}C]bicarbonate ($p = 0.99$) for 2 h (**Figures 3A,C,D**). In the labeling experiments with bicarbonate, the distribution of p was estimated from the observed isotopomer distribution.

In both exponential growth phase (48 h after inoculation) and early stationary growth phase (96 h), we found two populations of glucose in starch, one with ^{13}C at the natural abundance level (1.08% or *NA*) and another labeled with ^{13}C peaking at an average $p = 0.97$–0.98 ($p > 0.75$ in the four-step grading in the band model, but the actual distribution of p was also estimated by the C13dist program using the

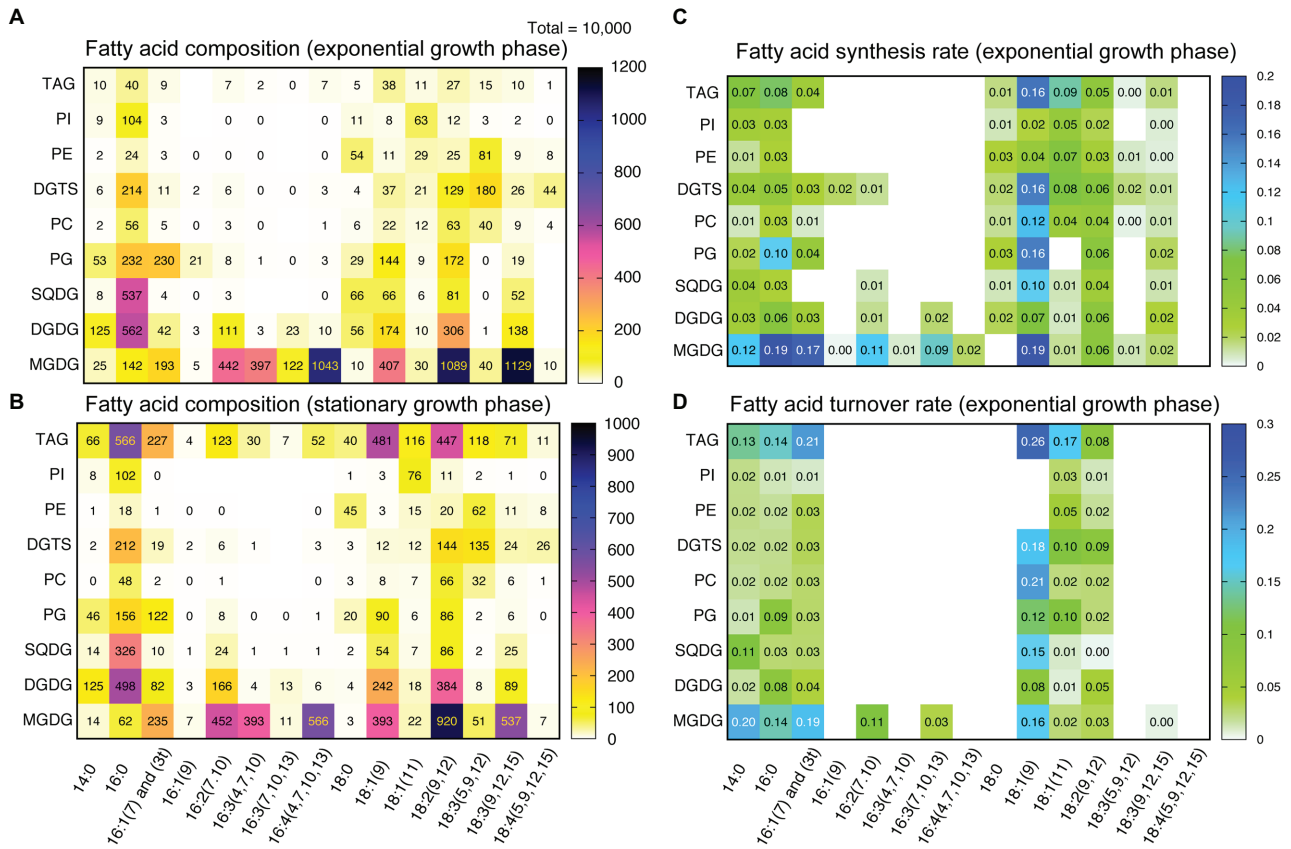

FIGURE 4 | Fatty acid composition and fatty acid turnover rates in individual lipid classes. **(A)** Fatty acid composition of lipid classes in the exponential growth phase (48 h). **(B)** Fatty acid composition of lipid classes in the stationary growth phase (144 h). **(C)** Fatty acid synthesis rates of individual lipid classes. The rates (in h^{-1}) were calculated for the data of 2-h labeling and 5-h labeling with [^{13}C]bicarbonate according to **Supplementary Material** and averaged. **(D)** Fatty acid turnover rates of individual lipid classes calculated for the chase data after the labeling with [^{13}C]bicarbonate according to **Supplementary Material**. In **(A,B)** contents of fatty acids are normalized by setting the amount of total fatty acids (of all lipid classes) to 10,000.

average model), which represented *de novo* synthesis resulting from photosynthetic carbon fixation (**Figure 3A**). As described already, we used the band model with five variables (four steps and an unlabeled population) for quantitation of differently labeled populations. In the 2-h labeling experiments, only the unlabeled and the high-p ($p > 0.75$) populations were observed. The labeled population amounted to 19.9% of glucose in starch in the exponential phase, but lowered in the early and late stationary phases (96 and 144 h) to 1.1 and 0.1%, respectively. This indicated a drastic decrease in photosynthetic starch production in the stationary phase. However, high-level accumulation of starch in the stationary phase suggested that starch could be synthesized from existing carbon source within the cell.

Lipid synthesis rate was estimated as the rate of ^{13}C incorporation into component fatty acids. We determined the proportion of ^{13}C abundance populations (14 steps plus the *NA* level, as shown in **Figure 2F**) in all major fatty acids in individual lipid classes, and summed the amount of each population over all these fatty acids. In this way, we present here the amount of labeled lipids with $p > 0.92$ and $p > 0.77$ during the 2-h labeling time (**Figures 3C,D**, respectively). The population with $p > 0.92$ represents the product of *de novo* photosynthesis, whereas the population with $0.77 < p \leq 0.92$ could result from a mixed precursor pool with photosynthates (with a high p value) and recycled carbon (with ^{13}C at the *NA* level). The amounts of labeled population of lipids estimated by the two criteria were similar in the exponential phase, whereas the two values differed considerably in the early and late stationary phases, suggesting that lowered rates of photosynthesis (more than about 10-fold in **Figure 3D**) resulted in imperfect incorporation of labeled carbon into long-chain fatty acid products.

In the exponential phase, the composition of labeled lipids was similar to the composition of lipids accumulated at that time. This suggests that all classes of lipids were synthesized in parallel by the supply of newly synthesized fatty acids. In the stationary phase, especially at 144 h, the labeling of chloroplast lipids, such as MGDG, DGDG, and SQDG, was drastically decreased, whereas the labeling of

PE and PC dominated. This could represent acyl recycling rather than *de novo* synthesis of the phospholipids. The *de novo* synthesis of TAG ($p > 0.92$; **Figure 3C**) also lowered in the stationary phase, but the relative activity of TAG synthesis became higher in the population with $p > 0.77$ (**Figure 3D**), suggesting that both new and recycled carbons contributed to the production of TAG.

The rates of synthesis of fatty acids in individual lipid classes were estimated from the results of labeling for 2 and 5 h (**Figure 4C**). The data of 5-h labeling were taken from the pulse-chase experiments described in the next section. Two major features are apparent: first, oleic acid [18:1(9)] was rapidly synthesized and incorporated into many classes of lipids, such as MGDG, PG, DGTS, PC, and TAG. Second, both C16 and C18 fatty acids in MGDG were rapidly synthesized. Unsaturated fatty acids, such as 16:1(7), 16:2(7,10), 16:3(7,10,13) and 18:2(9,12) were also labeled rather rapidly, suggesting that the desaturation of both C16 and C18 acids proceeds rapidly. This was consistent with the observation that the pools of desaturation intermediates were small (**Figure 4A**).

An interesting point to note is that DGDG was labeled efficiently in the exponential growth phase. This was evident in the amount of labeled DGDG as a whole (**Figure 3C**) and in the synthesis rates of various fatty acids in DGDG (**Figure 4C**). The distribution of labeled fatty acids in DGDG was similar to that of MGDG except that the labeling rate was about 1/3. This is a curious observation that we never found in other photosynthetic organisms, and will be discussed later.

Labeling and Chase Experiments: Overview

The flow of carbon in starch and TAG was analyzed by pulse-labeling for 5 h and chase for 4 days. Both sodium [^{13}C] bicarbonate and sodium [2-^{13}C]acetate were used in the labeling. Bicarbonate was expected to be incorporated into all organic compounds, whereas acetate was expected to be mainly incorporated into fatty acids. Here, the results with bicarbonate will be analyzed in detail, because the resolution of isotopomer analysis was limited in the acetate labeling experiments (note that a fatty acid is composed of C2 units resulting from acetate, and only one of two carbons are labeled). The results with acetate were mainly used to confirm the results with bicarbonate.

In the [^{13}C]bicarbonate experiments, the content of high-p starch ($p > 0.75$) decreased significantly during the chase period, whereas the content of total starch increased (**Figure 5A**). In the [2-^{13}C]acetate experiment, starch was not labeled to a significant level (**Figure 5B**). Namely, only a small proportion of starch glucose incorporated ^{13}C from acetate into the low-p population ($NA < p \leq 0.25$).

Figure 5C shows the amounts of variously labeled populations of lipids (exactly, their fatty acids) in the [^{13}C]bicarbonate experiments. The total amount of lipids is described on top of each bar. Note that the unlabeled population ($p = NA$) is not explicitly shown in the figure (it is obtained by subtracting the labeled amount shown by the height of the bar from the total amount described at the top). The total amount of differently labeled populations did not change with chase time, but the content of high-p lipids ($p > 0.92$, purple part at the top of each bar) significantly decreased during the chase time. In contrast, the content of very low-p lipids ($NA < p \leq 0.16$, the light gray and gray parts at the bottom of each bar) increased with time. This could reflect a dynamic turnover, either conversion of starch to lipids or degradation and re-synthesis of lipids, during the chase time. Comparable results were obtained in the experiments with [2-^{13}C]acetate. Namely, high-p lipids ($p > 0.84$, top part in purple of each bar) decreased while low-p lipids ($NA < p \leq 0.18$, bottom part in gray of each bar) increased (**Figure 5F**). Note that six steps of populations plus the unlabeled population was used in the analysis after [2-^{13}C]acetate labeling, which restricted resolution of populations with different p-values. The results with acetate had to be understood within the framework of degradation and re-synthesis of lipids, because starch was not likely to act as a high capacity source with a high-p value (**Figure 5B**).

Labeling and Chase Experiments: Bicarbonate Labeling

In the bicarbonate-labeling experiments, the rapid decrease of highly labeled starch and fatty acids (primary products of photosynthesis) during the chase period, and the concomitant increase of low-p population of fatty acids suggest that the degraded starch and fatty acids could be recycled in the synthesis of fatty acids. The carbon flow of re-synthesis must be fairly large. Judging from the data in **Figure 5C**, 6.65 fmol cell^{-1} (60%) of highly labeled fatty acids within the total of 11.09 fmol cell^{-1} were degraded within a day, and 5.27 fmol cell^{-1} (equivalent to 79% of the degraded fatty acids) poorly labeled fatty acids were re-synthesized. In the re-synthesis, only a small part (less than 10%) of carbon resulting from degradation of highly labeled fatty acids must be used because the p value of re-synthesized fatty acids was quite low (about 0.1). In other words, one part of carbon originating from degraded fatty acids (plus starch) is mixed with nine parts of newly fixed carbon to form a poorly labeled population with $p = 0.1$, which was used in *de novo* synthesis of fatty acids again.

The time course of changes in labeled population was analyzed kinetically. According to the theoretical treatment described in **Supplementary Material**, each time course consisting of a triplicate was fitted with a linear combination of two exponentials. The coefficients in the two exponents represented time constants of rapid and slow components, respectively. The slow components having k values of about 0.01–0.02 were likely to represent net degradation. The major decay rate k of starch (purple fraction) was 0.0759 ± 0.0285 h^{-1} (**Figure 6A**, average ± SE), while that of fatty acids (purple fraction) was 0.135 ± 0.067 h^{-1} (**Figure 6B**). Similar analysis was performed for each major fatty acid in individual lipid classes, but statistically meaningful results ($n = 3$) were obtained only for the fatty acids that

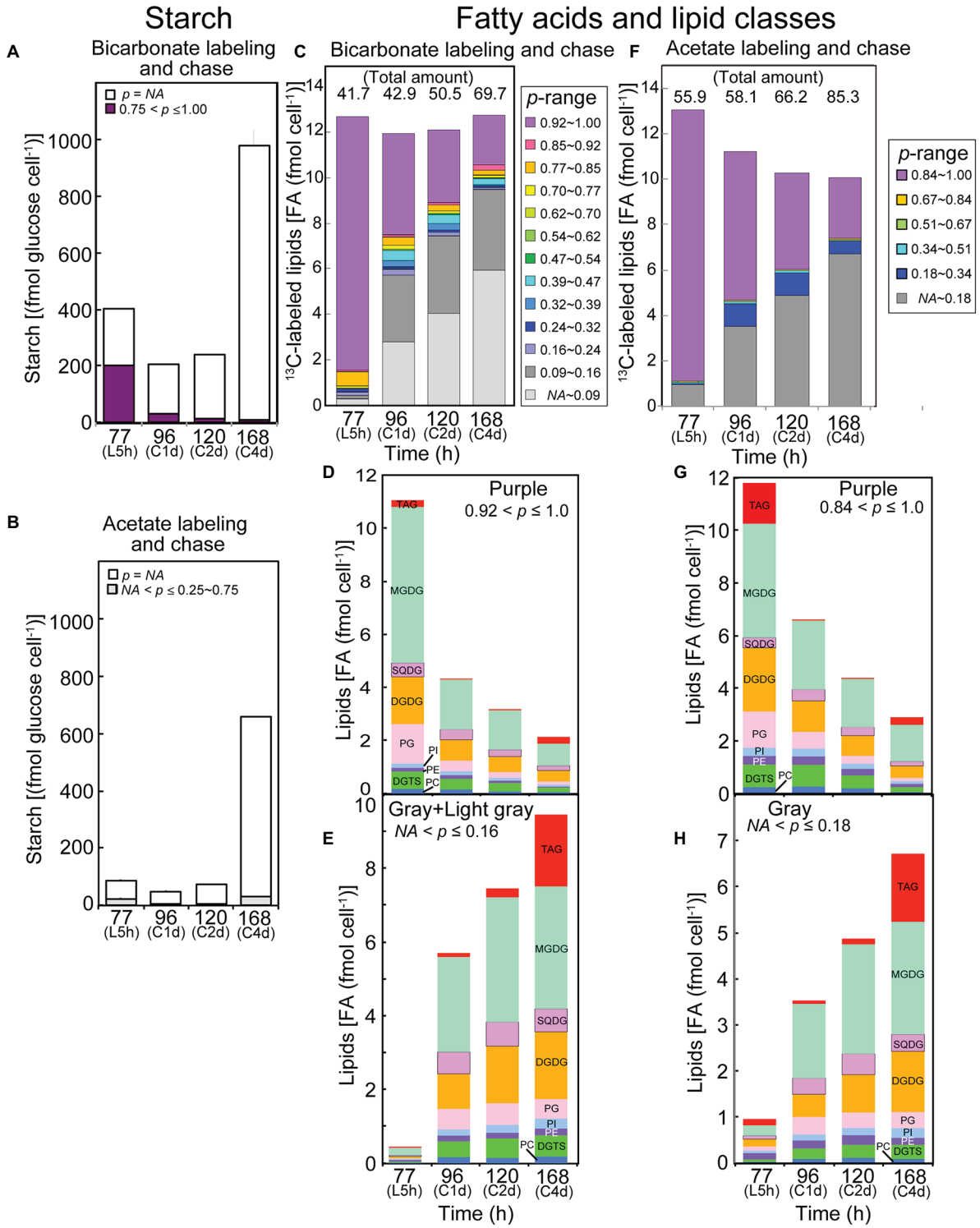

FIGURE 5 | Analysis of labeled starch and lipids in the labeling and chase experiments with [^{13}C]bicarbonate and [2-^{13}C]acetate. **(A,C–E)** Bicarbonate labeling; **(B,F–H)** Acetate labeling. **(A,B)** Labeled and unlabeled starch. **(C,F)** Composition of isotopic abundance populations in total fatty acids. The amount of total lipids (as labeled plus unlabeled fatty acids) is shown on top. **(D,G)** Amounts of highly labeled lipid classes [purple population in **(C,F)**, respectively]. **(E,H)** Amounts of low-*p* lipid classes [gray + light gray, or gray populations in **(C,F)**, respectively]. Note that the number of steps in isotopic abundance is different in bicarbonate labeling and acetate labeling, because the maximum number of labeled carbons is different in the two experiments.

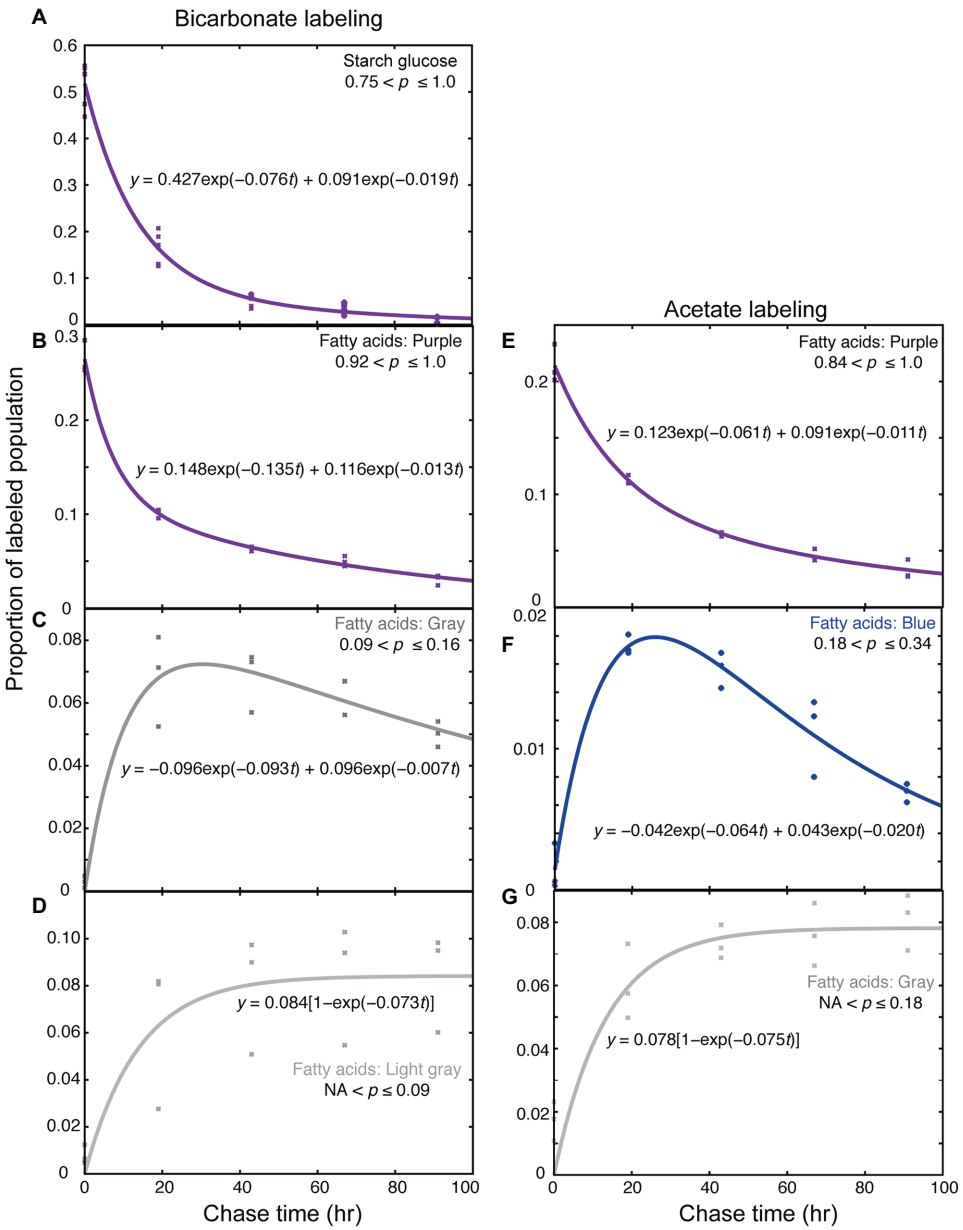

FIGURE 6 | Kinetic analysis of labeled populations during the chase. **(A–D)** Labeling with [^{13}C]bicarbonate. **(E–G)** Labeling with [2-^{13}C]acetate. **(A)** Starch glucose; **(B–E)** Highly labeled fatty acids; **(C)** Low-*p* (gray population) fatty acids; **(D)** Very low-*p* (light gray population) fatty acids; **(F)** Mid-low-*p* (blue population) fatty acids; and **(G)** Low-*p* (gray population) fatty acids. Kinetic analysis was performed with the R software according to **Supplementary Material**.

have incorporated high level of ^{13}C during the 5-h labeling. The decay rates of purple fraction (**Figure 4D**) were: 16:0 in MGDG: k = 0.138 ± 0.016, 18:1 in MGDG: k = 0.159 ± 0.371, 18:1 in DGDG: k = 0.083 ± 0.034, 18:1 in SQDG: k = 0.151 ± 0.027, 18:1 in PG: k = 0.122 ± 0.005, and 18:1 in DGTS: k = 0.182 ± 0.066. **Figure 4D** shows all values estimated in this way, including values with large estimated SE. Note that the labeling kinetics of 16:0 and 18:1 includes synthesis, desaturation, and degradation, but desaturation is compensated within total fatty acids. Therefore, the labeling kinetics of total fatty acids consists of only synthesis and degradation, and is simpler to analyze. Nevertheless, the turnover rates of fatty acids in individual lipid classes were roughly consistent with the corresponding synthesis rates (**Figure 4C**), supporting that the assumption of steady-state kinetics was applicable.

The increase rate of the gray ($0.09 < p \leq 0.16$) population of fatty acids (0.093 ± 0.040 h^{-1}, **Figure 6C**) and that of the light gray ($NA < p \leq 0.09$) population of fatty acids (0.073 ± 0.035 h^{-1}, **Figure 6D**) were similar, suggesting that both of these two populations were synthesized partially using the carbon supplied by degraded starch ($k = 0.075$) rather than degraded fatty acids ($k = 0.135$). Because the increase rates for fatty acids were an average of all fatty acids of total lipids, this does not exclude a possibility that a specific pool of fatty acids could supply materials for *de novo* fatty acid synthesis yielding the gray and light gray populations of fatty acids.

Labeling and Chase Experiments: Acetate Labeling

In the case of acetate labeling, too, we can calculate the carbon flow of re-synthesis. Using the data in **Figure 5F**, 5.39 fmol cell^{-1} (45%) of highly labeled fatty acids within the total of 11.93 fmol cell^{-1} were degraded and re-synthesized as 3.50 fmol cell^{-1} (equivalent to 65% of the degraded fatty acids) poorly labeled fatty acids. The proportion of re-synthesis is estimated to be lower than that in the bicarbonate labeling experiments, but, we can still imagine that a large fraction of newly synthesized fatty acids were degraded and re-used for the synthesis of fatty acids.

Kinetic analysis of the fatty acid labeling with [^{13}C]acetate was performed in a similar way (**Figures 6E–G**). The decrease of the high-p population (purple; $0.84 < p \leq 1.0$) consisted of two components, namely, rapid decay ($k = 0.061 \pm 0.030$) and slow decay ($k = 0.011 \pm 0.008$; **Figure 6E**). The kinetics of the blue population ($0.18 < p \leq 0.34$) was biphasic, consisting of increasing ($k = 0.064 \pm 0.025$) and decreasing ($k = 0.020 \pm 0.006$) components (**Figure 6F**). The increase rate of the gray population ($NA < p \leq 0.18$) was $k = 0.075 \pm 0.022$ (**Figure 6G**). These rate constants were roughly consistent with the corresponding rate constants obtained with [^{13}C]bicarbonate labeling. However, the rapid decrease rate of the high-p (purple) population was significantly higher in the bicarbonate labeling than in the acetate labeling. The difference in the p-range definition of the "purple" population in the two experiments ($0.84 < p \leq 1.0$ in acetate labeling, and $0.92 < p \leq 1.0$ in bicarbonate labeling) was not a reason, because the proportion in the "red" population ($0.85 < p \leq 0.92$) was quite low in bicarbonate labeling. An explanation might be that the high concentration (20 mM) of bicarbonate was a good carbon source to support (or activate) cell metabolism, whereas acetate was a poor carbon source, at least in photoautotrophically grown cells. Accordingly, lipids and starch were synthesized in excess during the labeling with bicarbonate (see the total amounts in **Figures 5A**,**C**), and then degraded after the shift to normal growth condition with 1.0% CO_2 to attain a steady state. Except this initial rate, the flow of carbon in the low-p populations of fatty acids was consistent in both acetate and bicarbonate labeling experiments.

Labeling and Chase Experiments: Lipid Classes

Dynamics of lipid labeling was analyzed in individual lipid classes in both bicarbonate labeling (**Figures 5D**,**E**) and acetate labeling (**Figures 5G**,**H**). **Figure 5D** shows the amounts of fatty acids of high-p population (purple in the bar graphs of fatty acid labeling) in lipid classes. The results were qualitatively similar to those in 2-h labeling (**Figure 3C**), but the proportion of labeled MGDG was higher in **Figure 5D**. The high-p population with acetate labeling contained high proportion of TAG (**Figure 5G**), although the composition of other lipid classes was similar to that in **Figure 5D** (bicarbonate labeling for 5 h). This suggests that TAG synthesis was stimulated by the supply of high concentration of acetate (20 mM).

During the following chase period, all classes of lipids lost the high-p population more or less similarly, except that the labeled TAG that accumulated during the labeling was lost rapidly, and accumulated in the stationary phase again (**Figures 5D**,**G**). Conversely, the low-p population of fatty acids accumulated in all lipid classes during the chase period (**Figures 5E**,**H**). The accumulation pattern was similar in bicarbonate and acetate labeling. In the stationary phase, accumulation of TAG was marked.

Figure 7 shows changes in the isotopic abundance distribution of polar lipids and TAG after the labeling with bicarbonate and chase. The changes in polar lipids (**Figure 7A**) were similar to those in total lipids (**Figure 5C**), but we noted a decrease in labeled population with concomitant increase in the total polar lipids (including unlabeled lipids) in the stationary phase (48–53 fmol cell^{-1} from 120 to 168 h; **Figure 7A**). High-level accumulation of TAG was found in the stationary phase (16.5 fmol cell^{-1}), and labeled population accounted for 2.4 fmol cell^{-1}, about 80% of which consisted of populations with $NA < p \leq 0.16$. The net increase in unlabeled fatty acids (14.1 fmol cell^{-1}) in TAG was accounted for by *de novo* synthesis. Interestingly, high-p population (purple) was found in 16:0, 18:2, and 18:3 in TAG (**Figure 7D**). Very low-p population (light gray) was abundant in 18:1 and 16:1. This suggests that labeled 16:0, 18:2 and 18:3 were mobilized from polar lipids (compare **Figures 7C**,**D**) to TAG, whereas the labeled 18:1 and 16:1 in TAG were products of re-synthesis from carbons recovered from degraded labeled fatty acids with newly fixed carbons or internal unlabeled carbon source.

Figure 8 shows composition of labeled populations in individual lipid classes in the bicarbonate-labeling experiments, namely, a decomposition of the data in **Figure 7A**. Clearly, the chloroplast lipids, MGDG, DGDG, SQDG, and PG contained the major part of high-p population (purple) of fatty acids after the 5-h labeling. The high rate of labeling of DGDG will be discussed later. Decrease in the high-p population and increase in low-p populations (gray and light gray) were found in all lipid classes during the chase. The net decrease in labeled fatty acids in MGDG and PG during the first day of chase was counter-balanced by the increase in labeled fatty acids in PC, DGTS, PE, PI and SQDG. Interestingly, the population shown in red corresponding to $0.85 < p \leq 0.92$ appeared at significant levels in PE after the first day of chase. This was, in fact, concentrated in 18:0 (**Figure 9C**).

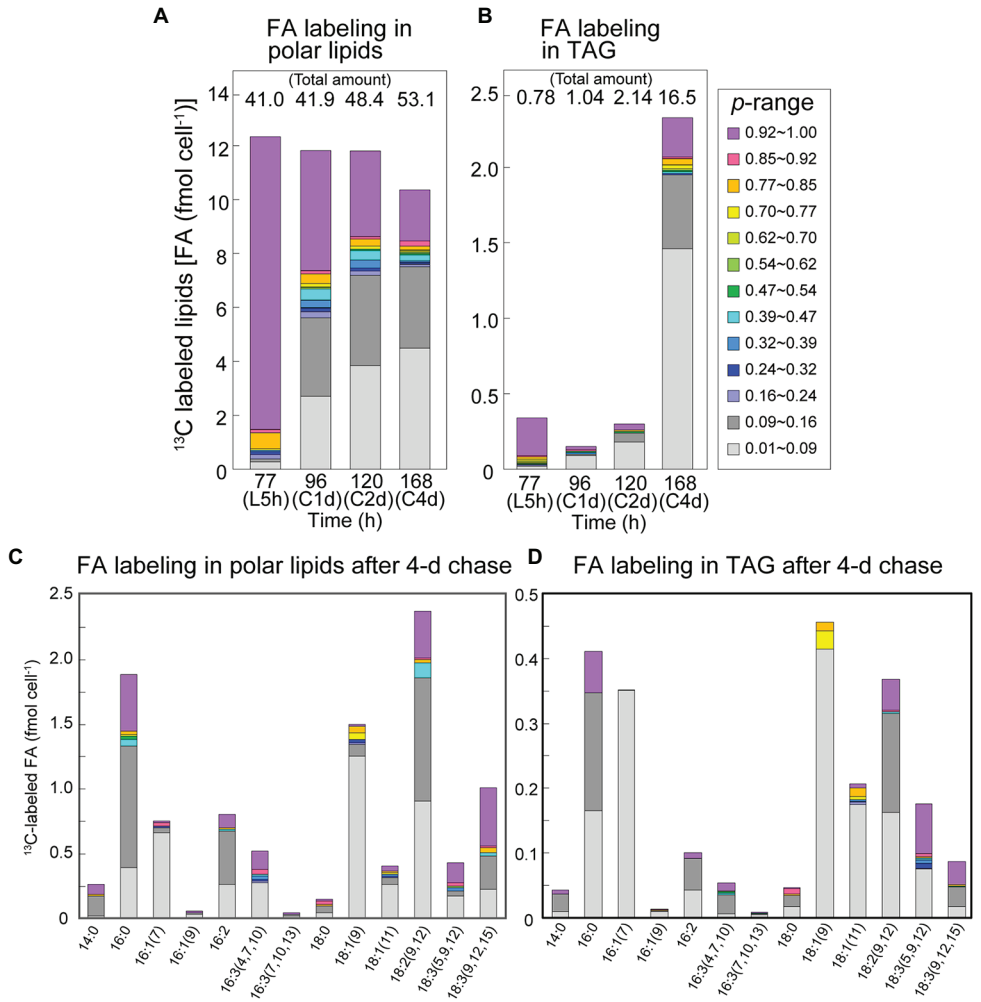

FIGURE 7 | Fatty acid labeling in polar lipids and TAG in the [^{13}C]bicarbonate labeling and chase experiments. **(A)** Composition of isotopic abundance populations in the fatty acids of polar lipids. **(B)** Composition of isotopic abundance populations in the TAG fatty acids. Total amount of lipids (as fatty acids) is shown on top. **(C)** Composition of labeled populations of fatty acids in polar lipids after the chase for 4 days. **(D)** Composition of labeled populations of fatty acids in TAG after the chase for 4 days.

Figure 9 shows labeled populations in saturated fatty acids and oleic acid. The composition of labeled populations in stearic acid (18:0) was quite different from that of other fatty acids. Namely, the proportion of purple population ($0.92 < p$) was lower (6.1% of total 18:0) and the proportion of gray population ($0.09 < p \leq 0.16$) was higher (11.3% of total 18:0) compared with other saturated fatty acids after the labeling with [^{13}C]bicarbonate for 5 h (**Figure 9A**). After the chase for first day onwards, the purple population diminished, whereas the red population ($0.85 < p \leq 0.92$) as well as the gray population became abundant. Close examination of the isotopomer distribution (**Figure 9B**) showed that the isotopomer containing 16 atoms of ^{13}C appeared after the chase, which represented the red population. The red population persisted until the fourth day of chase. As shown in **Figure 8C**, PE was the major lipid class that contained the red population of stearic acid. The red population ($0.85 < p \leq 0.92$) was only a minor component in all other fatty acids.

DISCUSSION

Methodological Advantage of Isotopomer Analysis

The present study was planned to exploit the possibility of stable isotope labeling in elucidating dynamism of carbon flux related to accumulation of starch and lipids. Detailed isotopomer analysis using C13dist software revealed both highly labeled population ($p > 0.92$) and low abundance population ($NA < p \leq 0.16$) in fatty acids. Labeling and chase studies showed distinct pools with differently labeled populations. The low abundance population is likely to result from degradation of highly labeled population and re-synthesis with about 9-fold excess of unlabeled, newly fixed carbon. The two substrates, bicarbonate and acetate, provided distinct but compatible information: namely, both starch and lipids were efficiently labeled with [^{13}C]bicarbonate, whereas only lipids were labeled significantly with [2-^{13}C]acetate. Bicarbonate

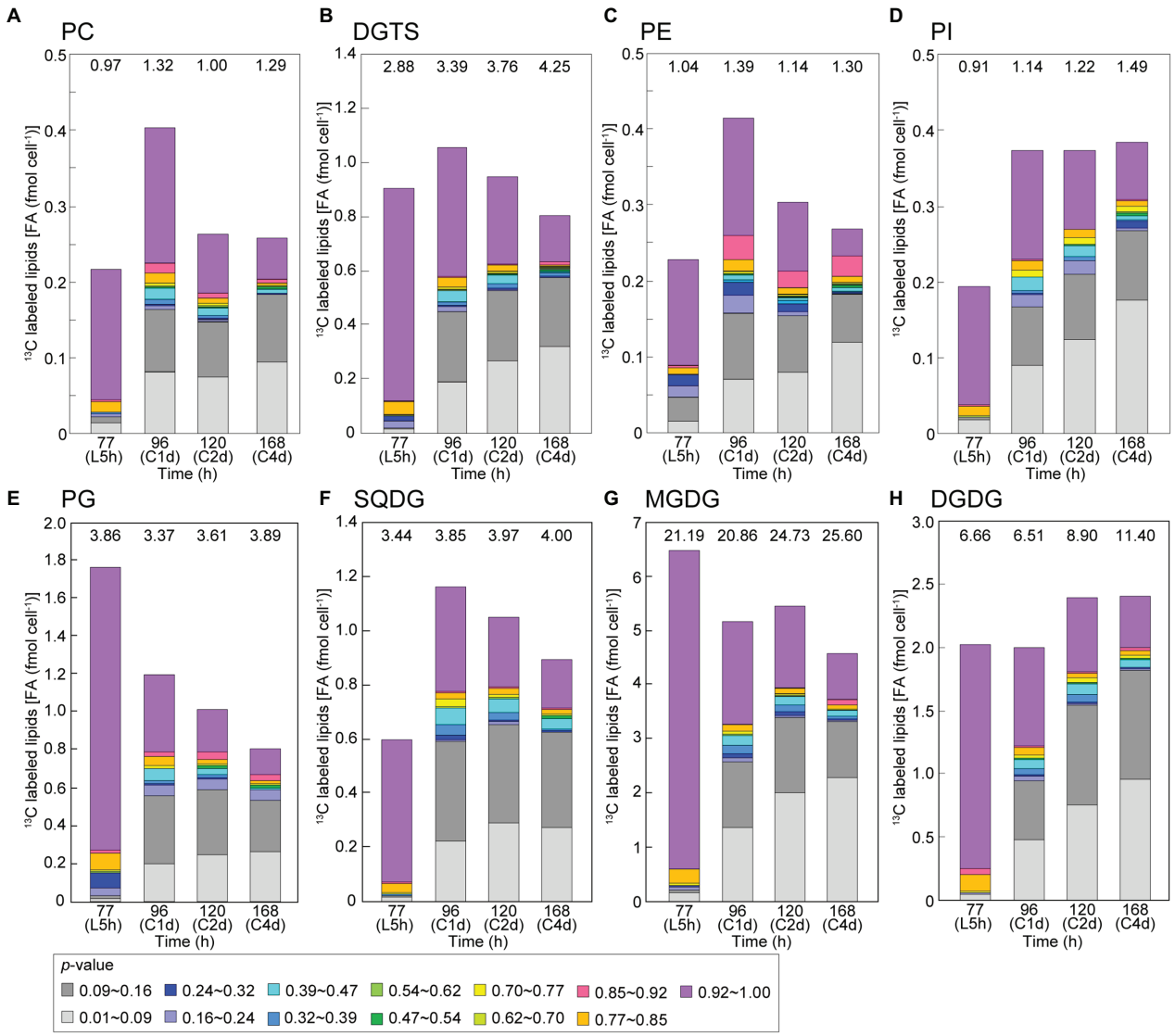

FIGURE 8 | Composition of isotopic abundance populations in the fatty acids in individual classes of polar lipids in the [^{13}C]bicarbonate labeling and chase experiments. **(A)** Phosphatidylcholine (PC); **(B)** diacylglyceryl-*N,N,N*-trimethylhomoserine (DGTS); **(C)** phosphatidylethanolamine (PE); **(D)** phosphatidylinositol (PI); **(E)** phosphatidylglycerol (PG); **(F)** sulfoquinovosyl diacylglycerol (SQDG); **(G)** monogalactosyl diacylglycerol (MGDG); and **(H)** digalactosyl diacylglycerol (DGDG). Total amount of lipids (as fatty acids) is shown on top.

is a good tracer for general metabolic flow, but acetate was useful in fatty acids labeling.

Turnover of Starch and Lipids: Labile and Stable Pools

Kinetic analysis suggested that both starch and TAG were subject to dynamic metabolism during both exponential and stationary growth phases. The turnover rate (kinetic constants of 0.075–0.135 h^{-1}, equivalent to half-lives of 9–5.1 h) was markedly higher than the growth rate (0.026 h^{-1} equivalent to a doubling time of 27 h). Abundant supply of ^{13}C-labeled substrate seemed to promote synthesis of starch and TAG, which were rapidly converted to other substances including fatty acids of polar lipids. Starch and fatty acids are different in metabolic turnover. Labeled starch is rapidly turned over, and no stable pool remained. In contrast, fatty acids also turned over rapidly to some extent, but a stable pool remained even after 4 days. The rapid and slow components in the kinetic analysis (**Figure 6**) represent labile and stable pools, respectively (**Figure 10**). This indicates that starch is present as a single pool, whereas different pools of fatty acids (in lipids) exist.

Close examination of the results of isotopomer analysis suggested that fatty acid synthesis seems to proceed using two carbon pools: the direct product of photosynthesis and the internal carbon pool resulting from degradation of fatty acids

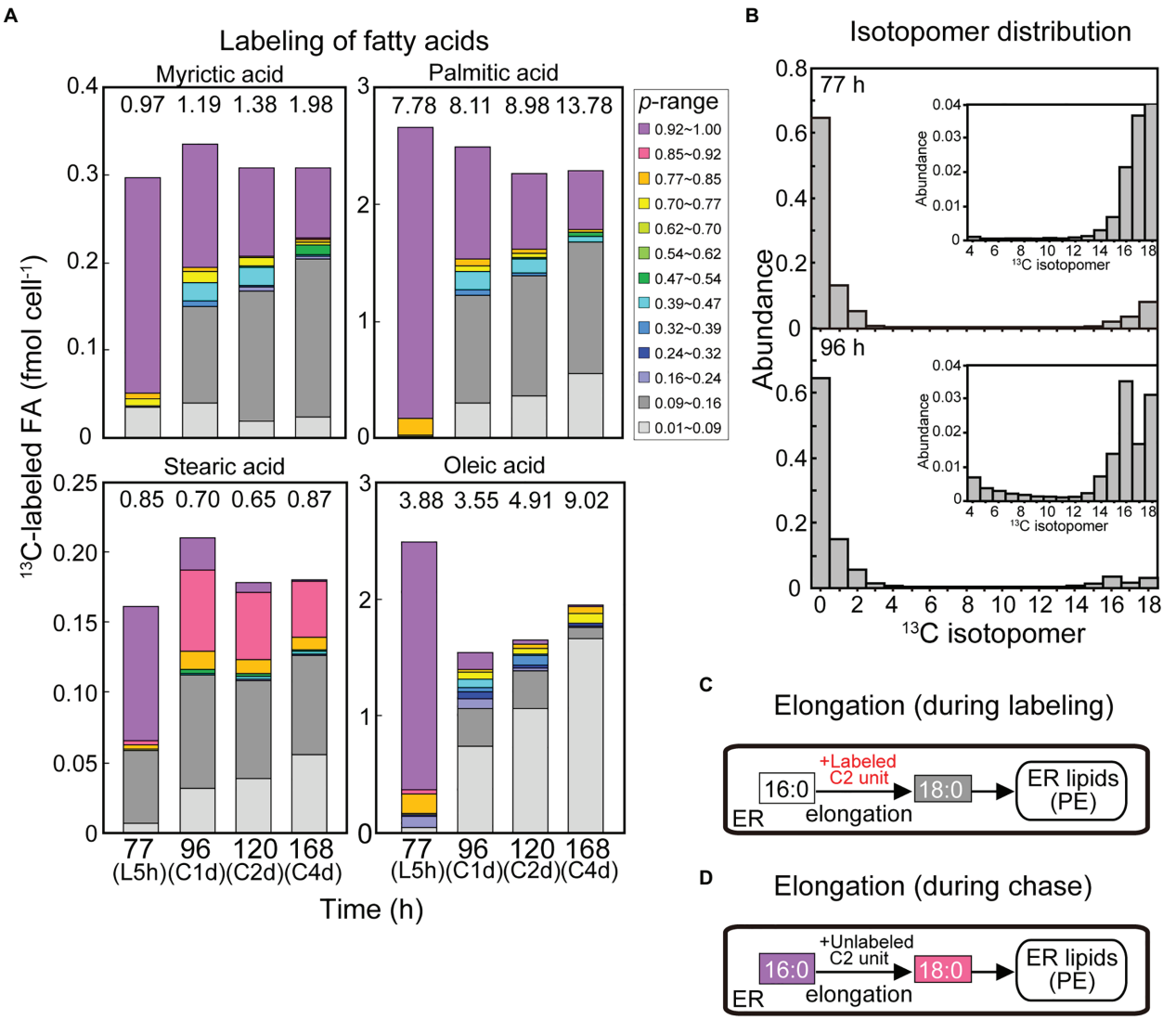

FIGURE 9 | Curious labeling pattern in stearic acid in the [^{13}C]bicarbonate labeling and chase experiments. **(A)** Composition of isotopic abundance populations in saturated fatty acids and oleic acid. **(B)** Isotopomer distribution of stearic acid after the labeling for 5 h and after the chase for 1 day. **(C,D)** Explanation of stearic acid labeling by elongation during the labeling **(C)** and the chase **(D)**.

and starch. Two lines of evidence support this view: The first was the presence of lipid population with $0.77 < p \leq 0.92$ (**Figure 3**, panels C and D) as pointed out previously (see section "*De novo* synthesis of starch lipids"). This suggests that newly fixed carbon is mixed with some internal carbon pool. Second, the conversion of the highly labeled population of fatty acids (shown in purple in **Figures 5, 8**) to the poorly labeled population (shown in gray and light gray) during the chase for 1 day showed a rapid turnover of newly synthesized fatty acids and re-synthesis. The degradation of highly labeled fatty acids results in highly labeled population of acetyl CoA, which is mixed with unlabeled acetyl CoA derived from photosynthetically produced glyceraldehyde 3-phosphate to re-synthesize fatty acids. This rapid remake is constantly functioning in this green alga. This is different from the situation in cyanobacteria that lack β-oxidation system (see Gclust database at http://gclust.c.u-tokyo.ac.jp/, Sato and Obayashi, 2021), in which highly labeled population of fatty acids remained stable for at least 1 day (Sato et al., 2016). The carbon flow of re-synthesis in *C. debaryana* must be fairly large, about 50% of the newly synthesized fatty acids were degraded within a day (see **Figure 10** for the sizes of labile and stable pools). Fatty acid synthesis and β-oxidation are likely to form a cycle to flexibly modulate the amounts of lipids and the fatty acid composition of lipids. This means that an excess of carbon source is rapidly compensated by the synthesis of fatty acids, which are then targeted to TAG. The following decrease in carbon supply accelerated degradation of TAG for the synthesis of

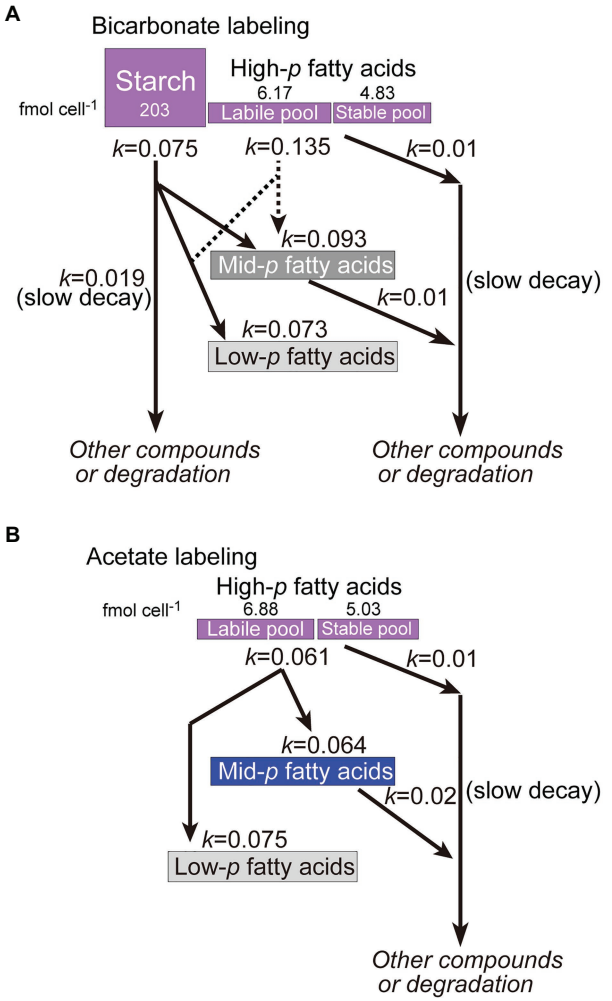

FIGURE 10 | Model of labeling and remodeling of starch and fatty acids as deduced from the labeling and chase experiments. **(A)** Bicarbonate labeling; **(B)** Acetate labeling.

other materials. This flexibility of fatty acid metabolism is a basis of TAG accumulation in the stationary growth phase.

Interestingly, however, not all labeled fatty acids were degraded during the 4 days of chase. About 20% of the initially synthesized, highly labeled population of fatty acids persisted as labeled 16:0 and other fatty acids (19.4% in **Figure 5C** for all fatty acids, and 20.2% in **Figure 9A** for 16:0). This suggests that there were two different pools of fatty acids: one (labile pool) that was subject to rapid turnover, and another (stable pool) that remained stable for a fairly long time. Curiously, only labile pool was found in oleic acid: namely, the highly labeled population of oleic acid disappeared within 2 days of chase, and replaced by a very low *p*-population. The decay kinetics of oleic acid consisted of a single component (k = 0.134 ± 0.008).

Various ideas can explain the two different pools of fatty acids, labile and stable ones. A rough estimate suggests that the stable pool consists about 40% of total newly synthesized lipids (**Figure 10**). An idea is the presence of different cell populations or cell differentiation. However, it is difficult to imagine that fatty acids are stable in some population of cells, because oleic acid is entirely labile. Another simple idea is that chloroplast lipids are more stable, because degradation of fatty acids takes place in the peroxisomes. Nevertheless, the data in **Figure 8** do not support this idea. Stable fatty acid pool is found in all classes of lipids. Stable fraction was found in 16:0, 18:2, 18:3(5,9,12) and 18:3(9,12,15). Another idea is that the stable lipids are localized to special sites. Alternatively, stable lipids are bound to membrane proteins. We might be able to explain the data by just assuming that some fraction of newly synthesized fatty acids are rapidly degraded and recycled, and some other fraction became stabilized. Mathematical modeling could be useful to check this metabolic dynamism in the future.

Metabolic relationship between starch and TAG has been studied in *C. reinhardtii* (Siaut et al., 2011; Singh et al., 2014; Smith and Gilmour, 2018). Because *C. reinhardtii* accumulates TAG only under nitrogen deprivation in these studies using Tris-acetate medium, acetate was also used for starch synthesis. This is an important difference from the present study, in which no nitrogen deprivation was imposed. As described above, acetate was a poor substrate for starch synthesis in *C. debaryana* under the nutrient replete condition. The relationship between starch and TAG could be different in the two species of *Chlamydomonas*. Siaut et al. (2011) did not find clear correlation between starch and TAG accumulations in various strains and mutants. This is consistent with our inability to provide evidence that starch is a direct precursor to TAG. Smith and Gilmour (2018) found a diurnal change in starch synthesis in the light period in the 12-h light/12-h dark cycles. Our findings suggest that starch is rapidly turned over even in the light. Therefore, the balance between synthesis and degradation, as well as nitrogen availability, should be important in evaluating the data in light/dark experiments. Singh et al. (2014) used ^{13}C-NMR for analyzing the fate of ^{13}C, supplied as [^{13}C]acetate or [^{13}C]bicarbonate. An important conclusion from the study was that acetate is degraded to bicarbonate/CO_2^{aq} before incorporation into TAG. This is not consistent with our data, showing that acetate is directly used in TAG synthesis (**Figure 5G**). If [2-^{13}C]acetate that we used were once degraded to inorganic carbon, then the synthesized fatty acids would have a different isotopomer distribution. Namely, palmitate could have isotopomers having more than eight ^{13}C atoms as in the experiments with [^{13}C]bicarbonate. However, our data showed only isotopomers 0–8 (mostly 8) in the palmitate after [2-^{13}C]acetate labeling (found as a purple population). This is evidence for the direct use of acetate in fatty acid synthesis for TAG production. The discrepancy could be explained by differences in time scale. The NMR experiments were performed after 24 h labeling when added acetate was exhausted. Alternatively, their data could reflect rapid recycling of added acetate after incorporation into labile pool of fatty acids as described above. NMR could be a good tool for the analysis of isotope incorporation at the cellular level, but it is usually difficult to analyze the label in different parts of molecules. Mass spectral analysis of various compounds can provide more detailed information on the incorporation of the label.

Source of TAG Accumulation in the Stationary Growth Phase

In the stationary growth phase, very high accumulation of TAG was observed. As stated above, *de novo* synthesis of TAG is also active in the stationary growth phase (**Figure 3D**), although the net synthesis of total lipids was reduced in the stationary growth phase. Close examination of the labeled populations in TAG showed that about 1/5 of TAG (**Figure 7B**) contained both highly labeled and low abundance population of fatty acids (16:0 and polyunsaturated fatty acids; **Figure 7D**), which indicated conversion of existing polar lipids to TAG. The presence of highly labeled population in 18:2 and 18:3 in both polar lipids and TAG (**Figures 7C**,**D**) can be explained by gradual progress of desaturation, in which 18:1 is desaturated to 18:2, and then to 18:3. Highly labeled population in 18:1 after the 5-h labeling was rapidly converted to 18:2 and 18:3, and remained as polyunsaturated fatty acids. The highly labeled population of 16:0 and 18:3(5,9,12) in TAG could originate from the corresponding population in DGTS (**Figure 8B**), which is a major lipid class containing 18:3(5,9,12) (**Figures 4A**,**B**) and estimated to be an important source of TAG as described in *C. reinhardtii* (Sakurai et al., 2014).

In a previous paper (Toyoshima and Sato, 2018), we found that accumulation of starch preceded accumulation of TAG, which suggested that starch was a source of TAG. In the present study, direct precursor-product relationship between starch and TAG was not identified, because labeled starch in the exponential phase was rapidly metabolized before the accumulation of TAG in the stationary phase. The relationship might be rather indirect, namely, starch is first converted to polar lipids, which is then converted to TAG in the stationary phase. This does not exclude the possibility that starch provides carbon for the synthesis of TAG as an unlabeled carbon flow in the stationary phase.

Detection of Palmitic Acid Elongation *in vivo*

The results shown in **Figure 9** are best explained by fatty acid elongation. We had two observations (**Figure 9A**): first, the abundance of gray population in 18:0 after the labeling for 5 h; second, the abundance of red population in 18:0 after the chase. The first observation can be explained by assuming that unlabeled 16:0 was elongated by the addition of a labeled C2 unit during the labeling period (**Figure 9C**). The second observation can be explained by the elongation of labeled 16:0 by the addition of an unlabeled C2 unit during the chase period (**Figure 9D**). In both cases, the substrate 16:0 could be supplied by an old pool already present in the cells either as free fatty acids or acyl lipids rather than by a pool of newly synthesized fatty acids. The added C2 unit could be supplied directly from photosynthesis, and represents the labeling status of the cells.

If this interpretation is correct, this is evidence for the elongation of fatty acids *in vivo*. Elongation of fatty acids, such as palmitic acid, is known to occur in the ER of eukaryotic cells. Elongation is characterized biochemically and genetically, but the *in vivo* evidence of elongation is a fortunate result of using this alga. In a red alga, *Cyanidioschyzon merolae*, 16:0 was found to be exported from the chloroplast and elongated to 18:0 in the ER (Mori et al., 2019). In plants, fatty acids are nearly exclusively synthesized within the chloroplasts (mitochondrial fatty acid synthesis is a very minor activity), in which 16:0 is elongated to 18:0, which is then desaturated to 18:1. In a typical view of plant fatty acid metabolism, the pool size of 18:0 (in the chloroplast) is very small, and 16:0 and 18:1 are either utilized in the chloroplast or exported to the cytoplasm. Elongation of both 16:0 and 18:1 results in the synthesis of very long chain fatty acids, such as C20 and C22, to even C30 depending on tissue. In *Arabidopsis*, the product of the *FATTY ACID ELONGATION1* (*FAE1*) gene extends the chain length of fatty acids from C18 to C20 and C22 (James et al., 1995; Millar and Kunst, 1997). In this context, the elongation of 16:0 to 18:0 in the ER is considered an initial step of synthesis of very long chain fatty acids, rather than a process of producing 18:0 *per se*. In contrast, the present study showed that the synthesis of 18:0 by elongation in the ER provides 18:0 in PE. This is a "late" reaction occurring after the synthesis of 16:0. In other words, the elongation occurs using a metabolically inert pool of 16:0, which stays several hours after its synthesis. The 18:0 in PE was rather stable during the chase, which also represents a distinct, stable pool.

Rapid DGDG Labeling

Rapid labeling of DGDG was found in the 2-h labeling experiments (**Figure 3**) as well as the 5-h labeling step of labeling and chase experiments (**Figure 5**). In many organisms, such as cyanobacteria (Sato and Murata, 1982), algae (Sato and Moriyama, 2007; Mori et al., 2019, in *Cyanidioschyzon merolae*, Sato, 1991 in *Cryptomonas*), and plants (Williams et al., 1975; Heemskerk et al., 1991), the acyl groups of DGDG are not readily labeled in typical labeling experiments for 1 or 2 h. We already demonstrated that the outer galactose of DGDG is preferentially labeled in cyanobacteria (Sato and Murata, 1982) and red algae (Sato and Moriyama, 2007). DGDG is synthesized by galactosylation of MGDG, which precludes direct acylation of newly synthesized fatty acids to DGDG. The results in *C. debaryana* suggest that a pool of newly synthesized MGDG is efficiently converted to DGDG, because the turnover rates of acyl groups of DGDG were smaller than those of MGDG acyl groups (**Figure 4D**). Among the two possible galactosylation mechanisms of MGDG to DGDG, galactolipid-galactolipid galactosyltransferase (*Arabidopsis* SFR2) is present in only land plants (see the Gclust database: Cluster 10,083 in Gclust2012_42: Sato and Obayashi, 2021). *Chlamydomonas reinhardtii* is unlikely to possess it (Riekhof et al., 2005). Only DGD1 is likely to transfer a galactose to MGDG from UDPgalactose to synthesize DGDG in *C. debaryana* according to the draft genome data (Hirashima et al., 2016). Curiously, Moseley and Thompson (1980) presented a preliminary result showing the rapid labeling of DGDG in *Volvox carteri*, a close relative of *Chlamydomonas*. We still do not know if rapid labeling of DGDG is common in green algae.

Concluding Remarks

In the present study, we performed labeling experiments with a stable carbon isotope coupled with detailed isotopomer analysis in

C. debaryana, to find the mechanism of TAG accumulation in the stationary growth phase. Carbon metabolism involving starch and lipids was rather complex, and we found various aspects of metabolism in this green alga: namely, two pools for the *de novo* synthesis of fatty acids, rapid turnover of starch and fatty acids including rapid TAG turnover, rapid DGDG synthesis, elongation of existing palmitic acid, degradation and re-synthesis of fatty acids, presence of a stable pool of lipids, and remodeling of polar lipids to TAG. Rapid turnover of starch was likely to provide carbon for the synthesis of fatty acids, but direct conversion of starch to TAG was not supported. In summary, the present study confirmed the power of isotopomer analysis in revealing dynamics of metabolic flow.

DATA AVAILABILITY STATEMENT

The raw data supporting the conclusions of this article will be made available by the authors, without undue reservation.

AUTHOR CONTRIBUTIONS

All authors listed, have made substantial, direct and intellectual contribution to the work, and approved it for publication.

FUNDING

This work was supported in part by a grant-in-aid for the Core Research for Evolutional Science and Technology (CREST) from the Japan Science and Technology Agency.

SUPPLEMENTARY MATERIAL

The Supplementary Material for this article can be found online at: https://www.frontiersin.org/articles/10.3389/fpls.2021.646498/full#supplementary-material

REFERENCES

Aikawa, S., Izumi, Y., Matsuda, F., Hasunuma, T., Chang, J. S., and Kondo, A. (2012). Synergistic enhancement of glycogen production in *Arthrospira platensis* by optimization of light intensity and nitrate supply. *Bioresour. Technol.* 108, 211–215. doi: 10.1016/j.biortech.2012.01.004

Aikawa, S., Joseph, A., Yamada, R., Izumi, Y., Yamatishi, T., Matsuda, F., et al. (2013). Direct conversion of *Spirulina* to ethanol without pretreatment or enzymatic hydrolysis processes. *Energy Environ. Sci.* 6, 1844–1849. doi: 10.1039/c3ee40305j

Bates, P. D. (2016). Understanding the control of acyl flux through the lipid metabolic network of plant oil biosynthesis. *Biochim. Biophys. Acta* 1861, 1214–1225. doi: 10.1016/j.bbalip.2016.03.021

Bates, P. D., Stymne, S., and Ohlrogge, J. (2013). Biochemical pathways in seed oil synthesis. *Curr. Opin. Plant Biol.* 16, 358–364. doi: 10.1016/j.pbi.2013.02.015

Bhowmick, G. D., Koduru, L., and Sen, R. (2016). Metabolic pathway engineering towards enhancing microalgal lipid biosynthesis for biofuel application—a review. *Renew. Sust. Energ. Rev.* 50, 1239–1253. doi: 10.1016/j.rser.2015.04.131

Bligh, E. G., and Dyer, W. J. (1959). A rapid method of total lipid extraction and purification. *Can. J. Biochem. Physiol.* 37, 911–917. doi: 10.1139/o59-099

Bréhélin, C., Kessler, F., and van Wijk, K. J. (2007). Plastoglobules: versatile lipoprotein particles in plastids. *Trends Plant Sci.* 12, 260–266. doi: 10.1016/j.tplants.2007.04.003

Chapman, K. D., Dyer, J. M., and Mullen, R. T. (2012). Biogenesis and functions of lipid droplets in plants: thematic review series: lipid droplet synthesis and metabolism: from yeast to man. *J. Lipid Res.* 53, 215–226. doi: 10.1194/jlr.R021436

Harris, E. H. (2009). *The Chlamydomonas sourcebook. 2nd Edn. Vol. 1*. Amsterdam: Academic Press.

Heemskerk, J. W., Schmidt, H., Hammer, U., and Heinz, E. (1991). Biosynthesis and desaturation of prokaryotic galactolipids in leaves and isolated chloroplasts from spinach. *Plant Physiol.* 96, 144–152. doi: 10.1104/pp.96.1.144

Hicks, G. R., Hironaka, C. M., Dauvillee, D., Funke, R. P., D'Hulst, C., Waffenschmidt, S., et al. (2001). When simpler is better. Unicellular green algae for discovering new genes and functions in carbohydrate metabolism. *Plant Physiol.* 127, 1334–1338. doi: 10.1104/pp.010821

Hirashima, T., Tajima, N., and Sato, N. (2016). Draft genome sequences of four species of *Chlamydomonas* containing phosphatidylcholine. *Genome Announc.* 4, e01070–e01016. doi: 10.1128/genomeA.01070-16

Hu, Q., Sommerfeld, M., Jarvis, E., Ghirardi, M., Posewitz, M., Seibert, M., et al. (2008). Microalgal triacylglycerols as feedstocks for biofuel production: perspectives and advances. *Plant J.* 54, 621–639. doi: 10.1111/j.1365-313X.2008.03492.x

Iwai, M., Ikeda, K., Shimojima, M., and Ohta, H. (2014). Enhancement of extraplastidic oil synthesis in *Chlamydomonas reinhardtii* using a type-2 diacylglycerol acyltransferase with a phosphorus starvation-inducible promoter. *Plant Biotechnol. J.* 12, 808–819. doi: 10.1111/pbi.12210

James, D. W. J., Lim, E., Keller, J., Plooy, I., Ralston, E., and Dooner, H. K. (1995). Directed tagging of the Arabidopsis *FATTY ACID ELONGATION1* (*FAE1*) gene with the maize transposon activator. *Plant Cell* 7, 309–319. doi: 10.1105/tpc.7.3.309

Juergens, M. T., Disbrow, B., and Shachar-Hill, Y. (2016). The relationship of triacylglycerol and starch accumulation to carbon and energy flows during nutrient deprivation in *Chlamydomonas reinhardtii*. *Plant Physiol.* 171, 2445–2457. doi: 10.1104/pp.16.00761

Li, X., Moellering, E. R., Liu, B., Johnny, C., Fedewa, M., Sears, B. B., et al. (2012). A galactoglycerolipid lipase is required for triacylglycerol accumulation and survival following nitrogen deprivation in *Chlamydomonas reinhardtii*. *Plant Cell* 24, 4670–4686. doi: 10.1105/tpc.112.105106

Li-Beisson, Y., Beisson, F., and Riekhof, W. (2015). Metabolism of acyl-lipids in *Chlamydomonas reinhardtii*. *Plant J.* 82, 504–522. doi: 10.1111/tpj.12787

Li-Beisson, Y., Shorrosh, B., Beisson, F., Andersson, M., Arondel, V., Bates, P., et al. (2013). "Acyl-lipid metabolism" in *The Arabidopsis book. Vol. 11*. Rockville, MD: American Society of Plant Biologists, e0161.

Lohscheider, J. N., and Bártulos, C. R. (2016). Plastoglobules in algae: a comprehensive comparative study of the presence of major structural and functional components in complex plastids. *Mar. Genomics* 28, 127–136. doi: 10.1016/j.margen.2016.06.005

Lung, S.-C., and Weselake, R. J. (2006). Diacylglycerol acyltransferase: a key mediator of plant triacylglycerol synthesis. *Lipids* 41, 1073–1088. doi: 10.1007/s11745-006-5057-y

Menetrez, M. Y. (2012). An overview of algae biofuel production and potential environmental impact. *Environ. Sci. Technol.* 46, 7073–7085. doi: 10.1021/es300917r

Merchant, S. A., Kropat, J., Liu, B., Shaw, J., and Warakanont, J. (2012). TAG, You're it! Chlamydomonas as a reference organism for understanding algal triacylglycerol accumulation. *Curr. Opin. Biotechnol.* 23, 352–363. doi: 10.1016/j.copbio.2011.12.001

Millar, A. A., and Kunst, L. (1997). Very-long-chain fatty acid biosynthesis is controlled through the expression and specificity of the condensing enzyme. *Plant J.* 12, 121–131. doi: 10.1046/j.1365-313X.1997.12010121.x

Misra, N., Panda, P. K., Parida, B. K., and Mishra, B. K. (2012). Phylogenomic study of lipid genes involved in microalgal biofuel production—candidate gene mining and metabolic pathway analyses. *Evol. Bioinform.* 8, 545–564. doi: 10.4137/EBO.S10159

Moellering, E. R., and Benning, C. (2010). RNA interference silencing of a major lipid droplet protein affects lipid droplet size in *Chlamydomonas reinhardtii*. *Eukaryot. Cell* 9, 97–106. doi: 10.1128/EC.00203-09

Mori, N., Moriyama, T., and Sato, N. (2019). Uncommon properties of lipid biosynthesis of isolated plastids in the unicellular red alga *Cyanidioschyzon merolae*. *FEBS Open Bio.* 9, 114–128. doi: 10.1002/2211-5463.12551

Moriyama, T., Toyoshima, M., Saito, M., Wada, H., and Sato, N. (2018). Revisiting the algal "chloroplast lipid droplet": the absence of an entity that is unlikely to exist. *Plant Physiol.* 176, 1519–1530. doi: 10.1104/pp.17.01512

Moseley, K. R., and Thompson, G. A. (1980). Lipid composition and metabolism of volvox carteri. *Plant Physiol.* 65, 260–265. doi: 10.1104/pp.65.2.260

Msanne, J., Xu, D., Konda, A. R., Casas-Mollano, J. A., Awada, T., Cahoon, E. B., et al. (2012). Metabolic and gene expression changes triggered by nitrogen deprivation in the photoautotrophically grown microalgae *Chlamydomonas reinhardtii* and *Coccomyxa* sp. C-169. *Phytochemistry* 75, 50–59. doi: 10.1016/j.phytochem.2011.12.007

Riekhof, W. R., Sears, B. B., and Benning, C. (2005). Annotation of genes involved in glycerolipid biosynthesis in *Chlamydomonas reinhardtii*: discovery of the betaine lipid synthase BTA1Cr. *Eukaryot. Cell* 4, 242–252. doi: 10.1128/EC.4.2.242-252.2005

Sakurai, K., Moriyama, T., and Sato, N. (2014). Detailed identification of fatty acid isomers sheds light on the probable precursors of triacylglycerol accumulation in photoautotrophically grown *Chlamydomonas reinhardtii*. *Eukaryot. Cell* 13, 256–266. doi: 10.1128/EC.00280-13

Sato, N. (1991). Lipids in Cryptomonas CR-1. II. Biosynthesis of betaine lipids and galactolipids. *Plant Cell Physiol.* 32, 845–851. doi: 10.1093/oxfordjournals.pcp.a078152

Sato, N. (2015). Is monoglucosyl diacylglycerol a precursor to monogalactosyl diacylglycerol in all cyanobacteria? *Plant Cell Physiol.* 56, 1890–1899. doi: 10.1093/pcp/pcv116

Sato, N., and Moriyama, T. (2007). Genomic and biochemical analysis of lipid biosynthesis in the unicellular rhodophyte *Cyanidioschyzon merolae*: lack of plastidic desaturation pathway results in mixed pathway of galactolipid synthesis. *Eukaryot. Cell* 6, 1006–1017. doi: 10.1128/EC.00393-06

Sato, N., Moriyama, T., Mori, N., and Toyoshima, M. (2017). Lipid metabolism and potentials of biofuel and high added-value oil production in red algae. *World J. Microbiol. Biotechnol.* 33:74. doi: 10.1007/s11274-017-2236-3.

Sato, N., and Murata, N. (1982). Lipid biosynthesis in the blue-green alga, *Anabaena variabilis* I. lipid classes. *Biochim. Biophys. Acta* 710, 271–278. doi: 10.1016/0005-2760(82)90109-6

Sato, N., and Obayashi, T. (2021). "Lipid pathway databases with a focus on algae" in *Methods in molecular biology: Plant lipids*. eds. D. Bartels and P. Dörmann (Springer Science) (in press).

Sato, N., Okazaki, Y., and Saito, K. (2016). Isotopic combinatomer analysis provides *in vivo* evidence of the direct epimerization of monoglucosyl diacylglycerol in cyanobacteria. *Biochemistry* 55, 5689–5701. doi: 10.1021/acs.biochem.6b00769

Siaut, M., Cuiné, S., Cagnon, C., Fessler, B., Nguyen, M., Carrier, P., et al. (2011). Oil accumulation in the model green alga *Chlamydomonas reinhardtii*: characterization, variability between common laboratory strains and relationship with starch reserves. *BMC Biotechnol.* 11:7. doi: 10.1186/1472-6750-11-7

Singh, H., Shukla, M. R., Chary, K. V. R., and Rao, B. J. (2014). Acetate and bicarbonate assimilation and metabolite formation in *Chlamydomonas reinhardtii*: a ^{13}C-NMR study. *PLoS One* 9:e106457. doi: 10.1371/journal.pone.0106457

Smith, R. T., and Gilmour, D. J. (2018). The influence of exogenous organic carbon assimilation and photoperiod on the carbon and lipid metabolism of *Chlamuydomonas reinhardtii*. *Algal Res.* 31, 122–137. doi: 10.1016/j.algal.2018.01.020

Tornabene, T. G., Holzer, G., Lien, S., and Burris, N. (1983). Lipid composition of the nitrogen starved green alga *Neochloris oleoabundans*. *Enzym. Microb. Technol.* 5, 435–440. doi: 10.1016/0141-0229(83)90026-1

Toyoshima, M., and Sato, N. (2015). High-level accumulation of triacylglycerol and starch in photoautotrophically grown *Chlamydomonas debaryana* NIES-2212. *Plant Cell Physiol.* 56, 2447–2456. doi: 10.1093/pcp/pcv163

Toyoshima, M., and Sato, N. (2018). Optimization of triacylglycerol and starch production in *Chlamydomonas debaryana* NIES-2212 with regard to light intensity and CO_2 concentration. *Microbiology* 164, 359–368. doi: 10.1099/mic.0.000603

Van den Koornhuyse, N., Libessart, N., Delrue, B., Zabawinski, C., Decq, A., Iglesias, A., et al. (1996). Control of starch composition and structure through substrate supply in the monocellular alga *Chlamydomonas reinhardtii*. *J. Biol. Chem.* 271, 16281–16287. doi: 10.1074/jbc.271.27.16281

Watanabe, A. (1960). List of algal strains in collection at the institute of applied microbiology, University of Tokyo. *J. Gen. Appl. Microbiol.* 6, 283–292. doi: 10.2323/jgam.6.283

Williams, J. P., Watson, G. R., Khan, M. U., and Leung, S. (1975). Galactolipid synthesis in *Vicia faba* leaves: I. Galactose, glycerol, and fatty acid labeling after CO_2 feeding. *Plant Physiol.* 55, 1038–1042. doi: 10.1104/pp.55.6.1038

Yoshitomi, T., Kaminaga, S., Sato, N., Toyoshima, M., Moriyama, T., and Yoshimoto, K. (2020). Formation of spherical palmelloid colony with enhanced lipid accumulation by gel encapsulation of *Chlamydomonas debaryana* NIES-2212. *Plant Cell Physiol.* 61, 158–168. doi: 10.1093/pcp/pcz188

Yumoto, K., Kasai, F., and Kawachi, M. (2013). Taxonomic re-examination of *Chlamydomonas* strains maintained in the NIES-collection. *Microbiol. Cult. Coll.* 2, 1–12.

Yusuf, C. (2007). Biodiesel from microalgae. *Biotechnol. Adv.* 25, 294–306. doi: 10.1016/j.biotechadv.2007.02.001.

Zhang, B., Wang, L., Hasan, R., and Shahbazi, A. (2014). Characterization of a native algae species *Chlamydonmonas debaryana*: strain selection, bioremediation ability, and lipid characterization. *Bioresources* 9, 6130–6140. doi: 10.15376/biores.9.4.6130-6140

Conflict of Interest: The authors declare that the research was conducted in the absence of any commercial or financial relationships that could be construed as a potential conflict of interest.

Copyright © 2021 Sato and Toyoshima. This is an open-access article distributed under the terms of the Creative Commons Attribution License (CC BY). The use, distribution or reproduction in other forums is permitted, provided the original author(s) and the copyright owner(s) are credited and that the original publication in this journal is cited, in accordance with accepted academic practice. No use, distribution or reproduction is permitted which does not comply with these terms.

frontiers in Plant Science

ORIGINAL RESEARCH
published: 13 April 2021
doi: 10.3389/fpls.2021.615577

Enhanced Lipid Production in *Chlamydomonas reinhardtii* Caused by Severe Iron Deficiency

*Elsinraju Devadasu and Rajagopal Subramanyam**

Department of Plant Sciences, School of Life Sciences, University of Hyderabad, Hyderabad, India

Microalgae are used as a source of lipids for the production of biofuels. Most algae produce neutral lipids under stress conditions. Here, lipid accumulation by the unicellular alga *Chlamydomonas reinhardtii* was examined during cultivation under iron-limiting conditions. Severe iron stress caused the cells to accumulate a significant amount of lipid, specifically triacylglycerols (TAGs), by compromising the growth. Semi-quantitative measurements by Fourier transform infrared (FTIR) spectroscopy showed an increase in both carbohydrate and lipid content in iron-stressed *C. reinhardtii* cells compared to control. Analysis by flow cytometry and thin layer chromatography confirmed that severe iron deficiency-induced TAG accumulation to fourfold higher than in iron-replete control cells. This accumulation of TAGs was mostly degraded from chloroplast lipids accompanied by overexpression of diacylglycerol acyltransferase (DGAT2A) protein. Furthermore, liquid chromatography-mass spectrometry (LC-MS) analysis demonstrated significantly enhanced levels of C16:0, C18:2, and C18:3 fatty acids (FAs). These results indicate that iron stress triggers the rapid accumulation of TAGs in *C. reinhardtii* cells. The enhanced production of these lipids caused by the iron deficiency may contribute to the efficient production of algal biofuels if we escalate to the photobioreactor's growth conditions.

Keywords: algae, *Chlamydomonas reinhardtii*, Fourier transform infrared spectroscopy, liquid chromatography, mass spectrometer, triacylglycerols, lipids

OPEN ACCESS

Edited by:
Mie Shimojima,
Tokyo Institute of Technology, Japan

Reviewed by:
Masataka Kajikawa,
Kindai University, Japan
Koichiro Awai,
Shizuoka University, Japan

***Correspondence:**
Rajagopal Subramanyam
srgsl@uohyd.ernet.in

Specialty section:
This article was submitted to Plant Physiology, a section of the journal Frontiers in Plant Science

Received: *09 October 2020*
Accepted: *23 March 2021*
Published: *13 April 2021*

Citation:
Devadasu E and Subramanyam R (2021) Enhanced Lipid Production in Chlamydomonas reinhardtii Caused by Severe Iron Deficiency. Front. Plant Sci. 12:615577. doi: 10.3389/fpls.2021.615577

INTRODUCTION

Photosynthetic algae capture solar energy and store it as chemical energy in the form of starch and lipids, particularly triacylglycerols (TAGs) (Merchant et al., 2007). The transesterification of TAGs achieves biodiesel production with methanol in the presence of a suitable catalyst (e.g., H_2SO_4). Most microalgae accumulate increased levels of TAGs under nutrient deficiency, such as nitrogen starvation. However, stress conditions like this are also accompanied by decreased growth rates. For the economical production of biodiesel from algae, increased lipid levels must be combined with a high percentage of algal growth. Various stress conditions like nitrogen starvation (Rios et al., 2015; Lin et al., 2018), iron starvation (Gorain et al., 2013), copper stress (Hamed et al., 2017), heat stress (Ördög et al., 2016), pH (Abinandan et al., 2019), and high-light stress (Fan and Zheng, 2017) have been reported to induce lipid accumulation in microalgae effectively. The nutritional requirements for the accumulation of TAGs by *Dunaliella tertiolecta* were investigated (Chen et al., 2011).

The soluble form of iron (Fe^{2+}) is very limited in soil. Its low bioavailability is a significant problem for photosynthetic organisms (Glaesener et al., 2013) because iron is essential in the biochemical pathways of plants and microalgae. In oxygenic photosynthesis, iron acts as a cofactor in all-electron transfer reactions and enhances the active photosynthetic reaction centers in algae. A lack of iron decreases photosystem (PS)II function, inter-photosystem electron transport, carbon fixation rates and ultimately affects the growth of cyanobacteria and algae (Singh et al., 2005; Devadasu et al., 2016).

Limitation of micronutrients (e.g., zinc and iron) results in the conversion of membrane lipids into individual fatty acids (FAs), which leads to the formation of lipid droplets (LDs) in *D. tertiolecta* (Chen et al., 2011). The impact of N, S, P, and Mg deficiency on microalgal metabolism has been studied in *Chlamydomonas reinhardtii* (Çakmak et al., 2014). Nitrogen starvation severely inhibits algal growth and induces TAG accumulation in *C. reinhardtii* cells (James et al., 2011). Iron stress has a wide range of effects on the endoplasmic reticulum (ER) and its membrane structures in this organism, which indicates its potential influence on TAG accumulation. Therefore, we hypothesized that two-stage iron starvation, i.e., cells initially subjected to iron deficiency are further cultured in an iron-depleted medium to cause severe iron starvation, might effectively induce lipid accumulation in *C. reinhardtii*. This so-far untested treatment regime could offer a simple way of increasing lipid content in microalgae.

The eukaryotic microalga, *C. reinhardtii,* is a model organism used extensively to study photosynthesis and primary metabolism (Merchant et al., 2007). Its genome has been sequenced; it is easy to grow in culture and has a well-characterized response to adverse environmental conditions. Therefore, this organism was selected to investigate the influence of two-stage iron starvation on TAG accumulation. We recently reported the effect of iron stress conditions on cellular biomass and the proteins involved in lipid biosynthesis in *C. reinhardtii* (Devadasu et al., 2019). In the present study, we examined the effect of two-stage iron starvation on growth rate and lipid production in this species. Cells cultivated in iron-deficient conditions were also examined for carbon partitioning into lipid and carbohydrate. Severe iron starvation conditions significantly increased the production of TAGs, which will help to make biofuel production for more efficient.

MATERIALS AND METHODS

Strain and Growth Conditions

The wild-type *C. reinhardtii* strain CC125 was obtained from the Chlamydomonas Resource Center[1]. Cells were grown photo-heterotrophically in acid-cleaned 1-L conical flasks containing 800 mL of tris acetate-phosphate (TAP) medium supplemented with Hutner's trace elements. Cultures were incubated at 22°C on an orbital shaker (120 rpm) with continuous illumination (50 μmol ± 5 photons m^{-2} s^{-1}). The media preparation method was followed according to Yadavalli et al. (2012). We have prepared the iron limiting TAP-Fe media by omitting the required concentration of iron from Hutner's trace elements. All culture flasks and plasticware were washed at least twice with 6 N HCl to remove the metal ions and later on washed six times with MilliQ water to remove the HCl and kept in oven at 50°C for over night. High-purity chemicals were used for preparation of iron-free stock solutions. Initially, a seed culture (30 mL) was grown in TAP medium to stationary phase, and 10 mL of culture was centrifuged (3,000 × *g* for 6 min at 25°C) to harvest the cells. The supernatant was removed. The cells washed twice with iron-free growth medium (TAP-Fe, 20 mL) before using them to inoculate TAP or TAP-Fe medium (1st generation) an initial optical density (OD_{750}) of 0.2 ± 0.024. After 3 days of incubation, the iron-deficient culture was used to inoculate another iron-free medium flask to an OD_{750} of 0.2 ± 0.04 to give 2nd stage iron deficiency (severe iron deficiency), where the iron concentration is negligible. Three independent cultures of each type were propagated for each experiment (n = 3). The growth measurements were carried out with spectrophotometer (Perkin Elmer LS-35, United States).

Cell Count and Dry Biomass Determination

Culture growth was monitored by counting cells using a hemocytometer. For dry cell weight (dw) measurement, the cells were collected by centrifugation at 2,000 × *g* for 5 min, washed twice with distilled water, transferred to a weighed tube, and then freeze-dried −105°C for 12 h. The tube was then weighed again, and the dry cell biomass calculated as follows:

$$dw = (w_2 - w_1)/v$$

Where w_1 is the mass of the empty tube, w_2 is the mass of the tube + dried cell pellet, and v is the sample's initial volume.

Measurement of Fourier Transform Infrared Spectra

Fourier transform infrared (FTIR) spectra were recorded with a Bruker Vertex 80 V (Bruker Optik GmbH) at a spectral resolution of 4 cm^{-1}. The spectra were acquired with a three-bounce diamond-attenuated total reflectance sampling accessory linked to a DTGS detector (64 scans per sample). Spectra were measured in the range from 800 to 1,800 cm^{-1} (protein amide bond I signals occur at 1,642 cm^{-1} and amide bond II signals at 1,541 cm^{-1}). Single-beam spectra were obtained from the dried algal cells under a nitrogen purge. Measurements were taken using an equal dw for all samples. Background single-beam spectra were recorded from the empty ATR plate under a nitrogen purge. Baseline offset corrections were made to the absorption spectra as required using the OPUS control software (v 6.5, Bruker Optik GmbH).

Quantification of Lipid Content

The total lipids include neutral lipids, membrane lipids, and other pigments, were quantified from all the conditions. The lipid content of dried *C. reinhardtii* cells was measured as a

[1]www.chlamycollection.org

percentage of the dry biomass. 20 mg of crushed cell powder were suspended in 1 mL of *n*-hexane. The mixture was transferred to a 10 mL glass tube, and 3 mL of *n*-hexane and 1.5 mL of isopropanol were added before shaking the tube (225 rpm) for 24 h at room temperature. 5 mL of distilled water were added, the tube was shaken for 1 min and then centrifuged (5,000 × *g*, 5 min). The n-hexane layer containing lipids was collected in a pre-weighed microfuge tube (1.5 mL), dried overnight at room temperature and then transferred to 60°C for 1 h. The prepared lipids were then weighed and the lipid content calculated as a percentage of dw.

Cell Staining for Lipids

Lipid droplets in *C. reinhardtii* cells were observed after staining with the lipophilic fluorescent dye Nile Red (NR) (Sigma-72485) as described previously (Moellering and Benning, 2010) with minor modifications. A 50 μg/mL stock solution of NR was prepared in methanol, and this was diluted to a final concentration of 0.5 μg/mL for staining. After adding the fluorescent dye, the cell suspension was vortexed for 30 s and incubated in darkness at room temperature for 10 min. The cells were then collected by centrifugation at 3,000 × *g* for 5 min, and unbound dye in the supernatant was removed, and cells were used for further analysis.

Confocal and Transmission Electron Microscopy of Intracellular LDs

Fluorescence and bright-field images of LDs in *C. reinhardtii* cells were acquired using a Zeiss LSM 880 confocal microscope system (Jena, Germany). Algal culture samples (1 mL) were fixed by adding iodine solution (5 μL, 2.5 mg/mL prepared in 95% ethanol). Stained (see section "Cell Staining for Lipids") cells were then mixed with 1% low melting-temperature agarose 1:1 (v/v) at 28°C and applied to a microscope slide. Images of agarose-embedded cells were captured using a Zeiss LSM 880 confocal microscope. Fluorescence images of the cells (λ excitation – 488 nm; λ emission scan – 560–600 nm) were recorded via a 60× oil objective at a pixel resolution of 1,024 × 1,024 in an 8-bit format. The scan and laser transmission settings remained constant for all scans.

For electron microscopic analysis, cells were resuspended in 0.1 M phosphate-buffer (pH 7.2) and cell fixation was done with 2% Glutaraldehyde (Sigma) solution for 2 h under dark and then cells were washed four times in PBS buffer each for 1 h and post-fixed in 2% aqueous Osmium Tetraoxide for 3 h, later washed with deionized distilled water for six times and dehydrated in series of ethanol solutions (30, 50, 70, 90%, and three changes of 100% for 10 min each), infiltrated and embedded in araldite resin. Further, incubated at 80°C for 72 h for complete polymerization and ultra thin sections (60 nm) were made with a glass ultramicrotome (Leica Ultra cut UCT-GA-D/E-1/100) and mounted on copper grids. The sections were stained with uranyl acetate and counter stained with Reynolds lead citrate as described albeit modifications (Bozzola and Russell, 1998). Transmission electron micrographs were captured using a Hitachi 7500 (Japan) instrument.

Nile Red Fluorescence Assay

Triolein (Sigma T9275) was used as a TAG standard for quantification. Samples (3×10^6 cells) of algal cultures grown under various growth conditions were transferred to the wells of black 96-well plates with transparent bottoms. NR solution (section "Cell Staining for Lipids") was added to each well and mixed with the cell suspension, followed by a 20-min incubation in the dark. Fluorescence produced by the interaction of NR with cellular neutral lipids was measured using a Tecan infinite 200 microplate reader (λ excitation–486 nm; λ emission–595 nm). The chlorophyll autofluorescence signal was subtracted from each measurement. The experiment was repeated with three individual cultures ($n = 3$).

Semi-Quantitative Analysis of TAGs by Fluorescence-Activated Cell Sorting

Relative neutral lipid levels in cells were monitored with fluorescence-activated cell sorting (FACS) analysis using a Calibur high-speed flow cytometer (BD Falcon, United States). Culture samples of 1 mL were gently mixed with NR stain (0.5 μg/mL), then held in the dark for 30 min before measuring fluorescence (λ excitation–488 nm; λ emission–545 nm). Each measurement, 10,000 events were kept as a cutoff. Chlorophyll autofluorescence was then subtracted from each reading, and mean fluorescence intensity values and images were analyzed using Flowing Software v2.5.1. Three replicates were carried out with three independent samples.

Lipid Extraction

Total lipids were extracted from cells described by Bligh and Dyer (1959) method with minor modifications. Dried algal samples of 20 mg were resuspended in 0.8 mL of chloroform/methanol (2:1, v/v) and 100 μL of 0.9% KCl solution for extraction of neutral lipids. For extraction of polar lipids, same amount of dw was taken and resuspended with chloroform/methanol (2:1, v/v). 100 μL of 1 M of KH_2PO_4 was added and vortexed. Sample mixture was centrifuged at 3,000 × *g* for 5 min at RT for phase separation. The lower chloroform phase containing lipids was collected. The remaining fractions were used for further lipid extraction, and this was repeated three times; the upper layer was collected, which was repeated three times. The lower chloroform phase was pooled and dried by evaporation in a stream of N_2, and the lipids were dissolved in 20 μL of chloroform then stored at −20°C.

Triacylglycerol Analysis by Thin-Layer Chromatography

Twenty microliter lipid extract samples were spotted onto a thin-layer chromatography (TLC) plate (TLC Silica gel 60, F254, Merck). 10 μg of glyceryl trioleate (Sigma) were also applied as a TAG standard. Chromatography was performed using a hexane/ether/acetic acid (70:30:1, v/v/v) mixture as the solvent system. The developed TLC plates were air-dried and the separated TAGs visualized by exposure to iodine vapor at 37°C for 5 min. The plates were photographed using a digital camera, and the TAG content in each sample was quantified by gray semi-quantitative analysis using Image J (ver1.45, NIH).

Polar lipids were separated by 2D TLC. The first dimension was run in the solvent system of chloroform/methanol/water (30:10:1, v/v/v) and the second dimension in chloroform/methanol/glacial acetic acid/water (35:7:6:1, v/v/v). The TLC plates were heated at 95°C to evaporate the solvent and lipids visualized by treatment with 5% phosphomolybdic acid (Sigma) in 95% ethanol. Three replicates were carried out with three independent samples.

Immunoblotting

Total protein was extracted from approximately 3×10^6 cells under severe iron starvation conditions using a buffer consisting of 0.1 M DTT, 4% SDS, 0.1 M *Tris*-HCl (pH 6.8). Extracted proteins were quantified using the Bradford method, and 5 μg samples were suspended in sample buffer, heated at 60°C for 5 min and loaded on a 15% SDS-polyacrylamide gel. After electrophoresis, the proteins were blotted onto a nitrocellulose membrane (Bio-Rad, United States) as described in Towbin et al. (1979). Equal loading was confirmed with Histone H3 antibody (Product Id: AS10 710A). The expression pattern of diacylglycerol acetyltransferase (DGAT2A) protein was determined by incubating the blot with anti-DGAT2A primary antibody (1:5,000) (Product Id: AS12 1874, Agrisera, Sweden) and then enzyme-conjugated IgG secondary antibody (1:10,000; Incell Technology). Immunoreactive bands were disclosed using the Chemidoc Touch system (Bio-Rad). Three replicates were carried out with three independent samples.

Liquid Chromatography-Mass Spectrometry

Liquid chromatography-mass spectrometry (LC-MS) analysis of FAs was performed using a modified high-pressure liquid chromatography (HPLC) method (Jouhet et al., 2017). Total lipid extracts from cultured cells were dissolved in 100 μL of 0.1% acetonitrile. As an internal standard, C17:0 FA (Sigma) dissolved in 0.1% acetonitrile was added to all the samples to a concentration of 0.5 μM. The samples were centrifuged for 30 min at 450 × *g* at RT to remove the insoluble pellet, and then the supernatants were transferred to fresh tubes and vacuum evaporated at 45°C for 15 min. FA derivatization was performed by resuspending the samples in *n*-butanol and incubating them at 60°C for 20 min (Martin et al., 2014). After vacuum evaporation at 65°C for 15 min, the lipid samples were re-extracted into 0.1% acetonitrile: formic acid. From each sample, 10 μL were injected into the LC-MS system (Shimadzu, 8045). The following mobile phase conditions were employed: Buffer A: water: 0.1% formic acid (v/v), Buffer B: acetonitrile: 0.1% formic acid (v/v) with run time for 1 min and, oven temperature: 25°C. The organic buffer consisting of acetonitrile/0.1% formic acid (Buffer-A) and aqueous buffer composed of water with formic acid (Buffer-B) total run time for 2 min with 0.0–0.2 min flow rate was at 0.1 mL/min 20% of buffer-B. The organic phase from the 0.2 to 1 flow rate was at 0.5 mL/min with 100% organic buffer and then 1–1.5 min for 0.1 mL/min of flow rate organic buffer with 20% buffer-B. In the end, 1.5–2 min for a run with a flow rate of 0.1 mL/min buffer of 100% aqueous phase. The direct molecular masses of separated compounds were determined using a coupled Shimadzu 8045 mass spectrometer. Specific multiple reaction monitoring (MRM) scans were used to quantify each ion's mass (**Supplementary Table 1**). The following conditions were employed for mass spectrometry (MS): source–ESI; nebulizing gas flow rate–2.5 L/min; heating gas flow rate–10 L/min; drying gas flow rate–10 L/min; interface temperature–300°C; DL temperature–250°C; heat block temperature–400°C.

Statistical Analysis

All the parameters were represented as mean ± SD (n = 3). Three individual cultures were taken for each treatment under each biological replicate, and the final results represented the data obtained from three biological replicates. The significance of the differences between mean values of control and all iron-deficient culture was determined using Student's t-test and showed $p < 0.05$ (*).

RESULTS AND DISCUSSION

Influence of Iron Deficiency on the Growth of *Chlamydomonas reinhardtii*

Tris-acetate-phosphate (TAP) medium, the standard growth medium for the culture of *C. reinhardtii,* contains 18–20 μM iron (Kropat et al., 2011). To examine the effect of iron-deficiency on growth, cells propagated in TAP were washed twice with TAP−Fe (iron-free medium) and then transferred to the same medium or TAP+Fe (iron-replete medium) as a control (**Figure 1A**) to give an optical density (OD_{750}) of approximately 0.2. The growth of these cultures was then monitored over 4 days. In iron-sufficient conditions, the OD was doubled in 2 days and reached a maximum value (OD_{750} = 1.01 ± 0.18) after 72 h. In the inoculum, traces of iron were utilized by the cells for initial multiplication in the iron-deficient medium, so genuine iron stress only occurred after the first cell division. The OD of the iron-deprived culture decreased (OD_{750} = 0.23 ± 0.02) over the early 2 days, but it then increased over the following 4 days to a maximum value of less than half iron-replete culture (OD_{750} = 0.42 ± 0.04). Moreover, since iron is a cofactor in several enzymes such as hydrogen dehydrogenase, nitrite reductase and superoxide dismutase, normal cellular metabolism required to maintain ATP production is depressed in cells lacking iron.

Further, the iron-limited culture (1st generation) was then used to inoculate into the same iron-free medium to see further consequences (severe iron starvation) (2nd generation). In severe iron-deficient culture, the cells were wholly starved due to lack of iron in the medium. During the severe iron starvation, the cells were in the dividing stage, and the photosynthesis process was reduced significantly as they do not have sufficient iron content in the cell (Devadasu et al., 2021).

The cell growth was reduced after 4 days (OD = 0.313 ± 0.03) in severe iron deficiency. Total biomass in dw was up to 2.1 g/L in cells grown in iron-replete medium (**Figure 1B**). In comparison, cell biomass in the iron-limited culture was 1.0 g/L, whereas the cultures with severe iron-deficiency were further reduced to 0.45 g/L (**Figure 1B**). Under optimal conditions, microalgae can grow

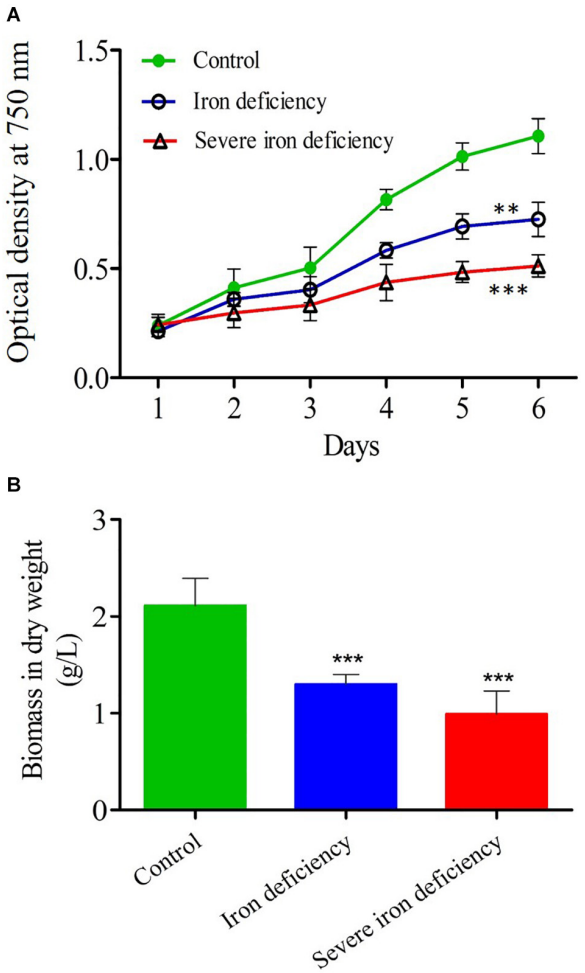

FIGURE 1 | Growth and biomass measurements of *Chlamydomonas reinhardtii* cells cultured under control and iron-deficient conditions. **(A)** The optical density (OD) of control culture [20 μM iron (Fe^{2+}) concentration], compared with those grown under iron deficiency and severe iron deficiency conditions. The statistical analysis was carried out from day 2 to day 6 of control and iron deficiency conditions. **(B)** Total biomass measured in the same cultures harvested after 4 days of growth. Values are mean ± SD. Statistical analysis was performed by Student *t*-test (non-paired) and *P* values were represented as $^{**}P < 0.01$; $^{***}P < 0.001$. Error bar indicates the standard deviation of three biological replicates.

and produce higher biomass with low lipid content. In contrast, nutrient limitation can accumulate high levels of lipid content but with low biomass (Tan and Lee, 2016). A previous study on nitrogen starvation in *C. reinhardtii* showed that cell growth was severely reduced, causing a decrease in total biomass, whereas increased lipid content (Park et al., 2015). Two major obstacles to the production of biodiesel from microalgae is (1) poor growth in culture leading to low cell density with low cellular lipid content and (2) stress conditions promotes neutral lipid content while decreasing growth (James et al., 2011). Previous reports show that total lipid levels in *C. reinhardtii* cells increased dramatically by iron starvation (Urzica et al., 2013; Devadasu et al., 2019). Since continuous exposure of cells to iron limitation causes plastid and ER stress and is highly likely to result in the degradation of cells (apoptosis). It is tempting to speculate that apoptosis may be involved in this cellular degradation. This process has recently been demonstrated in Chlamydomonas, and severe ER stress leads to apoptosis in many organisms (Howell, 2013). Other reports from nitrogen and phosphate starvation lead to LDs and TAG through apoptotic mechanism (Couso et al., 2018; Masclaux-Daubresse et al., 2020) indeed, in our case, also the apoptotic mechanism would have happened. Therefore LDs and TAG could have also occurred through the apoptotic mechanism under severe iron deficiency, and the results can be seen below.

Visualization of Intracellular LDs by Confocal and Transmission Electron Microscopy

The accumulation of LDs in *C. reinhardtii* cells was examined using confocal and transmission electron microscopy (TEM) (**Figure 2**). In iron deficiency, the size of the cells was decreased, and they displayed abnormal morphology. Cells were grown in an iron-replete (control) medium did not show any visible accumulation of lipid bodies (**Figure 2A**). In contrast, lipid production was induced in an iron-deficient medium, and LDs were present in cells in both iron deficiency and severe iron-limited cultures. Our study supports the earlier reports that the accumulation of LDs was seen in iron deficiency conditions (Urzica et al., 2013; Devadasu et al., 2019). Interestingly, severe iron deficiency (almost no iron in the cells or medium) caused the appearance of more abundant lipids and larger lipid bodies (**Figure 2A**), which has important implications for industrial applications. Previously, lipid body accumulation was observed in *Chlamydomonas* cells grown under nitrogen starvation conditions (James et al., 2011). *C. reinhardtii* cells accumulated lipids up to 45–50% of their total NR fluorescence (Moellering and Benning, 2010; James et al., 2011). In the present study, we observed lipid accumulation of 65% after 72 h of severe iron starvation compared with 45% in cells from the iron-limited 1st generation culture. This high lipid content in cells from severely iron starved cultures may make them a valuable starting material for biofuel production. TEM showed decreased unstacked thylakoid membranes in these cells. Also, the LDs observed in cells subjected to severe iron starvation (marked with "L") were more extensive than those grown in the iron deficiency conditions (**Figure 2B**).

Neutral Lipid Analysis by NR Staining

It has been shown that nutrient limitation causes decreased cell division in microalgae, and most studied species divert FAs into TAG accumulation (Sharma et al., 2012). To examine the effect of iron deficiency on neutral lipid accumulation at the population level, 10,000 *C. reinhardtii* cells from each group (i.e., control and iron-deficient) were stained with NR after 72 h in culture, and fluorescence intensity was analyzed using flow cytometry. Many more cells with raised fluorescence levels (threefold) were present in the iron-deficient conditions. The severely iron-deprived culture showed up to sixfold fluorescence values than the control culture (**Figure 3A**). These fluorescence data indicate

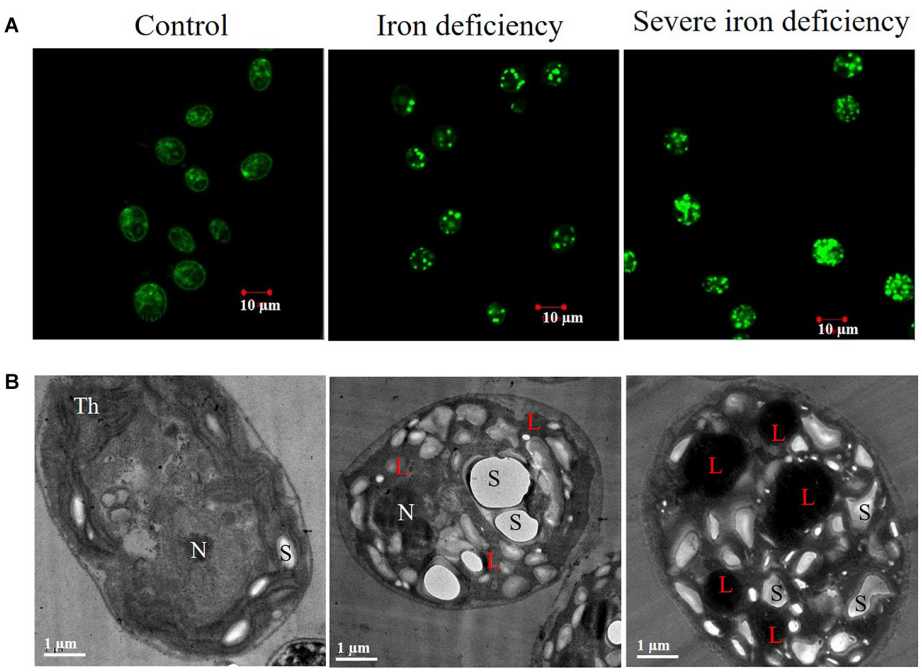

FIGURE 2 | Microscopic examination is of *Chlamydomonas reinhardtii* cells cultured under iron-replete and iron-deficient conditions. **(A)** Confocal fluorescence images of cells stained with Nile Red (NR) show the location and size of lipid droplets (scale bar = 10 µm). **(B)** Transmission electron microscopy (TEM) images showed lipids accumulated within cells under iron deficiency and severe iron deficiency conditions (scale bar = 1 µm). Symbols represent, Th, thylakoids; L, lipid droplet; N, nucleus; S, starch.

that cells subjected to severe iron deficiency are more stressed than control cells, which induces significant lipid accumulation (**Figure 3A**). Therefore, it is probable that the iron deficiency-induced lipid accumulation and the nitrogen starvation-induced pathway of LD formation are similar and involve the degradation and remodeling of chloroplast membrane lipids to form TAGs (Siaut et al., 2011). Notably, biomass was decreased while NR fluorescence increased when cells were grown in severe iron-depleted conditions for up to 72 h (**Figure 1B**). Decreased biomass and increased lipid content were observed in both iron deficiency stages, but higher levels of lipid were accumulated under severe iron starvation. The effect of iron limitation on lipid accumulation was observed from cell growth, but lipids' accumulation was highest at fourth-day cultures (**Figure 3B**). These results indicate that the metabolism of iron and carbon are interlinked in *C. reinhardtii*. Neutral lipid accumulation in iron-deficient conditions occurs primarily through photosynthetic carbon fixation via the Calvin-Benson cycle (Velmurugan et al., 2014; Devadasu et al., 2019).

Neutral lipid content of cells during growth under iron-replete and -deficient conditions was monitored by staining with NR. Samples of culture were taken throughout each experiment (12–72 h), and cell densities were normalized so that an equal number of cells (3×10^6) were stained (**Supplementary Figure 1**). As in previous studies, NR staining was employed to evaluate the neutral lipid content of *C. reinhardtii* cells and characterize the intracellular lipid bodies (James et al., 2011). Based on plate reader assay after 72 h of cell growth, the 1st and severe iron-deficient cells exhibited twofold and threefold increases in neutral lipid content, respectively, compared with the iron sufficient control cells. A previous study on *C. reinhardtii* cells cultured under N, S, and P limitation conditions also found an increased neutral lipid content (Çakmak et al., 2014). In our earlier investigation of iron limitation in *C. reinhardtii* (traces of iron still present), cells' neutral lipid content was increased (Devadasu et al., 2019). Similarly, TAG accumulation was observed when *C. reinhardtii* cells grown in iron deficiency (Urzica et al., 2013).

The total lipid content of cells was also determined following organic extraction and the results compared with NR staining data (**Figure 3B**). The level of lipid accumulation caused by severe iron deficiency was higher than that resulting from the first generation of iron deficiency (Urzica et al., 2013; Devadasu et al., 2019). Therefore, severe iron starvation conditions could be a valuable means of increasing the yield of neutral lipids in microalgae, which would benefit biodiesel production.

Lipid and Carbohydrate Measurements by FTIR

To corroborate the NR fluorescence and total lipid data, we used FTIR to monitor carbon partitioning between lipid and carbohydrate in *C. reinhardtii* cells cultured under iron-deficient conditions (**Figure 4**). Based on the vibrational stretches due to peptide bonds, carbohydrates and lipid molecules, we plotted lipid ratios: amide I and carbohydrate: amide I, according to

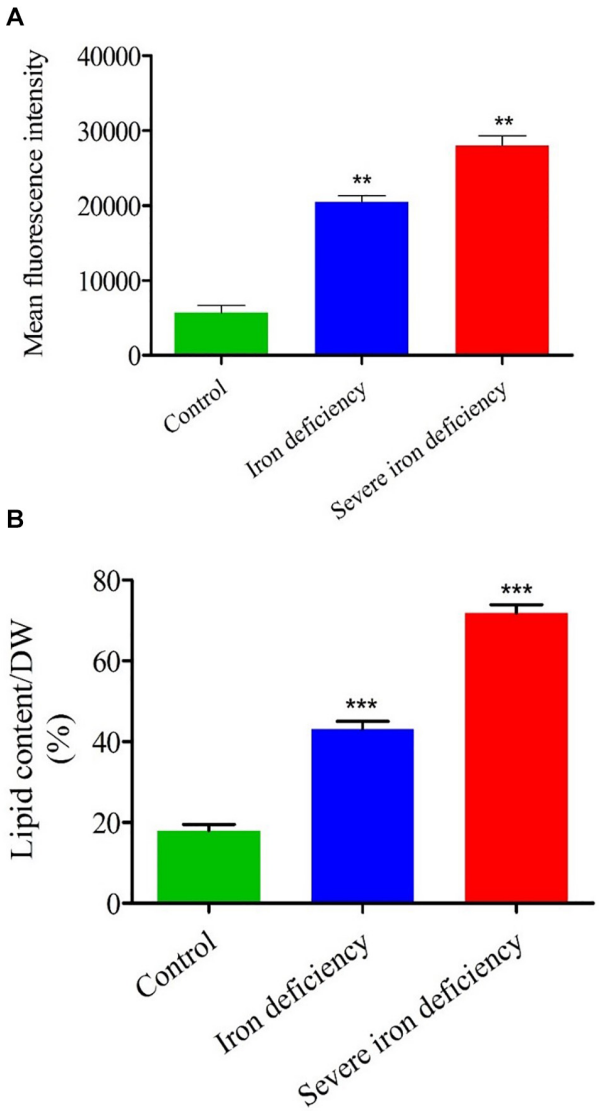

FIGURE 3 | Flow cytometry (FACS) and total lipid content analysis of *Chlamydomonas reinhardtii* cells cultured under iron-replete and iron-deficient conditions. **(A)** The mean fluorescence intensity of neutral lipids stained with NR was measured by FACS. **(B)** Total lipids recovered by organic extraction were quantified in cells over 4 days of growth. Values are mean ± SD. Statistical analysis was performed by Student *t*-test (non-paired) and *P* values were represented as $^{**}P < 0.01$; $^{***}P < 0.001$. Error bar indicates the standard deviation of three biological replicates.

previous reports by Dean et al. (2010). Previous reports have demonstrated that microalgae are grown under N, S, and P deprivation display decreased protein content (Kilham et al., 1997; Cakmak et al., 2012). Our results also showed a drastic decline in *C. reinhardtii* cells' protein content under 2nd stage severe iron starvation compared with 1st stage iron limitation (**Figure 4**). The FTIR spectra (**Figure 4A**) showed a strong absorption peak for the carbohydrate region (C–O–C) compared with weaker absorption for the protein amide I and amide II bands (C=O and N–H, respectively), and also for the lipid band (CO). The decrease in protein content produced by other elemental deprivations suggests that photosynthetic energy is used to synthesize more lipid and carbohydrate for storage, which correlates with our data from neutral lipid and carbohydrate measurements (**Figures 3**, **4**). Carbon storage as lipid and carbohydrate was measured in cells cultured under all conditions after 72 h. In the 1st stage of iron-deficiency, cells showed excess storage of carbon as starch due to increased operation of the Calvin-Benson cycle of carbon fixation as previously reported (Devadasu et al., 2019). This resulted in a substantial increase in the carbohydrate: amide I ratio (fourfold) (**Figure 4B**). The decrease in carbohydrate content in the severe iron deficiency may be due to carbon fixation toward lipid synthesis for energy storage. Lipid content was increased in both 1st and severe iron deficiency cells after 3 days of growth: the lipid: amide I ratio increased twofold in the former while a comparatively moderate increase of threefold occurred in the latter (**Figure 4C**).

In contrast, cells from the severe iron deficiency culture with 1st stage of iron deficiency showed a decrease (twofold) in the carbohydrate: amide ratio after 3 days of growth compare to iron sufficient condition (control) (**Figure 4C**). The results of a previous study suggest that the disassociation of glycolipids [monogalactosyldiacylglycerol (MGDG) and digalactosyldiacylglycerol (DGDG)], into their individual FAs and these FAs recycling to contributes to TAG accumulation in *C. reinhardtii* (Urzica et al., 2013). Similary, in nitrogen starvation the chloroplast membrane lipids have converted to TAG accumulation in *C. reinhardtii* (Yang et al., 2018). We assume that FAs dissociated from glycolipids enter the Kennedy pathway for the synthesis of TAGs. An analysis of lipids extracted from cells from iron-deficient cultures indicated that polar lipids, especially MGDG and DGDG, are degraded more rapidly in these conditions (**Supplementary Figure 2**). Therefore, it is likely that these two major class of lipids of FAs are diverted to participate in the formation of TAGs.

Interestingly, the other polar lipids, DGTS and SQDG, are also decreased in severe iron deficiency, and possibly these galactolipids could have dissociated into individual FAs. A previous study on the effects of N supplementation showed growth, and it produced enhanced cell growth in microalgae and decreased intracellular lipid content (Huang et al., 2013). Iron-induced TAG accumulation was observed following the alteration of chlorophyll content, indicating that iron deficiency affects chloroplast membranes without influencing lipid accumulation. These results are corroborated by TEM images of cells showing disturbance of thylakoid stacks (**Figure 2B**), which indicates that membrane lipids were converted to neutral lipids. It may be concluded that FTIR is a rapid and accurate means of confirming NR staining results when determining the quality of microalgae as a biodiesel feedstock.

Thin-Layer Chromatography Analysis of Accumulated TAGs

Previous studies showed that *C. reinhardtii* gets TAGs when grown under micronutrient limitation (Deng et al., 2011; Kropat et al., 2011). Another report showed epecifically, the

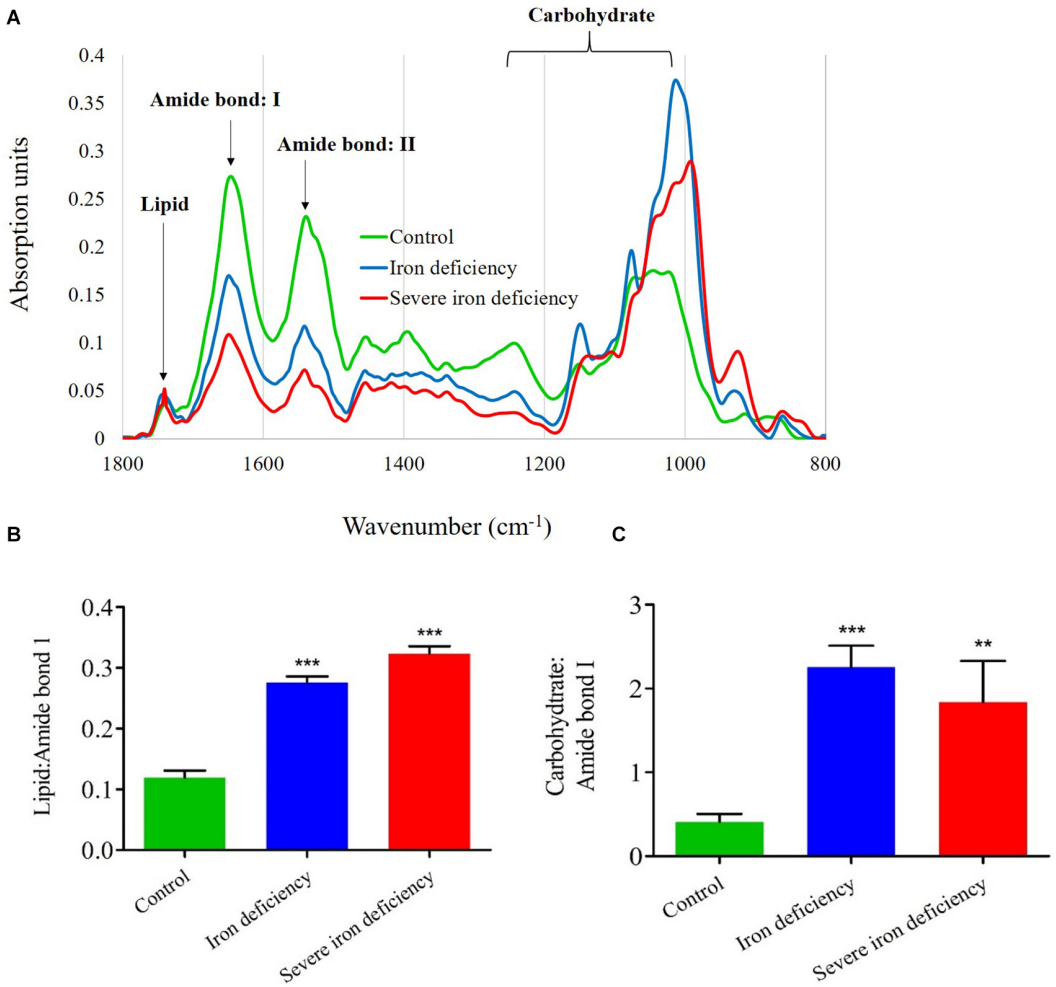

FIGURE 4 | Analysis of carbon storage in *Chlamydomonas reinhardtii* cells cultured under control and iron-deficient conditions by Fourier transform infrared (FTIR). **(A)** Representative FTIR spectra of cells. **(B)** Lipid: amide I ratios over the course of 4 days in culture. **(C)** Carbohydrate: amide I ratio for the iron-deprived culture. Three independent cultures propagated in each medium were examined, and Error bars represened the means ± SD ($n = 3$). The significance values were compared with the control and they represented as $^{***}P < 0.001$ for both iron deficiency conditions in panel **(B)**; $^{***}P < 0.001$ for iron deficiency condition; $^{**}P < 0.01$ value for severe iron deficiency condition in panel **(C)**.

TAG accumulations were observed in iron deficiency (Urzica et al., 2013). However, the accumulation of TAGs in severe iron deficiency is not known so far. Following in severe iron deficiency conditions caused enhanced lipid production by *C. reinhardtii* cells under photoheterotrophic conditions, we next semi-quantified the accumulated TAGs using TLC. Total lipids were extracted from cells following growth under control, iron deficiency, and severe iron deficiency for 72 h (**Figure 5**). TLC analysis of these lipid extracts confirmed increased TAG accumulation during iron starvation (**Figure 5A**). The TAG content (semi quanitiave) of control *C. reinhardtii* cells contained 0.036 mg/g dw of lipid. In comparison, cells cultured under the 1st stage of iron deficiency showed up to lipid content (threefold) (fold increased compare to control), and 2nd stage iron deficiency had lipid contents of fourfold. These results confirmed that two-stage iron stress is a promising method for inducing lipids accumulation, specifically TAGs, in microalgae (**Figure 5B**). It will be necessary to determine whether this strategy can be employed in high throughput photobioreactors to generate TAGs on an industrial scale.

Characterization of Lipids by LC-MS Analysis

Our recent report showed that *C. reinhardtii* cells subjected to 1st generation iron deficiency contain increased saturated FA levels (Devadasu et al., 2019). To determine the nature of lipids accumulation under iron deficiency conditions, we used LC-MS to characterize the FA composition. Extracted total FAs were analyzed by derivatization (transesterification), and the resultant fatty acid methyl esters (FAMEs) were analyzed by LC-MS. *C. reinhardtii* cultured under the two iron deficiency stages contained increased amounts of monounsaturated and saturated FAs compared with cells grown in iron-replete conditions

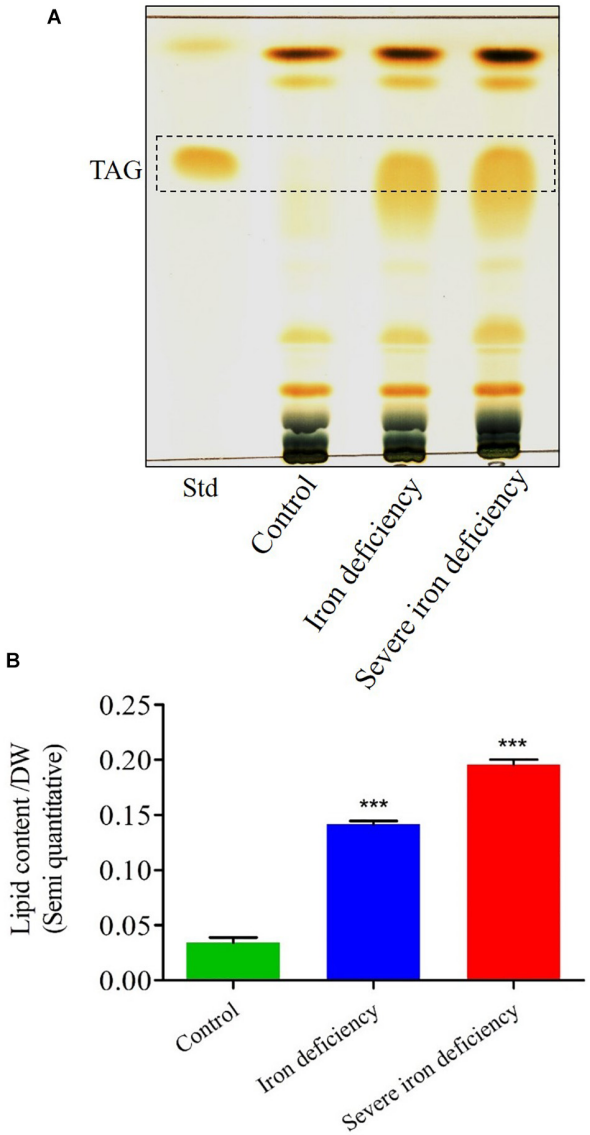

FIGURE 5 | Thin-layer chromatography (TLC) analysis of total triacylglycerol (TAG) content and semi-quantitative measurement of fatty acids in *Chlamydomonas reinhardtii* cells cultured under control and iron-deficient conditions. **(A)** Lipids were extracted from equal dry cell weights (dws), and similar concentrations were loaded in each lane. **(B)** Semi-quantitative measurements of TAGs bands from the cells under control and iron-deficient conditions. Data are the mean values from three replicates (n = 3) expressed as a percentage of dw. The data values were done with Student's t-test. Error bars represent the means ± SD (n = 3). ***P < 0.001.

(**Supplementary Table 1**). Levels of both FA types were higher in cells experiencing the most severe iron starvation. TAGs are rich in saturated FAs (16:0, 18:0), so their accumulation might be due to an increase in this class of FA as stated earlier (James et al., 2011; Urzica et al., 2013). A previous study demonstrated that saturated FAs form up to 20% of dw in *C. reinhardtii* cells grown under nitrogen-deficient conditions (James et al., 2011). Thus, the content of saturated FAs, which are useful for biofuels' production, appears to be increased more by iron deficiency (**Supplementary Table 1**). Our analysis demonstrated that the levels of all primary FAs found in *C. reinhardtii* cells (C16:0, C16:3, C18:0, C18:3, and C18:4) are significantly increased by iron starvation. Studies on iron starvation in *C. reinhardtii* leads to the most dramatic impact on MGDG levels that decreased very rapidly due to activation of MGDG-specific lipase, which predominantly acts on newly synthesized MGDG (Li et al., 2012), which suggests that it might be involved in re-shuffling of saturated FA from MGDG to TAG accumulation. Other reports also stated that the FA desaturation mechanism is played by diiron enzymes known as FA desaturases. These FA desaturases require electrons from NADPH and reduced ferredoxin (Wada et al., 1993; Urzica et al., 2013). Thus, due to lack of iron, FA desaturases are the most sensitive targets and inhibit FA's desaturation in *C. reinhardtii*; hence more saturated FA content was observed (**Supplementary Table 1**).

Moreover, other essential FAs, such as omega-3, α-linolenic acid (18:3), linoleic acid (18:2), and the omega-6 FA, oleic acid (18:1), were detected in cells subjected to iron deficiency. Alterations in FA composition have been reported previously in response to environmental changes, including temperature, pH and nitrogen deficiency in *Chlamydomonas* sp. (Poerschmann et al., 2004; James et al., 2011; Çakmak et al., 2014). The abundance of TAGs in severe iron deficiency could be an excellent strategy to boost biofuel production from green algae.

Iron Starvation Induces DGAT2A Expression

Triacylglycerols can also serve as storage lipids in both plants and algae. The final step in TAG biosynthesis, the incorporation of hydroxylated FAs, is catalyzed by diacylglycerol acyltransferase

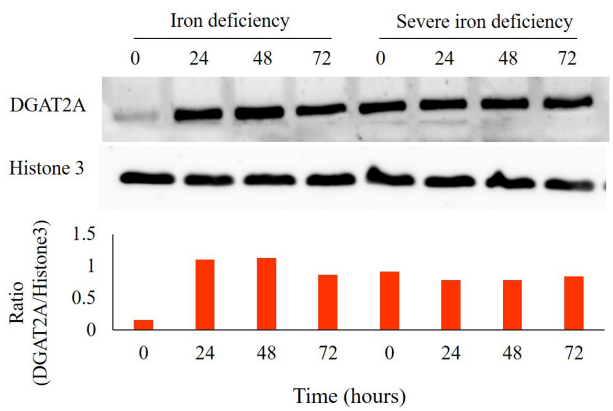

FIGURE 6 | Expression analysis of diacylglycerol acyltransferase (DGAT2A) levels in *Chlamydomonas reinhardtii* cells grown in iron-deprived as well as severe iron-deficient cultures grown from 0, 24, 48, and 72 h by immunoblotting. Total proteins were extracted, and 5 μg of protein were loaded per lane after quantification. Immunostaining of Histone (H) 3 was used as a loading control (C). DGAT2A bands were quantified with Image J software. Experiments were done with three biological replicates (n = 3).

(DGAT) (Zhang et al., 2009). Six genes encoding this enzyme are present in Chlamydomonas, and increased expression of DGAT2A has been reported in nitrogen-starved cells (Wase et al., 2015). Previously, we observed increased DGAT2A protein level expression in *C. reinhardtii* cells during the 1st stage of iron deficiency (Devadasu et al., 2019). We also observed increased expression of DGAT2A protein level during severe iron starvation (0–72 h) (**Figure 6**). It is known that DGAT2A catalyzes the incorporation of diacylglycerol with FA into TAG (Zhang et al., 2009).

CONCLUSION

Iron (Fe^{2+}) is an essential cofactor for photosynthesis since most photosynthetic complexes contain iron. If algal cells are propagated in a medium depleted of iron, photosynthetic efficiency is reduced, but cells remain viable after 72 h in culture. In response to iron deficiency, *C. reinhardtii* cells accumulate significant amounts of lipids. Here, we observed that cells were grown in low-iron conditions accumulated lipids to levels up to fourfold higher than iron-replete controls. Transmission electron micrographs showed large LDs formed in cells subjected to the most severe iron starvation.

Furthermore, we detected a significantly increased accumulation of TAGs in severe iron deficiency about sixfold higher than the control. We also analyzed cellular FA content, which demonstrated that iron starved cells accumulated more saturated than unsaturated FAs. Notably, saturated FAs are the preferred substrate for biodiesel production.

In summary, it indicates that severe iron deficiency hampers growth and triggers the glycolipid breakdown and high TAG accumulation levels. FAs accumulated in TAG are likely derived from the various cellular metabolic networks under iron deficiency. The accumulation of TAG is high in severe iron deficiency conditions which is very important for the feedstock and biodiesel. Hence, this study could be very important for the society to improve the fishery and poultry industries using algae as a feedstock. Therefore, the photobioreactors can enhance the growth and lipid accumulation on an industrial scale that could be important in producing biofuels or aquafeed.

DATA AVAILABILITY STATEMENT

The original contributions presented in the study are included in the article/**Supplementary Material**, further inquiries can be directed to the corresponding author.

AUTHOR CONTRIBUTIONS

ED carried out the experiments, analyzed the data, and drafted the manuscript. RS designed the experiments, drafted the manuscript, and secured the fund. Both authors contributed to the article and approved the submitted version.

FUNDING

RS was supported by the Council of Scientific and Industrial Research [Nos. 38 (1279)/11/EMR-II and 38 (1381)/14/EMR-II], UGC-ISF Research Grant – File No. 6-8/2018 (IC), UoH/IoE/RC1/RC1-20-019, Department of Biotechnology (BT/PR14964/BPA/118/137/2015), and DST-FIST, UGC-SAP, Government of India.

ACKNOWLEDGMENTS

ED acknowledges the receipt of a UGC-RGNF fellowship. We acknowledge John R. Gittins, University of Southampton, National Oceanography Center, Waterfront Road, Southampton, United Kingdom, for his critical reading and English correction.

SUPPLEMENTARY MATERIAL

The Supplementary Material for this article can be found online at: https://www.frontiersin.org/articles/10.3389/fpls.2021.615577/full#supplementary-material

Supplementary Figure 1 | Neutral lipid content of cells during growth (12–72 h) under control and iron deficiency and severe iron deficiency conditions. Cells were stained with Nile Red (NR), and fluorescence measured using a plate reader. Three independent cultures propagated in each medium were examined. Results are the mean ± SD (n = 3).

Supplementary Figure 2 | 2D thin-layer chromatography (TLC) analysis of polar lipids extracted from cells grown under control, iron deficiency and severe iron deficiency conditions. Degraded lipids, monogalactosyldiacylglycerol (MGDG) and digalactosyl diacylglycerol (DGDG), phosphatidyl glycerol (PG), Sulfoquinovosyl-diacylglycerol (SQDG), and Phosphatidylinositol (PI) were detected in cells subjected to severe iron starvation. The chromatography run was repeated three times, and representative results are shown. MGDG band was quantified with ImageJ software from all the conditions and showed a percentage (%). Three independent TLC experiments were done with each culture (n = 3).

REFERENCES

Abinandan, S., Subashchandrabose, S. R., Cole, N., Dharmarajan, R., Venkateswarlu, K., and Megharaj, M. (2019). Sustainable production of biomass and biodiesel by acclimation of non-acidophilic microalgae to acidic conditions. *Bioresour. Technol.* 271, 316–324. doi: 10.1016/j.biortech.2018.09.140

Bligh, E. G., and Dyer, W. J. (1959). A rapid method of total lipid extraction and purification. *Can. J. Biochem. Physiol.* 37, 911–917. doi: 10.1139/y59-099

Bozzola, J. J., and Russell, L. D. (1998). *Electron Microscopy: Principles and Techniques for Biologists*, 2nd Edn. Sudbury, MA: Jones and Bartlett publishers, 19–144.

Cakmak, T., Angun, P., Demiray, Y. E., Ozkan, A. D., Elibol, Z., and Tekinay, T. (2012). Differential effects of nitrogen and sulfur deprivation on growth and biodiesel feedstock production of *Chlamydomonas reinhardtii*. *Biotechnol. Bioeng.* 109, 1947–1957. doi: 10.1002/bit.24474

Çakmak, Z. E., Ölmez, T. T., Çakmak, T., Menemen, Y., and Tekinay, T. (2014). Induction of triacylglycerol production in *Chlamydomonas reinhardtii*:

comparative analysis of different element regimes. *Bioresour. Technol.* 155, 379–387. doi: 10.1016/j.biortech.2013.12.093

Chen, M., Tang, H., Ma, H., Holland, T. C., Ng, K. Y., and Salley, S. O. (2011). Effect of nutrients on growth and lipid accumulation in the green algae *Dunaliella tertiolecta*. *Bioresour. Technol.* 102, 1649–1655. doi: 10.1016/j.biortech.2010.09.062

Couso, I., Pérez-Pérez, M. E., Martínez-Force, E., Kim, H. S., He, Y., Umen, J. G., et al. (2018). Autophagic flux is required for the synthesis of triacylglycerols and ribosomal protein turnover in *Chlamydomonas*. *J. Exp. Bot.* 69, 1355–1367. doi: 10.1093/jxb/erx372

Dean, A. P., Sigee, D. C., Estrada, B., and Pittman, J. K. (2010). Using FTIR spectroscopy for rapid determination of lipid accumulation in response to nitrogen limitation in freshwater microalgae. *Bioresour. Technol.* 101, 4499–4507. doi: 10.1016/j.biortech.2010.01.065

Deng, X., Fei, X., and Li, Y. (2011). The effects of nutritional restriction on neutral lipid accumulation in *Chlamydomonas* and *Chlorella*. *Afr. J. Microbiol. Res.* 5, 260–270.

Devadasu, E., Chinthapalli, D. K., Chouhan, N., Madireddi, S. K., Rasineni, G. K., Sripadi, P., et al. (2019). Changes in the photosynthetic apparatus and lipid droplet formation in *Chlamydomonas reinhardtii* under iron deficiency. *Photosynth. Res.* 139, 253–266. doi: 10.1007/s11120-018-0580-2

Devadasu, E., Pandey, J., Dhokne, K., and Subramanyam, R. (2021). Restoration of photosynthetic activity and supercomplexes from severe iron starvation in *Chlamydomonas reinhardtii*. *Biochim. Biophys. Acta* 1862:148331. doi: 10.1016/j.bbabio.2020.148331

Devadasu, E. R., Madireddi, S. K., Nama, S., and Subramanyam, R. (2016). Iron deficiency cause changes in photochemistry, thylakoid organization, and accumulation of photosystem II proteins in *Chlamydomonas reinhardtii*. *Photosynth. Res.* 130, 469–478. doi: 10.1007/s11120-016-0284-4

Fan, J., and Zheng, L. (2017). Acclimation to NaCl and light stress of heterotrophic *Chlamydomonas reinhardtii* for lipid accumulation. *J. Biosci. Bioeng.* 124, 302–308. doi: 10.1016/j.jbiosc.2017.04.009

Glaesener, A. G., Merchant, S. S., and Blaby-Haas, C. E. (2013). Iron economy in *Chlamydomonas reinhardtii*. *Front. Plant Sci.* 4:337. doi: 10.3389/fpls.2013.00337

Gorain, P. C., Bagchi, S. K., and Mallick, N. (2013). Effects of calcium, magnesium and sodium chloride in enhancing lipid accumulation in two green microalgae. *Environ. Technol.* 34, 1887–1894. doi: 10.1080/09593330.2013.812668

Hamed, S. M., Selim, S., Klöck, G., and Abdelgawad, H. (2017). Sensitivity of two green microalgae to copper stress: growth, oxidative and antioxidants analyses. *Ecotoxicol. Environ. Saf.* 144, 19–25. doi: 10.1016/j.ecoenv.2017.05.048

Howell, S. H. (2013). Endoplasmic reticulum stress responses in plants. *Annu. Rev. Plant Biol.* 64, 477–499. doi: 10.1146/annurev-arplant-050312-120053

Huang, X., Huang, Z., Wen, W., and Yan, J. (2013). Effects of nitrogen supplementation of the culture medium on the growth, total lipid content and fatty acid profiles of three microalgae (*Tetraselmis subcordiformis*, *Nannochloropsis oculata* and *Pavlova viridis*). *J. Appl. Phycol.* 25, 129–137. doi: 10.1007/s10811-012-9846-9

James, G. O., Hocart, C. H., Hillier, W., Chen, H., Kordbacheh, F., Price, G. D., et al. (2011). Fatty acid profiling of *Chlamydomonas reinhardtii* under nitrogen deprivation. *Bioresour. Technol.* 102, 3343–3351. doi: 10.1016/j.biortech.2010.11.051

Jouhet, J., Lupette, J., Clerc, O., Magneschi, L., Bedhomme, M., Collin, S., et al. (2017). LC-MS/MS versus TLC plus GC methods: consistency of glycerolipid and fatty acid profiles in microalgae and higher plant cells and effect of a nitrogen starvation. *PLoS One* 12:e0182423. doi: 10.1371/journal.pone.0182423

Kilham, S., Kreeger, D., Goulden, C., and Lynn, S. (1997). Effects of nutrient limitation on biochemical constituents of *Ankistrodesmus falcatus*. *Freshw. Biol.* 38, 591–596. doi: 10.1046/j.1365-2427.1997.00231.x

Kropat, J., Hong-Hermesdorf, A., Casero, D., Ent, P., Castruita, M., Pellegrini, M., et al. (2011). A revised mineral nutrient supplement increases biomass and growth rate in *Chlamydomonas reinhardtii*. *Plant J.* 66, 770–780. doi: 10.1111/j.1365-313x.2011.04537.x

Li, X., Moellering, E. R., Liu, B., Johnny, C., Fedewa, M., Sears, B. B., et al. (2012). A galactoglycerolipid lipase is required for triacylglycerol accumulation and survival following nitrogen deprivation in *Chlamydomonas reinhardtii*. *Plant Cell* 24, 4670–4686. doi: 10.1105/tpc.112.105106

Lin, Q., Zhuo, W. H., Wang, X. W., Chen, C. P., Gao, Y. H., and Liang, J. R. (2018). Effects of fundamental nutrient stresses on the lipid accumulation profiles in two diatom species *Thalassiosira weissflogii* and *Chaetoceros muelleri*. *Bioprocess Biosyst. Eng.* 41, 1213–1224. doi: 10.1007/s00449-018-1950-z

Martin, G. J., Hill, D. R., Olmstead, I. L., Bergamin, A., Shears, M. J., Dias, D. A., et al. (2014). Lipid profile remodeling in response to nitrogen deprivation in the microalgae *Chlorella* sp. (Trebouxiophyceae) and *Nannochloropsis* sp. (Eustigmatophyceae). *PLoS One* 9:e103389. doi: 10.1371/journal.pone.0103389

Masclaux-Daubresse, C., d'Andrea, S., Bouchez, I., and Cacas, J. L. (2020). Reserve lipids and plant autophagy. *J. Exp. Bot.* 71, 2854–2861. doi: 10.1093/jxb/eraa082

Merchant, S. S., Prochnik, S. E., Vallon, O., Harris, E. H., Karpowicz, S. J., Witman, G. B., et al. (2007). The *Chlamydomonas* genome reveals the evolution of key animal and plant functions. *Science* 318, 245–250.

Moellering, E. R., and Benning, C. (2010). RNA interference silencing of a major lipid droplet protein affects lipid droplet size in *Chlamydomonas reinhardtii*. *Eukaryot Cell* 9, 97–106. doi: 10.1128/ec.00203-09

Ördög, V., Stirk, W. A., Bálint, P., Aremu, A. O., Okem, A., Lovász, C., et al. (2016). Effect of temperature and nitrogen concentration on lipid productivity and fatty acid composition in three *Chlorella* strains. *Algal Res.* 16, 141–149. doi: 10.1016/j.algal.2016.03.001

Park, J.-J., Wang, H. X., Gargouri, M., Deshpande, R. R., Skepper, J. N., Holguin, F. O., et al. (2015). The response of *Chlamydomonas reinhardtii* to nitrogen deprivation: a systems biology analysis. *Plant J.* 81, 611–624.

Poerschmann, J., Spijkerman, E., and Langer, U. (2004). Fatty acid patterns in *Chlamydomonas* sp. as a marker for nutritional regimes and temperature under extremely acidic conditions. *Microb. Ecol.* 48, 78–89. doi: 10.1007/s00248-003-0144-6

Rios, L. F., Klein, B. C., Luz, L. F. Jr., Maciel Filho, R., and Wolf Maciel, M. R. (2015). Nitrogen starvation for lipid accumulation in the microalga species *Desmodesmus* sp. *Appl. Biochem. Biotechnol.* 175, 469–476. doi: 10.1007/s12010-014-1283-6

Sharma, K. K., Schuhmann, H., and Schenk, P. M. (2012). High lipid induction in microalgae for biodiesel production. *Energies* 5, 1532–1553. doi: 10.3390/en5051532

Siaut, M., Cuiné, S., Cagnon, C., Fessler, B., Nguyen, M., Carrier, P., et al. (2011). Oil accumulation in the model green alga *Chlamydomonas reinhardtii*: characterization, variability between common laboratory strains and relationship with starch reserves. *BMC Biotechnol.* 11:7. doi: 10.1186/1472-6750-11-7

Singh, S. P., Zhou, X.-R., Liu, Q., Stymne, S., and Green, A. G. (2005). Metabolic engineering of new fatty acids in plants. *Curr. Opin. Plant Biol.* 8, 197–203. doi: 10.1016/j.pbi.2005.01.012

Tan, K. W. M., and Lee, Y. K. (2016). The dilemma for lipid productivity in green microalgae: importance of substrate provision in improving oil yield without sacrificing growth. *Biotechnol. Biofuels* 9:255.

Towbin, H., Staehelin, T., and Gordon, J. (1979). Electrophoretic transfer of proteins from polyacrylamide gels to nitrocellulose sheets: procedure and some applications. *Proc. Natl. Acad. Sci. U.S.A.* 76, 4350–4354. doi: 10.1073/pnas.76.9.4350

Urzica, E. I., Vieler, A., Hong-Hermesdorf, A., Page, M. D., Casero, D., Gallaher, S. D., et al. (2013). Remodeling of membrane lipids in iron-starved *Chlamydomonas*. *J. Biol. Chem.* 288, 30246–30258. doi: 10.1074/jbc.m113.490425

Velmurugan, N., Sung, M., Yim, S. S., Park, M. S., Yang, J. W., and Jeong, K. J. (2014). Systematically programmed adaptive evolution reveals potential role of carbon and nitrogen pathways during lipid accumulation in *Chlamydomonas reinhardtii*. *Biotechnol. Biofuels* 7:117. doi: 10.1186/preaccept-1279724404120676

Wada, H., Schmidt, H., Heinz, E., and Murata, N. (1993). In vitro ferredoxin-dependent desaturation of fatty acids in cyanobacterial thylakoid membranes. *J. Bacteriol.* 175, 544–547. doi: 10.1128/jb.175.2.544-547.1993

Wase, N., Tu, B., Black, P., and DiRusso, C. (2015). Phenotypic screening identifies Brefeldin A/Ascotoxin as an inducer of lipid storage in the algae *Chlamydomonas reinhardtii*. *Algal Res.* 11, 74–84. doi: 10.1016/j.algal.2015.06.002

Yadavalli, V., Jolley, C. C., Malleda, C., Thangaraj, B., Fromme, P., and Subramanyam, R. (2012). Alteration of proteins and pigments influence

the function of photosystem I under iron deficiency from *Chlamydomonas reinhardtii*. *PLoS One* 7:e35084. doi: 10.1371/journal.pone.0035084

Yang, M., Meng, Y., Chu, Y., Fan, Y., Cao, X., Xue, S., et al. (2018). Triacylglycerol accumulates exclusively outside the chloroplast in short-term nitrogen-deprived *Chlamydomonas reinhardtii*. *Biochim. Biophys. Acta Mol. Cell Biol. Lipids* 1863, 1478–1487. doi: 10.1016/j.bbalip.2018.09.009

Zhang, M., Fan, J., Taylor, D. C., and Ohlrogge, J. B. (2009). Acyltransferases have overlapping functions in *Arabidopsis* triacylglycerol biosynthesis and are essential for normal pollen and seed development. *Plant Cell* 21, 3885–3901. doi: 10.1105/tpc.109.071795

Conflict of Interest: The authors declare that the research was conducted in the absence of any commercial or financial relationships that could be construed as a potential conflict of interest.

Copyright © 2021 Devadasu and Subramanyam. This is an open-access article distributed under the terms of the Creative Commons Attribution License (CC BY). The use, distribution or reproduction in other forums is permitted, provided the original author(s) and the copyright owner(s) are credited and that the original publication in this journal is cited, in accordance with accepted academic practice. No use, distribution or reproduction is permitted which does not comply with these terms.

frontiers in Plant Science

ORIGINAL RESEARCH
published: 14 April 2021
doi: 10.3389/fpls.2021.658961

Arabidopsis thaliana EARLY RESPONSIVE TO DEHYDRATION 7 Localizes to Lipid Droplets via Its Senescence Domain

Nathan M. Doner[1], Damien Seay[2], Marina Mehling[2], Siqi Sun[3], Satinder K. Gidda[1], Kerstin Schmitt[4], Gerhard H. Braus[4], Till Ischebeck[3], Kent D. Chapman[5], John M. Dyer[2†] and Robert T. Mullen[1]*

[1]Department of Molecular and Cellular Biology, University of Guelph, Guelph, ON, Canada, [2]United States Department of Agriculture, US Arid-Land Agricultural Research Center, Agriculture Research Service, Maricopa, AZ, United States, [3]Department of Plant Biochemistry, Albrecht-von-Haller-Institute for Plant Sciences and Göttingen Center for Molecular Biosciences (GZMB), University of Göttingen, Göttingen, Germany, [4]Department of Molecular Microbiology and Genetics, Institute for Microbiology and Genetics and Göttingen Center for Molecular Biosciences (GZMB), University of Göttingen, Göttingen, Germany, [5]BioDiscovery Institute and Department of Biological Sciences, University of North Texas, Denton, TX, United States

Lipid droplets (LDs) are neutral-lipid-containing organelles found in all kingdoms of life and are coated with proteins that carry out a vast array of functions. Compared to mammals and yeast, relatively few LD proteins have been identified in plants, particularly those associated with LDs in vegetative (non-seed) cell types. Thus, to better understand the cellular roles of LDs in plants, a more comprehensive inventory and characterization of LD proteins is required. Here, we performed a proteomics analysis of LDs isolated from drought-stressed *Arabidopsis* leaves and identified EARLY RESPONSIVE TO DEHYDRATION 7 (ERD7) as a putative LD protein. mCherry-tagged ERD7 localized to both LDs and the cytosol when ectopically expressed in plant cells, and the protein's C-terminal senescence domain (SD) was both necessary and sufficient for LD targeting. Phylogenetic analysis revealed that ERD7 belongs to a six-member family in *Arabidopsis* that, along with homologs in other plant species, is separated into two distinct subfamilies. Notably, the SDs of proteins from each subfamily conferred targeting to either LDs or mitochondria. Further, the SD from the ERD7 homolog in humans, spartin, localized to LDs in plant cells, similar to its localization in mammals; although, in mammalian cells, spartin also conditionally localizes to other subcellular compartments, including mitochondria. Disruption of *ERD7* gene expression in *Arabidopsis* revealed no obvious changes in LD numbers or morphology under normal growth conditions, although this does not preclude a role for ERD7 in stress-induced LD dynamics. Consistent with this possibility, a yeast two-hybrid screen using ERD7 as bait identified numerous proteins involved in stress responses, including some that have been identified in other LD proteomes. Collectively, these observations provide new insight to ERD7 and the SD-containing family of proteins in plants and suggest that ERD7 may be involved in functional aspects of plant stress response that also include localization to the LD surface.

Keywords: EARLY RESPONSIVE TO DEHYDRATION 7, lipid droplet, plant lipids, senescence domain, senescence domain-containing protein, senescence/spartin-associated domain, spartin, stress

OPEN ACCESS

Edited by:
Juliette Jouhet, UMR5168 Laboratoire de Physiologie Cellulaire Vegetale (LPCV), France

Reviewed by:
Sabine D'andrea, AgroParisTech Institut des Sciences et Industries du Vivant et de L'environnement, France
Morgane Michaud, UMR5168 Laboratoire de Physiologie Cellulaire Vegetale (LPCV), France

***Correspondence:**
Robert T. Mullen
rtmullen@uoguelph.ca

†Present address:
John M. Dyer, United States Department of Agriculture, Agricultural Research Service, Albany, CA, United States

Specialty section:
This article was submitted to Plant Physiology, a section of the journal Frontiers in Plant Science

Received: *26 January 2021*
Accepted: *23 March 2021*
Published: *14 April 2021*

Citation:
Doner NM, Seay D, Mehling M, Sun S, Gidda SK, Schmitt K, Braus GH, Ischebeck T, Chapman KD, Dyer JM and Mullen RT (2021) Arabidopsis thaliana EARLY RESPONSIVE TO DEHYDRATION 7 Localizes to Lipid Droplets via Its Senescence Domain. Front. Plant Sci. 12:658961. doi: 10.3389/fpls.2021.658961

INTRODUCTION

Cells store neutral lipids, such as triacylglycerols (TAG) and sterol esters, in cytoplasmic lipid droplets (LDs), an organelle found in all kingdoms of life (Chapman et al., 2013; Lundquist et al., 2020). LDs are much more than simply lipid storage sites however, since they participate in a vast array of other cellular processes ranging from metabolism, protein turnover, signaling molecule biosynthesis, protein sequestration, and stress response (Pyc et al., 2017b; Kretzschmar et al., 2018; Olzmann and Carvalho, 2019; Lundquist et al., 2020). Underlying the control of these various processes are numerous LD "coat" proteins that reside on the surface of LDs and can be involved also in the formation of LDs at the endoplasmic reticulum (ER), mediating LD-LD or LD-organelle interactions, and LD turnover (Chapman et al., 2019; Thiam and Dugail, 2019; Ischebeck et al., 2020). While many LD proteins are conserved among evolutionarily-diverse organisms, some are unique to mammals, yeasts, or plants. Furthermore, the composition of LD coat proteins can vary even within the same species, depending on the tissue/cell type, developmental stage, and/or environmental cues. In *Arabidopsis thaliana*, for example, LD protein constituents differ in siliques, seeds, and seedlings (Kretzschmar et al., 2020), as well as in senescent (Brocard et al., 2017) or pathogen-challenged leaves (Shimada et al., 2014; Fernández-Santos et al., 2020).

Lipid droplets in plants are probably best known for their hyperaccumulation in oilseeds as a means to store carbon and energy. Once seed germination takes place, the stored lipids in oilseed LDs are catabolized to provide energy for seedling establishment until photoautotrophic growth can sustain the plant. However, in most other plant organs and tissues, including those that are typically not associated with lipid storage, such as in leaves, stems, and roots, the functions of LDs go beyond energy storage and include processes related to plant growth and development, lipid signaling, and biotic and abiotic stress responses (Pyc et al., 2017b; Ischebeck et al., 2020). Further, oleosins, which are involved with oilseed LD biology and are arguably the best characterized plant LD proteins, are not commonly found in vegetative tissues (Huang, 1996; Laibach et al., 2015). Our understanding of LD functions in non-seed tissues is limited, therefore, because relatively few LD-associated proteins have been studied in non-seed cell types. Nonetheless, recent efforts using mass-spectrometry (MS)-based proteomic analyses of purified LDs have led to the identification and subsequent characterization of several new plant-specific LD proteins. Pertinent examples include the LD-ASSOCIATED PROTEINS (LDAPs), which are required for proper LD biogenesis and neutral lipid homeostasis in vegetative tissues, including during stress responses (Gidda et al., 2013, 2016; Horn et al., 2013; Kim et al., 2016); PLANT UBX DOMAIN-CONTAINING PROTEIN 10 (PUX10), which is a member of the UBX-domain-containing protein family and is involved in LD protein degradation in *Arabidopsis* (Deruyffelaere et al., 2018; Kretzschmar et al., 2018); LDAP-INTERACTING PROTEIN (LDIP), which functions, presumably with LDAPs, in LD biogenesis (Pyc et al., 2017a; Coulon et al., 2020); and PHYTOALEXIN-DEFICIENT 3 (PAD3), which participates in the biosynthesis of antifungal compounds and localizes to leaf LDs during pathogen challenge (Fernández-Santos et al., 2020). As such, LD proteomics-based studies have not only provided important new insights into LD functioning in plants, they have led to the growing appreciation in the field that more LD proteins and the allied LD processes in which they are involved are yet to be discovered.

While LDs are known to proliferate during various biotic and abiotic stress treatments (reviewed in Xu and Shanklin, 2016; Pyc et al., 2017b; Yang and Benning, 2018; de Vries and Ischebeck, 2020; Lu et al., 2020), the linkage between LDs and stress responses is poorly understood, due in part to the limited numbers of LD-related proteins identified to date. Gene expression studies, on the other hand, have identified numerous genes that are differentially regulated during stress adaptation. Among these is EARLY RESPONSIVE TO DEHYDRATION 7 (ERD7), which is strongly upregulated by both biotic and abiotic stresses and, thus, commonly used as a marker for plant stress response (Cheng et al., 2013; Rasmussen et al., 2013). However, there is limited information on the function(s) of ERD7 and its subcellular localization in plant cells, with the exception of a recent study that demonstrated that ERD7 localizes in Arabidopsis protoplasts to membranes, albeit of uncertain identity (Barajas-Lopez et al., 2020). In the same study, ERD7 was shown to also bind to negatively-charged phospholipids *in vitro* and the composition of membrane lipids and membrane fluidity were altered in leaves of cold-stressed *erd7* mutant plants, suggesting that ERD7 plays a role in membrane lipid remodeling during cold stress response in Arabidopsis (Barajas-Lopez et al., 2020). ERD7 contains a predicted senescence domain (SD). The SD was originally named based on a protein that is upregulated in senescent daylily petals (Panavas et al., 1999), but is also found in other proteins in plants, metazoans, and fungi. Notably, in humans, the SD-containing protein spartin has been shown to localize to LDs (Eastman et al., 2009; Urbancyzk and Enz, 2011), as well as other subcellular compartments, including endosomes or mitochondria (Bakowska et al., 2007; Edwards et al., 2009; Joshi and Bakowska, 2011; Karlsson et al., 2014). While the spartin SD has been shown to bind the mitochondrial-associated phospholipid cardiolipin, which possibly serves as a mechanism for its mitochondrial localization (Joshi and Bakowska, 2011), how spartin targets to LDs and what its function(s) is on the LD surface are open questions.

In this study, the aim was to continue efforts to identify novel LD coat proteins in plant vegetative (non-seed) tissues. Toward that end, we analyzed the LD-enriched proteins isolated from drought-stressed Arabidopsis leaves, which is known to result in an accumulation of TAG and LD proliferation in plant vegetative tissues (Martin et al., 1986; Kong et al., 2013; Mukhopadhyay and Tyagi, 2015; Perlikowski et al., 2016; VanBuren et al., 2017; and reviewed in Xu and Shanklin, 2016; Yang and Benning, 2018; Lu et al., 2020). Among the various LD-related proteins we identified was ERD7, which we subsequently show using fluorescence microscopy localizes to LDs in plant cells. We also show that the protein's SD

mediates its LD localization. Interestingly, among the six SD-containing proteins in Arabidopsis, the SDs of ERD7 and both of its two closest homologs convey LD targeting in plant cells, as does the SD in human spartin, while the SD of other, more distantly-related Arabidopsis SD-containing proteins target to mitochondria. We discuss these and other findings, including a yeast two-hybrid (Y2H) screen that identified numerous stress-related proteins, and how they will provide new avenues for investigating the underlying mechanisms linking LDs and stress responses in plants.

MATERIALS AND METHODS

Plant Material, Growth Conditions, and Transformations

Experiments performed with *A. thaliana* involved the wild-type (WT) Columbia-0 (Col-0) ecotype, an *erd7-1* T-DNA insertional mutant line obtained from the Arabidopsis Biological Resource Center [ABRC; WiscDsLox452E10 (seed stock CS856515)], an *erd7-2* CRISPR/Cas9-based deletion mutant line, and an ERD7-mCherry stable expression line (see ERD7-mCherry-Expressing and CRISPR/Cas9 erd7 Knockout Arabidopsis Lines section for additional details on the latter two transgenic plant lines). Soil-grown Arabidopsis plants were cultivated with a 16/8-h day/night cycle at 22°C and a light intensity of 50 μmol m^{-2} s^{-1}. For growth on agar plates, seeds were sterilized with ethanol and plated on ½ strength Murashige and Skoog (Sigma-Aldrich) plates, and then stratified for 3 days at 4°C in the dark before being moved to a growth chamber with a 16/8-h day/night cycle at 22°C and a light intensity of 50 μmol m^{-2} s^{-1}. Arabidopsis (stable) transformations were carried out using the floral dip method (Clough and Bent, 1998) and *Agrobacterium tumefaciens* (strain GV3101) harboring the selected binary vector (see Molecular Cloning and Plasmid Construction section for details on all binary vectors used in this study), as described elsewhere (Clough and Bent, 1998; Petrie et al., 2010).

Nicotiana benthamiana plants were grown in soil with a 16/8-h day/night cycle at 22°C and a light intensity of 50 μmol m^{-2} s^{-1}. Leaves of ~4-week-old plants were transiently (co)transformed by infiltration with *A. tumefaciens* (strain LBA4404) carrying the selected binary vector(s), as described previously (McCartney et al., 2005; Cai et al., 2015). All (co) infiltrations with *N. benthamiana* were performed with the tomato bushy stunt virus (TBSV) *P19* gene in order to enhance ectopic gene expression (Petrie et al., 2010).

Suspension-cultured Arabidopsis cells were grown and transformed *via* biolistic bombardment, as described previously (Lingard and Trelease, 2006). Tungsten microparticles were coated with 10 μg of binary plasmid DNA [i.e., pMDC32-ChN/mCherry-ERD7 (see Molecular Cloning and Plasmid Construction section)] and 4 μg pRTL2/mGFP (Shockey et al., 2006), which encodes a monomerized version of the green fluorescent protein (GFP) and served as a cell (co)transformation marker. Approximately 24 h following bombardment, cells were prepared for confocal laser-scanning microscopy (CLSM), as described below (Microscopy section).

ERD7-mCherry-Expressing and CRISPR/Cas9 *erd7* Knockout Arabidopsis Lines

To generate Arabidopsis Col-0 plants stably-expressing ERD7-mCherry, selected hygromycin-resistant T_1 seedlings obtained after *Agrobacterium*-mediated plant transformation with pMDC32/ERD7-mCherry binary vector were advanced and resulting T_2 progeny were analyzed for ERD7-mCherry fluorescence using CLSM. Unfortunately, for reasons unknown, we were unable to generate homozygous T_3 lines stably-expressing ERD7-mCherry and, thus, experiments in this study were limited to assessing the subcellular localization of ERD7-mCherry in T_2 lines.

Arabidopsis *erd7-2* mutant plants were generated using CRISPR/Cas9 genome editing of Col-0 based on the procedures described by Wang et al. (2015). Briefly, a pBEE401E-based vector containing the egg-cell-expressed *CAS9* open reading frame (ORF) and a pair of single-guide RNAs (sgRNAs) corresponding to sequences near the 5' and 3' ends of the *ERD7* ORF was introduced into Arabidopsis using the floral dip method (Clough and Bent, 1998); refer to Molecular Cloning and Plasmid Construction section for additional details on the construction of the pBEE401E-based vector used for CRISPR/Cas9 genome editing of *ERD7* and **Supplementary Table 1** for sequences of sgRNAs and all other oligonucleotide primers used in this study. Genomic DNA (gDNA) of BASTA [i.e., phosphinothricin (Gold Biotechnology)]-resistant T_1 plants was screened for the loss of the *ERD7* ORF using the PCR and gene-specific primers (**Supplementary Table 1**) and selected *erd7* mutant plants were advanced. gDNA from T_2 progeny plants was then screened by PCR [and with the appropriate primers (**Supplementary Table 1**)] for the *CAS9*-containing T-DNA insert in order to identify plant lines that had lost the T-DNA through genetic segregation. Thereafter, edited *erd7* mutant and *CAS9*-deficient T_3 plants were analyzed by PCR genotyping and deletion of a sequence encoding 398 amino acids of the 452-amino-acid-long ERD7 polypeptide was confirmed by sequencing of the *ERD7* PCR product. Refer to **Supplementary Figure 1** for details on the relative locations of the sgRNAs and the region of the *ERD7* ORF that was removed by CRISPR/Cas9 genome editing in the *erd7-2* mutant line and the position of the T-DNA insertion in the *erd7-1* mutant line, as well as the genotyping and reverse transcriptase (RT)-PCR results for both mutant lines.

All DNA sequencing carried out in this study, including the sequencing of newly-constructed plasmids (see Molecular Cloning and Plasmid Construction section), was performed at the University of Guelph Genomics Facility or by Retrogen Inc.

Proteomics of Drought-Treated Arabidopsis Leaves

Wild-type (Col-0) Arabidopsis were grown on soil for 4 weeks as described above before watering was withheld for 1 week. Three biological replicates of rosette leaves were harvested, and then LDs were isolated and the associated proteins subjected to liquid chromatography-tandem MS (LC-MS/MS), as described previously (Schmitt et al., 2017; Kretzschmar et al., 2020), but

with the following modifications: centrifugation steps were carried out at 100,000 *g*, and the buffer used for grinding and all washing steps was supplemented with 0.4 M sucrose. Three technical replicates of LC-MS/MS analysis were performed on the peptide samples of each biological replicate.

The libraries, raw data files, MaxQuant search files, as well as protein groups and peptide search results created by MaxQuant are available on ProteomeXchange/PRIDE (Vizcaíno et al., 2014) under the identifier PXD023047. All LC-MS/MS data processing settings with MaxQuant can be found in the metadata file (**Supplementary Table 2**) and all raw and normalized/sorted proteomics data are shown in **Supplementary Datasets 1** and **2**, respectively.

Molecular Cloning and Plasmid Construction

The *ERD7* ORF was amplified from Arabidopsis rosette leaf cDNA using PCR and primers [i.e., ERD7-FP-*Sal*I and ERD7-RP-*Xho*I (**Supplementary Table 1**)] and then, following digestion with *Sal*I and *Xho*I, subcloned into similarly-digested donor vector pENTR3C (Invitrogen), yielding pENTR3C/ERD7. The *ERD7* ORF was subsequently transferred from pENTR3C/ERD7 into pMDC32-ChN using Gateway cloning technology (Curtis and Grossniklaus, 2003), yielding pMDC32/Ch-ERD7. pMDC32-ChN is a plant expression binary vector which contains two copies of the constitutive *35S* Cauliflower mosaic virus (CaMV) promoter, the ORF of the red fluorescent protein mCherry, and an adjacent 3' cloning site that allows for the translational (in-frame) fusion of mCherry to the N-terminus of a protein of interest (i.e., mCherry-X). To construct pMDC32-ChN, the mCherry ORF (without its stop codon; Shaner et al., 2004) was amplified by PCR from pRTL2/mCherry (Gidda et al., 2011) using primers mCherry-FP-*Kpn*I and mCherry-RP-*Asc*I (**Supplementary Table 1**) and inserted (*via* *Kpn*I/and *Asc*I restriction sites) upstream of the recombination site in pMDC32 (Curtis and Grossniklaus, 2003). To construct pMDC32/ERD7-mCherry, encoding ERD7 fused at its C-terminus to mCherry, primers ERD7-FP-pDONR and ERD7-RP-pDONR(NS) (**Supplementary Table 1**) were used to amplify the *ERD7* ORF from Arabidopsis rosette leaf cDNA. Thereafter, the *ERD7* ORF was transferred to pDONR-zeo and then pMDC32-ChC (Kretzschmar et al., 2020), *via* Gateway cloning.

All ERD7 mutants were amplified using pENTR3C/ERD7 (see above) as template DNA and the appropriate primers (**Supplementary Table 1**). Resulting PCR products were transferred into pMDC32-ChN using Gateway cloning, sometimes without being subcloned into the intermediate pDONR vector, as described in Müller et al. (2017) and referred to here as Fast Gateway cloning. *SENA2*, *SENA3*, *SENB1*, and *SENB2* full-length ORFs and their corresponding SD sequences were amplified from Arabidopsis rosette leaf cDNA using the appropriate gene-specific primers (**Supplementary Table 1**), followed by Gateway or Fast Gateway cloning into pMDC32-ChC. The coding region containing the SD in human (*Homo sapiens*) spartin [i.e., spartin-SD; amino acid residues 418–623, based on the InterPro domain database (see Bioinformatics section; accession no. NM_015087.5)] was amplified from cDNA derived from cultured human dopaminergic neurons using primers SPARTINSD-FP-pDONR and SPARTINSD-RP-pDONR (**Supplementary Table 1**) and cloned into pMDC32-ChC *via* Fast Gateway cloning. A full-length human spartin cDNA (CloneID HsCD00743790) was obtained from the DNASU Plasmid Repository[1] and used as a template, along with the appropriate primers, for Fast Gateway cloning into pMDC32-ChC. Note that compared to the reference sequence for spartin (i.e., NM_015087.5), the full-length spartin clone used in this study contained three point mutations (accession no. LT742893.1), resulting in two amino acid changes, P69T and P417H, both of which are outside of the protein's SD.

The construction of pMDC43/GFP-LPEAT1, encoding GFP-tagged Arabidopsis ACYL CoA:LYSOPHOSPHATIDYLETHANOLAMINE ACYLTRANSFERASE isoform 1 (LPEAT1), and pORE04/P19, encoding the Tomato bushy student virus (TBSV) RNA-silencing suppressor P19, has been described elsewhere (Petrie et al., 2010; Jasieniecka-Gazarkiewicz et al., 2021). The binary plasmid encoding the GFP-tagged mitochondrial marker protein (i.e., GFP-mito) was obtained from ABRC (plasmid stock CD3-987) and consists of the N-terminal mitochondrial targeting peptide from *Saccharomyces cerevisiae* cytochrome c oxidase subunit 4 fused to GFP (Nelson et al., 2007).

For Y2H screening with ERD7 (see Yeast-Two-Hybrid section), the Arabidopsis ERD7 ORF was amplified by PCR using appropriate primers (**Supplementary Table 1**), and then PCR products were digested with *Eco*RI and *Bam*HI, and subcloned into similarly-digested pGBKT7-DNA-BD (Clontech), yielding the "bait" vector pGBKT7/ERD7.

The pBEE401E-based vector used for CRISPR/Cas9 genome editing of Arabidopsis *ERD7* was constructed based on procedures described by Wang et al. (2015). Briefly, sgRNAs were designed using CRISPR-PLANT v2[2] (Minkenberg et al., 2019) to specifically target the *ERD7* ORF (refer to **Supplementary Figure 1** for the relative positions of the sgRNA regions targeted for CRISPR/Cas9 genome editing of the *Arabidopsis ERD7* gene). Primers ERD7-sgRNA1 and ERD7-sgRNA2 (**Supplementary Table 1**) were synthesized to contain each sgRNA sequence, as well as sequences complementary to the pCBC-DT1T2 template plasmid. A region of pCBC-DT1T2 (containing the sgRNA scaffold, promoters, and terminators) was then amplified and the resulting PCR products were digested with *Bsa*I, gel purified, and ligated using Golden Gate cloning into similarly-digested pBEE401E (Wang et al., 2015), yielding the binary vector pBEE401E/ERD7sgRNA.

Immunoblotting

Immunodetection of mCherry-tagged ERD7 protein in *Agrobacterium*-infiltrated *N. benthamiana* leaves 3 days post-infiltration was carried out as follows. Leaf material was snap-frozen in liquid nitrogen and ground into powder in extraction buffer consisting of 100 mM Tris-HCl pH 7.5, 150 mM NaCl, 10% (v/v) glycerol, 0.1% (v/v) Tween-20, 1 mM PMSF, and Protease Inhibitor Cocktail (Sigma-Aldrich). Extracts were clarified

[1]http://dnasu.org
[2]http://genome.arizona.edu/crispr2/

by centrifugation and the soluble (total) protein fraction was incubated with SDS Sample buffer (Laemmli, 1970) and boiled. Thereafter, proteins were separated by SDS-PAGE and electroblotted onto Hybond® nitrocellulose (GE LifeSciences). Membranes were stained with 0.5% (w/v) Ponceau S (Sigma-Aldrich) in 1% acetic acid, visualized, and then destained with ddH_20, blocked (and subsequently washed) in TBST buffer [20 mM Tris-HCl pH 7.5, 150 mM NaCl, 0.05% (v/v) Tween-20] containing 3% (w/v) skim milk powder, followed by incubations with anti-red fluorescent protein (RFP) antibodies, which recognize the mCherry protein (Invitrogen), and anti-mouse IgG-peroxidase antibodies (Sigma-Aldrich). Immunoreactive proteins were visualized using Amersham ECL Prime Western Blotting Detection Reagent, according to the manufacturer's instructions (GE Healthcare), and a ChemiDoc MP (Bio-Rad Laboratories).

RT-PCR and Genotyping

ERD7 gene expression in different WT Arabidopsis organs and tissues was assessed by RT-PCR. Plant material was snap-frozen and ground to a powder. RNA was then extracted using TRIzol reagent (Invitrogen) and an EZ-10 spin column plant RNA kit (Bio Basic Inc.), followed by cDNA synthesis using 750 ng RNA and qScript cDNA SuperMix (Quantabio). One microliter of cDNA was used per 20 µl reaction which consisted of 30 cycles of 30 s at 94°C, 45 s at 55°C, and 90 s at 72°C. *ERD7* and Arabidopsis β-TUBULIN isoform 4 (*TUB4*) serving as a reference gene, were amplified using gene-specific primers (**Supplementary Table 1**).

Genotyping and RT-PCR analysis of the Arabidopsis *erd7-1* and *erd7-2* mutants were carried out as follows. gDNA was isolated by grinding frozen rosette leaves from 4-week-old plants for each mutant line in extraction buffer [200 mM Tris-HCl pH 7.5, 250 mM NaCl, 25 mM EDTA, 0.5% (w/v) SDS] and then, following centrifugation, the supernatant was mixed 1:1 with isopropanol. Thereafter, samples were subjected to centrifugation, the resulting pellet washed with 70% ethanol and resuspended in 10 mM Tris-HCl pH 7.5, and PCR was performed using the appropriate gene-specific primers (**Supplementary Table 1**). RT-PCR to confirm the absence of *ERD7* transcript in the *erd7-1* and *erd7-2* mutant lines was performed as described above.

Microscopy

Wild-type and transgenic Arabidopsis seeds and leaves, *Agrobacterium*-infiltrated and drought-stressed *N. benthamiana* leaves, and biolistically-bombarded Arabidopsis suspension-cultured cells were processed for CLSM imaging, including staining of LDs with neutral lipid-selective fluorescent dyes boron-dipyrromethene (BODIPY) 493/503 (Invitrogen; Listenberger et al., 2007) and monodansylpentane (MDH; Abcepta; Yang et al., 2012), as previously described (Cai et al., 2015; Gidda et al., 2016).

Imaging of BODIPY-stained LDs in leaves of drought-stressed Arabidopsis plants, as described in Proteomics of Drought-Treated Arabidopsis Leaves section, was performed with a Zeiss LSM780 CLSM (Carl Zeiss Microscopy GmbH). All other imaging performed in this study was carried out using a Leica SP5 CLSM equipped with a Radius 405-nm laser (Leica Microsystems). Excitations and emission signals for fluorescent (mCherry or GFP) fusion proteins, BODIPY, and/or MDH were collected sequentially as single optical sections or *Z*-series in double-labeling experiments as described previously (Gidda et al., 2016). Single-labeling experiments showed no detectable crossover at the settings used for data collection. All fluorescence images of plant cells shown in individual figures are representative of at least three separate experiments, including >30 transformed *N. benthamiana* leaf cells and >10 Arabidopsis suspension cells; except for images of leaf cells from drought-stressed (and control) Arabidopsis plants whereby 10 leaf areas (i.e., two leaf areas from five different plants) per treatment were analyzed. Numbers and/or diameters of LDs in Arabidopsis seedling, senescing leaves, and drought-stressed (and control) leaves were quantified according to Cai et al. (2015), using the Analyze Particles function in ImageJ (v1.8.0; Schneider et al., 2012), and statistically analyzed using Student's *t*-test. All figure compositions were generated using Microsoft PowerPoint (Microsoft).

Yeast-Two-Hybrid

Screening of a Y2H library, consisting of Arabidopsis cDNA from various plant tissues and cloned into the appropriate prey vector, using Arabidopsis ERD7 [pGBKT7/ERD7 (see Molecular Cloning and Plasmid Construction section)] as "bait," was carried out with the Matchmaker Gold Y2H System (Clontech Laboratories, Inc.), as described by the manufacturer and as we have done so in previously-published Y2H screens (Park et al., 2013; Pyc et al., 2017a). All yeast strains that grew on selective media [synthetic dextrose media lacking tryptophan and leucine but containing X-α-Gal and Aureobasidin A (Takara Bio United States Inc.)], were designated as either "strong," "intermediate," or "weak" interactors based on the relative color of the colony, which corresponds to the activation of the *MEL1* reporter gene. Plasmids were extracted from yeast cells to determine the identity of encoded candidate ERD7-interacting (prey) proteins (listed in **Supplementary Table 3**) by automated DNA sequencing.

Bioinformatics

Annotations for the subcellular localizations of all detected proteins identified in proteomics analysis of drought-stressed Arabidopsis leaves were obtained from the Plant Proteome Database (PPDB[3]; Sun et al., 2009). The protein-protein network analysis of selected candidate LD-enriched proteins was performed using the Search Tool for Retrieval of Interacting Genes/Proteins (STRING) database[4] (Szklarczyk et al., 2019), with default settings and a minimum required interaction score = 0.400. Protein sequences of SD-containing proteins, including ERD7, in Arabidopsis and other plant species were obtained from The Arabidopsis Information Resource (TAIR[5]; Berardini et al., 2004),

[3]http://ppdb.tc.cornell.edu/dbsearch/subproteome.aspx
[4]http://string-db.org
[5]http://arabidopsis.org

UniProt,[6] or the Phytozome 12 database.[7] The SD in each protein was identified and the amino acid sequence defined based on information provided at the InterPro domain database[8] (Blum et al., 2021); note that the SD is referred to as senescence/spartin-associated domain. Sequences of ERD7 homologs in non-plant species (and their corresponding SDs), including human spartin, were obtained also from the InterPro database. Phylogenetic analyses were carried out using MEGA-X software (Kumar et al., 2018) and the phylogenetic tree was constructed using the neighbor-joining method. Microarray data for the relative expression of *ERD7* and selected *SEN* genes in Arabidopsis was obtained using the Arabidopsis electronic fluorescent pictographic (eFP) Browser hosted at The Bio-Analytic Resource for Plant Biology (BAR[9]; Kilian et al., 2007; Winter et al., 2007) and corresponding heat maps were generated using Microsoft Excel (Microsoft). Multiple sequence alignments used to calculate amino acid sequence identities/similarities between proteins were generated using Clustal Omega[10] (Madeira et al., 2019). Gene Ontology (GO) Slim terms were identified using the GO annotation search at TAIR. Putative amphipathic helices were predicted using the HeliQuest server[11] (Gautier et al., 2008), mitochondrial targeting sequences were predicted using the DeepLoc[12] (Almagro Armenteros et al., 2017) and Plant-mPLoc[13] (Chou and Shen, 2010) servers, and lipidation was predicted using the GPS-Lipid server[14] (Xie et al., 2016).

RESULTS

ERD7 Is Enriched With LDs Isolated From Drought-Stressed Arabidopsis Leaves

As an extension of our recent efforts to identify and characterize new LD proteins in plant vegetative (i.e., non-seed) tissues (Horn et al., 2013; Cai et al., 2015; Gidda et al., 2016; Pyc et al., 2017a; Kretzschmar et al., 2018, 2020; Greer et al., 2020), mature Arabidopsis plants were subject to 1 week of drought treatment in order to elicit TAG accumulation and LD proliferation of LDs, as reported previously in drought-stressed plants (reviewed in Xu and Shanklin, 2016; Yang and Benning, 2018; Lu et al., 2020). Consistent with this, we observed a significant increase in the number of LDs stained with the neutral lipid-selective dye BODIPY 493/503 in leaves from drought stress-treated vs. control (i.e., watered) Arabidopsis plants (**Supplementary Figure 2**). LDs were isolated (in triplicate) from leaves of stress-induced plants and proteins from LD-enriched fractions, as well as those from the corresponding total cellular extracts, were analyzed using quantitative MS based on the label-free quantification (LFQ) algorithm (Cox and Mann, 2008; Cox et al., 2014), similar to our other previously-published Arabidopsis LD proteomics studies (Pyc et al., 2017a; Kretzschmar et al., 2018, 2020). All detected proteins are listed, both as the raw and normalized data, in **Supplementary Datasets 1** and **2**, respectively, with the latter dataset also showing each protein's LFQ abundance and LD enrichment compared to the total cellular extracts (i.e., LD enrichment was calculated for each protein as the ratio of LFQ abundance in isolated LD fractions vs. total cellular extracts). Shown in **Supplementary Dataset 3** are the summed LFQ and enrichment values for all detected proteins at different subcellular localizations based on PPDB (Sun et al., 2009; Ischebeck et al., 2020), including proteins annotated to be localized at LDs, which were the most enriched in the LD fractions, as expected. Among the other notable groups of proteins enriched in the LD fractions were those annotated to be localized to tonoplasts or vacuoles (**Supplementary Dataset 3**), which might reflect the LD-vacuole interactions that are proposed to occur during autophagic degradation of LDs in plants (Ischebeck et al., 2020; Zienkiewicz and Zienkiewicz, 2020), as well as proteins localized to lipid-storing plastoglobuli, which, like cytosolic LDs, are known to be upregulated during plant stress (Rottet et al., 2015; Lundquist et al., 2020).

We further categorized all of the detected proteins in drought-stressed Arabidopsis leaves [based on the normalized dataset (**Supplementary Dataset 2**)] to include only those that (i) were found in all each of the three (replicate) LD-enriched fractions, (ii) had a relative LFQ abundance >0.2, and (iii) had an LD-enrichment score of >10. The resulting cohort of 89 proteins that co-purified with LDs are shown in **Supplementary Dataset 4** and a STRING-based protein-protein interaction network based on annotated functional associations and/or physical interactions of these proteins is shown in **Supplementary Figure 3**. Overall, the STRING network had three prominent clusters of proteins, including one enriched in vacuolar ATPase subunits, which was consistent with the enrichment of proteins in the LD fractions annotated (at PPBD) to be localized to vacuoles or tonoplasts (**Supplementary Table 3**). The two other main clusters of proteins in the network were enriched in translation-related proteins (e.g., ribosomal subunits and eukaryotic initiation factors) or stress-related proteins, the latter also including several well-known LD proteins, i.e., proteins experimentally confirmed *via* microscopy to be localized to LDs in plant cells (based on Ischebeck et al., 2020). To illustrate this further, all of the known LD proteins and the top candidate LD-associated proteins (based on **Supplementary Dataset 4**) are shown in **Table 1**. Notably, several of the known LD proteins that were either significantly enriched or only detected in LD-enriched fractions from drought-stressed Arabidopsis leaves (**Table 1**) have been also previously associated with plant stress, such as CALEOSIN 3 [CLO3, also referred to as RESPONSIVE TO DESSICATION 20 (RD20; Aubert et al., 2010; Park et al., 2018)], LDAP1 and LDAP3 (Gidda et al., 2016; Kim et al., 2016), and α-dioxygenase 1 (DOX1; Shimada et al., 2014). Also among the proteins exclusively detected in LD-enriched fractions were several previously found in other Arabidopsis LD proteomics studies but have not been experimentally characterized in terms their association with LDs and/or

[6]http://uniprot.org
[7]http://phytozome.jgi.doe.gov
[8]https://www.ebi.ac.uk/interpro/entry/InterPro/IPR009686/
[9]http://bar.utoronto.ca
[10]https://www.ebi.ac.uk/Tools/msa/clustalo/
[11]http://heliquest.ipmc.cnrs.fr
[12]http://cbs.dtu.dk/services/DeepLoc-1.0/
[13]http://www.csbio.sjtu.edu.cn/bioinf/plant-multi/
[14]http://lipid.biocuckoo.org

TABLE 1 | Known and candidate lipid droplet (LD) proteins enriched or only detected in LD fractions isolated from drought-stressed *Arabidopsis* leaves.

Name	AGI No.	Description	Total rLFQ	LD rLFQ	Other LD proteomes
Known LD proteins					
CLO3	AT2G33380	Caleosin 3/responsive to desiccation 20	0.606	37.96	Ref. 1
LDAP1	AT1G67360	Lipid droplet-associated protein 1	-	2.577	"
LDAP3	AT3G05500	Lipid droplet-associated protein 3	-	0.747	"
DOX1	AT3G01420	α-Dioxygenase 1	-	0.698	"
CAS1	AT2G07050	Cycloartenol synthase 1	-	0.209	"
LDIP	AT5G16550	LDAP-interacting protein	-	0.112	"
LIME	AT4G33110	Putative methyltransferase	-	0.085	"
Other proteins only found in LD fractions					
VHA-H	AT3G42050	Vacuolar ATP synthase subunit H family protein	-	2.305	Ref. 3–5
VHA-A3	AT4G39080	Vacuolar proton ATPase A3	-	1.647	Ref. 2, 3
VHA-D1	AT3G28710	ATPase, V_0/A_0 complex, subunit C/D	-	1.503	Ref. 3, 4
ERD10	AT1G20450	Dehydrin family protein	-	1.106	Ref. 3
COR47	AT1G20440	Cold-regulated 47	-	1.091	Ref. 3
NCL	AT1G53210	Sodium/calcium exchanger family protein	-	0.956	Ref. 2, 3, 5
EF1B	AT5G19510	Translation elongation factor EF1β	-	0.728	Ref. 4, 5
VAB2	AT4G38510	ATPase, V1 complex, subunit B protein	-	0.633	Ref. 3–5
AT3G57020	AT3G57020	Calcium-dependent phosphotriesterase superfamily protein	-	0.611	Ref. 4–6
MC4	AT1G79340	Metacaspase 4	-	0.575	Ref. 3, 4
AT4G17390	AT4G17390	Ribosomal protein L23/L15e family protein	-	0.573	Ref. 4, 5
VAM3	AT5G46860	Syntaxin/t-SNARE family protein	-	0.566	Ref. 3
CYP89A9	AT3G03470	Cytochrome P450, family 87, subfamily A, polypeptide 9	-	0.520	Ref. 3, 4
SS2	AT1G74020	Strictosidine synthase 2	-	0.518	Ref. 3, 5
AT3G17020	AT3G17020	Adenine nucleotide α-hydrolases-like superfamily	-	0.508	Ref. 3–5
VMA10	AT3G01390	Vacuolar membrane ATPase complex, subunit G	-	0.478	Ref. 3, 5
CHC1	AT3G11130	Clathrin heavy chain 1	-	0.464	Ref. 3, 4
ERD7	AT2G17840	Senescence/dehydration-associated protein-related	-	0.459	Ref. 2, 3
AVP1	AT1G15690	Inorganic H pyrophosphatase family protein	-	0.452	Ref. 3, 5
PATL3	AT1G72160	Sec14p-like phosphatidylinositol transfer family protein	-	0.449	Ref. 3
SYTA	AT2G20990	Synaptotagmin A	-	0.421	Ref. 2, 3, 5

All detected proteins identified in drought-stressed Arabidopsis leaves in this study are listed in **Supplementary Datasets 1** *and* **2**, *along with their respective LFQ abundance and LD enrichment compared to the total cellular extracts. All of the known and candidate LD-associated proteins that were enriched or only detected in LD fractions are also listed in* **Supplementary Dataset 4**. *Shown for each protein is its name (symbol), Arabidopsis Genome Initiative (AGI) identifier number, and description, as assigned by TAIR. Shown in the upper portion of the table are known (i.e., experimentally confirmed via microscopy) LD proteins, based on Ischebeck et al. (2020) and indicated as (Ref. 1), that were either significantly enriched (i.e., CLO3) or only detected (e.g., LDAP1/3) in LD-enriched fractions based on* **Supplementary Dataset 2**. *Shown in the lower portion of the table are the most abundant proteins in* **Supplementary Dataset 4** *found exclusively in LD-enriched fractions and which were also found in other previously-published Arabidopsis LD proteomics studies, including pathogen-challenged leaves (Fernández-Santos et al., 2020; Ref. 2), senescing leaves (Brocard et al., 2017; Ref. 3), and/or seeds or seedlings (Kretzschmar et al., 2020; Ref. 4; Kretzschmar et al., 2018; Ref. 5; Pyc et al., 2017a; Ref. 6). Relative label-free quantification (rLFQ) values reflect the protein abundance in the LD-enriched fractions (LD rLFQ) and the corresponding total cellular extracts (Total rLFQ) as measured by the LFQ algorithm (Cox and Mann, 2008; Cox et al., 2014), and normalized so that the abundance of all detected proteins sum to 1000 (i.e., rLFQ). Dashes in the Total rLFQ column indicate proteins that were not detected in total cellular extracts.*

LD-related function(s). Examples of these proteins are shown also in **Table 1** and included several of the abovementioned vacuolar ATPase subunits that were also found in the LD proteomes in senescent (Brocard et al., 2017) and/or pathogen (i.e., *Pseudomonas*)-challenged leaves (Fernández-Santos et al., 2020). In addition, several stress-related proteins were exclusively detected in LD-enriched fractions, including the dehydrin family members ERD10 and COLD-REGULATED 47, as well as ERD7 (**Table 1**), which, as discussed in the Introduction section, was selected for further study for several reasons.

Ectopically-Expressed ERD7 Is Localized to LDs and Cytosol in Plant Cells

To further evaluate the subcellular localization of ERD7 in plants, the protein was translationally appended, either at its N- or C-terminus, to the fluorescent protein mCherry (i.e., mCherry-ERD7 and ERD7-mCherry) and then transiently expressed in *N. benthamiana* leaves, which is a well-characterized model system for studying plant protein subcellular localization (Sparkes et al., 2006; Petrie et al., 2010). As shown in **Figure 1A**, CLSM imaging revealed that both of the ERD7 fusion proteins displayed similar fluorescence patterns in transformed *N. benthamiana* leaf (epidermal) cells, including distinct torus-shaped fluorescence patterns that encircled the BODIPY-stained LDs. While this staining pattern is reminiscent of other LD-related proteins transiently expressed in plant cells (Gidda et al., 2016; Pyc et al., 2017a; Kretzschmar et al., 2020), a portion of both ERD7 fusion proteins also displayed a more diffuse-like fluorescence pattern, suggesting localization to the cytosol. Indeed, a similar diffuse fluorescence pattern was observed in

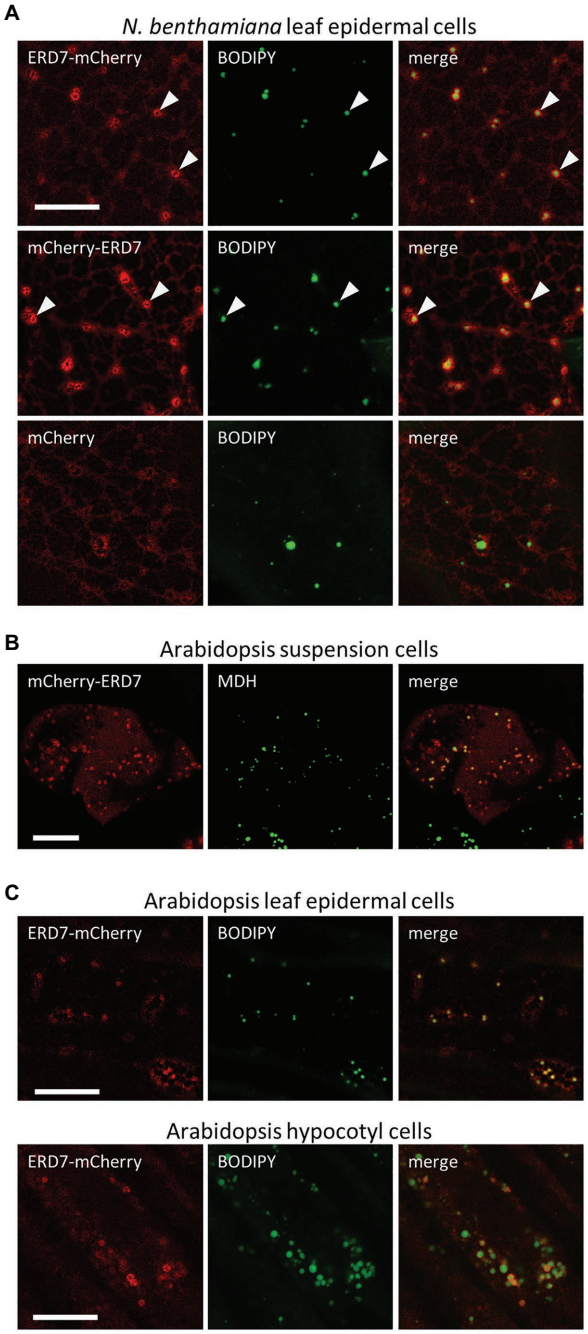

FIGURE 1 | Subcellular localization of EARLY RESPONSIVE TO DEHYDRATION 7 (ERD7) in plant cells. Representative confocal laser-scanning microscopy (CLSM) images (z-sections) of either **(A)** *Agrobacterium*-infiltrated *Nicotiana benthamiana* leaf epidermal cells, **(B)** biolistically-bombarded *Arabidopsis* suspension-cultured cells, or **(C)** transgenic *Arabidopsis* seedling leaf epidermal and hypocotyl cells, transiently- or stably-transformed with ERD7-mCherry, mCherry-ERD7, or mCherry alone (as indicated by the panel labels), and stained with the neutral lipid dyes BODIPY or MDH (false-colored green). Also shown for each set of images is the corresponding merged image. Arrowheads in the top two rows in **(A)** indicate obvious examples of mCherry-ERD7 and ERD7-mCherry fluorescence patterns surrounding the BODIPY-stained TAG core, indicating that ERD7 localizes to the surface of LDs. Scale bars in **(A–C)** = 10 μm.

N. benthamiana leaf cells transiently transformed with mCherry alone (**Figure 1A**). Furthermore, there was no obvious localization of ERD7 to the ER in *N. benthamiana* leaf cells, i.e., mCherry-ERD7 did not readily colocalize with a co-expressed GFP-LPEAT1 serving as an ER marker protein (Jasieniecka-Gazarkiewicz et al., 2021; **Supplementary Figure 4A**). We also performed immunoblotting with anti-mCherry antibodies to confirm that both mCherry-ERD7 and ERD7-mCherry transiently expressed in *N. benthamiana* leaves were of the expected molecular mass (i.e., ~77 kDa; **Supplementary Figure 4B**), indicating that the cytosolic localization observed for both fusion proteins was not simply due to cleavage of the appended mCherry moiety.

We also assessed the subcellular localization of mCherry-tagged ERD7 in Arabidopsis, the native (plant) environment for the ERD7 protein. As shown in **Figure 1B**, mCherry-ERD7 localized predominantly to MDH-stained LDs in transiently-transformed suspension-cultured Arabidopsis cells, although a portion of the fusion protein was also apparent in the cytosol, as in *N. benthamiana* leaf cells (**Figure 1A**). Similarly, ERD7-mCherry localized to BODIPY-stained LDs and the cytosol in both leaf epidermal and hypocotyl cells in stably-transformed Arabidopsis seedlings (**Figure 1C**). Collectively, these data support the results from our proteomics studies (**Table 1**) that ERD7 is localized to LDs, but further suggest that the expression levels of ERD7 and/or other factors might influence its distribution between LDs and the cytosol.

The LD Targeting Information in ERD7 Is Located in Its SD

In order to identify the putative LD targeting information in ERD7, we carried out a mutational analysis of the protein. As depicted in **Figure 2A**, we initially generated mCherry-tagged ERD7 mutants consisting of either the N-terminal [amino acids 1–253 (referred to as ERD7-N)] or C-terminal (amino acids 235–452) halves of ERD7, the latter of which being referred to as ERD7-SD since it included the protein's SD (amino acids 258–426). Each fusion construct was then transiently expressed in *N. benthamiana* leaves and their localization to BODIPY-stained LDs (or a lack thereof) was assessed using CLSM. As shown in **Figure 2B**, ERD7-N localized to the cytosol, with no apparent targeting to BODIPY-stained LDs. By contrast, ERD7-SD localized almost exclusively to LDs (**Figure 2B**), i.e., all of the fluorescence attributable to ERD7-SD in *N. benthamiana* leaf cells appeared to be enriched at BODIPY-stained LDs, with relatively little fluorescence observed in the cytosol (compare with images of ERD7-N and full-length ERD7 in **Figures 1A, 2B**). As shown also in **Figure 2**, additional fusion constructs consisting of different regions of the C-terminal half of ERD7 all mislocalized to the cytosol, with the exception of ERD7-C1, which consisted of amino acids 235–394, including the majority of the SD (fused to mCherry), and, similar to ERD7-SD, localized exclusively to LDs. These data indicate that the LD targeting information in ERD7 is located within a relatively long C-terminal region of the protein, including most of the SD.

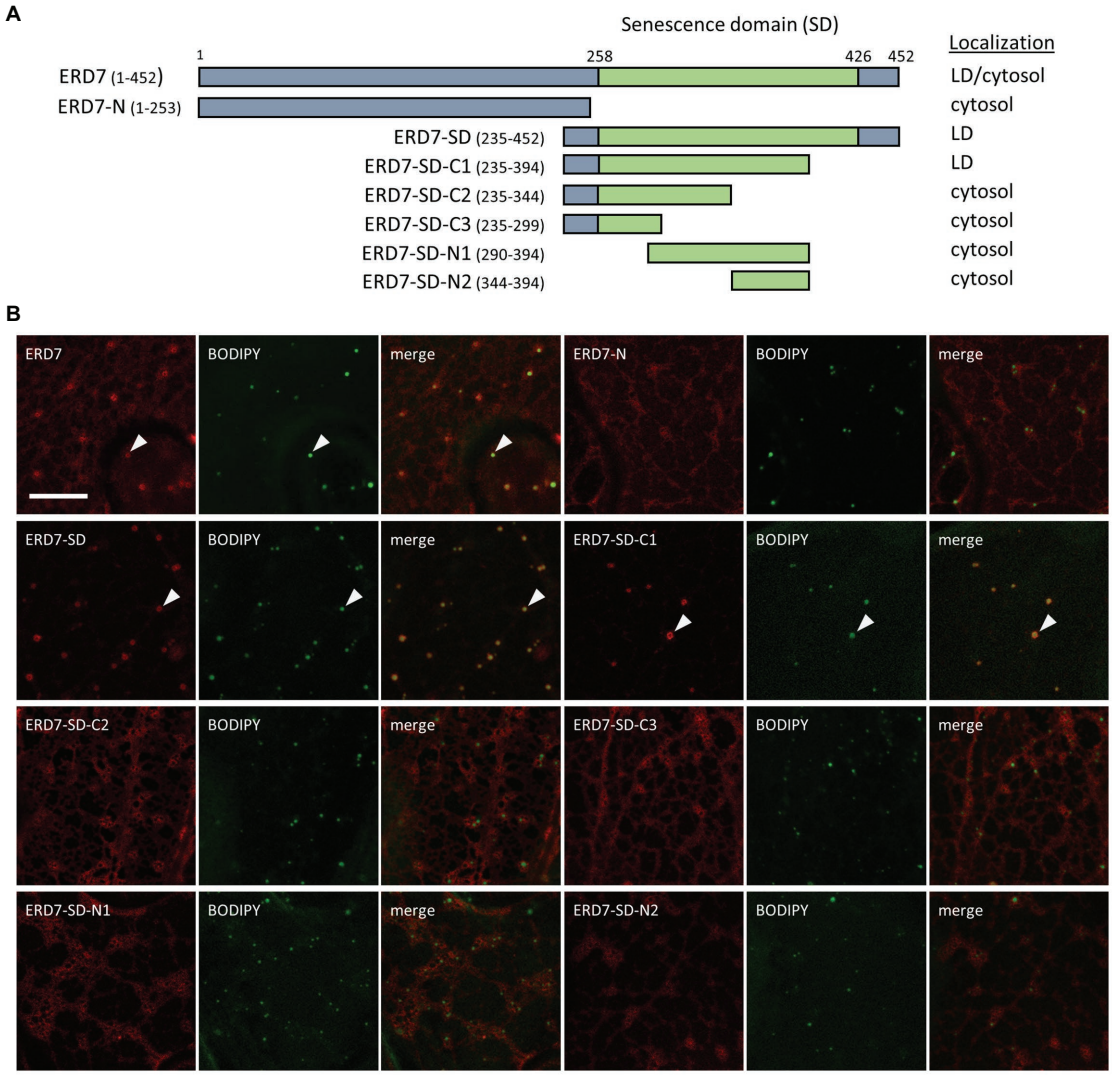

FIGURE 2 | Subcellular localization of various ERD7 truncation mutants in *N. benthamiana* leaves. *N. benthamiana* leaves were transiently transformed (*via Agrobacterium* infiltration) with either full-length or truncated versions of ERD7 and tagged at their N-termini with mCherry. Three days post-infiltration, leaves were stained with the neutral lipid dye BODIPY and imaged using CLSM. Shown in **(A)** are schematic representations of full-length ERD7 and the various ERD7 mutants and their corresponding subcellular localization(s) [i.e., cytosol and/or lipid droplet (LD)]. Numbers above the illustration of full-length ERD7 represent specific amino acids residues, and the SD (amino acid residues 258–426) is defined based on information obtained from the InterPro database. The numbers next to the name of each construct denote the amino acid residues in ERD7 that were fused to mCherry; note that the N-terminal-appended mCherry moiety is not depicted in the illustrations or construct names. The portion of ERD7 representing the SD or the other parts of the protein are depicted in the illustrations as green or gray boxes, respectively. Shown in **(B)** are representative CLSM images (z-sections) of each mCherry-ERD7 (mutant) protein, as indicated by the panel labels, along with the corresponding BODIPY-stained LDs in the same cell. Also shown is the corresponding merged image. Arrowheads indicate examples of mCherry-ERD7 and the selected (mutant) versions thereof (i.e., ERD7-SD and ERD7-C1) that localized to BODIPY-stained LDs; compare with the lack of LD localization for the other mutant versions of ERD7. Scale bar in **(B)** = 10 μm.

SEN Proteins Are Phylogenetically Organized Into Two Distinct Subfamilies in Plants, Including in Arabidopsis

Based on searches of the InterPro domain database, the SD is annotated to be of unknown function and found in proteins from a vast array of evolutionarily-diverse species, ranging from metazoans (animals), fungi, algae, and plants. Further, while most animal, fungal, and algal species have just one protein with an SD, multiple SD-containing proteins exist in land plants (**Figure 3A**), which we refer to collectively in all species as SENESCENCE DOMAIN-ASSOCIATED (SEN) proteins. For example, the SEN protein families in the seedless plant species *Marchantia polymorpha* and *Physcomitrella patens* possess two and 10 members, respectively. Monocots, such as *Zea mays* and *Oryza sativa*, each have three members, and Arabidopsis, a eudicot, has six members, including ERD7 (**Figure 3A**). These observations suggest that the expansion of the SEN protein families in land plants occurred early in

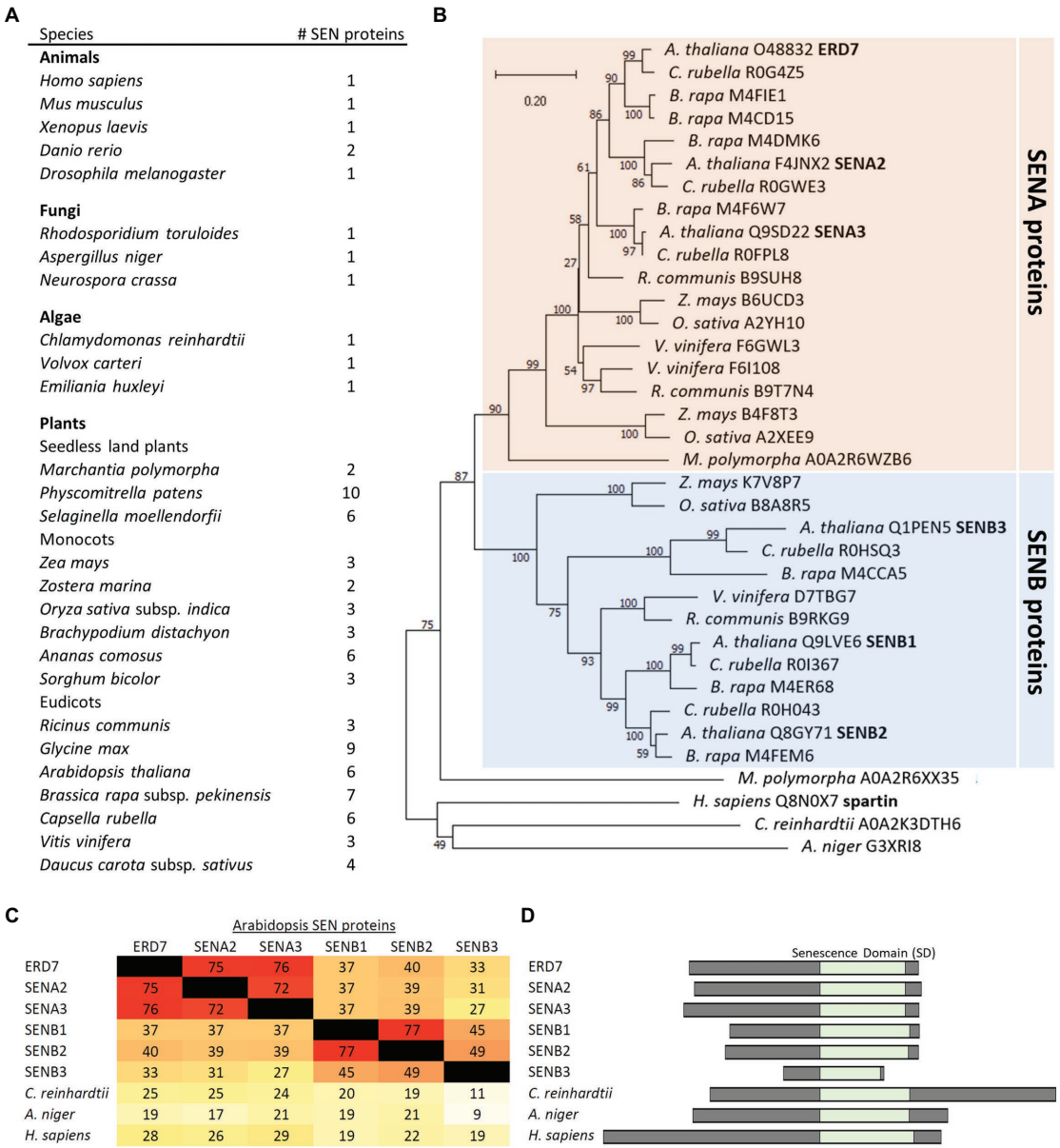

FIGURE 3 | Comparison of SEN protein families in plants and other evolutionarily-diverse species. **(A)** Shown are the number of proteins in selected species from plants, animals, fungi, and algae that are annotated to contain an SD, based on the InterPro domain database for SDs (InterPro entry: IPR009686), and ruling out redundant entries and splice isoforms based on the UniProt annotations for each protein. **(B)** Phylogenetic tree based on the SD sequences of SEN proteins from selected plant and non-plant species, obtained from the Uniprot or Phytozome databases, and constructed with the neighbor-joining method using MEGA-X (Kumar et al., 2018). Bootstrap values are indicated beside each branch point. The scale bar represents the number of amino acid substitutions per site. Note that, with exception of one protein from *M. polymorpha*, all of the plant SEN proteins shown group into either the SENA or SENB protein subfamilies. Each protein is listed by its species and Uniprot accession number. Also indicated in bold are the six SENA/B proteins, including ERD7, in Arabidopsis, as well as human spartin. **(C)** A heat map displaying the primary sequence identity (as a percentage) among the SDs of the six Arabidopsis SENA/B proteins and selected SEN proteins from other non-plant species, all which were calculated based on a ClustalO multiple sequence alignment. Darker (red) colors reflect higher sequence identities, while lighter (yellow) colors reflect lower sequence identities, consistent with the corresponding percent identities shown in each panel. **(D)** Schematic representations of the six Arabidopsis SENA/B proteins, as well as selected SEN proteins from algae, fungi, and animals (i.e., *Chlamydomonas reinhardtii*, *Aspergillus niger*, and human), depicting the relative location (and length) of their SDs and adjacent N- and C-terminal regions.

their evolution and that they may have acquired additional novel attributes (e.g., functions, subcellular localization, etc.) compared to their SEN homologs in other (non-land plant) species.

Phylogenetic analysis, based on sequences of plant homologs found in the Phytozome 12 database or non-plant homologs from the UniProt database, further revealed that the plant SEN proteins generally form two distinct subfamilies, termed

here SENA and SENB (**Figure 3B**). In Arabidopsis, the six SEN proteins are divided equally between each subfamily, with ERD7 (i.e., SENA1), SENA2, and SENA3 found in the SENA subfamily and SENB1-3 found in the SENB subfamily (**Figure 3B**). As depicted in **Figure 3C**, the C-terminal SDs in each of the Arabidopsis SENA and SENB proteins share their highest deduced amino acid sequence identities with the two other members of the same subfamily, while all of the Arabidopsis SENA/B proteins possess relatively low sequence identities with the SD sequences in their SEN protein homologs from non-plant species, such as *Chlamydomonas reinhardtii*, *Aspergillus niger*, and *H. sapiens*. The N-termini of the Arabidopsis SENB proteins are also generally shorter in length than those of their SENA protein counterparts, as well as those in SEN protein homologs from non-plant species (**Figure 3D**), with SENB3 having the shortest N-terminal sequence, as well as a C-terminal-truncated SD (**Figure 3D**).

The SDs of the Arabidopsis SENA and SENB Proteins Target Specifically to LDs and Mitochondria, Respectively

With the exception of ERD7, none of the other Arabidopsis SENA or SENB proteins were identified in our or other previously-published Arabidopsis LD proteomics studies (Brocard et al., 2017; Pyc et al., 2017a; Kretzschmar et al., 2018, 2020; Fernández-Santos et al., 2020) and all of these proteins, like ERD7, are annotated (based on TAIR) to have unknown function and subcellular localization. To determine the subcellular location of the other Arabidopsis SEN proteins and whether there might be differences between (or among) the members of each subfamily, full-length proteins or just the corresponding C-terminal portions, containing the SD regions, were appended to mCherry and transiently-expressed in *N. benthamiana* leaves. The subcellular localizations of the fusion proteins were then assessed using CLSM. As shown in **Figures 4A,B**, both full-length SENA2 and SENA3 localized to the cytosol, but not to BODIPY-stained LDs, unlike the LD and cytosolic localization observed for full-length ERD7 (**Figures 1, 2**). However, similar to the subcellular localization observed for ERD7-SD (**Figure 2**), the SENA2 and SENA3 C-terminal portions alone (i.e., SENA2-SD and SENA3-SD), which contain the SD, localized specifically to LDs (**Figures 4A,B**). Full-length SENB2 also localized only to the cytosol, but unlike the LD localization observed for the SD regions from the SENA proteins, SENB2-SD localized to punctate structures that were distinct from BODIPY-stained LDs (**Figures 4A,B**). Based on their size and shape, these structures were hypothesized to be mitochondria and, indeed, co-expression of SENB2-SD with a GFP-mitochondrial marker fusion protein (i.e., GFP-mito; Nelson et al., 2007) revealed that both proteins colocalized at mitochondria in *N. benthamiana* leaf cells (**Figure 4B**). Similarly, SENB1-SD colocalized with GFP-mito (**Figure 4B**), indicating that the SDs of the Arabidopsis SENB proteins contain mitochondrial targeting information.

We also assessed the subcellular localization of the human SEN protein, spartin, in *N. benthamiana* leaf cells in order to determine if this protein, similar to ERD7, might localize to LDs in plant cells, as it does in animal cells (Eastman et al., 2009; Urbancyzk and Enz, 2011). As shown in **Figure 4C**, transiently-expressed full-length spartin (fused to mCherry) localized to the cytosol, with no apparent localization to BODIPY-stained LDs nor to any other punctate structures [such as mitochondrial-localized SENB1-SD and SENB2-SD (**Figure 4B**)]. On the other hand, the region of spartin containing its SD alone fused to mCherry localized readily to LDs (**Figure 4C**), indicating that the LD targeting information in the SD region is likely conserved between Arabidopsis ERD7, SENA2, SENA3, and their human SEN protein counterpart, spartin. Further, in both sets of proteins, the LD targeting information is somewhat cryptic in nature, being more readily exposed when the N-terminal portion of each protein is removed.

LDs in *erd7* Mutant and WT Arabidopsis Leaves and Seeds Are Similar in Their Numbers and Sizes Under Normal Growth Conditions

Prior characterizations of plant LD-associated proteins, particularly those involved with LD biogenesis or turnover, have revealed conspicuous alterations in LD abundance and/or morphology in cells when their expression in disrupted (Siloto et al., 2006; Gidda et al., 2016; Pyc et al., 2017a; Kretzschmar et al., 2018). Considering that ERD7 localizes to LDs in leaves (**Figure 1**), we investigated if disruption of *ERD7* expression might alter LD homeostasis under normal growth conditions. Toward that end, an Arabidopsis mutant, which contains a T-DNA insertion in *ERD7* and termed here *erd7-1*, was obtained from ABRC, genotyped and advanced to homozygosity, then confirmed (*via* RT-PCR) to be devoid of any full-length *ERD7* transcripts (**Supplementary Figure 1**). We also generated a second independent homozygous Arabidopsis *ERD7* knockout mutant (i.e., *erd7-2*) using CRISPR/Cas9 genome editing (see ERD7-mCherry-Expressing and CRISPR/Cas9 erd7 Knockout Arabidopsis Lines section in the Materials and Methods for details), which was employed to remove most of the *ERD7* coding sequence, resulting also in no detectable *ERD7* expression (**Supplementary Figure 1**).

To begin to study any potential effects of *ERD7* disruption on LDs in Arabidopsis plants, we analyzed LDs with BODIPY staining and CLSM in dry seeds and seedlings during post-germinative growth, as well as in leaves of 15-day-old seedlings, all of which are organs that possess LDs with relatively high consistency in terms of their number and morphology and, thus, are often employed in studies of plant LDs (Gidda et al., 2016). Notably, RT-PCR-based analysis of *ERD7* gene expression in WT Arabidopsis confirmed that *ERD7* is expressed, albeit at varied levels, in a wide range of organs at different stages throughout plant growth and development, including in dry seeds, seedlings, mature plant leaves, and senescing leaves (**Supplementary Figure 5A**), and consistent with publicly-available Arabidopsis microarray expression data for *ERD7* (and other *SEN* genes; **Supplementary Figure 5B**). As shown in **Figure 5A**, CLSM analysis of BODIPY-stained cotyledons found no apparent visible differences in LD abundance and morphology

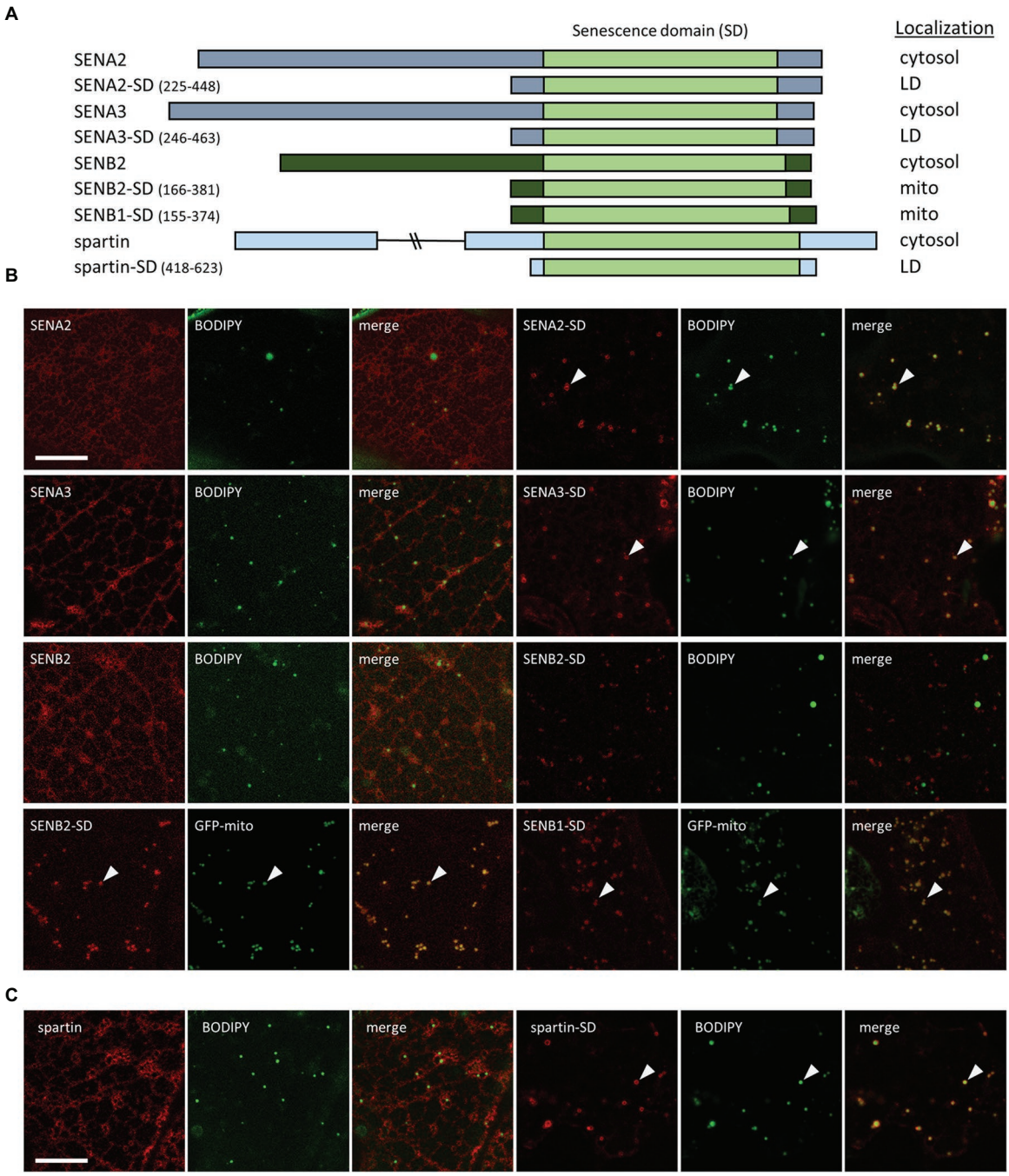

FIGURE 4 | Subcellular localization of various Arabidopsis SEN proteins and human spartin, and their corresponding SDs. *N. benthamiana* leaves were transiently transformed (*via Agrobacterium* infiltration) with either full-length or the C-terminal portion, including their SD, of Arabidopsis SENA2, SENA3, SENB1, SENB2, or human spartin, and tagged at their C-termini with mCherry. Three days post-infiltration, leaves were stained with the neutral lipid dye BODIPY and imaged using CLSM. Alternatively, leaves were co-transformed with either SENB2-SD-mCherry or SENB1-SD-mCherry and the mitochondrial marker protein GFP-mito. **(A)** Schematic representations of the full-length and/or C-terminal SD-containing portion of each *Arabidopsis* SENA/B protein and human spartin, and their corresponding subcellular localization(s) [i.e., cytosol, lipid droplet (LD), mitochondria (mito)]. The SD in each protein is based on information obtained from the InterPro domain database. The numbers next to the name of each SD construct denote the amino acid residues that were fused to mCherry. The portion of each protein representing the SD is depicted in the illustrations as a light green box, while other regions of the SENA, SENB, and spartin proteins are depicted as gray, dark green, and blue boxes, respectively. Note that the C-terminal-appended mCherry moiety is not depicted in the illustrations or construct names. Representative CLSM images (z-sections) of mCherry-tagged full-length or truncated SEN-family proteins **(B)** or spartin **(C)**, along with the corresponding BODIPY-stained LDs or co-expressed GFP-mito in the same cell, and as indicated by panel labels. Also shown is the corresponding merged image. Arrowheads indicate examples of SENA/B or spartin fusion proteins that localized to BODIPY-stained LDs or GFP-mito-labeled mitochondria. Scale bars in **(B,C)** = 10 μm.

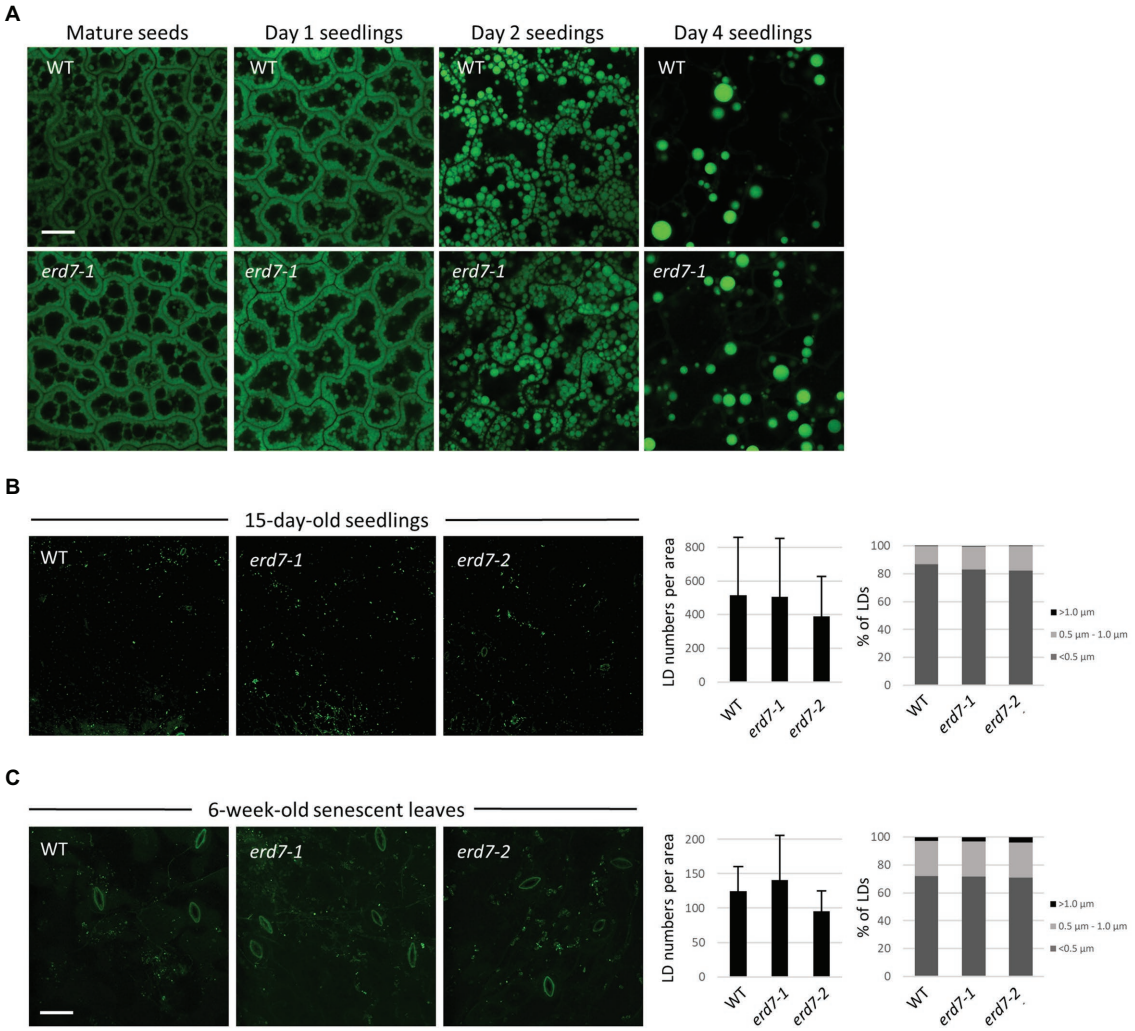

FIGURE 5 | ERD7 does not appear to be required for regulating LD numbers and sizes in *Arabidopsis* under normal growth conditions. Shown are representative CLSM images of BODIPY-stained LDs in leaf epidermal cells of **(A)** embryo cotyledon cells in mature (dry) seeds and germinating seedlings either 1, 2, or 4 days after germination; **(B)** 15-day-old *Arabidopsis* seedlings; and **(C)** 6-week-old, senescent *Arabidopsis* plants, from WT and *erd7-1* and/or *erd7-2* mutant lines, as indicated by labels. Scale bar = 20 µm. Shown also in **(B,C)** in the graphs on the right are the quantifications of LD numbers per area and LD sizes. Values of LD numbers in **(B)** are averages ± SD from three biological replicates, with each replicate consisting of two leaf samples from 3–4 plants per line. Values of LD numbers in **(C)** are averages ± SD from two biological replicates of 10 plants per line. LD diameters were calculated using the same data set (i.e., micrographs) and are presented as the percentage of LDs in three size classes: <0.5 µm (small), 0.5–1.0 µm (intermediate), and >1.0 µm (large); refer also to key. Overall, there were no significant differences in either LD numbers per area or LD sizes in leaves of 15-day-old seedlings or 6-week-old (senescing) plants from WT and both the *erd7-1* and *erd7-2* mutant lines, based on Student's *t*-tests ($p \leq 0.05$). Similarly, based on images presented in **(A)** and others, no obvious qualitative differences in LD numbers or sizes were observed between WT and *erd7-1* mutant seeds and seedlings.

in WT and *erd7-1* dry (mature) seeds or in seedlings 1, 2, or 4 days after the onset of germination, when storage oil (e.g., TAGs) and LDs are degraded to support seedling establishment. Similarly, visual comparisons and quantifications of BODIPY-stained LDs in 15-day-old seedlings from WT and both *erd7* mutant lines revealed no significant differences in LD numbers or size distributions (i.e., small, intermediate, and large-sized LDs; **Figure 5B**).

We also assessed the potential effects of *ERD7* disruption on LDs in senescing leaves of 6-week-old Arabidopsis plants, since ERD7 was previously reported to be enriched at LDs based on a proteomics analysis of Arabidopsis senescing leaves (Brocard et al., 2017). As shown in **Figure 5C**, visual comparisons and quantifications of BODIPY-stained LDs in senescent leaves from WT and both *erd7* mutant lines, similar to results from seedlings and seeds (**Figures 5A,B**), revealed no significant differences in LD numbers or size distributions in the *erd7* mutant lines compared with WT. However, as addressed in the Discussion section, whether the disruption in expression of *ERD7* and/or other *SEN* genes alters LD homeostasis in Arabidopsis during stress conditions, such as drought stress, is an important open question that requires further detailed investigation.

Several Putative ERD7-Interacting Proteins Participate in Plant Stress Responses

Given that the results presented in **Figure 5** indicate that ERD7 does not appear to play an essential role in LD homeostasis in plants, at least not in the organs and conditions examined, we sought to gain insight to possible function(s) of ERD7 by searching for potential interacting proteins, especially since many of the processes that LD-associated proteins are involved with are known to rely on protein-protein interaction networks (Kolkhof et al., 2017). Toward that end, a Y2H screen was conducted using ERD7 as bait along with a cDNA expression library derived from a variety of Arabidopsis tissues. In total, 36 candidate ERD7-interacting proteins were identified, as assessed by the relative growth of yeast (prey) transformants under selective conditions (**Supplementary Table 3**).

While none of the 36 candidate ERD7-interacting proteins identified are known LD proteins [i.e., proteins experimentally confirmed *via* microscopy to be localized to LDs in plant cells based on Ischebeck et al. (2020)], several of them were identified in our drought-stressed leaf LD proteome and/or in other previously-published Arabidopsis LD proteomics studies (**Supplementary Table 3**). Furthermore, several of the candidate ERD7-interacting proteins shared the same GO terms (GO Slim, as assigned by the TAIR GO annotation search) within the GO categories of "biological process," "molecular function," and/or "cellular compartment" (**Figure 6**; **Supplementary Table 3**), which, by extension, might reflect the general functions of ERD7. For example, several of the candidate proteins are annotated in the GO Slim category of "biological process" to be involved with "response to stress" (**Figure 6**), which is notable given that ERD7 has the same assigned GO Slim term, based on its upregulation during plant stress responses (Winter et al., 2007; Cheng et al., 2013; Rasmussen et al., 2013). Among these proteins was BINDING PARTNER OF ACCELERATED CELL DEATH 11 (ACD11) 1 (BPA1), which we identified as a relatively strong candidate interactor with ERD7 (**Supplementary Table 3**) and was also exclusively detected, like ERD7, in LD-enriched fractions isolated from drought-stressed Arabidopsis leaves (refer to **Supplementary Dataset 2**), as well as in other previously-published Arabidopsis LD proteomics studies (Kretzschmar et al., 2018, 2020). BPA1 is known to bind and stabilize ACD11 in plant immune defense and hypersensitive response pathways, which are elicited by biotic stresses (Petersen et al., 2009; Li et al., 2019). Other interesting candidate ERD7-interacting proteins included the relatively large number that were annotated in the GO Slim categories of molecular function and cellular compartment to be involved in DNA-binding transcription factor activity and localized to the nucleus, respectively (**Figure 6**). These included the entire S4 family of MYB transcription factors, namely MYB3, MYB4, MYB7, and MYB32 (Dubos et al., 2010), which function to suppress gene expression during plant stress responses (Fornalé et al., 2014; Zhou et al., 2017; Agarwal et al., 2020). As discussed below, these observations, as well as those for other candidate ERD7-interacting proteins we identified, collectively raise intriguing questions about the potential role of ERD7 in the link between LDs and plant stress responses.

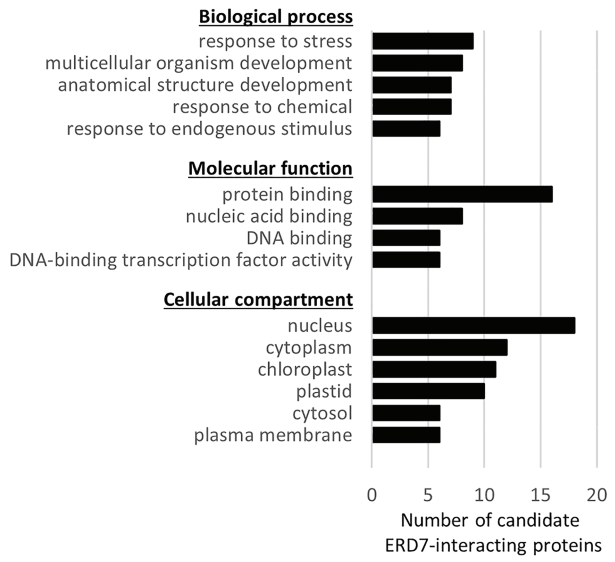

FIGURE 6 | Functional categorization, based on Gene Ontology (GO) terms, of candidate ERD7-interacting proteins identified in a Y2H screen. Each of the 36 Arabidopsis proteins identified in the Y2H screen using ERD7 as bait (refer to **Supplementary Table 3** for a list of all of the candidate ERD7-interacting proteins) were assigned GO terms based on the functional categorization of genes using the GO Slim annotation search tool at TAIR. Shown for each GO category (i.e., "Biological process," "Molecular function," and "Cellular component"), is the number of candidate ERD7-interacting proteins with the assigned GO annotation that appeared in at least six or more proteins.

DISCUSSION

ERD7 Is a Type II LD Protein That Targets to LDs *via* Its SD

The ongoing identification of novel LD-localized coat proteins affords us more tools to study LD-related processes in plants. Here, we show that a protein commonly associated with plant stress responses, ERD7 (Cheng et al., 2013; Rasmussen et al., 2013), is enriched with LDs isolated from drought-treated Arabidopsis leaves (**Table 1**), and targets to LDs when transiently- or stably-expressed in *N. benthamiana* and/or Arabidopsis (**Figures 1, 2**). While full-length ERD7 localized to both the cytosol and LDs, its C-terminal SD region alone localized almost entirely to LDs (**Figure 2**). This striking difference in subcellular localization indicates that the SD region of ERD7 is responsible for its LD localization, and further suggests that the N-terminal region potentiates LD localization of the full-length protein. Such regulated or potentiated protein localization might involve changes in protein conformation, due to the presence of post-translational modifications or perhaps through binding of a protein partner(s) that masks or reveals a protein targeting sequence (Bauer et al., 2015).

Lipid droplet coat proteins across eukaryotes are known to associate with LDs by two general mechanisms: (i) *via* a hydrophobic hairpin sequence that embeds into the neutral

lipid core of the LD and is employed by so-called type I LD proteins or (ii) associating with the LD surface *via* protein-protein and/or protein-phospholipid head group interactions, which is used by type II LD proteins (Kory et al., 2016). ERD7 is assumed to be a type II LD protein because it lacks a predicted hydrophobic region that could form a hairpin. Type II LD proteins are known to associate with LDs *via* either an amphipathic α-helix, a lipid modification, and/or by binding to another LD coat protein(s) (Kory et al., 2016). Consistent with this, ERD7 contains at least two regions within its SD sequence that have propensity to form an amphipathic α-helix (amino acids 308–325 and 355–372), as determined by HeliQuest (Gautier et al., 2008), and the GPS-Lipid server (Xie et al., 2016) predicts a putative S-palmitoylation site at the cysteine residue at position 281 in ERD7, a post-translational modification known to be responsible for proper localization of other LD coat proteins (Kory et al., 2016). However, whether either or both of these putative signals and/or interactions with other LD coat proteins contributes to the LD localization of ERD7 in plant cell, remains to be determined.

SENA and SENB Proteins Target to LDs or Mitochondria, Respectively

The localization of full-length ERD7 and the ERD7 SD region to cytosol and/or LDs (**Figure 2**) prompted us to investigate the subcellular localization of other SD-containing (i.e., SEN) proteins in plants. Land plants contain multiple SEN proteins separated into two distinct subfamilies, referred to in this study as SENA and SENB proteins (**Figures 3A,B**). Arabidopsis contains six SEN proteins, with three in each subfamily, including ERD7, which is a SENA-type protein (i.e., SENA1; **Figures 3A,B**). Unlike ERD7, which localized to both cytosol and LDs, transient expression of full-length Arabidopsis SENA2 and SENA3 in *N. benthamiana* leaves resulted in localization exclusively to the cytoplasm (**Figure 4**). Expression of the SENA2 and SENA3 SD regions alone; however, resulted in targeting almost exclusively to LDs (**Figure 4**), similar to what was observed for the ERD7 SD (**Figure 2**). The results together suggest that plant SENA-type proteins exhibit dual localization between cytosol and/or LDs, and that, as mentioned above, their subcellular distribution might be influenced by conformational changes that expose targeting signals within their SD regions. Expression of a full-length SENB-type protein (i.e., SENB2) in plant cells resulted also in localization to the cytosol, and surprisingly, the SD region of SENB2, as well as SENB1, did not target to LDs. Instead, both SENB1-SD and SENB2-SD targeted to mitochondria (**Figure 4**). Thus, the SEN protein family in plants appears to contain two distinct subfamilies whose members show potential for regulated distribution between cytosol and LDs or mitochondria, respectively. Notably, there are no obvious sequence motifs or conserved regions that are shared between the SDs in the LD-localized Arabidopsis SENA proteins and spartin, but absent in the SDs of the mitochondrial-localized SENB proteins. There are also no predicted mitochondrial targeting signals (based on the Plant-mPLoc and DeepLoc prediction programs) in the SDs of the Arabidopsis SENB proteins. Interestingly, ERD7 has been also reported to bind anionic phospholipids, such as phosphatidic acid (Barajas-Lopez et al., 2020), which is present in the LD monolayer (Thiam et al., 2013). It is plausible, therefore, that ERD7 (and the other Arabidopsis SENA proteins) localizes to LDs *via* binding anionic phospholipids on the LD surface, and similarly, mitochondrial targeting of SENB proteins could be mediated by binding to a different anionic phospholipid(s). How the SDs in these proteins are able to distinguish between different organelle locations in plant cells remains to be determined.

To determine whether this dual localization pattern might be an evolutionarily conserved feature of SEN-type proteins, we transiently expressed the human SEN protein spartin in plant cells. Notably, spartin is the only SD-containing protein found in humans (**Figure 3A**), where it localizes to LDs (Eastman et al., 2009; Urbancyzk and Enz, 2011), but also targets to mitochondria and other subcellular locations (Bakowska et al., 2007; Edwards et al., 2009; Joshi and Bakowska, 2011; Karlsson et al., 2014). When expressed in *N. benthamiana* leaf cells, the localization of spartin was similar to that of Arabidopsis SENA2 and SENA3, with full-length spartin localized to the cytosol, and the SD region alone targeting to LDs (**Figure 4**). This conservation of targeting suggests that the SD region of spartin might bind directly to LDs using biophysical features of LDs that are conserved between plants and animals, or by binding to an unidentified LD protein(s) conserved across plants and animals. Further, the differential localization of spartin to LDs or mitochondria in mammalian cells is interesting given that Arabidopsis SENA SDs localize to LDs and the SENB SDs localize to mitochondria. This suggests that plant SENA/SENB proteins might have diverged evolutionarily to have distinct subcellular localizations (i.e., LDs or mitochondria) and that multiple proteins evolved to carry out functions homologous to that of spartin in humans. However, it also cannot be ruled out that the SDs in plant SENA/SENB proteins might similarly localize to distinct subcellular organelles in different cellular and/or physiological contexts, since we only analyzed SD localization in one expression system, cell-type, and condition (i.e., transient-expression in *N. benthamiana* leaf epidermal cells subjected to standard growing conditions). Hence, the detailed characterization of the subcellular targeting signals in ERD7 and other plant SEN proteins and their potential modulation by cell type and/or stress conditions will be undoubtedly an important avenue of future investigation.

ERD7 Is Stress-Inducible and May Serve as a Link Between LDs and Stress Responses

While it is well-known that *ERD7* is transcriptionally upregulated by a variety of abiotic stresses, including drought, salt, and cold (Winter et al., 2007; Cheng et al., 2013; Rasmussen et al., 2013; refer also to Arabidopsis microarray expression data for *ERD7* and other *SEN* genes in response to various stresses shown in **Supplementary Figure 5C**), studies on its possible molecular function(s) have only recently been carried out.

That is, Barajas-Lopez et al. (2020) showed that ERD7 protein expression is similarly induced by cold and salt stress, and Arabidopsis mutants lacking *SENA2* and *SENA3* and heterozygous for *ERD7* (as the homozygous triple mutants were embryonic lethal) accumulated more anthocyanins during cold stress and leaves were more susceptible to freezing, perhaps due to decreased membrane flexibility. While the precise role(s) for ERD7 (and other plant SEN proteins) in membrane homeostasis during stress responses remains to be determined, our results from the Y2H screen conducted using ERD7 as bait (**Figure 6**; **Supplementary Table 3**) provide insight to help guide future studies. For instance, ERD7 potentially interacts with all four members of the S4 MYBs family, which are nuclear transcriptional repressors known to regulate phenylpropanoid biosynthesis (Zhou et al., 2017; Wang et al., 2020). It is possible, therefore, that ERD7 might regulate these transcriptional repressors by sequestering them in the cytosol, perhaps even at LDs, barring them from entering the nucleus. This premise is attractive given that other LD proteins have been shown to regulate nuclear protein factors by binding to and sequestering them on cytosolic LDs (Li et al., 2012; Ueno et al., 2013).

Among the other candidate ERD7-interacting proteins identified in our Y2H screen were two RING-type E3 ubiquitin ligases, SINAT2 and ATL72 (**Supplementary Table 3**). These proteins are notable given that human spartin has been shown to recruit E3 ubiquitin ligases to LDs and is proposed to function in controlling LD turnover by regulating the polyubiquitination and breakdown of LD proteins (Edwards et al., 2009; Hooper et al., 2010). This could point to an analogous role for ERD7 in controlling the turnover of LD proteins in plants, particularly during stress responses. In addition, the identification of BPA1 as a putative ERD7-interacting protein (**Supplementary Table 3**) is also notable, since BPA1 interacts with and stabilizes ACD11, which is a sphingolipid transfer protein involved in the plant immune defense and hypersensitive response pathways that are elicited by biotic stress (Petersen et al., 2009; Li et al., 2019). Since LDs are known to be involved in generation of lipid signals in eukaryotes, including in plants (Ischebeck et al., 2020), it is possible, therefore, that LD-localized ERD7 facilitates this process in response to stress. Whether ERD7 (or other Arabidopsis SEN proteins) serves to modulate MYB transcription factors, SINAT2/ATL72 E3 ubiquitin ligases, and/or BPA1/ACD11 activity remains to be determined. Of course, it will be important to first confirm in plant cells the putative interactions of ERD7 with these proteins or any of the other candidate ERD7-interacting proteins, we identified by Y2H analysis (**Supplementary Table 3**). Nonetheless, based on the results collectively presented in this study, ERD7 should serve as a unique tool for future studies aimed at elucidating the functional link between stress responses and LD biology in plants.

ACCESSION NUMBERS

Arabidopsis Genome Initiative (AGI) identifier numbers for the coding sequences of the Arabidopsis proteins examined in this study were obtained from TAIR and are as follows: *ERD7* (AT2G17840.1), *SENA2* (AT4G35985.1), *SENA3* (AT3G51250.1), *SENB1* (AT3G21600.1), *SENB2* (AT4G15450.1), *SENB3* (AT3G21590.1), *LPEAT1* (AT1G80950), and *TUBULIN 4* (AT5G44340). The National Center for Biotechnology Information (NCBI) Consensus CDS identifier numbers for *H. sapiens SPARTIN* and TBSV *P19* are NM_015087.5 and CAC01278.1, respectively.

DATA AVAILABILITY STATEMENT

The datasets presented in this study can be found in online repositories. The names of the repository/repositories and accession number(s) can be found in the article/**Supplementary Material**.

AUTHOR CONTRIBUTIONS

ND, DS, MM, SS, SG, and TI performed the experiments. KS and GB performed the mass spectrometry. ND and RM wrote the manuscript with input from JD, KC, and TI. All authors contributed to the article and approved the submitted version.

FUNDING

This work was funded by the US Department of Energy, Office of Science, BES-Physical Biosciences program (DE-SC0016536; to KC, JD, and RM), the Natural Sciences and Engineering Research Council of Canada (RGPIN-2018-04629; to RM), and the Deutsche Forschungsgemeinschaft (IS 273/2-2 to TI; and DFG-GZ: INST 186/1230-1 FUGG to Stefanie Pöggeler). Mention of trade names or commercial products in this article is solely for the purpose of providing specific information and does not imply recommendation or endorsement by the United States Department of Agriculture (USDA). The USDA is an equal opportunity provider and employer.

ACKNOWLEDGMENTS

We thank Daphne Goring (University of Toronto) for providing plasmids pBEE401E and pCBC-DT1T2 and advice on CRISPR/Cas9 genome editing in *Arabidopsis*, as well as Morgan Stykel and Scott Ryan (University of Guelph) for providing human neuron-derived mRNA used for cloning the spartin SD.

SUPPLEMENTARY MATERIAL

The Supplementary Material for this article can be found online at: https://www.frontiersin.org/articles/10.3389/fpls.2021.658961/full#supplementary-material

REFERENCES

Agarwal, P., Mitra, M., Banerjee, S., and Roy, S. (2020). MYB4 transcription factor, a member of R2R3-subfamily of MYB domain protein, regulates cadmium tolerance via enhanced protection against oxidative damage and increases expression of PCS1 and MT1C in Arabidopsis. *Plant Sci.* 297:110501. doi: 10.1016/j.plantsci.2020.110501

Almagro Armenteros, J. J., Sønderby, C. K., Sønderby, S. K., Nielsen, H., and Winther, O. (2017). DeepLoc: prediction of protein subcellular localization using deep learning. *Bioinformatics* 33, 3387–3395. doi: 10.1093/bioinformatics/btx431

Aubert, Y., Vile, D., Pervent, M., Aldon, D., Ranty, B., Simonneau, T., et al. (2010). RD20, a stress-inducible caleosin, participates in stomatal control, transpiration and drought tolerance in *Arabidopsis thaliana*. *Plant Cell Physiol.* 51, 1975–1987. doi: 10.1093/pcp/pcq155

Bakowska, J. C., Jupille, H., Fatheddin, P., Puertollano, R., and Blackstone, C. (2007). Troyer syndrome protein spartin is mono-ubiquitinated and functions in EGF receptor trafficking. *Mol. Biol. Cell* 18, 1683–1692. doi: 10.1091/mbc.e06

Barajas-Lopez, J. d. D., Tiwari, A., Zarza, X., Shaw, M. W., Pascual, J., Punkkinen, M., et al. (2020). EARLY RESPONSE TO DEHYDRATION 7 remodels cell membrane lipid composition during cold stress in Arabidopsis. *Plant Cell Physiol.* 62, 80–91. doi: 10.1093/pcp/pcaa139

Bauer, N. C., Doetsch, P. W., and Corbett, A. H. (2015). Mechanisms regulating protein localization. *Traffic* 16, 1039–1061. doi: 10.1111/tra.12310

Berardini, T. Z., Mundodi, S., Reiser, L., Huala, E., Garcia-hernandez, M., Zhang, P., et al. (2004). Functional annotation of the Arabidopsis genome using controlled vocabularies. *Plant Physiol.* 135, 745–755. doi: 10.1104/pp.104.040071

Blum, M., Chang, H., Chuguransky, S., Grego, T., Kandasaamy, S., Mitchell, A., et al. (2021). The InterPro protein families and domains database: 20 years on. *Nucleic Acids Res.* 49, 344–354. doi: 10.1093/nar/gkaa977

Brocard, L., Immel, F., Coulon, D., Esnay, N., Tuphile, K., Pascal, S., et al. (2017). Proteomic analysis of lipid droplets from Arabidopsis aging leaves brings new insight into their biogenesis and functions. *Front. Plant Sci.* 8:894. doi: 10.3389/fpls.2017.00894

Cai, Y., Goodman, J. M., Pyc, M., Mullen, R. T., Dyer, J. M., and Chapman, K. D. (2015). Arabidopsis SEIPIN proteins modulate triacylglycerol accumulation and influence lipid droplet proliferation. *Plant Cell* 27, 2616–2636. doi: 10.1105/tpc.15.00588

Chapman, K. D., Aziz, M., Dyer, J. M., and Mullen, R. T. (2019). Mechanisms of lipid droplet biogenesis. *Biochem. J.* 476, 1929–1942. doi: 10.1042/BCJ20180021

Chapman, K. D., Dyer, J. M., and Mullen, R. T. (2013). Commentary: why don't plant leaves get fat? *Plant Sci.* 207, 128–134. doi: 10.1016/j.plantsci.2013.03.003

Cheng, M., Liao, P., Kuo, W., and Lin, T. (2013). The Arabidopsis ETHYLENE RESPONSE FACTOR1 regulates abiotic stress-responsive gene expression by binding to different cis-acting elements in response to different stress signals. *Plant Physiol.* 162, 1566–1582. doi: 10.1104/pp.113.221911

Chou, K. C., and Shen, H. B. (2010). Plant-mPLoc: a top-down strategy to augment the power for predicting plant protein subcellular localization. *PLoS One* 5:e11335. doi: 10.1371/journal.pone.0011335

Clough, S. J., and Bent, A. F. (1998). Floral dip: a simplified method for *Agrobacterium*-mediated transformation of *Arabidopsis thaliana*. *Plant J.* 16, 735–743. doi: 10.1046/j.1365-313x.1998.00343.x

Coulon, D., Brocard, L., Tuphile, K., and Brehelin, C. (2020). Arabidopsis LDIP protein locates at a confined area within the lipid droplet surface and favors lipid droplet formation. *Biochimie* 169, 29–40. doi: 10.1016/j.biochi.2019.09.018

Cox, J., Hein, M. Y., Luber, C. A., Paron, I., Nagaraj, N., and Mann, M. (2014). Accurate proteome-wide label-free quantification by delayed normalization and maximal peptide ratio extraction, termed MaxLFQ. *Mol. Cell. Proteomics* 13, 2513–2526. doi: 10.1074/mcp.M113.031591

Cox, J., and Mann, M. (2008). MaxQuant enables high peptide identification rates, individualized p.p.b.-range mass accuracies and proteome-wide protein quantification. *Nat. Biotechnol.* 26, 1367–1372. doi: 10.1038/nbt.1511

Curtis, M., and Grossniklaus, U. (2003). A gateway cloning vector set for high-throughput functional analysis of genes *in planta*. *Plant Physiol.* 133, 462–469. doi: 10.1104/pp.103.027979

Deruyffelaere, C., Purkrtova, Z., Bouchez, I., Collet, B., Cacas, J., Chardot, T., et al. (2018). PUX10 is a CDC48A adaptor protein that regulates the extraction of ubiquitinated oleosins from seed lipid droplets in Arabidopsis. *Plant Cell* 30, 2116–2136. doi: 10.1105/tpc.18.00275

de Vries, J., and Ischebeck, T. (2020). Ties between stress and lipid droplets pre-date seeds. *Trends Plant Sci.* 25, 1203–1214. doi: 10.1016/j.tplants.2020.07.017

Dubos, C., Stracke, R., Grotewold, E., Weisshaar, B., Martin, C., and Lepiniec, L. (2010). MYB transcription factors in Arabidopsis. *Trends Plant Sci.* 15, 573–581. doi: 10.1016/j.tplants.2010.06.005

Eastman, S. W., Yassaee, M., and Bieniasz, P. D. (2009). A role for ubiquitin ligases and Spartin/SPG20 in lipid droplet turnover. *J. Cell Biol.* 184, 881–894. doi: 10.1083/jcb.200808041

Edwards, T. L., Clowes, V. E., Tsang, H. T. H., Connell, J. W., Sanderson, C. M., Luzio, J. P., et al. (2009). Endogenous spartin (SPG20) is recruited to endosomes and lipid droplets and interacts with the ubiquitin E3 ligases AIP4 and AIP5. *Biochem. J.* 423, 31–39. doi: 10.1042/BJ20082398

Fernández-Santos, R., Izquierdo, Y., López, A., Muñiz, L., Martínez, M., Cascón, T., et al. (2020). Protein profiles of lipid droplets during the hypersensitive defense response of Arabidopsis against *Pseudomonas* infection. *Plant Cell Physiol.* 61, 1144–1157. doi: 10.1093/pcp/pcaa041

Fornalé, S., Lopez, E., Salazar-Henao, J. E., Fernández-Nohales, P., Rigau, J., and Caparros-Ruiz, D. (2014). AtMYB7, a new player in the regulation of UV-sunscreens in *Arabidopsis thaliana*. *Plant Cell Physiol.* 55, 507–516. doi: 10.1093/pcp/pct187

Gautier, R., Douguet, D., Antonny, B., and Drin, G. (2008). HELIQUEST: a web server to screen sequences with specific α-helical properties. *Bioinformatics* 24, 2101–2102. doi: 10.1093/bioinformatics/btn392

Gidda, S. K., Park, S., Pyc, M., Yurchenko, O., Cai, Y., Wu, P., et al. (2016). Lipid droplet-associated proteins (LDAPs) are required for the dynamic regulation of neutral lipid compartmentation in plant cells. *Plant Physiol.* 170, 2052–2071. doi: 10.1104/pp.15.01977

Gidda, S. K., Shockey, J. M., Kim, P. K., Rothstein, S. J., Andrews, D. W., Dyer, J. M., et al. (2011). Hydrophobic-domain dependent protein–protein interactions mediate the localization of GPAT enzymes to ER subdomains. *Traffic* 12, 452–472. doi: 10.1111/j.1600-0854.2011.01160.x

Gidda, S., Watt, S., Collins-Silva, J., Kilaru, A., Arondel, V., Yurchenko, O., et al. (2013). Lipid droplet-associated proteins (LDAPs) are involved in the compartmentalization of lipophilic compounds in plant cells. *Plant Signal. Behav.* 8:e27141. doi: 10.4161/psb.27141

Greer, M. S., Cai, Y., Gidda, S. K., Esnay, N., Kretzschmar, F. K., Seay, D., et al. (2020). SEIPIN isoforms interact with the membrane-tethering protein VAP27-1 for lipid droplet formation. *Plant Cell* 32, 2932–2950. doi: 10.1105/tpc.19.00771

Hooper, C., Loring, Z., Shekhtman, A., Bakowska, J., and Puttamadappa, S. (2010). Spartin activates atrophin-1-interacting protein 4 (AIP4) E3 ubiquitin ligase and promotes ubiquitination of adipophilin on lipid droplets. *Biomed. Cent. Biol.* 8, 1–11. doi: 10.1186/1741-7007-8-72

Horn, P. J., James, C. N., Gidda, S. K., Kilaru, A., Dyer, J. M., Mullen, R. T., et al. (2013). Identification of a new slass of lipid droplet-associated proteins in plants. *Plant Physiol.* 162, 1926–1936. doi: 10.1104/pp.113.222455

Huang, A. H. C. (1996). Oleosins and oil bodies in seeds and other organs. *Plant Physiol.* 110, 1055–1061. doi: 10.1104/pp.110.4.1055

Ischebeck, T., Krawczyk, H. E., Mullen, R. T., Dyer, J. M., and Chapman, K. D. (2020). Lipid droplets in plants and algae: distribution, formation, turnover and function. *Semin. Cell Dev. Biol.* 108, 82–93. doi: 10.1016/j.semcdb.2020.02.014

Jasieniecka-Gazarkiewicz, K., Demski, K., Gidda, S. K., Klińska, S., Niedojadło, J., Lager, I., et al. (2021). Subcellular localization of acyl-CoA: lysophosphatidylethanolamine acyltransferases (LPEATs) and the effects of knocking-out and overexpression of their genes on autophagy markers level and life span of *A. thaliana*. *Int. J. Mol. Sci.* 22:3006. doi: 10.3390/ijms22063006

Joshi, D. C., and Bakowska, J. C. (2011). SPG20 protein spartin associates with cardiolipin via its plant-related senescence domain and regulates mitochondrial Ca^{2+} homeostasis. *PLoS One* 6:e19290. doi: 10.1371/journal.pone.0019290

Karlsson, A. B., Washington, J., Dimitrova, V., Hooper, C., Shekhtman, A., and Bakowska, J. C. (2014). The role of spartin and its novel ubiquitin binding region in DALIS occurrence. *Mol. Biol. Cell* 25, 1355–1365. doi: 10.1091/mbc.e13-11-0705

Kilian, J., Whitehead, D., Horak, J., Wanke, D., Weinl, S., Batistic, O., et al. (2007). The AtGenExpress global stress expression data set: protocols, evaluation and model data analysis of UV-B light, drought and cold stress responses. *Plant J.* 50, 347–363. doi: 10.1111/j.1365-313X.2007.03052.x

Kim, E. Y., Park, K. Y., Seo, Y. S., and Kim, W. T. (2016). Arabidopsis small rubber particle protein homolog SRPs play dual roles as positive factors for tissue growth and development and in drought stress responses. *Plant Physiol.* 170, 2494–2510. doi: 10.1104/pp.16.00165

Kolkhof, P., Werthebach, M., Van De Venn, A., Poschmann, G., Chen, L., Welte, M., et al. (2017). A luciferase-fragment complementation assay to detect lipid droplet-associated protein-protein interactions. *Mol. Cell. Proteomics* 16, 329–345. doi: 10.1074/mcp.M116.061499

Kong, Y., Chen, S., Yang, Y., and An, C. (2013). ABA-insensitive (ABI) 4 and ABI5 synergistically regulate DGAT1 expression in Arabidopsis seedlings under stress. *FEBS Lett.* 587, 3076–3082. doi: 10.1016/j.febslet.2013.07.045

Kory, N., Farese, R. V., and Walther, T. C. (2016). Targeting fat: mechanisms of protein localization to lipid droplets. *Trends Cell Biol.* 26, 535–546. doi: 10.1016/j.tcb.2016.02.007

Kretzschmar, F. K., Doner, N. M., Krawczyk, H. E., Scholz, P., Schmitt, K., Valerius, O., et al. (2020). Identification of low-abundant lipid droplet proteins in seeds and seedlings. *Plant Physiol.* 182, 1326–1345. doi: 10.1104/pp.19.01255

Kretzschmar, F. K., Mengel, L. A., Müller, A. O., Schmitt, K., Blersch, K. F., Valerius, O., et al. (2018). PUX10 is a lipid droplet-localized scaffold protein that interacts with CELL DIVISION CYCLE48 and is involved in the degradation of lipid droplet proteins. *Plant Cell* 30, 2137–2160. doi: 10.1105/tpc.18.00276

Kumar, S., Stecher, G., Li, M., Knyaz, C., and Tamura, K. (2018). MEGA X: molecular evolutionary genetics analysis across computing platforms. *Mol. Biol. Evol.* 35, 1547–1549. doi: 10.1093/molbev/msy096

Laemmli, U. K. (1970). Cleavage of structural proteins during the assembly of the head of bacteriophage T4. *Nature* 227, 680–685. doi: 10.1038/227680a0

Laibach, N., Post, J., Twyman, R. M., Gronover, C. S., and Prufer, D. (2015). The characteristics and potential applications of structural lipid droplet proteins in plants. *J. Biotechnol.* 201, 15–27. doi: 10.1016/j.jbiotec.2014.08.020

Li, Q., Ai, G., Shen, D., Zou, F., Wang, J., Bai, T., et al. (2019). A *Phytophthora capsici* effector targets ACD11 binding partners that regulate ROS-mediated defense response in Arabidopsis. *Mol. Plant* 12, 565–581. doi: 10.1016/j.molp.2019.01.018

Li, Z., Thiel, K., Thul, P. J., Beller, M., Kühnlein, R. P., and Welte, M. A. (2012). Lipid droplets control the maternal histone supply of *Drosophila* embryos. *Curr. Biol.* 22, 2104–2113. doi: 10.1016/j.cub.2012.09.018

Lingard, M. J., and Trelease, R. N. (2006). Five Arabidopsis peroxin 11 homologs individually promote peroxisome elongation, duplication or aggregation. *J. Cell Sci.* 119, 1961–1972. doi: 10.1242/jcs.02904

Listenberger, L. L., Ostermeyer-fay, A. G., Goldberg, E. B., Brown, W. J., and Brown, D. A. (2007). Adipocyte differentiation-related protein reduces the lipid droplet association of adipose triglyceride lipase and slows triacylglycerol turnover. *J. Lipid Res.* 48, 2751–2761. doi: 10.1194/jlr.M700359-JLR200

Lu, J., Xu, Y., Wang, J., Singer, S. D., and Chen, G. (2020). The role of triacylglycerol in plant stress response. *Plan. Theory* 9:472. doi: 10.3390/plants9040472

Lundquist, P. K., Shivaiah, K. K., and Espinoza-Corral, R. (2020). Lipid droplets throughout the evolutionary tree. *Prog. Lipid Res.* 78:101029. doi: 10.1016/j.plipres.2020.101029

Madeira, F., Park, Y. M., Lee, J., Buso, N., Gur, T., Madhusoodanan, N., et al. (2019). The EMBL-EBI search and sequence analysis tools APIs in 2019. *Nucleic Acids Res.* 47, 636–641. doi: 10.1093/nar/gkz268

Martin, B. A., Schoper, J. B., and Rinne, R. W. (1986). Changes in soybean (*Glycine max* [L.] Merr.) glycerolipids in response to water stress. *Plant Physiol.* 81, 798–801. doi: 10.1104/pp.81.3.798

McCartney, A. W., Greenwood, J. S., Fabian, M. R., White, K. A., and Mullen, R. T. (2005). Localization of the tomato bushy stunt virus replication protein p33 reveals a peroxisome-to-endoplasmic reticulum sorting pathway. *Plant Cell* 17, 3513–3531. doi: 10.1105/tpc.105.036350

Minkenberg, B., Zhang, J., Xie, K., and Yang, Y. (2019). CRISPR-PLANT v2: an online resource for highly specific guide RNA spacers based on improved off-target analysis. *Plant Biotechnol. J.* 17, 5–8. doi: 10.1111/pbi.13025

Mukhopadhyay, P., and Tyagi, A. K. (2015). OsTCP19 influences developmental and abiotic stress signaling by modulating ABI4-mediated pathways. *Sci. Rep.* 5, 1–12. doi: 10.1038/srep09998

Müller, A. O., Blersch, K. F., Gippert, A. L., and Ischebeck, T. (2017). Tobacco pollen tubes - a fast and easy tool for studying lipid droplet association of plant proteins. *Plant J.* 89, 1055–1064. doi: 10.1111/tpj.13441

Nelson, B. K., Cai, X., and Nebenführ, A. (2007). A multicolored set of *in vivo* organelle markers for co-localization studies in Arabidopsis and other plants. *Plant J.* 51, 1126–1136. doi: 10.1111/j.1365-313X.2007.03212.x

Olzmann, J. A., and Carvalho, P. (2019). Dynamics and functions of lipid droplets. *Nat. Rev. Mol. Cell Biol.* 20, 137–155. doi: 10.1038/s41580-018-0085-z

Panavas, T., Pikula, A., Reid, P. D., Rubinstein, B., and Walker, E. L. (1999). Identification of senescence-associated genes from daylily petals. *Plant Mol. Biol.* 40, 237–248. doi: 10.1023/A:1006146230602

Park, S., Gidda, S. K., James, C. N., Horn, P. J., Khuu, N., Seay, D. C., et al. (2013). The α/β hydrolase CGI-58 and peroxisomal transport protein PXA1 coregulate lipid homeostasis and signaling in Arabidopsis. *Plant Cell* 25, 1726–1739. doi: 10.1105/tpc.113.111898

Park, K. Y., Kim, W. T., and Kim, E. Y. (2018). The proper localization of RESPONSIVE TO DESICCATION 20 in lipid droplets depends on their biogenesis induced by STRESS-RELATED PROTEINS in vegetative tissues. *Biochem. Biophys. Res. Commun.* 495, 1885–1889. doi: 10.1016/j.bbrc.2017.12.068

Perlikowski, D., Kierszniowska, S., Sawikowska, A., Krajewski, P., Rapacz, M., Eckhardt, A., et al. (2016). Remodeling of leaf cellular glycerolipid composition under drought and re-hydration conditions in grasses from the Lolium-Festuca complex. *Front. Plant Sci.* 7:1027. doi: 10.3389/fpls.2016.01027

Petersen, N. H. T., Joensen, J., Mckinney, L. V., Brodersen, P., Petersen, M., Hofius, D., et al. (2009). Identification of proteins interacting with Arabidopsis ACD11. *J. Plant Physiol.* 166, 661–666. doi: 10.1016/j.jplph.2008.08.003

Petrie, J. R., Shrestha, P., Liu, Q., Mansour, M. P., Wood, C. C., Zhou, X., et al. (2010). Rapid expression of transgenes driven by seed-specific constructs in leaf tissue: DHA production. *Plant Methods* 6, 1–6. doi: 10.1186/1746-4811-6-8

Pyc, M., Cai, Y., Gidda, S. K., Yurchenko, O., Park, S., Kretzschmar, F. K., et al. (2017a). Arabidopsis lipid droplet-associated protein (LDAP) – interacting protein (LDIP) influences lipid droplet size and neutral lipid homeostasis in both leaves and seeds. *Plant J.* 92, 1182–1201. doi: 10.1111/tpj.13754

Pyc, M., Cai, Y., Greer, M. S., Yurchenko, O., Chapman, K. D., Dyer, J. M., et al. (2017b). Turning over a new leaf in lipid droplet biology. *Trends Plant Sci.* 22, 596–609. doi: 10.1016/j.tplants.2017.03.012

Rasmussen, S., Barah, P., Suarez-Rodriguez, M. C., Bressendorff, S., Friis, P., Costantino, P., et al. (2013). Transcriptome responses to combinations of stresses in Arabidopsis. *Plant Physiol.* 161, 1783–1794. doi: 10.1104/pp.112.210773

Rottet, S., Besagni, C., and Kessler, F. (2015). The role of plastoglobules in thylakoid lipid remodeling during plant development. *Biochim. Biophys. Acta* 1847, 889–899. doi: 10.1016/j.bbabio.2015.02.002

Schmitt, K., Smolinski, N., Neumann, P., Schmaul, S., Hofer-pretz, V., Braus, G. H., et al. (2017). Asc1p/RACK1 connects ribosomes to eukaryotic phosphosignaling. *Mol. Cell. Biol.* 37, 1–23. doi: 10.1128/MCB.00279-16

Schneider, C. A., Rasband, W. S., and Eliceiri, K. W. (2012). NIH image to ImageJ: 25 years of image analysis. *Nat. Methods* 9, 671–675. doi: 10.1038/nmeth.2089

Shaner, N. C., Campbell, R. E., Steinbach, P. A., Giepmans, B. N. G., Palmer, A. E., and Tsien, R. Y. (2004). Improved monomeric red, orange and yellow fluorescent proteins derived from *Discosoma* sp. red fluorescent protein. *Nat. Biotechnol.* 22, 1567–1572. doi: 10.1038/nbt1037

Shimada, T. L., Takano, Y., Shimada, T., Fujiwara, M., Fukao, Y., Mori, M., et al. (2014). Leaf oil body functions as a subcellular factory for the production of a phytoalexin in Arabidopsis. *Plant Physiol.* 164, 105–118. doi: 10.1104/pp.113.230185

Shockey, J. M., Gidda, S. K., Chapital, D. C., Kuan, J. C., Dhanoa, P. K., Bland, J. M., et al. (2006). Tung tree DGAT1 and DGAT2 have nonredundant functions in triacylglycerol biosynthesis and are localized to different subdomains of the endoplasmic reticulum. *Plant Cell* 18, 2294–2313. doi: 10.1105/tpc.106.043695

Siloto, R., Findlay, K., Lopez-Villalobos, A., Yeung, E., Nykiforik, C., and Moloney, M. (2006). The accumulation of oleosins determines the size of seed oilbodies in Arabidopsis. *Plant Cell* 18, 1961–1974. doi: 10.1105/tpc.106.041269

Sparkes, I. A., Runions, J., Kearns, A., and Hawes, C. (2006). Rapid, transient expression of fluorescent fusion proteins in tobacco plants and generation of stably transformed plants. *Nat. Protoc.* 1, 2019–2025. doi: 10.1038/nprot.2006.286

Sun, Q., Zybailov, B., Majeran, W., Friso, G., Olinares, P. D. B., and van Wijk, K. J. (2009). PPDB, the plant proteomics database at Cornell. *Nucleic Acids Res.* 37, 969–974. doi: 10.1093/nar/gkn654

Szklarczyk, D., Gable, A. L., Lyon, D., Junge, A., Wyder, S., Huerta-cepas, J., et al. (2019). STRING v11: protein-protein association networks with increased coverage, supporting functional discovery in genome-wide experimental datasets. *Nucleic Acids Res.* 47, 607–613. doi: 10.1093/nar/gky1131

Thiam, A. R., and Dugail, I. (2019). Lipid droplet–membrane contact sites – from protein binding to function. *J. Cell Sci.* 132, 1–12. doi: 10.1242/jcs.230169

Thiam, A. R., Farese, R. V., and Walther, T. C. (2013). The biophysics and cell biology of lipid droplets. *Nat. Rev. Mol. Cell Biol.* 14, 775–786. doi: 10.1038/nrm3699

Ueno, M., Shen, W. J., Patel, S., Greenberg, A. S., Azhar, S., and Kraemer, F. B. (2013). Fat-specific protein 27 modulates nuclear factor of activated T cells 5 and the cellular response to stress. *J. Lipid Res.* 54, 734–743. doi: 10.1194/jlr.M033365

Urbancyzk, A., and Enz, R. (2011). Spartin recruits PKC via the PCK-interacting proteins ZIP1 and ZIP3 to lipid droplets. *J. Neurochem.* 118, 737–748. doi: 10.1111/j.1471-4159.2011.07367.x

VanBuren, R., Wai, C. M., Zhang, Q., Song, X., Edger, P. P., Bryant, D., et al. (2017). Seed desiccation mechanisms co-opted for vegetative desiccation in the resurrection grass *Oropetium thomaeum*. *Plant Cell Environ.* 40, 2292–2306. doi: 10.1111/pce.13027

Vizcaíno, J. A., Deutsch, E. W., Wang, R., Csordas, A., Reisinger, F., Ríos, D., et al. (2014). ProteomeXchange provides globally coordinated proteomics data submission and dissemination. *Nat. Biotechnol.* 32, 223–226. doi: 10.1038/nbt.2839

Wang, X., Wu, J., Guan, M., Zhao, C., Geng, P., and Zhao, Q. (2020). Arabidopsis MYB4 plays dual roles in flavonoid biosynthesis. *Plant J.* 101, 637–652. doi: 10.1111/tpj.14570

Wang, Z. P., Xing, H. L., Dong, L., Zhang, H. Y., Han, C. Y., Wang, X. C., et al. (2015). Egg cell-specific promoter-controlled CRISPR/Cas9 efficiently generates homozygous mutants for multiple target genes in Arabidopsis in a single generation. *Genome Biol.* 16, 1–12. doi: 10.1186/s13059-015-0715-0

Winter, D., Vinegar, B., Nahal, H., Ammar, R., Wilson, G. V., and Provart, N. J. (2007). An "electronic fluorescent pictograph" browser for exploring and analyzing large-scale biological data sets. *PLoS One* 2:e718. doi: 10.1371/journal.pone.0000718

Xie, Y., Zheng, Y., Li, H., Luo, X., He, Z., Cao, S., et al. (2016). GPS-lipid: a robust tool for the prediction of multiple lipid modification sites. *Sci. Rep.* 6:28249. doi: 10.1038/srep28249

Xu, C., and Shanklin, J. (2016). Triacylglycerol metabolism, function, and accumulation in plant vegetative tissues. *Annu. Rev. Plant Biol.* 67, 179–206. doi: 10.1146/annurev-arplant-043015-111641

Yang, Y., and Benning, C. (2018). Functions of triacylglycerols during plant development and stress. *Curr. Opin. Biotechnol.* 49, 191–198. doi: 10.1016/j.copbio.2017.09.003

Yang, H., Hsu, C., Yang, J., and Yang, W. Y. (2012). Monodansylpentane as a blue-fluorescent lipid-droplet marker for multi-color live-cell imaging. *PLoS One* 7:e32693. doi: 10.1371/journal.pone.0032693

Zhou, M., Zhang, K., Sun, Z., Yan, M., Chen, C., Zhang, X., et al. (2017). LNK1 and LNK2 corepressors interact with the MYB3 transcription factor in phenylpropanoid biosynthesis. *Plant Physiol.* 174, 1348–1358. doi: 10.1104/pp.17.00160

Zienkiewicz, K., and Zienkiewicz, A. (2020). Degradation of lipid droplets in plants and algae—right time, many paths, one goal. *Front. Plant Sci.* 11:579019. doi: 10.3389/fpls.2020.579019

Conflict of Interest: The authors declare that the research was conducted in the absence of any commercial or financial relationships that could be construed as a potential conflict of interest.

Copyright © 2021 Doner, Seay, Mehling, Sun, Gidda, Schmitt, Braus, Ischebeck, Chapman, Dyer and Mullen. This is an open-access article distributed under the terms of the Creative Commons Attribution License (CC BY). The use, distribution or reproduction in other forums is permitted, provided the original author(s) and the copyright owner(s) are credited and that the original publication in this journal is cited, in accordance with accepted academic practice. No use, distribution or reproduction is permitted which does not comply with these terms.

frontiers in Plant Science

ORIGINAL RESEARCH
published: 15 April 2021
doi: 10.3389/fpls.2021.646938

In silico Analysis of Acyl-CoA-Binding Protein Expression in Soybean

Nur Syifaq Azlan[1], Ze-Hua Guo[1], Wai-Shing Yung[2], Zhili Wang[2], Hon-Ming Lam[2], Shiu-Cheung Lung[1] and Mee-Len Chye[1]**

[1] School of Biological Sciences, The University of Hong Kong, Pokfulam, Hong Kong, [2] School of Life Sciences and Center for Soybean Research of the State Key Laboratory of Agrobiotechnology, The Chinese University of Hong Kong, Shatin, Hong Kong

Plant acyl-CoA-binding proteins (ACBPs) form a highly conserved protein family that binds to acyl-CoA esters as well as other lipid and protein interactors to function in developmental and stress responses. This protein family had been extensively studied in non-leguminous species such as *Arabidopsis thaliana* (thale cress), *Oryza sativa* (rice), and *Brassica napus* (oilseed rape). However, the characterization of soybean (*Glycine max*) ACBPs, designated GmACBPs, has remained unreported although this legume is a globally important crop cultivated for its high oil and protein content, and plays a significant role in the food and chemical industries. In this study, 11 members of the GmACBP family from four classes, comprising Class I (small), Class II (ankyrin repeats), Class III (large), and Class IV (kelch motif), were identified. For each class, more than one copy occurred and their domain architecture including the acyl-CoA-binding domain was compared with Arabidopsis and rice. The expression profile, tertiary structure and subcellular localization of each GmACBP were predicted, and the similarities and differences between GmACBPs and other plant ACBPs were deduced. A potential role for some Class III GmACBPs in nodulation, not previously encountered in non-leguminous ACBPs, has emerged. Interestingly, the sole member of Class III ACBP in each of non-leguminous Arabidopsis and rice had been previously identified in plant-pathogen interactions. As plant ACBPs are known to play important roles in development and responses to abiotic and biotic stresses, the *in silico* expression profiles on GmACBPs, gathered from data mining of RNA-sequencing and microarray analyses, will lay the foundation for future studies in their applications in biotechnology.

Keywords: abiotic stress, acyl-CoA-binding protein, biotic stress, *Glycine max*, lipid trafficking, microarray, transcriptomics, protein structure

OPEN ACCESS

Edited by:
Eric Marechal, UMR 5168 Laboratoire de Physiologie Cellulaire Vegetale (LPCV), France

Reviewed by:
Guanqun (Gavin) Chen, University of Alberta, Canada
John Harwood, Cardiff University, United Kingdom

***Correspondence:**
Shiu-Cheung Lung
sclung@hku.hk
Mee-Len Chye
mlchye@hku.hk

Specialty section:
This article was submitted to Plant Physiology, a section of the journal Frontiers in Plant Science

Received: *28 December 2020*
Accepted: *12 March 2021*
Published: *15 April 2021*

Citation:
Azlan NS, Guo Z-H, Yung W-S, Wang Z, Lam H-M, Lung S-C and Chye M-L (2021) In silico Analysis of Acyl-CoA-Binding Protein Expression in Soybean. Front. Plant Sci. 12:646938. doi: 10.3389/fpls.2021.646938

INTRODUCTION

Soybean (*Glycine max*) is one of the most important global grain crops and plays a very prominent role in the food industry, because of its high protein (∼40%) and oil content in its seeds (∼20%) (Assefa et al., 2019). Soybean oil accounted for 362 of 596 million metric tons of total global oilseed production (George, 2021). In some parts of the world, especially in Asia, many types of dried and

fermented food are derived from soybean including soy sauce, soy milk, and tofu (Barrett, 2006). Furthermore, the production of soybean meal processed from soybean as a nutritious protein-rich food for livestock and poultry (Pantalone, 2012) totals 246.05 million metric tons globally (Soybean meal: world supply and demand, 2020). Soybean also supports several chemical industries related to the production of biodiesels, bioplastics and cosmetics (Gaonkar and Rosentrater, 2019).

Similar to many other important crops, soybean is subject to environmental challenges that disrupt growth and development which lead to reductions in yield and quality. A major problem faced in agriculture is salinity because excessive amounts of salt (exceeding 40 mM NaCl) in soils adversely affect the physiological and biochemical processes in plants (Miransari, 2016). Most legumes including soybean are sensitive to salinity (Hasanuzzaman et al., 2016) posing a severe threat to the soybean industry as land contaminated by high salt expands following saline intrusion by rising sea-water levels (FAO, 2018). Also, soybean is sensitive to cold environments of below 10°C that retard vegetative growth (Hasanuzzaman et al., 2016) as its optimal growth temperature ranges from 22.0 to 24.0°C (Choi et al., 2016). In soybean, water availability is especially crucial during the reproductive stage, particularly at seed filling (Desclaux et al., 2000), when seeds accumulate reserves of carbohydrate, protein and lipids (Goldberg et al., 1989). Drought and heat stress at the seed-filling stage are known to alter seed content, including lipid composition (Sehgal et al., 2018). During severe drought, reduction in soybean seed oil along with decrease in the percentages of linoleic and linolenic acids was reported, compromising on the quality of the seed oil (Dornbos and Mullen, 1991).

Besides abiotic stress factors, soybean is vulnerable to biotic stress. Soybean rust is one of the most threatening soybean diseases that affects production in the two biggest producers, United States and Brazil (Yorinori et al., 2005; Langenbach et al., 2016). In southern China, the loss suffered from soybean rust in the 1990s was estimated to be around 20 to 30 million US$/year (Li et al., 2010). Caused by a pathogenic fungus, *Phakopsora pachyrhizi*, this disease became more imminent as soybean *R* gene resistance responses were overcome and fungicide insensitivity escalated (Langenbach et al., 2016). Root and stem rot produced by an oomycete pathogen known as *Phytophthora sojae* is another soybean disease that causes million US$ losses in the United States (Tyler, 2007). An understanding of the molecular aspects underlying each of the abiotic and biotic stresses encountered will provide better strategies to enhance the crop value of soybean.

Lipids are organic molecules that can accomplish functions related to stress signaling and protection in many cellular processes. Besides their roles in response to stress and development (Colin and Jaillais, 2020; Huby et al., 2020; Rogowska and Szakiel, 2020; Wan et al., 2020), they are important in the formation of membranes for compartmentalization of cells and organelles (Goñi, 2014). Waxes and suberin which can be found on the epidermis and endodermis, respectively, participate in defense to protect against pathogenic attack (Seigler, 1998). The *de novo* synthesis of fatty acid (FA) in plants occurs in the plastids after which lipid biosynthesis takes place *via* the 'prokaryotic' or 'eukaryotic' pathways (Ohlrogge and Jaworski, 1997). In the 'prokaryotic' pathway, FA are made and utilized within the plastids while for the 'eukaryotic' pathway they must first be exported out of the plastids to the endoplasmic reticulum (ER) for further modifications and integration in lipid assembly (Ohlrogge and Jaworski, 1997). Hence, proteins which transfer lipids play an important role in the mobilization of lipids/FA within the cell (Li et al., 2016). While FATTY ACID EXPORT1 (FAX1) is a membrane protein responsible for the delivery of FA across the chloroplast inner membranes (Li et al., 2015), acyl carrier proteins (ACPs) bind to fatty acyl intermediates during fatty acid synthesis (Mofid et al., 2002). The utilization of FA outside plastids in many cellular pathways will require them to be esterified to acyl-CoA esters by long-chain acyl-CoA synthetase (LACS) (Shockey et al., 2002). It has been reported that candidates for transfer of acyl-CoA esters from the plastids to the ER include the acyl-CoA-binding proteins (ACBPs) (Du et al., 2016).

Acyl-CoA-binding proteins comprise a protein family that share a highly conserved acyl-CoA-binding (ACB) domain of about 80–90 residues (Burton et al., 2005). ACBPs are found in animals, plants, fungi, some eubacteria and archaebacteria (Burton et al., 2005; Islinger et al., 2020). Besides having a canonical role in channeling acyl-CoA esters within subcellular components, their roles can be very diverse in both plants and animals, given the presence of adjoining domains or motifs (Lung and Chye, 2016; Islinger et al., 2020). In plants, ACBPs can be grouped into four classes as dictated by molecular mass and the presence of other functional domain, ankyrin repeats or kelch motif (Du et al., 2016). Besides acyl-CoA esters, to which ACBP classes show different binding affinities, ACBPs also bind to phospholipids (Lung and Chye, 2016). Studies conducted in identifying their subcellular localization as well as their protein interactors have revealed that the roles of ACBPs include mediating stress responses and plant development (Du et al., 2016). This *in silico* study summarizes tissue-specificity and stress-responsiveness of soybean ACBPs, as extracted from data available in SoyBase[1] and the Soybean eFP Browser[2]. Together with the predicted tertiary structure and subcellular localization, this work provides a foundation in understanding GmACBPs.

MATERIALS AND METHODS

Classification and Homology Modeling of ACBP Homologs in Soybean

Soybean ACBPs (GmACBPs) were identified by BLASTp search using query protein sequences from each class of *Arabidopsis thaliana* (thale cress). Accession numbers of GmACBPs were retrieved from the Phytozome v12.1 database[3]. The GmACBPs were then classified by characterizing their domain architecture. Conserved domains used in the classification of plant ACBPs,

[1]https://www.soybase.org/

[2]http://bar.utoronto.ca/efpsoybean/cgi-bin/efpWeb.cgi

[3]https://phytozome.jgi.doe.gov/pz/portal.html

namely the acyl-CoA-binding domain (cd00435), ankyrin-repeat domain (cd00204) and kelch motif (pfam01344, pfam07646, pfam13415, pfam13418, and pfam13854) in GmACBP protein sequences were identified by performing an NCBI protein BLAST search[4] together with the ACBP protein sequences of Arabidopsis and *Oryza sativa* (rice). The domain arrangement and their boundaries were annotated by aligning them with the sequences from the Conserved Domain Database (CDD)[5]. Homology modeling in tertiary structure of GmACBPs was predicted using online tools, Phyre2[6] (Kelley et al., 2015) and SWISS-MODEL[7] (Waterhouse et al., 2018). The predicted 3D structures were viewed using NCBI iCn3D[8] (Wang J. et al., 2020).

Multiple Protein Sequence Alignment and Sequence Identity of Each Class ACB Domain Between Arabidopsis, Rice and Soybean

Protein sequences of the ACB domain from each class of Arabidopsis ACBPs, rice ACBPs, and soybean ACBPs were aligned using *ClustalW* in MEGA X (Kumar et al., 2018). Geneious Prime version 2021.0.1 software[9] was used for viewing the alignment and generating the sequence identity between Arabidopsis, rice and soybean.

Subcellular Localization Prediction of GmACBPs

Subcellular localization of GmACBPs was predicted using TargetP 1.1[10] (Emanuelsson et al., 2000) and PSORT for plant sequences[11] (Nakai and Horton, 1999). For both online tools, the prediction was performed using the protein sequences from each GmACBP retrieved from Phytozome v12.1 database (see text footnote 3).

Data Mining of *GmACBP* Expression in Different Organs and in Response to Stress

GmACBP expression data in young leaves, flowers, nodules, roots, developing seeds, and pod shells at different ages were retrieved from the RNA-seq transcriptomic data (Severin et al., 2010) available online at the Soybean eFP Browser (see text footnote 2). Data on the GmACBP expression was derived by using the soybean gene model ID from the Wm82.a1 assembly (Schmutz et al., 2010).

Information on *GmACBP* expression in response to abiotic and biotic stresses was retrieved from SoyBase (see text footnote 1) under SoyBase Expression Explorer[12]. The website hosts expression profiles of soybean gene models that include numerous tissues and organs at different developmental stages from various experiments and publications (Grant et al., 2010). Expression data on each *GmACBP* was explored by inputting the respective gene ID in the provided search bar and clicking on 'Display Expression.' RNA-seq and microarray experiments related to the gene of interest would then be displayed. Subsequently, specific *GmACBP* expression profiles in response to abiotic and biotic stresses were collected and tabulated.

For abiotic stress, *GmACBP* expression was analyzed in response to salinity, dehydration and cold stress. The *GmACBP* expression profile in response to salinity and dehydration stress was retrieved from a study using soybean cultivar Williams 82 (Belamkar et al., 2014). A high saline environment was created by placing young soybeans in 100 mM NaCl solution (Belamkar et al., 2014). For dehydration stress, the plants were exposed to air with reduced water availability (Belamkar et al., 2014). Root tissues harvested at 0, 1, 6, and 12 h were used for generating the expression profiles in both stress situations (Belamkar et al., 2014).

For cold stress, the *GmACBP* expression profile was adapted from the RNA-seq data generated from Yamasaki and Randall (2016) and Robison et al. (2019). The seedlings were left at 4°C until harvest at 0, 1 and 24 h (Robison et al., 2019).

The *GmACBP* expression profile in response to *P. pachyrhizi* was plotted based on the microarray data generated by Gregory Alvord et al. (2007) in which two different strains of *P. pachyrhizi* were used, the avirulent Hawaii 94-1 and virulent Taiwan 80-2 (Gregory Alvord et al., 2007). The *GmACBP* expression profile in response to *P. sojae* was retrieved from microarray analysis performed using isolate PT2004C2.S1 (Wang et al., 2010). Inoculation was conducted by Wang et al. (2010) at 24, 48, 72, and 120 h, each with an independent mock-treatment. For sample collection at 24 and 48 hpi (hours post inoculation), the sample was harvested directly at the inoculation site. At 72 and 120 hpi, the samples were taken 7.5 mm below and above the lesion margin of the seedlings (Wang et al., 2010).

Quantitative Real-Time PCR Analysis of *GmACBPs* in Soybean Root Nodules

Nodule samples and nodular RNA were prepared as previously described (Wang Q. et al., 2020) in which surface-sterilized *Glycine max* cv. C08 seeds were germinated in autoclaved vermiculite. *Sinorhizobium fredii* CCBAU45436 was used for inoculation at 4 days after sowing. Seedlings were watered with Milli-Q water at 3-day interval and grown at 28°C under a 16 h/8 h light-dark cycle. Nodules were harvested at 28 days post-inoculation. Samples were snap-frozen with liquid nitrogen and stored at −80°C before use. Total RNA was extracted with TRIzol reagent (Thermo Fisher, United States) and treated with DNase I, Amplification Grade (Thermo Fisher, United States) following manufacturer's instructions and cDNA was generated using High-Capacity cDNA Reverse Transcription Kit (Thermo Fisher, United States) with 18-mer oligo dT. The cDNA was diluted 10-fold with Milli-Q water before use in qPCR.

[4]http://blast.ncbi.nlm.nih.gov/Blast.cgi
[5]https://www.ncbi.nlm.nih.gov/Structure/cdd/cdd.shtml
[6]http://www.sbg.bio.ic.ac.uk/phyre2/
[7]https://swissmodel.expasy.org/
[8]https://www.ncbi.nlm.nih.gov/Structure/icn3d/full.html
[9]https://www.geneious.com
[10]http://www.cbs.dtu.dk/services/TargetP-1.1/
[11]http://psort1.hgc.jp/form.html
[12]https://www.soybase.org/expression/

Quantitative real-time PCR (qRT-PCR) was performed using TB Green *Premix Ex Taq* II (Tli RNaseH Plus) (TaKaRa Bio, United States) with Real-Time PCR Detection System, Bio-Rad CFX96 Touch. The program was carried out as follows: 95°C at 30 s, then 95°C at 5 s and 60°C for 30 s with 40 cycles. The experiment was conducted in two biological replicates and the calculation of relative expression level performed using the $2^{-\Delta\Delta Ct}$ method (Livak and Schmittgen, 2001) with normalization to the housekeeping gene *F-BOX PROTEIN2* (Libault et al., 2008). The average of $2^{-\Delta\Delta Ct}$ and standard error of mean, $n = 3$ from two biological replicates were used to plot the graph by using stripped roots (the remaining roots after nodule excision) as the control following (Wang Q. et al., 2020). Gene-specific primers used are listed in **Supplementary Table 1**.

Statistical Analysis

Analyses of *GmACBP* expression were carried out using the Student's *t*-test to determine any significant differences between means.

Accession Numbers

All the sequence information used in this work was retrieved using the following identifiers: Arabidopsis *AtACBPs* (At5g53470, At4g27780, At4g24230, At3g05420, At5g27630 and At1g31812), rice *OsACBPs* (LOC_Os08g06550.1, LOC_Os06g02490.1, LOC_Os03g37960.1, LOC_Os04g58550.1, LOC_Os03g14000.1 and LOC_Os03g61930.1), soybean *GmACBPs* (Glyma.09g214500, Glyma.04g122900, Glyma.04g233600, Glyma.06g131200, Glyma.01g191900, Glyma.11g050200, Glyma.14g087600, Glyma.17g236700, Glyma.03g236500, Glyma.19g234400, and Glyma.20g235500), and *F-BOX PROTEIN2* (Glyma.02G273700).

RESULTS

Classification and Homology Modeling of GmACBPs

Eleven identified GmACBPs were grouped by protein sequence alignment into four classes, based on domain architecture and molecular mass following the classification of the Arabidopsis and rice homologs (**Figure 1**). The 11 putative GmACBP homologs included two Class I small ACBPs (i.e., GmACBP1 and GmACBP2), two Class II ankyrin-repeat ACBPs (i.e., GmACBP3 and GmACBP4), four Class III large ACBPs (i.e., GmACBP5, GmACBP6, GmACBP7 and GmACBP8) and three Class IV kelch-ACBPs (i.e., GmACBP9, GmACBP10, and GmACBP11).

Each soybean Class I ACBP (GmACBP1 and GmACBP2) consists of 90 amino acids with a single ACB domain similar to Arabidopsis AtACBP6 (**Figure 1**). In each of Class II GmACBP3 and GmACBP4, a signal peptide absent in Arabidopsis Class II ACBPs, was detected within the transmembrane domain (**Figure 1**) similar to rice Class II OsACBP4. Class III GmACBP5 and GmACBP6 were more related in protein size and domain arrangement to each other than to GmACBP7 and GmACBP8 which are the largest amongst these four. Each of them contains a signal peptide and a transmembrane domain at the *N*-terminus (**Figure 1**). Interestingly, GmACBP7 possesses an additional DnaJ superfamily domain, which is absent in rice and Arabidopsis (**Figure 1**). Class IV GmACBP9, GmACBP10 and GmACBP11 showed conservation to Arabidopsis and rice Class IV ACBPs with the ACB domain at *N*-terminus and kelch motifs in the middle of the protein sequence.

Homology modeling in tertiary structure prediction of GmACBPs revealed that each of Class I and Class III GmACBPs consists of four α-helices at the ACB domain (**Figure 2A**). For Class I GmACBP1 and GmACBP2 the ACB domain was located within amino acid residues 3 to 87 while for Class III GmACBP5 and GmACBP6, the ACB domain spanned from residues 192 to 276 (**Figures 1**, **2A**). The helical structure in Class III GmACBP7 was predicted to be within residues 245 to 327, and the ACB helices in Class III GmACBP8 occurred at residues 258 to 339 (**Figure 2A**). For Class II GmACBPs, the predicted 3D model (**Figure 2B**) corresponded to the region of ankyrin repeats at residues 228 to 334 in GmACBP3 and residues 238 to 342 in GmACBP4 (**Figure 1**). The tertiary structures of Class IV GmACBP9, GmACBP10 and GmACBP11 (**Figure 2C**) were modeled against the kelch-motif-containing Arabidopsis nitrile-specifier protein (Zhang et al., 2017).

Conservation at the ACB Domain Within Arabidopsis, Rice, and Soybean Classes

Multiple sequence alignment of ACB domain of Class I ACBPs from Arabidopsis, rice and soybean revealed that GmACBP1 and GmACBP2 shared higher sequence identity with rice than Arabidopsis (**Figure 3**). GmACBP1 and GmACBP2 displayed higher identity to OsACBP1, at 80.46% and 82.76% respectively, than the other two Class I OsACBPs (**Figure 3**). GmACBP1 shared 72.41% identity while GmACBP2 shared 73.56% identity to Arabidopsis AtACBP6 (**Figure 3**). Class II GmACBP3 and GmACBP4 showed higher identity at the ACB domain with Arabidopsis, especially AtACBP2 with 87.13% identity in comparison to rice (69.31% and 70.30%, respectively) (**Figure 3**). For Class III, alignment at the ACB domain showed that the sequence identity amongst Arabidopsis, rice, and soybean was below 70% (**Figure 3**). Among the four members of soybean Class III, GmACBP7 shared highest identity with AtACBP3 and OsACBP5 at 60.42% and 51.52%, respectively (**Figure 3**). In the alignment of the ACB domain of Class IV, GmACBPs showed higher identity to Arabidopsis than rice, with GmACBP9 and GmACBP10 more similar to AtACBP4, and GmACBP11 to AtACBP5 (**Figure 3**).

Subcellular Localization Prediction of GmACBPs

Subcellular localization of GmACBPs was predicted by TargetP 1.1 (**Table 1**) and PSORT (**Table 2**). For TargetP 1.1, all proteins were predicted to be localized either at the chloroplast, mitochondria, secretory pathway or any other location. Based on the highest score in TargetP 1.1, Classes I and IV GmACBP were predicted not to be sorted to the chloroplast, mitochondria or secretory pathway while Classes II and III GmACBPs were

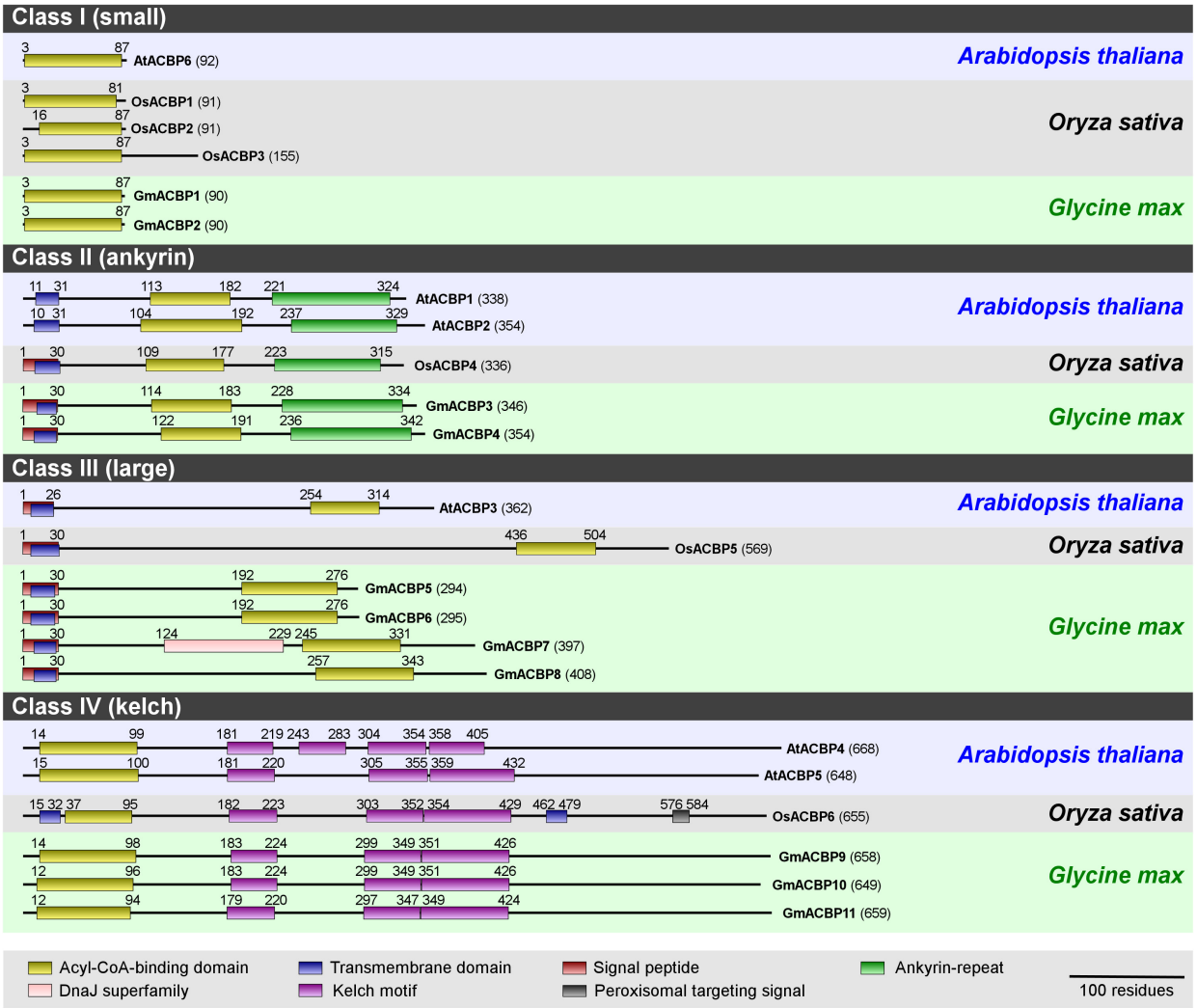

FIGURE 1 | Domain architecture of ACBPs from Arabidopsis, rice, and soybean. ACBP protein sequences from Arabidopsis (*Arabidopsis thaliana*), rice (*Oryza sativa*), and soybean (*Glycine max*) were submitted to the NCBI protein BLAST search (http://blast.ncbi.nlm.nih.gov/Blast.cgi) to identify conserved domains, and their boundaries are annotated by alignment with the Conserved Domain Database (CDD) collection including acyl-CoA-binding domain (cd00435), ankyrin-repeat domain (cd00204) and kelch motif (pfam01344, pfam07646, pfam13415, pfam13418, and pfam13854). Residue numbers are indicated in parentheses. This schematic diagram was modified from Lung and Chye (2016).

predicted to be targeted to the secretory pathway (**Table 1**). Using PSORT, Classes I and IV GmACBPs were deemed cytosolic while Class II GmACBPs scored highest for the plasma membrane (**Table 2**). For Class III, PSORT predicted that GmACBP5 would most certainly localize outside the cell, while GmACBP6 was predicted to be destined to the vacuole (**Table 2**). Class III GmACBP7 and GmACBP8 were both predicted to be targeted to the ER membrane (**Table 2**).

GmACBP Expression Profiles Across Various Organs of Soybean

Figure 4A shows *GmACBP* expression in developing seeds and Class I *GmACBP1* and *GmACBP2* exhibited elevated expression in all stages of seed development while Class III *GmACBP5* and *GmACBP6* have the lowest expression throughout. Class I *GmACBP1* and *GmACBP2* showed similar pattern in expression starting from 28 days after fertilization (DAF) (**Figure 4A**). Class II *GmACBP3* and *GmACBP4* displayed distinctive patterns of expression throughout seed development. For *GmACBP3*, its expression was maintained at the same level from 14 to 17 DAF until 25 DAF (**Figure 4A**). For *GmACBP4*, its expression peaked at 21 DAF and was constant from 35 to 42 DAF (**Figure 4A**). Lowest expression was detected for Class III *GmACBP5* and *GmACBP6* at 10–13 and 14–17 DAF (**Figure 4A**). *GmACBP5* lacked expression throughout every stage of seed development while *GmACBP6* exhibited low expression from 21 DAF (**Figure 4A**). Class III *GmACBP7* and *GmACBP8* both showed different expression profiles during seed development

A Class I (small) and Class III (large)

		H1	H2	H3	H4
GmACBP1 (Class I)	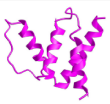	2-14	23-37	51-62	68-86
GmACBP2 (Class I)	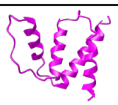	2-14	23-37	51-62	68-86
GmACBP5 (Class III)	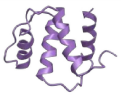	192-204	213-227	241-252	258-272
GmACBP6 (Class III)	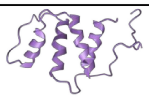	193-203	213-227	241-251	258-272
GmACBP7 (Class III)	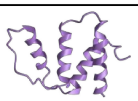	245-262	268-282	296-307	313-327
GmACBP8 (Class III)	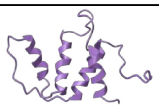	258-268	280-294	308-318	325-339

B Class II (Ankyrin repeats)

GmACBP3 (Class II)

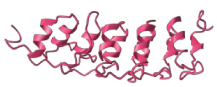

GmACBP4 (Class II)

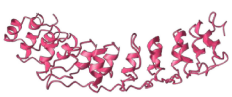

C Class IV (Kelch moif)

GmACBP9 (Class IV)

GmACBP10 (Class IV)

GmACBP11 (Class IV)

FIGURE 2 | Predicted tertiary structure of GmACBPs. The model was generated by using Phyre2 and SWISS-MODEL. **(A)** Class I and III GmACBPs with their corresponding position of the amino acid residues in the formation of the four helical structures, H1, H2, H3, and H4. **(B)** Predicted 3D model for Class II GmACBPs and their structure included the ankyrin-repeat regions. **(C)** 3D structure of Class IV GmACBPs predicted from SWISS-MODEL, including the region of kelch motif.

(**Figure 4A**). At 10–13 DAF, *GmACBP7* was highly expressed while *GmACBP8* expression was highest at 14–17 DAF. In Class IV, the expression profiles for all members were similar and *GmACBP10* and *GmACBP11* patterns were identical to each other (**Figure 4A**).

GmACBP expression in developing pods is shown in **Figure 4A**. Class I again showed very high expression at all three developmental stages. The expression of *GmACBP1* was notably similar across the three stages while *GmACBP2* expression was highest in 14–17 DAF pod shells (**Figure 4A**). Class II *GmACBP3* showed an upward trend as the pod shells matured in contrast to *GmACBP4* (**Figure 4A**). For Class III *GmACBP5* and *GmACBP8* lowest expression was evident in seven DAF pod shells (**Figure 4A**). *GmACBP6* indicated highest expression at 14–17 DAF while *GmACBP7* appeared constant across the different stages (**Figure 4A**). Class IV *GmACBP9*, *GmACBP10* and *GmACBP11* displayed different expression patterns at all three stages of pod development (**Figure 4A**).

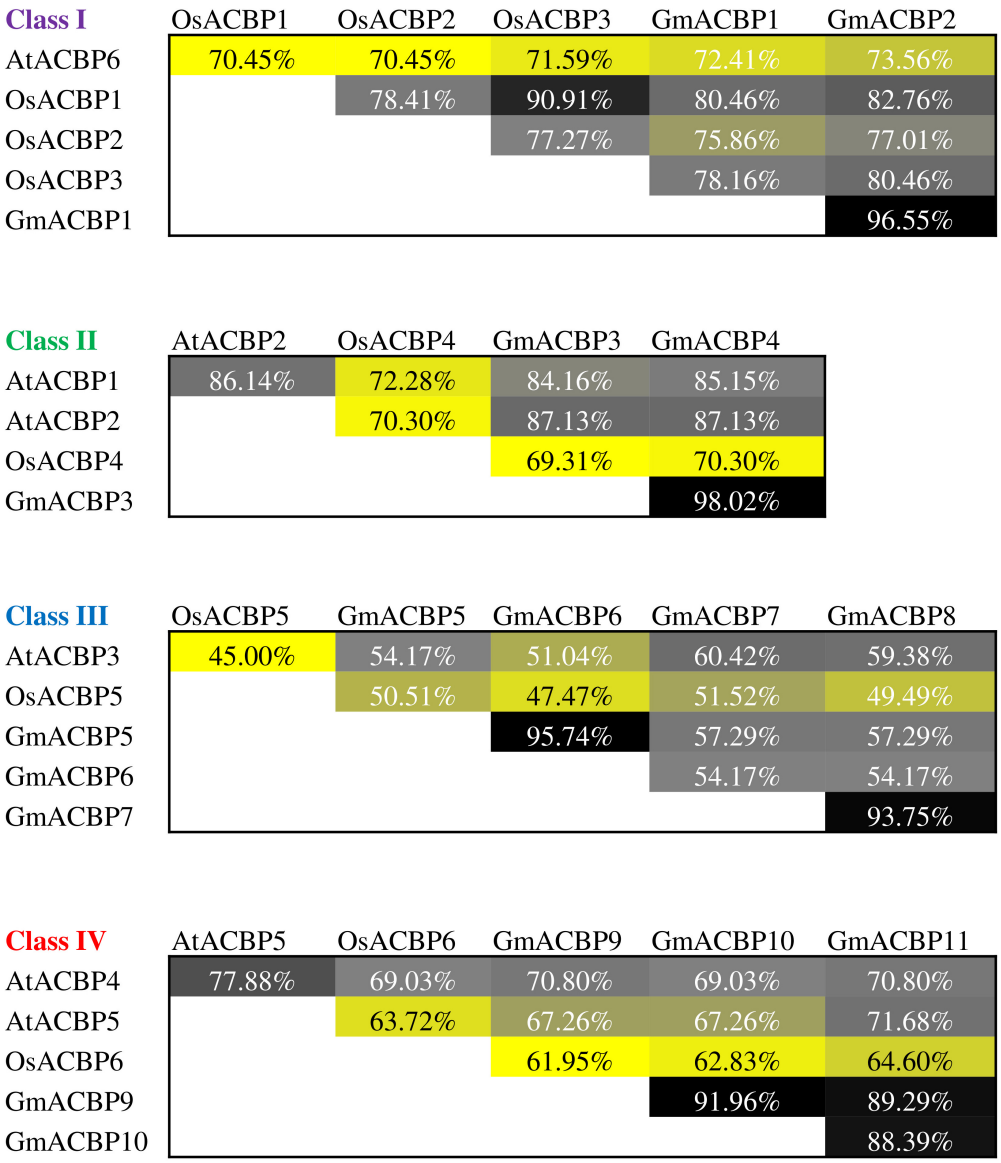

FIGURE 3 | Protein sequence identity of ACB domain in Arabidopsis, rice, and soybean ACBPs within the same classes. Percentage of identical residues was obtained by sequence alignment of the ACB domain in ACBPs from different species using *ClustalW* in MEGA X. The identity values are presented in heatmap in a descending order from black, gray, grayish yellow to yellow.

Figure 4B shows *GmACBP* expression in young leaves, flowers, roots, and nodules. Class I *ACBP*s are highly expressed in young leaves and roots. Of the four organs, *GmACBP1* showed strongest expression in roots and weakest in young leaves while *GmACBP2* was similarly expressed in roots, nodules, and flowers, but displayed lowest expression in young leaves (**Figure 4B**). Class II *GmACBP3* and *GmACBP4* showed higher expression in nodules and roots than flowers and young leaves. Members of Class III *GmACBP5, GmACBP6, GmACBP7,* and *GmACBP8* projected divergent expression patterns in young leaves, flowers, nodules, and roots (**Figure 4B**). *GmACBP5* expression was greatest in roots but very low in young leaves, flowers, and nodules. In contrast, the expression of *GmACBP6* was highest in roots and well expressed in flowers. *GmACBP7* and *GmACBP8* shared greatest expression in the nodules. Class IV *GmACBP9*, *GmACBP10,* and *GmACBP11* showed about similar expression patterns in all four organs with highest expression in young leaves and roots (**Figure 4B**).

GmACBP Expression in Response to Abiotic Stress

Figure 5A shows *GmACBP* expression when subjected to salinity stress. Class I *GmACBP2* expression decreased within 6 h of treatment (**Figure 5A**). The expression of Class II

TABLE 1 | Subcellular localization prediction of GmACBPs by TargetP 1.1.

GmACBP	Chloroplast	Mitochondrion	Secretory pathway	Other
GmACBP1	0.136	0.109	0.102	**0.872**
GmACBP2	0.150	0.103	0.115	**0.838**
GmACBP3	0.009	0.036	**0.981**	0.036
GmACBP4	0.008	0.046	**0.974**	0.036
GmACBP5	0.005	0.046	**0.986**	0.030
GmACBP6	0.007	0.049	**0.987**	0.025
GmACBP7	0.010	0.013	**0.961**	0.096
GmACBP8	0.004	0.013	**0.954**	0.181
GmACBP9	0.025	0.326	0.044	**0.668**
GmACBP10	0.077	0.343	0.041	**0.488**
GmACBP11	0.084	0.275	0.045	**0.539**

Value is certainty score. Highest score marked in bold indicates that the prediction is most certain to be in that location.

GmACBP3 was higher than the control after 12 h of salt treatment (**Figure 5A**). Class III *GmACBP7* expression pattern was different from *GmACBP5, GmACBP6* and *GmACBP8* because it appeared higher than the control within 12 h (**Figure 5A**). In Class IV, *GmACBP10* showed lower expression than the control at 12 h while *GmACBP9* expression was higher than the control at 1 h (**Figure 5A**). **Figure 5B** reports on *GmACBP* expression in response to dehydration and Class II *GmACBP3* and *GmACBP4* portrayed a similar expression pattern in which expression slightly increased and then was kept constant within 12 h (**Figure 5B**). Class III *GmACBP7* expression was upregulated within 1 h but after 6 h, expression dipped lower than the control (**Figure 5B**). Class IV *GmACBP9* displayed higher expression than the control after 6 h dehydration treatment (**Figure 5B**). **Figure 6** shows that during cold stress no difference in expression was detected between the control and *GmACBPs*, with the exception of Class IV *GmACBP11* of which expression was lower than the control at 24 h.

GmACBP Expression in Response to Biotic Stress

In microarray analysis of *GmACBP* expression during fungal *P. pachyrhizi* infection (**Figure 7**), only the expression of seven out of 11 was detected, albeit all classes were represented (Gregory Alvord et al., 2007) including Class I (*GmACBP2*), Class II (*GmACBP4*), Class III (*GmACBP5, GmACBP6* and *GmACBP7*), and Class IV (*GmACBP9* and *GmACBP11*). Similar expression patterns were observed for the seven *GmACBP*s in both susceptible- and resistant-reactions (**Figures 7A,B**). The expression of Class I *GmACBP2*, Class II *GmACBP4*, Class III *GmACBP5* and *GmACBP6,* and Class IV *GmACBP11* showed a reduction after 6 h (**Figures 7A,B**). For Class III *GmACBP5* and *GmACBP6,* expression was lower than the control up to 48 h (**Figures 7A,B**).

Figure 8 portrays the expression of seven *GmACBPs* in response to *P. sojae*. Class I *GmACBP2* expression was significantly downregulated at 48, 72, and 120 hpi from the mock (**Figure 8**). Class III *GmACBP5, GmACBP6* and *GmACBP7* exhibited a reduction at 48, 72, 120 hpi (**Figure 8**). Class IV *GmACBP9* showed a slight increase over the mock at 72 hpi (upper section of lesion margin) while *GmACBP11* was downregulated at 48 and 72 hpi (lower section of lesion margin).

GmACBP Expression in Soybean Root Nodules

Analysis by qRT-PCR on *GmACBP* expression in soybean root nodules showed that the expression of at least one member in each GmACBP class differed from the stripped root control (**Figure 9**). Expression of Class I *GmACBP2* and Class II *GmACBP3* were slightly higher in the nodules. While, the expression of Class IV *GmACBP10* and *GmACBP11* decreased in the nodules (**Figure 9**). For Class III, high expression in the nodules displayed by *GmACBP7* and *GmACBP8* corresponded to the expression pattern generated from RNA-seq (Severin et al., 2010) in which similar high expression occurred for *GmACBP7*

TABLE 2 | Subcellular localization prediction of GmACBPs by PSORT.

	Cy	Mit		PM	ER		GB	Out	Vac	Chl (TM)	Mic (Px)
		MtS	IM		M	L					
GmACBP1	**0.650**	0.100									
GmACBP2	**0.650**	0.100									
GmACBP3				**0.811**	0.640	0.100	0.370				
GmACBP4				**0.460**	0.100	0.100		0.100			
GmACBP5					0.100	0.100		**0.820**	0.445		
GmACBP6					0.100	0.100		0.820	**0.868**		
GmACBP7			0.100	0.100	**0.600**					0.302	
GmACBP8			0.100	0.100	**0.600**					0.302	
GmACBP9	**0.650**	0.100									
GmACBP10	**0.450**	0.100								0.100	0.321
GmACBP11	**0.450**	0.100								0.100	0.321

Value is certainty score. Highest score marked in bold indicated the prediction is most certain to be in that location.
Cy, cytoplasm; Mit, mitochondria; MtS, matrix space; IM, inner membrane; PM, plasma membrane; ER, endoplasmic reticulum; M, membrane; L, lumen; GB, Golgi body; Out, outside; Vac, vacuole; Chl, chloroplast; TM, thylakoid membrane; Mic, microbody; Px, peroxisome.

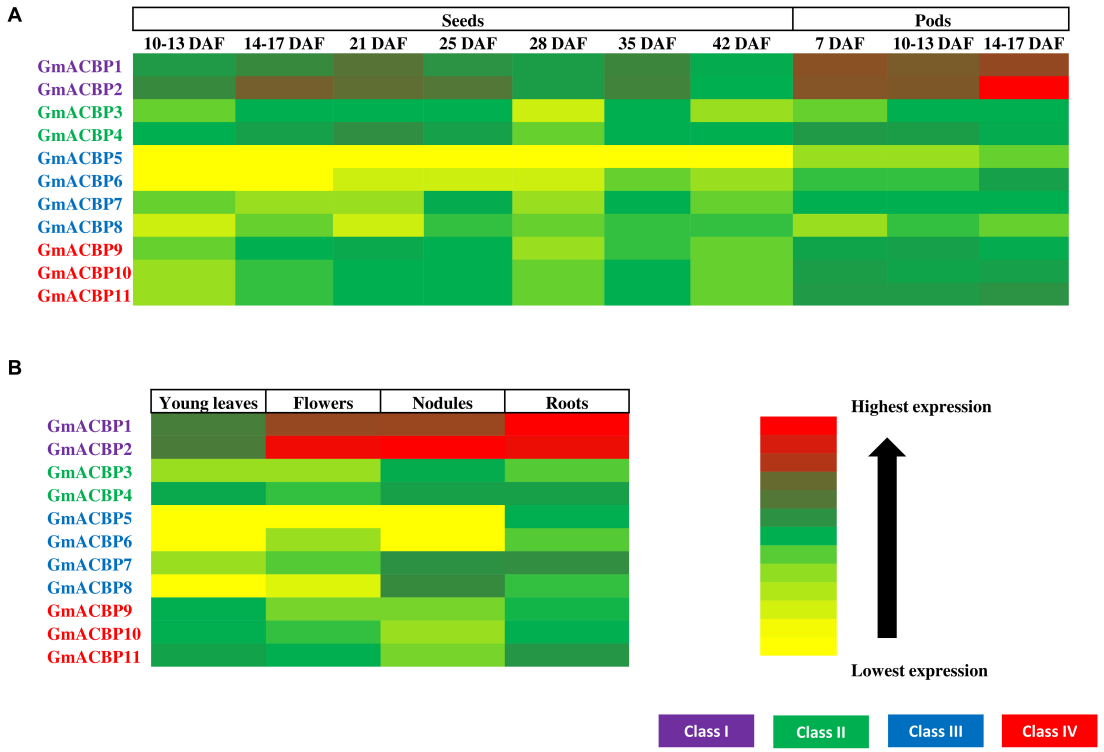

FIGURE 4 | *GmACBP* expression in different organs in the form of a heatmap generated using Microsoft Excel 2010. **(A)** Developing seeds and pods. **(B)** *GmACBP* expression in young leaves, flowers, nodules, and roots. The data were retrieved from RNA-seq analysis performed by Severin et al. (2010) from the Soybean eFP Browser (http://bar.utoronto.ca/efpsoybean/cgi-bin/efpWeb.cgi). The expression level was calculated using RPKM (Severin et al., 2010). The cultivar used was an introgression of *Glycine soja* (PI468916) and *Glycine max* (A81-356022) (Severin et al., 2010). The data were generated by pooled samples of three plants by Severin et al. (2010). Harvested samples by Severin et al. (2010) were based on the ontology terms described in SoyBase Soybean Ontologies (https://www.soybase.org/ontology.php) as follow: young leaves (SOY:0000252), flower (SOY:0001277), nodule (SOY:0001301), roots (SOY:0001183), 10–13 DAF seeds (SOY:0001290), 14–17 DAF seeds (SOY:0001290), 21 DAF seeds (SOY:0001291), 25 DAF seeds (SOY:0001291), 28 DAF seeds (SOY:0001291), 35 DAF seeds (SOY:0001292), 42 DAF seeds (SOY:0001293), 7 DAF pods (SOY:0001280), 10–13 DAF pods (SOY:0001281), and 14–17 DAF pods (SOY:0001282). *GmACBP* classes are shown in different colors.

and *GmACBP8* (**Figure 4B**). Such expression was again observed in qRT-PCR analysis of the second biological replicate and Class III *GmACBP8* exhibited very high expression in the nodules in comparison to the stripped roots (**Supplementary Figure 1**).

DISCUSSION

Eleven GmACBPs Map Into Four ACBP Classes

All ACBP homologs in soybean could be classified into four classes similar to non-leguminous species Arabidopsis and rice. The classification of *GmACBP* members into the four respective plant ACBP classes had previously been displayed in phylogenetic analysis (Meng et al., 2011). Class I comprises small (10-kDa of ∼92 amino acids) proteins that contain only a single ACB domain. Class II consists of large ACBPs with additional functional motifs, ankyrin repeats at the *C*-terminus and transmembrane domain at the *N*-terminus (Li and Chye, 2003). Class III is defined by large (∼39.3 kDa) ACBPs in which the ACB domain resides at the *C*-terminus (Leung et al., 2006). Class IV is characterized by the ACB domain at the *N*-terminus and presence of kelch motif at the middle region of the protein (Leung et al., 2004). Genome-wide mining of ACBPs in several plant species has shown that at least one copy has been identified in each class indicating that plant ACBPs play non-redundant roles (Meng et al., 2011). On top of that, in soybean, the Class III GmACBP7 was predicted to contain an additional DnaJ domain which has not been reported in other plant ACBPs. DnaJ proteins are co-chaperone that interacts with HSP70 for activating its function in protein folding (Pulido and Leister, 2018). The discovery of the DnaJ domain in GmACBP7 is deemed interesting as DnaJ proteins are characterized by the J-domain where HSP70 interaction occurs, with the addition of a zinc-finger domain and/or *C*-terminal substrate-binding domain (Pulido and Leister, 2018).

ACB Domain Sequence Conservation Amongst Arabidopsis, Rice, and Soybean

Alignment of ACB domains within the same classes revealed high conservation amongst Arabidopsis, rice and soybean. This

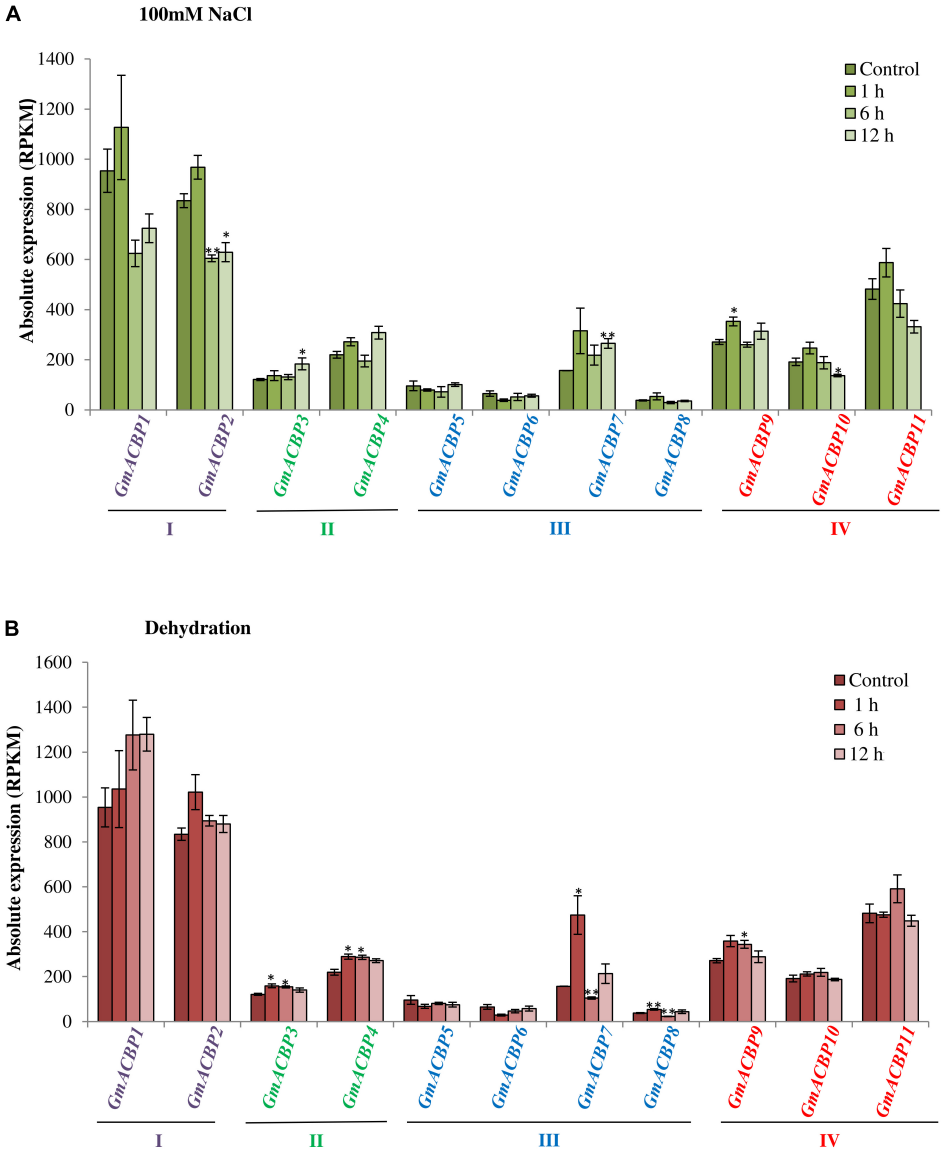

FIGURE 5 | *GmACBP* expression in response to salinity and dehydration stress. Expression profiles were retrieved from transcriptomic data generated by Belamkar et al. (2014) accessible at SoyBase (https://www.soybase.org/) with the identifier GSE57252. **(A)** Salinity stress was imposed on Williams 82 soybean seedlings of V1 stage by Belamkar et al. (2014) by treating the plants with 100 mM NaCl solution at 1, 6, and 12 h. **(B)** The dehydration treatment was conducted by exposing the seedlings in the air with less water for 1, 6, and 12 h (Belamkar et al., 2014). Root tissues of five plants for each treatment were used for the RNA-seq (Belamkar et al., 2014). *GmACBP* classes are shown in different colors. The expression pattern was plotted based on the average expression value of three plants. Error bars indicate the standard error of mean for each sample. Control and treatment groups were compared using Student's *t*-test. Statistically significant difference (**$P < 0.01$, $n = 3$; *$P < 0.05$, $n = 3$) is indicated.

may be explained by the selection pressure on *ACBP* genes in monocots and eudicots by which any deleterious mutation in *ACBP* will be eliminated to retain its biological function in binding acyl-CoA esters (Burton et al., 2005; Cvijović et al., 2018). Multiple protein sequence alignment of ACBPs from Arabidopsis, *Brassica napus*, rice, *Ricinus communis* (castor bean), man and cow showed that several amino acid residues are conserved in all, including YKQATVGP and KAKWDAW, which corresponded to the acyl-CoA-binding site (Engeseth et al., 1996). Considering the high homology amongst ACBP amino acid sequences, the 3D structure of the ACB domain in GmACBPs was predicted based on published ACBP structures from other plants or organisms. The structure of ACBPs as of bovine ACBP determined by nuclear magnetic resonance spectroscopy (Andersen et al., 1991), and those from man (Taskinen et al., 2007), *Plasmodium falciparum* (van Aalten et al., 2001) and rice (Guo et al., 2017; Jin et al., 2020) showed that each ACBP is made of four α-helices displayed in an up-and-down configuration. In rice, the acyl-CoA ester C18:3-CoA was shown to bind to Class I OsACBP2 in a pocket formed by the two helical structures and

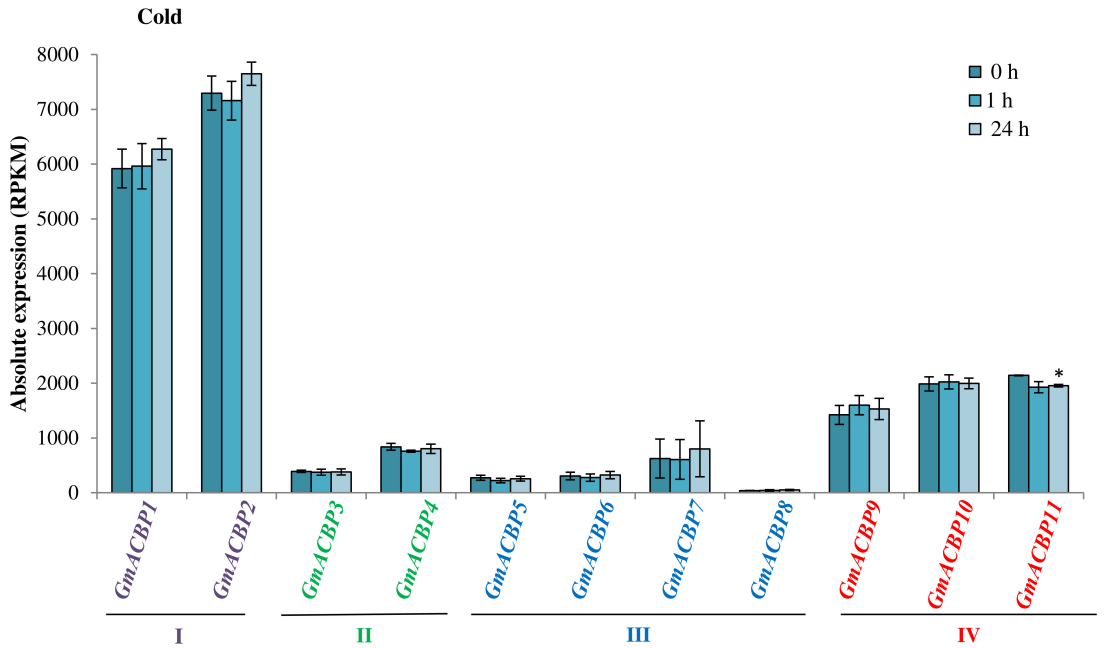

FIGURE 6 | *GmACBP* expression profile following cold stress. The expression data were taken from SoyBase (https://www.soybase.org/) (GSE117686) based on the RNA-seq transcriptome generated by Robison et al. (2019). Two-week-old Williams 82 soybean seedlings were exposed to 4°C for 0, 1, and 24 h (Robison et al., 2019). RNA-seq was generated by harvesting the cold-treated unifoliate leaves of more than six plants per biological replicates of three (Robison et al., 2019). The control (0 h) was not subject to treatment at 4°C (Robison et al., 2019). *GmACBP* classes are represented by different colors. The expression profile was charted based on the average expression value of three plants. Error bars indicate the standard error of mean for each sample. Control and treatment groups were compared using Student's *t*-test. Statistically significant difference (*$P < 0.05$, $n = 3$) is indicated.

the fatty acyl group of the ester was accommodated in the region of hydrophobic residues (Jin et al., 2020).

Subcellular Localization of GmACBPs

Subcellular localization of GmACBPs as analyzed using two different online tools, TargetP 1.1 (Emanuelsson et al., 2000) and PSORT (Nakai and Horton, 1999), revealed variation in the results, which may have arisen from different methods applied in each prediction. TargetP 1.1 specifically analyzes the *N*-terminal amino acid sequence for targeting into chloroplast, mitochondrion, ER/Golgi/secreted and 'other' (Emanuelsson et al., 2000). Meanwhile, PSORT takes into account the full amino acid sequence and also its organism origin, which is either prokaryotes, yeasts, animals or plants. In addition, PSORT analyzes various sequence features that range more than just the chloroplast or mitochondrion including the peroxisomal-targeting signal, ER-lumen-retention signal, nuclear-localization signals and vacuolar-targeting signal (Nakai and Horton, 1999) which may result in a more diverse prediction than TargetP 1.1.

Classes I and IV GmACBPs were deemed to be cytosolic using PSORT similar to Arabidopsis Class I AtACBP6 and Class IV AtACBP4 and AtACBP5, which had been verified by western blot analysis of subcellular protein fractionation, immuno-electron microscopy and confocal laser scanning microscopy of autofluorescence-tagged AtACBPs (Chen et al., 2008; Xiao et al., 2008). For Class II GmACBPs, both members were predicted to localize at the plasma membrane, similarly to Arabidopsis Class II as substantiated by transient expression of AtACBP-GFP fusion in onion epidermal cells and immuno-electron microscopy (Li and Chye, 2003), and expression of DsRed-AtACBP1 fusion protein in transgenic Arabidopsis (Lung et al., 2017, 2018). In rice, Class II OsACBP4 was validated to be localized at the plasma membrane and ER by confocal laser scanning microscopy of transgenic rice roots expressing *OsACBP4pro:GFP* (Liao et al., 2020). Extracellular targeting of Class III GmACBP5 according to PSORT is consistent with findings on Class III Arabidopsis AtACBP3 and rice OsACBP5, which were localized to the apoplast (Leung et al., 2006; Liao et al., 2020).

GmACBP Expression in Different Organs

High expression of Class I *GmACBP* in the flowers, roots, nodules and young leaves (**Figure 4**) indicated an expression profile suitable to housekeeping functions of Class I *ACBPs* (Du et al., 2016). Interestingly, Class III *GmACBP7* and *GmACBP8* displayed high expression in the nodules as shown by RNA-seq (**Figure 4B**) and experimentally validated by qRT-PCR analysis (**Figure 9**) suggesting their involvement in nodulation. Expression of *GmACBPs* in nodules is unique for soybean as this specialized organ does not occur in Arabidopsis or rice (Stacey, 2007). Nodules are organs developed from symbiosis in relation with rhizobia for atmospheric nitrogen fixation (Ferguson, 2013). An understanding on how GmACBPs can regulate nodulation would be essential as this symbiosis process is a good alternative to nitrogen-based fertilizers which contribute to air pollution

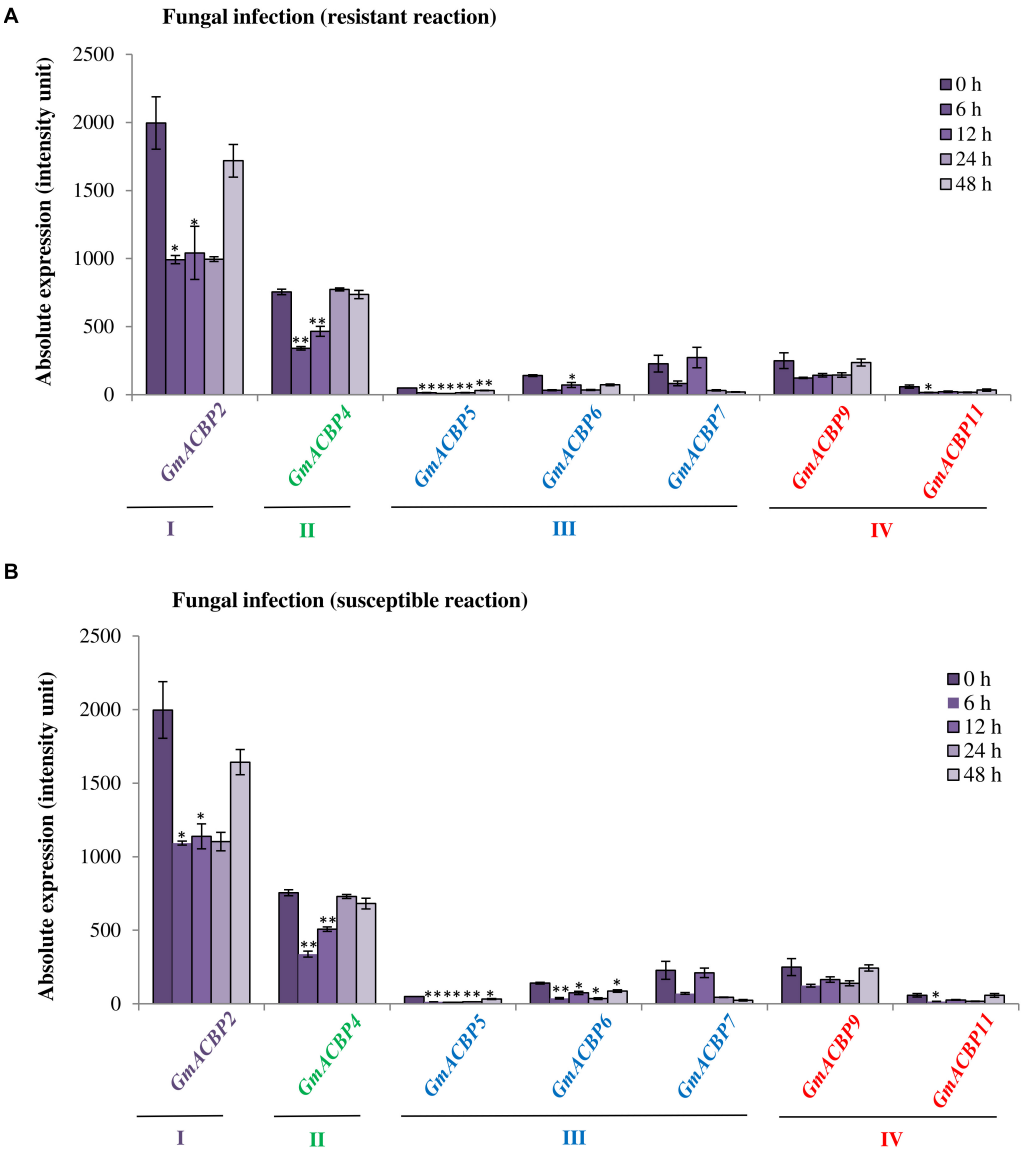

FIGURE 7 | *GmACBP* expression in response to fungal infection by two different *Phakopsora pachyrhizi* strains. Expression data were extracted from the microarray analysis by Gregory Alvord et al. (2007) available in SoyBase (https://www.soybase.org/) with identifier (GDS3230). Isolates of *P. pachyrhizi* used in the microarray analysis by Gregory Alvord et al. (2007) produced either resistant or susceptible physiological response in the soybean host. **(A)** The *P. pachyrhizi* strain that produced resistant reaction was Hawaii 94-1, while **(B)** Taiwan 80-2 caused a susceptible reaction (Gregory Alvord et al., 2007). Microarray data were generated from RNA isolation of infected leaves from 0 to 48 h, and expression was plotted based on the average of three biological replicates. *GmACBP* classes are displayed in different colors. Error bars indicate the standard error of mean for each sample. Control and treatment groups were compared using Student's *t*-test. Statistically significant difference (**$P < 0.01$, $n = 3$; *$P < 0.05$, $n = 3$) is indicated.

in its production and the product itself can be very costly (Crutzen et al., 2016).

The seed development of a legume can be divided into three main phases, namely embryogenesis, maturation, and dormant/matured stages (Le et al., 2007). The embryogenesis stage is further categorized into globular, heart and cotyledon stages. In general, the early stage in seed development is for cell division and cell differentiation of embryo axis and cotyledons (Le et al., 2007). After embryogenesis, the seed will enter maturation stage which is divided into early-, mid-, and late-stage (Le et al., 2007). The seed-filling stage is considered to be the most crucial phase in the seed development (Le et al., 2007) because this is the stage where the accumulation of reserves such as lipids, carbohydrate and protein occurs (Le et al., 2007). If disruption takes place during the accumulation process, it will negatively affect yield (Sehgal et al., 2018). The final stage in seed development is the dormant stage during which the seeds lose water and stay dormant until favorable conditions are available for germination (Sehgal et al., 2018). The seeds that Severin et al. (2010) collected are classified into cotyledon stage (10–13 and

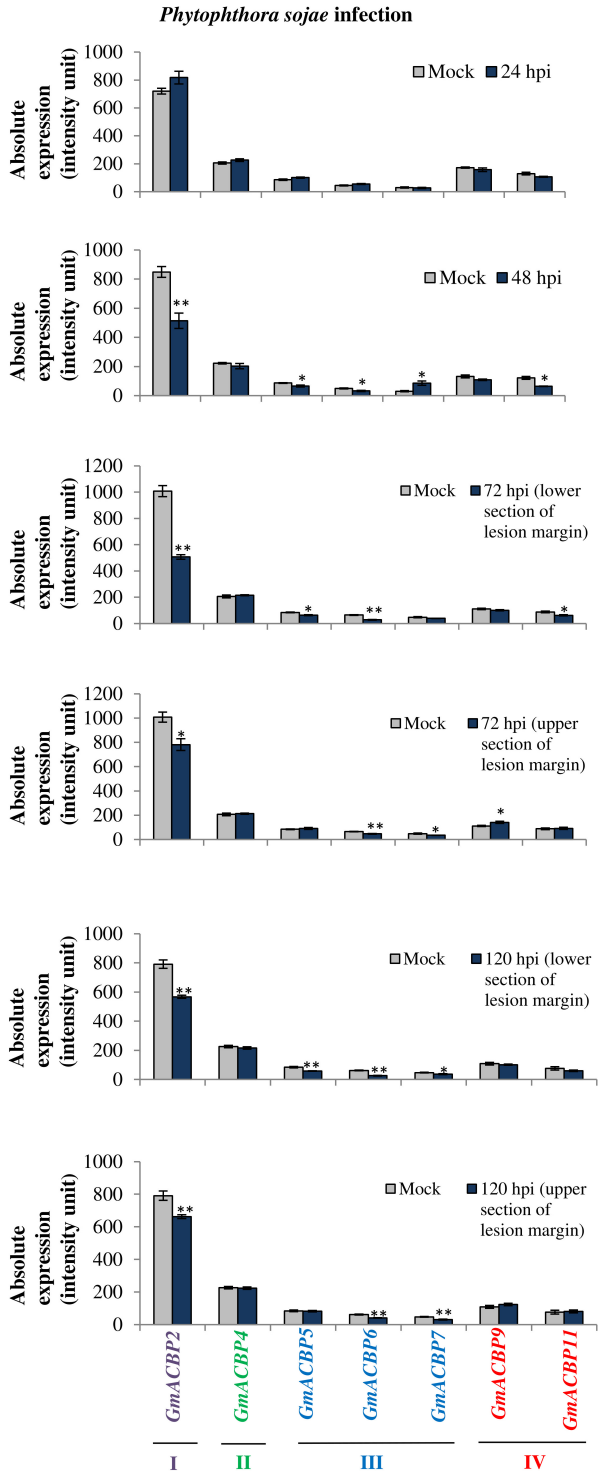

FIGURE 8 | *GmACBP* expression in response to *Phytophthora sojae*. The data were plotted based on the microarray analysis performed by Wang et al. (2010) available at SoyBase (https://www.soybase.org/) with identifier GDS3244. Inoculation of *P. sojae* by Wang et al. (2010) was conducted by injuring the seedling tap root with a 5 mm wound using a scalpel and at 24 and 48 hpi the samples were taken at the inoculation site, while at 72 and 120 hpi, they were derived from 7.5 mm below and above the lesion margin of the seedlings. *GmACBP* classes are represented in different colors. The expression profile was generated based on the average of four biological replicates (Wang et al., 2010). Error bars indicate the standard error of mean for each sample. Control and treatment groups were compared using Student's *t*-test. Statistically significant difference (**$P < 0.01$, $n = 4$; *$P < 0.05$, $n = 4$) is indicated.

14–17 DAF), early-maturation 1 (21, 25, and 28 DAF), early-maturation 2 (35 DAF) and mid-maturation (42 DAF) stage according to plant ontology provided by SoyBase[13].

High expression of Class I *GmACBP1* and *GmACBP2* in developing seeds suggests that Class I GmACBPs play important roles during seed development. Their expression remained high during early maturation which was the beginning of seed-filling stage. Studies conducted on Class I ACBPs in Arabidopsis (Guo et al., 2019b), *Helianthus annuus* (sunflower) (Aznar-Moreno et al., 2016), rice (Guo et al., 2019a), *Elaeis guineensis* (oil palm) (Amiruddin et al., 2019), and *B. napus* (Yurchenko et al., 2009, 2014) suggested their involvement in seed oil biosynthesis. Comparative transcriptomic analysis followed by qRT-PCR on developing embryos and seed coats of *B. napus*, showed that the Class I *BnACBP6* displayed the highest of all *BnACBP* expression throughout seed development suggesting it plays a potential role in oil accumulation (Liao et al., 2019). In oil palm and sunflower, the expression of their Class I *ACBPs* in the seeds was highest during the oil accumulation period (Aznar-Moreno et al., 2016; Amiruddin et al., 2019). In transgenic rice, the overexpression of Class I *OsACBP2* increased grain size and oil content (Guo et al., 2019a). Knockout of *atacbp6* affected seed oil content and composition (Guo et al., 2019b), leading to reduction in seed weight (Hsiao et al., 2014). This is not surprising given the main components for the biosynthesis of oil in seeds are glycerol-3-phosphate (G3P) and acyl-CoA esters, which act as substrates for the acylation of G3P catalyzed by acyltransferases to form triacylglycerol (TAG) (Bates et al., 2013). *In vitro* studies on recombinant *B. napus* Class I ACBP (rBnACBP) have already shown that it can stimulate the activity of acyltransferases involved in TAG synthesis (Brown et al., 2002).

GmACBP Expression in Response to Abiotic Stress

RNA-seq analysis for salinity and drought stress response (**Figures 5A,B**) showed that the increase in Class II *GmACBP3* expression is similar to Arabidopsis and rice (Du et al., 2013; Chen et al., 2018; Guo et al., 2020) but Class III *GmACBP7* was also induced. In Arabidopsis, it has been shown that Class II AtACBPs play essential roles in both drought and salinity stress (Du et al., 2013; Chen et al., 2018). *AtACBP1* expression was induced greater than five-fold after 48 h NaCl treatment (Chen et al., 2018). Studies using *AtACBP1*-overexpressors, *atacbp1*, and *AtACBP1*-complemented lines in response to different salinity concentrations revealed that AtACBP1 is involved in the abscisic acid (ABA)-signaling pathway and interacted with

[13]https://www.soybase.org/ontology.php

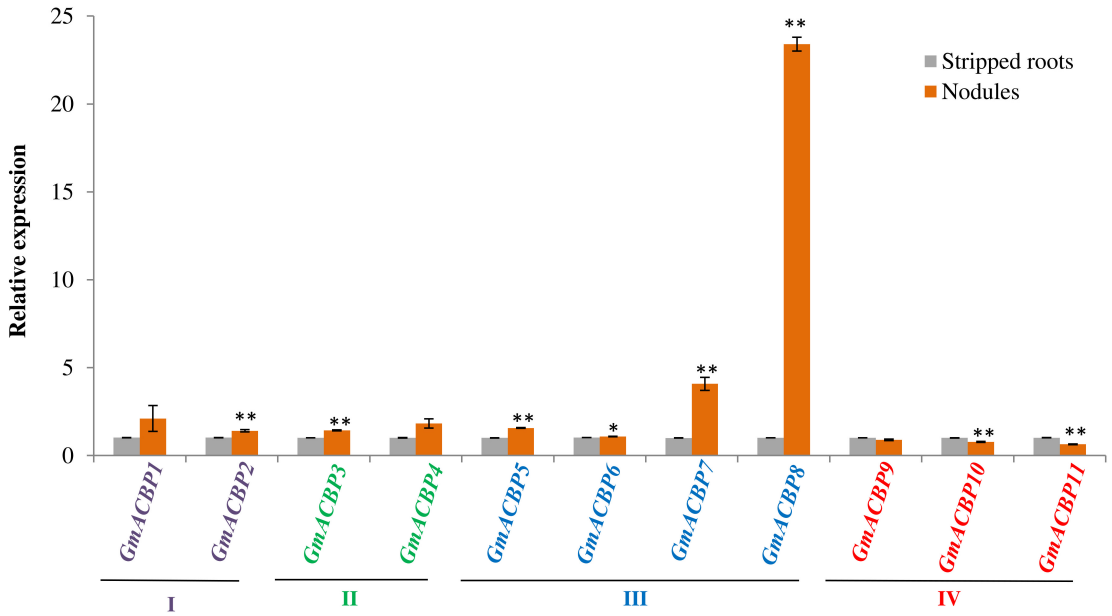

FIGURE 9 | Quantitative real-time PCR of *GmACBP* expression in root nodules. The control for the experiment consisted of stripped roots, the main and lateral root regions after the removal of nodules following Wang Q. et al. (2020). The expression level was normalized to the housekeeping gene, *F-BOX PROTEIN2*. qRT-PCR analysis was performed in two biological replicates. A similar expression pattern was also observed in the second biological replicate. Error bars indicate the standard error of mean, $n = 3$. Control and target groups were compared using the Student's *t*-test with statistically significant difference between the two groups as indicated (**$P < 0.01$; *$P < 0.05$).

ABA-RESPONSIVE ELEMENT BINDING PROTEIN1 (AREB1) through its ankyrin repeats to regulate salinity responses during seed germination and seedling development (Chen et al., 2018). Meanwhile, the expression of *AtACBP2* in the guard cells supported its role in the drought stress response through an ABA-mediated pathway in the production of reactive oxygen species (ROS) and *AtACBP2*-overexpression in transgenic Arabidopsis conferred drought tolerance (Du et al., 2013). In rice, Class II *OsACBP4* expression was induced by both salt and drought treatment (Meng et al., 2011). Furthermore, the overexpression of *OsACBP4* enhanced tolerance to salinity stress in transgenic rice and Arabidopsis (Guo et al., 2020). In this study, the Class III member *GmACBP7* was found to be more greatly induced by salinity and drought than the two Class II members, *GmACBP3* and *GmACBP4* (**Figure 5**), which makes soybean different from rice and Arabidopsis because in these species only Class II *ACBPs* have been reported to be upregulated after salinity or drought treatment. This may imply different roles played by GmACBPs in soybean stress responses.

When soybean seedlings were subjected to cold stress (Robison et al., 2019), the expression of most *GmACBPs* from Classes I, II, and III did not exhibit any difference between control and the cold-treated samples. In contrast, Arabidopsis Class II AtACBP1 and Class I AtACBP6 played a role in response to cold stress (Chen et al., 2008; Du et al., 2010). AtACBP1 was implicated in the cold stress response through the regulation of phospholipase Dα1 (PLDα1) and phospholipase Dδ (PLDδ) that were related to the changes in phosphatidylcholine (PC) and phosphatidic acid (PA) contents although *AtACBP1* expression was not cold-inducible (Du et al., 2010). Initial studies conducted on rosettes of 4-week-old Arabidopsis (Chen et al., 2008) and subsequently in the flowers of 5-week-old plants (Liao et al., 2014) revealed that the overexpression of *AtACBP6* conferred cold tolerance through different mechanisms in different organs that were related to the expression of *COLD-RESPONSIVE (COR)*-related, PC-related and monogalactosyldiacylglycerol (MGDG)-related genes. The expression of rice Class I ACBPs (*OsACBP1*, *OsACBP2*, and *OsACBP3*) was down-regulated in 12 h but at 24 h their expression had resumed to level similar to the control (Meng et al., 2011). In each of Arabidopsis, rice, and soybean, distinct patterns in Class I ACBP expression upon cold stress suggest that variation probably arose from differences in tissues used in each study. In rice, 2-week-old rice seedlings were used (Meng et al., 2011) while in soybean, RNA-seq data were generated from unifoliate 2-week-old soybean seedlings (Robison et al., 2019).

GmACBP Expression in Response to Biotic Stress

Various strains of *P. pachyrhizi* can have specific host-strain reactions resulting in differential resistance reactions (Hartman et al., 2011). The strains used in Gregory Alvord et al. (2007), were Hawaii 94-1, an avirulent strain that produced resistant-reaction for the soybean host and Taiwan 80-2, a virulent strain that resulted in susceptible-reaction (Bonde et al., 2006). In the analysis of *GmACBP* expression toward different strains of

P. pachyrhizi, there was a lack in distinct variation in expression between the susceptible and resistant reactions suggesting that *GmACBPs* may not function directly in producing these reaction types. Studies on identification on differentially expressed genes (Gregory Alvord et al., 2007) or accumulation of metabolites (Silva et al., 2020) between two conditions of susceptibility and resistance are expected to achieve an understanding of the molecular pathway for soybean resistance against the pathogen (Hartman et al., 2016).

In soybean, single dominant genes that conferred resistance toward *P. sojae* were identified as *Rps* genes and had been applied in breeding resistant cultivars (Gordon et al., 2007). However, some populations of *P. sojae* that surpass the resistance genes do exist (Dorrance et al., 2003). In a study by Wang et al. (2010), the cultivar Conrad used was a variety that conferred partial resistance toward the pathogen. Partial resistance was characterized by reduction in pathogen colonization and size of lesions (Mideros et al., 2007). Inoculation of cultivar Conrad with *P. sojae* revealed that most members of Classes I, III, and IV exhibited slight downregulation in expression from the control. This situation appeared to differ from ACBPs of other plants such as Arabidopsis, grapevine and rice, in which Class III ACBPs, AtACBP3 (Xiao and Chye, 2011), VvACBP (Takato et al., 2013), and OsACBP5 (Panthapulakkal Narayanan et al., 2020) respectively, respond to plant pathogens. In transgenic Arabidopsis, *AtACBP3*-overexpressors and *acbp3* showed contrasting reactions to biotrophic and necrotrophic pathogens. *AtACBP3*-overexpressors were resistant to infection by biotrophic pathogen *Pseudomonas syringae* pv. *tomato* DC3000, but was susceptible to infection by necrotrophic fungus *Botrytis cinerea* (Xiao and Chye, 2011). In contrast, transgenic rice *OsACBP5*-overexpressors displayed disease resistance toward biotrophic (*Xanthomonas oryzae*), hemibiotrophic (*Magnaporthe oryzae* and *Fusarium graminearum*) and necrotrophic (*Rhizoctonia solani* and *Cercospora oryzae*) pathogens *via* both jasmonic acid (JA)- and salicylic acid (SA)-mediated pathways (Panthapulakkal Narayanan et al., 2020). Also transgenic Arabidopsis overexpressing *V. vinifera* Class III ACBP was tolerant to *P. syringae* and *Colletotrichum higginsianum*, a pathogenic hemibiotrophic ascomycetous fungus (Takato et al., 2013).

CONCLUSION

In this analysis of GmACBPs, their protein domain architecture and their sequences were demonstrated to be well conserved to ACBPs from non-leguminous plants such as Arabidopsis and rice. The analysis on putative *GmACBP* spatial expression at various organs and different developmental stages, along with expression in response to stress showed that GmACBPs may play important roles in nodule formation that would be unique from Arabidopsis and rice ACBPs.

DATA AVAILABILITY STATEMENT

The raw data supporting the conclusions of this article will be made available by the authors, without undue reservation.

AUTHOR CONTRIBUTIONS

NSA, S-CL, and M-LC designed the research. NSA analyzed the data and conducted qRT-PCR analysis. Z-HG and S-CL helped in data analyses. ZW, W-SY, and H-ML prepared RNA and cDNA from soybean root nodules and stripped roots. NSA and M-LC wrote the manuscript with contributions of all authors. All authors contributed to the article and approved the submitted version.

FUNDING

This work was supported by the Wilson and Amelia Wong Endowment Fund, Hong Kong Research Grants Council Area of Excellence Scheme of Hong Kong (AoE/M-403/16), and Innovation Technology Fund (funding support to State Key Laboratory of Agrobiotechnology). Any opinions, findings, conclusions or recommendations expressed in this publication do not reflect the views of the Government of the Hong Kong Special Administrative Region or the Innovation and Technology Commission.

SUPPLEMENTARY MATERIAL

The Supplementary Material for this article can be found online at: https://www.frontiersin.org/articles/10.3389/fpls.2021.646938/full#supplementary-material

Supplementary Figure 1 | Quantitative real-time PCR of *GmACBP* expression in root nodules in second biological replicate. The expression level was normalized to the housekeeping gene, *F-BOX PROTEIN2*. Error bars indicate the standard error of mean, $n = 3$. Control and target groups were compared using Student's *t*-test. Statistically significant difference (**$P < 0.01$; *$P < 0.05$) is indicated.

Supplementary Table 1 | Gene-specific primers for qRT-PCR analysis of *GmACBP* in nodules.

REFERENCES

Amiruddin, N., Chan, P.-L., Azizi, N., Morris, P. E., Chan, K.-L., Ong, P. W., et al. (2019). Characterization of oil palm acyl-CoA-binding proteins and correlation of their gene expression with oil synthesis. *Plant Cell Physiol.* 61, 735–747. doi: 10.1093/pcp/pcz237

Andersen, K. V., Ludvigsen, S., Mandrup, S., Knudsen, J., and Poulsen, F. M. (1991). The secondary structure in solution of acyl-coenzyme A binding protein from bovine liver using 1H nuclear magnetic resonance spectroscopy. *Biochemistry* 30, 10654–10663. doi: 10.1021/bi00108a008

Assefa, Y., Purcell, L. C., Salmeron, M., Naeve, S., Casteel, S. N., Kovács, P., et al. (2019). Assessing variation in US soybean seed composition (protein and oil). *Front. Plant Sci.* 10:298. doi: 10.3389/fpls.2019.00298

Aznar-Moreno, J. A., Venegas-Calerón, M., Du, Z. Y., Garcés, R., Tanner, J. A., Chye, M. L., et al. (2016). Characterization of a small acyl-CoA-binding protein (ACBP) from *Helianthus annuus* L. and its binding

affinities. *Plant Physiol. Biochem.* 102, 141–150. doi: 10.1016/j.plaphy.2016.02.025

Barrett, J. R. (2006). The science of soy: What do we really know? *Environ. Health Perspect.* 114, A352–A358.

Bates, P. D., Stymne, S., and Ohlrogge, J. (2013). Biochemical pathways in seed oil synthesis. *Curr. Opin. Plant Biol.* 16, 358–364. doi: 10.1016/j.pbi.2013.02.015

Belamkar, V., Weeks, N. T., Bharti, A. K., Farmer, A. D., Graham, M. A., and Cannon, S. B. (2014). Comprehensive characterization and RNA-Seq profiling of the HD-Zip transcription factor family in soybean (*Glycine max*) during dehydration and salt stress. *BMC Genomics* 15:950. doi: 10.1186/1471-2164-15-950

Bonde, M., Nester, S., Austin, C., Stone, C., Frederick, R. D., Hartman, G. L., et al. (2006). Evaluation of virulence of *Phakopsora pachyrhizi* and *P. meibomiae* isolates. *Plant Dis.* 90, 708–716. doi: 10.1094/pd-90-0708

Brown, A. P., Slabas, A. R., and Denton, H. (2002). Substrate selectivity of plant and microbial lysophosphatidic acid acyltransferases. *Phytochemistry* 61, 493–501. doi: 10.1016/s0031-9422(02)00290-x

Burton, M., Rose, T. M., Faergeman, N. J., and Knudsen, J. (2005). Evolution of the acyl-CoA binding protein (ACBP). *Biochem. J.* 392, 299–307. doi: 10.1042/bj20050664

Chen, M.-X., Hu, T.-H., Xue, Y., Zhu, F.-Y., Du, Z.-Y., Lo, C., et al. (2018). Arabidopsis acyl-coenzyme-A-binding protein ACBP1 interacts with AREB1 and mediates salt and osmotic signaling in seed germination and seedling growth. *Environ. Exp. Bot.* 156, 130–140. doi: 10.1016/j.envexpbot.2018.09.007

Chen, Q. F., Xiao, S., and Chye, M. L. (2008). Overexpression of the Arabidopsis 10-kilodalton acyl-coenzyme-A-binding protein ACBP6 enhances freezing tolerance. *Plant Physiol.* 148, 304–315. doi: 10.1104/pp.108.123331

Choi, D.-H., Ban, H.-Y., Seo, B.-S., Lee, K.-J., and Lee, B.-W. (2016). Phenology and seed yield performance of determinate soybean cultivars grown at elevated temperatures in a temperate region. *PLoS One* 11:e0165977. doi: 10.1371/journal.pone.0165977

Colin, L. A., and Jaillais, Y. (2020). Phospholipids across scales: lipid patterns and plant development. *Curr. Opin. Plant Biol.* 53, 1–9. doi: 10.1016/j.pbi.2019.08.007

Crutzen, P. J., Mosier, A. R., Smith, K. A., and Winiwarter, W. (2016). "N2O release from agro-biofuel production negates global warming reduction by replacing fossil fuels," in *Paul J Crutzen: A Pioneer on Atmospheric Chemistry and Climate Change in the Anthropocene*, eds P. J. Crutzen and H. G. Brauch (Cham: Springer), 227–238. doi: 10.1007/978-3-319-27460-7_12

Cvijović, I., Good, B. H., and Desai, M. M. (2018). The effect of strong purifying selection on genetic diversity. *Genetics* 209:1235. doi: 10.1534/genetics.118.301058

Desclaux, D., Huynh, T.-T., and Roumet, P. (2000). Identification of soybean plant characteristics that indicate the timing of drought stress. *Crop Sci.* 40, 716–722. doi: 10.2135/cropsci2000.403716x

Dornbos, D. L. Jr., and Mullen, R. E. (1991). Influence of stress during soybean seed fill on seed weight, germination, and seedling growth rate. *Can. J. Plant Sci.* 71, 373–383. doi: 10.4141/cjps91-052

Dorrance, A. E., Mcclure, S. A., and Desilva, A. (2003). Pathogenic diversity of *Phytophthora sojae* in Ohio soybean fields. *Plant Dis.* 87, 139–146. doi: 10.1094/pdis.2003.87.2.139

Du, Z.-Y., Arias, T., Meng, W., and Chye, M.-L. (2016). Plant acyl-CoA-binding proteins: an emerging family involved in plant development and stress responses. *Prog. Lipid Res.* 63, 165–181. doi: 10.1016/j.plipres.2016.06.002

Du, Z. Y., Chen, M. X., Chen, Q. F., Xiao, S., and Chye, M. L. (2013). Overexpression of Arabidopsis acyl-CoA-binding protein ACBP2 enhances drought tolerance. *Plant Cell Environ.* 36, 300–314. doi: 10.1111/j.1365-3040.2012.02574.x

Du, Z. Y., Xiao, S., Chen, Q. F., and Chye, M. L. (2010). Depletion of the membrane-associated acyl-coenzyme A-binding protein ACBP1 enhances the ability of cold acclimation in *Arabidopsis*. *Plant Physiol.* 152, 1585–1597. doi: 10.1104/pp.109.147066

Emanuelsson, O., Nielsen, H., Brunak, S., and Von Heijne, G. (2000). Predicting subcellular localization of proteins based on their N-terminal amino acid sequence. *J. Mol. Biol.* 300, 1005–1016. doi: 10.1006/jmbi.2000.3903

Engeseth, N. J., Pacovsky, R. S., Newman, T., and Ohlrogge, J. B. (1996). Characterization of an acyl-CoA-binding protein from *Arabidopsis thaliana*. *Arch. Biochem. Biophys.* 331, 55–62.

FAO (2018). *Saline Agriculture in a Context of Water Scarcity and the Establishment of a WASAG Working Group*. Rome: Food and Agriculture Organization of the United Nations.

Ferguson, B. J. (2013). "Rhizobia and legume nodulation genes," in *Brenner's Encyclopedia of Genetics*, 2nd Edn, eds S. Maloy and K. Hughes (San Diego, CA: Academic Press), 236–239. doi: 10.1016/b978-0-12-374984-0.01046-9

Gaonkar, V., and Rosentrater, K. A. (2019). "Chapter 4 - soybean," in *Integrated Processing Technologies for Food and Agricultural By-Products*, eds Z. Pan, R. Zhang, and S. Zicari (San Diego, CA: Academic Press), 73–104.

George, B. (2021). *Oilseeds: World Markets and Trade*. Washington, DC: United States Department of Agriculture.

Goldberg, R. B., Barker, S. J., and Perez-Grau, L. (1989). Regulation of gene expression during plant embryogenesis. *Cell* 56, 149–160. doi: 10.1016/0092-8674(89)90888-x

Goñi, F. M. (2014). The basic structure and dynamics of cell membranes: an update of the Singer–Nicolson model. *Biochim. Biophys. Acta* 1838, 1467–1476. doi: 10.1016/j.bbamem.2014.01.006

Gordon, S. G., Kowitwanich, K., Pipatpongpinyo, W., St. Martin, S. K., and Dorrance, A. E. (2007). Molecular marker analysis of soybean plant introductions with resistance to *Phytophthora sojae*. *Phytopathology* 97, 113–118. doi: 10.1094/phyto-97-0113

Grant, D., Nelson, R. T., Cannon, S. B., and Shoemaker, R. C. (2010). SoyBase, the USDA-ARS soybean genetics and genomics database. *Nucleic Acids Res.* 38, D843–D846.

Gregory Alvord, W., Roayaei, J. A., Quiñones, O. A., and Schneider, K. T. (2007). A microarray analysis for differential gene expression in the soybean genome using Bioconductor and R. *Brief. Bioinform.* 8, 415–431. doi: 10.1093/bib/bbm043

Guo, Z. H., Chan, W. H. Y., Kong, G. K. W., Hao, Q., and Chye, M. L. (2017). The first plant acyl-CoA-binding protein structures: the close homologues OsACBP1 and OsACBP2 from rice. *Acta Crystallogr. D Struct. Biol.* 73, 438–448. doi: 10.1107/s2059798317004193

Guo, Z. H., Haslam, R. P., Michaelson, L. V., Yeung, E. C., Lung, S. C., Napier, J. A., et al. (2019a). The overexpression of rice ACYL-CoA-BINDING PROTEIN2 increases grain size and bran oil content in transgenic rice. *Plant J.* 100, 1132–1147. doi: 10.1111/tpj.14503

Guo, Z.-H., Pogancev, G., Meng, W., Du, Z.-Y., Liao, P., Zhang, R., et al. (2020). The overexpression of rice ACYL-COA-BINDING PROTEIN4 improves salinity tolerance in transgenic rice. *Environ. Exp. Bot.* 183:104349. doi: 10.1016/j.envexpbot.2020.104349

Guo, Z.-H., Ye, Z.-W., Haslam, R. P., Michaelson, L. V., Napier, J. A., and Chye, M.-L. (2019b). Arabidopsis cytosolic acyl-CoA-binding proteins function in determining seed oil composition. *Plant Direct* 3:e00182.

Hartman, G. L., Hill, C., Twizeyimana, M., MR, M., and Bandyopadhyay, R. (2011). Interaction of soybean and *Phakopsora pachyrhizi*, the cause of soybean rust. *CAB Rev. Perspect. Agric. Vet. Sci. Nutr. Nat. Resour.* 6:25. doi: 10.1079/PAVSNNR20116025

Hartman, G. L., Pawlowski, M. L., Chang, H. X., and Hill, C. B. (2016). "3 - Successful technologies and approaches used to develop and manage resistance against crop diseases and pests," in *Emerging Technologies for Promoting Food Security*, ed. C. Madramootoo (Oxford: Woodhead Publishing), 43–66. doi: 10.1016/b978-1-78242-335-5.00003-2

Hasanuzzaman, M., Nahar, K., Rahman, A., Mahmud, J. A., Hossain, M. S., and Fujita, M. (2016). "4 - Soybean production and environmental stresses," in *Environmental Stresses in Soybean Production*, ed. M. Miransari (San Diego, CA: Academic Press), 61–102. doi: 10.1016/b978-0-12-801535-3.00004-8

Hsiao, A. S., Haslam, R. P., Michaelson, L. V., Liao, P., Chen, Q. F., Sooriyaarachchi, S., et al. (2014). Arabidopsis cytosolic acyl-CoA-binding proteins ACBP4, ACBP5 and ACBP6 have overlapping but distinct roles in seed development. *Biosci. Rep.* 34:e00165.

Huby, E., Napier, J. A., Baillieul, F., Michaelson, L. V., and Dhondt-Cordelier, S. (2020). Sphingolipids: towards an integrated view of metabolism during the plant stress response. *New Phytol.* 225, 659–670. doi: 10.1111/nph.15997

Islinger, M., Costello, J. L., Kors, S., Soupene, E., Levine, T. P., Kuypers, F. A., et al. (2020). The diversity of ACBD proteins – from lipid binding to protein modulators and organelle tethers. *Biochim. Biophys. Acta Mol. Cell Res.* 1867, 118675. doi: 10.1016/j.bbamcr.2020.118675

Jin, J., Guo, Z.-H., Hao, Q., and Chye, M.-L. (2020). Crystal structure of the rice acyl-CoA-binding protein OsACBP2 in complex with C18:3-CoA reveals a novel pattern of binding to acyl-CoA esters. *FEBS Lett.* 594, 3568–3575. doi: 10.1002/1873-3468.13923

Kelley, L. A., Mezulis, S., Yates, C. M., Wass, M. N., and Sternberg, M. J. E. (2015). The Phyre2 web portal for protein modeling, prediction and analysis. *Nat. Protoc.* 10, 845–858. doi: 10.1038/nprot.2015.053

Kumar, S., Stecher, G., Li, M., Knyaz, C., and Tamura, K. (2018). MEGA X: molecular evolutionary genetics analysis across computing platforms. *Mol. Biol. Evol.* 35, 1547–1549. doi: 10.1093/molbev/msy096

Langenbach, C., Campe, R., Beyer, S. F., Mueller, A. N., and Conrath, U. (2016). Fighting Asian soybean rust. *Front. Plant Sci.* 7:797. doi: 10.3389/fpls.2016.00797

Le, B. H., Wagmaister, J. A., Kawashima, T., Bui, A. Q., Harada, J. J., and Goldberg, R. B. (2007). Using genomics to study legume seed development. *Plant Physiol.* 144, 562–574. doi: 10.1104/pp.107.100362

Leung, K. C., Li, H. Y., Mishra, G., and Chye, M. L. (2004). ACBP4 and ACBP5, novel Arabidopsis acyl-CoA-binding proteins with kelch motifs that bind oleoyl-CoA. *Plant Mol. Biol.* 55, 297–309. doi: 10.1007/s11103-004-0642-z

Leung, K.-C., Li, H.-Y., Xiao, S., Tse, M.-H., and Chye, M.-L. (2006). Arabidopsis ACBP3 is an extracellularly targeted acyl-CoA-binding protein. *Planta* 223, 871–881. doi: 10.1007/s00425-005-0139-2

Li, H.-Y., and Chye, M.-L. (2003). Membrane localization of Arabidopsis acyl-CoA binding protein ACBP2. *Plant Mol. Biol.* 51, 483–492.

Li, N., Gügel, I. L., Giavalisco, P., Zeisler, V., Schreiber, L., Soll, J., et al. (2015). FAX1, a novel membrane protein mediating plastid fatty acid export. *PLoS Biol.* 13:e1002053. doi: 10.1371/journal.pbio.1002053

Li, N., Xu, C., Li-Beisson, Y., and Philippar, K. (2016). Fatty acid and lipid transport in plant cells. *Trends Plant Sci.* 21, 145–158. doi: 10.1016/j.tplants.2015.10.011

Li, X., Esker, P. D., Pan, Z., Dias, A. P., Xue, L., and Yang, X. B. (2010). The uniqueness of the soybean rust pathosystem: an improved understanding of the risk in different regions of the world. *Plant Dis.* 94, 796–806. doi: 10.1094/pdis-94-7-0796

Liao, P., Chen, Q.-F., and Chye, M.-L. (2014). Transgenic Arabidopsis flowers overexpressing acyl-CoA-binding protein ACBP6 are freezing tolerant. *Plant Cell Physiol.* 55, 1055–1071. doi: 10.1093/pcp/pcu037

Liao, P., Leung, K. P., Lung, S.-C., Panthapulakkal Narayanan, S., Jiang, L., and Chye, M.-L. (2020). Subcellular localization of rice acyl-CoA-binding proteins ACBP4 and ACBP5 supports their non-redundant roles in lipid metabolism. *Front. Plant Sci.* 11:331. doi: 10.3389/fpls.2020.00331

Liao, P., Woodfield, H. K., Harwood, J. L., Chye, M. L., and Scofield, S. (2019). Comparative transcriptomics analysis of *Brassica napus* L. during seed maturation reveals dynamic changes in gene expression between embryos and seed coats and distinct expression profiles of acyl-CoA-binding proteins for lipid accumulation. *Plant Cell Physiol.* 60, 2812–2825. doi: 10.1093/pcp/pcz169

Libault, M., Thibivilliers, S., Bilgin, D. D., Radwan, O., Benitez, M., Clough, S. J., et al. (2008).). Identification of four soybean reference genes for gene expression normalization. *Plant Genome* 1, 44–54. doi: 10.3835/plantgenome2008.02.0091

Livak, K. J., and Schmittgen, T. D. (2001). Analysis of relative gene expression data using real-time quantitative PCR and the 2(-Delta Delta C(T)) Method. *Methods* 25, 402–408. doi: 10.1006/meth.2001.1262

Lung, S. C., and Chye, M. L. (2016). Deciphering the roles of acyl-CoA-binding proteins in plant cells. *Protoplasma* 253, 1177–1195. doi: 10.1007/s00709-015-0882-6

Lung, S.-C., Liao, P., Yeung, E. C., Hsiao, A.-S., Xue, Y., and Chye, M.-L. (2017). Acyl-CoA-binding protein ACBP1 modulates sterol synthesis during embryogenesis. *Plant Physiol.* 174, 1420–1435. doi: 10.1104/pp.17.00412

Lung, S. C., Liao, P., Yeung, E. C., Hsiao, A. S., Xue, Y., and Chye, M. L. (2018). Arabidopsis ACYL-COA-BINDING PROTEIN1 interacts with STEROL C4-METHYL OXIDASE1-2 to modulate gene expression of homeodomain-leucine zipper IV transcription factors. *New Phytol.* 218, 183–200. doi: 10.1111/nph.14965

Meng, W., Su, Y. C., Saunders, R. M., and Chye, M. L. (2011). The rice acyl-CoA-binding protein gene family: phylogeny, expression and functional analysis. *New Phytol.* 189, 1170–1184. doi: 10.1111/j.1469-8137.2010.03546.x

Mideros, S., Nita, M., and Dorrance, A. E. (2007). Characterization of components of partial resistance, Rps2, and root resistance to Phytophthora sojae in soybean. *Phytopathology* 97, 655–662. doi: 10.1094/phyto-97-5-0655

Miransari, M. (2016). "1 - Use of biotechnology in soybean production under environmental stresses," in *Environmental Stresses in Soybean Production*, ed. M. Miransari (San Diego, CA: Academic Press), 1–22. doi: 10.1016/b978-0-12-801535-3.00001-2

Mofid, M. R., Finking, R., and Marahiel, M. A. (2002). Recognition of hybrid peptidyl carrier proteins/acyl carrier proteins in nonribosomal peptide synthetase modules by the 4′-phophopantetheinyl transferases AcpS and Sfp. *J. Biol. Chem.* 277, 17023–17031. doi: 10.1074/jbc.m200120200

Nakai, K., and Horton, P. (1999). PSORT: a program for detecting sorting signals in proteins and predicting their subcellular localization. *Trends Biochem. Sci.* 24, 34–35. doi: 10.1016/s0968-0004(98)01336-x

Ohlrogge, J. B., and Jaworski, J. G. (1997). Regulation of fatty acid synthesis. *Annu. Rev. Plant Physiol. Plant Mol. Biol.* 48, 109–136.

Pantalone, V. R. (2012). "11 - Modern breeding approaches to enhancing soy protein quality," in *Designing Soybeans for 21st Century Markets*, ed. R. F. Wilson (Urbana, IL: AOCS Press), 197–226. doi: 10.1016/b978-0-9830791-0-1.50015-7

Panthapulakkal Narayanan, S., Lung, S.-C., Liao, P., Lo, C., and Chye, M.-L. (2020). The overexpression of OsACBP5 protects transgenic rice against necrotrophic, hemibiotrophic and biotrophic pathogens. *Sci. Rep.* 10:14918.

Pulido, P., and Leister, D. (2018). Novel DNAJ-related proteins in *Arabidopsis thaliana*. *New Phytol.* 217, 480–490. doi: 10.1111/nph.14827

Robison, J. D., Yamasaki, Y., and Randall, S. K. (2019). The ethylene signaling pathway negatively impacts CBF/DREB-regulated cold response in soybean (Glycine max). *Front. Plant Sci.* 10:121. doi: 10.3389/fpls.2019.00121

Rogowska, A., and Szakiel, A. (2020). The role of sterols in plant response to abiotic stress. *Phytochem. Rev.* 19, 1525–1538. doi: 10.1007/s11101-020-09708-2

Schmutz, J., Cannon, S. B., Schlueter, J., Ma, J., Mitros, T., Nelson, W., et al. (2010). Genome sequence of the palaeopolyploid soybean. *Nature* 463, 178–183. doi: 10.1038/nature08670

Sehgal, A., Sita, K., Siddique, K. H. M., Kumar, R., Bhogireddy, S., Varshney, R. K., et al. (2018). Drought or/and heat-stress effects on seed filling in food crops: impacts on functional biochemistry, seed yields, and nutritional quality. *Front. Plant Sci.* 9:1705. doi: 10.3389/fpls.2018.01705

Seigler, D. S. (ed). (1998). "Plant waxes ," in *Plant Secondary Metabolism*, (Boston, MA: Springer), 51–55. doi: 10.1007/978-1-4615-4913-0_4

Severin, A. J., Woody, J. L., Bolon, Y.-T., Joseph, B., Diers, B. W., Farmer, A. D., et al. (2010). RNA-seq atlas of *Glycine max*: a guide to the soybean transcriptome. *BMC Plant Biol.* 10:160. doi: 10.1186/1471-2229-10-160

Shockey, J. M., Fulda, M. S., and Browse, J. A. (2002). Arabidopsis contains nine long-chain acyl-coenzyme a synthetase genes that participate in fatty acid and glycerolipid metabolism. *Plant Physiol.* 129, 1710–1722. doi: 10.1104/pp.003269

Silva, E., Da Graça, J. P., Porto, C., Martin Do Prado, R., Hoffmann-Campo, C. B., Meyer, M. C., et al. (2020). Unraveling Asian soybean rust metabolomics using mass spectrometry and molecular networking approach. *Sci. Rep.* 10:138.

Soybean meal: world supply and demand (2020). *Soybean Growers for the Feed Industry*. Available online at: https://www.soymeal.org/newsletter/june-2020/

Stacey, G. (2007). "Chapter 10 - the rhizobium-legume nitrogen-fixing symbiosis," in *Biology of the Nitrogen Cycle*, eds H. Bothe, S. J. Ferguson, and W. E. Newton (Amsterdam: Elsevier), 147–163. doi: 10.1016/b978-044452857-5.50011-4

Takato, H., Shimidzu, M., Ashizawa, Y., Takei, H., and Suzuki, S. (2013). An acyl-CoA-binding protein from grape that is induced through ER stress confers morphological changes and disease resistance in Arabidopsis. *J. Plant Physiol.* 170, 591–600. doi: 10.1016/j.jplph.2012.11.011

Taskinen, J. P., Van Aalten, D. M., Knudsen, J., and Wierenga, R. K. (2007). High resolution crystal structures of unliganded and liganded human liver ACBP reveal a new mode of binding for the acyl-CoA ligand. *Proteins* 66, 229–238. doi: 10.1002/prot.21124

Tyler, B. M. (2007). *Phytophthora sojae*: root rot pathogen of soybean and model oomycete. *Mol. Plant Pathol.* 8, 1–8. doi: 10.1111/j.1364-3703.2006.00373.x

van Aalten, D. M. F., Milne, K. G., Zou, J. Y., Kleywegt, G. J., Bergfors, T., Ferguson, M. A. J., et al. (2001). Binding site differences revealed by crystal structures of Plasmodium falciparum and bovine acyl-CoA binding protein. *J. Mol. Biol.* 309, 181–192. doi: 10.1006/jmbi.2001.4749

Wan, X., Wu, S., Li, Z., An, X., and Tian, Y. (2020). Lipid metabolism: critical roles in male fertility and other aspects of reproductive development in plants. *Mol. Plant* 13, 955–983. doi: 10.1016/j.molp.2020.05.009

Wang, H., Waller, L., Tripathy, S., St. Martin, S. K., Zhou, L., Krampis, K., et al. (2010). Analysis of genes underlying soybean quantitative trait loci conferring partial resistance to *Phytophthora sojae*. *Plant Genome* 3, 23–40. doi: 10.3835/plantgenome2009.12.0029

Wang, J., Youkharibache, P., Zhang, D., Lanczycki, C. J., Geer, R. C., Madej, T., et al. (2020). iCn3D, a web-based 3D viewer for sharing 1D/2D/3D representations of biomolecular structures. *Bioinformatics* 36, 131–135. doi: 10.1093/bioinformatics/btz502

Wang, Q., Yung, W.-S., Wang, Z., and Lam, H.-M. (2020). The histone modification H3K4me3 marks functional genes in soybean nodules. *Genomics* 112, 5282–5294. doi: 10.1016/j.ygeno.2020.09.052

Waterhouse, A., Bertoni, M., Bienert, S., Studer, G., Tauriello, G., Gumienny, R., et al. (2018). SWISS-MODEL: homology modelling of protein structures and complexes. *Nucleic Acids Res.* 46, W296–W303.

Xiao, S., and Chye, M.-L. (2011). Overexpression of Arabidopsis ACBP3 enhances NPR1-dependent plant resistance to *Pseudomonas syringe* pv tomato DC3000. *Plant Physiol.* 156, 2069–2081. doi: 10.1104/pp.111.176933

Xiao, S., Li, H.-Y., Zhang, J.-P., Chan, S.-W., and Chye, M.-L. (2008). Arabidopsis acyl-CoA-binding proteins ACBP4 and ACBP5 are subcellularly localized to the cytosol and ACBP4 depletion affects membrane lipid composition. *Plant Mol. Biol.* 68, 571–583. doi: 10.1007/s11103-008-9392-7

Yamasaki, Y., and Randall, S. K. (2016). Functionality of soybean CBF/DREB1 transcription factors. *Plant Sci.* 246, 80–90. doi: 10.1016/j.plantsci.2016.02.007

Yorinori, J. T., Paiva, W. M., Frederick, R. D., Costamilan, L. M., Bertagnolli, P. F., Hartman, G. E., et al. (2005). Epidemics of soybean rust (*Phakopsora pachyrhizi*) in Brazil and Paraguay from 2001 to 2003. *Plant Dis.* 89, 675–677. doi: 10.1094/pd-89-0675

Yurchenko, O., Singer, S. D., Nykiforuk, C. L., Gidda, S., Mullen, R. T., Moloney, M. M., et al. (2014). Production of a *Brassica napus* low-molecular mass acyl-coenzyme-A-binding protein in *Arabidopsis* alters the acyl-coenzyme A pool and acyl composition of oil in seeds. *Plant Physiol.* 165, 550–560. doi: 10.1104/pp.114.238071

Yurchenko, O. P., Nykiforuk, C. L., Moloney, M. M., Stahl, U., Banas, A., Stymne, S., et al. (2009). A 10-kDa acyl-CoA-binding protein (ACBP) from *Brassica napus* enhances acyl exchange between acyl-CoA and phosphatidylcholine. *Plant Biotechnol. J.* 7, 602–610. doi: 10.1111/j.1467-7652.2009.00427.x

Zhang, W., Zhou, Y., Wang, K., Dong, Y., Wang, W., and Feng, Y. (2017). Crystal structure of the nitrile-specifier protein NSP1 from *Arabidopsis thaliana*. *Biochem. Biophys. Res. Commun.* 488, 147–152. doi: 10.1016/j.bbrc.2017.05.027

Conflict of Interest: The authors declare that the research was conducted in the absence of any commercial or financial relationships that could be construed as a potential conflict of interest.

The reviewer JH declared a past co-authorship with one of the authors M-LC to the handling editor.

Copyright © 2021 Azlan, Guo, Yung, Wang, Lam, Lung and Chye. This is an open-access article distributed under the terms of the Creative Commons Attribution License (CC BY). The use, distribution or reproduction in other forums is permitted, provided the original author(s) and the copyright owner(s) are credited and that the original publication in this journal is cited, in accordance with accepted academic practice. No use, distribution or reproduction is permitted which does not comply with these terms.

frontiers in Plant Science

ORIGINAL RESEARCH
published: 22 April 2021
doi: 10.3389/fpls.2021.652319

CRISPR/Cas9-Induced *fad2* and *rod1* Mutations Stacked With *fae1* Confer High Oleic Acid Seed Oil in Pennycress (*Thlaspi arvense* L.)

*Brice A. Jarvis[1], Trevor B. Romsdahl[2], Michaela G. McGinn[1], Tara J. Nazarenus[3], Edgar B. Cahoon[3], Kent D. Chapman[2] and John C. Sedbrook[1]**

[1] School of Biological Sciences, Illinois State University, Normal, IL, United States, [2] BioDiscovery Institute and Department of Biological Sciences, University of North Texas, Denton, TX, United States, [3] Department of Biochemistry and Center for Plant Science Innovation, University of Nebraska-Lincoln, Lincoln, NE, United States

OPEN ACCESS

Edited by:
Juliette Jouhet, UMR 5168 Laboratoire de Physiologie Cellulaire Vegetale (LPCV), France

Reviewed by:
José Manuel Martínez-Rivas, Instituto de la Grasa (CSIC), Spain
Clay Carter, University of Minnesota Twin Cities, United States

***Correspondence:**
John C. Sedbrook
jcsedbr@ilstu.edu

Specialty section:
This article was submitted to Plant Physiology, a section of the journal Frontiers in Plant Science

Received: *12 January 2021*
Accepted: *23 March 2021*
Published: *22 April 2021*

Citation:
Jarvis BA, Romsdahl TB, McGinn MG, Nazarenus TJ, Cahoon EB, Chapman KD and Sedbrook JC (2021) CRISPR/Cas9-Induced fad2 and rod1 Mutations Stacked With fae1 Confer High Oleic Acid Seed Oil in Pennycress (Thlaspi arvense L.). Front. Plant Sci. 12:652319. doi: 10.3389/fpls.2021.652319

Pennycress (*Thlaspi arvense* L.) is being domesticated as an oilseed cash cover crop to be grown in the off-season throughout temperate regions of the world. With its diploid genome and ease of directed mutagenesis using molecular approaches, pennycress seed oil composition can be rapidly tailored for a plethora of food, feed, oleochemical and fuel uses. Here, we utilized Clustered Regularly Interspaced Short Palindromic Repeats (CRISPR)/Cas9 technology to produce knockout mutations in the *FATTY ACID DESATURASE2* (*FAD2*) and *REDUCED OLEATE DESATURATION1* (*ROD1*) genes to increase oleic acid content. High oleic acid (18:1) oil is valued for its oxidative stability that is superior to the polyunsaturated fatty acids (PUFAs) linoleic (18:2) and linolenic (18:3), and better cold flow properties than the very long chain fatty acid (VLCFA) erucic (22:1). When combined with a *FATTY ACID ELONGATION1* (*fae1*) knockout mutation, *fad2 fae1* and *rod1 fae1* double mutants produced ∼90% and ∼60% oleic acid in seed oil, respectively, with PUFAs in *fad2 fae1* as well as *fad2* single mutants reduced to less than 5%. MALDI-MS spatial imaging analyses of phosphatidylcholine (PC) and triacylglycerol (TAG) molecular species in wild-type pennycress embryo sections from mature seeds revealed that erucic acid is highly enriched in cotyledons which serve as storage organs, suggestive of a role in providing energy for the germinating seedling. In contrast, PUFA-containing TAGs are enriched in the embryonic axis, which may be utilized for cellular membrane expansion during seed germination and seedling emergence. Under standard growth chamber conditions, *rod1 fae1* plants grew like wild type whereas *fad2* single and *fad2 fae1* double mutant plants exhibited delayed growth and overall reduced heights and seed yields, suggesting that reducing PUFAs below a threshold in pennycress had negative physiological effects. Taken together, our results suggest that combinatorial knockout of *ROD1* and *FAE1* may be a viable route to commercially increase oleic acid content in pennycress seed oil whereas mutations in *FAD2* will likely require at least partial function to avoid fitness trade-offs.

Keywords: CRISPR, MALDI-MSI, oilseed, oleic acid, pennycress, polyunsaturated fatty acid, *Thlaspi arvense*, triacylglycerol

INTRODUCTION

There is overwhelming evidence that the use of fossil fuels is driving climate change, the mitigation of which may benefit from replacement with increased production of biofuels derived from oilseed crops grown sustainably (Vollmann and Rajcan, 2009; Fan et al., 2013; IPCC, 2013; Hill et al., 2016; Drake et al., 2017; Masson-Delmotte et al., 2018). Demands on oilseed production for food and other uses are also intensifying due to population growth and improved standards of living. Two well-established oilseed crops are soybean (*Glycine max* L.) and canola (*Brassica napus*), producing over 400 million metric tons of seed, annually, rich in both oil and protein (USDA, United States Department of Agriculture Foreign Agriculture Services, 2013). The oils from these crops can be used in a plethora of products including foodstuffs, feed, cosmetics, and industrial lubricants along with biodiesel and biojet fuels (Dyer et al., 2008; Volkova et al., 2016). However, it is important to balance needs for human nutrition with those of bio-based products. Taken together, there is impetus to develop new oilseed crops that can be grown with relatively low greenhouse gas emissions and without causing detrimental land use changes (Fulton et al., 2015).

Pennycress (*Thlaspi arvense* L.) is an emerging oilseed crop and member of the Brassicaceae family (mustard family), native to Eurasia and naturalized throughout temperate regions of the world (Mc Intyre and Best, 1978; Sharma et al., 2007). Pennycress can be grown as a winter annual cover crop on otherwise fallow farmland, providing ecosystems benefits and avoiding displacement of established food crops (Isbell, 2008; Phippen and Phippen, 2012; Fan et al., 2013). Pennycress is self-pollinating with a diploid genome that shares ∼86% nucleotide sequence identity with the genome of the well-studied model organism *Arabidopsis thaliana* (Arabidopsis) (Dorn et al., 2013, 2015). Like Arabidopsis, pennycress is well-suited for laboratory studies, growing well side by side with Arabidopsis in growth chambers and greenhouses and being readily genetically transformable using an *Agrobacterium tumefaciens*-mediated floral dip method, albeit requiring vacuum application during the floral dip (McGinn et al., 2019). Ease of pennycress mutagenesis using ethyl methanesulfonate (EMS) as well as Clustered Regularly Interspaced Short Palindromic Repeats (CRISPR)/Cas9 gene editing, along with its ease of growth and study in farm field settings, makes pennycress an attractive multifunctional model system for simultaneous basic and applied research (Sedbrook et al., 2014; Chopra et al., 2018, 2020; Sedbrook and Durrett, 2020; Tsogtbaatar et al., 2020).

Pennycress seeds naturally accumulate high amounts of oil (∼35%) and protein (∼20%), similar to other established and emerging Brassicaceae oilseed crops such as canola, carinata (*Brassica carinata*), and camelina (*Camelina sativa*) (Moser et al., 2009; Kang et al., 2011; Selling et al., 2013; Hossain et al., 2019; Kumar et al., 2020). Pennycress can yield up to 840 liters of oil per hectare, with a potential of United States Midwest Corn Belt-grown pennycress to replace ∼5% of petroleum sources currently used in the United States (Moser et al., 2009; Boateng et al., 2010; Fan et al., 2013; Mousavi-Avval and Shah, 2020). In addition to possible uses for biofuels, food, and feed production, the seed oil-derived fatty acids (FAs) can be processed to produce wax esters which are used in cosmetics, surfactants, lubricants, and plastics (Volkova et al., 2016). A main objective of research on pennycress is altering its seed lipid profile to create value-added feedstocks better suited for specific applications. For example, pennycress seed TAGs naturally contain high amounts of very long chain fatty acids (VLCFAs) mostly in the form of erucic acid (22:1; ∼35%), which could be genetically enhanced further through breeding and engineering (Li et al., 2012; Guan et al., 2014; Altendorf et al., 2019; Claver et al., 2020). Erucic acid has multiple industrial uses and is suitable for hydrocracking to produce dodecane (C11) and other medium and long chain fatty acids (MCFAs, LCFAs) for aviation fuel and biodiesel (Bezergianni and Kalogianni, 2009; Sotelo-Boyás et al., 2012; Isbell et al., 2015). Pennycress can also be engineered to produce seed TAGs and acetyl-TAGs containing MCFAs suitable for industrial, biojet fuel and improved biodiesel applications (Esfahanian et al., 2021). It has also been shown in different plant species that specific mutations and mutation combinations can substantially decrease VLCFAs and polyunsaturated fatty acids (PUFAs, e.g., 18:2 linoleic acid and 18:3 linolenic acid) thereby increasing 18:1 oleic acid content in seed oil, which is a desirable biodiesel component (Sivaraman et al., 2004; Kang et al., 2011; McGinn et al., 2019; Chopra et al., 2020; Neumann et al., 2021). Oleic acid has increased oxidative stability compared to linoleic acid and linolenic acid thereby improving fuel stability as well as improving the oil's suitability for high-temperature food applications such as frying (Frega et al., 1999; Serrano et al., 2014; Lanjekar and Deshmukh, 2016). Oleic acid also has better cold-flow properties than VLCFAs, making it more suitable as a component of biodiesel (Stournas et al., 1995; Verma et al., 2016; Sia et al., 2020). From a nutritional motivation, erucic acid levels are limited in food and feed due to potential toxicity when eaten in large amounts (Millar and Kunst, 1997), so reductions in VCLFA amounts in pennycress could be beneficial from this standpoint.

Pennycress seeds store lipids as TAGs within embryonic tissues, which serve as an energy source for the seed embryo upon germination (Goffman et al., 2005; Tsogtbaatar et al., 2020). TAGs are composed of a glycerol backbone with three ester-linked fatty acid carbon chains of different lengths and levels of unsaturation (Chapman and Ohlrogge, 2012). Oleic acid linked to CoA is converted by the enzyme FAE1 (FATTY ACID ELONGATION1) to eicosenoic acid then erucic acid (**Figure 1**). Oleic acid esterified to PC is also converted to linoleic acid by the enzyme FATTY ACID DESATURASE2 (FAD2), which is further reduced to linolenic acid by FATTY ACID DESATURASE3 (FAD3) (**Figure 1**; Browse and Somerville, 1991; Browse et al., 1993; Okuley et al., 1994). Linoleic and linolenic acids are omega-6 and omega-3 PUFAs, respectively, shown to have dietary "heart-health" benefits when balanced in the diet (Simopoulos, 2011; de Lorgeril and Salen, 2012; Ruiz-Núñez et al., 2013). Claver et al. (2017, 2020) performed enzymatic and functional analyses on the pennycress FAE1 enzyme, in the process finding that pennycress embryos incorporate erucic acid into TAG very early during seed maturation, concomitant with decreased desaturase activity, and that erucic acid is preferentially incorporated into

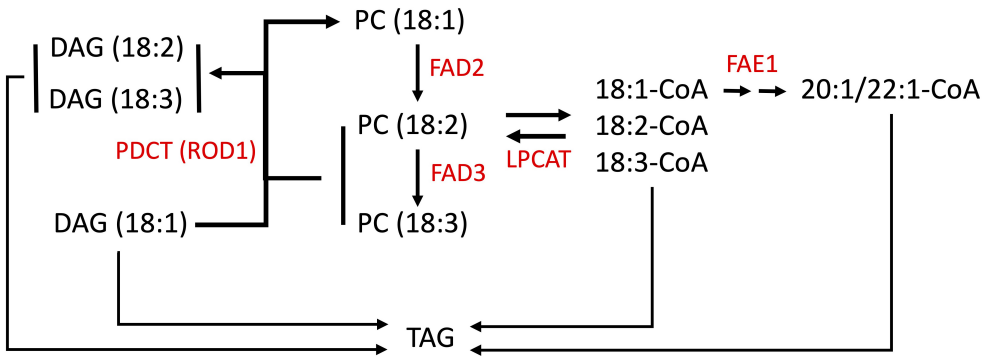

FIGURE 1 | Simplified scheme for fatty acid modification in Brassicas. Fatty acid (FA) elongation of 18:1-CoA is carried out by a protein complex containing the FA elongase, FAE1. Lysophosphatidylcholine acyltransferase (LPCAT) shuttles acyl groups between PC and the acyl-CoA pool. The polyunsaturated FA pathway involves desaturation of 18:1 (esterified to PC) by the FA desaturases, FAD2 and FAD3. 18:1-CoA and acyl-PC are the substrates for FAE1 and the FA desaturases, respectively. PDCT (phosphatidylcholine (PC):diacylglycerol (DAG) cholinephosphotransferase) is also named REDUCED OLEATE DESATURATION (ROD1) that modulates polyunsaturated FA (PUFA) content by interconverting PC and DAG, transferring 18:1 into PC for desaturation, and 18:2 and 18:3 into the triacylglycerol (TAG) biosynthetic pathway thereby increasing PUFA content in TAG (Lu et al., 2009). Choline phosphotransferase (CPT) may also mediate the interconversion of DAG and PC but is not shown here for simplicity.

TAG via DGAT1. Mutations in *FAE1* can block seed oil erucic and eicosenoic acids production resulting in increased oleic, linoleic, and linolenic acids content, whereas mutations in *FAD2* genes have been found in different species to reduce seed oil PUFAs content and increase oleic acid content (Demorest et al., 2016; Li et al., 2016; Jiang et al., 2017; Lakhssassi et al., 2017).

ROD1 (*REDUCED OLEATE DESATURASE1*) is another gene involved with modulating unsaturated fatty acid levels (reviewed in Bates, 2016). The *ROD1* gene encodes a phosphatidylcholine:diacylglycerol cholinephosphotransferase (PDCT) which interconverts diacylglycerol (DAG) and phosphatidylcholine (PC). ROD1 transfers a phosphocholine from a PC molecule to the *sn*-3 position of a DAG molecule, and acts as a gatekeeper enzyme by directing 18:1 molecules for further desaturation on PCs (**Figure 1**). It also provides a mechanism for returning the products (18:2 and 18:3) back into the DAG pool for membrane and storage lipid synthesis (Lu et al., 2009; Bates and Browse, 2012; Bai et al., 2020). In addition to the action of PDCT on PC, an acyl editing cycle catalyzed by lyso phosphatidylcholine acyltransferase (LPCAT) shuttles fatty acids between PC and the acyl-CoA pools, and this pathway plays an important role in providing unsaturated acyl-CoAs for incorporation into TAGs (**Figure 1**). Hence there are multiple steps which may influence the fatty acid composition of seed oils. Researchers discovered in Arabidopsis that loss-of-function mutations in the *rod1* gene reduced the amounts of PUFAs produced. Further, combining either a *rod1* or *fad2* mutation with an *fae1* mutation can produce even more dramatic changes to the seed lipid composition, greatly increasing the amounts of oleic acid (Nguyen et al., 2013; Chopra et al., 2020; Neumann et al., 2021).

In this study, our objective was to provide evidence that pennycress seed genotypes with elevated oleic acid content could be produced by the targeted knockout of the putative pennycress *FAD2* and *ROD1* genes using CRISPR gene editing. Further, we combined each single mutation with a CRISPR/Cas9-edited *fae1* knockout mutation to block both desaturation and elongation of oleic acid (**Figure 1**). Homozygous *fad2* and *rod1* mutants were generated and further gene combinations created through crossing with the previously generated *fae1-3* mutant (McGinn et al., 2019), creating *fad2 fae1* and *rod1 fae1* double knockout mutants. Growth phenotypes and overall fitness of the mutants were characterized, documenting traits such as germination rates, flowering times, and seed yields. Additionally, using GC-FID (Gas Chromatography-Flame Ionization Detection), ESI-MS (electrospray ionization-mass spectrometry), and MALDI-MSI (matrix assisted desorption/ionization-mass spectrometry imaging), we quantified the changes in the different FA species and determined the relative amounts and distributions of PC and TAG molecular species (Sturtevant et al., 2016, 2018; Woodfield et al., 2017) in pennycress wild-type and mutant embryos, which indicated different impacts to overall lipid metabolic processes in each of the mutant genotypes. Our data show that the oleic acid content in pennycress seed TAGs can be substantially increased by combining a *fae1* knockout mutation with either a *fad2* or *rod1* knockout mutation, attaining 90% oleic acid in *fad2 fae1* double mutant seed TAGs. However, *fad2* knockout mutations slowed plant growth considerably, likely due to reducing PUFAs below physiologically important levels.

RESULTS

CRISPR/SaCas9-Induced Mutations in the Putative *TaFAD2* Gene Greatly Reduce Linoleic and Linolenic Acid Content in Pennycress Seed TAGs

The seeds of *Thlaspi arvense* (pennycress) accumulate triacylglycerols (TAGs) containing about 12% oleic acid (18:1), 18% linoleic acid (18:2), and 12% linolenic acid (18:3) (**Figure 2** and **Supplementary Table 1**). The presence of high

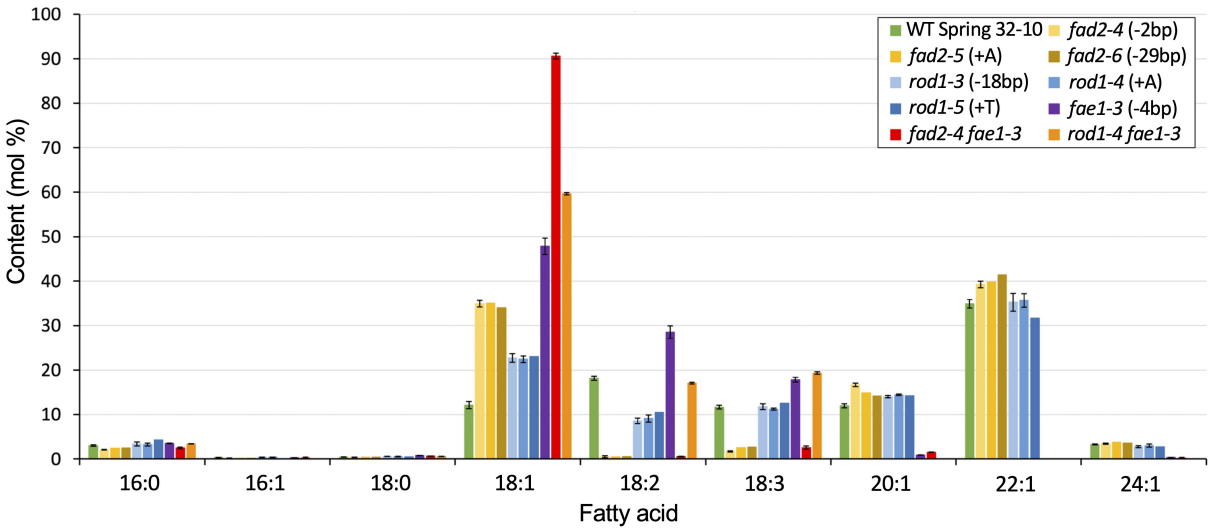

FIGURE 2 | Fatty acid composition of seed TAGs for the different lipid mutants versus WT. Graph shows mean weight percents of the different lipid species. Error bars represent standard deviations of the means where n = 2 or 3 biological reps and 3 technical reps. Those without error bars are single samples. See **Supplementary Table 1** for values and statistical differences.

levels of linoleic and linolenic acids suggest that pennycress has active *FAD2* and *FAD3* fatty acid desaturase genes. Since monounsaturated oleic acid is preferred over the PUFAs for many commercial applications including biodiesel production owing to its superior oxidative stability, we set out to identify the pennycress *TaFAD2* coding sequences and to determine how CRISPR/Cas9 knock out of its function would affect pennycress seed TAG fatty acid composition along with plant and seed health. Using *Arabidopsis thaliana FAD2* (*AtFAD2*; AT3G12120.1) coding sequences as the query, we searched the *T. arvense* genome sequences database using a pennycress-specific Basic Local Alignment Search Tool (BLAST) program available at http://pennycress.umn.edu. We also used *AtFAD2* coding sequences and National Center for Biotechnology Information (NCBI) nucleotide BLAST to search the *T. arvense* transcriptome shotgun assembly database (TSA; Dorn et al., 2013, 2015). Together, these searches identified the putative *TaFAD2* gene and the TSA sequence GAKE01001774.1[1]. Alignment of the *TaFAD2* genomic sequence with the GAKE01001774.1 sequence showed 100% identity and no introns and an open reading frame (ORF) 1,152 nucleotides in length. Sequence alignment also showed that the *TaFAD2* ORF shares 88.8% nucleotide sequence identity with the 1,152 nucleotides *AtFAD2* ORF (AT3G12120.1) (**Supplementary Figure 1**).

To target knockout of the *TaFAD2* gene, we created a CRISPR/SaCas9 binary vector construct named TaFAD2-CRISPR-Cas9_Hyg, utilizing a vector set containing *Staphylococcus aureus* Cas9 (*Sa*Cas9) that was adapted for use in Arabidopsis by Steinert et al. (2015). The TaFAD2-CRISPR-Cas9_Hyg vector was designed to introduce edits ∼263 nucleotides downstream of the *TaFAD2* translational start site (**Supplementary Figure 1**). The TaFAD2-CRISPR-Cas9_Hyg vector was introduced into pennycress plants using the *Agrobacterium*-mediated vacuum infiltration method developed by McGinn et al. (2019). Hygromycin selection of the progeny from the *Agrobacterium*-dipped plants identified eight independent T_1-generation transformants. To screen for Cas9 editing activity, we performed T7 endonuclease I digestion (Pyott et al., 2016) of *FAD2* PCR products amplified from leaf genomic DNA purified from these plants. T7 endonuclease I cuts double-stranded DNA at sites where there is DNA base-pair mismatch, in this case originating from CRISPR/SaCas9-induced mutations. No mismatches were detected in the analyzed T_1-generation plant tissues. Therefore, we planted out at least 16 T_2 progeny from three of the T_1 plants, speculating that SaCas9-induced edits might be detected with the T7 endonuclease method in the T_2 generation. This approach identified progeny from one of the three T_1 plants as having putative mutations at the *FAD2* gene target site (**Supplementary Figure 2A**). Two T_2 plants were chosen for further analyses based on DNA sequence analysis that showed one was heterozygous for a 2 base-pair (bp) deletion and the other heterozygous for an adenine (A) nucleotide insertion. Both mutations were located as expected at the CRISPR-targeted site within the *FAD2* ORF (**Supplementary Figures 1**, **2B**). These mutations segregated as recessive, with the seeds of homozygous mutants exhibiting altered fatty acid profiles (described below). Moreover, during these analyses, a new *fad2* mutation (29 bp deletion; **Supplementary Figure 2B**) was detected in one of the plants whose parent had been heterozygous for the 2 bp deletion. The 29 bp deletion likely was introduced in the wild-type *FAD2* allele by continued activity of the CRISPR/SaCas9 machinery. Lines homozygous and stable for each of these three mutations, having the CRISPR/Cas9 construct segregated away, were subsequently isolated and

[1]https://www.ncbi.nlm.nih.gov/nuccore/%20GAKE01001774.1

named *fad2-4* (2 bp deletion), *fad2-5* (single A insertion), and *fad2-6* (29 bp deletion) (**Supplementary Figure 2B**). All three mutations result in frameshifts in the *FAD2* open reading frame and therefore likely confer total loss of *FAD2* function (knockout mutants) by preventing translation of a full-length FAD2 polypeptide (**Supplementary Figures 2C–F**), resulting in production of truncated fad2 protein and/or causing *fad2* transcript degradation due to nonsense mediated mRNA decay (Conti and Izaurralde, 2005).

Note that pennycress *fad2-1*, *fad2-2*, and *fad2-3* mutant alleles, which are not part of this study, were identified in an ethyl methanesulfonate (EMS) mutant population by screening for altered seed lipid fingerprints using near-infrared spectroscopic (NIRS) analysis. Little has been published on those EMS alleles (Chopra et al., 2019). Also note that all of the mutant lines in this study had the CRISPR/CAS9 constructs segregated away before in-depth genotypic and phenotypic analyses were performed. Moreover, the chosen CRISPR/Cas9 protospacer sequences had less than 70% sequence identity with any other pennycress sequences (based on BLAST searches of the pennycress genome), in order to avoid off-target mutations. In addition, since the *fad2* mutants had strong growth phenotypes in addition to the expected seed lipid compositional changes, we PCR amplified and sequenced the potential chromosomal off-target sites sharing at least 50% sequence identity with the *FAD2* protospacer and, as expected, found no mutations.

Seeds from homozygous *fad2-4*, *fad2-5*, and *fad2-6* plants were analyzed for TAG fatty acid composition, revealing identical fatty acid profiles that were significantly different from wild type (**Figure 2** and **Supplementary Table 1**). On average, seeds of *fad2* mutants exhibited nearly three times higher proportion of oleic acid (18:1) than wild type (35% versus 12%), whereas PUFAs content was drastically reduced. Compared to wild type, linoleic acid (18:2) content was 97% reduced (<1% versus 18%) and linolenic acid (18:3) content was 80% reduced (∼2.5% versus ∼12%). As anticipated, *fad2* seeds showed higher erucic acid (22:1) content compared to wild type (40% versus 35%) (**Figure 2** and **Supplementary Table 1**). The observed relative changes in *Tafad2* mutants seed FA profiles are consistent with those reported in other Brassica species, including *A. thaliana* and *Camelina sativa*. These results support the concept that the loss of *fad2* function results in higher amounts of oleic acid and erucic acid content in seed TAGs due to blockage of oleic acid flux into PUFA synthesis and enhanced availability of oleic acid for elongation (**Figure 1**) (Jiang et al., 2017).

CRISPR/SpCas9-Induced Mutations in the Putative *TaROD1* Gene Modestly Increase Oleic Acid Content in Pennycress Seed TAGs

To identify the putative *TaROD1* gene in pennycress, we again searched the *T. arvense* genome sequence database and the *T. arvense* transcriptome shotgun assembly, using the *A. thaliana AtROD1* coding sequence as the query. Together, these searches identified the putative *TaROD1* gene and the TSA sequence GAKE01006801.1[2], which shared 100% nucleotide sequence identity with each other. The *TaROD1* gene is predicted to have three exons (two introns) and an open reading frame (ORF) 906 nucleotides in length sharing 85.5% nucleotide sequence identity with the 906 bp *AtROD1* ORF (AT3G15820.1) (**Supplementary Figure 3**).

We created a CRISPR/SpCas9 binary vector construct named TaROD1-CRISPR-Cas9_Hyg, utilizing a vector set developed by Fauser et al. (2014), which contains *Streptococcus pyogenes* Cas9 (*Sp*Cas9) coding sequences. The TaROD1-CRISPR-Cas9_Hyg vector was designed to target edits ∼176 bp downstream of the *TaROD1* translational start site (**Supplementary Figure 3**). T7 endonuclease screening of PCR products amplified from seven independent T_1-generation transformants identified four of the seven plants harboring putative edits at or near the targeted *ROD1* gene site. DNA sequence analysis led us to focus on three of the T_1 plants, which were heterozygous for either an A nucleotide insertion, a thymine (T) nucleotide insertion, or an 18 bp deletion at the CRISPR-targeted site within the *ROD1* gene. T7 endonuclease I analysis of 20 T_2 progeny arising from these three T_1 plants along with DNA sequence analyses and phenotypic analyses (described below) confirmed that the mutations were inherited and segregated as recessive. We named the corresponding mutant lines *rod1-3* (18 bp deletion), *rod1-4* (single A insertion), and *rod1-5* (single T insertion) (**Supplementary Figure 4**). Note that pennycress *rod1-1* and *rod1-2* mutant alleles, which are not part of this study, were generated by ethyl methanesulfonate (EMS) mutagenesis and were found to have seed TAG fatty acid compositions identical to those of the CRISPR-induced *rod1* mutant alleles reported here (Chopra et al., 2020).

Seeds from homozygous *rod1-3*, *rod1-4*, and *rod1-5* plants were analyzed for TAG fatty acid composition, revealing all had identical profiles which were significantly different from wild type (**Figure 2** and **Supplementary Table 1**). These results suggest that all three mutations likely confer total loss of *ROD1* function. The *rod1-3* mutation is predicted to produce a "TGA" stop codon at the deletion site (**Supplementary Figures 4A,C**), whereas the *rod1-4* and *rod1-5* mutations cause frameshifts, in this case abolishing translation of 80% of the downstream portions of the ROD1 polypeptide (**Supplementary Figures 4A–E**). These frameshift mutations introduced premature stop codons which can cause nonsense-mediated mRNA decay – a mechanism used by cells to avoid production of truncated proteins that could be toxic (Conti and Izaurralde, 2005). On average, seeds of all *rod1* mutants had a nearly two-fold increase in oleic acid percentage (∼23% versus 12%), about a two-fold decrease in linoleic acid (∼9% versus 18%), and relatively no changes in linolenic or erucic acids content compared to wild type (**Figure 2** and **Supplementary Table 1**). These relative fatty acid changes were comparable to those observed with *rod1* loss-of-function in *A. thaliana* and *Brassica napus*, although the magnitudes of changes were found to be different between Arabidopsis and canola (Lu et al., 2009; Bai et al., 2020).

[2]https://www.ncbi.nlm.nih.gov/nuccore/%20GAKE01006801.1

Stacking *fad2* or *rod1* Mutations With *fae1* Knockout Substantially Increased Seed Oil Oleic Acid Content

Wild-type pennycress seed TAGs contain about 35% erucic acid (22:1), which is produced by sequential fatty acid elongation of oleic acid (18:1) involving a protein complex containing the FA elongase enzyme, FAE1 (Haslam and Kunst, 2013; McGinn et al., 2019; Chopra et al., 2020). We reasoned that TAG oleic acid content could be increased further in the pennycress *fad2* and *rod1* knockout mutants by stacking each with an *fae1* CRISPR-induced knockout mutant we previously showed abolished erucic acid production (McGinn et al., 2019), in this way creating ultra-high (*fad2 fae1*) and high (*rod1 fae1*) oleic acid seed oil varieties. To accomplish this, we cross-pollinated *rod1* and *fad2* mutants with the *fae1-3* knockout mutant and screened for double mutants in the F_2 generation using the above-described T7 Endonuclease method. Double homozygous *fad2-4 fae1-3*, *fad2-5 fae1-3*, and *rod1-4 fae1-3* lines were confirmed by DNA sequence analysis of gene-specific PCR products amplified from F_3 plants. Fatty acid compositional analyses of TAGs extracted from seeds harvested from senesced plants revealed that *fad2-4 fae1-3* seed TAGs contained, on average, 91% oleic acid (compared to 12% for WT), less than 1% linoleic acid (18% for WT), less than 3% linolenic acid (12% for WT), and no erucic acid (35% for WT), whereas *rod1-4 fae1-3* seed TAGs contained about 60% oleic acid, 17% linoleic acid, 19% linolenic acid, and no erucic acid (**Figure 2** and **Supplementary Table 1**). Both of these mutant combinations increased seed TAG oleic acid content over the 48% present in the *fae1-3* single mutant. Notably, only the *fad2-4 fae1-3* mutant combination, like the *fad2* single mutants, and not *rod1-4 fae1-3*, had greatly reduced PUFAs content.

fad2 Knockout Mutants Displayed Delayed Growth and Reduced Seed Yield

To determine if any of the mutations detailed above also affected plant growth and/or seed viability, homozygous mutant plants and wild-type controls were grown side by side in growth chambers and assessed for relative growth characteristics including morphologies, growth rates, flowering times, final plant heights, seed quantities and weights, and seed germination rates. Growth experiments were repeated at least two times for each genotype. The following data are from a representative experiment, where 12 plants per each mutant line were grown alongside wild type (see the section "Materials and Methods"). The number of days to first flower, final flower, and total flowering times were quantified along with final plant heights and seed yields (**Figure 3** and **Supplementary Figure 5**). No obvious morphological differences were observed between the different mutant and wild-type plants. However, *fad2* and *fad2 fae1* mutant plants consistently grew much slower than wild type, whereas the other genotypes grew similar to wild type (**Figures 3A–D** and **Supplementary Figure 5**). In terms of flowering, first-flower opening for *fae1*, *rod1*, and *rod1 fae1* mutant plants occurred an average of 20.5 days post planting, similar to wild-type Spring 32-10 control plants (**Figure 3A**). In contrast, *fad2* and *fad2 fae1* mutant plants took, on average 6.5 days (32%) and 9.2 days (44.3%) longer to flower than wild type, respectively (**Figure 3A**). The days the last flowers opened also were recorded, with *fae1*, *rod1*, and *rod1 fae1* mutant plants completing flowering similarly to the 41 days taken by wild-type plants. By contrast, *fad2* and *fad2 fae1* mutant plants consistently completed flowering much later than wild type, in this case, 22 and 23 days later on average than wild type (**Figure 3B** and **Supplementary Figure 5**). Moreover, the total durations of flowering for *fad2* and *fad2 fae1* plants were significantly longer than wild-type and the other mutants (36.2 days total flowering time for *fad2*, 37 days for *fad2 fae1*, versus 20.7 days for wild type; one-way ANOVA; Tukey test, $p < 0.01$) (**Figure 3C**).

Final plant heights along with total amounts of seed produced and single seed weights were also quantified for all of the genotypes. **Figure 3D** shows that *fad2-4* and *fad2-4 fae1-3* plants grew to be significantly shorter than wild type, on average 56.8 cm for *fad2-4* and 62.8 cm for *fad2-4 fae1-3* versus 72.5 cm for wild type, representing 15–21% shorter heights (one-way ANOVA; Tukey test, $p < 0.01$). Moreover, *fad2* and *fad2 fae1* mutant plants produced significantly less seeds than wild type, on average 0.15 grams and 0.34 grams seed per *fad2-4* and *fad2-4 fae1-3* plant, respectively, versus 0.59 grams per wild-type plant (42 to 75% less; one-way ANOVA; Tukey test, $p < 0.01$) (**Figure 3E**). Individual seed weights were no different between the mutants and wild type (**Figure 3F**). For this particular experiment, *fae1-3* mutant plants grew on average to be ∼17% shorter than wild type. However, this difference was not consistently observed from experiment to experiment. Moreover, the *fae1-3* knockout mutation stacked with *rod1-4* (*rod1-4 fae1-3* plants) were on average the same height as wild type (**Figure 3E**), suggesting the *fae1-3* single mutant height difference may be due to factors unrelated to *fae1* loss of function, unless the *rod1* mutation is somehow compensating for the *fae1* mutation. Field studies are underway to determine what growth differences may exist between the mutants versus wild type under United States Midwest farm field conditions.

The seeds of the mutant genotypes and wild type also were scored for germination under various temperatures and light regimes. Described first is an experiment consisting of 150 seeds from each line spread onto three agar growth media plates (50 seeds per plate; each plate was scored as a biological rep), incubated in a growth chamber at 22°C with a 16 h/8 h light/dark cycle. Seeds were scored each day over a 10-day period for radical emergence. The data in **Figure 4** and **Supplementary Table 2** show that no germination occurred until 2 days after plating. After 3 days, 88% to 99% of wild-type, *rod1-3*, *fae1-3*, and *rod1-4 fae1*-3 seeds had germinated whereas only 20% to 62% of *fad2-4*, *fad2-5*, *fad2-4 fae1-3*, and *fad2-5 fae1-3* seeds had germinated. Statistical analysis of the data showed that the *fad2* genotypes germinated significantly slower than wild type (one-way ANOVA; Tukey test $p < 0.01$; **Supplementary Table 2**). In fact, it took an additional 2–5 days for *fad2*-containing genotypes to attain the 88% or greater amounts of germination seen for wild type and the other mutant genotypes. While significantly more *rod1-4 fae1*-3 and *fae1-3* seeds had germinated after 2 days relative to wild type (**Figure 4** and **Supplementary Table 2**), *rod1-4* and wild type germinated similarly, putting in

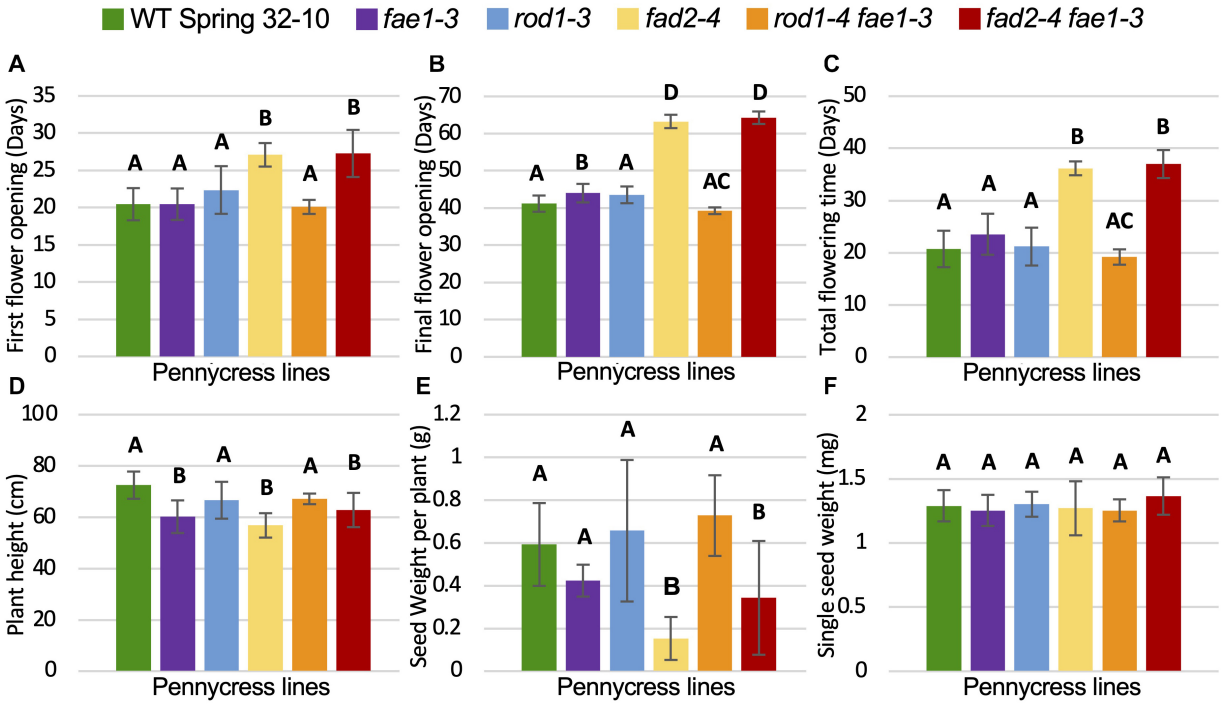

FIGURE 3 | Plant growth and seed yield comparisons. **(A–F)** Graphs showing average **(A)** time until first flower opening, **(B)** time until final flower opening, **(C)** duration of flowering, **(D)** plant height upon senescence, **(E)** total weight of seeds per plant, and **(F)** single seed weight. Bars are standard deviations. Different letters above columns represent significant differences between genotypes (one-way ANOVA; Tukey test, $p < 0.01$). $n = 11$ biological reps. For **(E,F)**, all seeds from each plant were measured.

to question whether there is a germination benefit to *fae1* and/or *rod1* mutations. Regardless, these data show that *fae1* and *rod1* knockout mutations do not negatively affect germination under the growth conditions used. It is important to note that it is not uncommon for the germination of pennycress seeds of a given genotype including wild type to vary from batch to batch.

Plants adjust PUFA content in membranes to adapt to different temperatures, with PUFA content increasing with colder temperatures to maintain membrane fluidity (Menard et al., 2017). To see how seed germination of the different mutants might be affected by different temperatures, we performed germination assays at four different temperatures (4°C, 14°C, 22°C, and 28°C), under constant light as well as constant dark conditions. Of particular interest was how well the *fad2* mutation-containing genotypes would perform, given their severely hampered ability to produce PUFAs and the observed delays in adult plant growth. The data in **Supplementary Figure 6** and **Supplementary Tables 2, 3** show that seeds of all genotypes including the *fad2* single and *fad2 fae1* double mutants germinated very well at 28°C under both light and dark conditions, with most seeds germinating within 2–3 days. At 22°C, 14°C, as well as 4°C, *fad2* single mutant seeds tended to germinate slower than wild type, with the differences becoming more noticeable at the lower temperatures, especially under the constant dark conditions (**Supplementary Figures 6B,D**). For the most part, though, all except the *fad2* genotypes germinated comparably well to wild type under all the conditions tested. Studies are underway to determine how the various genotypes germinate and establish under farm field conditions.

Heterogeneous Distributions of PC and TAG in Mutant and Wild-Type Seeds

To test whether spatial changes in seed lipid metabolites accompanied changes in composition, the distributions of PC and TAG molecular species were analyzed by MALDI-MS imaging of sectioned seeds harvested from senesced plants. PC is both a major structural membrane lipid as well as an important source of acyl chains that are incorporated into TAGs through the acyl editing pathway (Bates et al., 2013). Specifically, PC is the metabolite on which FAD2 adds a second double bond at the Δ12 position of an oleate moiety (Okuley et al., 1994). Hence, a disruption of the *FAD2* gene was suspected to impact the overall unsaturation of the PC pool within *fad2* containing mutants. Similarly, ROD1 acts on PC by interconverting PC and DAG by swapping the phosphocholine moiety from PC to DAG (Lu et al., 2009), which may also influence the PC molecular composition or distribution. As FAE1 acts on acyl-CoA substrates rather than on PC (James et al., 1995), the PC composition is not expected to change much in *fae1* mutants, but the length of the fatty acids in TAG is expected to change significantly.

In the wild type, Spring 32-10, the most abundant of PC molecular species included PC-36:3 and 36:4 (**Figure 5**) as well as PC-34:1, 34:2, 34:3 (**Supplementary Figure 7**). The more

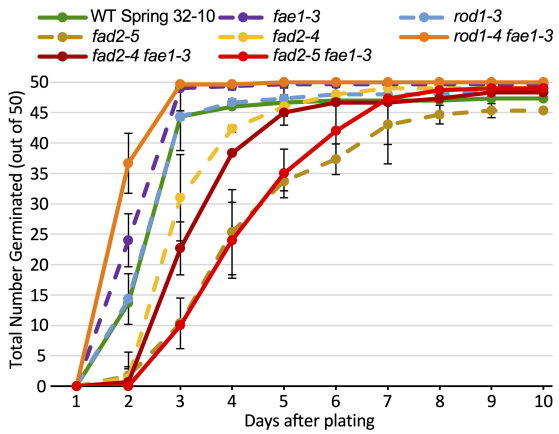

FIGURE 4 | Amounts of seed germination over a 10-day period of the different lipid mutants versus wild type grown at 22°C. One hundred and fifty seeds from each line were plated on three agar growth media plates (50 seeds per plate; each plate treated as a biological rep). The data for single mutants are graphs as dashed lines, whereas double mutants and wild type (WT) are graphed as solid lines. Error bars represent standard deviations of the means. Values and significant differences can be found in **Supplementary Table 2**.

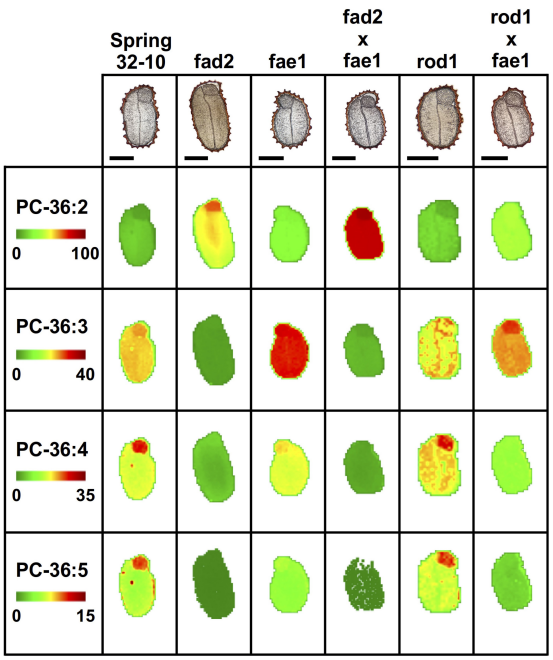

FIGURE 5 | Mass spectrometry (MS) imaging of selected phosphatidylcholine (PC) molecular species in wild-type and CRISPR mutant *T. arvense* seeds. MS images are presented as false colored images with each pixel representing an individual scan rastered over the imaged seed section (microscopy image above, scale bar = 500 μm). The color intensity scale ranges from green (low) to red (high) as the mol% value of the metabolite class. Each row of images are set to the same mol% scale to show relative differences in abundance and localization between each seed type.

unsaturated PC molecular species were primarily localized within the embryonic axis, while the less unsaturated PC species were found more enriched in the cotyledons. Disruption of the *fad2* gene had the expected result of diminishing the abundance of PC with polyunsaturated FAs and increasing the abundance of PC molecular species with more saturated FAs, such as PC-36:2 (**Figure 5**). While the abundance of the different PC molecular species within the single *fae1* mutant did not change much compared to wild type (**Figure 5** and **Supplementary Figure 7**), the mutants did show an unexpected ablation of the unequal heterogeneous distribution of PC species. The double mutant *fad2 fae1* showed an expected reduction of PC molecular species diversity with PC-36:2 most dominant (**Figure 5**), likely containing two oleate moieties that accumulate without the action of *fad2* for further desaturation or *fae1* for elongating beyond an 18 carbon FA in acyl-CoA substrates. The single *rod1* mutant appeared to effect little change in either the abundance or distributions of PC molecular species, and the double mutant of *rod1 fae1* showed a similar abundance and distribution as the single *fae1* mutant (**Figure 5** and **Supplementary Figure 7**).

Like PC, different TAG molecular species of oilseeds have previously been observed to localize preferentially to different seed tissues (Marmon et al., 2017; Woodfield et al., 2017; Lu et al., 2018, 2020; Sturtevant et al., 2019). In wild-type seeds, the most abundant TAG molecular species were the erucic acid-containing TAG-62:4, 62:5 (**Figure 6**) and TAG-60:4, 60:5 (**Supplementary Figure 8**), preferentially localized to the cotyledons, while the embryonic axis showed a relative enrichment in 52 and 54 carbon TAG species (**Supplementary Figure 8** and **Figure 6**). The *fad2* mutant showed similar distributions as the wild type but much less of the polyunsaturated TAG molecular species and instead an accumulation of the more saturated TAG-62:3 (**Figure 6**) and TAG-60:3 (**Supplementary Figure 8**). The *fae1* mutant showed a complete lack of TAG containing very long chain FAs, such as erucic acid, as expected without the elongation pathway. Instead, *fae1* mutants accumulated 54 carbon containing TAG in the cotyledons where previously there had been much less in the wild-type seeds (**Figure 6** and **Supplementary Figure 8**). The added *fad2* disruption in the double mutant of *fad2 fae1* simplified the TAG molecular species present to mostly TAG-54:3 in both the cotyledons and embryonic axis uniformly, likely containing three oleic fatty acids (**Figure 6**).

Similar to the wild type, the *rod1* mutant showed a greater abundance of 60 and 62 carbon containing TAG, especially TAG-60:3 (**Supplementary Figure 8**) and TAG-62:3 (**Figure 6**), but showed a decrease in the more unsaturated TAG molecular species with the same number of carbons reflecting the reduced abundance of PUFAs in these mutants (**Supplementary Table 1**). The double mutant *rod1 fae1* showed a similar abundance and distribution of TAG molecular species as the *fae1* single mutant (**Figure 6** and **Supplementary Figure 8**).

Quantification of TAG and PC Content and Composition Within Wild-Type and Mutant Seeds

While MALDI-MS imaging is able to provide information on the spatial distribution and the relative abundance PC and

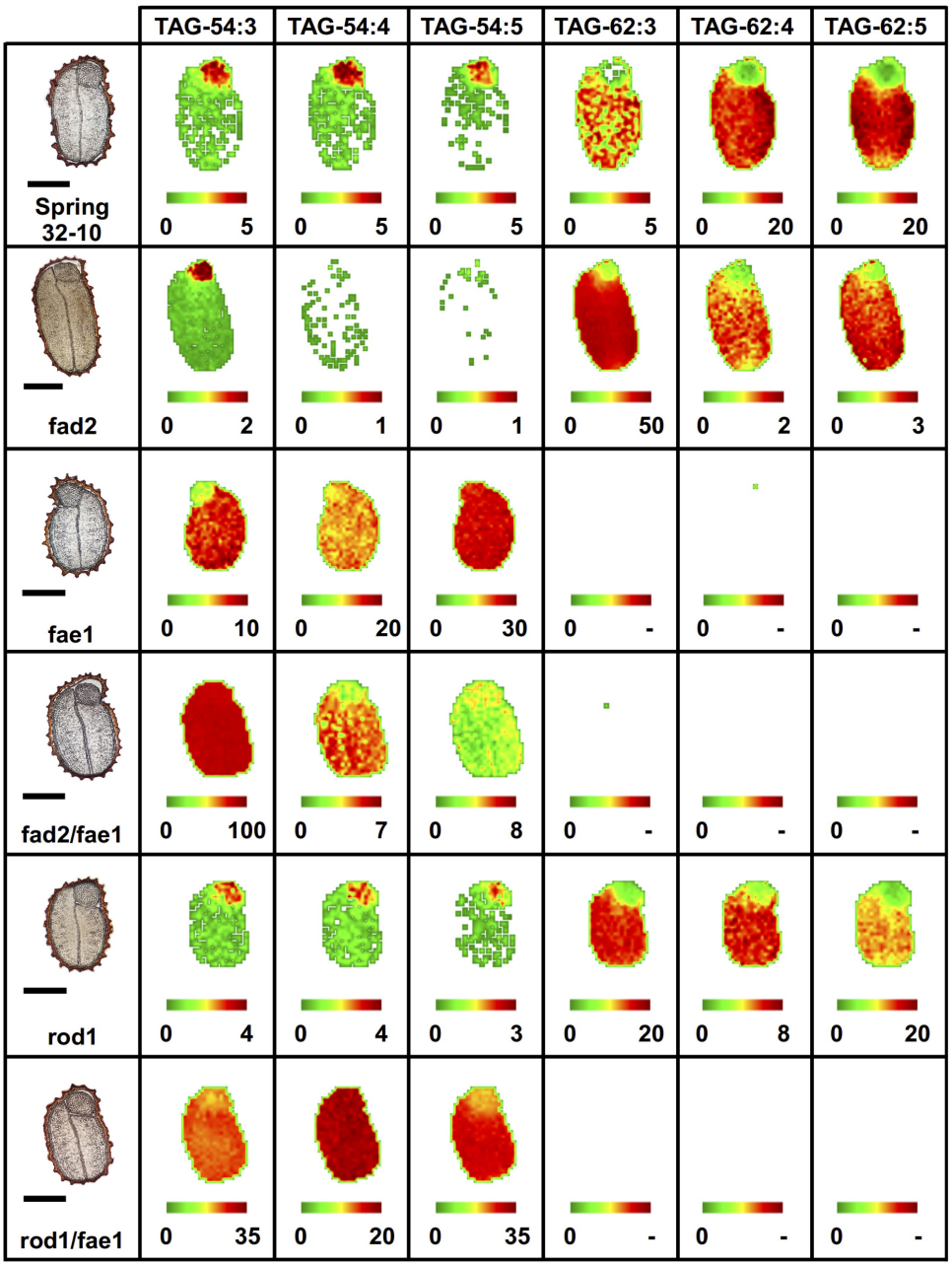

FIGURE 6 | Imaging of selected triacylglycerol (TAG) molecular species (54 vs. 62 carbon TAG) in wild-type and mutant *fad2*, *fae1*, *fad2 fae1*, *rod1*, and *rod1 fae1* *T. arvense* mature seed sections. MS images are presented as false colored images with each pixel representing an individual scan rastered over the imaged seed section (microscopy image left, scale bar = 500 μm). The color intensity scale ranges from green (low) to red (high) as the mol% value of the metabolite class. Each image mol% value is set individually (color scale below image) to show relative differences in abundance and localization between each seed type.

TAG molecular species, it is limited in its ability to provide a quantitative measure of the amounts of these PC and TAG metabolites (Sturtevant et al., 2016). To determine the amounts of PC and TAG within the wild-type seeds and the different mutants, direct infusion ESI-MS was performed on lipid extracts made from each genotype. The total TAG measured from wild-type seeds was 405.5 ± 27.6 nmol/mg, which was nearly the same as in *rod1* seeds with 400.5 ± 24.3 nmol/mg (**Figure 7B**). The TAG content from *fae1* (287.7 ± 20.4 nmol/mg), *fad2 fae1* (316.8 ± 23.4 nmol/mg), and *rod1 fae1* (288.8 ± 36.0 nmol/mg) was significantly less than wild type or *rod1*, while *fad2* had an intermediate amount of TAG (348.5 ± 22.4 nmol/mg) (one-way ANOVA; Tukey test, $p < 0.01$; **Figure 7B**).

The major TAG molecular species found in wild-type Spring 32-10 were 60:3, 60:4, 60:5, 62:3, 62:4, and 62:5, containing the very long chain erucic acid. The two most abundant molecular

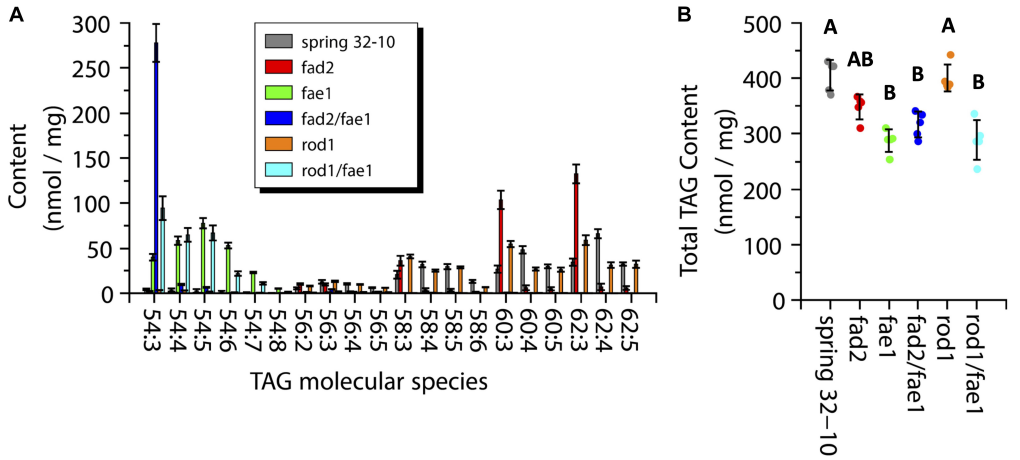

FIGURE 7 | Measurements of triacylglycerol (TAG) molecular species composition **(A)** and total content **(B)** within wild-type Spring 32-10 (dark gray) and CRISPR/Cas9 mutant *T. arvense* seeds *fad2* (red), *fae1* (green), *fad2 fae1* (dark blue), *rod1* (orange), and *rod1 fae1* (light blue). Error bars represent standard deviations of the means. (n = 5, ±SD, one-way ANOVA; Tukey test, $p < 0.01$).

species in wild-type seeds were 60:4 (48.3 ± 4.1 nmol/mg) and 62:4 (66.1 ± 5.0 nmol/mg) (**Figure 7A**, dark gray bars). In *fad2* seeds the TAG composition shifted to more saturated species, as seen in **Figure 7A** (red bars) and consistent with total FA profiles (**Supplementary Table 1**), with the most abundant molecular species being 60:3 (103.6 ± 10.2 nmol/mg) and 62:3 (132.5 ± 10.4 nmol/mg), which is nearly equal to the sum of all 60 and 62 carbon TAG found in wild-type seeds when including the more unsaturated species, respectively. The *fae1* seeds showed a major shift in TAG composition where the most abundant molecular species shifted to 54 carbon TAG with between three and seven double bonds in the FAs (**Figure 7A**, green bars). The *fad2 fae1* seeds essentially contained only the 54:3 TAG molecular species, made of three oleic fatty acids (**Figure 7A**, dark blue bar). The *rod1* seeds showed a similar TAG composition as wild-type seeds but with a trend toward more saturated molecular species, like *fad2* seeds with less of a stark difference (**Figure 7A**, orange bars). The *rod1 fae1* double mutant showed a similar composition as *fae1* seeds but with a higher content of 54:3 TAG (94.5 ± 13.1 vs. 40.1 ± 3.8 nmol/mg) (**Figure 7A**, light blue bars). These quantitative data from ESI-MS/MS analyses corroborated analyses of total fatty acid compositions (**Supplementary Table 1**) and the relative distributions determined by MALDI-MS imaging (**Figure 6**).

The total PC content across the wild-type and mutant seeds ranged from 9 to 11 nmol/mg with the exception of *fad2 fae1* seeds showing a significantly greater amount at ∼13 nmol/mg (one-way ANOVA; Tukey test, $p < 0.01$; **Figure 8B**). The major PC molecular species measured in wild-type seeds were the 36 carbon species containing between two and four double bonds, as well as PC-34:1 and 34:2 (**Figure 8A**, dark gray bars). Like TAG, the PC molecular species in *fad2* seeds shifted to more saturated species compared to the wild-type seeds, such as PC-36:2 (4.8 ± 0.6 vs. 1.3 ± 0.3 nmol/mg) and PC-38:2 (1.3 ± 0.1 vs. 0.4 ± 0.1 nmol/mg) (**Figure 8A**, red bars). The *fae1* seeds showed a PC molecular species composition similar to wild-type seeds with a slight increase in PC-36:2 and 36:3 (**Figure 8A**, green bars). The PC composition of the *fad2 fae1* double mutant was nearly entirely PC-36:2 (10.4 ± 1.2 nmol/mg) (**Figure 8A**, dark blue bars). Seeds from *rod1* mutants contained nearly the same composition as wild type seeds, as did *rod1 fae1* seeds with a slight increase of PC-36:2 (3.1 ± 0.5 vs. 1.3 ± 0.3 nmol/mg) (**Figure 8A**, orange and light blue bars, respectively). These quantitative data from ESI-MS/MS analyses corroborated analyses of total fatty acid compositions (**Supplementary Table 1**) and the relative distributions determined by MALDI-MS imaging (**Figure 6**).

DISCUSSION

Pennycress is being developed as an off-season oilseed-producing cash cover crop for the 80 million-acre United States Midwest Corn Belt and other temperate regions (Moser et al., 2009; Phippen and Phippen, 2012; Cubins et al., 2019; Chopra et al., 2020). As part of those efforts, we sought to determine how pennycress would respond to CRISPR/Cas9 knockout of key FA biosynthetic genes involved in FA elongation (*FAE1*), FA desaturation (*FAD2*), and trafficking of mono- and poly-unsaturated FAs between PC, DAG and TAG (*ROD1*) (**Figure 1**). Disruption of *FAE1*, *FAD2*, and *ROD1* function individually and in combination is known to increase the oleic acid content of seed oil in other species (Peng et al., 2010; Bates et al., 2013; Li et al., 2016; Neumann et al., 2021), although the magnitudes of changes have been found to vary from species to species, reinforcing the importance of testing hypotheses in different Brassicas instead of assuming all behave the same (Bai et al., 2020; Claver et al., 2020). This may be particularly true when comparing Brassica species having diploid genomes (e.g., *Thlaspi arvense*, *Arabidopsis thaliana*, and *Lepidium campestre*) to those having polyploid genomes (*Brassica napus*, *Camelina sativa*, and *Brassica carinata*), given that genome duplications afford the opportunity

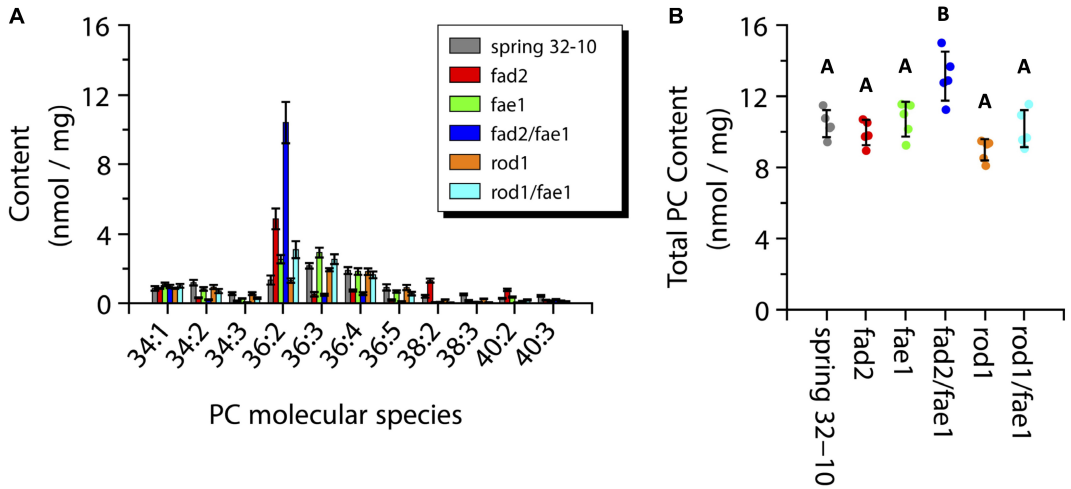

FIGURE 8 | Measurements of phosphatidylcholine (PC) molecular species composition **(A)** and total PC content **(B)** within wild-type Spring 32-10 (dark gray) and CRISPR/Cas9 mutant *T. arvense* seeds *fad2* (red), *fae1* (green), *fad2 fae1* (dark blue), *rod1* (orange), and *rod1 fae1* (light blue). Error bars represent standard deviations of the means (n = 5, ±SD, one-way ANOVA; Tukey test, $p < 0.01$).

for duplicated genes to diverge in function to varying degrees (Dar et al., 2017).

Pennycress *rod1 fae1* double mutants interrogated in this study, as well as EMS-generated pennycress *rod1 fae1* double mutants reported by Chopra et al. (2020), displayed a seed TAG FA composition nearly identical to that of canola (Singh and Singh, 2010), which makes this pennycress genotype attractive commercially. Here, we also report that pennycress *fad2 fae1* double mutants produce about 90% oleic acid in the seed oil. High-oleic oil has added value for food, fuel, and industrial uses owing to its relatively lower viscosity and oxidative stability compared to genetically unimproved oils from oilseed crops. Along with compositional analyses, we sought to determine how these genetic changes might affect plant growth and health, as it is important that crop stress resilience and grain yields not be compromised by genetic changes introduced into commercial varieties. In that regard, *rod1 fae1* double mutant plants grew indistinguishable from wild type whereas *fad2* knockout mutants exhibited delayed growth (discussed below). We also documented changes to the lipid composition and spatial heterogeneity of PC and TAG species specifically within the seed via MALDI-MSI, shedding light on where different lipids are synthesized and stored in pennycress embryos derived from varying lipid metabolic pathways.

Engineering Pennycress to Confer High Oleic Seed Oil Phenotypes

We successfully employed the *S. pyogenes* and *S. aureus* CRISPR/Cas9 systems to create mutations in the *ROD1* and *FAD2* genes, respectively. Five of the six CRISPR/Cas9-induced mutations resulted in frameshifts whereas the sixth created a premature stop codon. As such, all of the mutations in this study are likely complete loss-of-function alleles, which is supported by the fact that the mutant alleles of each gene exhibited identical phenotypes including identical FA compositional changes (**Figure 2** and **Supplementary Table 1**). The lipid profile changes were also consistent between siblings and from generation to generation, suggesting low plasticity to these traits, at least under our controlled growth chamber conditions. It remains to be seen how plastic pennycress seed FA composition is under variable farm field conditions. Reports with other species in this regard have been mixed, with camelina varieties showing no variation in seed oil FA composition based on different weather conditions (Kurasiak-Popowska et al., 2021), whereas oilseed rape was found to have higher and lower seed oil linolenic acid content corresponding with warmer and cooler weather conditions, respectively (Wójtowicz and Wójtowicz, 2020).

Notably, PUFA content was drastically reduced in the *fad2* mutants (<5%), revealing the nearly exclusive role of *TaFAD2* in FA desaturation in pennycress seed TAGs. BLAST searches of the pennycress genome, using *TaFAD2* sequences as the query, did not identify any close *FAD2* homologs. *FAD2* in *Arabidopsis thaliana* also occurs as a single-copy gene (Beisson et al., 2003). It is possible that the small amounts of PUFAs found in seeds of *fad2* mutants were derived from the action of FAD6, a plastidial delta-12 desaturase which has similar enzymatic activity to the endoplasmic reticulum-localized FAD2 while sharing limited sequence homology (Falcone et al., 1994).

We found that pennycress *fae1* and *fad2* mutants had undesirable reductions in total amounts of seed oil compared to wild type, although those reductions varied between experiments, possibly due to differences in growing conditions. Similar relative reductions in seed oil content were reported for *Brassica napus fae1* and *fad2* RNA interference (RNAi) mutants (Shi et al., 2017). Reduced oil production in these mutants may in part be due to feedback inhibition of plastidic acetyl-CoA carboxylase (ACCase) by 18:1-acyl carrier protein (ACP), as found by Andre et al. (2012) in *Brassica napus* embryo-derived cell cultures that were fed oleic acid Tween esters. It may be possible to overcome this feedback

inhibition by reducing function of the ACCase inhibiting proteins, BIOTIN ATTACHMENT DOMAIN-CONTAINING1 (BADC1) and BADC3 (Yu et al., 2021).

Characterization of Different Plant Growth Phenotypes

While not measured in the *fad2* mutant plants' vegetative tissues, it is possible that PUFA levels were also reduced throughout the plant. This would explain the delayed plant growth phenotypes we observed with the *fad2* knockout mutant plants (**Figure 3A** and **Supplementary Figure 7**). PUFAs are known to play important physiologic and biophysical roles, participating in signaling, regulating membrane fluidity at different temperatures, and providing resilience against environmental stressors including cold and salt stress (Browse et al., 1993; Okuley et al., 1994; Kodama et al., 1995; Weber, 2002; Zhang et al., 2012; Dar et al., 2017; Nguyen et al., 2019). Notably, linolenic acid is a precursor to the synthesis of jasmonic acid, which is a plant hormone that plays a central role in stress responses, development and growth (Huang et al., 2017). More work will be necessary to determine how these mutations affect hormone production and signaling and if the different mutants and mutant combinations are susceptible to specific abiotic and biotic stressors including drought stress and herbivory. Our germination and growth data suggest this may be the case with pennycress *fad2* loss of function. By contrast, to date, the pennycress *rod1* and *fae1* mutants and mutant combinations have performed very similar to wild type in both growth chamber (this study) and field settings (unpublished). Field conditions from fall pennycress planting to spring harvest in the United States Midwest, where these lines have been grown, are highly variable and challenging due to freeze-thaw cycles, waterlogging, and wind-blown conditions, which bodes well for the agronomic relevance of *rod1* and *fae1* mutations in improving pennycress crop characteristics. It seems likely that partial loss-of-function *fad2* mutations will also be relevant agronomically, even though our data show that total loss of *fad2* function causes agronomically unacceptable delays in growth and reduced seed yields (**Figure 3** and **Supplementary Figure 5**). It remains to be determined what are the threshold changes in lipids composition that can be tolerated by pennycress and how undesirable phenotypes can be mitigated with compensatory genetic changes.

Visualizing Heterogeneous Distributions of PC and TAG in Pennycress Mutant and Wild-Type Seeds via MALDI-MSI

Differences in fatty acid composition seen by GC-FID assay prompted us to investigate the distribution of the major classes of lipids in these seeds—PC and TAG. PC is an important structural membrane lipid in seeds and is also an intermediate in the biosynthesis of TAG. Given that different molecular species of PC and TAG have been found to be distributed in an unequal manner in seed tissues of many plant species (Marmon et al., 2017; Woodfield et al., 2017; Lu et al., 2018, 2020; Sturtevant et al., 2019), it was not clear how the mutant genotypes generated here would influence those normal distributions. MALDI-MS imaging allows for a comprehensive view of the lipid metabolites distributed in seed sections. Here, the spatial distribution for different molecular species of PC and TAG were visualized, and these mutations in enzymes of seed lipid metabolism influenced these metabolite distributions in some surprising ways. In wild-type seeds, the more unsaturated PC species containing 34 and 36 fatty acid carbons were localized mostly within the embryonic axis, while those that were more saturated were found more throughout the cotyledons (**Supplementary Figures 7**, **8**). This distribution was largely the same in the *rod1* mutant. The *fad2* seeds retained some heterogeneous separation between the cotyledonary and embryonic axis tissues, most easily seen with PC-34:1 (**Supplementary Figure 7**), but with a somewhat less diverse PC lipid profile. However, *fae1*, *fad2 fae1*, and *rod1 fae1* revealed a lack of heterogeneity in seed tissues, suggesting the mutations made in *FAE1* were most impactful on pathways that would otherwise establish that heterogeneity observed in wild-type seeds. Likewise, many of the distributions of 54 carbon TAG species in these same three mutants were uniform across the seed tissues (**Figure 6**), reinforcing the precursor-product relationship between acyl groups in PC and those in TAG. The 54 carbon TAG species became the major molecular species in *fae1*-containing mutant seeds, made up of 18 carbon fatty acids with varying levels of unsaturation between the three mutants, with *fad2 fae1* being the most saturated (i.e., TAG-54:3 with 18:1/18:1/18:1) and the single *fae1* mutant being the most unsaturated. Among all the wild-type and mutant seeds, those TAG molecular species that were lower molecular weight, such as 52 carbon, but also 54 and 56 carbon species in wild type, *fad2*, and *rod1*, were primarily enriched in the embryonic axis and less abundant, relatively speaking, in the cotyledons (**Supplementary Figure 8**), suggesting that elongation of fatty acids normally predominates in cotyledonary tissues and that this drives the unequal accumulation of erucic-acid containing TAGs in these parts of the seed. The loss of heterogeneity observed in *fae1*, *fad2 fae1*, and *rod1 fae1* most likely is attributed to the mutation in *FAE1*, as it is common to all three mutant genotypes, and *FAE1* has been found to be primarily expressed in cotyledonary tissues in developing seeds (Rossak et al., 2001; Lu et al., 2020). Lipid species containing VLCFAs, like those produced via FAE1, have previously been found to accumulate in cotyledonary tissues of seeds (Horn et al., 2013; Woodfield et al., 2017; Lu et al., 2020). The interruption of *FAE1* in the pennycress mutant seeds may result in remaining metabolic pathways for TAG accumulations in cotyledons to more resemble what is found in the embryonic axis tissues, resulting in less heterogeneous distributions of both PC and TAG molecular species.

Quantifying the Changes in PC and TAG Profiles in Pennycress Wild-Type and Mutant Seeds

Most of the mutations made here in this study produced results within PC and TAG profiles that were expected: *fad2* produced more saturated lipid species, likely one double bond in every fatty acid of either PC or TAG; *fae1* resulted in a shifted TAG

profile from those containing very long chain fatty acids (56, 58, 60, 62) to those containing largely 18 carbon fatty acids (54), but had little effect on PC; the double mutant *fad2 fae1* reduced the diversity of PC and TAG to largely PC-36:2 and TAG-54:3; *rod1* resulted in slightly more saturated TAG species, though much more subtly than *fad2*, and having little effect on PC; and *rod1 fae1* with a TAG profile most similar to the single *fae1* mutant, but with an increase in TAG-54:3, and overall little effect on the PC profile (**Figures 7**, **8**). One interesting set of mutants were those containing an interruption in ROD1. Though ROD1 is involved with PC/DAG interconversion, neither the PC composition nor total content differed greatly with the wild-type pennycress seeds. As desaturation occurs on PC, it might be expected that ROD1 would have a greater effect on the level of unsaturation in TAG, as DAG could then become interconverted to PC and become more unsaturated, and, indeed, *rod1* mutants tended to have more saturated TAG, but the overall effect of the mutation was fairly modest (**Figure 7**). The PC and TAG distributions as revealed by MALDI-MS imaging and the total TAG content between the single *rod1* mutant and wild-type seeds were nearly identical (**Figures 5**, **6**). Likely this was a reflection of the contribution of LPCAT as a route for the release of PUFA-CoAs, and their incorporation into TAG by the Kennedy pathway (**Figure 1**); or by cholinephosphotransferase (CPT) as a partially redundant activity for the interconversion of PC and DAG in the absence of *rod1*. The mutants that appeared to show the greatest changes in TAG composition and content were those containing an interruption in FAE1. The three mutants *fae1, fad2 fae1*, and *rod1 fae1* all showed a significantly lower amount of TAG compared to either wild type or the single mutant *rod1*, whereas *fad2* contained a TAG content intermediate between wild type and its double mutant with *fae1* (**Figure 7**). This may suggest FAE1 exerts a much greater influence on the total TAG content and composition stored within pennycress seeds, which in wild type seeds are notable for accumulating a high amount of erucic acid (22:1). Future engineering efforts will need to overcome this obstacle when creating new pennycress lines with altered TAG compositions in order to create not only pennycress seed oils with oil compositions more suitable to their intended applications, such as drop-in fuels, but also high oil producing lines.

CONCLUSION

Pennycress is proving to be a useful model system for translational biology research, allowing for comparative analyses and the implementation of powerful genetics tools such as CRISPR/Cas9 gene editing for rapid and efficient production of mutants and corresponding genotypic and phenotypic analyses. The different pennycress single and double mutants that were generated for this study displayed unique plant and seed phenotypes captured in a variety of characterization methods, the data of which will be useful in guiding future studies of mutant performance under different stressors in both laboratory and field conditions. Here, we also provide data showing that pennycress *rod1 fae1* double mutations confer a lipid profile similar to that of canola seed TAGs. The pennycress *rod1 fae1* mutant combination appears to be an attractive genotype for commercialization into food, feed, and fuel products including biodiesel given that these genotypes grow as well as wild type, although more growth tests remain to be performed to determine how resilient the genotypes are to a variety of abiotic and biotic stresses. Furthermore, this study sheds light on tissue-specific localizations of PC and TAG molecular species within pennycress embryos and how lipid metabolic fluxes may be affected by various mutations in the targeted fatty acid modifying genes, hinting at useful metabolic studies and related genetic changes aimed at optimizing lipid compositions while also enhancing total oil yields and avoiding disruption of important physiologic functions (Sedbrook and Durrett, 2020; Tsogtbaatar et al., 2020).

MATERIALS AND METHODS

Surface Sterilization of Pennycress Seeds and Growth Conditions

Pennycress seeds were surface sterilized with a brief rinse of 70% ethanol followed by a 10-min incubation in a sterilization solution consisting of 30% bleach and 0.01% SDS. After sterilization solution removal, the seeds were rinsed three times with sterile water. Gibberellin treatment was not necessary for Spring 32 seed germination as it has low primary seed dormancy.

Surface-sterilized pennycress seeds were sown onto "agar growth media," consisting of 0.8% agar media containing one-half-strength Murashige and Skoog salts in petri dishes wrapped in Parafilm. Immediately after seed sowing, the plates were placed into a Percival Scientific CU-36L5 incubator (16 h 4100K fluorescent light ∼150–200 $\mu E/m^2/s$/8 h dark, 22°C). For growth in soil, seedlings were transplanted at a density of four plants per 4-inch pot (Gage Dura Pots 4″ × 3–3/8″, OBC Northwest Inc. catalog no. PPG4) in autoclaved Miracle Grow soil mix (or a 50/50 mix of Redi-Earth plug and seedling mix and Berger BM 7 bark mix) intermixed with 0.03 g/4-inch pot of the insecticide Marathon (Marathon 1% Granular[3]). When making up the 4-inch pots with Redi-Earth and BM 7 soils, a thin layer of wet soil (∼1/4 inch) was first put in the bottom of the pot, on top of which 1/8 teaspoon of prilled urea (46-0-0; Greenway Biotech, Inc.) was sprinkled before the pot was entirely filled with the wet soil mix. For the flowering time assays, time zero was when seedlings were transplanted into soil. Plants were grown in environment-controlled growth chambers cycling 16 h light/8 h dark (light was either 6500K fluorescent or a combination 4100K fluorescent/incandescent lighting, 175–250 $\mu E/m^2/s$ light intensity), at 21 or 22°C.

Vectors

The TaFAD2_CRISPR-Sa-Cas9_Hyg and TaROD1_CRISPR-Sp-Cas9_Hyg binary vectors were constructed and generated, as described in Fauser et al. (2014); Steinert et al. (2015), and at http://www.botanik.kit.edu/molbio/940.php, using the vectors pEn-Sa-Chimera and pDe-Sa-Cas9 or pEn-Sp-Chimera and pDe-Sp-Cas9, respectively. The plant selectable marker (Bar gene) in

[3]www.domyown.com/

the pDe-sa-Cas9 binary vector was replaced with the Hygromycin phosphotransferase (hpt) gene (40 U/ml hygromycin selection in plants) to create a pDe-Sa-Cas9_Hyg and pDe-Sp-Cas9_Hyg vectors. Bacterial selection used for the binary vector was 75 μg/ml spectinomycin.

The following two oligos were annealed to create the 20-mer protospacer specific to the open reading frame of the putative pennycress *TaFAD2* gene. Note that the nucleotides ATTG on the FWD primer and CAAT on the REV primer serve as overhangs for annealing to the vector's *Bsa*I restriction sites:

PennyFAD2_CRISPR_FWD:
ATTGTACTTGGCTTGGCCTCTCTA
PennyFAD2_CRISPR_REV:
TAGAGAGGCCAAGCCAAGTACAAT

The following two oligos were annealed to create the 20-mer protospacer specific to the open reading frame of the putative pennycress *TaROD1* gene:

PennyROD1_CRISPR_FWD:
ATTGGACGACGGCTACGCAAACGG
PennyROD1_CRISPR_REV:
CCGTTTGCGTAGCCGTCGTCCAAT

Constructs were introduced into *Agrobacterium tumefaciens* strain GV3101 using a standard $CaCl_2$ flash-freeze/thaw transformation method (Holsters et al., 1978).

Agrobacterium-Mediated Transformation of Pennycress

Cultures of *Agrobacterium tumefaciens* strain GV3101 containing either the TaFAD2-CRISPR-SaCas9_Hyg or TaROD1-CRISPR-SpCas9_Hyg plasmid were grown from glycerol stocks (∼200 uL inoculated into 50 mL Luria Broth (LB) containing 50 μg/ml gentamycin, 50 μg/ml rifampicin, and 75 μg/ml spectinomycin. The 50 mL cultures were shaken overnight at 28°C, then added to an additional 200 mL LB antibiotic-containing media and again incubated overnight, then centrifuged at 3,500 RPM for 10 min and resuspended in an equal volume of 5% (w/v) sucrose plus 0.02% (v/v) Silwet L-77. The floral portion of inflorescences of plants that had flowers opening for ∼5 days were submerged in this *Agrobacterium* solution, then placed under ∼30 inches mercury (14.7 psi) vacuum in a 26 cm × 25 cm × 36.5 cm vacuum chamber for 10 min, using a diaphragm vacuum pump (60 L/Min pump speed, 200 mBar ultimate vacuum). After dipping, the floral portions of the inflorescences were wrapped in plastic wrap sealed around the stems with twist ties, and the plants placed back into an environmental growth chamber. The plastic wrap covering was removed the following day.

Identification of Transgenic and CRISPR-Cas9-Edited Pennycress Plants

Antibiotic Selection

Putative TaFAD2-CRISPR-SaCas9_Hyg or TaROD1-CRISPR_SpCas9 transgenic seeds were surface sterilized and plated onto 0.8% agar/one half-strength Murashige and Skoog salts containing 40 U/mL *hygromycin* B. Seedlings that continued to grow on the antibiotic-containing media were transferred to soil ∼8 days after plating, then after establishment were further confirmed as being transgenic by PCR analysis.

Screening for CRISPR/Cas9 Edits: T7 Endonuclease I

Leaf-extracted genomic DNA was PCR amplified using *FAD2* or *ROD1* primers spanning the CRISPR-Cas9 target site (see **Supplementary Materials**), followed by T7 endonuclease I digestion of the PCR product as described by Pyott et al. (2016). Template for PCR reactions was a 50:50 mix of each putative mutant prep and wild type to ensure that even in the case of a homozygous mutation, a DNA mismatch would be PCR amplified and detected. PCR template was extracted from fresh leaf tissue using the Phire Plant Direct PCR Kit (Thermo #F130WH). For T7 endonuclease I analysis, 10 μl of each 20 μl PCR reaction was denatured by heating at 95°C for 5 min in a thermocycler (Fisher) and annealed using gradual cooling: −2°C per second decrease from 95°C to 85°C then −0.1°C per second decrease from 85°C to 25°C, followed by T7 endonuclease I (Fisher Scientific cat. #50-995-224) digestion for 30 min. The digested product was electrophoresed in a 1% agarose gel to identify samples that partially digested, indicating an SaCas9 or SpCas9-induced edit in *TaFAD2* or *TaROD1* genes, respectively, which were confirmed by Sanger DNA sequence analyses of PCR products amplified from cetyltrimethyl ammonium bromide (CTAB)-purified genomic DNA (Clarke, 2009).

Characterization Assays

Germination Studies

Seeds were surface sterilized and plated onto 0.8% agar/one half-strength Murashige and Skoog salts (agar growth media) with no antibiotics and no sucrose. Plates were observed at the same time daily for radical emergence until all seeds germinated or 16 days. Seed germination times were compared to wild type using one-way ANOVA; Tukey test, $p < 0.01$. $n = 150$ seeds split in to three biological reps (50-seed replicates plated on to agar growth media).

Flowering Times

Plants were observed and scored at a daily time for the opening of the first flower on their inflorescences. The same plants were also observed and scored daily at the same time for the final flower to open. These time points were compared to the time of transplant and to each other for total flower time window.

Plant Heights

Final plant heights were recorded by cutting the plants at the base by the soil and measuring the length from the base to the top of the main stem, straightening the stem against a measuring stick.

Seed Analysis Data

Quantifications of numbers of seeds, total seed weights per plant, and single-seed weight of the different CRISPR mutants and wild type were performed using a MARViTECH MARViN 5.0 Seed Analyzer instrument along with an Ohaus STX223 balance (Single-seed weight = total seed weight/number of seeds).

Lipid Analysis

Total lipids were extracted from pennycress seeds harvested from senesced plants, and fatty acid methyl esters (FAMEs) were generated and analyzed by gas chromatography, as described in Cahoon et al. (2006). For ESI-MS analysis, neutral lipids were purified from total seed lipids on a small silica column with 99:1 (v/v) chloroform: methanol. Samples were then analyzed on an API4000 triple quadrupole mass spectrometer (Applied Biosystems) as described previously (Bansal and Durrett, 2016). To quantify fatty acid composition, total seed lipids were separated using thin layer chromatography on Silica gel 60 plates (Merck) with a 70:30:1 hexane:diethyl-ether:acetic acid (v/v/v) solvent system. Lipids were visualized by spraying with 0.075% 20,70 -dichlorofluorescein in 95% methanol and exposing to UV light. The bands were scraped and directly transmethylated using a base-catalyzed method (Ichihara et al., 1996); the resulting FAMEs were analyzed using gas chromatography.

MALDI-MS Imaging of Pennycress Seed Sections

Pennycress seeds harvested from senesced plants were sectioned then imaged by MALDI-MS imaging using methods as previously described by Rolletschek et al. (2020). Data collected from MS imaging experiments used the same parameters described previously, and were analyzed in a similar manner with the exception that PC images were derived from the sum of the $[M + H]^+$ and $[M + K]^+$ adducts, and TAG as the sum of the $[M + Na]^+$ and $[M + K]^+$ adducts.

ESI-MS Quantification of PC and TAG From Lipid Extracts of Pennycress Seeds

Total lipids from whole seeds (10–15 mg) were extracted into $CHCl_3$ using procedures previously described (Sturtevant et al., 2019). Lipid extracts were diluted by 1:50 into 1:1:0.01 $CHCl_3$/MeOH/5 mM NH_4Ac prior to analysis. Diluted extracts were analyzed via direct infusion ESI-MS using a Waters Synapt G2-Si mass spectrometer (Waters Corporation, Milford, MA, United States). The mass spectrometer and direct infusion parameters were set as follows: an *m/z* range of 600–1200, source temperature of 80°C, desolvation gas set to 500 L/h, capillary voltage set to 3 kV, and an injection rate of 20 μl/min. Data was collected with MassLynx software (Waters Corporation, Milford, MS, United States). A mixture of PC and TAG standards consisting of tripentadecanoin (15:0/15:0/15:0, 1.05 μM), tripalmitin (16:0/16:0/16:0, 0.99 μM), triheptadecanoin (17:0/17:0/17:0, 0.94 μM), tristearin (18:0/18:0/18:0, 1.01 μM), triolein (18:1/18:1/18:1, 1.02 μM), trilinolein (18:2/18:2/18:2, 1.02 μM), trilinolenin (18:3/18:3/18:3, 1.03 μM), triheneicosanoin (21:0/21:0/21:0, 0.98 μM), dimyristoylphosphocholine (PC-14:0/14:0, 0.1 μM), diheptadecanoylphosphocholine (PC-17:0/17:0), and diheneicosanoylphosphocholine (PC-21:0/21:0, 0.1 μM) was used to determine the correction factors for carbon number and unsaturations for ESI-MS data. TAG standards were synthesized by Nu-Chek Prep. Inc. (Elysian, MN, United States), and the PC standards were purchased from Sigma Aldrich (St. Louis, MO, United States; PC-14:0/14:0: ca. no. P2663; PC-17:0/17:0: ca. no. 850360C, PC-21:0/21:0: ca. no. 850370P). Relative correction factors were calculated from the intensities of each standard and then plotted against either the number of fatty acid carbons or number of fatty acid double bonds. The equation for the fitted linear trend line was used to calculate the adjustment factors for each potential number of carbon or double bond found in the detected TAG and PC molecular species of the pennycress lipid extracts. The product of the two correction factors (carbon no. and double bond number) was multiplied by the calculated nmol/mg of TAG or PC detected to produce the final corrected amount. Samples were spiked with 1 nmol of dimyristoylphosphocholine and 1 nmol of triheptadecanoin as internal standards prior to analysis.

DATA AVAILABILITY STATEMENT

The original contributions presented in the study are included in the article/**Supplementary Material**, further inquiries can be directed to the corresponding author.

AUTHOR CONTRIBUTIONS

BJ and MM generated the CRISPR/Cas9 constructs and mutants. BJ genotypically and phenotypically characterized the CRISPR/Cas9 mutants. TN performed the fatty acids analyses. TR performed MALDI-MS imaging and ESI-MS/MS quantification of PC and TAG. BJ, MM, TN, EC, KC, and JS designed and interpreted experiments. BJ, TR, KC, and JS wrote and edited the manuscript. All authors contributed to the article and approved the submitted version.

FUNDING

This material is based upon work that is supported by the National Institute of Food and Agriculture, United States Department of Agriculture, under award number 2018-67009-27374, the Agriculture and Food Research Initiative Competitive Grant No. 2019-69012-29851, and the United States Department of Energy, Office of Science, Office of Biological and Environmental Research, Genomic Science Program grant no. DE-SC0021286 to JS. MS imaging studies and ESI-MS/MS quantification were supported by the United States Department of Energy, Office of Science, Division of Biological and Environmental Research under contract number DE-SC0020325 to KC. EC was funded by grants from USDA-NIFA (2018-38821-28111 and 2019-67021-29946).

ACKNOWLEDGMENTS

We thank Friedrich Fauser, Jeannette Steinert, and Holger Puchta for providing the CRISPR/SpCas9 and CRISPR/SaCas9 vector sets. Special thanks to Dalton Williams, Matt Maynard, and Matt Reuss for their assistance as undergraduate researchers in the lab, and David Marks and Ratan Chopra for fruitful conversations.

SUPPLEMENTARY MATERIAL

The Supplementary Material for this article can be found online at: https://www.frontiersin.org/articles/10.3389/fpls.2021.652319/full#supplementary-material

Supplementary Figure 1 | Nucleotide sequence alignment of the *AtFAD2* and *TaFAD2* ORFs.

Supplementary Figure 2 | T7 endonuclease analysis and sequences of the *fad2* mutants.

Supplementary Figure 3 | Nucleotide sequence alignment of the *AtROD1* and *TaROD1* ORFs.

Supplementary Figure 4 | Sequences of the *rod1* mutants.

Supplementary Figure 5 | Pictures of mutants and wild type growth over time.

Supplementary Figure 6 | Graphed amounts of seed germination over a 16-day period under different temperatures and light regimes.

Supplementary Figure 7 | MS imaging of PC molecular species detected in wild-type and mutant embryos.

Supplementary Figure 8 | MS imaging of TAG molecular species detected in wild-type and mutant embryos.

Supplementary Table 1 | Seed TAG fatty acid compositions of the different mutants.

Supplementary Table 2 | Total seed germination on agar growth media plates.

Supplementary Table 3 | Amounts of seed germination in constant light at different temperatures.

Supplementary Table 4 | Amounts of seed germination in constant darkness at different temperatures.

REFERENCES

Altendorf, K., Isbell, T., Wyse, D. L., and Anderson, J. A. (2019). Significant variation for seed oil content, fatty acid profile, and seed weight in natural populations of field pennycress (*Thlaspi arvense* L.). *Ind. Crops Prod.* 129, 261–268. doi: 10.1016/j.indcrop.2018.11.054

Andre, C., Haslam, R. P., and Shanklin, J. (2012). Feedback regulation of plastidic acetyl-CoA carboxylase by 18:1-acyl carrier protein in *Brassica napus*. *Proc. Natl. Acad. Sci. U.S.A.* 109, 10107–10112. doi: 10.1073/pnas.1204604109

Bai, S., Wallis, J. G., Denolf, P., Engelen, S., Bengtsson, J. D., Van Thournout, M., et al. (2020). The biochemistry of headgroup exchange during triacylglycerol synthesis in canola. *Plant J.* 103:83. doi: 10.1111/tpj.14709

Bansal, S., and Durrett, T. P. (2016). Defining the extreme substrate specificity of *Euonymus alatus* diacylglycerol acetyltransferase, an unusual membrane-bound O-acyltransferase. *Biosci. Rep.* 36:e00406. doi: 10.1042/BSR20160277

Bates, P. D. (2016). Understanding the control of acyl flux through the lipid metabolic network of plant oil biosynthesis. *Biochim. Biophys. Acta (BBA) Mol. Cell Biol. Lipids* 1861, 1214–1225. doi: 10.1016/j.bbalip.2016.03.021

Bates, P. D., and Browse, J. (2012). The significance of different diacylgycerol synthesis pathways on plant oil composition and bioengineering. *Front. Plant Sci.* 3:147. doi: 10.3389/fpls.2012.00147

Bates, P. D., Stymne, S., and Ohlrogge, J. (2013). Biochemical pathways in seed oil synthesis. *Curr. Opin. Plant Biol.* 16, 358–364. doi: 10.1016/j.pbi.2013.02.015

Beisson, F., Koo, A. J., Ruuska, S., Schwender, J., Pollard, M., Thelen, J. J., et al. (2003). *Arabidopsis* genes involved in acyl lipid metabolism. A 2003 census of the candidates, a study of the distribution of expressed sequence tags in organs, and a web-based database. *Plant Physiol.* 132, 681–697.

Bezergianni, S., and Kalogianni, A. (2009). Hydrocracking of used cooking oil for biofuels production. *Bioresour. Technol.* 100, 3927–3932. doi: 10.1016/j.biortech.2009.03.039

Boateng, A. A., Mullen, C. A., and Goldberg, N. M. (2010). Producing stable pyrolysis liquids from the oil-seed presscakes of mustard family plants: Pennycress (*Thlaspi arvense* L.) and Camelina (*Camelina sativa*). *Energy Fuels* 24, 6624–6632. doi: 10.1021/ef101223a

Browse, J., and Somerville, C. (1991). Glycerolipid synthesis: biochemistry and regulation. *Annu. Rev. Plant Biol.* 42, 467–506. doi: 10.1146/annurev.pp.42.060191.002343

Browse, J., McConn, M., James, D., and Miquel, M. (1993). Mutants of *Arabidopsis* deficient in the synthesis of alpha-linolenate. Biochemical and genetic characterization of the endoplasmic reticulum linoleoyl desaturase. *J. Biol. Chem.* 268, 16345–16351.

Cahoon, E. B., Dietrich, C. R., Meyer, K., Damude, H. G., Dyer, J. M., and Kinney, A. J. (2006). Conjugated fatty acids accumulate to high levels in phospholipids of metabolically engineered soybean and *Arabidopsis* seeds. *Phytochemistry* 67, 1166–1176. doi: 10.1016/j.phytochem.2006.04.013

Chapman, K. D., and Ohlrogge, J. B. (2012). Compartmentation of triacylglycerol accumulation in plants. *J. Biol. Chem.* 287, 2288–2294. doi: 10.1074/jbc.R111.290072

Chopra, R., Folstad, N., Lyons, J., Ulmasov, T., Gallaher, C., Sullivan, L., et al. (2019). The adaptable use of *Brassica* NIRS calibration equations to identify pennycress variants to facilitate the rapid domestication of a new winter oilseed crop. *Ind. Crops Prod.* 128, 55–61. doi: 10.1016/j.indcrop.2018.10.079

Chopra, R., Johnson, E. B., Daniels, E., McGinn, M., Dorn, K. M., Esfahanian, M., et al. (2018). Translational genomics using *Arabidopsis* as a model enables the characterization of pennycress genes through forward and reverse genetics. *Plant J.* 96, 1093–1105. doi: 10.1111/tpj.14147

Chopra, R., Johnson, E. B., Emenecker, R., Cahoon, E. B., Lyons, J., Kliebenstein, D. J., et al. (2020). Identification and stacking of crucial traits required for the domestication of pennycress. *Nat. Food* 1, 84–91. doi: 10.1038/s43016-019-0007-z

Clarke, J. D. (2009). Cetyltrimethyl ammonium bromide (CTAB) DNA miniprep for plant DNA isolation. *Cold Spring Harb. Protoc.* 2009:pdb.prot5177. doi: 10.1101/pdb.prot5177

Claver, A., de la Vega, M., Rey-Giménez, R., Luján, M. Á, Picorel, R., López, M. V., et al. (2020). Functional analysis of β-ketoacyl-CoA synthase from biofuel feedstock *Thlaspi arvense* reveals differences in the triacylglycerol biosynthetic pathway among *Brassicaceae*. *Plant Mol. Biol.* 104, 283–296. doi: 10.1007/s11103-020-01042-7

Claver, A., Rey, R., López, M. V., Picorel, R., and Alfonso, M. (2017). Identification of target genes and processes involved in erucic acid accumulation during seed development in the biodiesel feedstock Pennycress (*Thlaspi arvense* L.). *J. Plant Physiol.* 208, 7–16. doi: 10.1016/j.jplph.2016.10.011

Conti, E., and Izaurralde, E. (2005). Nonsense-mediated mRNA decay: molecular insights and mechanistic variations across species. *Curr. Opin. Cell Biol.* 17, 316–325. doi: 10.1016/j.ceb.2005.04.005

Cubins, J. A., Wells, M. S., Frels, K., Ott, M. A., Forcella, F., Johnson, G., et al. (2019). Management of pennycress as a winter annual cash cover crop. A review. *Agron. Sustain. Dev.* 39:46. doi: 10.1007/s13593-019-0592-0

Dar, A. A., Choudhury, A. R., Kancharla, P. K., and Arumugam, N. (2017). The *FAD2* gene in plants: occurrence, regulation, and role. *Front. Plant Sci.* 8:1789. doi: 10.3389/fpls.2017.01789

de Lorgeril, M., and Salen, P. (2012). New insights into the health effects of dietary saturated and omega-6 and omega-3 polyunsaturated fatty acids. *BMC Med.* 10:50. doi: 10.1186/1741-7015-10-50

Demorest, Z. L., Coffman, A., Baltes, N. J., Stoddard, T. J., Clasen, B. M., Luo, S., et al. (2016). Direct stacking of sequence-specific nuclease-induced mutations to produce high oleic and low linolenic soybean oil. *BMC Plant Biol.* 16:225. doi: 10.1186/s12870-016-0906-1

Dorn, K. M., Fankhauser, J. D., Wyse, D. L., and Marks, M. D. (2013). De novo assembly of the pennycress (*Thlaspi arvense*) transcriptome provides tools for the development of a winter cover crop and biodiesel feedstock. *Plant J.* 75, 1028–1038. doi: 10.1111/tpj.12267

Dorn, K. M., Fankhauser, J. D., Wyse, D. L., and Marks, M. D. (2015). A draft genome of field pennycress (*Thlaspi arvense*) provides tools for the domestication of a new winter biofuel crop. *DNA Res.* 22, 121–131. doi: 10.1093/dnares/dsu045

Drake, B. L., Hanson, D. T., Lowrey, T. K., and Sharp, Z. D. (2017). The carbon fertilization effect over a century of anthropogenic CO_2 emissions: higher intracellular CO_2 and more drought resistance among invasive and native grass species contrasts with increased water use efficiency for woody plants in the US Southwest. *Glob. Chang. Biol.* 23, 782–792. doi: 10.1111/gcb.13449

Dyer, J. M., Stymne, S., Green, A. G., and Carlsson, A. S. (2008). High-value oils from plants. *Plant J.* 54, 640–655. doi: 10.1111/j.1365-313X.2008.03430.x

Esfahanian, M., Nazarenus, T. J., Freund, M. M., McIntosh, G., Phippen, W. B., Phippen, M. E., et al. (2021). Generating pennycress (*Thlaspi arvense*) seed triacylglycerols and acetyl-triacylglycerols containing medium-chain fatty acids. *Front. Energy Res.* 10:620118. doi: 10.3389/fenrg.2021.620118

Falcone, D. L., Gibson, S., Lemieux, B., and Somerville, C. (1994). Identification of a gene that complements an *Arabidopsis* mutant deficient in chloroplast [omega]6 desaturase activity. *Plant Physiol.* 106, 1453–1459. doi: 10.1104/pp.106.4.1453

Fan, J., Shonnard, D. R., Kalnes, T. N., Johnsen, P. B., and Rao, S. (2013). A life cycle assessment of pennycress (*Thlaspi arvense* L.)-derived jet fuel and diesel. *Biomass Bioenergy* 55, 87–100. doi: 10.1016/j.biombioe.2012.12.040

Fauser, F., Schiml, S., and Puchta, H. (2014). Both CRISPR/Cas-based nucleases and nickases can be used efficiently for genome engineering in *Arabidopsis thaliana*. *Plant J.* 79, 348–359. doi: 10.1111/tpj.12554

Frega, N., Mozzon, M., and Lercker, G. (1999). Effects of free fatty acids on oxidative stability of vegetable oil. *J. Am. Oil Chem. Soc.* 76, 325–329. doi: 10.1007/s11746-999-0239-4

Fulton, L. M., Lynd, L. R., Körner, A., Greene, N., and Tonachel, L. R. (2015). The need for biofuels as part of a low carbon energy future. *Biofuels Bioprod. Biorefin.* 9, 476–483. doi: 10.1002/bbb.1559

Goffman, F. D., Alonso, A. P., Schwender, J., Shachar-Hill, Y., and Ohlrogge, J. B. (2005). Light enables a very high efficiency of carbon storage in developing embryos of rapeseed. *Plant Physiol.* 138, 2269–2279. doi: 10.1104/pp.105.063628

Guan, R., Lager, I., Li, X., Stymne, S., and Zhu, L. H. (2014). Bottlenecks in erucic acid accumulation in genetically engineered ultrahigh erucic acid *Crambe abyssinica*. *Plant Biotechnol. J.* 12, 193–203. doi: 10.1111/pbi.12128

Haslam, T. M., and Kunst, L. (2013). Extending the story of very-long-chain fatty acid elongation. *Plant Sci.* 210, 93–107. doi: 10.1016/j.plantsci.2013.05.008

Hill, J., Tajibaeva, L., and Polasky, S. (2016). Climate consequences of low-carbon fuels: the United States renewable fuel standard. *Energy Policy* 97, 351–353. doi: 10.1016/j.enpol.2016.07.035

Holsters, M., De Waele, D., Depicker, A., Messens, E., Van Montagu, M., and Schell, J. (1978). Transfection and transformation of *Agrobacterium tumefaciens*. *Mol. Gen. Genet. MGG* 163, 181–187. doi: 10.1007/BF00267408

Horn, P. J., Silva, J. E., Anderson, D., Fuchs, J., Borisjuk, L., Nazarenus, T. J., et al. (2013). Imaging heterogeneity of membrane and storage lipids in transgenic *Camelina sativa* seeds with altered fatty acid profiles. *Plant J.* 76, 138–150. doi: 10.1111/tpj.12278

Hossain, Z., Johnson, E. N., Wang, L., Blackshaw, R. E., and Gan, Y. (2019). Comparative analysis of oil and protein content and seed yield of five *Brassicaceae* oilseeds on the Canadian prairie. *Ind. Crops Prod.* 136, 77–86. doi: 10.1016/j.indcrop.2019.05.001

Huang, H., Liu, B., Liu, L., and Song, S. (2017). Jasmonate action in plant growth and development. *J. Exp. Bot.* 68, 1349–1359. doi: 10.1093/jxb/erw495

Ichihara, K. I., Shibahara, A., Yamamoto, K., and Nakayama, T. (1996). An improved method for rapid analysis of the fatty acids of glycerolipids. *Lipids* 31, 535–539. doi: 10.1007/BF02522986

IPCC (2013). *Fifth Assessment Report of the United Nations Intergovernmental Panel on Climate Change*. Geneva: IPCC.

Isbell, T. (2008). "Thlaspi arvense (Pennycress) as a biodiesel in a one year-two crop rotation with soybean [Abstract]," in *Proceedings of the 20th Annual Meeting of the Association for the Advancement of Industrial Crops*, (College Station, TX), 6.

Isbell, T. A., Evangelista, R., Glenn, S. E., Devore, D. A., Moser, B. R., Cermak, S. C., et al. (2015). Enrichment of erucic acid from pennycress (*Thlaspi arvense* L.) seed oil. *Ind. Crops Prod.* 66, 188–193. doi: 10.1016/j.indcrop.2014.12.050

James, D. W., Lim, E., Keller, J., Plooy, I., Ralston, E., and Dooner, H. K. (1995). Directed tagging of the *Arabidopsis FATTY ACID ELONGATION1* (*FAE1*) gene with the maize transposon activator. *Plant Cell* 7, 309–319.

Jiang, W. Z., Henry, I. M., Lynagh, P. G., Comai, L., Cahoon, E. B., and Weeks, D. P. (2017). Significant enhancement of fatty acid composition in seeds of the allohexaploid, *Camelina sativa*, using CRISPR/Cas9 gene editing. *Plant Biotechnol. J.* 15, 648–657. doi: 10.1111/pbi.12663

Kang, J., Snapp, A. R., and Lu, C. (2011). Identification of three genes encoding microsomal oleate desaturases (FAD2) from the oilseed crop *Camelina sativa*. *Plant Physiol. Biochem.* 49, 223–229. doi: 10.1016/j.plaphy.2010.12.004

Kodama, H., Horiguchi, G., Nishiuchi, T., Nishimura, M., and Iba, K. (1995). Fatty acid desaturation during chilling acclimation is one of the factors involved in conferring low-temperature tolerance to young tobacco leaves. *Plant Physiol.* 107, 1177–1185. doi: 10.1104/pp.107.4.1177

Kumar, S., Seepaul, R., Mulvaney, M. J., Colvin, B., George, S., Marois, J. J., et al. (2020). *Brassica carinata* genotypes demonstrate potential as a winter biofuel crop in South East United States. *Ind. Crops Prod.* 150:112353. doi: 10.1016/j.indcrop.2020.112353

Kurasiak-Popowska, D., Graczyk, M., Przybylska-Balcerek, A., and Stuper-Szablewska, K. (2021). Influence of variety and weather conditions on fatty acid composition of winter and spring *Camelina sativa* varieties in Poland. *Eur. Food Res. Technol.* 247, 465–473. doi: 10.1007/s00217-020-03639-0

Lakhssassi, N., Zhou, Z., Liu, S., Colantonio, V., AbuGhazaleh, A., and Meksem, K. (2017). Characterization of the *FAD2* gene family in soybean reveals the limitations of gel-based TILLING in genes with high copy number. *Front. Plant Sci.* 8:324. doi: 10.3389/fpls.2017.00324

Lanjekar, R. D., and Deshmukh, D. (2016). A review of the effect of the composition of biodiesel on NOx emission, oxidative stability and cold flow properties. *Renew. Sustain. Energy Rev.* 54, 1401–1411. doi: 10.1016/j.rser.2015.10.034

Li, X., Mei, D., Liu, Q., Fan, J., Singh, S., Green, A., et al. (2016). Down-regulation of crambe fatty acid desaturase and elongase in *Arabidopsis* and crambe resulted in significantly increased oleic acid content in seed oil. *Plant Biotechnol. J.* 14, 323–331. doi: 10.1111/pbi.12386

Li, X., van Loo, E. N., Gruber, J., Fan, J., Guan, R., Frentzen, M., et al. (2012). Development of ultra-high erucic acid oil in the industrial oil crop *Crambe abyssinica*. *Plant Biotechnol. J.* 10, 862–870. doi: 10.1111/j.1467-7652.2012.00709.x

Lu, C., Xin, Z., Ren, Z., Miquel, M., and Browse, J. (2009). An enzyme regulating triacylglycerol composition is encoded by the ROD1 gene of *Arabidopsis*. *Proc. Natl. Acad. Sci.* 106, 18837–18842. doi: 10.1073pnas.0908848106

Lu, S., Aziz, M., Sturtevant, D., Chapman, K. D., and Guo, L. (2020). Heterogeneous distribution of erucic acid in *Brassica napus* seeds. *Front. Plant Sci.* 10:1744. doi: 10.3389/fpls.2019.01744

Lu, S., Sturtevant, D., Aziz, M., Jin, C., Li, Q., Chapman, K. D., et al. (2018). Spatial analysis of lipid metabolites and expressed genes reveals tissue-specific heterogeneity of lipid metabolism in high-and low-oil *Brassica napus* L. seeds. *Plant J.* 94, 915–932. doi: 10.1111/tpj.13959

Marmon, S., Sturtevant, D., Herrfurth, C., Chapman, K., Stymne, S., and Feussner, I. (2017). Two acyltransferases contribute differently to linolenic acid levels in seed oil. *Plant Physiol.* 173, 2081–2095. doi: 10.1104/pp.16.01865

Masson-Delmotte, V., Zhai, P., Pörtner, H.-O., Roberts, D., Skea, J., Shukla, P. R., et al. (eds) (2018). *IPCC, 2018: Global Warming of 1.5°C. An IPCC Special Report on the Impacts of Global Warming of 1.5°C Above Pre-Industrial Levels and Related Global Greenhouse Gas Emission Pathways, in the Context of Strengthening the Global Response to the Threat of Climate Change, Sustainable Development, and Efforts to Eradicate Poverty*. Cambridge: Cambridge University Press.

Mc Intyre, G. I., and Best, K. F. (1978). Studies on the flowering of *Thlaspi arvense* L. IV. Genetic and ecological differences between early-and late-flowering strains. *Bot. Gaz.* 139, 190–195. doi: 10.1086/336986

McGinn, M., Phippen, W. B., Chopra, R., Bansal, S., Jarvis, B. A., Phippen, M. E., et al. (2019). Molecular tools enabling pennycress (*Thlaspi arvense*) as a model plant and oilseed cash cover crop. *Plant Biotechnol. J.* 17, 776–788.

Menard, G. N., Moreno, J. M., Bryant, F. M., Munoz-Azcarate, O., Kelly, A. A., Hassani-Pak, K., et al. (2017). Genome wide analysis of fatty acid desaturation and its response to temperature. *Plant Physiol.* 173, 1594–1605. doi: 10.1104/pp.16.01907

Millar, A. A., and Kunst, L. (1997). Very-long-chain fatty acid biosynthesis is controlled through the expression and specificity of the condensing enzyme. *Plant J.* 12, 121–131. doi: 10.1046/j.1365-313X.1997.12010121.x

Moser, B. R., Knothe, G., Vaughn, S. F., and Isbell, T. A. (2009). Production and evaluation of biodiesel from field pennycress (*Thlaspi arvense* L.) oil. *Energy Fuels* 23, 4149–4155. doi: 10.1021/ef900337g

Mousavi-Avval, S. H., and Shah, A. (2020). Techno-economic analysis of pennycress production, harvest and post-harvest logistics for renewable jet fuel. *Renew. Sustain. Energy Rev.* 123:109764. doi: 10.1016/j.rser.2020.109764

Neumann, N. G., Nazarenus, T. J., Aznar-Moreno, J. A., Rodriguez-Aponte, S. A., Veintidos, V. A. M., Comai, L., et al. (2021). Generation of camelina mid-oleic acid seed oil by identification and stacking of fatty acid biosynthetic mutants. *Ind. Crops Prod.* 159:113074. doi: 10.1016/j.indcrop.2020.113074

Nguyen, H. T., Silva, J. E., Podicheti, R., Macrander, J., Yang, W., Nazarenus, T. J., et al. (2013). Camelina seed transcriptome: a tool for meal and oil improvement and translational research. *Plant Biotechnol. J.* 11, 759–769. doi: 10.1111/pbi.12068

Nguyen, V. C., Nakamura, Y., and Kanehara, K. (2019). Membrane lipid polyunsaturation mediated by FATTY ACID DESATURASE 2 (FAD2) is involved in endoplasmic reticulum stress tolerance in *Arabidopsis thaliana*. *Plant J.* 99, 478–493. doi: 10.1111/tpj.14338

Okuley, J., Lightner, J., Feldmann, K., Yadav, N., and Lark, E. (1994). *Arabidopsis FAD2* gene encodes the enzyme that is essential for polyunsaturated lipid synthesis. *Plant Cell* 6, 147–158. doi: 10.1105/tpc.6.1.147

Peng, Q., Hu, Y., Wei, R., Zhang, Y., Guan, C., Ruan, Y., et al. (2010). Simultaneous silencing of *FAD2* and *FAE1* genes affects both oleic acid and erucic acid contents in *Brassica napus* seeds. *Plant Cell Rep.* 29, 317–325. doi: 10.1007/s00299-010-0823-y

Phippen, W. B., and Phippen, M. E. (2012). Soybean seed yield and quality as a response to field pennycress residue. *Crop Sci.* 52, 2767–2773. doi: 10.2135/cropsci2012.03.0192

Pyott, D. E., Sheehan, E., and Molnar, A. (2016). Engineering of CRISPR/Cas9-mediated potyvirus resistance in transgene-free *Arabidopsis* plants. *Mol. Plant Pathol.* 17, 1276–1288. doi: 10.1111/mpp.12417

Rolletschek, H., Schwender, J., König, C., Chapman, K. D., Romsdahl, T., Lorenz, C., et al. (2020). Cellular plasticity in response to suppression of storage proteins in the *Brassica napus* embryo. *Plant Cell* 32, 2383–2401. doi: 10.1105/tpc.19.00879

Rossak, M., Smith, M., and Kunst, L. (2001). Expression of the *FAE1* gene and *FAE1* promoter activity in developing seeds of *Arabidopsis thaliana*. *Plant Mol. Biol.* 46, 717–725. doi: 10.1023/A:1011603923889

Ruiz-Núñez, B., Pruimboom, L., Dijck-Brouwer, D. A. J., and Muskiet, F. A. J. (2013). Lifestyle and nutritional imbalances associated with Western diseases: causes and consequences of chronic systemic low-grade inflammation in an evolutionary context. *J. Nutr. Biochem.* 24, 1183–1201. doi: 10.1016/j.jnutbio.2013.02.009

Sedbrook, J. C., and Durrett, T. P. (2020). Pennycress, carbon wise: labeling experiments reveal how pennycress seeds efficiently incorporate carbon into biomass. *J. Exp. Bot.* 71, 2842–2846. doi: 10.1093/jxb/eraa136

Sedbrook, J. C., Phippen, W. B., and Marks, M. D. (2014). New approaches to facilitate rapid domestication of a wild plant to an oilseed crop: example pennycress (*Thlaspi arvense* L.). *Plant Sci.* 227, 122–132. doi: 10.1016/j.plantsci.2014.07.008

Selling, G. W., Hojilla-Evangelista, M. P., Evangelista, R. L., Isbell, T. A., Price, N., and Doll, K. M. (2013). Extraction of proteins from pennycress seeds and press cake. *Ind. Crops Prod.* 41, 113–119. doi: 10.1016/j.indcrop.2012.04.009

Serrano, M., Oliveros, R., Sánchez, M., Moraschini, A., Martínez, M., and Aracil, J. (2014). Influence of blending vegetable oil methyl esters on biodiesel fuel properties: oxidative stability and cold flow properties. *Energy* 65, 109–115. doi: 10.1016/j.energy.2013.11.072

Sharma, N., Cram, D., Huebert, T., Zhou, N., and Parkin, I. A. (2007). Exploiting the wild crucifer *Thlaspi arvense* to identify conserved and novel genes expressed during a plant's response to cold stress. *Plant Mol. Biol.* 63, 171–184. doi: 10.1007/s11103-006-9080-4

Shi, J., Lang, C., Wang, F., Wu, X., Liu, R., Zheng, T., et al. (2017). Depressed expression of *FAE1* and *FAD2* genes modifies fatty acid profiles and storage compounds accumulation in *Brassica napus* seeds. *Plant Sci.* 263, 177–182. doi: 10.1016/j.plantsci.2017.07.014

Sia, C. B., Kansedo, J., Tan, Y. H., and Lee, K. T. (2020). Evaluation on biodiesel cold flow properties, oxidative stability and enhancement strategies: a review. *Biocatal. Agric. Biotechnol.* 24:101514. doi: 10.1016/j.bcab.2020.101514

Simopoulos, A. P. (ed.) (2011). Healthy agriculture, healthy nutrition, healthy people. *World Rev. Nutr. Diet.* 102, 10–21. doi: 10.1159/000327785

Singh, S. P., and Singh, D. (2010). Biodiesel production through the use of different sources and characterization of oils and their esters as the substitute of diesel: a review. *Renew. Sust. Energ. Rev.* 14, 200–216. doi: 10.1016/j.rser.2009.07.017

Sivaraman, I., Arumugam, N., Sodhi, Y. S., Gupta, V., Mukhopadhyay, A., Pradhan, A. K., et al. (2004). Development of high oleic and low linoleic acid transgenics in a zero erucic acid *Brassica juncea* L. (Indian mustard) line by antisense suppression of the *fad2* gene. *Mol. Breed.* 13, 365–375. doi: 10.1023/B:MOLB.0000034092.47934.d6

Sotelo-Boyás, R., Trejo-Zárraga, F., and Hernández-Loyo, F. (2012). Hydroconversion of triglycerides into green liquid fuels. *IntechOpen* 8:199. doi: 10.5772/48710

Steinert, J., Schiml, S., Fauser, F., and Puchta, H. (2015). Highly efficient heritable plant genome engineering using Cas9 orthologues from *Streptococcus thermophilus* and *Staphylococcus aureus*. *Plant J.* 84, 1295–1305. doi: 10.1111/tpj.13078

Stournas, S., Lois, E., and Serdari, A. (1995). Effects of fatty acid derivatives on the ignition quality and cold flow of diesel fuel. *J. Am. Oil Chem. Soc.* 72, 433–437. doi: 10.1007/BF02636084

Sturtevant, D., Aziz, M., and Chapman, K. D. (2018). Visualizing the oilseed lipidome. *Inform* 29, 21–24. doi: 10.21748/inform.04.2018.21

Sturtevant, D., Lee, Y. J., and Chapman, K. D. (2016). Matrix assisted laser desorption/ionization-mass spectrometry imaging (MALDI-MSI) for direct visualization of plant metabolites in situ. *Curr. Opin. Biotechnol.* 37, 53–60. doi: 10.1016/j.copbio.2015.10.004

Sturtevant, D., Romsdahl, T. B., Yu, X. H., Burks, D. J., Azad, R. K., Shanklin, J., et al. (2019). Tissue-specific differences in metabolites and transcripts contribute to the heterogeneity of ricinoleic acid accumulation in *Ricinus communis* L.(castor) seeds. *Metabolomics* 15:6. doi: 10.1007/s11306-018-1464-3

Tsogtbaatar, E., Cocuron, J. C., and Alonso, A. P. (2020). Non-conventional pathways enable pennycress (*Thlaspi arvense* L.) embryos to achieve high efficiency of oil biosynthesis. *J. Exp. Bot.* 71, 3037–3051. doi: 10.1093/jxb/eraa060

USDA, United States Department of Agriculture Foreign Agriculture Services (2013). *Data & Analysis*. Available online at: https://www.fas.usda.gov/data/oilseeds-world-markets-and-trade and http://www.indexmundi.com/agriculture/?commodity=soybean-meal (accessed 2020).

Verma, P., Sharma, M. P., and Dwivedi, G. (2016). Evaluation and enhancement of cold flow properties of palm oil and its biodiesel. *Energy Rep.* 2, 8–13. doi: 10.1016/j.egyr.2015.12.001

Volkova, N., Li, X., Zhu, L. H., and Adlercreutz, P. (2016). Combination of modern plant breeding and enzyme technology to obtain highly enriched erucic acid from Crambe oil. *Sustain. Chem. Process.* 4:1. doi: 10.1186/s40508-016-0045-x

Vollmann, J., and Rajcan, I. (2009). "Oil crop breeding and genetics," in *Oil Crops*, eds J. Vollmann and I. Rajcan (New York, NY: Springer), 1–30. doi: 10.1007/978-0-387-77594-4_1

Weber, H. (2002). Fatty acid-derived signals in plants. *Trends Plant Sci.* 7, 217–224. doi: 10.1016/S1360-1385(02)02250-1

Wójtowicz, M., and Wójtowicz, A. (2020). The effect of climate change on linolenic fatty acid in oilseed rape. *Agronomy* 10:2003. doi: 10.3390/agronomy10122003

Woodfield, H. K., Sturtevant, D., Borisjuk, L., Munz, E., Guschina, I. A., Chapman, K., et al. (2017). Spatial and temporal mapping of key lipid species in *Brassica napus* seeds. *Plant Physiol.* 173, 1998–2009. doi: 10.1104/pp.16.01705

Yu, X.-H., Cai, Y., Keereetaweep, J., Wei, K., Chai, J., Deng, E., et al. (2021). Biotin attachment domain-containing proteins mediate hydroxy fatty acid-dependent inhibition of acetyl CoA carboxylase. *Plant Physiol.* kiaa109. doi: 10.1093/plphys/kiaa109

Zhang, J., Liu, H., Sun, J., Li, B., Zhu, Q., Chen, S., et al. (2012). *Arabidopsis* fatty acid desaturase FAD2 is required for salt tolerance during seed germination and early seedling growth. *PLoS One* 7:e30355. doi: 10.1371/journal.pone.0030355

Conflict of Interest: Illinois State University has entered a licensing agreement with CoverCress, Inc. for use of the *fae1* germplasm.

Copyright © 2021 Jarvis, Romsdahl, McGinn, Nazarenus, Cahoon, Chapman and Sedbrook. This is an open-access article distributed under the terms of the Creative Commons Attribution License (CC BY). The use, distribution or reproduction in other forums is permitted, provided the original author(s) and the copyright owner(s) are credited and that the original publication in this journal is cited, in accordance with accepted academic practice. No use, distribution or reproduction is permitted which does not comply with these terms.

frontiers in Plant Science

REVIEW
published: 22 April 2021
doi: 10.3389/fpls.2021.639276

Lipid Droplets in Unicellular Photosynthetic Stramenopiles

*Nolwenn Guéguen, Damien Le Moigne, Alberto Amato, Juliette Salvaing and Eric Maréchal**

Laboratoire de Physiologie Cellulaire et Végétale, INRAE, CNRS, CEA, IRIG, CEA Grenoble, Université Grenoble Alpes, Grenoble, France

The Heterokonta or Stramenopile phylum comprises clades of unicellular photosynthetic species, which are promising for a broad range of biotechnological applications, based on their capacity to capture atmospheric CO_2 via photosynthesis and produce biomolecules of interest. These molecules include triacylglycerol (TAG) loaded inside specific cytosolic bodies, called the lipid droplets (LDs). Understanding TAG production and LD biogenesis and function in photosynthetic stramenopiles is therefore essential, and is mostly based on the study of a few emerging models, such as the pennate diatom *Phaeodactylum tricornutum* and eustigmatophytes, such as *Nannochloropsis* and *Microchloropsis* species. The biogenesis of cytosolic LD usually occurs at the level of the endoplasmic reticulum. However, stramenopile cells contain a complex plastid deriving from a secondary endosymbiosis, limited by four membranes, the outermost one being connected to the endomembrane system. Recent cell imaging and proteomic studies suggest that at least some cytosolic LDs might be associated to the surface of the complex plastid, via still uncharacterized contact sites. The carbon length and number of double bonds of the acyl groups contained in the TAG molecules depend on their origin. *De novo* synthesis produces long-chain saturated or monounsaturated fatty acids (SFA, MUFA), whereas subsequent maturation processes lead to very long-chain polyunsaturated FA (VLC-PUFA). TAG composition in SFA, MUFA, and VLC-PUFA reflects therefore the metabolic context that gave rise to the formation of the LD, either via an early partitioning of carbon following FA *de novo* synthesis and/or a recycling of FA from membrane lipids, e.g., plastid galactolipids or endomembrane phosphor- or betaine lipids. In this review, we address the relationship between cytosolic LDs and the complex membrane compartmentalization within stramenopile cells, the metabolic routes leading to TAG accumulation, and the physiological conditions that trigger LD production, in response to various environmental factors.

Keywords: heterokont, stramenopile, *Nannochloropsis*, *Microchloropsis*, *Phaeodactylum*, lipid droplet (LD), triacylglycerol (TAG), seipin

OPEN ACCESS

Edited by:
Peter J. Lammers, Arizona State University, United States

Reviewed by:
Taraka Dale, Biosciences Division, Los Alamos National Laboratory, United States
Inna Khozin-Goldberg, Ben-Gurion University of the Negev, Israel
Ansgar Gruber, Institute of Parasitology, Academy of Sciences of the Czech Republic (ASCR), Czechia

***Correspondence:**
Eric Maréchal
eric.marechal@cea.fr

Specialty section:
This article was submitted to Marine and Freshwater Plants, a section of the journal Frontiers in Plant Science

Received: *08 December 2020*
Accepted: *17 March 2021*
Published: *22 April 2021*

Citation:
Guéguen N, Le Moigne D, Amato A, Salvaing J and Maréchal E (2021) Lipid Droplets in Unicellular Photosynthetic Stramenopiles. Front. Plant Sci. 12:639276. doi: 10.3389/fpls.2021.639276

INTRODUCTION

Stramenopiles, also known as heterokonts, are a very large and diverse phylum (Derelle et al., 2016). They are originally defined as eukaryotic protists producing asymmetrically biflagellated zoospores, characterized by an anterior flagellum bearing ciliary hairs and a short posterior one (Cavalier-Smith, 2018). They include more than 100,000 species ranging from microscopic unicellular

organisms to large multicellular organisms such as the giant seaweeds of the kelp forest. Most of the groups belonging to this phylum are photosynthetic, but it also includes some colorless non-photosynthetic stramenopiles such as Thraustochytrids populating a variety of habitats from polar areas to tropical mangroves (Fossier Marchan et al., 2018; Strassert et al., 2019).

Efforts to propose a consensus eukaryotic Tree of Life (eToL) have benefited from the progress in phylogenomics developed in the past decades and the recent addition of evolutionarily key protist taxa. In the latest eToL, based almost entirely on multigene molecular phylogenies (**Figure 1**; Burki et al., 2020), microalgae cluster in numerous supergroups. Previously, all organisms bearing a red algal-derived plastid were assigned to Chromalveolata following the assumption that their plastids had been acquired from a common ancestor. Nowadays, this hypothesis is controversial, with a reassignment of Chromalveolata lines into TSAR (telonemids, stramenopiles, alveolates, and Rhizaria), Haptista, and Cryptista. Stramenopiles belong to the TSAR supergroup.

Oleaginous stramenopile species, such as the diatom *Phaeodactylum tricornutum* and the eustigmatophyte *Nannochloropsis s.l.* (*sensu lato*, i.e., including the recently described genus *Microchloropsis,* Fawley et al., 2015) have attracted the attention for a broad range of potential biotechnological applications. Oleaginous strains accumulate oil rich in triacylglycerol (TAG), whose fatty acids (FAs) comprise long-chain saturated or monounsaturated FAs (SFA, MUFA, with 16 or 18 carbons), and very long-chain polyunsaturated FA (VLC-PUFA, with 20 or 22 carbons and up to five or six double bonds). TAGs enriched in SFA and MUFA are often considered as a feedstock for biofuels and green chemistry (Lupette and Maréchal, 2018), whereas TAGs enriched in VLC-PUFA are valuable for feed, food, and human health (Lupette and Benning, 2020). Understanding the physiological contexts leading to the formation of TAG with various FA composition is therefore essential.

In this review, we summarize the current knowledge on the relationship between cytosolic lipid droplets (LDs) and the complex membrane compartmentalization within stramenopile cells, the metabolic routes leading to TAG accumulation, and the physiological conditions in which LDs are produced, in response to various environmental factors.

EVOLUTION AND PLASTID ARCHITECTURE IN STRAMENOPILES

The Origin of Secondary Plastids in Stramenopiles

Eukaryotes acquired photosynthesis through the engulfment of a photosynthetic cyanobacterium (primary endosymbiosis) or of another photosynthetic eukaryote (secondary endosymbiosis). The engulfed organisms underwent genetic reductions, a loss of autonomy to such an extent that they fully integrated the host cell, giving rise to organelles, usually photosynthetic, collectively termed "plastids." The initial acquisition of a cyanobacterium by an unknown ancestral heterotrophic eukaryote occurred around 1 to 1.5 billion years ago (Jensen and Leister, 2014) leading to the emergence of the "primary plastid"—the so-called chloroplast (**Figure 2**). This view is now considered as partly incomplete, since numerous chloroplastic proteins, including the majority of enzymes involved in membrane lipid biosynthesis, are of non-cyanobacterial origin (Petroutsos et al., 2014; Cenci et al., 2017; Sato and Awai, 2017; Marechal, 2018). It is thus considered that other prokaryotes were present with the ancestral cyanobacterium and contributed to the settlement and integration of the structure that eventually became the primary chloroplast, as we know it today (Cenci et al., 2017). Unicellular organisms possessing a primary plastid all derive from the same first endosymbiosis event. They are called Archaeplastida (Adl et al., 2005) and radiated into three major lineages, the Glaucophyta, the Rhodophyceae or red algae, and the Chloroplastida (Adl et al., 2005), also known as Viridiplantae (Cavalier-Smith, 1981). Recently, Li et al. (2020) described the new phylum/division Prasinodermophyta and demonstrated that Prasinodermophyta belongs to Viridiplantae (Li et al., 2020).

Secondary endosymbiosis refers to the acquisition of a secondary plastid by eukaryote-to-eukaryote endosymbiosis (Dorell et al., 2017). The engulfed organism is indeed a photosynthetic eukaryote containing a primary plastid (**Figure 2**). Secondary endosymbiosis is thought to have occurred several times during evolution and has been performed by heterotroph eukaryotes, consequently becoming phototrophs (Reyes-Prieto et al., 2007). Higher-order endosymbiosis events also took place during evolution and involved more complex interactions, also leading to complex plastid formation (Keeling, 2010, 2013; Jackson et al., 2012; Oborník, 2019).

Nannochloropsis s.l. and *P. tricornutum* both stem from two endosymbiosis events, where the last endosymbiosis involved the engulfment of a microalga from the red lineage. However, the second endosymbiosis may imply different red algae and/or different heterotrophic cells (Keeling, 2013), as well as distinct patterns of horizontal gene transfers (Fan et al., 2020; Vancaester et al., 2020). Thus, although phylogenetically close, their metabolisms might differ.

The Complex Plastids of *Phaeodactylum* and *Nannochloropsis s.l.* Present a Nucleus-Plastid Continuum

A common feature of complex plastids is the presence of more than two surrounding membranes. Some complex plastids can even still contain a relic of the nucleus from the ancestral eukaryotic endosymbiont, called the nucleomorph (Maier et al., 1991; Gilson et al., 2006; Curtis et al., 2012). *Nannochloropsis s.l.* and *P. tricornutum* possess plastids bounded by four membranes and lack the nucleomorph. The lipid composition of plastidial membranes is still unknown and is often inferred based on their evolutionary origins.

The origin of the two innermost membranes of the plastid is not or little debated, and assumed to correspond to the chloroplast envelope of the symbiont, called the

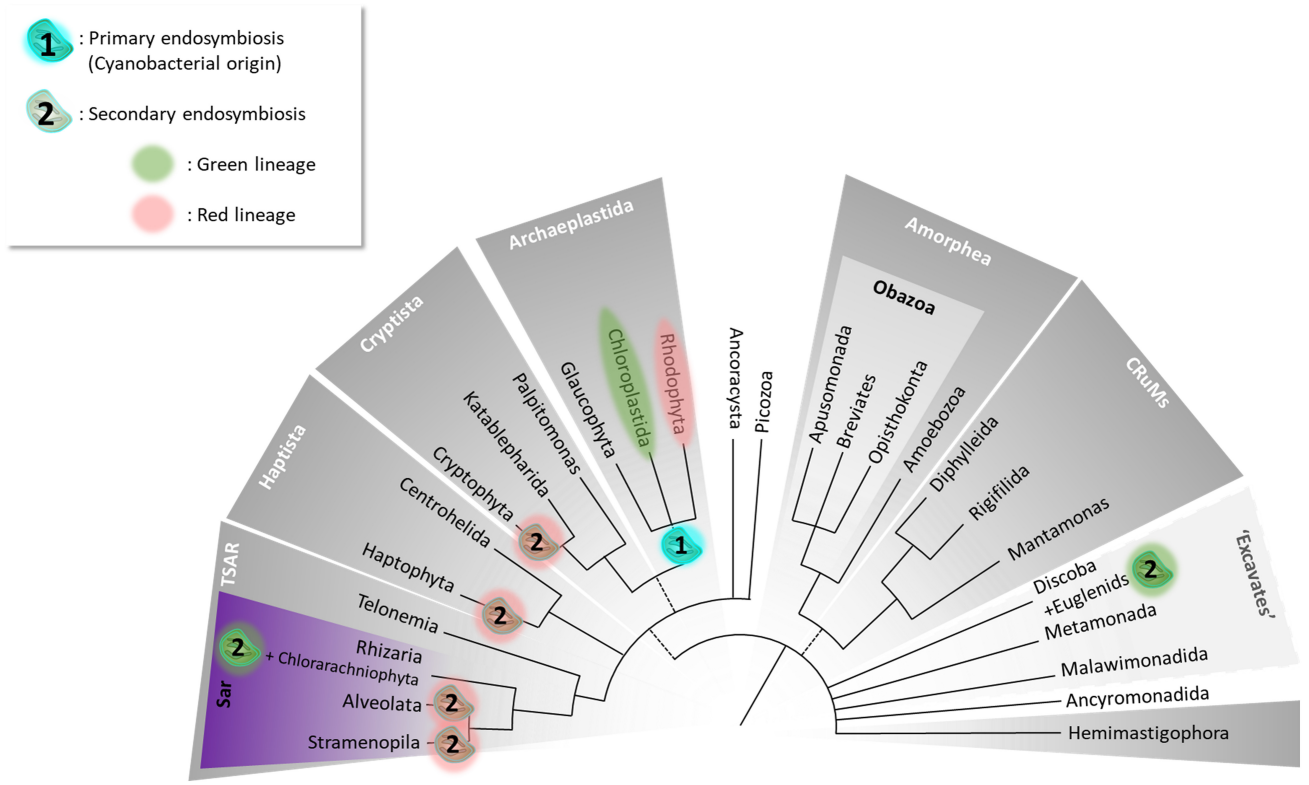

FIGURE 1 | The Tree of Eukaryotes. The colored groupings correspond to currently defined "supergroups." Unresolved branching orders among lineages are shown as multifurcations. Broken lines reflect minor uncertainties about the monophyly of certain groups. (1) Unique primary endosymbiosis event; (2) multiple secondary endosymbiosis events identified by Oborník (2019) as "complex endosymbioses." The tree topology was adapted from Burki et al. (2020).

outer and inner envelope membranes (P-oEM and P-iEM, respectively). However, different suppositions have been made about the origin of the additional bounding membranes. The outermost membrane, called the epiplastidial membrane (EpM), could derive from the host phagocytic membrane. Underneath, the periplastidial membrane (PPM) is considered to derive from the symbiont plasma membrane (Grosche et al., 2014). Alternatively, it has been hypothesized that the outer envelope membranes of red complex plastids could derive from the host ER (Gould et al., 2015). Interestingly, a vesicular network forming a "blob-like" structure has been detected between the PPM and the EpM in *P. tricornutum*, but its function is still elusive (Kilian and Kroth, 2004; Flori et al., 2016).

The EpM can also be found under the name "chloroplastic endoplasmic reticulum," as its particularity in *P. tricornutum* and *Nannochloropsis s.l.* is to be continuous with the ER and the outer membrane of the nuclear envelope, forming a nucleus-plastid Continuum (NPC) (Murakami and Hashimoto, 2009; Flori et al., 2016). In addition, membrane contact sites were detected between the inner membrane of the nuclear envelope and the PPM (Flori et al., 2016). Such a tight association between the plastid and the nucleus is hypothesized to facilitate exchanges of small molecules, RNAs, proteins, etc.

Based on the suggested origin of the four membranes around the secondary plastid, it is plausible but still not demonstrated that the two innermost membranes contain plastid-specific lipids such as monogalactosyldiacylglycerol, digalactosyldiacylglycerol, and sulfoquinovosyldiacylglycerol (MGDG, DGDG, and SQDG, respectively) (Boudière et al., 2014), whereas the two outermost membranes may be related to the ER lipid composition, with lipids such as phosphatidylcholine (PC) and betaine lipids (Boudière et al., 2014; Dolch and Maréchal, 2015).

The events that led to the emergence of secondary plastids are critical milestones in the evolution of eukaryotes, and their impact on cell biology is still poorly understood. The structure of the complex/secondary plastids differs radically from other well-known semi-autonomous organelles such as the mitochondria or "classical" chloroplasts. The tight structural and physical interactions of the secondary plastid with other organelles of the endomembrane system, such as the ER, the nucleus, or uncharacterized networks of vesicles, challenge our understanding of cellular processes usually assumed to be restricted to the ER. This holds particularly true for the formation of LDs in oleaginous stramenopiles. Such missing knowledge is critical, when trying to optimize stramenopile algae for biotechnological purposes.

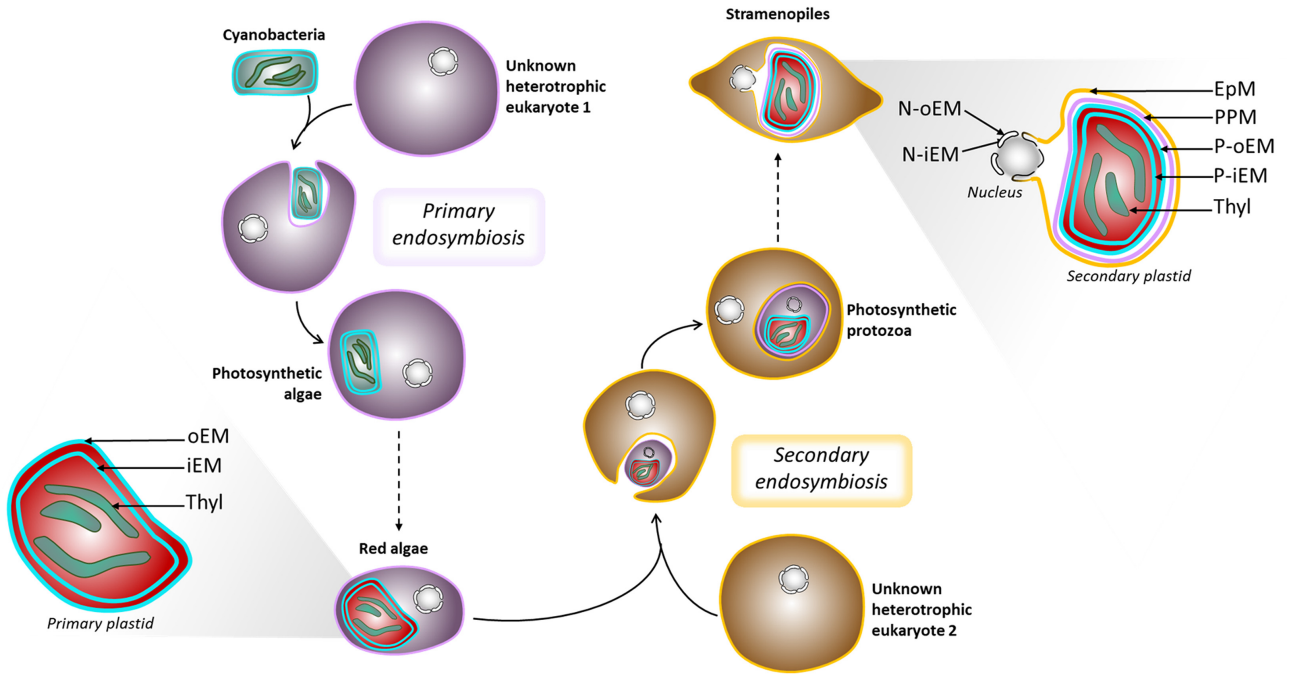

FIGURE 2 | Schematic representation of plastid evolution. Schematic representation of primary and secondary endosymbiosis, and organelle architecture. EpM, epiplastidial membrane; PPM, periplastidial membrane; P-oEM and P-iEM, plastid outer and inner envelope membranes respectively; Thyl, thylakoids; N-oEM and P-iEM, nucleus outer and inner envelope membranes respectively.

COMPOSITION OF THE LIPID DROPLET, A STORAGE FOR TRIACYLGLYCEROL AND OTHER LIPOPHILIC COMPOUNDS

A Limiting Monolayer Made of Glyco-, Phospho-, and Betaine Lipids

While cytosolic LDs are classically described to be limited by a phospholipid monolayer in non-photosynthetic eukaryotes (Tauchi-Sato et al., 2002; Bartz et al., 2007), this is not always the case for some photosynthetic microalgae recently characterized, from Chlorophytes to Stramenopila (Peled et al., 2011; Tsai et al., 2015; Lupette et al., 2019). Glycerolipid composition of LDs in *P. tricornutum* has been described on a fraction purified with great attention (Lupette et al., 2019). Besides the 99.0 mol% of TAG, it comprises a betaine lipid, diacylglycerylhydroxymethyl-*N*,*N*,*N*-trimethyl-beta-alanine or DGTA (0.4 mol%), a plastid sulfolipid SQDG (0.35 mol%), and a prominent phospholipid of the ER, PC (0.15 mol%). The latter three lipids probably make up the LD bounding monolayer. Brassicasterol is also copurified with LDs, presumed to be included in the limiting monolayer, where it represents almost 5 mol% of total sterols and glycerolipids (Lupette et al., 2019). Such a profile differs from the general assumption of LD monolayer exclusively composed of phospholipids. A set of possible hypotheses about the site of biogenesis of lipid droplets is discussed further below.

To our knowledge, lipid composition of the LD membrane in *Nannochloropsis s.l.* has yet to be described, although it has been referred to as a phospholipid monolayer (Vieler et al., 2012a). In the light of recent studies in microalgae, it appears of pivotal importance to verify lipid composition in *Nannochloropsis s.l.* LDs as well (Peled et al., 2011; Tsai et al., 2015; Lupette et al., 2019).

Proteins are inserted into or associated to the LD bounding lipid monolayer. Their nature and function are discussed further, later in this review.

The Core of the Lipid Droplet: More Than Triacylglycerol Molecules

The LD core is mainly made of TAGs, but pigments have also been detected, and the presence of other hydrophobic compounds cannot be excluded. Cytological studies very often highlight the detection of pigmented LDs in the cytosol in a large variety of species, like in the green alga *Haematococcus lacustris* (as *H. pluvialis* in Peled et al., 2011; Gao et al., 2013). LDs in both *P. tricornutum* and *Nannochloropsis s.l.* also contain carotenoids (Vieler et al., 2012a; Yoneda et al., 2016; Lupette et al., 2019). Pigment detection has to be taken cautiously given some plastoglobules from the stroma of plastids may be at the origin of part of the carotenoids unavoidably contaminating cytosolic LD fractions. In *P. tricornutum*, fucoxanthin, and β-carotene are the main carotenoids in LD-enriched fractions, while only traces of other pigments were detected (Lupette et al., 2019). The light harvesting complex in *P. tricornutum* is made of fucoxanthin, chlorophyll a, and chlorophyll c. The presence of fucoxanthin and absence of chlorophylls in purified LDs suggest that in *P. tricornutum* LD, fucoxanthin may be part

of a distinct pool (Lupette et al., 2019). The function of LD pigments is currently poorly understood in stramenopiles and often considered as secondary, compared with the function of LDs as TAG reserves.

LD FORMATION, A CELL RESPONSE TO ADAPT TO A CHALLENGING ENVIRONMENT

Growth Conditions and Abiotic Parameters of the Environment Influence Lipid Droplet Formation

Several abiotic factors influence TAG accumulation in microalgae, though it is often difficult to identify which specific parameter, or combination of parameters, indeed triggers this accumulation. In standard "unstressed" conditions, light regime and intensity play a crucial role on lipid metabolism (Janssen et al., 2018, 2019b). Basically, TAG often accumulates during the light period and is consumed in the dark (Sukenik and Carmeli, 1990; Fábregas et al., 2002; Chauton et al., 2013; Poliner et al., 2015). Temperature variations were also reported to alter the extent of TAG accumulation (Pasquet et al., 2014; Gill et al., 2018). When light or temperature values exceed the tolerance threshold, becoming hence a stressing factor, TAG accumulation may be triggered (Alboresi et al., 2016). The availability of an organic carbon source can also increase the magnitude of TAG production in unstressed conditions. *P. tricornutum* and *Nannochloropsis s.l.* can grow in mixotrophy, with the provision of additional carbon sources like glycerol, glucose, starch, arginine, and acetate, each with a distinct effect on TAG accumulation (Cerón García et al., 2000; Fang et al., 2004; Villanova et al., 2017; Menegol et al., 2019; Munz et al., 2020).

Various environmental stresses can affect microalgal physiology and lead to the production of LDs in the cytosol. Nutrient starvation is widely studied (Vieler et al., 2012b; Simionato et al., 2013; Mayers et al., 2014; Abida et al., 2015; Mühlroth et al., 2017; Liang et al., 2019a,b), nitrogen in particular (Hu et al., 2008). Phosphate and nitrate limitations are supposed to induce an imbalance between carbon and the missing nutrient, with a carbon excess diverted to storage forms including TAG. Cells exposed to nitric oxide, hydrogen peroxide, and other oxidative reactive species, also respond by increasing TAG accumulation in LD (Dolch et al., 2017a; Conte et al., 2018). A plethora of chemicals proved efficient in triggering TAG accumulation in *P. tricornutum* (Conte et al., 2018) and *Nannochloropsis s.l.* (Franz et al., 2013).

Triacylglycerol Formation, From *de novo* Synthesis to Lipid Remodeling

Nitrogen starvation can trigger a rapid TAG accumulation in organisms spanning from bacteria (Santucci et al., 2019), green algae (Goncalves et al., 2016), dinoflagellates (Weng et al., 2015), to different stramenopiles (Li et al., 2014; Abida et al., 2015; Jia et al., 2015; Dellero et al., 2018b; Janssen et al., 2019a). The mechanisms of TAG synthesis are well described, and two routes lead to the accumulation of neutral lipids. Part of it stems from *de novo* biosynthesis, the rest from intense lipid remodeling.

Triacylglycerol molecules are composed of three FAs esterified onto a glycerol backbone. The Kennedy pathway that leads to TAG *de novo* formation, also called the acyl-CoA-dependent pathway, is partially involved in the synthesis of all other glycerolipids. The series of reactions for this pathway can occur in both the ER, using acyl-CoA (canonical Kennedy pathway), and the plastid, using acyl-ACP as substrate (Kennedy-like pathway) (Kennedy and Weiss, 1956). The last step of TAG formation can alternatively occur using FA transferred from an existing membrane glycerolipid used as a donor. This pathway is then termed acyl-CoA independent (Dahlqvist et al., 2000).

Common Initial Steps for the Formation of Membrane Glycerolipids and Triacylglycerol

The scaffolding starts with the esterification of an acyl-CoA at position *sn*-1 of a glycerol-3-phosphate (G3P) by a glycerol-3-phosphate-*sn*1-acyl-CoA-acyltransferase (GPAT) leading to lysophosphatidic acid (LPA). The addition of a second acyl-group at position sn-2 by a lysophosphatidic acid acyltransferase (LPAT) produces phosphatidic acid (PA). PA can be used either to synthesize phosphatidylglycerol (PG) via a cytidine diphosphate diacylglycerol intermediate or dephosphorylated by a PA phosphatase (PAP) to produce diacylglycerol (DAG). Most glycerolipids can be synthesized from DAG. In the plastid, DAG is the substrate for SQDG and MGDG syntheses, while in the ER, DAG is the substrate for the synthesis of PC, phosphatidylethanolamine (PE), and betaine lipids. The last step of TAG synthesis is commonly performed in the ER by a DAG acyltransferase (DGAT) that esterifies a third acyl-CoA in position *sn-3*. DAG used in the last step of the Kennedy pathway can stem from *de novo* synthesis as described here, but also from the recycling of membrane lipids (Li-Beisson et al., 2010, 2019; Boudière et al., 2012; Petroutsos et al., 2014).

Schematically, FAs *de novo* synthesized in the plastid of *P. tricornutum* and *Nannochloropsis s.l.* contain 16 carbons, whereas longer chained FAs are produced by an elongation process occurring in the ER (Dolch et al., 2017b). The early steps of the Kennedy-like pathway in the plastid is often referred to as the prokaryotic pathway, although this term was recently contested (Sato and Awai, 2017), and membrane glycerolipids characterized by 16-carbon FAs at position *sn*-2 are considered to harbor a prokaryotic signature. Elongation of FAs to 18 or more carbons involves the export of C16 from the plastid to the ER. The ER pathway is often referred to as the eukaryotic pathway, and leads to glycerolipids with various signatures, depending on the species. While such a distinction between topologically distinct pathways is quite evident in plants (Roughan and Slack, 1982), in most stramenopiles, a more thorough investigation is needed to depict the exact origin of the different building blocks of glycerolipids (Mühlroth et al., 2013).

In *Nannochloropsis s.l.* and *P. tricornutum*, both prokaryotic (plastid) and eukaryotic (ER) pathways seem to provide DAG substrates for TAG biosynthesis (Radakovits et al., 2012; Vieler et al., 2012b). A recent analysis in *N. oceanica* has focused on the four copies of LPATs, addressing their subcellular location

and function in the synthesis of eukaryotic precursors, based on single and double knockout (KO) studies (Nobusawa et al., 2017). NoLPAT1 proved to be mainly involved in the transfer of 16:1 to the *sn*-2 position of LPA used for the synthesis of membrane glycerolipids, particularly PC and DGTS. This isoform does not influence TAG biosynthesis. By contrast, NoLPAT4 transfers 16:0 to the *sn*-2 position of LPA purely dedicated to TAG. Eventually, NoLPAT2 and NoLPAT3 are mainly involved in the transfer of 18:1 at the *sn*-2 position of precursors used for PC, PE, and of 16:0 at the *sn*-2 position of precursors for TAG (Nobusawa et al., 2017). Thus, in the early step of the Kennedy pathway, LPAT isoforms seem to control the fate of the produced phosphatidic acid, upstream membrane glycerolipid, and/or TAG pathways. Based on GFP-fusion analyses, NoLPAT1 and NoLPAT2 were likely localized at the ER, whereas NoLPAT3 and NoLPAT4 were located at the periphery of cytosolic LDs (Nobusawa et al., 2017). Based on this differential pattern, the role of NoLPAT2 in TAG formation would suggest that membranes related to the ER may be a platform for LD formation, at least in the early stages of LD biogenesis. The location of NoLPAT3 and NoLPAT4 suggests that they may be involved in the production of TAG loaded in more mature LDs. The location of NoLPAT3 further suggests that some part of the membrane lipid synthesis might occur at the vicinity of LDs. The role of LPATs is therefore likely to be critical in the control of metabolic routes directed to membrane glycerolipids, TAG, or both.

In addition, DAG may derive from membrane glycerolipids, like PC, via the action of phospholipases C (PLC) or phosphatidylcholine:diacylglycerol choline transferases (PDAT). PLC is discussed further below. In *P. tricornutum*, genes coding for a putative PDAT have been predicted (Dolch et al., 2017b), but to our knowledge, not formally characterized. Their roles and possible involvement in the production of TAG substrates deserve investigation.

Acyl-coA-Dependent Pathway

DGAT enzymes catalyze the committed step from acyl-CoA and DAG to TAG. Because of its pivotal role in TAG synthesis and of the increasing importance gained by TAGs produced by oleaginous algae like *P. tricornutum* and *Nannochloropsis s.l.* in biotechnology (Ma et al., 2016; Butler et al., 2020), it is no surprise that the number of studies involving DGAT drastically raised in the last decade.

Recently, the human DGAT1 enzyme (HsDGAT1) was structurally characterized (Sui et al., 2020) by cryo-electron microscopy, revealing that the protein contains nine transmembrane helices with the amino-terminus (N-ter) spreading in the cytosol and the carboxyl-terminus (C-ter) in the ER lumen. The HsDGAT1 forms dimers via hydrogen bonds and hydrophobic interaction between the N-termini of each monomer. The dimerization is essential to the acyltransferase activity because N-ter truncated proteins, unable to dimerize, show dramatically reduced activity. The active site, His415 in HsDGAT1 (McFie et al., 2010), is embedded in a tunnel that opens up toward the cytosol formed by four transmembrane (TM) domains (**Figure 3**), and that serves the acyl-CoA binding function. Laterally, a gate was identified that opens up in between

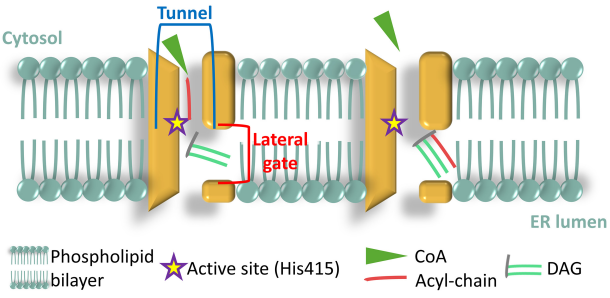

FIGURE 3 | Architecture of the membrane bound *O*-acyl transferase (MBOAT)-core of human diacylglycerol acyltransferase (DGAT1) enzyme (HsDGAT1). Adapted from Sui et al. (2020).

the two membrane sheets (**Figure 3**) and driving the DAG to the core of the dimer, where the active histidine is located (Sui et al., 2020). Such architectural structure is specific to membrane-bound *O*-acyl transferase (MBOAT) enzymes and was hence named MBOAT-core (Sui et al., 2020). DGAT1 from a green unicellular alga [*Chromochloris zofingiensis*, formerly known as *Chlorella zofingiensis* (Fucikova and Lewis, 2012)] was recently characterized and showed a similar structure of the protein and a crucial role played by its N-ter in protein activity (Xu et al., 2020). DGAT2 family has not yet been characterized in such detail. Murine DGAT2 shows two TM domains and both N- and C- termini in the cytosol (Stone et al., 2006). A highly conserved sequence (HPHG) found in all DGAT2 proteins are the possible catalytic residues (Xu et al., 2018). DGAT3 is the only cytosolic DGAT and was first characterized in peanut (*Arachis hypogaea*), AhDGAT3 (AY875644) (Saha et al., 2006) then in *Arabidopsis thaliana*, AtDGAT3 (At1g48300) (Hernández et al., 2012; Aymé et al., 2018) where it was shown to harbor a [2Fe–2S] cluster, characteristic to some ferredoxins, but whose function is still unknown (Aymé et al., 2018). Moreover, the AtDGAT3 has a chloroplast transit peptide, absent in other higher plant DGAT3.

The protist DGATs have not been yet characterized to such a deep level of detail, and the most recent review focusing solely on algal DGATs dates back to 2012 (Chen and Smith, 2012). A comprehensive review dealing with mainly plant but also algal DGAT and PDAT was recently published (Xu et al., 2018). *P. tricornutum* possesses several DGATs, namely, one PtDAGT1, five PtDGAT2, and a PtDGATX (Cui et al., 2018) or PtDGAT3 (Zhang et al., 2020), with a double wax ester synthase (WS) and DGAT function (Cui et al., 2013, 2018). All the PtDGATs were tested for activity either *in vitro* or by heterologous expression in the *Saccharomyces cerevisiae* quadruple mutant H1246.

PtDGAT1 (GenBank accession MN061782) was recently reannotated and characterized (Zhang et al., 2020). The authors showed that the original annotation Phatr3_J9794 locus on chromosome 2 lacked part of the N-ter (Guihéneuf et al., 2011). The novel annotation identified a gene composed of a 265-bp 5′-UTR, a 511-bp 3′-UTR, and a 2,271-bp coding sequence interrupted by three introns, encoding for a 756-AA protein (Zhang et al., 2020). PtDGAT1 is a cER (Zhang et al., 2020) membrane-bound protein (eight TM domains were predicted;

Guihéneuf et al., 2011) as demonstrated by topology analysis via Western blot (Cui et al., 2018). The novel annotation pointed out the presence in the N-ter of the protein of a pleckstrin homology (PH) domain (Zhang et al., 2020), involved in signaling and membrane binding. The protein shows 55% identity with *Thalassiosira pseudonana* DGT-1 (THAPSDRAFT_261279 on chromosome 2) and 35% with DGAT1 from higher plants. Its function, activity, and specificity were characterized both *in vitro* and by heterologous expression in yeast (Zhang et al., 2020). Among the tested PtDGAT, PtDGAT1 is the most active and presented a slight preference toward mono-unsaturated medium chain FA like C16:1 over saturated medium chain ones (Zhang et al., 2020). A detectable, although reduced, activity was recorded on eicosapentaenoic acid (EPA, C20:5) too. *PtDGAT1* seems to play a crucial role during nitrogen starvation, its expression being highly upregulated in a time-dependent manner at early and late starvation, i.e., when TAG cellular content was highly augmented (Guihéneuf et al., 2011; Cui et al., 2018; Zhang et al., 2020). Overexpression of PtDGAT1 in *P. tricornutum* showed little effect on cell growth, but induced a twofold accumulation of lipids (Zhang et al., 2020). In nitrogen starvation conditions, PtDGAT1 overexpressing (OE) lines redirect carbon from carbohydrates and proteins toward lipid synthesis (Zhang et al., 2020).

The PtDGAT2 family is represented by five protein coding genes in *P. tricornutum*, namely, *PtDGAT2A* (JX469835, Phatr3_49462 on chromosome 22), *PtDGAT2* [JQ837823, Phatr3_49544 on chromosome 22 henceforth referred to as *PtDGAT2B*, as in references (Gong et al., 2013; Haslam et al., 2020; Zhang et al., 2020)], *PtDGAT2C* (JX469836, Phatr3_31662 on chromosome 2), *PtDGAT2D* (JX469837, Phatr3_43469 on chromosome 1), and *PtDGAT2E* (Phatr3_EG00369 on chromosome 19) (Chen and Smith, 2012). *PtDGAT2B* is the only one that rescued the phenotype of the H1246 mutant (Gong et al., 2013; Zhang et al., 2020), had an *in vitro* activity (Zhang et al., 2020), and presented a considerable overexpression in nitrogen starvation (Gong et al., 2013; Zhang et al., 2020).

PtDGAT2B localizes at the cER, like PtDAGT1 (Zhang et al., 2020) and has been more intensively studied (Gong et al., 2013; Haslam et al., 2020; Zhang et al., 2020) compared with other PtDGAT2. It was demonstrated that *PtDGAT2B* expression varies along the growth curve in nitrogen replete condition with a peak at the end of the exponential phase (Gong et al., 2013), while in nitrogen starvation, its expression stays invariably high (Gong et al., 2013; Zhang et al., 2020). Such an expression pattern correlates quite well with the TAG accumulation. Indeed, *PtDGAT2B*-overexpressing lines, accumulate TAGs with no impaired growth in either N-replete nor N-depleted condition (Haslam et al., 2020; Zhang et al., 2020). Coincidently to TAG accumulation, *PtDGAT2B* OE slightly accumulate EPA in N-repletion and show a sharper effect on the accumulation of C16:0 and C16:1 in N-depletion compared with the WT. Analyses of TAG species in the OE lines show an increase in C48 containing TAG, suggesting that PtDGAT2B may prefer C16 species and C16-containing DAG as substrates (Haslam et al., 2020). The very low levels of TAG containing only saturated FA (C48:0) at least partially corroborates previous findings that have shown substrate specificity toward unsaturated FA (Gong et al., 2013; Zhang et al., 2020).

The role played by *PtDGAT2A*, *PtDGAT2C*, and *PtDGAT2D* in the Kennedy pathway remains uncertain because besides not complementing the phenotype of the H1246 mutant neither showing any or very low activity *in vitro*, they are all poorly expressed in both nitrogen replete and deplete conditions (Gong et al., 2013; Zhang et al., 2020).

In *P. tricornutum* genome, the locus Phatr3_J49708, encoding for a predicted protein (XM_002184438, protein ID: XP_002184474), was first isolated from cDNA (Cui et al., 2013) and characterized by heterologous expression in the H1246 mutant and *in vitro* assay (Cui et al., 2013; Zhang et al., 2020). Sequence identity and domain identification revealed that the product of Phatr3_J49708 might be identified as PtDAGT3 by homology to *Acinetobacter calcoaceticus* DGAT3 (AE529086) and because it showed poor similarity to other DGATs found in *P. tricornutum* itself or in other algal species (Cui et al., 2013). PtDGAT3 is localized to the cER (Zhang et al., 2020) unlike the cytosolic AhDGAT3 (Saha et al., 2006), and noteworthy, it presents two domains, namely, a wax ester acyltransferase and acyl-CoA:diacylglycerol acyltransferase domains (Cui et al., 2013). Intriguingly, a few years later, the same predicted protein (XP_002184474) was identified as a novel dual-function PtWS/DGAT and named PtDGATX (Cui et al., 2018). In 2020, the Phatr3_J49708 locus was investigated again and named back as a PtDGAT3 (Zhang et al., 2020). This nomenclatural inhomogeneity should be solved, but it goes beyond the aims of the present review. Nonetheless, henceforth, the Phatr3_J49708 locus product will be referred to as PtDGAT3 (Cui et al., 2013; Zhang et al., 2020). *PtDGAT3* transcript is weakly expressed compared with *PtDGAT1* and *PtDGAT2B* (Cui et al., 2018; Zhang et al., 2020), and along a growth curve, its expression peaks in the middle of the exponential phase. The overexpression of *PtDGAT3* in alga did not impair growth nor photosynthesis efficiency, though it induced a TAG accumulation in both N-replete and N-deplete conditions (Cui et al., 2018; Zhang et al., 2020), which is coherent with the DGAT activity of the protein. Moreover, expression of *PtDGAT3* in the H1246 mutant induced an accumulation, although to a lesser extent, of wax, as expected from the WS domain identified (Cui et al., 2013, 2018).

In conclusion, *P. tricornutum* shows a rather broad toolkit to esterify acyl chains onto a DAG molecule deriving from the Kennedy pathway. Different DGAT proteins presumably exhibit different substrate specificities in order to cope with the wide array of FAs synthesized by *P. tricornutum*. Nevertheless, *in vitro* enzymatic activity tests on C16:0, C16:1, and C20:5 show no striking differences among the PtDGATs (Zhang et al., 2020). It is not excluded, though, that *in vitro* as well as *in vivo* assays tested to date were not adequate to determine PtDGAT's slight differences in substrate specificity. Moreover, the set of FAs tested *in vitro* was rather reduced. It is not possible to exclude a role of the inactive PtDGAT2s in very specific conditions. DGAT involved in peculiar yet to discover functions to cope with still undetermined conditions may be the reason for a huge gene dose expansion in stramenopiles. Gene duplication in diatom is a relatively frequent event (Parks et al., 2018;

Osuna-Cruz et al., 2020) and has been suggested as one of the reasons for the undeniable success of diatoms in the world oceans (Busseni et al., 2019).

The *Nannochloropsis* and *Microchloropsis* genera show the highest number of DGAT genes (Wang D. et al., 2014; Alboresi et al., 2016), namely, two DGAT1 (1A found in *N. oceanica* IMET1, *N. oceanica* CCMP531, *M. gaditana* CCMP526, and CCAP849/5, *N. oculata* CCMP525; 1B found in IMET1, CCMP531, *N. granulata* CCMP529, and CCMP525) and 11 DGAT2 (2A through K) with a very interesting pattern of orthology. *DGAT2* genes are all present in all the strains analyzed, while *DGAT1* genes are not (Wang D. et al., 2014). The strain *N. oceanica* CCMP1779 shows only one *DGAT1* (*NoDGAT1*) and up to 12 *DGAT2* (NoDGTT1 through NoDGTT12) genes (out of which 11 show a EST support) (Vieler et al., 2012b). From phenotype restoration in the TAG-deficient *S. cerevisiae* mutant assay, it emerged that not all the proteins are able to rescue the lipid phenotype, like, e.g., NoGAT1B in *N. oceanica* IMET1 (Li et al., 2016).

Multi-omics analyses performed on several *M. gaditana* (CCAP 849/5, B-31, CCFM-01, and CCMP526) and *N. oceanica* (IMET1, CCAP1779) strains exposed to different stressors showed contrasting results. While some *DGATs* are downregulated in N-starvation, others are upregulated, and others do not change, pointing at the need of more thorough molecular physiology studies on this group of unicellular algae (Corteggiani Carpinelli et al., 2014; Li et al., 2014; Poliner et al., 2015; Alboresi et al., 2016; Xin et al., 2017; Zienkiewicz et al., 2017, 2020; Hulatt et al., 2020; Janssen et al., 2020). Different *DGAT* genes may act on different substrates and/or at different moments along the life cycle of the species, as hypothesized above for *P. tricornutum*. Disentangling the mechanism of each of the DGAT proteins may not only increase our knowledge of stramenopile metabolisms but also can be functional to biotechnological aims.

The non-photosynthetic stramenopiles *Aurantiochytrium limacinum* and *Hondaea fermentalgiana*, although being strong TAG accumulators, possess a reduced DGAT toolkit with two DGAT1 (only one in *H. fermentalgiana*), one DGAT2 and one dual-functioning DGAT/Wes (Dellero et al., 2018a; Seddiki et al., 2018; Morabito et al., 2020), likely involved in the synthesis of wax esters. Although poorly investigated, the possibility of Wes activities may be considered in photosynthetic heterokonts as well.

Acyl-CoA-Independent Pathway

Besides *de novo* synthesis via DGATs, TAGs may accumulate through glycerolipid recycling via the activity of a so-called phospholipid:diacylglycerol acyltransferase, or PDAT (Dahlqvist et al., 2000; Ma et al., 2016; Zulu et al., 2018; Falarz et al., 2020). The acyl-CoA-independent pathway consists in the transfer of an FA from the *sn*-2 position of a membrane lipid (usually PC, in non-photosynthetic organisms) to the *sn*-3 position of the glycerol backbone of DAG. This pathway was far less investigated than the acyl-CoA-dependent route in algae. Whereas in non-photosynthetic models, such as yeast, PDAT is located at the ER and using phospholipid as an acyl-donor, functional analysis of *Chlamydomonas reinhardtii* PDAT suggested a role in transferring FA groups from plastid membrane lipids as well (Yoon et al., 2012). By contrast with the vast number of DGATs, only one copy of PDAT is usually encountered in photosynthetic stramenopiles, such as *Nannochloropsis s.l.* (Dolch et al., 2017b; Nobusawa et al., 2017). On the basis of transcriptomic results, the PDAT pathway was suggested to be responsible for TAG accumulation in *M. gaditana* CCAP 849/5 alongside the DGAT-dependent synthesis (Mus et al., 2013; Yang et al., 2013; Alboresi et al., 2016). It seems that some physiological conditions may be in favor of a prominence of the DGAT- or the PDAT-dependent routes; however these conditions have not yet been characterized, and the level of possible redundancy/compensation is unknown. Thus, on the one hand, ^{13}C isotopic labeling results showed that at least in *M. gaditana* strain CCFM-01, most of the FAs in TAGs stemmed from *de novo* synthesis (Janssen et al., 2019a). On the other hand, in a knockdown (KD) line of an elongase converting 16:0-CoA into 18:0-CoA in the cytosol of *M. gaditana*, disturbing membrane glycerolipid composition, only the *MgPDAT* gene proved to be upregulated and likely responsible for the observed accumulation of TAG (Dolch et al., 2017b). The control of the acyl-CoA-independent pathway needs to be addressed in stramenopiles, as well as possible redundancy with the acyl-CoA dependent routes. Since PDAT allows a connection between TAG production and membrane lipid turnover, a role of the reorganization of cellular membranes needs also to be investigated.

Stepwise Formation of Lipid Droplet Subpopulations in *Phaeodactylum*

Lipid Droplet Biogenesis Steps

Stepwise LD formation has been mostly described in non-photosynthetic organisms (Walther et al., 2017; Nettebrock and Bohnert, 2020; Renne et al., 2020) even though recent review articles have underlined some specificities of plastid-containing organisms (Chapman et al., 2019; Ischebeck et al., 2020; Leyland et al., 2020a). Cytosolic LD biogenesis is usually described as an ER process. Briefly, TAG and sterol ester synthesis occurs between the two leaflets of the ER membrane leading to the formation of lenses once they reach a certain concentration (Choudhary et al., 2015; Thiam and Forêt, 2016). After lense growth, complex mechanisms lead to the budding of an LD from the ER membrane at specialized domains. Data from yeast as well as animals suggest that such domains are sites of both LD and peroxisome biogenesis (Joshi et al., 2018; Wang et al., 2018), thus linking the two processes. LD budding is mostly described in biophysical terms. Specific lipid composition at LD budding sites locally changes the membrane curvature (Ben M'barek et al., 2017; Choudhary et al., 2018; Santinho et al., 2020), and the introduction of an imbalance in surface tensions between the two membrane leaflets is essential for directional budding (Chorlay and Thiam, 2018; Chorlay et al., 2019). The role of proteins in the budding is therefore important to regulate local lipid composition and locally modify surface tension, as well as to stabilize the junction between the nascent LD and the ER

and to ensure the unidirectional filling of the LD. Only a few proteins involved in LD biogenesis have been identified in all eukaryotic models.

First identified in humans as responsible for the Bardinelli–Seip congenital lipodystrophy (Magré et al., 2001), the seipin protein is a key player in LD biosynthesis in all organisms in which it has been investigated (Chapman et al., 2019; Nettebrock and Bohnert, 2020; Renne et al., 2020). Seipin proteins localize in discrete ER domains that define LD biogenesis sites (Wang C.-W. et al., 2014; Wang et al., 2016; Grippa et al., 2015; Salo et al., 2016). Seipin proteins contain at least two transmembrane domains that anchor them in the ER membrane. The central luminal part is involved in seipin's oligomerization, thus forming a channel-like structure that stabilizes the ER–LD junction (Binns et al., 2010; Sui et al., 2018; Yan et al., 2018) and is essential to ensure unidirectionality of the TAG and/or sterol–ester flow from the ER to the LD (Salo et al., 2019). Moreover, in humans, such channel-like domain can interact *in vitro* with anionic phospholipids, in particular, PA (Yan et al., 2018). If confirmed *in vivo*, such an interaction could contribute to local changes in the ER membrane composition that is involved in budding, as depicted above. Finally, seipin plays a role in metabolism regulation, through its interactions with lipid biosynthesis enzymes (Boutet et al., 2009; Sim et al., 2013; Talukder et al., 2015; Pagac et al., 2016; Su et al., 2019). While yeast and animals possess only one seipin isoform, three have been identified in *Arabidopsis thaliana* (Cai et al., 2015), and it has been shown that the N-terminal tail of seipins is involved in LD size control. Seipin isoforms are supposed to have distinct functions depending on the tissue, and all of the three are required for proper LD biogenesis in embryos (Taurino et al., 2018). In addition to lipid metabolism enzymes as mentioned above, seipin interacts with different proteins depending on the organism. In yeast, the seipin homolog Fld1 function depends on its interaction with Ldb16 (Wang C.-W. et al., 2014). Yet this seems to be yeast specific as no homolog of Ldb16 has been identified in other eukaryotes. The expression of human seipin is sufficient to rescue the double *Fld1/Ldb16* KO (Wang C.-W. et al., 2014). The Fld1/Ldb16 complex interacts with Ldo16 and Ldo45 (Lipid Droplet Organization proteins) (Eisenberg-Bord et al., 2018). This interaction is conserved in mammals for which Promethin/TMEM159/LDAF1 (lipid droplet assembly factor) has been identified as the Ldo45 homolog (Castro et al., 2019; Chung et al., 2019). In both yeast and humans, the abovementioned interaction of seipin may determine the sites of LD formation (Bohnert, 2020). Recently, the yeast phosphatase Nem1 has also been identified as an interactor of seipin, playing a major role in the recruitment of TAG synthesis enzymes to LD biogenesis sites (Choudhary et al., 2020). In *Arabidopsis thaliana*, seipins 2 and 3 interact with the vesicle-associated membrane protein (VAMP) -associated protein VAP27, and this interaction proved crucial for LD formation, although the underlying mechanism still needs to be investigated (Greer et al., 2020). A seipin homolog has been identified in *P. tricornutum* (Lu et al., 2017) and confirmed as an important factor in LD biogenesis as its overexpression leads to TAG accumulation and increased LD formation. By sequence homology, the *Thalassiosira pseudonana* locus *THAPSDRAFT_1237* could encode a seipin homolog. Conversely, no homologs have been found in *Nannochloropsis s.l.*

Other factors have been involved in LD biogenesis in Opisthokonts and Viridiplantae. Interestingly, some seem to be specific to one or the other phylum, e.g., the FIT proteins that play a major role in Opisthokonts (Renne et al., 2020) could not be identified in Viridiplantae nor in the *P. tricornutum* genome. Likewise, the LD major structural proteins identified in stramenopiles (see below) are different from perilipins found in Opisthokonts or oleosins found in Viridiplantae.

Another major peculiarity of stramenopiles is the biogenesis site of LD. As mentioned above, the ER is widely considered as the site of LD biogenesis. Yet, studies in the green alga *C. reinhardtii* suggest that the chloroplast and the ER are jointly involved in LD biogenesis (Fan et al., 2011; Goodson et al., 2011; Tsai et al., 2015). The architecture of the secondary plastids is unique, and the outermost membrane, the EpM, is in continuity with the ER (see above). Electron microscopy analyses have shown very close contacts between the plastid and the LD in *P. tricornutum* (Flori et al., 2016; Lupette et al., 2019; Jaussaud et al., 2020). Moreover, the lipid monolayer surrounding the LD includes the plastid glycolipid SQDG as well as PC and the betaine lipid DGTA (Lupette et al., 2019) (see above) that is considered to be synthesized in the ER. Two major DGTA species are found in the LD, namely, DGTA C20:5/C16:1 and C20:5/C16:2 (Lupette et al., 2019), the latter being a minor DGTA species in *P. tricornutum* (Abida et al., 2015; Lupette et al., 2019). While C20:5 biosynthesis occurs in the ER (Dolch and Maréchal, 2015), C16:2 is a major FA in MGDG and DGDG but is mostly absent from ER lipids (Abida et al., 2015). This particular composition thus suggests an interplay between ER and plastid functions, and two main hypotheses could explain it (**Figure 4**). First, the EpM could be the site of LD biogenesis instead of the ER (**Figure 4A**). EpM is continuous with the ER, and hence, it may exert some classical ER functions (Flori et al., 2016). Alternatively, as hypothesized in *C. reinhardtii*, LD biogenesis could occur through links with both the plastid and the ER (**Figure 4B**). In support to the latter hypothesis, electron microscopy inspections show association of the LD with endomembranes in *P. tricornutum* (Lupette et al., 2019). Another corroboration to this hypothesis is supplied by the tight links between the LD and the ER in *Fistulifera* sp. (Nojima et al., 2013), suggested by proteomics analysis of oil bodies.

Contact points and molecular transfers between LD and mitochondria may also occur and need to be characterized. They may, in particular, be important for TAG degradation (Jallet et al., 2020).

Several Populations of Lipid Droplets Observed Within *Phaeodactylum tricornutum* Cells Under Nitrogen Deprivation

While proteomics and lipidomics analyses are performed on the global population of lipid droplets, there may be heterogeneity among them. Indeed, the accumulation of LD upon nitrogen starvation in *P. tricornutum* involves several populations of LD biogenesis (Jaussaud et al., 2020). The initial population P1 LD grows in size until a maximal size is reached at day 3, then two additional populations formed. While P3 LD also

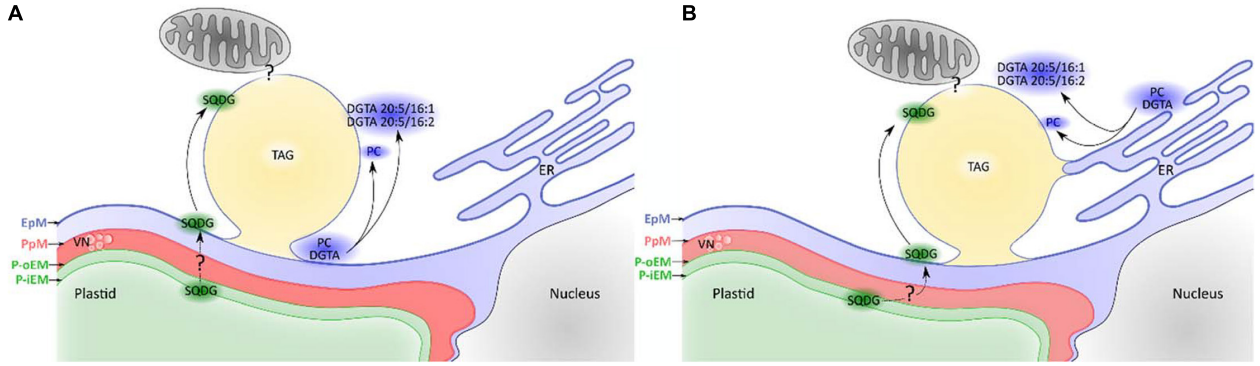

FIGURE 4 | Different hypotheses regarding lipid droplet (LD) biogenesis in *Phaeodactylum tricornutum*. EpM, epiplastidial membrane; PpM, Periplastidial membrane; P-oEM, plastid outer envelope membrane; P-iEM, plastid inner envelope membrane; ER, endoplasmic reticulum; VN, vesicular network; SQDG, sulfoquinovosyldiacylglycerol; PC, phosphatidylcholine; DGTA, diacylglycerylhydroxymethyl-*N*,*N*,*N*-trimethyl-β-alanine; TAG, triacylglycerol). **(A)** Lipid droplets emerge from the EpM. The EpM membrane contains PC and specific DGTA species, but also SQDG. The abundance of C16:2 on the betaine lipid DGTA found in the lipid droplet monolayer (Lupette et al., 2019) supports a plastid emerging hypothesis as this fatty acid is major in the plastid but very minor in endomembranes (Abida et al., 2015). The origin of SQDG in the EpM is unknown and may be explained either by an export from the plastid or a synthetic pathway located in the EpM. **(B)** Lipid droplets form at an interface between the ER and the EpM. PC and DGTA can originate from both membranes, while SQDG comes from the EpM as described above. The peculiar DGTA composition (Lupette et al., 2019) suggests that only certain species are present at LD biogenesis sites although the sorting mechanism is unknown.

expand, although not as much as P1 LD, P2 LD stays small. The maximal size of P1 and P3 LD is increased in mutants with a larger cell size, suggesting that the rigid cell wall of *P. tricornutum* is a determinant limiting factor for LD expansion in WT cells (Jaussaud et al., 2020). This may be a difference among stramenopiles. While *P. tricornutum* does not increase in cell size, either phosphate or nitrogen deprivation induces a cell volume increase in *N. oceanica* (Mühlroth et al., 2017) or *Nannochloropsis* sp. PJ12 (Liang et al., 2019b). Thus, cell volume increase may be a common trait under nutrient stress in *Nannochloropsis s.l.* Interestingly, the size of P2 LD in *P. tricornutum* is not changed in larger cells (Jaussaud et al., 2020), raising the possibility that the composition of P2 LD population is different from that of P1 and P3. Additionally, P1 LD growth is concomitant with a general increase in the cell lipid content, suggesting that TAG filling P1 LD population, mostly come from *de novo* synthesis. On the other hand, the emergence of P2 and P3 population correlates with a decrease in polar glycerolipids, ventilating the hypothesis that most of their TAG content may derive from membrane lipid recycling. It must be noticed that the fine sequence of biogenesis of LD subpopulation deciphered in the Pt1 ecotype of *P. tricornutum* (Jaussaud et al., 2020) was not detected in the Pt4 ecotype (Leyland et al., 2020b). Further studies are needed to disentangle the origin, composition, and functions of the different populations of LD.

LIPID DROPLET FORMATION IN RESPONSE TO NITROGEN AND PHOSPHATE STARVATION

Accumulation of LDs in response to nutrient limitation is often correlated with a major lipid remodeling, a decrease in photosynthetic activity, and a much slower growth (Meng et al., 2017; Janssen et al., 2019b). Indeed, shortage of nitrogen and phosphate has striking consequences on cell phenotypes. Nitrogen is an essential component of nucleobases, proteins, and many glycerolipids (e.g., PC, DGTS, and PE), while phosphate is required in nucleic acids, sugar molecules, phosphoproteins, and phospholipids. Phosphate may also be a critical element for such molecules as adenosine phosphates or NADPH, the "energy" currencies of the cell to perform its metabolism. The metabolism of all organisms is therefore finely adjusted and tuned in response to the availability of these nutrients.

An Intense Lipid Remodeling Is Triggered Upon Nitrogen or Phosphate Starvation

Stress-induced lipid remodeling corresponds to changes in the proportions of glycerolipid classes, in the FA contained in each class, and sometimes includes modification of subcellular location (Jaussaud et al., 2020). Upon nitrogen deprivation, the level of all glycerolipid classes decreases in *Nannochloropsis s.l.* (Simionato et al., 2013; Meng et al., 2017). Only in *Nannochloropsis* sp. PJ12 were PC and PE found to possibly increase during nitrogen deprivation (Liang et al., 2019b). The authors suggest that the increase in PC and PE could be due to their important role in acyl editing, providing a pool of elongated and desaturated FAs (Schneider and Roessler, 1994; Benning, 2009). In *P. tricornutum*, MGDG, PG, and PE decrease, while other lipid classes are stable (Abida et al., 2015; **Figure 5**).

Phosphate deprivation is apparently a less severe stress compared with nitrogen deprivation, possibly due to the presence of intracellular storage forms; nonetheless, it also leads to an intense lipid remodeling. Phosphate deprivation triggers a breakdown of membrane phospholipids (Abida et al., 2015; Cañavate et al., 2017a,b; Mühlroth et al., 2017;

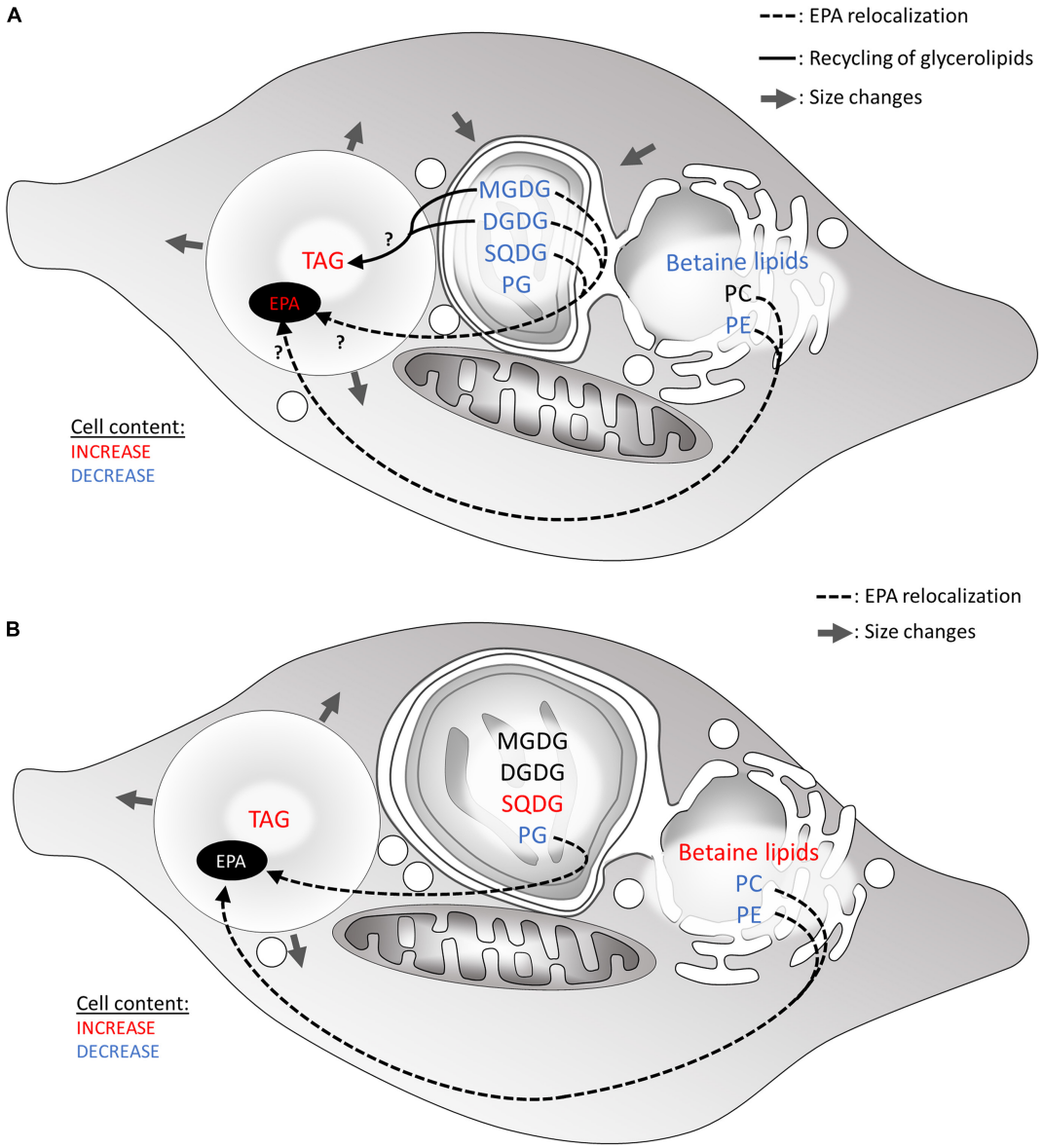

FIGURE 5 | Hypothetical recycling of products of membrane glycerolipid breakdown for the formation of TAG in heterokonts subjected to a nitrogen or phosphate shortage. **(A)** Lipid remodeling under nitrogen starvation. Most glycerolipids are degraded, affecting the plastid size. **(B)** Lipid remodeling under phosphate starvation. In both scenarios, FA released from membrane lipids may be consumed via the β-oxidation pathway in the mitochondrion. Alternatively, down-products can be recycled to form TAG. Arrows show hypothetical conversions of membrane lipid down-products in the production of TAG, as well as in the increase in very long-chained PUFA (e.g., 20:5) in LDs. Glycerolipid conversions occur to rescue phospholipid degradation. DGDG, digalactosyldiacylglycerol; EPA, eicosapentaenoic acid; MGDG, monogalactosyldiacylglycerol; PC, phosphatidylcholine; PG, phosphatidylglycerol; SQDG, sulfoquinovosyldiacylglycerol; TAG, triacylglycerol.

Liang et al., 2019a). Such a decline designates phospholipids as a possible substantial P storage form. Whereas in plants, a PC-to-DGDG appeared as a general phosphorus-saving process, no such mechanism could be evidenced in any stramenopile model studied to date (Abida et al., 2015). Rather, the proportion of another class of non-phosphorus lipid, i.e., betaine lipids, increases (Abida et al., 2015; Cañavate et al., 2017a,b; Mühlroth et al., 2017; Liang et al., 2019a; Meng et al., 2019); it was suggested that phospholipids were replaced by betaine lipids in membranes (Abida et al., 2015; Cañavate et al., 2017a; Mühlroth et al., 2017; Meng et al., 2019), as also suggested in other phytoplankton species (Van Mooy et al., 2009; Cañavate et al., 2017b). This specific conversion of PC-to-betaine lipids has been proposed in several studies (Abida et al., 2015; Iwai et al., 2015; Meng et al., 2019). In particular, in *N. oceanica*, DGTS replaces PC and becomes central during lipid remodeling as a platform for C18 desaturation, maintaining eicosapentaenoic acid (EPA or C20:5) biosynthesis and providing EPA for plastid glycolipids synthesis (Meng et al., 2019), as it was already suggested during nitrogen deprivation (Meng et al., 2017).

The PC-to-betaine lipid switch is considered as specific to the endomembrane system.

By the same token, in plastid membranes, phosphate deprivation triggers a striking increase in SQDG proportion in *P. tricornutum* and *N. oceanica* (Abida et al., 2015; Cañavate et al., 2017b; Mühlroth et al., 2017), while it decreases in *Nannochloropsis* sp. PJ12 (Liang et al., 2019a), and is stable in *M. gaditana* (Cañavate et al., 2017b). In *P. tricornutum* and *N. oceanica*, the decrease in PG is concomitant with the increase in SQDG (Abida et al., 2015; Cañavate et al., 2017b; Mühlroth et al., 2017), reflecting a specific PG-to-SQDG conversion (Abida et al., 2015; Iwai et al., 2015; Cañavate et al., 2017b). This conversion is reminiscent to that established in other organisms, such as *Arabidopsis* under phosphate deprivation (Nakamura, 2013) and has been reported in other phytoplankton exposed to a phosphate shortage as well (Van Mooy et al., 2009; Cañavate et al., 2017b).

Degraded phospholipids can provide building blocks for TAG accumulation. FA released from membrane glycerolipids may be consumed via the β-oxidation pathway in the mitochondrion. Alternatively, down-products can be recycled to form TAG. In particular, PC is supposed to be involved in acyl-CoA-independent synthesis of TAG as inferred by the activation of the Land's cycle and the PDAT enzymes upon phosphate depletion (Mühlroth et al., 2017). Hypothetical flows of materials released from membrane lipid breakdown to TAG are summarized in **Figure 5**.

Eicosapentaenoic Content in Lipid Class, a Signature to Trace Lipid Remodeling

Under nitrogen as well as phosphate deprivations, the EPA level in total lipid decreases in *Nannochloropsis s.l.* (Simionato et al., 2013; Abida et al., 2015; Meng et al., 2015; Liang et al., 2019a,b), while it is stable in *P. tricornutum* (Abida et al., 2015). However, EPA accumulation in TAG increases in both taxa (Abida et al., 2015; Meng et al., 2017; Janssen et al., 2019b; Liang et al., 2019b). Due to the interest toward EPA for several industrial applications, the source of EPA during lipid remodeling has been further investigated in order to find new ways to improve EPA content in TAG (Simionato et al., 2013; Abida et al., 2015; Jia et al., 2015; Meng et al., 2015; Liang et al., 2019b). For example, contribution of galactolipids to TAG synthesis is emphasized by the probability that, under nitrogen deprivation, the EPA present in TAG partly stems from galactolipid recycling, based on FA balance between these lipid classes (Simionato et al., 2013; Abida et al., 2015; Jia et al., 2015; Meng et al., 2015; Liang et al., 2019b; **Figure 5**). In *P. tricornutum* under phosphate deprivation, phospholipids are supposed to also provide part of the EPA in TAG molecular species (Abida et al., 2015), and this was also hypothesized in *M. gaditana* under nitrogen deprivation (Janssen et al., 2019a). In *N. oceanica* under normal growth conditions, PE and DGTS seem to provide EPA to other lipids, in particular to MGDG (Vieler et al., 2012b; Meng et al., 2017). However, it was not shown whether translocation of EPA to TAG under nitrogen deprivation originated from PE and DGTS and/or from MGDG (Meng et al., 2017). In *P. tricornutum*, the role of EPA source is apparently played by PC (Mühlroth et al., 2013). By monitoring EPA within membrane glycerolipids and TAG, various routes for very long-chain polyunsaturated FAs are highlighted within glycerolipid metabolism, and an important future challenge is to decipher the molecular determinants of each route, and their controlling and regulatory mechanisms.

Enzymes Involved in Lipid Reshuffling Are Upregulated at the Transcriptional Level

Transcriptomic analyses revealed that lipases involved in lipid remodeling were activated during nitrogen and phosphate deprivation. In *N. oceanica* under nitrogen shortage, a homolog of the *Arabidopsis* galactolipase *PSD1* is upregulated, coincidently with degradation of MGDG (Li et al., 2014). Diverse phospholipases A, C, and D (PLA, PLC, and PLD, respectively) were also identified in both *P. tricornutum* and *Nannochloropsis s.l.* In *P. tricornutum*, under both nitrogen and phosphate starvation, several *PLC* and *PLD* isoforms were upregulated (Alipanah et al., 2015, 2018; Cruz de Carvalho et al., 2016; Remmers et al., 2018). The upregulated *PLC* isoforms are all predicted to encode for PI-specific PLCs in the case of the phosphate deprivation (Cruz de Carvalho et al., 2016; Alipanah et al., 2018). In *N. oceanica* under nitrogen deprivation, several genes encoding for putative patatin and one putative lysophospholipase were upregulated under nitrogen deprivation (Li et al., 2014; Jia et al., 2015). Meng et al. (2019) did not find any upregulated genes related to phospholipid degradation under phosphate deprivation in *N. oceanica* (Meng et al., 2019). Conversely, Mühlroth et al. (2017) found three patatin-like PLAs together with two glycerophosphoryldiester phosphodiesterases (GDPDs) upregulated, which could lead to the release of FAs and G3P from phospholipids, leading to the complete recycling of phospholipids in *N. oceanica* (Mühlroth et al., 2017).

Key enzymes of the Land's cycle were also found to be upregulated. Both phosphate and nitrogen deprivation induced upregulation of one putative PDAT in *Nannochloropsis s.l.* and *P. tricornutum* (Li et al., 2014; Alipanah et al., 2015, 2018; Jia et al., 2015; Cruz de Carvalho et al., 2016; Mühlroth et al., 2017). One LPCAT and one PLA2 were also overexpressed under phosphate deprivation in *N. oceanica* (Mühlroth et al., 2017), completing the Land's cycle.

MORE LIPID DROPLET FUNCTION IN THE CELL: HYPOTHESIS DEDUCED FROM PROTEOMIC STUDIES

As mentioned above, TAG production and storage are induced under stress conditions, which results in cell cycle slowdown or arrest. The energy excess produced by photosynthesis that still works during the first phases of stress is stocked and constitutes a pool of carbon and energy available upon stress release. However, in stramenopiles, as in other organisms (Welte, 2015),

LD function is not limited to an energy reservoir as can be hypothesized from proteomics analyses.

The Protein Equipment of Lipid Droplets, Insights Into Lipid Droplet Function and Connection to Other Organelles

Identification of Major Structural Lipid Droplet Proteins

Several proteomics analyses have been performed in different stramenopiles, e.g., *Nannochloropsis oceanica* (Vieler et al., 2012a), *Fistulifera* sp. (Nojima et al., 2013; Nonoyama et al., 2019), and *P. tricornutum* (Yoneda et al., 2016; Wang et al., 2017; Lupette et al., 2019; Leyland et al., 2020b). Purification of LDs consisted in (i) treatment of cells to nutrient starvation (mostly nitrogen deprivation) to trigger LD formation, (ii) cell disruption, and (iii) LD isolation, generally through sucrose density centrifugation. This classical method was particularly improved in proteomic analysis in *P. tricornutum* (Lupette et al., 2019) where it greatly reduced contamination from plastid and other cellular compartments.

With the noticeable exception of *Fistulifera* sp., proteomics analysis revealed the presence of quantitatively major LD proteins. In *Nannochloropsis* sp., the main protein was named the lipid droplet surface protein (LDSP, accession number AFB75402) and immunodetected in four *Nannochloropsis s.l.* species among which are *M. gaditana* and *N. oceanica* (Vieler et al., 2012a). The LDSP had no previously assigned function and was first hypothesized to serve as a major structural component (Vieler et al., 2012a). It was later on shown to be likely involved in LD degradation through binding to autophagy-related protein 8 (ATG8) (Zienkiewicz et al., 2020). A detailed comparison of stramenopile LDPs characterized to date is provided in **Figure 6**.

For *P. tricornutum*, the two first LD proteomic analyses unexpectedly identified distinct sets of proteins. The first analysis identified nine proteins, among which the most abundant is the Stramenopile-type lipid droplet protein (StLDP, accession number XP_002183367), named based on the homology found in six other stramenopiles including *M. gaditana* (Yoneda et al., 2016). StLDP possibly plays a role in the maintenance, distribution, and degradation of TAG in LDs (Yoneda et al., 2016). The second analysis identified five proteins, with PtLDP1 (accession number XP_002178287) being the most represented (Wang et al., 2017). OE and KD of PtLDP1 led to changes in lipid content, LD size, and relative expression levels of key genes involved in TAG and FA biosynthesis (Wang et al., 2017), suggesting an important role in LD biogenesis and regulation of lipid synthesis. Interestingly, PtLDP1 shares high similarities with one of the LD protein identified in *Fistulifera* sp., DOAP1 (accession number BAO47264) (Nojima et al., 2013; Maeda et al., 2014; Wang et al., 2017). DOAP1 and PtLDP1 both possess a terminal signal peptide, and further analyses suggested that DOAP1 may localize to the ER prior to the transfer to LDs (Maeda et al., 2014). The difference between the two studies may be due to different nitrogen starvation conditions (6 vs. 2 days), corresponding to late and early LD formation, respectively (Yoneda et al., 2016; Wang et al., 2017). Protein equipment of nascent and budding LDs is indeed thought to differ from that of mature LDs. In the study performed by Lupette et al. (2019) on mature LDs (7 days of nitrogen starvation), StLDP and PtLDP1 were both recorded in the LD proteome, although no major LD protein was pointed out. The presence of StLDP was further confirmed in a more recent analysis of LD proteome in the Pt4 ecotype of *P. tricornutum* (Leyland et al., 2020b).

LD-associated proteins have been classified according to their structure and provenance (Kory et al., 2016). Class I proteins are inserted in the membrane through a hydrophobic hairpin structure and access the LD surface *via* the ER, while class II proteins access the LD from the cytosol, using other hydrophobic domains. Both LDSP and StLDP are class I proteins, while PtLDP1 and DOAP1 are class II proteins (**Figure 6**).

LDSP, StLDP, and PtLDP1 all contain hydrophobic sequences harboring a proline-rich region (**Figure 6**), similar to the proline knot motif found in plant oleosins (Abell et al., 2004). *LDSP*, *StLDP*, and *PtLDP1* gene expression can be induced by stress conditions leading to lipid accumulation (Yoneda et al., 2016; Wang et al., 2017; Zienkiewicz et al., 2020), and their function is related to the modulation of LD size (Vieler et al., 2012a; Yoneda et al., 2016; Wang et al., 2017).

Altogether, it seems that like in other eukaryotic lineages, it is difficult to identify major LDPs conserved at the whole clade level. This diversity of LPDs is puzzling. Either LDPs are simply protective proteins, which assemble into a subspherical "shield" preventing free interaction between the LD core and the cytosol, possibly acting as a docking surface for more peripheral proteins, or LDPs may act in dynamic processes as well, for metabolic or signaling processes that need to be uncovered.

Mining *Phaeodactylum tricornutum* Lipid Droplet Protein Equipment

As mentioned above, very low contamination was observed in the mature LD proteome produced by Lupette et al. (2019), leading to highly pure LDs and the identification of a core proteome made of 86 proteins. LD function depends on its protein equipment. Based on gene ontology, LD-associated proteins can be divided in seven large functional and structural groups: metabolism, membrane organelle, chaperones/protein folding/post translational modification/quality control, cytoskeleton, genomic information processing, plastoglobules, and "unknown" (Lupette et al., 2019). Plastoglobule-specific proteins probably prove the unavoidable contamination of the purified LD faction by plastid lipid bodies.

Proteins involved in metabolism were mainly cytosolic enzymes participating in the glycolytic and pentose phosphate pathways (Lupette et al., 2019). Others were mitochondrial components of the Kreb's cycle, and two were the plastidial carbonic anhydrase and acetyl-coA carboxylase (ACC1) (Yoneda et al., 2016; Lupette et al., 2019). The latter two enzymes reveal the proximity of the LD to the plastid, i.e., the compartment devoted to the initiation of FA biosynthesis.

Proteins related to membrane organelles stemmed mainly from the endomembrane, and support a connection between

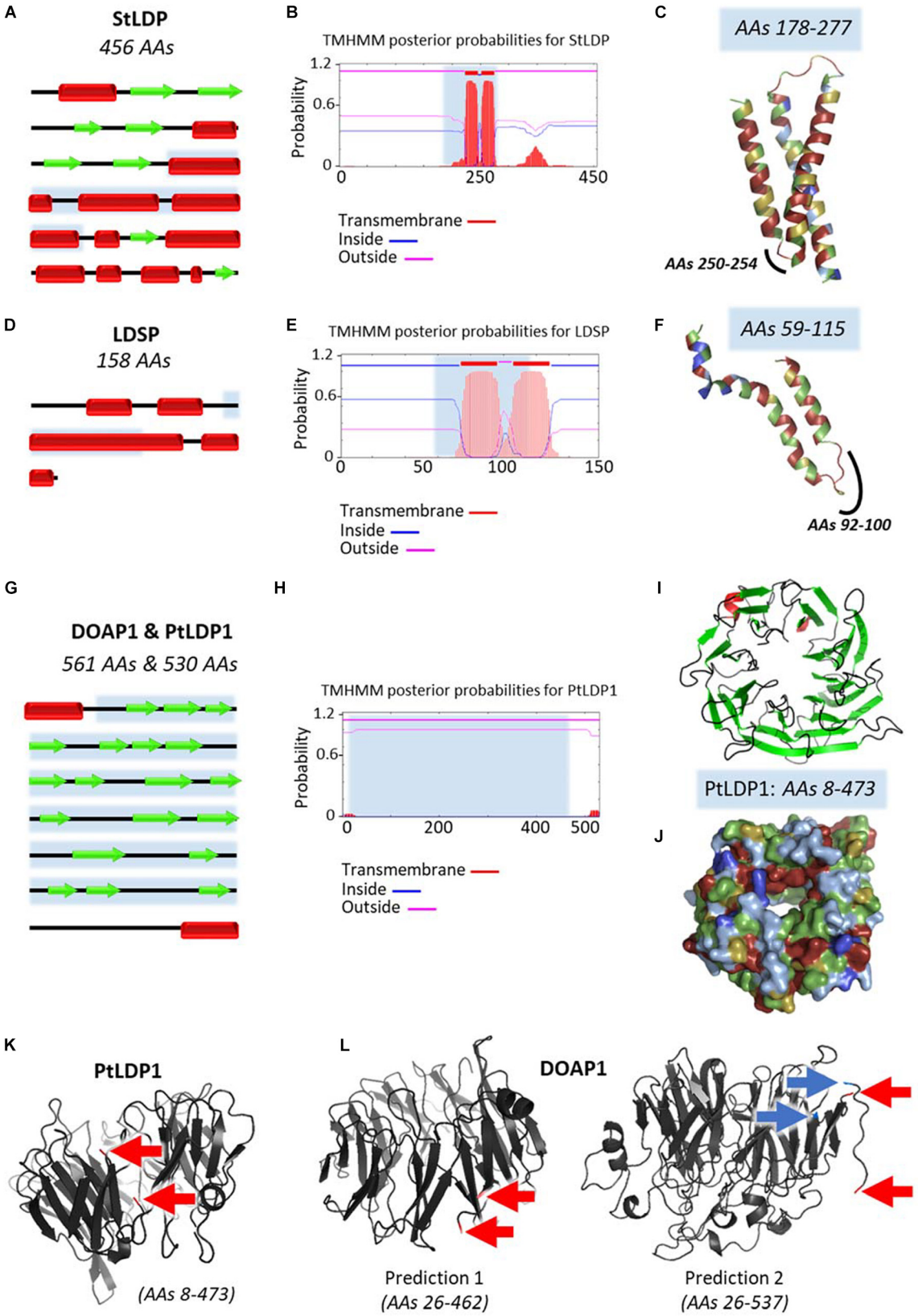

FIGURE 6 | Continued

FIGURE 6 | Predicted structures of major lipid droplet proteins found in stramenopile models. Analysis of predicted structures and hydrophobic regions in **(A–C)** StLDP from *Phaeodactylum tricornutum*, **(D–F)** LDSP from *Nannochloropsis s.l.*, and the highly similar **(G–L)** DOAP1 and PtLDP1 from *Fistulifera solaris* and *P. tricornutum*, respectively. **(A,D,G)** Secondary structure representations adapted from results obtained with Jpred4 prediction server (http://www.compbio.dundee.ac.uk/jpred/). Beta sheets are represented with red rectangles, and alpha helices with green arrows. **(B,E,H)** Predictions of transmembrane helices obtained with TMHMM prediction server (http://www.cbs.dtu.dk/services/TMHMM/). **(C,F,I,J,K,L)** Predicted tertiary structures obtained with Phyre^2 (Protein Homology/analogy Recognition Engine V2.0) prediction server (http://www.sbg.bio.ic.ac.uk/~phyre2/html/page.cgi?id = index) in ribbon diagrams **(C,F,I,K,L)**, and surface representation **(J)**. Obtained Phyre^2 predictions span only a portion of the proteins, first and last amino acids (AAs) are specified in the figures. These regions are indicated in blue in the secondary structures representations **(A,D,G)** and TMHMM results **(B,E,H)**. Hydrophobicity level of AAs is represented with a color code in **(C,F,I,J)**, ranging from dark blue for very hydrophobic AAs, light blue for hydrophobic AAs, green for poorly hydrophobic or hydrophilic AAs, yellow for hydrophilic AAs, and red for very hydrophilic AAs. These predictions show that StLDP and LDSP have a hairpin structure, with the hairpin being enriched in hydrophobic residues. For DOAP1 and PtLDP1, a beta barrel structure bordered with two alpha helices is predicted. The membrane-spanning sequences of the beta barrel do not seem as enriched in hydrophobic residues as the alpha-helices of the hairpin structures of StLDP and LDSP, as already observed in the literature for these structures (Tamm et al., 2004; Wimley, 2009). The alpha helices potentially anchor the protein in the membrane as suggested by the TMHMM results. These alpha helices seen in the secondary structure are not present in the predicted tertiary structure due to incomplete models. To infer the position of the alpha helices regarding the beta barrel, first and last amino acids of the spanned regions are indicated with red arrows for one PtLDP1 model **(K)** and two possible DOAP1 models **(L)**. DOAP1 model spanning the AAs 26–537 offers a more complete model than the model covering the AAs 26–462. However, a break in the predicted tertiary structure appears in this model between the two AAs indicated with blue arrows. The two alpha helices appear to be close to each other. However, it is not possible to conclude if the helices are in the same direction. AAs, amino acids; DOAP1, diatom oleosome-associated protein1; LDSP, lipid droplet surface protein; PtLDP1, *P. tricornutum* lipid droplet protein1; StLDP, stramenopile lipid droplet protein.

the LD and cytosolic vesicles. The presence of two subunits of the coat protein complex 1 (COP1) coatomer (COPA and COPBETA2) were identified (Lupette et al., 2019). COP1 complex participates in the retrograde transport of vesicles from the *trans*-Golgi network to the ER and in intra-Golgi transport, and depends on ARF1 to be operational (Serafini et al., 1991), which was identified in the unfiltered LD proteome (326 proteins) (Lupette et al., 2019). Two components of the clathrin vesicle coating system (CHC and PTAP1/2BETA) were also identified (Lupette et al., 2019). Clathrins participate in the transfer of proteins outside *trans* Golgi network (Jürgens, 2004). These components could be linked with the presence in the unfiltered proteome of SNARE proteins, whose function is necessary for fusion of transport vesicle with target membrane (Tanaka et al., 2015), and which play a role in COP1 transport (Lupette et al., 2019). Finally, a proton pump found in endomembrane vesicle, V-ATPase, and an ABC-transporter, are also present (Lupette et al., 2019). SLC25A4 (an adenine nucleotide translocator) is located in the inner mitochondrial envelope membrane, supporting a possible connection of the LD with the mitochondrion (Lupette et al., 2019). Some of these protein components were confirmed in a more recent proteomic study of LD purified from the Pt4 ecotype of *P. tricornutum* (Leyland et al., 2020b).

No proteins were identified as originating from the plastid, or more exactly the EpM in the LD proteome of Lupette et al. (2019). Nonetheless, predictions suggest that five out of the 10 proteins classified as "unknown" possess either a signal peptide or a chloroplast transit peptide (cTP) (Lupette et al., 2019). Connection between the LD and the endomembrane, the mitochondria, and the EpM were further supported with electron microscopy images (Flori et al., 2016).

Several proteins were related to mRNA translation and control of misfolded proteins. On one hand, chaperones including heat shock proteins (HSP, HSP70A, HSP90, and HSP40), ribosomal subunits (40S and 60S), and components of the RNA translation machinery (EF1A, EF2, and EIF4A) were identified (Yoneda et al., 2016; Lupette et al., 2019). On the other hand, proteins involved in post translational modification such as ubiquitination (UBI3 and PUB39) and phosphorylation (STK and EPK2) were found, as well as proteins involved in the endoplasmic reticulum-associated degradation (ERAD) system (CDC48 and BIP) (Lupette et al., 2019). Consistent with the presence of ubiquitination proteins, four 26S proteasome proteins are also present in the LD proteome (Lupette et al., 2019). Altogether, the presence of the aforementioned proteins supports the hypothesis for the LD as a potential site for mRNA storage and as platform for specific synthesis and folding of proteins at the periphery of the LD.

Histones H2B-1B, H3-1C, H3.3, and H4-1B were identified in the LD proteome as well. Histone proteins are involved in genome information processing, and their presence in the LD suggests that the LD plays a role in storing and protecting specific proteins during starvation, i.e., a context of intense protein degradation (Lupette et al., 2019). Protection of nucleosome components could prepare for a quick recovery of cell division and chromatin packaging upon the stressing condition (e.g., nutrient starvation) release.

Getting Ready to Recover From Stress

When favorable growth conditions are restored, the energy stored in LDs is used to reactivate cell cycle and photosynthesis activity. In algae, several forms of lipophagy (lipid degradation by autophagy) may be involved in LD mobilization. Macrolipophagy is characterized by the formation of an autophagosome triggered by autophagy-related (ATG) proteins (Ward et al., 2016). The autophagosome carries, within a double membrane, molecules or damaged organelles to the vacuole for degradation. Fusion of the autophagosome with the vacuole also requires ATG proteins. By microlipophagy, the components to degrade are delivered to the vacuole by invagination of the tonoplast (Ward et al., 2016). Finally, chaperone-mediated autophagy (CMA) is a process by which proteins directly enter the vacuole *via* a translocation complex localized on the vacuole membrane by the heat shock cognate protein 70 (HSC70) and other cytosolic chaperones (Yim and Mizushima, 2020).

Autophagy components and chaperones were regularly detected in stramenopile LD proteomes.

In *N. oceanica*, the ATG8 expression level is induced directly after the transition from nitrogen-depleted condition to nitrogen replete (Zienkiewicz et al., 2020). As mentioned above, ATG8 binds to the major LD surface protein LDSP, in which an ATG8 interaction motif (AIM) was detected (Zienkiewicz et al., 2020). Interestingly, one of the major LD surface proteins in *P. tricornutum*, StLDP, also possesses an AIM (Leyland et al., 2020a). This suggests that macrolipophagy might be involved in LD breakdown. Transmission electron microscopy observations showed that in *N. oceanica*, LDs fuse with the vacuole after transition from nitrogen-depleted to nitrogen-replete condition (Zienkiewicz et al., 2020). This strongly suggests that microlipophagy is also involved in LD turnover in *N. oceanica*.

The LD proteome of *Fistulifera solaris* also reveals the presence of clathrin vesicle coating system and of COP1 coatomer (Nonoyama et al., 2019), like that of *P. tricornutum*. Clathrins have been shown to be involved in macrolipophagy (Oku et al., 2017); hence, in *P. tricornutum* and *F. solaris*, LD breakdown may occur by microlipophagy. In addition, both *P. tricornutum* and *F. solaris* LD proteomes contain a HSP70 homolog. Hsp70 family (which includes HSC70) was shown to play a role in LD protein degradation by CMA (Cuervo and Wong, 2014; Kaushik and Cuervo, 2015), and in the removal of clathrin from clathrin-coated vesicles (Barouch et al., 1994; Rapoport et al., 2008), which is an important step for vesicle fusion and cargo delivery.

To test the potential role of lipophagy in LD mobilization in *F. solaris* and *P. tricornutum*, Nonoyama et al. (2019) used inhibitors of membrane trafficking-related proteins and lipophagy (Nonoyama et al., 2019). Chloroquine was used to prevent fusion of LD and autophagosome, VER-155008 was used to bind to HSP70, and Pitstop 2 was used to bind clathrin. All three inhibitors limited LD shrinkage in *F. solaris* and in *P. tricornutum*, supporting the occurrence of lipophagy processes in LD breakdown, with the probable involvement of HSP70 and clathrin. More specifically, these results are coherent with CMA and microlipophagy playing a role in LD breakdown.

Remobilization of stored energy in LD involves the disassembly of TAG molecules into glycerol and free FAs. Glycerol will then be redirected to the glycolysis pathway, while FA will undergo β-oxidation, which in diatoms can occur in the mitochondria and in the peroxisomes (Chauton et al., 2013). It was recently shown that mitochondrial β-oxidation was prominent in diatoms (Jallet et al., 2020). The first step to catabolize TAG is generally performed by TAG lipases. In *Arabidopsis*, AtSDP1 is a TAG lipase that plays a key role in TAG hydrolysis during seed germination (Eastmond, 2006). Homologs of AtSDP1 have been characterized in stramenopiles, named tgl1 in *P. tricornutum* (Barka et al., 2016), and NoTGL1 and NoTGL2 in *N. oceanica* (Nobusawa et al., 2019). *tgl1* KD and *NoTGL1* KO lead to over-accumulation of TAG, corroborating their role in TAG hydrolysis. NoTGL2, on the other hand, was shown to have a more specific role than NoTGL1, with the degradation of 16:1-containing molecular species of TAG (Nobusawa et al., 2019). Many other putative TAG lipases have been predicted in *P. tricornutum*, *N. oceanica*, and *F. solaris* but need to be investigated (Barka et al., 2016; Nomaguchi et al., 2018; Zienkiewicz et al., 2020).

CONCLUDING REMARKS

Secondary endosymbiosis-derived organisms, with their complicated cellular organizations, have been far less studied than simpler photosynthetic eukaryotes, such as the green alga *C. reinhardtii* or the plant *A. thaliana*. These Archaeplastida models contain primary chloroplasts and have been our reference for decades to unravel unique features of the plant kingdom, such as the synthesis of FA within the stroma, or the coordination of two membrane systems for the biosynthesis of membrane glycerolipids, schematically the ER for the bulk of phospholipids and the plastid for glycolipids. Enzymes have been purified, functionally and molecularly characterized, and metabolic pathways reconstructed at the cellular level. The localization of TAG biogenesis at the ER has been discussed in green algae, likely involving the chloroplast. Trafficking of FA and lipid intermediates and FA editing appear as the last challenges we need in order to collectively comprehend lipid metabolism in Archaeplastida. On the basis of knowledge gathered in other model organisms, we elaborated paradigms that need evaluation in stramenopiles. The structure of the secondary plastid is probably one of the major obstacles to transfer knowledge from *C. reinhardtii* or *A. thaliana*, since no such ER–plastid hybrid structure has ever been studied before. Here, we attempted to summarize efforts put recently on stramenopile models, which emerged also as oleaginous strains for possible biotechnological applications. The secondary plastid appears as a pivotal cellular factory for membrane glycerolipid and TAG production, as well as for the biogenesis of the LD, so we need to refine our understanding of the cooperation of the secondary plastid with other organelles. Many biochemical, cell biology, and genetic analyses still need to be performed. Resolving some of the questions we listed in this review is necessary for biotechnological purposes. Exploring this *terra incognita* is definitely a fascinating mission.

AUTHOR CONTRIBUTIONS

All authors listed have made a substantial, direct and intellectual contribution to the work, and approved it for publication.

FUNDING

This work was supported by the French National Research Agency (Oceanomics ANR-11-BTBR-0008, GlycoAlps ANR-15-IDEX-02, GRAL Labex ANR-10-LABEX-04, and EUR CBS ANR-17-EURE-0003).

REFERENCES

Abell, B. M., Hahn, M., Holbrook, L. A., and Moloney, M. M. (2004). Membrane topology and sequence requirements for oil body targeting of oleosin: role of oleosin topology in oil body targeting. *Plant J.* 37, 461–470. doi: 10.1111/j.1365-313X.2003.01988.x

Abida, H., Dolch, L.-J., Meï, C., Villanova, V., Conte, M., Block, M. A., et al. (2015). Membrane glycerolipid remodeling triggered by nitrogen and phosphorus starvation in *Phaeodactylum tricornutum*. *Plant Physiol.* 167, 118–136. doi: 10.1104/pp.114.252395

Adl, S. N., Simpson, A. G. B., Farmer, M. A., Andersen, R. A., Anderson, R. O., Barta, J. R., et al. (2005). The new higher level classification of eukaryotes with emphasis on the taxonomy of protists. *J Eukaryot. Microbiol.* 52, 399–451. doi: 10.1111/j.1550-7408.2005.00053.x

Alboresi, A., Perin, G., Vitulo, N., Diretto, G., Block, M. A., Jouhet, J., et al. (2016). Light remodels lipid biosynthesis in *Nannochloropsis gaditana* by modulating carbon partitioning between organelles. *Plant Physiol.* 171, 2468–2482. doi: 10.1104/pp.16.00599

Alipanah, L., Rohloff, J., Winge, P., Bones, A. M., and Brembu, T. (2015). Whole-cell response to nitrogen deprivation in the diatom *Phaeodactylum tricornutum*. *J. Exp. Bot.* 66, 6281–6296. doi: 10.1093/jxb/erv340

Alipanah, L., Winge, P., Rohloff, J., Najafi, J., Brembu, T., and Bones, A. M. (2018). Molecular adaptations to phosphorus deprivation and comparison with nitrogen deprivation responses in the diatom *Phaeodactylum tricornutum*. *PLoS One* 13:e0193335. doi: 10.1371/journal.pone.0193335

Aymé, L., Arragain, S., Canonge, M., Baud, S., Touati, N., Bimai, O., et al. (2018). *Arabidopsis thaliana* DGAT3 is a [2Fe-2S] protein involved in TAG biosynthesis. *Sci. Rep.* 8:17254. doi: 10.1038/s41598-018-35545-7

Barka, F., Angstenberger, M., Ahrendt, T., Lorenzen, W., Bode, H. B., and Büchel, C. (2016). Identification of a triacylglycerol lipase in the diatom *Phaeodactylum tricornutum*. *Biochim. Biophys. Acta* 1861, 239–248. doi: 10.1016/j.bbalip.2015.12.023

Barouch, W., Prasad, K., Greene, L. E., and Eisenberg, E. (1994). ATPase activity associated with the uncoating of clathrin baskets by Hsp70. *J. Biol. Chem.* 269, 28563–28568.

Bartz, R., Li, W.-H., Venables, B., Zehmer, J. K., Roth, M. R., Welti, R., et al. (2007). Lipidomics reveals that adiposomes store ether lipids and mediate phospholipid traffic ,. *J. Lipid Res.* 48, 837–847. doi: 10.1194/jlr.M600413-JLR200

Ben M'barek, K., Ajjaji, D., Chorlay, A., Vanni, S., Forêt, L., and Thiam, A. R. (2017). ER Membrane phospholipids and surface tension control cellular lipid droplet formation. *Dev. Cell* 41, 591–604.e7. doi: 10.1016/j.devcel.2017.05.012

Benning, C. (2009). Mechanisms of lipid transport involved in organelle biogenesis in plant cells. *Annu. Rev. Cell Dev. Biol.* 25, 71–91. doi: 10.1146/annurev.cellbio.042308.113414

Binns, D., Lee, S., Hilton, C. L., Jiang, Q.-X., and Goodman, J. M. (2010). Seipin is a discrete homooligomer. *Biochemistry* 49, 10747–10755. doi: 10.1021/bi1013003

Bohnert, M. (2020). New friends for seipin — Implications of seipin partner proteins in the life cycle of lipid droplets. *Semin. Cell Dev. Biol.* 108, 24–32. doi: 10.1016/j.semcdb.2020.04.012

Boudière, L., Botté, C. Y., Saidani, N., Lajoie, M., Marion, J., Bréhélin, L., et al. (2012). Galvestine-1, a novel chemical probe for the study of the glycerolipid homeostasis system in plant cells. *Mol. BioSyst.* 8:2023. doi: 10.1039/c2mb25067e

Boudière, L., Michaud, M., Petroutsos, D., Rébeillé, F., Falconet, D., Bastien, O., et al. (2014). Glycerolipids in photosynthesis: composition, synthesis and trafficking. *Biochim. Biophys. Acta* 1837, 470–480. doi: 10.1016/j.bbabio.2013.09.007

Boutet, E., El Mourabit, H., Prot, M., Nemani, M., Khallouf, E., Colard, O., et al. (2009). Seipin deficiency alters fatty acid Δ9 desaturation and lipid droplet formation in Berardinelli-Seip congenital lipodystrophy. *Biochimie* 91, 796–803. doi: 10.1016/j.biochi.2009.01.011

Burki, F., Roger, A. J., Brown, M. W., and Simpson, A. G. B. (2020). The new tree of eukaryotes. *Trends Ecol. Evol.* 35, 43–55. doi: 10.1016/j.tree.2019.08.008

Busseni, G., Rocha Jimenez Vieira, F., Amato, A., Pelletier, E., Pierella Karlusich, J. J., Ferrante, M. I., et al. (2019). Meta-omics reveals genetic flexibility of diatom nitrogen transporters in response to environmental changes. *Mol. Biol. Evol.* 36, 2522–2535. doi: 10.1093/molbev/msz157

Butler, T., Kapoore, R. V., and Vaidyanathan, S. (2020). *Phaeodactylum tricornutum*: a diatom cell factory. *Trends Biotechnol.* 38, 606–622. doi: 10.1016/j.tibtech.2019.12.023

Cai, Y., Goodman, J. M., Pyc, M., Mullen, R. T., Dyer, J. M., and Chapman, K. D. (2015). *Arabidopsis* SEIPIN proteins modulate triacylglycerol accumulation and influence lipid droplet proliferation. *Plant Cell* 27, 2616–2636. doi: 10.1105/tpc.15.00588

Cañavate, J. P., Armada, I., and Hachero-Cruzado, I. (2017a). Aspects of phosphorus physiology associated with phosphate-induced polar lipid remodelling in marine microalgae. *J. Plant Physiol.* 214, 28–38. doi: 10.1016/j.jplph.2017.03.019

Cañavate, J. P., Armada, I., and Hachero-Cruzado, I. (2017b). Interspecific variability in phosphorus-induced lipid remodelling among marine eukaryotic phytoplankton. *New Phytol.* 213, 700–713. doi: 10.1111/nph.14179

Castro, I., Eisenberg-Bord, M., Persiani, E., Rochford, J., Schuldiner, M., and Bohnert, M. (2019). Promethin is a conserved seipin partner protein. *Cells* 8:268. doi: 10.3390/cells8030268

Cavalier-Smith, T. (1981). Eukaryote kingdoms: seven or nine? *Biosystems* 14, 461–481. doi: 10.1016/0303-2647(81)90050-2

Cavalier-Smith, T. (2018). Kingdom Chromista and its eight phyla: a new synthesis emphasising periplastid protein targeting, cytoskeletal and periplastid evolution, and ancient divergences. *Protoplasma* 255, 297–357. doi: 10.1007/s00709-017-1147-3

Cenci, U., Bhattacharya, D., Weber, A. P. M., Colleoni, C., Subtil, A., and Ball, S. G. (2017). Biotic host–pathogen interactions as major drivers of plastid endosymbiosis. *Trends Plant Sci.* 22, 316–328. doi: 10.1016/j.tplants.2016.12.007

Cerón Garcí, M. C., Fernández Sevilla, J. M., Acién Fernández, F. G., Molina Grima, E., and García Camacho, F. (2000). Mixotrophic growth of *Phaeodactylum tricornutum* on glycerol: growth rate and fatty acid profile. *J. Appl. Phycol.* 12, 239–248. doi: 10.1023/A:1008123000002

Chapman, K. D., Aziz, M., Dyer, J. M., and Mullen, R. T. (2019). Mechanisms of lipid droplet biogenesis. *Biochem. J.* 476, 1929–1942. doi: 10.1042/BCJ20180021

Chauton, M. S., Winge, P., Brembu, T., Vadstein, O., and Bones, A. M. (2013). Gene regulation of carbon fixation, storage, and utilization in the diatom *Phaeodactylum tricornutum* acclimated to light/dark cycles. *Plant Physiol.* 161, 1034–1048. doi: 10.1104/pp.112.206177

Chen, J. E., and Smith, A. G. (2012). A look at diacylglycerol acyltransferases (DGATs) in algae. *J. Biotechnol.* 162, 28–39. doi: 10.1016/j.jbiotec.2012.05.009

Chorlay, A., Monticelli, L., Veríssimo Ferreira, J., Ben M'barek, K., Ajjaji, D., Wang, S., et al. (2019). Membrane asymmetry imposes directionality on lipid droplet emergence from the ER. *Dev. Cell* 50, 25–42.e7. doi: 10.1016/j.devcel.2019.05.003

Chorlay, A., and Thiam, A. R. (2018). An asymmetry in monolayer tension regulates lipid droplet budding direction. *Biophys. J.* 114, 631–640. doi: 10.1016/j.bpj.2017.12.014

Choudhary, V., El Atab, O., Mizzon, G., Prinz, W. A., and Schneiter, R. (2020). Seipin and Nem1 establish discrete ER subdomains to initiate yeast lipid droplet biogenesis. *J. Cell Biol.* 219:e201910177. doi: 10.1083/jcb.201910177

Choudhary, V., Golani, G., Joshi, A. S., Cottier, S., Schneiter, R., Prinz, W. A., et al. (2018). Architecture of lipid droplets in endoplasmic reticulum is determined by phospholipid intrinsic curvature. *Curr. Biol.* 28, 915–926.e9. doi: 10.1016/j.cub.2018.02.020

Choudhary, V., Ojha, N., Golden, A., and Prinz, W. A. (2015). A conserved family of proteins facilitates nascent lipid droplet budding from the ER. *J. Cell Biol.* 211, 261–271. doi: 10.1083/jcb.201505067

Chung, J., Wu, X., Lambert, T. J., Lai, Z. W., Walther, T. C., and Farese, R. V. (2019). LDAF1 and Seipin form a lipid droplet assembly complex. *Dev. Cell* 51, 551.e–563.e. doi: 10.1016/j.devcel.2019.10.006

Conte, M., Lupette, J., Seddiki, K., Meï, C., Dolch, L.-J., Gros, V., et al. (2018). Screening for biologically annotated drugs that trigger triacylglycerol accumulation in the diatom *Phaeodactylum*. *Plant Physiol.* 177, 532–552. doi: 10.1104/pp.17.01804

Corteggiani Carpinelli, E., Telatin, A., Vitulo, N., Forcato, C., D'Angelo, M., Schiavon, R., et al. (2014). Chromosome scale genome assembly and transcriptome profiling of *Nannochloropsis gaditana* in nitrogen depletion. *Mol. Plant* 7, 323–335. doi: 10.1093/mp/sst120

Cruz de Carvalho, M. H., Sun, H.-X., Bowler, C., and Chua, N.-H. (2016). Noncoding and coding transcriptome responses of a marine diatom to phosphate fluctuations. *New Phytol.* 210, 497–510. doi: 10.1111/nph.13787

Cuervo, A. M., and Wong, E. (2014). Chaperone-mediated autophagy: roles in disease and aging. *Cell Res.* 24, 92–104. doi: 10.1038/cr.2013.153

Cui, Y., Zhao, J., Wang, Y., Qin, S., and Lu, Y. (2018). Characterization and engineering of a dual-function diacylglycerol acyltransferase in the oleaginous marine diatom *Phaeodactylum tricornutum*. *Biotechnol. Biofuels* 11:32. doi: 10.1186/s13068-018-1029-8

Cui, Y., Zheng, G., Li, X., Lin, H., Jiang, P., and Qin, S. (2013). Cloning and characterization of a novel diacylglycerol acyltransferase from the diatom *Phaeodactylum tricornutum*. *J. Appl. Phycol.* 25, 1509–1512. doi: 10.1007/s10811-013-9991-9

Curtis, B. A., Tanifuji, G., Burki, F., Gruber, A., Irimia, M., Maruyama, S., et al. (2012). Algal genomes reveal evolutionary mosaicism and the fate of nucleomorphs. *Nature* 492, 59–65. doi: 10.1038/nature11681

Dahlqvist, A., Stahl, U., Lenman, M., Banas, A., Lee, M., Sandager, L., et al. (2000). Phospholipid:diacylglycerol acyltransferase: an enzyme that catalyzes the acyl-CoA-independent formation of triacylglycerol in yeast and plants. *Proc. Natl. Acad. Sci. U.S.A.* 97, 6487–6492. doi: 10.1073/pnas.120067297

Dellero, Y., Cagnac, O., Rose, S., Seddiki, K., Cussac, M., Morabito, C., et al. (2018a). Proposal of a new thraustochytrid genus *Hondaea* gen. nov. and comparison of its lipid dynamics with the closely related pseudo-cryptic genus *Aurantiochytrium*. *Algal Res.* 35, 125–141. doi: 10.1016/j.algal.2018.08.018

Dellero, Y., Rose, S., Metton, C., Morabito, C., Lupette, J., Jouhet, J., et al. (2018b). Ecophysiology and lipid dynamics of a eukaryotic mangrove decomposer: autecology and ecophysiology of *Aurantiochytrium limacinum*. *Environ. Microbiol.* 20, 3057–3068. doi: 10.1111/1462-2920.14346

Derelle, R., López-García, P., Timpano, H., and Moreira, D. (2016). A phylogenomic framework to study the diversity and evolution of Stramenopiles (=Heterokonts). *Mol. Biol. Evol.* 33, 2890–2898. doi: 10.1093/molbev/msw168

Dolch, L.-J., Lupette, J., Tourcier, G., Bedhomme, M., Collin, S., Magneschi, L., et al. (2017a). Nitric oxide mediates nitrite-sensing and acclimation and triggers a remodeling of lipids. *Plant Physiol.* 175, 1407–1423. doi: 10.1104/pp.17.01042

Dolch, L.-J., and Maréchal, E. (2015). Inventory of fatty acid desaturases in the pennate diatom *Phaeodactylum tricornutum*. *Mar. Drugs* 13, 1317–1339. doi: 10.3390/md13031317

Dolch, L.-J., Rak, C., Perin, G., Tourcier, G., Broughton, R., Leterrier, M., et al. (2017b). A palmitic acid elongase affects eicosapentaenoic acid and plastidial monogalactosyldiacylglycerol levels in *Nannochloropsis*. *Plant Physiol.* 173, 742–759. doi: 10.1104/pp.16.01420

Dorell, R. G., Gile, G., McCallum, G., Méheust, R., Bapteste, E. P., and Klinger, C. M. (2017). Chimeric origins of ochrophytes and haptophytes revealed through an ancient plastid proteome. *eLife* 6:e23717. doi: 10.7554/eLife.23717

Eastmond, P. J. (2006). *SUGAR-DEPENDENT1* encodes a patatin domain triacylglycerol lipase that initiates storage oil breakdown in germinating *Arabidopsis* Seeds. *Plant Cell* 18, 665–675. doi: 10.1105/tpc.105.040543

Eisenberg-Bord, M., Mari, M., Weill, U., Rosenfeld-Gur, E., Moldavski, O., Castro, I. G., et al. (2018). Identification of seipin-linked factors that act as determinants of a lipid droplet subpopulation. *J. Cell Biol.* 217, 269–282. doi: 10.1083/jcb.201704122

Fábregas, J., Maseda, A., Domínguez, A., Ferreira, M., and Otero, A. (2002). Changes in the cell composition of the marine microalga, *Nannochloropsis gaditana*, during a light:dark cycle. *Biotechnol. Lett.* 24, 1699–1703. doi: 10.1023/A:1020661719272

Falarz, L. J., Xu, Y., Caldo, K. M. P., Garroway, C. J., Singer, S. D., and Chen, G. (2020). Characterization of the diversification of phospholipid:diacylglycerol acyltransferases in the green lineage. *Plant J.* 103, 2025–2038. doi: 10.1111/tpj.14880

Fan, J., Andre, C., and Xu, C. (2011). A chloroplast pathway for the de novo biosynthesis of triacylglycerol in *Chlamydomonas reinhardtii*. *FEBS Lett.* 585, 1985–1991. doi: 10.1016/j.febslet.2011.05.018

Fan, X., Qiu, H., Han, W., Wang, Y., Xu, D., Zhang, X., et al. (2020). Phytoplankton pangenome reveals extensive prokaryotic horizontal gene transfer of diverse functions. *Sci. Adv.* 6:eaba0111. doi: 10.1126/sciadv.aba0111

Fang, X., Wei, C., Zhao-Ling, C., and Fan, O. (2004). Effects of organic carbon sources on cell growth and eicosapentaenoic acid content of *Nannochloropsis* sp. *J. Appl. Phycol.* 16, 499–503. doi: 10.1007/s10811-004-5520-1

Fawley, M. W., Jameson, I., and Fawley, K. P. (2015). The phylogeny of the genus *Nannochloropsis* (Monodopsidaceae, Eustigmatophyceae), with descriptions of *N. australis* sp. nov. and *Microchloropsis* gen. nov. *Phycologia* 54, 545–552. doi: 10.2216/15-60.1

Flori, S., Jouneau, P.-H., Finazzi, G., Maréchal, E., and Falconet, D. (2016). Ultrastructure of the periplastidial compartment of the diatom *Phaeodactylum tricornutum*. *Protist* 167, 254–267. doi: 10.1016/j.protis.2016.04.001

Fossier Marchan, L., Lee Chang, K. J., Nichols, P. D., Mitchell, W. J., Polglase, J. L., and Gutierrez, T. (2018). Taxonomy, ecology and biotechnological applications of thraustochytrids: a review. *Biotechnol. Adv.* 36, 26–46. doi: 10.1016/j.biotechadv.2017.09.003

Franz, A. K., Danielewicz, M. A., Wong, D. M., Anderson, L. A., and Boothe, J. R. (2013). Phenotypic screening with oleaginous microalgae reveals modulators of lipid productivity. *ACS Chem. Biol.* 8, 1053–1062. doi: 10.1021/cb300573r

Fucikova, K., and Lewis, L. A. (2012). Intersection of *Chlorella*, *Muriella* and *Bracteacoccus*: resurrecting the genus *Chromochloris* Kol et Chodat (Chlorophyceae, Chlorophyta). *Fottea* 12, 83–93. doi: 10.5507/fot.2012.007

Gao, Z., Meng, C., Gao, H., Zhang, X., Xu, D., Su, Y., et al. (2013). Analysis of mRNA expression profiles of carotenogenesis and astaxanthin production of *Haematococcus pluvialis* under exogenous 2, 4-epibrassinolide (EBR). *Biol. Res.* 46, 201–206. doi: 10.4067/S0716-97602013000200012

Gill, S., Willette, S., Dungan, B., Jarvis, J., Schaub, T., VanLeeuwen, D., et al. (2018). Suboptimal temperature acclimation affects kennedy pathway gene expression, lipidome and metabolite profile of *Nannochloropsis salina* during PUFA enriched TAG synthesis. *Mar. Drugs* 16:425. doi: 10.3390/md16110425

Gilson, P. R., Su, V., Slamovits, C. H., Reith, M. E., Keeling, P. J., and McFadden, G. I. (2006). Complete nucleotide sequence of the chlorarachniophyte nucleomorph: nature's smallest nucleus. *Proc. Natl. Acad. Sci. U.S.A.* 103, 9566–9571. doi: 10.1073/pnas.0600707103

Goncalves, E. C., Wilkie, A. C., Kirst, M., and Rathinasabapathi, B. (2016). Metabolic regulation of triacylglycerol accumulation in the green algae: identification of potential targets for engineering to improve oil yield. *Plant Biotechnol. J.* 14, 1649–1660. doi: 10.1111/pbi.12523

Gong, Y., Zhang, J., Guo, X., Wan, X., Liang, Z., Hu, C. J., et al. (2013). Identification and characterization of PtDGAT2B, an acyltransferase of the DGAT2 acyl-Coenzyme A: diacylglycerol acyltransferase family in the diatom *Phaeodactylum tricornutum*. *FEBS Lett.* 587, 481–487. doi: 10.1016/j.febslet.2013.01.015

Goodson, C., Roth, R., Wang, Z. T., and Goodenough, U. (2011). Structural correlates of cytoplasmic and chloroplast lipid body synthesis in chlamydomonas reinhardtii and stimulation of lipid body production with acetate boost. *Eukaryot. Cell* 10, 1592–1606. doi: 10.1128/EC.05242-11

Gould, S. B., Maier, U.-G., and Martin, W. F. (2015). Protein import and the origin of red complex plastids. *Curr. Biol.* 25, R515–R521. doi: 10.1016/j.cub.2015.04.033

Greer, M. S., Cai, Y., Gidda, S. K., Esnay, N., Kretzschmar, F. K., Seay, D., et al. (2020). SEIPIN isoforms interact with the membrane-tethering protein VAP27-1 for lipid droplet formation. *Plant Cell* 32, 2932–2950. doi: 10.1105/tpc.19.00771

Grippa, A., Buxó, L., Mora, G., Funaya, C., Idrissi, F.-Z., Mancuso, F., et al. (2015). The seipin complex Fld1/Ldb16 stabilizes ER–lipid droplet contact sites. *J. Cell Biol.* 211, 829–844. doi: 10.1083/jcb.201502070

Grosche, C., Hempel, F., Bolte, K., Zauner, S., and Maier, U. G. (2014). The periplastidal compartment: a naturally minimized eukaryotic cytoplasm. *Curr. Opin. Microbiol.* 22, 88–93. doi: 10.1016/j.mib.2014.09.017

Guihéneuf, F., Leu, S., Zarka, A., Khozin-Goldberg, I., Khalilov, I., and Boussiba, S. (2011). Cloning and molecular characterization of a novel acyl-CoA:diacylglycerol acyltransferase 1-like gene (PtDGAT1) from the diatom *Phaeodactylum tricornutum*: *P. tricornutum* DGAT1 cloning and characterization. *FEBS J.* 278, 3651–3666. doi: 10.1111/j.1742-4658.2011.08284.x

Haslam, R. P., Hamilton, M. L., Economou, C. K., Smith, R., Hassall, K. L., Napier, J. A., et al. (2020). Overexpression of an endogenous type 2 diacylglycerol acyltransferase in the marine diatom *Phaeodactylum tricornutum* enhances lipid production and omega-3 long-chain polyunsaturated fatty acid content. *Biotechnol. Biofuels* 13:87. doi: 10.1186/s13068-020-01726-8

Hernández, M. L., Whitehead, L., He, Z., Gazda, V., Gilday, A., Kozhevnikova, E., et al. (2012). A cytosolic acyltransferase contributes to triacylglycerol synthesis

in sucrose-rescued arabidopsis seed oil catabolism mutants. *Plant Physiol.* 160, 215–225. doi: 10.1104/pp.112.201541

Hu, Q., Sommerfeld, M., Jarvis, E., Ghirardi, M., Posewitz, M., Seibert, M., et al. (2008). Microalgal triacylglycerols as feedstocks for biofuel production: perspectives and advances. *Plant J.* 54, 621–639. doi: 10.1111/j.1365-313X.2008.03492.x

Hulatt, C. J., Smolina, I., Dowle, A., Kopp, M., Vasanth, G. K., Hoarau, G. G., et al. (2020). Proteomic and transcriptomic patterns during lipid remodeling in *Nannochloropsis gaditana*. *IJMS* 21:6946. doi: 10.3390/ijms21186946

Ischebeck, T., Krawczyk, H. E., Mullen, R. T., Dyer, J. M., and Chapman, K. D. (2020). Lipid droplets in plants and algae: distribution, formation, turnover and function. *Semin. Cell Dev. Biol.* 108, 82–93. doi: 10.1016/j.semcdb.2020.02.014

Iwai, M., Hori, K., Sasaki-Sekimoto, Y., Shimojima, M., and Ohta, H. (2015). Manipulation of oil synthesis in *Nannochloropsis* strain NIES-2145 with a phosphorus starvation–inducible promoter from *Chlamydomonas reinhardtii*. *Front. Microbiol.* 6:912. doi: 10.3389/fmicb.2015.00912

Jackson, C. J., Gornik, S. G., and Waller, R. F. (2012). A tertiary plastid gains RNA editing in its new host. *Mol. Biol. Evol.* 30, 788–792. doi: 10.1093/molbev/mss270

Jallet, D., Xing, D., Hughes, A., Moosburner, M., Simmons, M. P., Allen, A. E., et al. (2020). Mitochondrial fatty acid β−oxidation is required for storage-lipid catabolism in a marine diatom. *New Phytol.* 228, 946–958. doi: 10.1111/nph.16744

Janssen, J. H., Driessen, J. L. S. P., Lamers, P. P., Wijffels, R. H., and Barbosa, M. J. (2018). Effect of initial biomass-specific photon supply rate on fatty acid accumulation in nitrogen depleted *Nannochloropsis gaditana* under simulated outdoor light conditions. *Algal Res.* 35, 595–601. doi: 10.1016/j.algal.2018.10.002

Janssen, J. H., Lamers, P. P., de Vos, R. C. H., Wijffels, R. H., and Barbosa, M. J. (2019a). Translocation and de novo synthesis of eicosapentaenoic acid (EPA) during nitrogen starvation in *Nannochloropsis gaditana*. *Algal Res.* 37, 138–144. doi: 10.1016/j.algal.2018.11.025

Janssen, J. H., Spoelder, J., Koehorst, J. J., Schaap, P. J., Wijffels, R. H., and Barbosa, M. J. (2020). Time-dependent transcriptome profile of genes involved in triacylglycerol (TAG) and polyunsaturated fatty acid synthesis in *Nannochloropsis gaditana* during nitrogen starvation. *J. Appl. Phycol.* 32, 1153–1164. doi: 10.1007/s10811-019-02021-2

Janssen, J. H., Wijffels, R. H., and Barbosa, M. J. (2019b). Lipid production in *Nannochloropsis gaditana* during nitrogen starvation. *Biology* 8:5. doi: 10.3390/biology8010005

Jaussaud, A., Lupette, J., Salvaing, J., Jouhet, J., Bastien, O., Gromova, M., et al. (2020). Stepwise biogenesis of subpopulations of lipid droplets in nitrogen starved *Phaeodactylum tricornutum* cells. *Front. Plant Sci.* 11:48. doi: 10.3389/fpls.2020.00048

Jensen, P. E., and Leister, D. (2014). Chloroplast evolution, structure and functions. *F1000Prime Rep.* 6:40. doi: 10.12703/P6-40

Jia, J., Han, D., Gerken, H. G., Li, Y., Sommerfeld, M., Hu, Q., et al. (2015). Molecular mechanisms for photosynthetic carbon partitioning into storage neutral lipids in *Nannochloropsis oceanica* under nitrogen-depletion conditions. *Algal Res.* 7, 66–77. doi: 10.1016/j.algal.2014.11.005

Joshi, A. S., Nebenfuehr, B., Choudhary, V., Satpute-Krishnan, P., Levine, T. P., Golden, A., et al. (2018). Lipid droplet and peroxisome biogenesis occur at the same ER subdomains. *Nat. Commun.* 9:2940. doi: 10.1038/s41467-018-05277-3

Jürgens, G. (2004). Membrane trafficking in plants. *Annu. Rev. Cell Dev. Biol.* 20, 481–504. doi: 10.1146/annurev.cellbio.20.082503.103057

Kaushik, S., and Cuervo, A. M. (2015). Degradation of lipid droplet-associated proteins by chaperone-mediated autophagy facilitates lipolysis. *Nat. Cell Biol.* 17, 759–770. doi: 10.1038/ncb3166

Keeling, P. J. (2010). The endosymbiotic origin, diversification and fate of plastids. *Phil. Trans. R. Soc. Lond. B* 365, 729–748. doi: 10.1098/rstb.2009.0103

Keeling, P. J. (2013). The number, speed, and impact of plastid endosymbioses in eukaryotic evolution. *Annu. Rev. Plant Biol.* 64, 583–607. doi: 10.1146/annurev-arplant-050312-120144

Kennedy, E. P., and Weiss, S. B. (1956). The function of cytidine coenzymes in the biosynthesis of phospholipides. *J. Biol. Chem.* 222, 193–214. doi: 10.1016/S0021-9258(19)50785-2

Kilian, O., and Kroth, P. G. (2004). Identification and characterization of a new conserved motif within the presequence of proteins targeted into complex diatom plastids: protein targeting into diatom plastids. *Plant J.* 41, 175–183. doi: 10.1111/j.1365-313X.2004.02294.x

Kory, N., Farese, R. V., and Walther, T. C. (2016). Targeting fat: mechanisms of protein localization to lipid droplets. *Trends Cell Biol.* 26, 535–546. doi: 10.1016/j.tcb.2016.02.007

Leyland, B., Boussiba, S., and Khozin-Goldberg, I. (2020a). A review of diatom lipid droplets. *Biology* 9:38. doi: 10.3390/biology9020038

Leyland, B., Zarka, A., Didi-Cohen, S., Boussiba, S., and Khozin-Goldberg, I. (2020b). High resolution proteome of lipid droplets isolated from the pennate diatom *Phaeodactylum tricornutum* (Bacillariophyceae) strain pt4 provides mechanistic insights into complex intracellular coordination during nitrogen deprivation. *J. Phycol.* 56, 1642–1663. doi: 10.1111/jpy.13063

Li, D.-W., Cen, S.-Y., Liu, Y.-H., Balamurugan, S., Zheng, X.-Y., Alimujiang, A., et al. (2016). A type 2 diacylglycerol acyltransferase accelerates the triacylglycerol biosynthesis in heterokont oleaginous microalga *Nannochloropsis oceanica*. *J. Biotechnol.* 229, 65–71. doi: 10.1016/j.jbiotec.2016.05.005

Li, J., Han, D., Wang, D., Ning, K., Jia, J., Wei, L., et al. (2014). Choreography of transcriptomes and lipidomes of *Nannochloropsis* reveals the mechanisms of oil synthesis in microalgae. *Plant Cell* 26, 1645–1665. doi: 10.1105/tpc.113.121418

Li, L., Wang, S., Wang, H., Sahu, S. K., Marin, B., Li, H., et al. (2020). The genome of *Prasinoderma coloniale* unveils the existence of a third phylum within green plants. *Nat. Ecol. Evol.* 4, 1220–1231. doi: 10.1038/s41559-020-1221-7

Liang, J., Iqbal, S., Wen, F., Tong, M., and Liu, J. (2019a). Phosphorus-induced lipid class alteration revealed by lipidomic and transcriptomic profiling in oleaginous microalga *Nannochloropsis* sp. PJ12. *Mar. Drugs* 17:519. doi: 10.3390/md17090519

Liang, J., Wen, F., and Liu, J. (2019b). Transcriptomic and lipidomic analysis of an EPA-containing *Nannochloropsis* sp. PJ12 in response to nitrogen deprivation. *Sci. Rep.* 9:4540. doi: 10.1038/s41598-019-41169-2

Li-Beisson, Y., Shorrosh, B., Beisson, F., Andersson, M. X., Arondel, V., Bates, P. D., et al. (2010). Acyl-lipid metabolism. *Arabidopsis Book* 8:e0133. doi: 10.1199/tab.0133

Li-Beisson, Y., Thelen, J. J., Fedosejevs, E., and Harwood, J. L. (2019). The lipid biochemistry of eukaryotic algae. *Prog. Lipid Res.* 74, 31–68. doi: 10.1016/j.plipres.2019.01.003

Lu, Y., Wang, X., Balamurugan, S., Yang, W.-D., Liu, J.-S., Dong, H.-P., et al. (2017). Identification of a putative seipin ortholog involved in lipid accumulation in marine microalga *Phaeodactylum tricornutum*. *J. Appl. Phycol.* 29, 2821–2829. doi: 10.1007/s10811-017-1173-8

Lupette, J., and Benning, C. (2020). Human health benefits of very-long-chain polyunsaturated fatty acids from microalgae. *Biochimie* 178, 15–25. doi: 10.1016/j.biochi.2020.04.022

Lupette, J., Jaussaud, A., Seddiki, K., Morabito, C., Brugière, S., Schaller, H., et al. (2019). The architecture of lipid droplets in the diatom *Phaeodactylum tricornutum*. *Algal Res.* 38:101415. doi: 10.1016/j.algal.2019.101415

Lupette, J., and Maréchal, E. (2018). "Phytoplankton glycerolipids: challenging but promising prospects from biomedicine to green chemistry and biofuels," in *Blue Biotechnology*, eds S. La Barre and S. S. Bates (Weinheim: Wiley-VCH), 191–215. doi: 10.1002/9783527801718.ch6

Ma, X.-N., Chen, T.-P., Yang, B., Liu, J., and Chen, F. (2016). Lipid production from *Nannochloropsis*. *Mar. Drugs* 14:61. doi: 10.3390/md14040061

Maeda, Y., Sunaga, Y., Yoshino, T., and Tanaka, T. (2014). Oleosome-associated protein of the oleaginous diatom *Fistulifera solaris* contains an endoplasmic reticulum-targeting signal sequence. *Mar. Drugs* 12, 3892–3903. doi: 10.3390/md12073892

Magré, J., Delépine, M., Khallouf, E., Gedde-Dahl, T., Van Maldergem, L., Sobel, E., et al. (2001). Identification of the gene altered in Berardinelli–Seip congenital lipodystrophy on chromosome 11q13. *Nat. Genet.* 28, 365–370. doi: 10.1038/ng585

Maier, U. G., Hofmann, C. J., Eschbach, S., Wolters, J., and Igloi, G. L. (1991). Demonstration of nucleomorph-encoded eukaryotic small subunit ribosomal RNA in cryptomonads. *Mol. Gen. Genet.* 230, 155–160. doi: 10.1007/BF00290663

Marechal, E. (2018). Primary endosymbiosis: emergence of the primary chloroplast and the chromatophore, two independent events. *Methods Mol. Biol.* 1829, 3–16. doi: 10.1007/978-1-4939-8654-5_1

Mayers, J. J., Flynn, K. J., and Shields, R. J. (2014). Influence of the N:P supply ratio on biomass productivity and time-resolved changes in elemental and bulk biochemical composition of *Nannochloropsis* sp. *Bioresour. Technol.* 169, 588–595. doi: 10.1016/j.biortech.2014.07.048

McFie, P. J., Stone, S. L., Banman, S. L., and Stone, S. J. (2010). Topological orientation of Acyl-CoA:Diacylglycerol Acyltransferase-1 (DGAT1) and identification of a putative active site histidine and the role of the n terminus in dimer/tetramer formation. *J. Biol. Chem.* 285, 37377–37387. doi: 10.1074/jbc.M110.163691

Menegol, T., Romero-Villegas, G. I., López-Rodríguez, M., Navarro-López, E., López-Rosales, L., Chisti, Y., et al. (2019). Mixotrophic production of polyunsaturated fatty acids and carotenoids by the microalga *Nannochloropsis gaditana*. *J. Appl. Phycol.* 31, 2823–2832. doi: 10.1007/s10811-019-01828-3

Meng, Y., Cao, X., Yang, M., Liu, J., Yao, C., and Xue, S. (2019). Glycerolipid remodeling triggered by phosphorous starvation and recovery in *Nannochloropsis oceanica*. *Algal Res.* 39:101451. doi: 10.1016/j.algal.2019.101451

Meng, Y., Cao, X., Yao, C., Xue, S., and Yang, Q. (2017). Identification of the role of polar glycerolipids in lipid metabolism and their acyl attribution for TAG accumulation in *Nannochloropsis oceanica*. *Algal Res.* 24, 122–129. doi: 10.1016/j.algal.2017.03.004

Meng, Y., Jiang, J., Wang, H., Cao, X., Xue, S., Yang, Q., et al. (2015). The characteristics of TAG and EPA accumulation in *Nannochloropsis oceanica* IMET1 under different nitrogen supply regimes. *Bioresour. Technol.* 179, 483–489. doi: 10.1016/j.biortech.2014.12.012

Morabito, C., Aiese Cigliano, R., Maréchal, E., Rébeillé, F., and Amato, A. (2020). Illumina and PacBio DNA sequencing data, de novo assembly and annotation of the genome of *Aurantiochytrium limacinum* strain CCAP_4062/1. *Data Brief* 31:105729. doi: 10.1016/j.dib.2020.105729

Mühlroth, A., Li, K., Røkke, G., Winge, P., Olsen, Y., Hohmann-Marriott, M., et al. (2013). Pathways of lipid metabolism in marine algae, co-expression network, bottlenecks and candidate genes for enhanced production of EPA and DHA in species of chromista. *Mar. Drugs* 11, 4662–4697. doi: 10.3390/md11114662

Mühlroth, A., Winge, P., El Assimi, A., Jouhet, J., Maréchal, E., Hohmann-Marriott, M. F., et al. (2017). Mechanisms of phosphorus acquisition and lipid class remodeling under P limitation in a marine microalga. *Plant Physiol.* 175, 1543–1559. doi: 10.1104/pp.17.00621

Munz, J., Xiong, Y., Kim, J. Y. H., Sung, Y. J., Seo, S., Hong, R. H., et al. (2020). Arginine-fed cultures generates triacylglycerol by triggering nitrogen starvation responses during robust growth in *Chlamydomonas*. *Algal Res.* 46:101782. doi: 10.1016/j.algal.2019.101782

Murakami, R., and Hashimoto, H. (2009). Unusual nuclear division in *Nannochloropsis oculata* (Eustigmatophyceae, Heterokonta) which may ensure faithful transmission of secondary plastids. *Protist* 160, 41–49. doi: 10.1016/j.protis.2008.09.002

Mus, F., Toussaint, J.-P., Cooksey, K. E., Fields, M. W., Gerlach, R., Peyton, B. M., et al. (2013). Physiological and molecular analysis of carbon source supplementation and pH stress-induced lipid accumulation in the marine diatom *Phaeodactylum tricornutum*. *Appl. Microbiol. Biotechnol.* 97, 3625–3642. doi: 10.1007/s00253-013-4747-7

Nakamura, Y. (2013). Phosphate starvation and membrane lipid remodeling in seed plants. *Prog. Lipid Res.* 52, 43–50. doi: 10.1016/j.plipres.2012.07.002

Nettebrock, N. T., and Bohnert, M. (2020). Born this way – Biogenesis of lipid droplets from specialized ER subdomains. *Biochim. Biophys. Acta* 1865:158448. doi: 10.1016/j.bbalip.2019.04.008

Nobusawa, T., Hori, K., Mori, H., Kurokawa, K., and Ohta, H. (2017). Differently localized lysophosphatidic acid acyltransferases crucial for triacylglycerol biosynthesis in the oleaginous alga *Nannochloropsis*. *Plant J.* 90, 547–559. doi: 10.1111/tpj.13512

Nobusawa, T., Yamakawa-Ayukawa, K., Saito, F., Nomura, S., Takami, A., and Ohta, H. (2019). A homolog of *Arabidopsis* SDP1 lipase in *Nannochloropsis* is involved in degradation of de novo-synthesized triacylglycerols in the endoplasmic reticulum. *Biochim. Biophys. Acta* 1864, 1185–1193. doi: 10.1016/j.bbalip.2019.05.013

Nojima, D., Yoshino, T., Maeda, Y., Tanaka, M., Nemoto, M., and Tanaka, T. (2013). Proteomics analysis of oil body-associated proteins in the oleaginous diatom. *J. Proteome Res.* 12, 5293–5301. doi: 10.1021/pr4004085

Nomaguchi, T., Maeda, Y., Liang, Y., Yoshino, T., Asahi, T., and Tanaka, T. (2018). Comprehensive analysis of triacylglycerol lipases in the oleaginous diatom *Fistulifera solaris* JPCC DA0580 with transcriptomics under lipid degradation. *J. Biosci. Bioeng.* 126, 258–265. doi: 10.1016/j.jbiosc.2018.03.003

Nonoyama, T., Nojima, D., Maeda, Y., Noda, M., Yoshino, T., Matsumoto, M., et al. (2019). Proteomics analysis of lipid droplets indicates involvement of membrane trafficking proteins in lipid droplet breakdown in the oleaginous diatom *Fistulifera solaris*. *Algal Res.* 44:101660. doi: 10.1016/j.algal.2019.101660

Oborník, M. (2019). Endosymbiotic evolution of algae, secondary heterotrophy and parasitism. *Biomolecules* 9:266. doi: 10.3390/biom9070266

Oku, M., Maeda, Y., Kagohashi, Y., Kondo, T., Yamada, M., Fujimoto, T., et al. (2017). Evidence for ESCRT- and clathrin-dependent microautophagy. *J. Cell Biol.* 216, 3263–3274. doi: 10.1083/jcb.201611029

Osuna-Cruz, C. M., Bilcke, G., Vancaester, E., De Decker, S., Bones, A. M., Winge, P., et al. (2020). The *Seminavis robusta* genome provides insights into the evolutionary adaptations of benthic diatoms. *Nat. Commun.* 11:3320. doi: 10.1038/s41467-020-17191-8

Pagac, M., Cooper, D. E., Qi, Y., Lukmantara, I. E., Mak, H. Y., Wu, Z., et al. (2016). SEIPIN regulates lipid droplet expansion and adipocyte development by modulating the activity of Glycerol-3-phosphate Acyltransferase. *Cell Rep.* 17, 1546–1559. doi: 10.1016/j.celrep.2016.10.037

Parks, M. B., Nakov, T., Ruck, E. C., Wickett, N. J., and Alverson, A. J. (2018). Phylogenomics reveals an extensive history of genome duplication in diatoms (Bacillariophyta). *Am. J. Bot.* 105, 330–347. doi: 10.1002/ajb2.1056

Pasquet, V., Ulmann, L., Mimouni, V., Guihéneuf, F., Jacquette, B., Morant-Manceau, A., et al. (2014). Fatty acids profile and temperature in the cultured marine diatom *Odontella aurita*. *J. Appl. Phycol.* 26, 2265–2271. doi: 10.1007/s10811-014-0252-3

Peled, E., Leu, S., Zarka, A., Weiss, M., Pick, U., Khozin-Goldberg, I., et al. (2011). Isolation of a novel oil globule protein from the green alga *Haematococcus pluvialis* (Chlorophyceae). *Lipids* 46, 851–861. doi: 10.1007/s11745-011-3579-4

Petroutsos, D., Amiar, S., Abida, H., Dolch, L.-J., Bastien, O., Rébeillé, F., et al. (2014). Evolution of galactoglycerolipid biosynthetic pathways – From cyanobacteria to primary plastids and from primary to secondary plastids. *Prog. Lipid Res.* 54, 68–85. doi: 10.1016/j.plipres.2014.02.001

Poliner, E., Panchy, N., Newton, L., Wu, G., Lapinsky, A., Bullard, B., et al. (2015). Transcriptional coordination of physiological responses in *Nannochloropsis oceanica* CCMP1779 under light/dark cycles. *Plant J.* 83, 1097–1113. doi: 10.1111/tpj.12944

Radakovits, R., Jinkerson, R. E., Fuerstenberg, S. I., Tae, H., Settlage, R. E., Boore, J. L., et al. (2012). Draft genome sequence and genetic transformation of the oleaginous alga *Nannochloropsis gaditana*. *Nat. Commun.* 3:686. doi: 10.1038/ncomms1688

Rapoport, I., Boll, W., Yu, A., Böcking, T., and Kirchhausen, T. (2008). A motif in the clathrin heavy chain required for the Hsc70/Auxilin uncoating reaction. *MBoC* 19, 405–413. doi: 10.1091/mbc.e07-09-0870

Remmers, I. M., D'Adamo, S., Martens, D. E., de Vos, R. C. H., Mumm, R., America, A. H. P., et al. (2018). Orchestration of transcriptome, proteome and metabolome in the diatom *Phaeodactylum tricornutum* during nitrogen limitation. *Algal Res.* 35, 33–49. doi: 10.1016/j.algal.2018.08.012

Renne, M. F., Klug, Y. A., and Carvalho, P. (2020). Lipid droplet biogenesis: a mystery "unmixing"? *Semin. Cell Dev. Biol.* 108, 14–23. doi: 10.1016/j.semcdb.2020.03.001

Reyes-Prieto, A., Weber, A. P. M., and Bhattacharya, D. (2007). The origin and establishment of the plastid in algae and plants. *Annu. Rev. Genet.* 41, 147–168. doi: 10.1146/annurev.genet.41.110306.130134

Roughan, P. G., and Slack, C. R. (1982). Cellular organization of glycerolipid metabolism. *Annu. Rev. Plant. Physiol.* 33, 97–132. doi: 10.1146/annurev.pp.33.060182.000525

Saha, S., Enugutti, B., Rajakumari, S., and Rajasekharan, R. (2006). Cytosolic triacylglycerol biosynthetic pathway in oilseeds. molecular cloning and expression of peanut cytosolic Diacylglycerol Acyltransferase. *Plant Physiol.* 141, 1533–1543. doi: 10.1104/pp.106.082198

Salo, V. T., Belevich, I., Li, S., Karhinen, L., Vihinen, H., Vigouroux, C., et al. (2016). Seipin regulates ER –lipid droplet contacts and cargo delivery. *EMBO J.* 35, 2699–2716. doi: 10.15252/embj.201695170

Salo, V. T., Li, S., Vihinen, H., Hölttä-Vuori, M., Szkalisity, A., Horvath, P., et al. (2019). Seipin facilitates triglyceride flow to lipid droplet and counteracts droplet ripening via endoplasmic reticulum contact. *Dev. Cell* 50, 478–493.e9. doi: 10.1016/j.devcel.2019.05.016

Santinho, A., Salo, V. T., Chorlay, A., Li, S., Zhou, X., Omrane, M., et al. (2020). Membrane curvature catalyzes lipid droplet assembly. *Curr. Biol.* 30, 2481–2494.e6. doi: 10.1016/j.cub.2020.04.066

Santucci, P., Johansen, M. D., Point, V., Poncin, I., Viljoen, A., Cavalier, J.-F., et al. (2019). Nitrogen deprivation induces triacylglycerol accumulation, drug tolerance and hypervirulence in mycobacteria. *Sci. Rep.* 9:8667. doi: 10.1038/s41598-019-45164-5

Sato, N., and Awai, K. (2017). "Prokaryotic Pathway" is not prokaryotic: noncyanobacterial origin of the chloroplast lipid biosynthetic pathway revealed by comprehensive phylogenomic analysis. *Genome Biol. Evol.* 9, 3162–3178. doi: 10.1093/gbe/evx238

Schneider, J. C., and Roessler, P. (1994). Radiolabeling studies of lipids and fatty acids in *Nannochloropsis* (Eustigmatophyceae), an oleaginous marine alga. *J. Phycol.* 30, 594–598. doi: 10.1111/j.0022-3646.1994.00594.x

Seddiki, K., Godart, F., Aiese Cigliano, R., Sanseverino, W., Barakat, M., Ortet, P., et al. (2018). Sequencing, *de novo* assembly, and annotation of the complete genome of a new Thraustochytrid species, strain CCAP_4062/3. *Genome Announc.* 6, e1335-e17. doi: 10.1128/genomeA.01335-17

Serafini, T., Orci, L., Amherdt, M., Brunner, M., Kahn, R. A., and Rothmant, J. E. (1991). ADP-Ribosylation factor is a subunit of the coat of Golgi-derived COP-coated vesicles: a novel role for a GTP-binding protein. *Cell* 67, 239–253. doi: 10.1016/0092-8674(91)90176-Y

Sim, M. F. M., Dennis, R. J., Aubry, E. M., Ramanathan, N., Sembongi, H., Saudek, V., et al. (2013). The human lipodystrophy protein seipin is an ER membrane adaptor for the adipogenic PA phosphatase lipin 1. *Mol. Metab.* 2, 38–46. doi: 10.1016/j.molmet.2012.11.002

Simionato, D., Block, M. A., La Rocca, N., Jouhet, J., Maréchal, E., Finazzi, G., et al. (2013). The response of *Nannochloropsis gaditana* to nitrogen starvation includes *de novo* biosynthesis of triacylglycerols, a decrease of chloroplast galactolipids, and reorganization of the photosynthetic apparatus. *Eukaryot. Cell* 12, 665–676. doi: 10.1128/EC.00363-12

Stone, S. J., Levin, M. C., and Farese, R. V. (2006). Membrane topology and identification of key functional amino acid residues of murine Acyl-CoA:Diacylglycerol Acyltransferase-2. *J. Biol. Chem.* 281, 40273–40282. doi: 10.1074/jbc.M607986200

Strassert, J. F. H., Jamy, M., Mylnikov, A. P., Tikhonenkov, D. V., and Burki, F. (2019). New phylogenomic analysis of the enigmatic phylum telonemia further resolves the eukaryote tree of life. *Mol. Biol. Evol.* 36, 757–765. doi: 10.1093/molbev/msz012

Su, W.-C., Lin, Y.-H., Pagac, M., and Wang, C.-W. (2019). Seipin negatively regulates sphingolipid production at the ER–LD contact site. *J. Cell Biol.* 218, 3663–3680. doi: 10.1083/jcb.201902072

Sui, X., Arlt, H., Brock, K. P., Lai, Z. W., DiMaio, F., Marks, D. S., et al. (2018). Cryo–electron microscopy structure of the lipid droplet–formation protein seipin. *J. Cell Biol.* 217, 4080–4091. doi: 10.1083/jcb.201809067

Sui, X., Wang, K., Gluchowski, N. L., Elliott, S. D., Liao, M., Walther, T. C., et al. (2020). Structure and catalytic mechanism of a human triacylglycerol-synthesis enzyme. *Nature* 581, 323–328. doi: 10.1038/s41586-020-2289-6

Sukenik, A., and Carmeli, Y. (1990). Lipid synthesis and fatty acid composition in *Nannochloropsis* sp. (eustigmatophyceae) grown in a light-dark cycle. *J. Phycol.* 26, 463–469. doi: 10.1111/j.0022-3646.1990.00463.x

Talukder, M. M., Sim, M. F. M., O'Rahilly, S., Edwardson, J. M., and Rochford, J. J. (2015). Seipin oligomers can interact directly with AGPAT2 and lipin 1, physically scaffolding critical regulators of adipogenesis. *Mol. Metab.* 4, 199–209. doi: 10.1016/j.molmet.2014.12.013

Tamm, L. K., Hong, H., and Liang, B. (2004). Folding and assembly of β-barrel membrane proteins. *Biochim. Biophys. Acta* 1666, 250–263. doi: 10.1016/j.bbamem.2004.06.011

Tanaka, A., De Martino, A., Amato, A., Montsant, A., Mathieu, B., Rostaing, P., et al. (2015). Ultrastructure and membrane traffic during cell division in the marine pennate diatom *Phaeodactylum tricornutum*. *Protist* 166, 506–521. doi: 10.1016/j.protis.2015.07.005

Tauchi-Sato, K., Ozeki, S., Houjou, T., Taguchi, R., and Fujimoto, T. (2002). The surface of lipid droplets is a phospholipid monolayer with a unique fatty acid composition. *J. Biol. Chem.* 277, 44507–44512. doi: 10.1074/jbc.M207712200

Taurino, M., Costantini, S., De Domenico, S., Stefanelli, F., Ruano, G., Delgadillo, M. O., et al. (2018). SEIPIN proteins mediate lipid droplet biogenesis to promote pollen transmission and reduce seed dormancy. *Plant Physiol.* 176, 1531–1546. doi: 10.1104/pp.17.01430

Thiam, A. R., and Forêt, L. (2016). The physics of lipid droplet nucleation, growth and budding. *Biochim. Biophys. Acta* 1861, 715–722. doi: 10.1016/j.bbalip.2016.04.018

Tsai, C.-H., Zienkiewicz, K., Amstutz, C. L., Brink, B. G., Warakanont, J., Roston, R., et al. (2015). Dynamics of protein and polar lipid recruitment during lipid droplet assembly in *Chlamydomonas reinhardtii*. *Plant J.* 83, 650–660. doi: 10.1111/tpj.12917

Van Mooy, B. A. S., Fredricks, H. F., Pedler, B. E., Dyhrman, S. T., Karl, D. M., Koblížek, M., et al. (2009). Phytoplankton in the ocean use non-phosphorus lipids in response to phosphorus scarcity. *Nature* 458, 69–72. doi: 10.1038/nature07659

Vancaester, E., Depuydt, T., Osuna-Cruz, C. M., and Vandepoele, K. (2020). Comprehensive and functional analysis of horizontal gene transfer events in diatoms. *Mol. Biol. Evol.* 37, 3243–3257. doi: 10.1093/molbev/msaa182

Vieler, A., Brubaker, S. B., Vick, B., and Benning, C. (2012a). A lipid droplet protein of *Nannochloropsis* with functions partially analogous to plant oleosins. *Plant Physiol.* 158, 1562–1569. doi: 10.1104/pp.111.193029

Vieler, A., Wu, G., Tsai, C.-H., Bullard, B., Cornish, A. J., Harvey, C., et al. (2012b). Genome, functional gene annotation, and nuclear transformation of the heterokont oleaginous alga *Nannochloropsis oceanica* CCMP1779. *PLoS Genet.* 8:e1003064. doi: 10.1371/journal.pgen.1003064

Villanova, V., Fortunato, A. E., Singh, D., Bo, D. D., Conte, M., Obata, T., et al. (2017). Investigating mixotrophic metabolism in the model diatom *Phaeodactylum tricornutum*. *Phil. Trans. R. Soc. Lond. B* 372, 20160404. doi: 10.1098/rstb.2016.0404

Walther, T. C., Chung, J., and Farese, R. V. (2017). Lipid droplet biogenesis. *Annu. Rev. Cell Dev. Biol.* 33, 491–510. doi: 10.1146/annurev-cellbio-100616-060608

Wang, C.-W., Miao, Y.-H., and Chang, Y.-S. (2014). Control of lipid droplet size in budding yeast requires the collaboration between Fld1 and Ldb16. *J. Cell Sci.* 127, 1214–1228. doi: 10.1242/jcs.137737

Wang, D., Ning, K., Li, J., Hu, J., Han, D., Wang, H., et al. (2014). *Nannochloropsis* genomes reveal evolution of microalgal oleaginous traits. *PLoS Genet.* 10:e1004094. doi: 10.1371/journal.pgen.1004094

Wang, H., Becuwe, M., Housden, B. E., Chitraju, C., Porras, A. J., Graham, M. M., et al. (2016). Seipin is required for converting nascent to mature lipid droplets. *eLife* 5:e16582. doi: 10.7554/eLife.16582

Wang, S., Idrissi, F.-Z., Hermansson, M., Grippa, A., Ejsing, C. S., and Carvalho, P. (2018). Seipin and the membrane-shaping protein Pex30 cooperate in organelle budding from the endoplasmic reticulum. *Nat. Commun.* 9:2939. doi: 10.1038/s41467-018-05278-2

Wang, X., Hao, T.-B., Balamurugan, S., Yang, W.-D., Liu, J.-S., Dong, H.-P., et al. (2017). A lipid droplet-associated protein involved in lipid droplet biogenesis and triacylglycerol accumulation in the oleaginous microalga *Phaeodactylum tricornutum*. *Algal Res.* 26, 215–224. doi: 10.1016/j.algal.2017.07.028

Ward, C., Martinez-Lopez, N., Otten, E. G., Carroll, B., Maetzel, D., Singh, R., et al. (2016). Autophagy, lipophagy and lysosomal lipid storage disorders. *Biochim. Biophys. Acta* 1861, 269–284. doi: 10.1016/j.bbalip.2016.01.006

Welte, M. A. (2015). Expanding roles for lipid droplets. *Curr. Biol.* 25, R470–R481. doi: 10.1016/j.cub.2015.04.004

Weng, L.-C., Pasaribu, B., -Ping Lin, I., Tsai, C.-H., Chen, C.-S., and Jiang, P.-L. (2015). Nitrogen deprivation induces lipid droplet accumulation and alters fatty acid metabolism in symbiotic dinoflagellates isolated from *Aiptasia pulchella*. *Sci. Rep.* 4:5777. doi: 10.1038/srep05777

Wimley, W. C. (2009). Toward genomic identification of β-barrel membrane proteins: composition and architecture of known structures. *Protein Sci.* 11, 301–312. doi: 10.1110/ps.29402

Xin, Y., Lu, Y., Lee, Y.-Y., Wei, L., Jia, J., Wang, Q., et al. (2017). Producing designer oils in industrial microalgae by rational modulation of co-evolving Type-2 Diacylglycerol Acyltransferases. *Mol. Plant* 10, 1523–1539. doi: 10.1016/j.molp.2017.10.011

Xu, Y., Caldo, K. M. P., Falarz, L., Jayawardhane, K., and Chen, G. (2020). Kinetic improvement of an algal diacylglycerol acyltransferase 1 via fusion with an acyl-CoA binding protein. *Plant J.* 102, 856–871. doi: 10.1111/tpj.14708

Xu, Y., Caldo, K. M. P., Pal-Nath, D., Ozga, J., Lemieux, M. J., Weselake, R. J., et al. (2018). Properties and biotechnological applications of Acyl-CoA:diacylglycerol Acyltransferase and Phospholipid:diacylglycerol Acyltransferase from terrestrial plants and microalgae. *Lipids* 53, 663–688. doi: 10.1002/lipd.12081

Yan, R., Qian, H., Lukmantara, I., Gao, M., Du, X., Yan, N., et al. (2018). Human SEIPIN binds anionic phospholipids. *Dev. Cell* 47, 248–256.e4. doi: 10.1016/j.devcel.2018.09.010

Yang, Z.-K., Niu, Y.-F., Ma, Y.-H., Xue, J., Zhang, M.-H., Yang, W.-D., et al. (2013). Molecular and cellular mechanisms of neutral lipid accumulation in diatom following nitrogen deprivation. *Biotechnol. Biofuels* 6:67. doi: 10.1186/1754-6834-6-67

Yim, W. W.-Y., and Mizushima, N. (2020). Lysosome biology in autophagy. *Cell Discov.* 6:6. doi: 10.1038/s41421-020-0141-7

Yoneda, K., Yoshida, M., Suzuki, I., and Watanabe, M. M. (2016). Identification of a major lipid droplet protein in a marine diatom *Phaeodactylum tricornutum*. *Plant Cell Physiol.* 57, 397–406. doi: 10.1093/pcp/pcv204

Yoon, K., Han, D., Li, Y., Sommerfeld, M., and Hu, Q. (2012). Phospholipid:diacylglycerol acyltransferase is a multifunctional enzyme involved in membrane lipid turnover and degradation while synthesizing triacylglycerol in the unicellular green microalga *Chlamydomonas reinhardtii*. *Plant Cell* 24, 3708–3724. doi: 10.1105/tpc.112.100701

Zhang, Y., Pan, Y., Ding, W., Hu, H., and Liu, J. (2020). Lipid production is more than doubled by manipulating a diacylglycerol acyltransferase in algae. *GCB Bioenergy* 13, 185–200. doi: 10.1111/gcbb.12771

Zienkiewicz, A., Zienkiewicz, K., Poliner, E., Pulman, J. A., Du, Z.-Y., Stefano, G., et al. (2020). The microalga *Nannochloropsis* during transition from quiescence to autotrophy in response to nitrogen availability. *Plant Physiol.* 182, 819–839. doi: 10.1104/pp.19.00854

Zienkiewicz, K., Zienkiewicz, A., Poliner, E., Du, Z.-Y., Vollheyde, K., Herrfurth, C., et al. (2017). *Nannochloropsis*, a rich source of diacylglycerol acyltransferases for engineering of triacylglycerol content in different hosts. *Biotechnol. Biofuels* 10:8. doi: 10.1186/s13068-016-0686-8

Zulu, N. N., Zienkiewicz, K., Vollheyde, K., and Feussner, I. (2018). Current trends to comprehend lipid metabolism in diatoms. *Prog. Lipid Res.* 70, 1–16. doi: 10.1016/j.plipres.2018.03.001

Conflict of Interest: The authors declare that the research was conducted in the absence of any commercial or financial relationships that could be construed as a potential conflict of interest.

Copyright © 2021 Guéguen, Le Moigne, Amato, Salvaing and Maréchal. This is an open-access article distributed under the terms of the Creative Commons Attribution License (CC BY). The use, distribution or reproduction in other forums is permitted, provided the original author(s) and the copyright owner(s) are credited and that the original publication in this journal is cited, in accordance with accepted academic practice. No use, distribution or reproduction is permitted which does not comply with these terms.

frontiers in Plant Science

ORIGINAL RESEARCH
published: 27 April 2021
doi: 10.3389/fpls.2021.648426

Semi-Quantitative Targeted Gas Chromatography-Mass Spectrometry Profiling Supports a Late Side-Chain Reductase Cycloartenol-to-Cholesterol Biosynthesis Pathway in Brown Algae

*Jean Girard[1], Goulven Lanneau[1,2†], Ludovic Delage[1], Cédric Leroux[2], Arnaud Belcour[3], Jeanne Got[3], Jonas Collén[1], Catherine Boyen[1], Anne Siegel[3], Simon M. Dittami[1], Catherine Leblanc[1] and Gabriel V. Markov[1]**

[1]CNRS, Integrative Biology of Marine Models (LBI2M, UMR8227), Station Biologique de Roscoff (SBR), Sorbonne Université, Roscoff, France, [2]CNRS, Plateforme Corsaire-METABOMER (FR2424), Station Biologique de Roscoff, Sorbonne Université, Roscoff, France, [3]Univ Rennes, Inria, CNRS, IRISA, Equipe Dyliss, Rennes, France

Sterols are biologically important molecules that serve as membrane fluidity regulators and precursors of signaling molecules, either endogenous or involved in biotic interactions. There is currently no model of their biosynthesis pathways in brown algae. Here, we benefit from the availability of genome data and gas chromatography-mass spectrometry (GC-MS) sterol profiling using a database of internal standards to build such a model. We expand the set of identified sterols in 11 species of red, brown, and green macroalgae and integrate these new data with genomic data. Our analyses suggest that some metabolic reactions may be conserved despite the loss of canonical eukaryotic enzymes, like the sterol side-chain reductase (SSR). Our findings are consistent with the principle of metabolic pathway drift through enzymatic replacement and show that cholesterol synthesis from cycloartenol may be a widespread but variable pathway among chlorophyllian eukaryotes. Among the factors contributing to this variability, one could be the recruitment of cholesterol biosynthetic intermediates to make signaling molecules, such as the mozukulins. These compounds were found in some brown algae belonging to Ectocarpales, and we here provide a first mozukulin biosynthetic model. Our results demonstrate that integrative approaches can already be used to infer experimentally testable models, which will be useful to further investigate the biological roles of those newly identified algal pathways.

Keywords: sterol, brown alga, gas chromatography-mass spectrometry, biosynthesis pathway evolution, side-chain reduction

OPEN ACCESS

Edited by:
Juliette Jouhet, UMR5168 Laboratoire de Physiologie Cellulaire Vegetale (LPCV), France

Reviewed by:
Hubert Schaller, UPR2357 Institut de Biologie Moléculaire des Plantes (IBMP), France
Xin Wang, Miami University, United States

***Correspondence:**
Gabriel V. Markov
gabriel.markov@sb-roscoff.fr

†Deceased

Specialty section:
This article was submitted to Marine and Freshwater Plants, a section of the journal Frontiers in Plant Science

Received: *31 December 2020*
Accepted: *06 April 2021*
Published: *27 April 2021*

Citation:
Girard J, Lanneau G, Delage L, Leroux C, Belcour A, Got J, Collén J, Boyen C, Siegel A, Dittami SM, Leblanc C and Markov GV (2021) Semi-Quantitative Targeted Gas Chromatography-Mass Spectrometry Profiling Supports a Late Side-Chain Reductase Cycloartenol-to-Cholesterol Biosynthesis Pathway in Brown Algae. Front. Plant Sci. 12:648426. doi: 10.3389/fpls.2021.648426

INTRODUCTION

Sterols are biologically important molecules in eukaryotes, which function as membrane fluidity regulators and precursors of signaling molecules, either endogenous or involved in biotic interactions. The associated biosynthetic pathways are good models to study metabolic pathway evolution because the enzymes involved are well-known across eukaryotes and relatively conserved despite some variation (Desmond and Gribaldo, 2009). Recently, several studies have enabled to better understand the history of this pathway in land plants (Sonawane et al., 2016), diatoms (Gallo et al., 2020), or red algae (Belcour et al., 2020). However, a general model for sterol biosynthesis in brown algae – a vast diversified and independent eukaryotic lineage (Bringloe et al., 2020) – is still lacking.

The main brown algal sterol is fucosterol, but C28 and C27 sterols have also been reported, for example, in the model brown alga *Ectocarpus siliculosus* (Mikami et al., 2018). Among C27 derivatives, specialized metabolites have also been identified, such as a molecule bearing structural similarity to a brassinosteroid biosynthesis precursors in the fucale *Cytoseira myrica* (Hamdy et al., 2009), or the mozukulins from another ectocarpale species, the mozuku *Cladosiphon okamuranus* (Cheng et al., 2016). Some of these specialized metabolites could be important signaling or defense molecules, but so far there is little knowledge about their potential biological roles (Markov et al., 2018).

In order to build sterol biosynthesis pathway models that take into account data on metabolite distribution, we carried out semi-quantitative gas chromatography-mass spectrometry (GC-MS) profiling of sterols present in the two brown algal orders, the Ectocarpales and the Laminariales, for which genome-scale metabolic networks have been recently reconstructed (Aite et al., 2018; Nègre et al., 2019; Dittami et al., 2020). Specifically, we explored the sterol profiles of the two *Ectocarpus* species for which genome sequences are available, *E. siliculosus* and *Ectocarpus subulatus*, as well as two local species from Roscoff: *Ectocarpus fasciculatus* and *Ectocarpus crouanorium*, and one additional member from the Ectocarpales order: *Pylaiella littoralis*. We also explored the sterol profiles of two kelp species (Laminariales) from Roscoff: *Saccharina latissima* and *Laminaria digitata*. Furthermore, we analyzed these profiles in three red algae (*Chondrus crispus*, *Mastocarpus stellatus*, and *Palmaria palmata*), and one green alga (*Ulva* sp.), as a basis for comparison and to further investigate the intriguing issue of undetectable cycloartenol that we noticed previously in *C. crispus* (Belcour et al., 2020).

MATERIALS AND METHODS

Sampling of Algae

Macroalgal samples from *L. digitata*, *Ulva* sp., *C. crispus*, and *M. stellatus* were collected at low tides on the shore at Roscoff, France, in front of the Station Biologique (48°43′38″ N; 3°59′04″ W) for *Ulva* sp., *C. crispus*, and *M. stellatus*, and at the Bloscon site (48°43"31"N; 3°58"8"W) for *L. digitata*. Samples from *E. fasciculatus* and *E. crouaniorum* came from frozen samples collected at Roscoff (Perharidy site, 48.73° N, 4.00° W) in 2009. Samples of *S. latissima*, *E. subulatus* Ec371 (CCAP accession 1310), *E. siliculosus* Ec32 (CCAP accession 1310/04), and *P. palmata* came from cultures and were maintained in 10 L Nalgene flasks in a culture room at 14°C using filtered and autoclave seawater enriched with Provasoli nutrients (Bold and Wynne, 1978) and aerated with 0.22 µm-filtered compressed air to avoid CO_2 depletion. The cultures of *S. latissima* were started from freshly released spores of mature sporophytes collected at Perharidy as described previously (Bernard et al., 2018). Photosynthetically active radiation was provided by Philips daylight fluorescence tubes at a photon flux density of 40 $\mu mol.m^{-2}.s^{-1}$ for 14 $h.d^{-1}$. The algal samples were freeze-dried, ground to powder and stored at −80°C up to chemical extraction.

Standards and Reagents

Cholesterol, stigmasterol, β-sitosterol, 7-dehydrocholesterol, lathosterol (5α-cholest-7-en-3β-ol), squalene, campesterol, brassicasterol, desmosterol, lanosterol, fucosterol, cycloartenol, and 5α-cholestane (internal standard) were acquired from Sigma-Aldrich (Saint-Quentin-Fallavier, France), cycloartanol and cycloeucalenol from Chemfaces (Wuhan, China), and zymosterol from Avanti Polar Lipids (Alabaster, United States). The C7-C40 Saturated Alkanes Standards were acquired from Supelco (Bellefonte, United States). Reagents used for extraction, saponification, and derivation steps were n-hexane, ethyl acetate, acetonitrile, methanol (Carlo ERBA Reagents, Val de Reuil, France), (trimethylsilyl)diazomethane, toluene (Sigma-Aldrich) and N,O-bis(trimethylsilyl)trifluoroacetamide with trimethylcholorosilane [BSTFA:TMCS (99:1); Supelco].

Standard Preparation

Stock solutions of cholesterol, stigmasterol, β-sitosterol, 7-dehydrocholesterol, lathosterol (5α-cholest-7-en-3β-ol), squalene, campesterol, brassicasterol, desmosterol, lanosterol, fucosterol, cycloartenol, and 5α-cholestane were prepared in hexane at a concentration of 5 $mg.ml^{-1}$. Working solutions were made at a concentration of 1 $mg.ml^{-1}$, in hexane, by diluting stock solutions. The C7-C40 Saturated Alkanes Standard stock had a concentration of 1 $mg.ml^{-1}$ and a working solution was prepared at a concentration of 0.1 $mg.ml^{-1}$. All solutions were stored at −20°C. The 24-alkylsterols from algae are often epimers from their land plant counterparts that can be distinguished by NMR (Rubinstein et al., 1976; Nes, 2011), so here campesterol, brassicasterol, sitosterol, and stigmasterol were used as proxies for both epimers of, respectively, 24-methylcholesterol, 24-methylcholest-22-enol, 24-ethylcholesterol and 24-ethylcholest-22-enol.

Calibration of Standard Quantification Curves

To avoid biases linked to the variation of the behavior of individual sterols during the ionization step, a quantification method specific to the available standards was developed, according to the recommendations of the community (Khoury et al., 2018). We choosed to use a method with a correction on average

standard curves between mix standards, which contained all sterols of the global mix standards, but divided in two new mixes with time retention well distinct, because this appears to give the best accurate relative quantification (details are given in **Supplementary Material**, **Supplementary Figures S1–S5** and **Supplementary Tables S1–S5**).

Sample Preparation

Algal samples (60 mg) were extracted with 2 ml ethyl acetate by continuous agitation for 1 h at 4°C. After 10 min of centrifugation at 4,000 rpm, the solvent was removed, the extracts were saponified in 3 ml of methanolic potassium hydroxide solution (1 M) during 1 h of incubation at 90°C. The saponification reaction was stopped by plunging samples into an ice bath for 30 min minimum. The unsaponifiable fraction was extracted with 2 ml of hexane and 1.2 ml of water and centrifuged at 2,000 rpm for 5 min. The upper phase was collected, dried under N_2, and resuspended with 120 µl of (trimethylsilyl)diazomethane, 50 µl of methanol:toluene [2:1 (v/v)] and 5 µl of 5α-cholestane (1 mg. ml^{-1}) as internal standard. The mixture was vortexed for 30 s and then heated to 37°C for 30 min. After a second evaporation under N_2, 50 µl of acetonitrile and 50 µl of BSTFA:TMCS (99:1) were added to the dry residue, vortexed for 30 s and heated to 60°C for 30 min. After final evaporation under N_2, the extract was resuspended in 100 µl of hexane, transferred into a sample vial and stored at −80°C until the GC-MS analysis.

Gas Chromatography-Mass Spectrometry Analysis

The sterols were analyzed on a 7890 Agilent Technologies gas chromatography coupled with a 5975C Agilent Technologies mass spectrometer (GC-MS). A HP-5MS capillary GC column (30 m × 0.25 mm × 0.25 µm) from J&W Scientific (CA, United States) was used for separation and UHP helium was used as carrier gas at a flow rate to 1 $ml.min^{-1}$. The temperature of the injector was 280°C and the detector temperature was 315°C. After injection, the oven temperature was kept at 60°C for 1 min. The temperature was increased from 60 to 100°C at a rate of 25°C.min^{-1}, then to 250°C at a rate of 15°C.min^{-1}, then to 315°C at a rate of 3°C.min^{-1} and then held at 315°C for 2 min, resulting in a total run time of 37 min. Electronic impact mass spectra were measured at 70 eV and an ionization temperature of 250°C. The mass spectra were scanned from m/z 50 to m/z 500. Peaks were identified based on the comparisons with the retention times and the mass spectra (**Supplementary Table S1**).

Searches for Orthologous Genes

Similarity searches for orthologous genes were performed using BLAST either against protein sequences, when available, or directly on translated nucleotidic sequences on the sequence read archive (SRA) or transcriptome shotgun assemblies (TSA). Project accession numbers for SRA and TSA are indicated in **Supplementary Table S6**.

Ab-initio Inference of Biosynthesis Pathways

Ab-initio inference of biosynthesis pathway was performed using the Pathmodel program (Belcour et al., 2020). The encoding source files for the mozukulins pathway and the brown sterol biosynthetic pathways were added in a new version of Pathmodel (0.2.0). See full links in the data availability statement.

Ancestral Character Mapping

Mitochondrial *cox3* nucleotidic sequences from GenBank (Accession numbers in **Supplementary Table S7**) were aligned using Clustal Omega (Sievers and Higgins, 2014) as implemented in Seaview version 4.5.4 (Gouy et al., 2010). Phylogenetic trees were built using PHYML 3.1 (Guindon and Gascuel, 2003) using the GTR with a gamma law and estimation of the proportion of invariable sites. Ancestral character reconstruction and stochastic mapping (Huelsenbeck et al., 2003) were performed under R version 3.2.2 (R Core Team, 2015) using the make.simmap function as implemented in the phytools package version 0.5.0 (Revell, 2012). Character evolution was inferred using a model of symmetrical transition rates between the character states (SYM). About 1,000 character histories were sampled to allow the incorporation of the uncertainty associated with the transition between different states. Inferred state frequencies for ancestral nodes were plotted using the describe.simmap function. See the link for commands and sources files in the data availability statement.

Update of Genome-Scale Metabolic Networks

Update of the genome-scale metabolic networks is available at genouest.org for four brown algal species (*E. siliculosus*, *E. subulatus*, *C. okamuranus*, and *Saccharina japonica*) was performed using the curation function of AuReMe (Aite et al., 2018). The added reactions are also available as **Supplementary Material** (**Supplementary Tables S8–S11**).

RESULTS

Targeted GC-MS Profiling and Quantification of Sterols in Seven Brown Algae and Four Red and Green Algae

We identified and quantified 12 sterols plus their common biosynthetic precursor squalene. The total quantity of sterols varied between 0.28 and 4.25 $\mu g.mg^{-1}$ dry weight (DW) across samples (**Figure 1**). Among them, seven sterols were found in at least some brown algae, fucosterol being the most abundant in brown and green algae, whereas cholesterol or desmosterol were the most abundant sterols in red algae (**Figure 1**). In order to get a more synthetic overview of the variation of sterol profiles in a phylogenetic context, we plotted the sterol profiles on a cladogram showing the phylogenetic relationships between the investigated species (**Figure 1**).

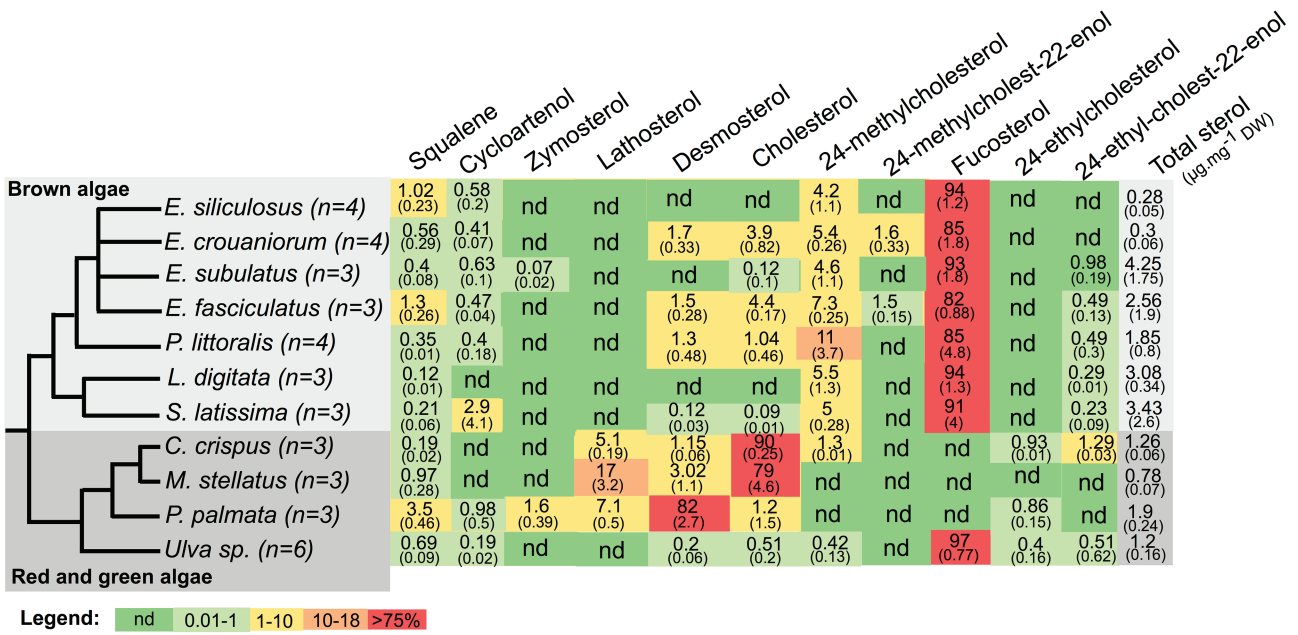

FIGURE 1 | Relative abundances of squalene and sterols detected in algal samples measured by semi-quantitative gas chromatography-mass spectrometry (GC-MS) profiling. Relative abundance values are expressed as a percentage of total sterol content, mean of multiple replicates, with SD in brackets. "nd" means not detectable (<0.01%). The tree represents the consensus view of the species phylogeny, with number of biological replicates indicated for each species. Last column (in gray) indicates the abundance of sterols relative to dry weight (DW).

Among the remaining sterols, cycloartenol was found in all algae except *C. crispus*, as previously noticed (Belcour et al., 2020), and *L. digitata*, where we could also interpret this absence as it being below the detection limit. Indeed, its precursor, squalene, is also found in the lowest concentration in *L. digitata* compared to the other examined brown algae. 24-methylcholesterol also turned out to be an important component of brown algal sterol profiles, representing between 4.2 and 11% of total sterols, whereas 24-ethylcholest-22-enol, 24-methylcholest-22-enol, desmosterol, and cholesterol were not always detectable and showed variable patterns. 24-ethylcholest-22-enol was always a rare sterol (between 0 and 0.98% in all brown algae), whereas cholesterol ranged from 0 to 4.4%. Among the other investigated sterols, lanosterol was never found, whereas 24-ethylcholesterol and lathosterol were found only in the three red algal species, and zymosterol was found only in *P. palmata* and in *E. subulatus*. The fact that we did not detect ergosterol in any of the analyzed algae was particularly striking because it was recently reported to be present in *E. siliculosus*, using a different separation technique, HPLC coupled to fluorescence detection (Mikami et al., 2018). Therefore, we checked using a spiked extract that we were technically able to identify the standard in an extract from *E. siliculosus* tissue (**Supplementary Figure S1**). We also tentatively identified small amounts of coprostanol, a degradation product of cholesterol, in *P. littoralis*, but did not include it in the table because we do not have the corresponding analytical standard. Altogether, our analysis indicates that some closely related species share similar features that are linked to a common evolutionary history. For example, the three red algal species synthesize mainly sterols with 27 carbons, which correlate with the loss of the canonical sterol methyltransferases, transferring additional methyl groups in other lineages (Belcour et al., 2020; Gallo et al., 2020). However, *C. crispus* and *M. stellatus*, which belong to the Gigartinales, produce mainly cholesterol, whereas *P. palmata* belonging to the Palmariales produces mainly desmosterol. For brown algae, the variation across the four species of *Ectocarpus* indicates that, even among close relatives, there can also be important variations both in terms of total sterol content, equivalent to the variation observed across the three phyla, and also in terms of relative sterol abundance. In that case, as we did not specifically control for developmental stage or physiological state among samples, those parameters can contribute as much as phylogenetic history to the observed variation.

A General Model for Sterol Biosynthesis in Brown Algae

In order to build a general biosynthesis model for the brown algal sterols confirmed by GC-MS profiling, we used the previously developed Pathmodel program (Belcour et al., 2020) to infer pathways based on the data about the presence and absence of sterols in brown alga and the related biochemical reactions registered in the MetaCyc database (Caspi et al., 2020). This model shows a mixture of features that are either conserved in other lineages or specific to brown algae (**Figure 2**).

The biosynthesis pathway from cycloartenol to cholesterol is similar to one of the two alternative pathways potentially present in the red alga *C. crispus* (Belcour et al., 2020), and identical to the biosynthesis pathway proposed independently

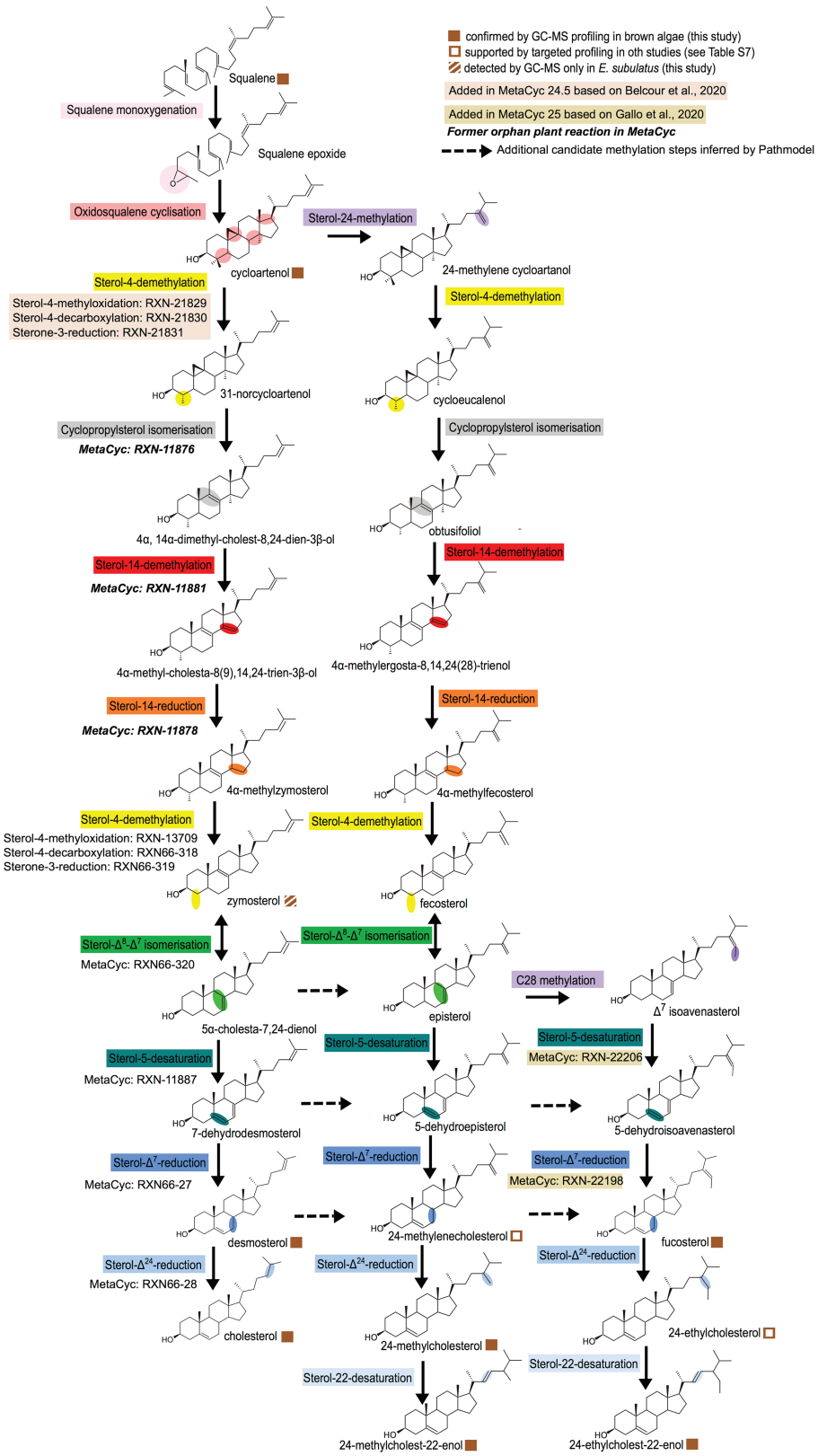

FIGURE 2 | General model for sterol biosynthesis in brown algae. The model was generated with Pathmodel, using the end metabolites isolated by GC-MS as targets and using known reactions. The colors indicate similar molecular transformations occurring on different substrates in the various pathway branches.

for two diatoms (Gallo et al., 2020). The difference in both pathways is that, in brown algae and diatoms, the second sterol-4-demethylation occurs before the sterol-Δ^8-Δ^7-isomerization, to accommodate the presence of zymosterol that we observed in at least one species (**Figure 2**), whereas in the red alga, the isomerization was inferred to occur before the demethylation, in line with the lack of zymosterol detection in this species (Belcour et al., 2020). Interestingly, during the incorporation of the *C. crispus* model in the MetaCyc database by manual curation, we noticed that not all reactions needed to be added. Some (in *bold italics* on **Figure 2**) were already present in the database, as orphan reactions not connected to a pathway. Their presence was established using enzymatic assays on sterol bioconversion performed with cellular extracts (Paik et al., 1984) or using biochemical characterization of recombinant plant enzymes in yeast (Grebenok et al., 1998; Lovato et al., 2000; Rahier et al., 2009). This therefore suggests that a cycloartenol-to-cholesterol pathway with late sterol-Δ^{24}-reduction may be present as a whole in plants that synthesize cholesterol, additional to the cycloartenol-to-cholesterol pathway with early sterol-Δ^{24}-reduction that has already been proposed for solanaceae (Sonawane et al., 2016).

The biosynthetic pathway from cycloartenol to 24-methylcholest-22-enol shares many steps with the classical land plant biosynthesis pathway from cycloartenol to campesterol (Desmond and Gribaldo, 2009), the main difference being that as for the pathway from cycloartenol to cholesterol, the second sterol-4-demethylation is inferred here to occur before the sterol-Δ^8-Δ^7-isomerization. The pathway leading to fucosterol may end up in a diatom-like way with a sterol-5-desaturation and a sterol-Δ^7-reduction following a sterol-28-methylation leading to different epimers than in land plants (Gallo et al., 2020). However, since the main biochemical requirement for sterol side chain alkylation at carbons 24 and 28 is the presence of a $\Delta^{24(25)}$ or $\Delta^{24(28)}$ double bond (Nes, 2003), alternative routes may be possible from other precursors having those double bonds (dotted arrows on **Figure 2**). Finally, to explain the observation of 24-ethylcholest-22-enol in some brown algae, it is necessary to infer the presence of 24-ethylcholesterol as an intermediate, because in that case the lack of $\Delta^{24(25)}$ or $\Delta^{24(28)}$ would render impossible a sterol-28-methylation from 24-methylcholest-22-enol. Actually, 24-ethylcholesterol has been reported in other brown algae by different groups (Kamenarska et al., 2003; Lopes et al., 2011; Mikami et al., 2018).

Most of the enzymes involved in the sterol biosynthesis pathway are globally conserved across eukaryotes (**Supplementary Table S6**), but there are some notable exceptions. The sterone-3-reductase performing the third step in the sterol-4-demethylation is known only in animals and fungi (Desmond and Gribaldo, 2009), and its absence in brown algae is consistent with the previously reported absence in plants. The canonical sterol-Δ^{24}-reductase and sterol-22-desaturases were lost in brown algae and were most likely replaced by paralogs, given that the metabolic profiling data indicate that those reactions occur (**Figure 2**). The canonical sterol-4-methyloxidase is found only in *E. subulatus* and in the transcriptome of a fucale, *Sargassum vulgare*. This suggests that this gene may be present in brown algae, but that it is currently unpredicted in the other brown algal genomes due to assembly issues. Altogether, those genomic data indicate that, as for other lineages, the sterol synthesis pathways in brown algae show both conservation and variation regarding other eukaryotic lineages.

The Late SSR Pathway as a Starting Point for the Biosynthesis of Specialized Metabolites

In addition to the sterols that are widespread across brown algae, some derived metabolites of this biosynthetic pathway seem to be restricted to certain species. This is the case of one of the algae for which, we previously performed a GSMN reconstruction (Nègre et al., 2019), the Japanese mozuku *C. okamuranus*. Two sterol derivatives, named mozukulin A and mozukulin B, have been identified in this species (Cheng et al., 2016). In the purpose of globally updating the sterol-related pathway in the GSMN, we also inferred *ab initio* a metabolic pathway model for those molecules using Pathmodel. For this, we could use some molecular transformations already present in the late SSR pathway (in yellow and blue on **Figure 3**) but also needed to incorporate three other reactions (in brown on **Figure 3**). The first one, a sterone-$\Delta^{1(2)}$-desaturation, has been described in bacteria degrading human sterols in sewage water sediments (Rohman and Dijkstra, 2019), fungi (Lv et al., 2017), and animals (Mahanti et al., 2014). The second one, a sterone-23-hydroxylation, comes from land plant brassinosteroid synthesis (Bajguz et al., 2020). Those two reactions could be easily inferred based on the knowledge from other organisms by the molecular transformation approach as implemented in Pathmodel. For the third reaction, a sterone-23-reduction, we did not find any other similar reactions either in databases or even using classical bibliographic search. However, reduction of hydroxylated carbon residues occurs at various other positions in the sterol backbone: this has been documented on carbons 3, 7, 11, 12, 17, and 20 (Caspi et al., 2020). In that case, the inference is based on a more relaxed concept of molecular transformations (Cunchillos and Lecointre, 2007). We previously justified its use from a biological viewpoint on sterols (Markov et al., 2017), but did not yet implement in Pathmodel. Finally, the sterone-Δ^{24}-reduction of Mozukulin A into Mozukulin B is a new variant of reactions observed at the end of the general brown algal sterol biosynthesis pathway (compare with **Figure 2**). Thus, the first sterol-4-demethylation steps of the late SSR could serve as a branching point for new enzymatic activities leading to the production of specialized molecules. The brown alga-specific sterol-Δ^{24} -reductase, distinct from the ancestral eukaryotic one, may have also been recruited into this pathway due to catalytic promiscuity.

Integrating Additional Brown Algal Metabolic Profiling Data to Inform Decisions About Genome-Scale Metabolic Network Curation

The four brown algae for which, we already reconstructed a GSMN illustrate well the classical challenge of heterogeneous

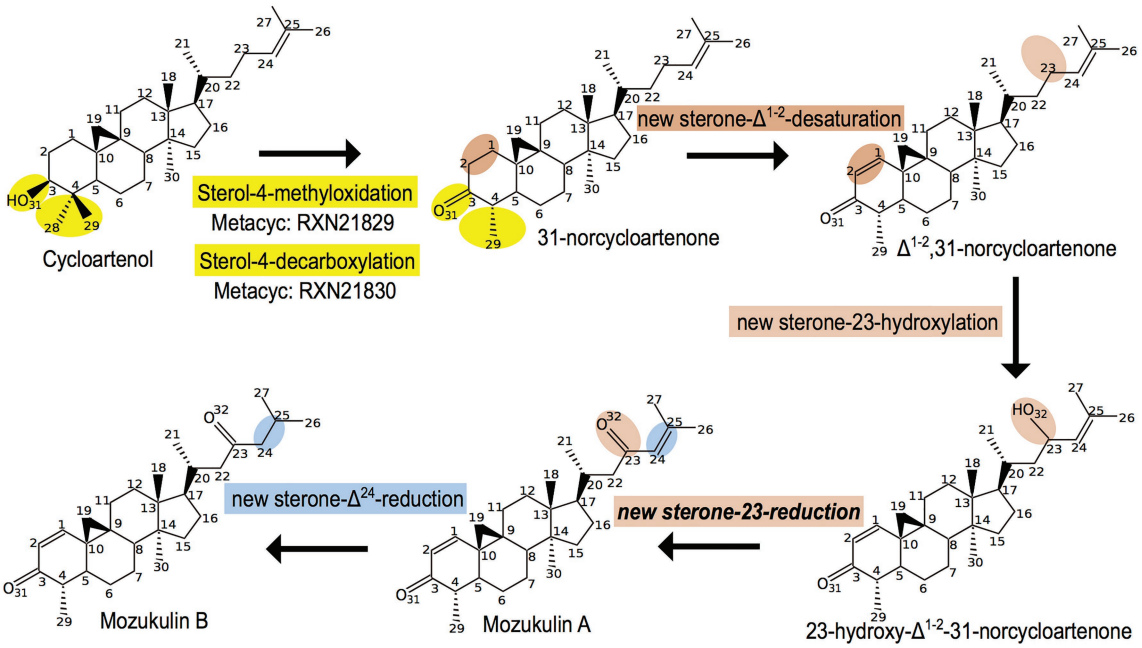

FIGURE 3 | *Ab initio* inference of the mozukulin pathway in the Ectocarpale alga *Cladosiphon okamuranus*. In yellow: reactions identical to the late sterol side-chain reductase (SSR) biosynthesis pathway. In blue: new variant from the Δ^{24}-reduction, distinct from those present in the early or late sterol biosynthesis pathways. In brown: reactions variants coming either from other pathways (bacterial steroid degradation or brassinosteroid synthesis) or even more distant type of molecular transformation, previously defined as "type hIIc homologies" (Cunchillos and Lecointre, 2007).

data integration. For the two *Ectocarpus* species, we had GC-MS profiling data, partially overlapping, but also partially contradicting those published by others (Mikami et al., 2018). For *S. japonica*, the published sterol profiles (Honya et al., 1994) were in agreement with our own observations in the closely related *S. latissima*. However for *C. okamuranus*, we only had data on specialized metabolites (mozukulins). In order to make a curation decision as well informed as possible, we decided to integrate our profiling results with the rest of the available knowledge on brown algal sterol profiling, which we gathered into an internal database (**Supplementary Table S7**). There is no experimental support yet for extending the distribution of the mozukulin pathway, for which evidence is up to now limited to *C. okamuranus*. On the contrary, for the fucosterol pathway, there is no reason to doubt about its presence in *C. okamuranus*, because fucosterol is systematically identified in brown algal sterol profiling. However, for the late SSR pathway, the 24-methyl-cholest-22-enol pathway and the pathway from fucosterol to 24-ethyl-cholest-22-enol, the distribution of sterols across species was much variable. This is illustrated with the late SSR pathway in **Figure 4**, where the data in favor of its wide distribution across brown algae are the strongest among those three pathways.

The topology of this *cox3*-based tree reflects well the current knowledge of phylogenetic relationships among crown brown algae (Bringloe et al., 2020). However, the four Dictyotales species at the basis of the brown algal group (*Dictyota dichotoma*, *Padina pavonica*, *Canistrocarpus cervicornis* and *Halopteris filicina*) do not cluster together, which we interpret as a technical artifact, leading to the overweighting of weak evidence for the late SSR pathway at the ancestral node. Even with this limitation, the probability that the late SSR pathway was present in the common ancestor of Laminariales and Ectocarpales with strong support is 51%. This probability stays identical for the last common ancestor of *C. okamuranus* and the *Punctaria*, *Striata*, and *Stilophora* genera, all corresponding to the Chordariaceae family (Silberfeld et al., 2014). However, because desmosterol has so far not been detected in any species of this group, we decided not to include yet a late SSR pathway in the genome-scale metabolic network for *C. okamuranus*.

DISCUSSION

In this study, we performed targeted profiling of 12 sterols in 11 algal species and integrated our findings regarding brown algae into biochemical pathway models. We establish a general model for the biosynthesis of the sterols that are widespread across brown algae, but also for some specialized metabolites that are derived from those general pathways. Our analysis therefore provides a starting point for biochemical tests of candidate enzymatic activities.

In addition to the biochemical validation, there are still some issues to further clarify from the metabolomic viewpoint. In particular, there are very few data, to date, on the biosynthetic intermediates between cycloartenol and end-pathway products

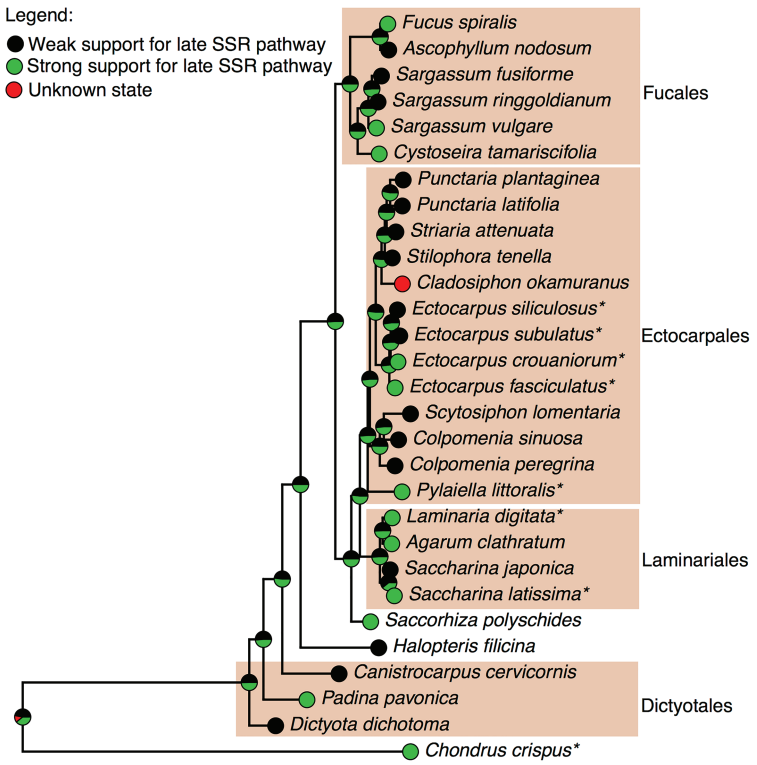

FIGURE 4 | Mapping the degree of support for the late SSR cholesterol pathway in brown algae. The maximum-likelihood tree was inferred based on publicly available data of the *cox3* mitochondrial marker. The four color boxes indicate algal orders where multiple species were analyzed. Strong support: cholesterol and desmosterol detected. Weak support: only cholesterol detected. *represents species with GC-MS data reported in this paper.

that we reported here. The only robust evidence here is available for the presence of 24-methylenecholesterol, which was reported in at least 11 other brown algal species (**Supplementary Table S7**). Those transient compounds are indeed difficult to detect because their abundance is very low in normal physiological states. However, evidence is accumulating in animals, fungi, and land plants that some of them are critical regulators of sterol homeostasis (Darnet and Schaller, 2019). Regarding the end-product sterols, we have to note that although we systematically found 24-methylcholesterol, it was only rarely reported by other studies in different species (**Supplementary Table S7**), while others reported 24-ethylcholesterol in brown algae, which we found only in the three red algae. This variability is similar to the one found in diatoms: while dihydrobrassicasterol, fucosterol, and clionasterol have been identified in the diatoms *Skeletonema marinoi* and *Cyclotella criptica*, the most abundant sterol in the lipid droplet of the diatom *Phaeodactylum tricornutum* was found to be brassicasterol (Lupette et al., 2019). In addition to the interspecies variations, other factors, like seasonality, are also known to influence the sterol profile variability (Honya et al., 1994). This probably contributed to the variability that we observed across the four *Ectocarpus* species.

Even if important biological variability could impact both quality and quantity of sterols in brown algae, some general patterns, either conserved or not, can be drawn, in relationships with evolution of this pathway. When comparing diatoms and brown algae, which belong both to the stramenopile lineage, it is interesting to note that a pathway identical to the late SSR pathway has been independently proposed (Gallo et al., 2020), the only difference with the late SSR pathway from red algae being that sterol-Δ^8-Δ^7 isomerization occurs before the second sterol-4-demethylation, leading to the production of zymosterol. Consistently with this, we inferred the same reaction order for the sterol-Δ^8-Δ^7 isomerization and sterol-4-demethylation occurring on methylated sterols, in contrast with the inferences in diatoms that keep the plant-like sterol-4-demethylation before the isomerization step. Regarding this, we have to stress that both hypotheses are equally speculative in light of data about the corresponding biosynthetic intermediates. Another difference between diatoms and brown algae is that some diatoms still retain the canonical SSR enzyme that has been lost in brown algae, despite the evidence that steroid side-chain reduction at carbon 24 does occur in brown algae, according to our profiling data and to independent NMR-based data on specialized metabolites in *C. okamuranus* (Cheng et al., 2016). This observation further supports the hypothesis of metabolic pathway drift by enzymatic replacement, the fact that a pathway can be maintained even if some enzymes are replaced by others over time (Belcour et al., 2020).

CONCLUSION

In this paper, we gathered GC-MS data from representatives of two brown algal orders to fuel a first model of sterol biosynthesis pathways and provide a case-study example of how to integrate these data with the literature in an evolutionary context. Specifically, we show that although the most likely way to synthesize cholesterol implies a late SSR pathway, this pathway shows variation either in terms of involved enzymes or in the succession of steps, highlighting the need for experimental data in multiple species to better understand the dynamics of metabolic pathway evolution across the eukaryotic tree of life.

DATA AVAILABILITY STATEMENT

Data to construct the brown algal biosynthesis pathway: https://github.com/pathmodel/pathmodel/blob/master/pathmodel/data/brown_sterols_pwy.lp. Data to construct the mozukulin biosynthesis pathway in *C. okamuranus*: https://github.com/pathmodel/pathmodel/blob/master/pathmodel/data/mozukulins_pwy.lp. Commands and sources files for ancestral mapping: https://github.com/gabrielmarkov/AncCharMapping. Updated versions of the brown algal genome-scale metabolic networks: http://aureme.genouest.org/wiki.html. All other original contributions presented in the study are included in the article/Supplementary Material; further inquiries can be directed to the corresponding author.

AUTHOR CONTRIBUTIONS

GM, LD, SD, CB, CLb, AS, and JC conceived the project. JGi conducted sterol profiling with help from GM, GL, LD, CLr, and CLb. GM encoded the mozukulin, brown algal biosynthesis pathways into the Pathmodel program with input from AB and AS, and wrote the manuscript with input and edits from all authors. LD performed reciprocal blast searches of orthologs in the sterol pathway. JGo updated the genome-scale metabolic network models on the AuReMe website based on input files prepared by GM. All authors contributed to the article and approved the submitted version.

FUNDING

This work benefited from the support of the French Government *via* the National Research Agency investment expenditure program IDEALG (ANR-10-BTBR-04) and from Région Bretagne *via* the grant SAD 2016 - METALG (9673). This chemical analytic work was carried in conjunction with the European Marine Biological Resource Centre (EMBRC-ERIC), EMBRC-France within the Investments of the Future program (ANR-10-INSB-02) and on the Corsaire-Metabomer platform supported by BioGenouest.

ACKNOWLEDGMENTS

We thank Philippe Potin, Miriam Bernard, and Sylvie Rousvoal for providing algal cultures, and Ron Caspi for curating the new red algal and diatom sterol biosynthesis pathways into the Metacyc database.

SUPPLEMENTARY MATERIAL

The Supplementary Material for this article can be found online at: https://www.frontiersin.org/articles/10.3389/fpls.2021.648426/full#supplementary-material

REFERENCES

Aite, M., Chevallier, M., Frioux, C., Trottier, C., Got, J., Cortés, M. P., et al. (2018). Traceability, reproducibility and wiki-exploration for "à-la-carte" reconstructions of genome-scale metabolic models. *PLOS Comp. Biol.* 14, 1–25. doi: 10.1371/journal.pcbi.1006146

Bajguz, A., Chmur, M., and Gruszka, D. (2020). Comprehensive overview of the brassinosteroid biosynthesis pathways: substrates, products, inhibitors, and connections. *Front. Plant Sci.* 11:1034. doi: 10.3389/fpls.2020.01034

Belcour, A., Girard, J., Aite, M., Delage, L., Trottier, C., Marteau, C., et al. (2020). Inferring biochemical reactions and metabolite structures to understand metabolic pathway drift. *iScience* 23:100849. doi: 10.1016/j.isci.2020.100849

Bernard, M., Rousvoal, S., Jacquemin, B., Ballenghien, M., Peters, A. F., and Leblanc, C. (2018). qPCR-based relative quantification of the brown algal endophyte *Laminarionema elsbetiae* in *Saccharina latissima*: variation and dynamics of host-endophyte interactions. *J. Appl. Phycol.* 30, 2901–2911. doi: 10.1007/s10811-017-1367-0

Bold, H. C., and Wynne, M. J. (1978). *Introduction to the Algae*. Englewood Cliffs. New Jersey: Prentice-Hall, xiv+706.

Bringloe, T. T., Starko, S., Wade, R. M., Vieira, C., Kawai, H., de Clerck, O., et al. (2020). Phylogeny and evolution of the brown algae. *Crit. Rev. Plant Sci.* 39, 281–321. doi: 10.1080/07352689.2020.1787679

Caspi, R., Billington, R., Keseler, I. M., Kothari, A., Krummenacker, M., Midford, P. E., et al. (2020). The MetaCyc database of metabolic pathways and enzymes - a 2019 update. *Nucleic Acids Res.* 48, D445–D453. doi: 10.1093/nar/gkz862

Cheng, K. C., Kuo, P. C., Hung, H. Y., Yu, K. H., Hwang, T. L., Shieh, P. C., et al. (2016). Four new compounds from edible algae *Cladosiphon okamuranus* and *Chlorella sorokiniana* and their bioactivities. *Phytochem. Lett.* 18, 113–116. doi: 10.1016/j.phytol.2016.09.008

Cunchillos, C., and Lecointre, G. (2007). Ordering events of biochemical evolution. *Biochimie* 89, 555–573. doi: 10.1016/j.biochi.2006.12.007

Darnet, S., and Schaller, H. (2019). Metabolism and biological activities of 4-methyl-sterols. *Molecules* 24:451. doi: 10.3390/molecules24030451

Desmond, E., and Gribaldo, S. (2009). Phylogenomics of sterol synthesis: insights into the origin, evolution, and diversity of a key eukaryotic feature. *Genome Biol. Evol.* 1, 364–381. doi: 10.1093/gbe/evp036

Dittami, S. M., Corre, E., Brillet-Guéguen, L., Lipinska, A. P., Pontoizeau, N., Aite, M., et al. (2020). The genome of *Ectocarpus subulatus* – A highly stress-tolerant brown alga. *Mar. Genomics* 52:100740. doi: 10.1016/j.margen.2020.100740

Gallo, C., Landi, S., d'Ippolito, G., Nuzzo, G., Manzo, E., Sardo, A., et al. (2020). Diatoms synthesize sterols by inclusion of animal and fungal genes in the plant pathway. *Sci. Rep.* 10:4204. doi: 10.1038/s41598-020-60993-5

Gouy, M., Guindon, S., and Gascuel, O. (2010). SeaView version 4: a multiplatform graphical user interface for sequence alignment and phylogenetic tree building. *Mol. Biol. Evol.* 27, 221–224. doi: 10.1093/molbev/msp259

Grebenok, R. J., Ohnmeiss, T. E., Yamamoto, A., Huntley, E. D., Galbraith, D. W., and Della Penna, D. (1998). Isolation and characterization of an *Arabidopsis thaliana* C-8,7 sterol isomerase: functional and structural similarities to

mammalian C-8,7 sterol isomerase/emopamil-binding protein. *Plant Mol. Biol.* 38, 807–815. doi: 10.1023/A:1006028623875

Guindon, S., and Gascuel, O. (2003). A simple, fast, and accurate algorithm to estimate large phylogenies by maximum likelihood. *Syst. Biol.* 52, 696–704. doi: 10.1080/10635150390235520

Hamdy, A. H. A., Aboutabl, E. A., Sameer, S., Hussein, A. A., Diaz-Marrero, A. R., Darias, J., et al. (2009). M. 3-Keto-22-epi-28-nor-cathasterone, a brassinosteroid-related metabolite from *Cystoseira myrica*. *Steroids* 74, 927–930. doi: 10.1016/j.steroids.2009.06.008

Honya, M., Kinoshita, T., Ishikawa, M., Mori, H., and Nisizawa, K. (1994). Seasonal variation in the lipid content of cultured *Laminaria japonica*: fatty acids, sterols, β-carotene and tocopherol. *J. Appl. Phycol.* 6, 25–29. doi: 10.1007/BF02185900

Huelsenbeck, J. P., Nielsen, R., and Bollback, J. P. (2003). Stochastic mapping of morphological characters. *Syst. Biol.* 52, 131–158. doi: 10.1080/10635150390192780

Kamenarska, Z. G., Dimitrova-Konaklieva, S. D., Stefanov, K. L., and Popov, S. S. (2003). A comparative study on the sterol composition of some brown algae from the Black Sea. *J. Serb. Chem. Soc.* 68, 269–275. doi: 10.2298/JSC0305269K

Khoury, S., Canlet, C., Lacroix, M. Z., Berdeaux, O., Jouhet, J., and Bertrand-Michel, J. (2018). Quantification of lipids: model, reality, and compromise. *Biomol. Ther.* 8:174. doi: 10.3390/biom8040174

Lopes, G., Sousa, C., Bernardo, J., Andrade, P. B., Valentão, P., Ferreres, F., et al. (2011). Sterol profiles in 18 macroalgae of the portuguese coast. *J. Phycol.* 47, 1210–1218. doi: 10.1111/j.1529-8817.2011.01028.x

Lovato, M. A., Hart, E. A., Segura, M. J., Giner, J. L., and Matsuda, S. P. (2000). Functional cloning of an *Arabidopsis thaliana* cDNA encoding cycloeucalenol cycloisomerase. *J. Biol. Chem.* 275, 13394–13397. doi: 10.1074/jbc.275.18.13394

Lupette, J., Jaussaud, A., Seddiki, K., Morabito, C., Brugière, S., Schaller, H., et al. (2019). The architecture of lipid droplets in the diatom *Phaeodactylum tricornutum*. *Algal Res.* 38:101415. doi: 10.1016/j.algal.2019.101415

Lv, J.-M., Hu, D., Gao, H., Kushiro, T., Awakawa, T., Chen, G.-D., et al. (2017). Biosynthesis of helvolic acid and identification of an unusual C-4-demethylation process distinct from sterol biosynthesis. *Nat. Commun.* 8:1644. doi: 10.1038/s41467-017-01813-9

Mahanti, P., Bose, N., Bethke, A., Judkins, J. C., Wollam, J., Dumas, K. J., et al. (2014). Comparative metabolomics reveals endogenous ligands of DAF-12, a nuclear hormone receptor, regulating *C. elegans* development and lifespan. *Cell Metab.* 19, 73–83. doi: 10.1016/j.cmet.2013.11.024

Markov, G. V., Girard, J., Laudet, V., and Leblanc, C. (2018). Hormonally active phytochemicals from macroalgae: a largely untapped source of ligands to deorphanize nuclear receptors in emerging marine animal models. *Gen. Comp. Endocrinol.* 265, 41–45. doi: 10.1016/j.ygcen.2018.06.004

Markov, G. V., Gutierrez-Mazariegos, J., Pitrat, D., Billas, I. M. L., Bonneton, F., Moras, D., et al. (2017). Origin of an ancient hormone/receptor couple revealed by resurrection of an ancestral estrogen. *Sci. Adv.* 3:e1601778. doi: 10.1126/sciadv.1601778

Mikami, K., Ito, M., Taya, K., Kishimoto, I., Kobayashi, T., Itabashi, Y., et al. (2018). Parthenosporophytes of the brown alga *Ectocarpus siliculosus* exhibit sex-dependent differences in thermotolerance as well as fatty acid and sterol composition. *Mar. Environ. Res.* 137, 188–195. doi: 10.1016/j.marenvres.2018.02.003

Nègre, D., Aite, M., Belcour, A., Frioux, C., Brillet-Guéguen, L., Liu, X., et al. (2019). Genome-scale metabolic networks shed light on the carotenoid biosynthesis pathway in the brown algae *Saccharina japonica* and *Cladosiphon okamuranus*. *Antioxidants* 8:564. doi: 10.3390/antiox8110564

Nes, W. (2003). Enzyme mechanisms for sterol C-methylations. *Phytochemistry* 64, 75–95. doi: 10.1016/S0031-9422(03)00349-2

Nes, W. D. (2011). Biosynthesis of Cholesterol and Other Sterols. *Chem. Rev.* 111, 6423–6451. doi: 10.1021/cr200021m

Paik, Y. K., Trzaskos, J. M., Shafiee, A., and Gaylor, J. L. (1984). Microsomal enzymes of cholesterol biosynthesis from lanosterol. Characterization, solubilization, and partial purification of NADPH-dependent delta 8,14-steroid 14-reductase. *J. Biol. Chem.* 259, 13413–13423. doi: 10.1016/S0021-9258(18)90710-6

Rahier, A., Bergdoll, M., Génot, G., Bouvier, F., and Camara, B. (2009). Homology modeling and site-directed mutagenesis reveal catalytic key amino acids of 3beta-hydroxysteroid-dehydrogenase/C4-decarboxylase from *Arabidopsis*. *Plant Physiol.* 149, 1872–1886. doi: 10.1104/pp.108.132282

R Core Team (2015). R: A language and environment for statistical computing. R Foundation for Statistical Computing, Vienna, Austria. Available at: https://www.R-project.org/

Revell, L. J. (2012). Phytools: an R package for phylogenetic comparative biology (and other things). *Methods Ecol. Evol.* 3, 217–223. doi: 10.1111/j.2041-210X.2011.00169.x

Rohman, A., and Dijkstra, B. W. (2019). The role and mechanism of microbial 3-ketosteroid Δ(1)-dehydrogenases in steroid breakdown. *J. Steroid Bioch.* 191:105366. doi: 10.1016/j.jsbmb.2019.04.015

Rubinstein, I., Goad, L., Clague, A., and Mulheirn, L. J. (1976). The 220 MHz NMR spectra of phytosterols. *Phytochemistry* 15, 195–200. doi: 10.1016/S0031-9422(00)89083-4

Sievers, F., and Higgins, D. G. (2014). Clustal omega, accurate alignment of very large numbers of sequences. *Methods Mol. Biol.* 1079, 105–116. doi: 10.1007/978-1-62703-646-7_6

Silberfeld, T., Rousseau, F., and de Reviers, B. (2014). An updated classification of brown algae (Ochrophyta, Phaeophyceae). *Cryptogam. Algol.* 35, 117–156. doi: 10.7872/crya.v35.iss2.2014.117

Sonawane, P. D., Pollier, J., Panda, S., Szymanski, J., Massalha, H., Yona, M., et al. (2016). Plant cholesterol biosynthetic pathway overlaps with phytosterol metabolism. *Nat. plants* 3:16205. doi: 10.1038/nplants.2016.205

Conflict of Interest: The authors declare that the research was conducted in the absence of any commercial or financial relationships that could be construed as a potential conflict of interest.

Copyright © 2021 Girard, Lanneau, Delage, Leroux, Belcour, Got, Collén, Boyen, Siegel, Dittami, Leblanc and Markov. This is an open-access article distributed under the terms of the Creative Commons Attribution License (CC BY). The use, distribution or reproduction in other forums is permitted, provided the original author(s) and the copyright owner(s) are credited and that the original publication in this journal is cited, in accordance with accepted academic practice. No use, distribution or reproduction is permitted which does not comply with these terms.

frontiers in Plant Science

REVIEW
published: 19 May 2021
doi: 10.3389/fpls.2021.665206

Phytosterol Profiles, Genomes and Enzymes – An Overview

*Sylvain Darnet, Aurélien Blary, Quentin Chevalier and Hubert Schaller**

Plant Isoprenoid Biology Team, Institut de Biologie Moléculaire des Plantes du CNRS, Université de Strasbourg, Strasbourg, France

The remarkable diversity of sterol biosynthetic capacities described in living organisms is enriched at a fast pace by a growing number of sequenced genomes. Whereas analytical chemistry has produced a wealth of sterol profiles of species in diverse taxonomic groups including seed and non-seed plants, algae, phytoplanktonic species and other unicellular eukaryotes, functional assays and validation of candidate genes unveils new enzymes and new pathways besides canonical biosynthetic schemes. An overview of the current landscape of sterol pathways in the tree of life is tentatively assembled in a series of sterolotypes that encompass major groups and provides also peculiar features of sterol profiles in bacteria, fungi, plants, and algae.

Keywords: phytosterol, cholesterol, algae, plant, eukaryote, prokaryote

OPEN ACCESS

Edited by:
Eric Marechal, UMR 5168 Laboratoire de Physiologie Cellulaire Vegetale (LPCV), France

Reviewed by:
Angelo Fontana, Istituto di Chimica Biomolecolare, Consiglio Nazionale delle Ricerche (CNR), Italy
Michele Fabris, University of Southern Denmark, Denmark

***Correspondence:**
Hubert Schaller
hubert.schaller@ibmp-cnrs.unistra.fr

Specialty section:
This article was submitted to Marine and Freshwater Plants, a section of the journal Frontiers in Plant Science

Received: *07 February 2021*
Accepted: *20 April 2021*
Published: *19 May 2021*

Citation:
Darnet S, Blary A, Chevalier Q and Schaller H (2021) Phytosterol Profiles, Genomes and Enzymes – An Overview. Front. Plant Sci. 12:665206. doi: 10.3389/fpls.2021.665206

INTRODUCTION

Sterols are mandatory components of eukaryotic life as building blocks of cellular membranes and as bioactive signals both functions having specific molecular structural requirements (Schaller, 2010; Darnet and Schaller, 2019). The sterol repertoire, which is built from the $C_{30}H_{50}O$ triterpenic committed precursors cycloartenol and lanosterol is part of the ubiquitous terpenome that is inseparable from the origin of life (Ourisson and Nakatani, 1994), just as DNA, RNA, and proteins. Sterols are also found in some bacterial groups but not in archaea (Salvador-Castell et al., 2019). Hopanoids in bacteria are considered as functional triterpenic counterparts of sterols in eukaryotes, but their presence is not strictly restricted to prokaryotes since some lycophyte species synthesize hopanoids (Kushiro and Ebizuka, 2010). Such an overlapping distribution of structurally different triterpenes and terpenogenic enzymes at play in distantly related taxa illustrates the fact that those pathways are quite ancient acquisitions, which have evolved through multiple mechanisms (Keeling and Palmer, 2008). The diversity and complexity of sterol pathways and the evolution of enzymes is closely associated to the rise of oxygen on earth about two billion years ago (Holland, 2002; Summons et al., 2006). In fact, the enzymatic conversion of squalene to diploptene (the simplest hopanoid) in bacteria is a one-step dioxygen-independent biosynthetic process, whereas the nineteen-enzymatic step conversion of squalene into 24-ethylsterols in viridiplantae requires 12 molecules of dioxygen (Nes, 2011; Gold et al., 2017). The analysis and dating of hydrocarbon biomarkers particularly steranes, which are molecular fossils produced by the diagenetic transformation of sterols, have helped to apprehend the importance of certain eukaryotic groups in geological periods. For instance, isopropylcholestane is debated as the most probable marker of chlorophyta in neoproterozoic sediments (Bobrovskiy et al., 2021).

The elucidation of sterol pathways from biosynthetic to genetic studies has attracted immense research efforts over the last decades (Cornforth, 2002). Major findings from the initial cyclization of the oxidized squalene (3*S*)-2,3-oxidosqualene into steroidal triterpenols

(cycloartenol, lanosterol) to their conversion into cholesterol, ergosterol and phytosterols and the biological significance of those have been assembled in a global picture proposed for mammal, invertebrate, fungi, and plant model species (Nes, 2011; Brown et al., 2018; Moreau et al., 2018). The understanding of accurate biosynthetic processes for example with chemical radiotracers (Cornforth, 2002) preceded the characterization of corresponding enzyme activities but was limited to a small number of laboratory-compatible organisms. The growing access to genome mining is now rapidly broadening the understanding of the origin and distribution of sterol biosynthetic capabilities in the tree of life. The best example when considering sterol pathways is the widespread occurrence of cycloartenol (and cycloartenol synthase, CAS) in prokaryotes (Bode et al., 2003) and eukaryotes like *Dictyostelium discoidum* (Godzina et al., 2000; Meyer et al., 2002) or Naegleria (Raederstorff and Rohmer, 1987). In fact, novel and massive genome and metagenome analysis coupled with *ad hoc* functional validation assays will facilitate the access to yet undisclosed sterol biosynthetic enzymes or more generally new pathways and therefore new aspects of cellular homeostasis.

Here, the purpose is to provide an overview of main aspects of sterol profiles and corresponding enzymes from various organisms including plants and algae but not exclusively, and to tentatively classify organisms into sterolotypes, considering a wealth of genetic, biochemical, and phylogenomic data.

CANONICAL FEATURES OF STEROL BIOSYNTHESIS IN EUKARYOTES

Enzymes implied in the post-squalene pathways to sterols in model organisms (mammals: human, mouse; fungi: *Saccharomyces cerevisiae*; and chlorophyta: *Arabidopsis thaliana*) have been quite comprehensively described and orthologous or paralogous enzymes were found in related species or taxonomic groups based on functional genomics (Bloch, 1989; Benveniste, 2004; Schaller, 2010; Nes, 2011; Sonawane et al., 2016; Darnet and Schaller, 2019). Initial biosynthetic studies have led to the characterization of enzyme activities responsible for the successive substrate-product bioconversions identified in incorporation experiments or by the targeted action of chemical inhibitors (Guo et al., 1997). Organic analytical chemistry also preceded functional genomics to unveil a major pathway for the production in C_5 isoprenic units (isopentenyl diphosphate, dimethylallyl diphosphate) in prokaryotes and some eukaryotes, condensed in linear terpenic precursors (Rohmer, 1999). The occurrence of this so-called methylerythritol 4-phosphate (MEP) pathway in prokaryotes and plastids of the chlorophyta and apicomplexa, along with the classical (first described) mevalonate pathway in vertebrates, invertebrates, fungi and plants is now mapped on the tree of life with an increasing precision and consequently with exceptions or alternatives (Lombard and Moreira, 2011). Forward and reverse genetic screens and genome mining provided scientists with a compendium of genes implied in the conversion of squalene into sterol end-products like cholesterol, ergosterol, stigmasterol, and poriferasterol in human, yeast, land plants and algae, respectively (**Figure 1**). In brief, human (or mammals and other groups of sterol autotroph animals) and fungi use lanosterol as a committed precursor to produce cholesterol, a C_{27} product with an 8-carbon atom side chain, and ergosterol, a C_{28} product with one additional exocyclic carbon atom at C-24 added by a sterol-C-methyltransferase [SMT, here a zymosterol-C24-methyltransferase (SMT1)], respectively. Differences between mammals and fungi includes also a sterol-C22(23)-desaturase (C22D) present in yeast only and a sterol-7-reductase (C7R) absent from yeast only, indicative of gene gain and loss as a powerful driver of sterol profile diversification. The *A. thaliana* sterol pathway as a model for higher plants displays very strong differences with human and yeast canonical pathways. Plants use cycloartenol as a committed precursor. A further sterol diversification by the action of two distinct SMT1 and SMT2 is responsible for the formation of 24-methylsterols and 24-ethylsterols (C_{29} products), respectively, (Bouvier-Nave et al., 1998; Schaeffer et al., 2001; Nakamoto et al., 2015). The Arabidopsis pathway also includes a C22D of the same cytochrome P450-dependent monooxygenases group (CYP710A) as the fungi enzyme (Morikawa et al., 2006). Arabidopsis has also evolved two distinct sterol methyl oxidases SMO1 and SMO2 acting non-consecutively during the course of the conversion of cycloartenol into the complex 24-alkyl-Δ^5-sterol mixture typical of plants (Darnet and Rahier, 2004). Conversely, a single SMO in fungi and mammals contributes to the C4-demethylation complex of enzymes [including in addition to SMO, a 3β-hydroxysteroid dehydrogenase/C4-decarboxylase (βHSD), a sterone ketoreductase (SR), and a tethering ERG28 protein] that removes successively both methyl groups at C-4 (**Figure 1**; Bouvier et al., 2005). In addition, the mandatory biosynthesis of phytosterols from cycloartenol (Babiychuk et al., 2008) requires a cyclopropyl sterol isomerase (CPI; Men et al., 2008), which is also present in some protists like *D. discoidum* that use the cycloartenol pathway (Lovato et al., 2000). Mammalian, fungi and plant sterol pathways therefore define major sterolotypes based on sterol profiles and the associated enzymes like lanosterol synthase (LAS) in mammals, LAS and SMT1 in fungi, and CAS and SMT1 and SMT2 in higher plants (**Figure 2**). Gene gain or loss differentiate these pathways, otherwise sharing significant orthology and paralogy thus enabling functional cloning in yeast of human and plant enzymes for biochemical complementation or metabolic interference (Corey et al., 1993; Lecain et al., 1996; Husselstein et al., 1999). Those canonical pathways have been quite extensively reviewed (Benveniste, 2004; Schaller, 2010; Nes, 2011; Brown et al., 2018; Moreau et al., 2018). Very strikingly, further gene discovery in sterol metabolism still relies on direct and possibly challenging biochemical approaches. The recent finding of aspartyl ergosterol and the set of enzymes promoting conjugation and deconjugation of ergosterol with amino acids represent a prominent example in the field. This novel group of sterols restricted to fungi (except in *S. cerevisiae* where the gene is absent) is formed by the action of non-canonical tRNA acyltransferases (Yakobov et al., 2020).

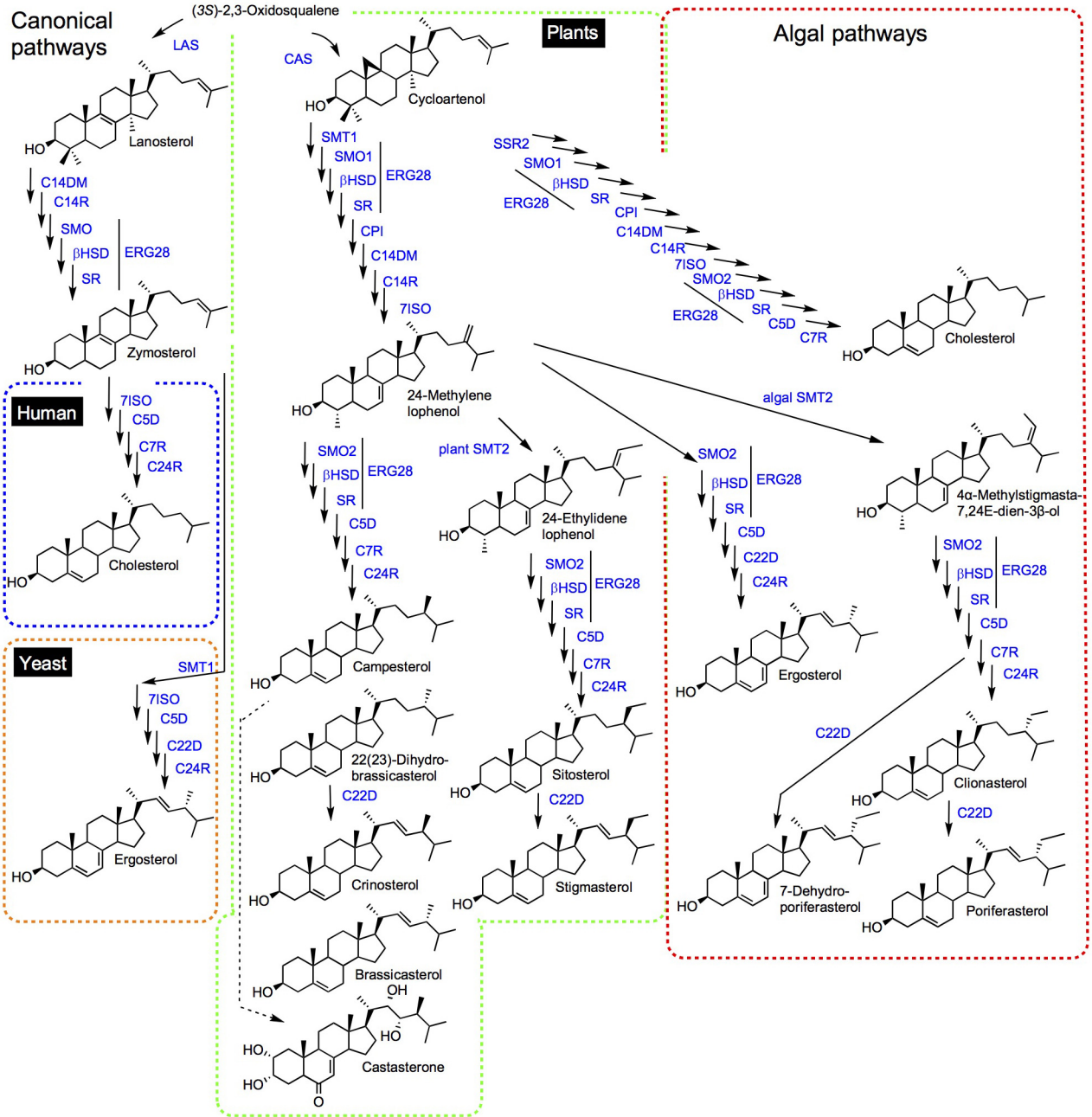

FIGURE 1 | Synthetic view of sterol pathways. Dashed lines discriminate mammalian (blue), fungal (red), and plants (green) canonical pathways. The so-called non-canonical pathways shown for algae is framed in mixed red and green colors to point out $\Delta^{5,7}$-sterols in both fungal and algal groups, and to recall common side chain modifying enzymes SSR2 and SMTs. Substrate-product enzymatic conversion is visualized with a single arrow. The dashed line between campesterol and castasterone (brassinosteroids) represents multiple steps. Sterol names are non-systematic names. The comprehensive IUPAC recommendations and conventional system for sterol nomenclature based on cholestane, ergostane, and stigmastane scaffolds, and the associated stereochemistry is given in Moss (1989) and also commented in Nes (2011). LAS, lanosterol synthase; CAS, cycloartenol synthase; C14DM, sterol-14-demethylase; C14R, sterol-14-reductase; SMO, sterol methyl oxidase; βHSD, 3β-hydroxysteroid dehydrogenase/C4-decarboxylase; SR, sterone ketoreductase; 7ISO, sterol-7(8)-isomerase; C5D, sterol-5(6)-desaturase; C7R, sterol-7-reductase; C24R, sterol-24-reductase; SMT1, sterol-C24-methyltransferase; SMT2, sterol-C28-methyltransferase; CPI, cyclopropyl isomerase; and C22D, sterol-22-desaturase.

Besides canonical pathways, sterol biosynthetic processes in non-model eukaryotes are often overlooked, since sterol profiles only are reported but genomic data are just emerging. This is particularly the case for the vast group of algae (chromalveolate microalgae, rhodophyta, and green algae, etc.), which had been described for their sterol content in authoritative reports years

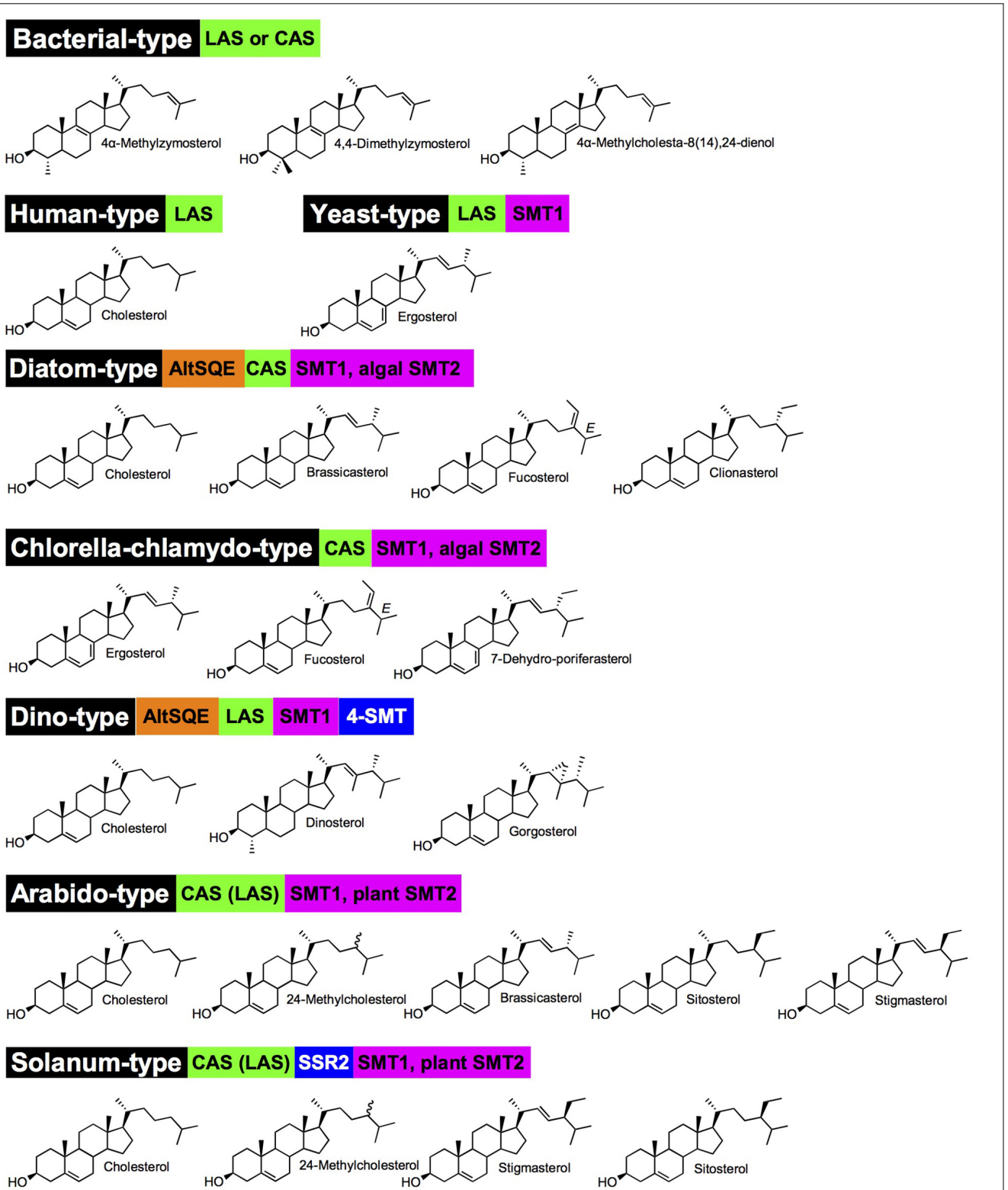

FIGURE 2 | Major sterolotypes defined in living organisms. Names in black boxes are chosen according to species or taxonomic groups for which a sterol pathway is well documented. Green boxes indicated whether a CAS (cycloartenol synthase) or LAS (lanosterol synthase) defines a sterol pathway; brackets are for minor contribution of a pathway as currently understood. Orange boxes are marking an AltSQE, alternative squalene epoxidase (canonical SQE otherwise not indicated in sterolotypes). Blue and magenta boxes are for sterol side chain modifications by SSR2 (sterol side chain reductase 2), SMT, sterol-C-methyltransferases. Major or representative sterols are represented for each sterolotype. Nomenclature as in **Figure 1**. Arabido-type and Solanum-type exhibit the epimeric pair of campesterol (C24α-methylcholesterol) and 22(23)-dihydrobrassicasterol (C24β-methylcholesterol) represented by 24-methylcholesterol.

ago (Patterson, 1971, 1974) or more recently (Kumari et al., 2013; Volkman, 2016; **Figure 1**). Major catalysts that generate the above-mentioned sterol diversity are SMT and sterol-Δ^{24}-reductases (C24R) or C22D implied in the modification of the sterol side chain (Nes, 2011). These enzymes are of pivotal importance for producing the epimeric 24-alkyl-sterols in different groups. The big picture obtained from decades of analytical work shows a taxonomy that recapitulates sterol stereochemistry at C24, with algae producing C24β-ethylsterols (clionasterol, poriferasterol) and higher plants producing C24α-ethylsterols (β-sitosterol, stigmasterol; Goad and Goodwin, 1972; **Figure 1**). Epimeric pairs of sterols like campesterol (C24α) and 22(23)-dihydrobrassicasterol (C24β), sitosterol (C24α), and clionasterol (C24β), stigmasterol (C24α), and poriferasterol (C24β; **Figures 1**, **3**) can be distinguished by NMR spectroscopic methods (Rubinstein et al., 1976). Studies with biological membrane mimics have shown equivalent structural behavior of 24-ethyl epimers (Marsan et al., 1996). The unequal distribution in taxa of those epimers is raising the interesting question of stereochemistry possibly recapitulating biology, as suggested from the progress in brassinosteroid signaling and biosynthesis made at a fast pace since 1996 (Li et al., 1996). In Arabidopsis, campesterol (24α-methylcholesterol) is the committed precursor of brassinosteroids through a C22 hydroxylation pathway whereas the epimeric 22(23)-dihydrobrassicasterol has not been reported as an active brassinosteroid precursor (Fujita et al., 2006; Bajguz et al., 2020). The astonishing diversity of sterol side chain biosynthetic modifications will be further scrutinized thanks to the growing number of eukaryotic genome and metagenome sequencing initiatives. The current global picture of sterol profiles across phyla shows a widespread distribution of C_{27}, C_{28}, and C_{29} sterols whereas C_{30} products are restricted to a few species (**Figure 4**).

SQUALENE METABOLISM INTO COMMITTED TRITERPENES

Squalene is the committed C_{30} isoprenic precursor of tetrahymanol and hopanoids, and after its conversion into (3*S*)-2,3-oxidosqualene, of steroidal (cycloartenol, lanosterol, and parkeol) and non-steroidal triterpenoids (**Figure 5**). While squalene- and (3*S*)-2,3-oxidosqualene-derived non-steroidal triterpenoids exhibit a skeletal chemical structure distinct from that of steroidal compounds (Xu et al., 2004), tetrahymanol and hopanoids do exert membrane structural functions classically assigned to sterols, as described below. Tetrahymanol is produced in the ciliate *Tetrahymena pyriformis* by a squalene-tetrahymanol cyclase (THC; Saar et al., 1991; Wiersma et al., 2020). A *S. cerevisiae* loss-of-function mutant impaired in ergosterol biosynthesis was able to grow autotrophically when expressing the *Tetrahymena* THC, indicating therefore a functionality of tetrahymanol as a sterol surrogate (Wiersma et al., 2020). Some bacteria are also tetrahymanol producers, however, their biosynthetic process leading to tetrahymanol requires first a squalene-hopene cyclase (SHC) that generates a product on which the bacterial tetrahymanol synthase (THS) performs additional ring expansion of the triterpenic product (Banta et al., 2015). Consequently, THC and THS enzymes define distinct systematic groups, which possess identical triterpene products resulting from evolutionary convergent processes.

Hopanoids are widely distributed in ecosystems. This is shown by their presence in sediments as stable hopane derivatives (or geohopanoids), which are markers of life of particular interest in petroleum geochemistry (Ourisson et al., 1982). These hopanoids are found in many prokaryotic groups (bacteria, cyanobacteria) and are quite often designated as "sterol surrogates" acting as phospholipidic bilayer stabilizers or reinforcers (Bird et al., 1971; De Rosa et al., 1971; Rohmer et al., 1979; Delgado-Baquerizo et al., 2018). This was established in a series of *in vitro* experiments showing that diplopterol and cholesterol achieved identical effects on phase behavior and ordering of sphingolipids in model membranes (Saenz et al., 2012; Mangiarotti et al., 2019). Hopanoids have attracted considerable research focus on plant-bacteria interactions particularly in legume-rhizobia symbiotic root nodulation since the initial characterization of hopanoid-lipid A conjugates (Silipo et al., 2014; Belin et al., 2018). Hopanoid producers are found within eukaryotes, in lichens and ferns producing both squalene-derived products, and (3*S*)-2,3-oxidosqualene-derived sterols just like canonical land plants. A cycloartenol to β-sitosterol pathway was described in *Selaginella* (Weng and Noel, 2013) and in *Azolla filiculoides* (Brouwer et al., 2015). Genome mining in these species provided new observations on fern-cyanobacteria symbiosis, with the identification of the cyanobacterial origin (from *Nostoc azollae* also called *Anabaena azollae*) of the lycophytic SHC (Pereira and Vasconcelos, 2014; Li et al., 2018). Functions of hopanoids as membrane lipids have been more specifically assigned in oxygenic photosynthetic cyanobacteria to the efficient protection through compartmentation, of the essential nitrogenase implied in nitrogen fixation, which is a dioxygen-sensitive process. At the most global scale of the oceans it is proposed that hopanoids are recruited to optimize the efficiency of cyanobacterial diazotrophs (Cornejo-Castillo and Zehr, 2019). This is of course reminiscent of the role of hopanoids as reinforcers of the vesicular structure that protects the site of nitrogenase activity in plant-rhizobia symbiotic relationships (Berry et al., 1993).

The mandatory biosynthetic route to sterols through cycloartenol and not lanosterol in plants was established in a series of comprehensive biosynthetic and genetic studies (Corey et al., 1993; Benveniste, 2004; Babiychuk et al., 2008; Gas-Pascual et al., 2015). However, extensive genome mining based on protein motifs and specific amino acid residue conservation or variation unveiled the presence of LASs in many plant species (Kolesnikova et al., 2006; Suzuki et al., 2006). The significance of a catalytically functional LAS from plants, when expressed in a heterologous yeast, is yet asking for more studies since a loss of function *las* allele from Arabidopsis displayed no morphogenetic inhibitions (Ohyama et al., 2009). In *Euphorbiaceae*, a LAS ortholog is producing loads of lanosterol in the cytoplasm of laticifers, in combination with other triterpene synthases like CAS and a butyrospermol synthase (Forestier et al., 2019). *Solanaceae* do have a LAS, but produce high amounts of cholesterol through the cycloartenol route like it is the case for other phytosterols. In fact,

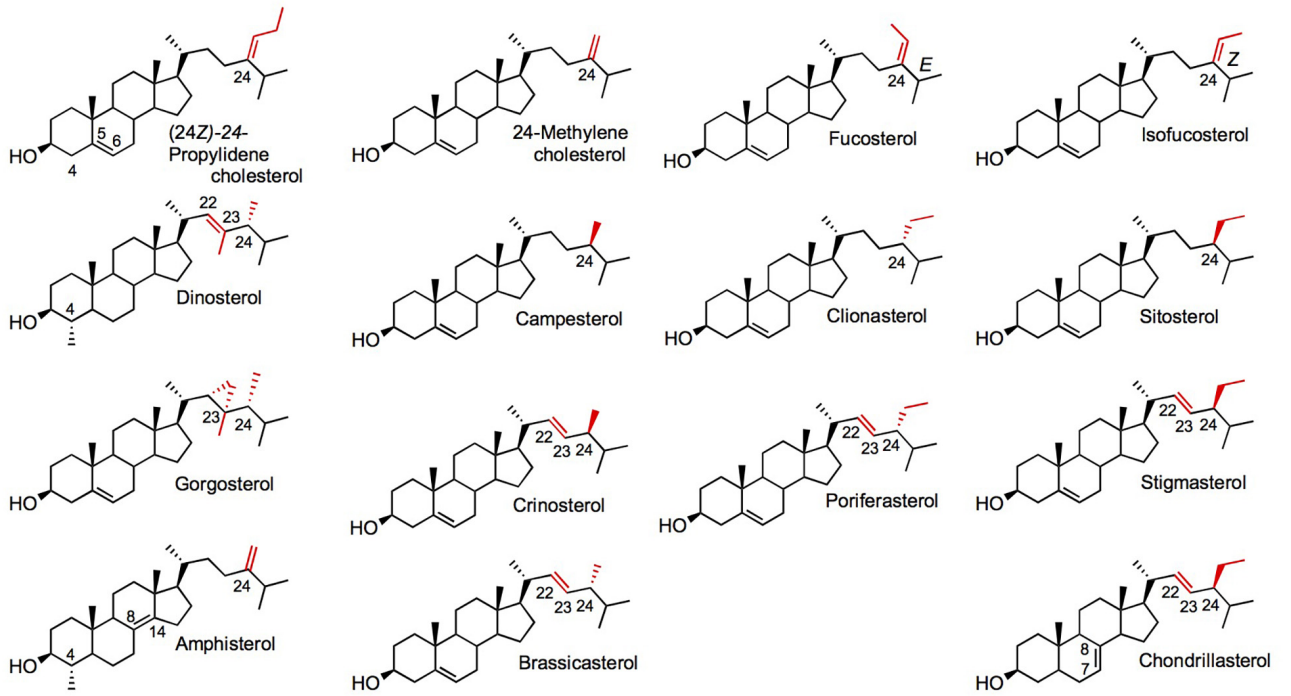

FIGURE 3 | Diverse sterols found in algae and plants. Side chain C22, C23, and C24 positions are in red. Chiral substituents at C24 of the sterol side chain are C24α for a methyl or ethyl group in front: campesterol, sitosterol, crinosterol, stigmasterol, chondrillasterol; or C24β for a methyl or ethyl group in back: dinosterol, clionasterol, gorgosterol, poriferasterol. Nomenclature as in **Figure 1**.

the lanosterol-unrelated cholesterol is a precursor of solanine and chaconine and of some other steroidal glycoalkaloids in tomato and potato, accounting for some 15–20% of total sterols. Besides a canonical plant sterol-$\Delta^{24(28)}$-reductase (**Figure 1**), a solanaceae-specific sterol-$\Delta^{24(25)}$-reductase also named sterol side chain reductase 2 (SSR2) reduces the $\Delta^{24(25)}$ of the 8-carbon side chain of cycloartenol and desmosterol, yielding cholesterol (Sawai et al., 2014; Sonawane et al., 2016). Consequently, a sterol pathway based on a CAS, SSR2, and SMT1 and SMT2 defines a major sterolotype among eukaryotes (**Figure 2**). The solanaceae *Withania somnifera* (Indian ginseng or ashwagandha) has a sterol-Δ^{24}-reductase coined 24ISO performing the conversion of 24-methylenecholesterol to 24-methyldesmosterol and consequently channeling the latter substrate into the specific biosynthetic segment for withanolides (Knoch et al., 2018).

MINIMAL STEROL PATHWAY IN PROKARYOTES

Sterols are quite often classified as eukaryotic lipids but in fact some bacterial species synthesize sterols. A prominent example of a bacterial pathway is given by the methylotroph *Methylococcus capsulatus*, which produces unique $\Delta^{8(14)}$ -sterols (Bouvier et al., 1976). *M. capsulatus* genes encoding a squalene epoxidase, a LAS and a lanosterol-14-demethylase have been identified (Lamb et al., 2007). This bacterial pathway converts lanosterol into a series of metabolites of which 4α-methylcholesta-8(14),24-dienol could be the end-product, which implies a set of enzymes for the demethylation at C-4, reduction at C-24, and isomerization of the lanosterol double bond 8(9) into 8(14). The discovery of C-4 demethylation proteins SdmA (a Rieske-type oxygenase) and SdmB [a NAD(P)-dependent reductase], which convert lanosterol into the corresponding 4-demethylated product shows that a sterol C4-demethylation process has evolved independently in prokaryotes and in eukaryotes (in which a C4-methyl group oxidation is carried out by enzymes from the fatty hydroxylase group; Lee et al., 2018). Other bacteria have evolved other minimal sterol pathways. *Gemmata obscuriglobus* is a planctomycetes that contains a (3*S*)-2,3-oxidosqualene cyclase (OSC) responsible for the formation of the isomers lanosterol and parkeol, without further metabolization of these steroidal triterpenes (Pearson et al., 2007). *Stigmatella aurantiaca* is a myxobacterium that produce sterols from cycloartenol (Bode et al., 2003). Genomic and metagenomic surveys pointed out the presence of OSCs in several bacterial phyla (bacteroidetes, planctomycetes, proteobacteria, and some others), broadening thus the evolutionary success of a bacterial type of sterol pathway (Wei et al., 2016). Although scarce some recent data indicate possible symbiotic interactions at the sterol metabolism interface: the combination of genomics and isotopic ratio mass spectrometry of sterols has been exploited in a probably unique study suggesting a metabolic cooperation between a methanotroph endosymbiont and its eukaryotic host, the mussel *Bathymodiolus genus*. As a matter of fact, the isotopic ratio $\delta^{13}C$ measured for the host cholesterol suggest a direct biogenetic

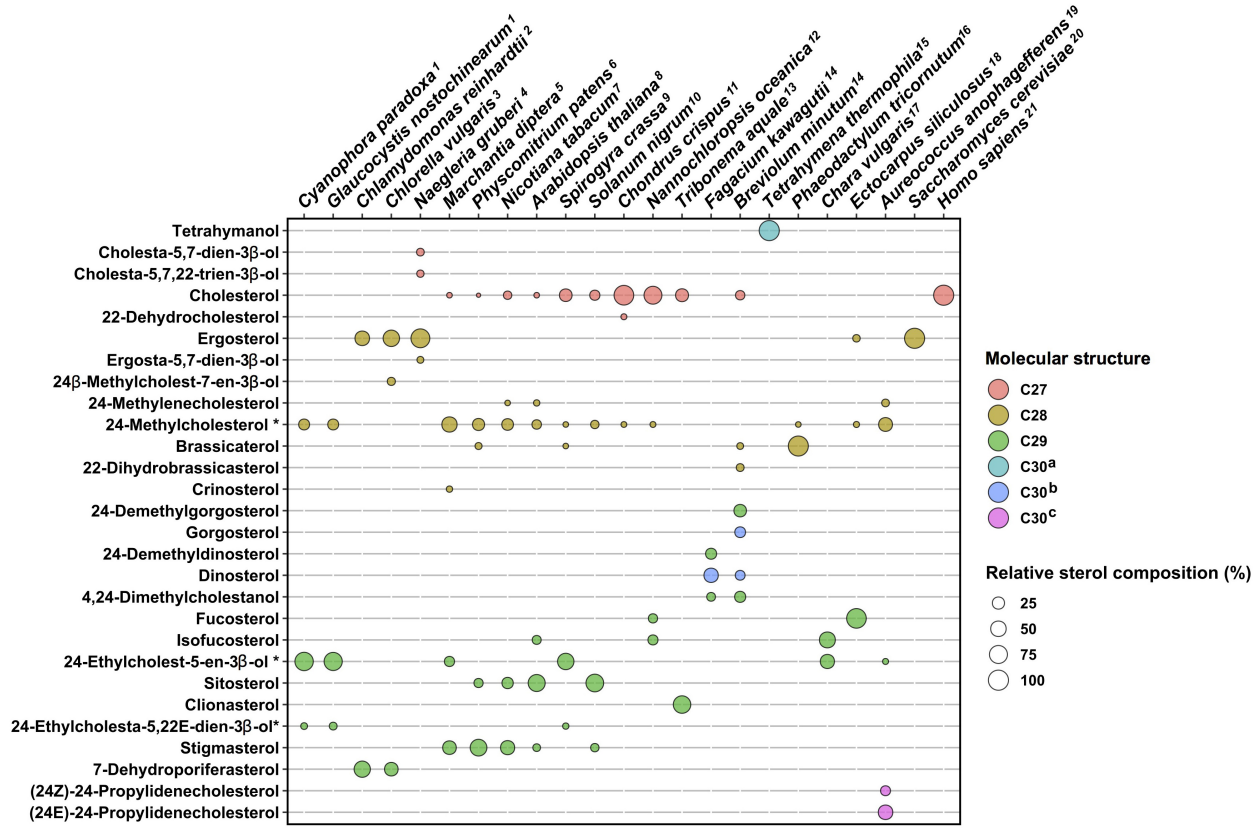

FIGURE 4 | Sterol profiles in algae and plants. Sterol compositions of twenty species are plotted on a schematic diagram, which indicates proportions in percent and molecular structures by color codes. C_{27}, sterols bearing a C_8-side chain (e.g., cholesterol); C_{28}, C_9-side chain (e.g., ergosterol); and C_{29}, C_{10}-side chain (e.g., fucosterol). $C_{30}{}^a$, $C_{30}H_{50}O$ direct cyclization products of (3*S*)-2,3-oxidosqualene (e.g., tetrahymanol). $C_{30}{}^b$, sterol products with additional methyl groups on the tetracyclic moiety and on the side chain (e.g., dinosterol). $C_{30}{}^c$, sterol products with a C_{11}-side chain (e.g., propylidene sterols). Sterol compositions as percent of the total were found in published references indicated by upper case numbering of species. Sterols contributing less than 2% of a total were not considered for clarity of this schematic representation. 1, Leblond et al. (2011); 2, Miller et al. (2012); 3, Akihisa et al. (1992); 4, Raederstorff and Rohmer (1987); 5, Chiu et al. (1985); 6, Morikawa et al. (2009); 7, Schaller et al. (1998); 8, Schaeffer et al. (2000); 9, Mitova et al. (1999); 10, Bhatt and Bhatt (1984); 11, Tasende (2000); 12, Lu et al. (2014); 13, Mercer et al. (1974); 14, Lu et al. (2020); 15, Conner et al. (1982); 16, Rampen et al. (2010); 17, Patterson and Nes (1991); 18, Mikami et al. (2018); 19, Giner et al. (2009); 20, Lamacka and Sajbidor (1997); and 21, Chakrabarti et al. (2017). *Tetrahymena thermophila*, *Saccharomyces cerevisiae*, and *Homo sapiens* are shown as single pathway end-product species. Sterols tagged with an asterisk * are C-24 epimeric mixtures.

link with methane from deep sea environments. In addition, transcripts for steroidogenic enzymes from the endosymbiont -which would provide the upstream biosynthetic pathway- and the host -which would provide the downstream biosynthetic pathway- were colocalized at the gills of the bivalves in *in situ* hybridization experiments (Takishita et al., 2017).

Cyanobacteria and other oxygenic photosynthetic bacteria from the genera *Anabaena*, *Nodularia*, *Nostoc*, *Spirulina*, *Chlorogloeopsis*, *Phormidium* conceal some sterol producing species as it was debated in the sixties especially with the detection of 24-ethylcholesterol (De Souza and Nes, 1968) and reviewed more recently (Volkman, 2003, 2016). Biosynthetic studies showing the conversion of isoprenic precursors to sterol products were not recently reported in any of the common cyanobacteria. *Phormidium autumnale* was shown to produce sterols albeit in heterotrophic culture systems compatible with an industrial scale-up (Fagundes et al., 2018). Metagenomic analysis of prokaryotic sequences pointed out OSC genes in some other genera of cyanobacteria like *Planktothrix* or *Prochloron* (Wei et al., 2016), but not in the genome of one of the most popular cyanobacterium *Synochocystis* sp. (Kaneko et al., 1996).

STEROL AUXOTROPHY IN CILIATES

Tetrahymena spp. and *Paramecium tetraurelia* are sterol auxotrophs that develop on dietary sterols unless degraded environmental conditions like starvation switches on a capacity to make tetrahymanol (Raederstorff and Rohmer, 1988; Najle et al., 2020). The enzymes recruited for metabolization of exogenous sterols are a canonical sterol-C5-desaturase (Poklepovich et al., 2012) belonging to the fatty acid hydroxylase group (Sperling et al., 2003), a C24-dealkylase (or sterol-24-de ethylase) acting on the sterol side chain (Tomazic et al., 2011, 2014), and a Rieske Oxygenase performing a sterol-C7-desaturation (Nusblat et al., 2005; Najle et al., 2013). Enzymes of the same type are found in distant sterol-auxotroph,

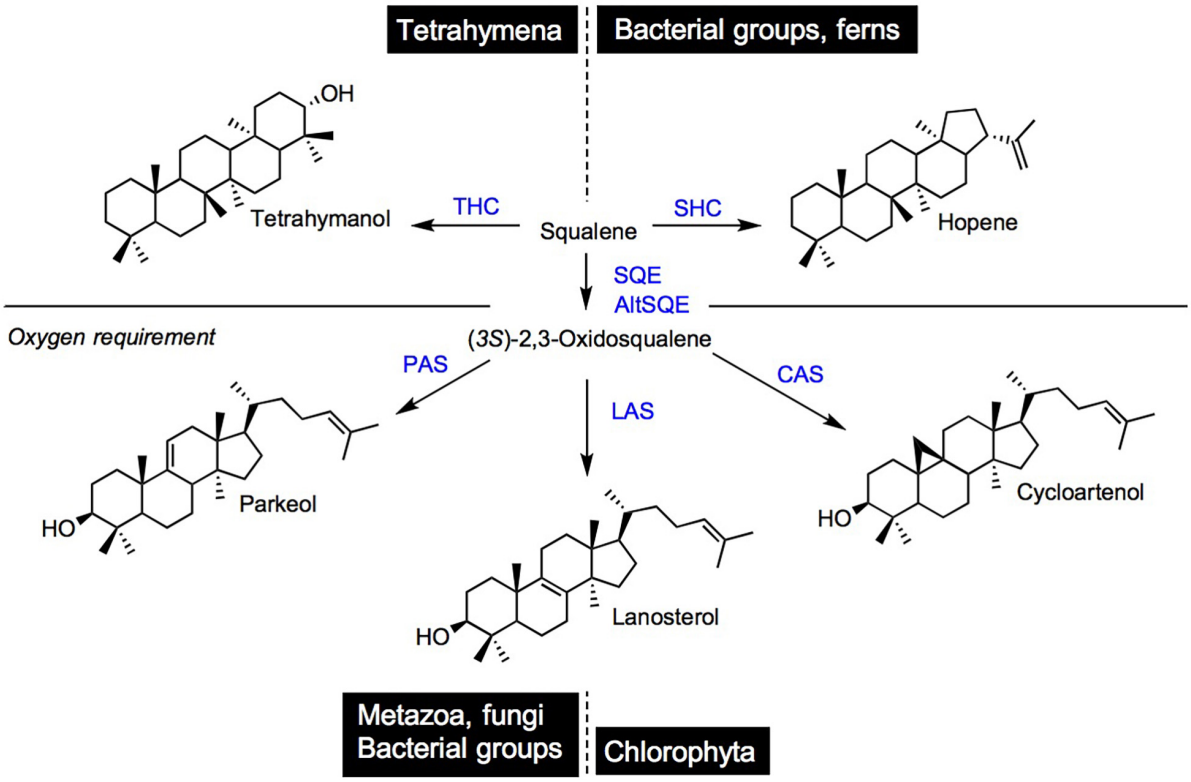

FIGURE 5 | Cyclization products of squalene and (3*S*)-2,3-oxidosqualene in species and taxonomic groups. THC, tetrahymanol synthase; SHC, squalene hopene cyclase; SQE, squalene epoxidase; AltSQE, alternative squalene epoxidase; PAS, parkeol synthase; LAS, lanosterol cyclase; and CAS, cycloartenol cyclase.

namely, insects, and nematodes (Zhou et al., 2020). This observation adds on typical cases of convergent evolution, here for a functional remodeling of phytosterols, by enzymes most probably acquired by horizontal gene transfer (Darnet et al., 2020). Genome wide investigations in *Tetrahymena* led to the identification of a sterol-22-desaturase belonging to the super family of fatty acid hydroxylases, and not to the canonical P450 monooxygenases (Najle et al., 2020). The multiple desaturations of exogenous cholesterol by *Tetrahymena thermophila* (**Figure 6**) is reminiscent of the conversion of dietary cholesterol into dafachronic acids – a class of signaling steroids- by *Caenorhabditis elegans*, a distantly related sterol-auxotroph (Zhou et al., 2020). Enzyme evolution and innovations (Newton et al., 2018) particularly in the super group of fatty acid hydroxylases is not restricted to ciliates when it comes to the post-squalene pathway. An enzyme of the fatty acid hydroxylase type was shown to use squalene as a substrate to produce (3*S*)-2,3-oxidosqualene in a diatom, therefore named alternative squalene epoxidase (AltSQE; Pollier et al., 2019).

LANOSTEROL TO 4-METHYLSTEROL PATHWAY IN DINOFLAGELLATES

Dinoflagellates from the SAR group (comprising stramenopila, alveolate, and rhizaria) shown in the new tree of eukaryotes (Burki et al., 2020) exhibit very striking sterol biosynthetic peculiarities. This group is widespread in aquatic ecosystems and is most importantly hosting symbiotic species required for the remarkable biology of cnidaria and especially reef-building corals, which depend on their symbionts for nutrients and sterols (Lu et al., 2020). The sterol supply to an anemone from its *symbiodinaceae* symbionts was shown to be associated with a symbiosome enriched with a Niemann-Pick type C2 (NPC2) transporter protein (Hambleton et al., 2019). The implication in sterol transport of NPC proteins are otherwise well characterized in mammalian lysosomal cholesterol metabolism (Strauss et al., 2002; Kidambi and Patel, 2008).

Dinoflagellates produce a specific 4-methylsterol called dinosterol and some other particular sterols like gorgosterol (C_{30} sterol products). These organisms use lanosterol as a sterol precursor (Shimizu et al., 1976; Alam, 1979; Volkman, 2016; Lu et al., 2020), and have evolved a so-called alternative squalene epoxidase to produce (3*S*)-2,3-oxidosqualene (Pollier et al., 2019). Dinosterol amounts are highly variable between dinoflagellates species in the genera *Symbiodinium*, *Gymnodinium*, *Fragilidium,* and *Gonyaulax* (Piretti et al., 1997; Amo et al., 2010). Dinosterol (4α,22,23-trimethylcholesta-5,22-dienol; **Figure 3**) has 3 exocyclic carbon atoms when compared to cholesterol. Sterols with an exocyclic methyl group at C4 are found in roundworms like *Caenorhabditis elegans* (Hannich et al., 2009; Zhou et al., 2020). In these invertebrates, which

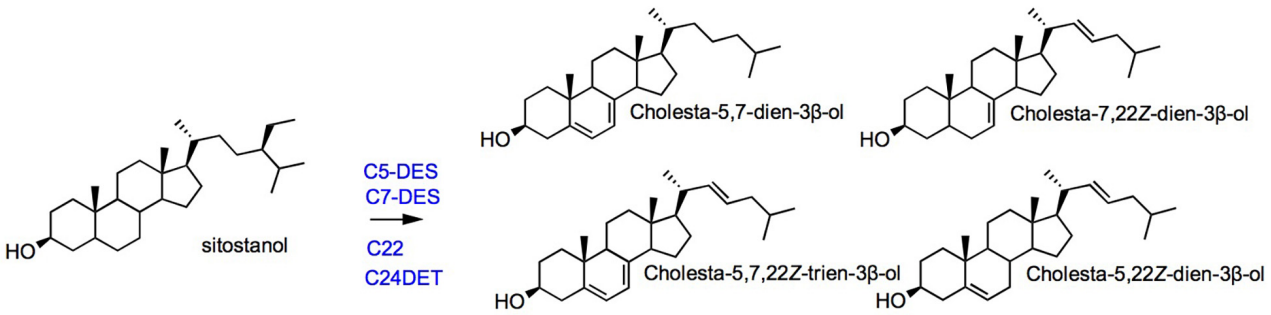

FIGURE 6 | Sterol metabolization reactions in the ciliate *Tetrahymena*. The conversion of sitostanol is shown [adapted from Najle et al. (2013)]. C5-DES, sterol-5(6)-desaturase; C7-DES, sterol-7-desaturase; C22-DES, sterol-22-desaturase; and C24DET, sterol-24-de-ethylase enzyme abbreviations from Najle et al. (2013).

are sterol auxotrophs, dietary cholesterol is metabolized by several enzymes into 4α-methyllophenol just like in a cholesterol retro-biosynthetic segment. Among these enzymes, STRM-1 is a sterol-C4-methyltransferase (4-SMT) from the orthologous group of SMT (Zhou et al., 2020). 4-SMT has distinct specificity and substrate recognition characteristics when compared to SMT1 and SMT2 that catalyze methyl transfers on olefinic sterol side chains (Darnet et al., 2020). An orthologous 4-SMT sequence from *Symbiodinium* is reported in databases suggesting that 4-methylsterols in dinoflagellates originate from the same biosynthetic process functionally described in the case of round worms (Lu et al., 2020). The occurrence of 4-methylsterols produced through C4-methylation in very distant taxa suggest a convergent evolutionary process at play to gain biological functions, yet unclear in the case of dinoflagellates. *Fugacium kawagutii* exhibits a sterol profile with all compounds methylated at C4, and dinosterol and 24-desmethyldinosterol accounting for sixty percent of the total (Lu et al., 2020). Dinosterol has also two exocyclic carbon atoms in its side chain, at C24 and at the unusual C23 position for a sterol side chain alkylation, and a double bond at C22. This favors the existence of an additional SMT to SMT1, yet to be identified. Dinoflagellates may probably have a sterol-C22-desaturase reminiscent of the type of reaction catalyzed by a cytochrome P450 dependent monooxygenase in canonical pathways but this particular point requires further genome mining and functional assays in heterologous systems to uncover orthologous or novel side chain modifying enzymes. Besides dinosterol other sterol molecules like gorgosterol are considered as taxonomic markers of the dinoflagellates (Mackenzie et al., 1982). Gorgosterol is a very particular sterol not seen in canonical models but it features the wealth of complex sterol structures describes in marine organisms (Giner and Djerassi, 1991). Gorgosterol harbors a cyclopropyl group at C22 indicative of a side chain rearrangement most probably through reactions well studied in the case of cyclopropyl and cyclopropenyl sterols found in sponges (Giner, 1993). The sterolotype defined by dinoflagellates with a LAS and the particular 4-SMT in addition to SMT1 (**Figure 2**) would certainly urge further research effort to clarify a possible role of specific 4-methylsterols in the success of symbiotic association with the sterol auxotrophic cnidarians and this in the context of strong abiotic environmental stress leading to coral bleaching (Lu et al., 2020).

STEROIDOGENIC ENZYMES AS TARGETS FOR ANTIPARASITIC DRUGS

Two major groups found in Alveolata and Excavata (Burki et al., 2020) are the apicomplexan parasites, which are sterol auxotrophs, and the kinetoplastida *trypanosomatidae*, which are sterol autotrophs. The search for therapeutic chemicals has driven significant aspects of sterol research in these organisms particularly on sterol uptake and biosynthesis that are targets of unbroken medical and economic interest (Roberts et al., 2003; Chaudhary and Roos, 2005).

Species from the *trypanosomatidae* are causing severe parasitic diseases in human and other mammals like *T. cruzi* causes Chagas disease, *T. brucei* causes sleeping sickness (African trypanosomiasis), and Leishmania causes leishmaniasis. Trypanosomes synthesize their 24-alkylsterols *de novo* from isoprenic precursors produced through the mevalonate pathway (El-Sayed et al., 2005; Cosentino and Aguero, 2014; Gold et al., 2016). The conversion of lanosterol to ergosterol has been demonstrated in these parasites, which display therefore a fungal type of sterol pathway (Fügi et al., 2014; Gold et al., 2016). Some enzymes implied in this pathway especially those that are major targets for biocides have been the focus of intensive research. These enzymes are 3-hydroxy-3-methylglutaryl-CoA-reductase (HMGR), squalene epoxidase, lanosterol-C14-demethylase and sterol-C24-methyltransferase (SMT), inhibited by statins, allylamines, azoles, and azasterols, respectively, Buckner et al. (2000), Urbina et al. (2002), Roberts et al. (2003), Lepesheva et al. (2004, 2018), Friggeri et al. (2018), Darnet and Schaller (2019). Remarkably, a distinct sterol composition of specific parasitic developmental stages was described in *T. cruzi*. Epimastigotes contain ergosterol and amastigotes produce 24-methyl-Δ^7-sterols and 24-ethylidene-Δ^7-sterols (Cosentino and Aguero, 2014). In *T. brucei*, a complex network of ergosterol and novel ergostatrienols coined ETO [ergosta-5,7,25(27)-trien-3β-ol] and 24-DTO [dimethyl ergosta-5,7,25(27)-trienol] were detected in

procyclic and bloodstream forms of the parasite (Nes et al., 2012). Amoeba and other metamonada are classified with the excavates (Burki et al., 2020). Some species present a sophisticated sterol metabolism that includes an endogenous sterol biosynthetic pathway and an additional capacity to metabolize exogenous cholesterol. *Naegleria lovaniensis*, *Naegleria gruberi,* and *Acanthamoeba polyphaga* are producing ergosterol, cholesterol, and poriferasterol derivatives (Raederstorff and Rohmer, 1987; Zhou et al., 2018). In these unicellulars, ergosterol biosynthesis occurs via cycloartenol (and not lanosterol), which is converted into 31-norlanosterol and from that point a pathway closely identical to the algae pathway is leading to the above-mentioned end-products. More recent studies combining chemistry and genomics in *Naegleria fowleri* confirmed a cycloartenol to cholesterol pathway in the amoeba, and also a dual origin of cholesterol of both biosynthetic and dietary origin (Zhou et al., 2018). *Naegleria* converts cholesterol into $\Delta^{5,7}$-dienic sterols most probably using a sterol-C7-desaturase of the Rieske oxygenase type, which has been initially discovered in sterol auxotrophs like *Drosophila* and round worms or *Tetrahymena*. These organisms require specific sterols at specific developmental stages of their life span and for this recruit specific enzymes yet considered as unusual with respect to the canonical view on sterol pathways.

DIATOMS AND OTHER STRAMENOPILA

The sterol content of diatoms has been reported (Volkman, 2003, 2016). The search for biomarkers of these planktonic organisms is motivated by the tremendous role they play in carbon dioxide fixation through photosynthesis and this at a global scale (Gold et al., 2017). An attempt to link a 18S RNA-based molecular phylogeny to sterol profiles of hundreds of species including raphid pennates, araphid pennates, radial centrics, and others came to the conclusive evidence that diatoms may not be specifically marked with a sterol profile (Rampen et al., 2010). In rare cases 23-methylsterols and 23,24-dimethylsterols were found, eventually distinguishing those species from other microalgae. The unusual sterol side chains with a methyl group at C-23, a 22-cyclopropane or a 24-propylidene is also found in dinoflagellates or sponges (Giner et al., 1991). In diatoms, the isoprenic precursors are provided by the plastidial MEP pathway but some species produce the C_5 building blocks from mevalonate (Cvejic et al., 2000). The quite well studied *Phaeodactylum tricornutum* performs squalene epoxidation to (3*S*)-2,3-oxidosqualene using the alternative squalene epoxidase AltSQE that belongs to the fatty acid hydroxylase type of oxygenases, is widely distributed in many eukaryotic groups, and is distinct from the flavoprotein-type of squalene epoxidase (Pollier et al., 2019). Diatoms produce 24-alkyl-Δ^5-sterols through the cycloartenol route (Fabris et al., 2014; Gallo et al., 2020). The effect of light spectral quality and temperature were shown as major physiological parameters acting on the sterol composition and quantity in *Phaeodactylum tricornutum* (Veron et al., 1996). *P. tricornutum*, *Thalassiosira* sp. and *Nannochloropsis oceanica* have been studied with an objective to assess their biotechnological potential for hydrocarbon or fine chemical industrial supply (Lu et al., 2014). Proteomic and chemical lipid profiling in these organisms unveiled particular aspects of sterol compartmentation and lipid homeostasis (Lupette et al., 2019). Interference with synthetic estrogens observed in a chemical screening for strong triacylglycerol producers in *P. tricornutum* resulted in a reallocation of acetyl-CoA building blocks from the isoprenoid/sterol pool to the fatty acyl-CoA pool (Conte et al., 2018). Two diatoms *Skeletonema marinoi* and *Cyclotella cryptica* were subjected to transcriptome profiling and sterol biosynthetic studies implementing ^{13}C-glucose feeding to cultures (Gallo et al., 2020). Clionasterol (C24β-ethylcholesterol) and fucosterol were identified in these species (Gallo et al., 2020). A considerable amount of analytical work carried out on algae around the seventies has firmly established the distribution of epimeric pairs of C24-alkylsterols in eukaryotes as already depicted above, with pairs such as β-sitosterol (24α) and clionasterol (24β) found in higher plants and in algae, respectively. Likewise, the stereoisomers isofucosterol (*trans*C24) and fucosterol (*cis*C24) are found in higher plants and in algae, respectively, (Patterson, 1971). *In silico* analysis of the transcriptomes from *S. marinoi* and *C. cryptica* suggest that the formation of fucosterol is mediated by an algal SMT2 (in diatoms and red algae, therefore named red SMT), which may have diverged from an ancestor quite early in the evolution toward canonical SMT1 and SMT2 enzymes (Gallo et al., 2020). Alltogether the combination of AltSQE, CAS, and algal SMT2 defines an interesting diatom sterolotype (**Figure 2**). Strikingly, *P. tricornatum* is lacking a SMT2, which explains the absence of 24-ethylsterols in *P. tricornutum* (Rampen et al., 2010; Lu et al., 2014). The cycloartenol-to-cholesterol route was recently confirmed in the chaetocerid diatom *Chaetoceros muelleri* (Jaramillo-Madrid et al., 2020b).

Conjugation of sterols in diatoms is suggested to play a role in growth dynamics and particularly oceanic phytoplankton blooming, a process which is controlled by programmed cell death (Gallo et al., 2017). Sulfonation of sterols in diatoms may regulate blooming dynamics. In fact, organic extracts prepared from growth phase declining cultures of *S. marinoi* were used in bio-guided fractionation assays to isolate sterol sulfates. Cholesterol and dihydrobrassicasterol sulfates were found, but also sitosterol sulfate in the active fractions. In the latter case one may find intriguing that diatoms biosynthesize clionasterol (24β-ethylcholesterol) but use sitosterol and stigmasterol (24α-ethylsterols) as a substrate for sulfotransferases (Gallo et al., 2018; Nuzzo et al., 2018).

Emiliania huxleyi is a phytoplanktonic prymnesiophyte (haptophyte). This ubiquitous coccolithophore that is forming large blooms in the oceans has a tremendous impact on carbon and sulfur cycling, ecosystems, and ultimately on climate (Holligan et al., 1983; Rivero-Calle et al., 2015). *E. huxleyi* is certainly not the only unicellular phytoplanktonic alga with such an ecological importance (Rivero-Calle et al., 2015) but recent work showed that its growth and bloomings regulated by coccolithoviruses implied a considerable metabolic remodeling and reprogramming of the host lipid metabolism during the infection process (Rosenwasser et al., 2014; Frada et al.,

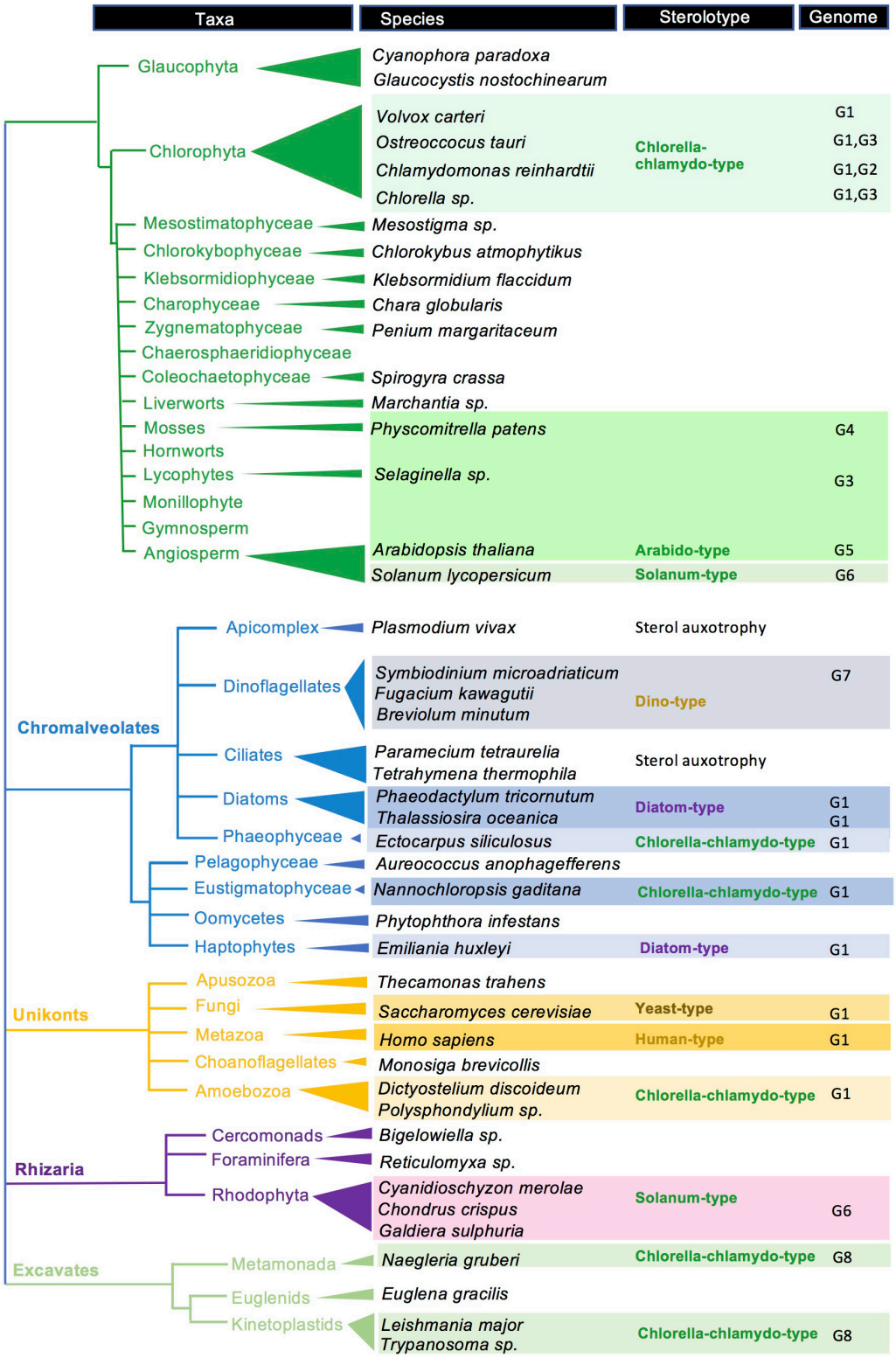

FIGURE 7 | Sterolotype distribution over a tree of eukaryotes. A selection of species is tagged with sterolotypes presented in **Figure 2**. References about genomes and gene functions, and sterol profiles, are indicated by G1 to G8. G1, (Lu et al., 2014); G2, (Brumfield et al., 2017); G3, (Gold et al., 2016); G4, (Morikawa et al., 2009); G5, (Schaller, 2010); G6, (Sonawane et al., 2016); G7, (Lu et al., 2020); and G8, (Fügi et al., 2014). Species with no sterolotype indications are awaiting for a comprehensive mining of corresponding genomes. Gene nomenclature for *Arabidopsis thaliana*, *Saccharomyces cerevisiae*, *Homo sapiens,* and *Chlamydomonas reinhardtii* is given in **Supplementary Table 1**.

2017). Major effects were seen on fatty acid and sphingolipid metabolism but also on the mevalonate/isoprenoid and sterol pathways apparently hijacked by the virus for its replication (Rosenwasser et al., 2014). The exact nature of all coccolithophore sterols was not reported in this study although previous chemotaxonomic studies established those sterol profiles in the context of geochemistry surveys (Taipale et al., 2016; Volkman, 2016). *E. huxleyi* produces a 24-ethylsterol (24-ethylcholesta-5,22E-dien-3β-ol) as a major component and small amount of cholesterol among other sterols (Volkman et al., 1981). Genome mining in this species points out an almost complete pathway and therefore the indication of a cycloartenol route in agreement with recent evolutionary studies (Gold et al., 2016).

STEROL PATHWAYS IN BROWN, RED, AND GREEN ALGAE

Algae from diverse groups of phaeophyta (brow algae), rhodophyta (red algae), and chlorophyta (green algae) have triggered the interest of analytical biochemists since the initial characterization of fucosterol (*cis*-24-ethylidenecholesterol) in *Fucus vesiculosus* (Heilbron et al., 1934; Patterson, 1971; McKean and Nes, 1977; Heilbron and Kevles, 1988; Komura et al., 2014). Genome sequences have been produced for the brown algae *Ectocarpus siliculosus* (Cock et al., 2010) and *Saccharina japonica* (Ye et al., 2015). *E. siliculosus* exhibits a sterol profile with cholesterol, ergosterol and fucosterol as prominent compounds and also some 24-ethylsterols (Mikami et al., 2018). Sterol enzymes predicted from the *E. siliculosus* sequence were closely similar to those of the diatoms *Thalassiosira oceanica* and *T. pseudomona* (Lommer et al., 2012), however, the epoxidation of squalene to (3*S*)-2,3-oxidosqualene is done by the canonical squalene epoxidase, not by the alternative squalene epoxidase found in diatoms (Lu et al., 2014; Gold et al., 2016; Pollier et al., 2019). Two distinct SMTs were identified in genomes of *E. siliculosus* and *E. subulatus* sp. Ec32 genomes (Dittami et al., 2020), in agreement with sterol profiles. Further genome mining and experimental validation of candidate genes are required to document the apparent absence in these genomes of sterol-24-reductases (24RED) and sterol-22-desaturases (C22D) of the canonical type (Dittami et al., 2020). High amounts of fucosterol in brown algae are often accompanied by saringosterol, a 24-hydroxy-24-vinylcholesterol that arise from non-enzymatic oxidative conversion of fucosterol (Knights, 1970).

The red and brown algae synthesize cholesterol, with red algae being very strong producers (Tsuda et al., 1957; Gibbons, 1967). *Chondrus crispus* has more than 94% of cholesterol in its total sterols but desmosterol or Δ^{22}-cholestenol were detected as well (Tasende, 2000). These species may represent a rich source of bio-based non-animal cholesterol. *C. crispus* and *Cyanidioschyzon merolae* were selected for in-depth genomic studies, from which a sterol pathway was inferred and modeled (Belcour et al., 2020). Sterol profiles were not established in the case of *C. merolae* but genomic datasets indicated the presence of a complete pathway from cycloartenol to cholesterol (Desmond and Gribaldo, 2009; Lu et al., 2014). The mixotrophic and thermophilic unicellular red algae *Galdieria sulphuria* and *Cyanidium caldarium* produce ergosterol and other dienic or polyenic ergosterol derivatives, in addition to 24-ethylsterols (Seckbach et al., 1993). Genomes of *G. sulphuria* and from *Porphyridium purpureum* have been sequenced, however, a curated catalog of sterol genes is not fully available, although annotations provided by databases (KEGG, MetaCyc, and others) indicate a cycloartenol route for sterol production in red algae and furthermore suggest a monophyletic evolutionary relationship between red algae and plants (Bhattacharya et al., 2013; Schonknecht et al., 2013).

Green algae from the chlorophyta like *Chlorella* sp., *Volvox* sp., *Chlamydomonas* sp., *Ostreococcus* sp., and some other genera like *Monodus* sp., and *Ochromonas* sp., from the chrysophyta (golden brown algae) have been studied decades ago (Moseley and Thompson, 1980; Gealt et al., 1981) with a continuous interest to depict the evolutionary relationship between, e.g., a fungal ergosterol pathway and an algal ergosterol pathway (Miller et al., 2012). The overall published data on algal sterols provides a clear-cut dichotomy of sterols structures found in large taxonomic groups (as already discussed in a previous section of this review): the sterol profiles established for all species of the chlorophyta and chrysophta exhibit C24β-methylsterols (brassicasterol, ergosterol) and C24β-ethylsterols (clionasterol, poriferasterol, and 7-dehydroporiferasterol). The technical requirements for the distinction of C24α - and C24β-ethylsterols (Rubinstein et al., 1976) most probably led to misnaming epimeric pairs of sterols here or there. Genome and proteomes of algae (Nguyen et al., 2011) are confirming the cycloartenol route for the production of 24-alkylsterols in green algae, which define a Chlorella-chlamydo-type of sterol pathways (**Figure 2**) (Miller et al., 2012). Pathways inferred from *in silico* analysis using canonical data sets as usual queries generally unclose orthologs and paralogs of steroidogenic enzymes. However, genes and enzymes acting on the sterol side chain modification (SMT, sterol-22-desaturases, sterol-24-reductase) or genes and enzymes required for the metabolization of the tetracyclic nucleus (sterone-3-reductase, sterol-C5-desaturase, sterol-C7-reductase and other putative enzymes) certainly deserve a further attention (Lu et al., 2014; Brumfield et al., 2017). Interestingly, the Chlamydomonas single SMT upon expression in yeast produces $\Delta^{7,22}$-poriferasterol, a C24β sterol epimer typical of algae (Brumfield et al., 2017). The access to novel sequence data for species like *Chlorokybus atmophyticus* (Wang et al., 2020) or *Penium maragaritaceum* (Jiao et al., 2020) will provide additional resources to enrich sterol profile records and to examine a sterol profile-genome congruence.

CONCLUDING REMARKS

The access to novel sequenced genomes and the increasing quality of their expert annotation and curation is opening the search for interesting new genes, pathways and for a more exhaustive view upon the sterol biosynthetic capacities and distribution in eukaryotes (**Figure 7**). The integration of a considerable body of published data on the sterol composition of a multitude of species – sometimes in ancient and overlooked

papers and repositories – with genome sequencing led us to tentatively visualize major taxonomic groups with sterolotypes, which may evolve as far as more information will be produced from genome surveys (Wong, 2019), especially those genomes coming from the oceans (Carradec et al., 2018; Canals et al., 2020). To reach this goal, indissociable efforts of investigating and validating accurate gene functions in dedicated heterologous expression systems will further support advanced phylogenomic studies (Desmond and Gribaldo, 2009; Gold et al., 2016). In the same vein, progresses in sterolomics will in turn provide users with powerful methods to envisage large-scale metaphenomics for a data-driven treatment of biological questions (Griffiths and Wang, 2019). Nonetheless, yet unknown genes and enzymes may well arise from forward and serendipitous genetic screenings. It is also worth noting that subtle variations in enzyme sequences like single amino acid substitution(s) may define a pathway, like for instance mutation(s) in cycloartenol synthase converts the latter into a LAS (Meyer et al., 2002). Consequently, genomic analyses *per se* are not sufficient to define sterolotypes, which are based on both decisive enzymes and accurate sterol compositions (**Figure 2**). The inherent limited potential of expert BLAST searches for predicting orthology and paralogy is especially emphasized when comparing protein sequences of selected species including canonical models, and enzyme-based sterolotypes. Species that belong to a same sterolotype as defined in this study display for each sterol biosynthetic enzymes a remarkably wide range of sequence identities (**Supplementary Figure 1**).

Sterolotypes defined in this paper readily stand on the AltSQE/SQE, CAS/LAS distinction, and on the sterol side chain modification enzymes (**Figure 2**). The exclusive choice of CAS or LAS is not fully understood as for instance the evolutionary conserved LAS in land plants has not been integrated as an essential contributor to sterol homeostasis. Sterolotypes flagged with CAS also highlight the remarkable conversion of cycloartenol to cholesterol in viridiplantae (Babiychuk et al., 2008; Ohyama et al., 2009; Sawai et al., 2014; Sonawane et al., 2016). This pathway recruits a particular sterol-Δ^{24}-reductase paralog (SSR2 in *Solanum lycopersicum*) also found in rhodophyta (Calegario et al., 2016), for the synthesis of cholesterol. Distinct pathways for the production of that unique sterol in red algae or plants, and in mammals, speaks therefore in favor of convergent evolutionary process in sterol biology, as depicted in other eukaryotic groups in this brief overview.

Finally, sterols have raised interest from the biotech and industrial field due to their multiple pharmaceutical, cosmetic and food applications like blood cholesterol-lowering, anticancer, antiangiogenic, anti-inflammatory, antiatherosclerotic, anthelminthic, and antioxidant effects (Martin-Creuzburg and Elert, 2009; Martin-Creuzburg and Merkel, 2016). The sterol supply for a global market could possibly shift from agricultural waste products (Maniet et al., 2019) or plants (Zhang et al., 2020), to diatoms and other microalgae as a versatile system (Singh et al., 2017). Successful achievements in specific pathway engineering, for instance expected from the expression of limiting enzymes (Jaramillo-Madrid et al., 2020a), certainly require a further picturing of the intricate regulatory metabolic networks and cellular homeostasis of these producers (Marechal and Lupette, 2019), in order to provide at source to sink production of sterols compatible with the market demand (Luo et al., 2015).

AUTHOR CONTRIBUTIONS

SD and HS conceived the overview and wrote the manuscript with contributions from AB and QC. All authors contributed to the article and approved the submitted version.

FUNDING

The authors wish to acknowledge the European commission for a MCSA H2020 grant no 897283 to SD, Carlsberg group/Kronenbourg breweries for financial support (CNRS contract no 174144) to AB, and the University of Strasbourg for supporting QC (ATER contract 2020–2021). HS acknowledges funding from the Agence Nationale de la Recherche (grant ANR-20-CE44-0002-02).

SUPPLEMENTARY MATERIAL

The Supplementary Material for this article can be found online at: https://www.frontiersin.org/articles/10.3389/fpls.2021.665206/full#supplementary-material

Supplementary Figure 1 | Protein sequence comparison between species and sterolotypes. The orthologs were retrieved by BLAST search and the amino acid percent identity was reported in the matrix. Proteomes are imported from UniProt database. The accession numbers for *Homo sapiens*, HsLAS, *Saccharomyces cerevisiae*, ScLAS, ScSMT1, and *Arabidopsis thaliana*, AtCAS1, AtLAS1, AtSMT1, At plant SMT2 are indicated in **Supplementary Table 1**. Accessions for other protein sequences as follows. *Phaeodactylum tricornutum*: PtAltSQE, B7FXW1; PtCAS1, XP_002185678.1; PtSMT1, XP_002186194.1; Pt algal SMT2, XP_002178531.1; *Chlorella variabilis*: CvCAS1, XP_005848291.1; CvSMT1, XP_005845039.1; Cv algal SMT2, XP_005844298.1; *Symbiodinium microadriaticum*: SmCAS1, OLP86082.1; SmSMT1, OLP85101.1; Sm4-SMT, OLQ09145.1; SmAltSQE, CAE7673970.1; and *Solanum lycopersicum*: SlCAS1, NP_001233784.1; SlLAS1, XP_004240118.1; SlSMT1, XP_004229650.1; Sl plant SMT2, XP_004248642.1; SlSSR2, NP_001306251.1. Horizontal frames, species assigned to a sterolotype. Vertical frames, exemplified enzyme sequence diversity.

REFERENCES

Akihisa, T., Hayashi, Y., Patterson, G. W., Shimizu, N., and Tamura, T. (1992). 4α-methylvernosterol and other sterols from *Vernonia anthelmintica* seeds. *Phytochemistry* 31, 1759–1763.

Alam, M. (1979). Dinoflagellate sterols I: sterol composition of the dinoflagellates of ? species. *Steroids* 33, 197–203.

Amo, M., Suzuki, N., Kawamura, H., Yamaguchi, A., Takano, Y., and Horiguchi, T. (2010). Sterol composition of dinoflagellates: different abundance and composition in heterotrophic species and resting cysts. *Geochem. J.* 44, 225–231.

Babiychuk, E., Bouvier-Nave, P., Compagnon, V., Suzuki, M., Muranaka, T., Van Montagu, M., et al. (2008). Allelic mutant series reveal distinct functions for *Arabidopsis* cycloartenol synthase 1 in cell viability and plastid biogenesis.

Proc. Natl. Acad. Sci. U.S.A. 105, 3163–3168. doi: 10.1073/pnas.0712190105

Bajguz, A., Chmur, M., and Gruszka, D. (2020). Comprehensive overview of the brassinosteroid Biosynthesis pathways: substrates. products, inhibitors, and connections. *Front. Plant Sci.* 11:1034. doi: 10.3389/fpls.2020.01034

Banta, A. B., Wei, J. H., and Welander, P. V. (2015). A distinct pathway for tetrahymanol synthesis in bacteria. *Proc. Natl. Acad. Sci. U.S.A.* 112, 13478–13483. doi: 10.1073/pnas.1511482112

Belcour, A., Girard, J., Aite, M., Delage, L., Trottier, C., Marteau, C., et al. (2020). Inferring biochemical reactions and metabolite structures to understand metabolic pathway drift. *iScience* 23:100849. doi: 10.1016/j.isci.2020.100849

Belin, B. J., Busset, N., Giraud, E., Molinaro, A., Silipo, A., and Newman, D. K. (2018). Hopanoid lipids: from membranes to plant-bacteria interactions. *Nat. Rev. Microbiol.* 16, 304–315. doi: 10.1038/nrmicro.2017.173

Benveniste, P. (2004). Biosynthesis and accumulation of sterols. *Annu. Rev. Plant Biol.* 55, 429–457.

Berry, A. M., Harriott, O. T., Moreau, R. A., Osman, S. F., Benson, D. R., and Jones, A. D. (1993). Hopanoid lipids compose the *Frankia* vesicle envelope, presumptive barrier of oxygen diffusion to nitrogenase. *Proc. Natl. Acad. Sci. U.S.A.* 90, 6091–6094. doi: 10.1073/pnas.90.13.6091

Bhatt, P. N., and Bhatt, D. P. (1984). Changes in sterol content during leaf aging and in vitro differentiation in *Solanum nigrum*. *J. Nat. Prod.* 47, 426–432.

Bhattacharya, D., Price, D. C., Chan, C. X., Qiu, H., Rose, N., Ball, S., et al. (2013). Genome of the red alga *Porphyridium purpureum*. *Nat. Commun.* 4:1941.

Bird, C. W., Lynch, J. M., Pirt, F. J., and Reid, W. W. (1971). Steroids and squalene in *Methylococcus capsulatus* grown on methane. *Nature* 230, 473–474. doi: 10.1038/230473a0

Bloch, K. (1989). Sterol structure and function. *Steroids* 53, 261–270.

Bobrovskiy, I., Hope, J. M., Nettersheim, B. J., Volkman, J. K., Hallmann, C., and Brocks, J. J. (2021). Algal origin of sponge sterane biomarkers negates the oldest evidence for animals in the rock record. *Nat. Ecol. Evol.* 5, 165–168. doi: 10.1038/s41559-020-01334-7

Bode, H. B., Zeggel, B., Silakowski, B., Wenzel, S. C., Reichenbach, H., and Muller, R. (2003). Steroid biosynthesis in prokaryotes: identification of myxobacterial steroids and cloning of the first bacterial 2,3(S)-oxidosqualene cyclase from the myxobacterium *Stigmatella aurantiaca*. *Mol. Microbiol.* 47, 471–481. doi: 10.1046/j.1365-2958.2003.03309.x

Bouvier, F., Rahier, A., and Camara, B. (2005). Biogenesis, molecular regulation and function of plant isoprenoids. *Prog. Lipid Res.* 44, 357–429.

Bouvier, P., Rohmer, M., Benveniste, P., and Ourisson, G. (1976). Delta8(14)-steroids in the bacterium *Methylococcus capsulatus*. *Biochem. J.* 159, 267–271. doi: 10.1042/bj1590267

Bouvier-Nave, P., Husselstein, T., and Benveniste, P. (1998). Two families of sterol methyltransferases are involved in the first and the second methylation steps of plant sterol biosynthesis. *Eur. J. Biochem.* 256, 88–96. doi: 10.1046/j.1432-1327.1998.2560088.x

Brouwer, P., Van Der Werf, A., Schluepmann, H., Reichart, G.-J., and Nierop, K. G. J. (2015). Lipid yield and composition of *Azolla filiculoides* and the implications for biodiesel production. *Bioenergy Res.* 9, 369–377.

Brown, M. S., Radhakrishnan, A., and Goldstein, J. L. (2018). Retrospective on cholesterol homeostasis: the central role of scap. *Annu. Rev. Biochem.* 87, 783–807. doi: 10.1146/annurev-biochem-062917-011852

Brumfield, K. M., Laborde, S. M., and Moroney, J. V. (2017). A model for the ergosterol biosynthetic pathway in *Chlamydomonas reinhardtii*. *Eur. J. Phycol.* 52, 64–74.

Buckner, F. S., Nguyen, L. N., Joubert, B. M., and Matsuda, S. P. T. (2000). Cloning and heterologous expression of the *Trypanosoma brucei* lanosterol synthase gene. *Mol. Biochem. Parasitol.* 110, 399–403. doi: 10.1016/s0166-6851(00)00267-x

Burki, F., Roger, A. J., Brown, M. W., and Simpson, A. G. B. (2020). The new tree of eukaryotes. *Trends Ecol. Evol.* 35, 43–55.

Calegario, G., Pollier, J., Arendt, P., De Oliveira, L. S., Thompson, C., Soares, A. R., et al. (2016). Cloning and functional characterization of cycloartenol synthase from the red seaweed *Laurencia dendroidea*. *PLoS One* 11:e0165954. doi: 10.1371/journal.pone.0165954

Canals, O., Obiol, A., Muhovic, I., Vaque, D., and Massana, R. (2020). Ciliate diversity and distribution across horizontal and vertical scales in the open ocean. *Mol. Ecol.* 29, 2824–2839. doi: 10.1111/mec.15528

Carradec, Q., Pelletier, E., Da Silva, C., Alberti, A., Seeleuthner, Y., Blanc-Mathieu, R., et al. (2018). A global ocean atlas of eukaryotic genes. *Nat. Commun.* 9:373.

Chakrabarti, R. S., Ingham, S. A., Kozlitina, J., Gay, A., Cohen, J. C., Radhakrishnan, A., et al. (2017). Variability of cholesterol accessibility in human red blood cells measured using a bacterial cholesterol-binding toxin. *eLife* 6:e23355. doi: 10.7554/eLife.23355

Chaudhary, K., and Roos, D. S. (2005). Protozoan genomics for drug discovery. *Nat. Biotechnol.* 23, 1089–1091.

Chiu, P. L., Patterson, G. W., and Fenner, G. P. (1985). Sterols of bryophytes. *Phytochemistry* 24, 263–266.

Cock, J. M., Sterck, L., Rouze, P., Scornet, D., Allen, A. E., Amoutzias, G., et al. (2010). The Ectocarpus genome and the independent evolution of multicellularity in brown algae. *Nature* 465, 617–621.

Conner, R. L., Landrey, J. R., and Czarkowski, N. (1982). The effect of specific sterols on cell size and fatty acid composition of*Tetrahymena* pyriformisW. *J. Protozool.* 29, 105–109.

Conte, M., Lupette, J., Seddiki, K., Mei, C., Dolch, L. J., Gros, V., et al. (2018). Screening for biologically annotated drugs that trigger triacylglycerol accumulation in the diatom *Phaeodactylum*. *Plant Physiol.* 177, 532–552. doi: 10.1104/pp.17.01804

Corey, E. J., Matsuda, S. P., and Bartel, B. (1993). Isolation of an *Arabidopsis thaliana* gene encoding cycloartenol synthase by functional expression in a yeast mutant lacking lanosterol synthase by the use of a chromatographic screen. *Proc. Natl. Acad. Sci. U.S.A.* 90, 11628–11632. doi: 10.1073/pnas.90.24.11628

Cornejo-Castillo, F. M., and Zehr, J. P. (2019). Hopanoid lipids may facilitate aerobic nitrogen fixation in the ocean. *Proc. Natl. Acad. Sci. U.S.A.* 116, 18269–18271. doi: 10.1073/pnas.1908165116

Cornforth, J. W. (2002). Sterol biosynthesis: the early days. *Biochem. Biophys. Res. Commun.* 292, 1129–1138.

Cosentino, R. O., and Aguero, F. (2014). Genetic profiling of the isoprenoid and sterol biosynthesis pathway genes of *Trypanosoma cruzi*. *PLoS One* 9:e96762. doi: 10.1371/journal.pone.0096762

Cvejic, J. H., Putra, S. R., El-Beltagy, A., Hattori, R., Hattori, T., and Rohmer, M. (2000). Bacterial triterpenoids of the hopane series as biomarkers for the chemotaxonomy of *Burkholderia*. *Pseudomonas* and *Ralstonia* spp. *FEMS Microbiol. Lett.* 183, 295–299. doi: 10.1111/j.1574-6968.2000.tb08974.x

Darnet, S., Fliesler, S. J., and Schaller, H. (2020). Worming our way toward multiple evolutionary origins of convergent sterol pathways. *J. Lipid Res.* 61, 129–132. doi: 10.1194/jlr.C119000600

Darnet, S., and Rahier, A. (2004). Plant sterol biosynthesis: identification of two distinct families of sterol 4α-methyl oxidases. *Biochem. J.* 378, 889–898. doi: 10.1042/BJ20031572

Darnet, S., and Schaller, H. (2019). Metabolism and biological activities of 4-methyl-sterols. *Molecules* 24:451.

De Rosa, M., Gambacorta, A., Minale, L., and Bu'lock, J. D. (1971). Bacterial triterpenes. *J. Chem. Soc. Chem. Commun.* 1971, 619–620. doi: 10.1039/C29710000619

De Souza, N. J., and Nes, W. R. (1968). Sterols: isolation from a blue-green alga. *Science* 162:363.

Delgado-Baquerizo, M., Oliverio, A. M., Brewer, T. E., Benavent-Gonzalez, A., Eldridge, D. J., Bardgett, R. D., et al. (2018). A global atlas of the dominant bacteria found in soil. *Science* 359, 320–325. doi: 10.1126/science.aap9516

Desmond, E., and Gribaldo, S. (2009). Phylogenomics of sterol synthesis: insights into the origin, evolution, and diversity of a key eukaryotic feature. *Genome Biol. Evol.* 1, 364–381. doi: 10.1093/gbe/evp036

Dittami, S. M., Corre, E., Brillet-Gueguen, L., Lipinska, A. P., Pontoizeau, N., Aite, M., et al. (2020). The genome of *Ectocarpus subulatus* - A highly stress-tolerant brown alga. *Mar. Genomics* 52:100740. doi: 10.1016/j.margen.2020.100740

El-Sayed, N. M., Myler, P. J., Blandin, G., Berriman, M., Crabtree, J., Aggarwal, G., et al. (2005). Comparative genomics of trypanosomatid parasitic protozoa. *Science* 309, 404–409.

Fabris, M., Matthijs, M., Carbonelle, S., Moses, T., Pollier, J., Dasseville, R., et al. (2014). Tracking the sterol biosynthesis pathway of the diatom *Phaeodactylum tricornutum*. *New Phytol.* 204, 521–535. doi: 10.1111/nph.12917

Fagundes, M. B., Vendruscolo, R. G., Maroneze, M. M., Barin, J. S., De Menezes, C. R., Zepka, L. Q., et al. (2018). Towards a sustainable route for the production of squalene using cyanobacteria. *Waste Biomass Valori.* 10, 1295–1302.

Forestier, E., Romero-Segura, C., Pateraki, I., Centeno, E., Compagnon, V., Preiss, M., et al. (2019). Distinct triterpene synthases in the laticifers of *Euphorbia lathyris*. *Sci. Rep.* 9:4840. doi: 10.1038/s41598-019-40905-y

Frada, M. J., Rosenwasser, S., Ben-Dor, S., Shemi, A., Sabanay, H., and Vardi, A. (2017). Morphological switch to a resistant subpopulation in response to viral infection in the bloom-forming coccolithophore *Emiliania huxleyi*. *PLoS Pathog.* 13:e1006775. doi: 10.1371/journal.ppat.1006775

Friggeri, L., Hargrove, T. Y., Rachakonda, G., Blobaum, A. L., Fisher, P., De Oliveira, G. M., et al. (2018). Sterol 14alpha-demethylase structure-based optimization of drug candidates for human infections with the protozoan *Trypanosomatidae*. *J. Med. Chem.* 61, 10910–10921. doi: 10.1021/acs.jmedchem.8b01671

Fügi, M. A., Gunasekera, K., Ochsenreiter, T., Guan, X., Wenk, M. R., and Maser, P. (2014). Genome profiling of sterol synthesis shows convergent evolution in parasites and guides chemotherapeutic attack. *J. Lipid Res.* 55, 929–938. doi: 10.1194/jlr.M048017

Fujita, S., Ohnishi, T., Watanabe, B., Yokota, T., Takatsuto, S., Fujioka, S., et al. (2006). *Arabidopsis* CYP90B1 catalyses the early C-22 hydroxylation of C27. C28 and C29 sterols. Plant J. 45, 765–774. doi: 10.1111/j.1365-313X.2005.02639.x

Gallo, C., D'ippolito, G., Nuzzo, G., Sardo, A., and Fontana, A. (2017). Autoinhibitory sterol sulfates mediate programmed cell death in a bloom-forming marine diatom. *Nat. Commun.* 8:1292. doi: 10.1038/s41467-017-01300-1

Gallo, C., Landi, S., D'ippolito, G., Nuzzo, G., Manzo, E., Sardo, A., et al. (2020). Diatoms synthesize sterols by inclusion of animal and fungal genes in the plant pathway. *Sci. Rep.* 10:4204. doi: 10.1038/s41598-020-60993-5

Gallo, C., Nuzzo, G., D'ippolito, G., Manzo, E., Sardo, A., and Fontana, A. (2018). Sterol sulfates and sulfotransferases in marine diatoms. *Methods Enzymol.* 605, 101–138.

Gas-Pascual, E., Simonovik, B., Schaller, H., and Bach, T. J. (2015). Inhibition of cycloartenol synthase (CAS) function in tobacco BY-2 cells. *Lipids* 50, 761–772.

Gealt, M. A., Adler, J. H., and Nes, W. R. (1981). The sterols and fatty acids from purified flagella of *Chlamydomonas reinhardi*. *Lipids* 16, 133–136.

Gibbons, G. (1967). The sterols of some marine red algae. *Phytochemistry* 6, 677–683.

Giner, J. L. (1993). Biosynthesis of marine sterol side-chains. *Chem. Rev.* 93, 1735–1752.

Giner, J. L., and Djerassi, C. (1991). Biosynthetic studies of marine lipids. 33. Biosynthesis of dinosterol, peridinosterol and gorgosterol: unusual patterns of bioalkylation in dinoflagellate sterols. *J. Org. Chem.* 56, 2357–2363.

Giner, J.-L., Wünsche, L., Andersen, R. A., and Djerassi, C. (1991). Dinoflagellates cyclize squalene oxide to lanosterol. *Biochem. Syst. Ecol.* 19, 143–145.

Giner, J.-L., Zhao, H., Boyer, G. L., Satchwell, M. F., and Andersen, R. A. (2009). Sterol chemotaxonomy of marine pelagophyte algae. *Chem. Biodivers.* 6, 1111–1130. doi: 10.1002/cbdv.200800316

Goad, L. J., and Goodwin, T. W. (1972). "The biosynthesis of plant sterols," in *Progress in Phytochemistry*, eds L. Reinhold and Y. Liwschitz (London: Interscience Publishers).

Godzina, S. M., Lovato, M. A., Meyer, M. M., Foster, K. A., Wilson, W. K., Gu, W., et al. (2000). Cloning and characterization of the *Dictyostelium discoideum* cycloartenol synthase cDNA. *Lipids* 35, 249–255. doi: 10.1007/s11745-000-0520-3

Gold, D. A., Caron, A., Fournier, G. P., and Summons, R. E. (2017). Paleoproterozoic sterol biosynthesis and the rise of oxygen. *Nature* 543, 420–423. doi: 10.1038/nature21412

Gold, D. A., Grabenstatter, J., De Mendoza, A., Riesgo, A., Ruiz-Trillo, I., and Summons, R. E. (2016). Sterol and genomic analyses validate the sponge biomarker hypothesis. *Proc. Natl. Acad. Sci. U.S.A.* 113, 2684–2689. doi: 10.1073/pnas.1512614113

Griffiths, W. J., and Wang, Y. (2019). Sterolomics in biology, biochemistry, medicine. *Trends Analyt. Chem.* 120:115280. doi: 10.1016/j.trac.2018.10.016

Guo, D.-A., Mangla, A. T., Zhou, W., Lopez, M., Jia, Z., Derrek Nichols, S., et al. (1997). "Antifungal sterol biosynthesis inhibitors," in *Subcellular Biochemistry*, ed. D. B. Roodyn (New York, NY: Springer US).

Hambleton, E. A., Jones, V. A. S., Maegele, I., Kvaskoff, D., Sachsenheimer, T., and Guse, A. (2019). Sterol transfer by atypical cholesterol-binding NPC2 proteins in coral-algal symbiosis. *eLife* 8:e43923. doi: 10.7554/eLife.43923

Hannich, J. T., Entchev, E. V., Mende, F., Boytchev, H., Martin, R., Zagoriy, V., et al. (2009). Methylation of the sterol nucleus by STRM-1 regulates dauer larva formation in *Caenorhabditis elegans*. *Dev. Cell* 16, 833–843. doi: 10.1016/j.devcel.2009.04.012

Heilbron, I., Phipers, R. F., and Wright, H. R. (1934). The chemistry of the algae. Part I. The algal sterol fucosterol. *J. Chem. Soc.*, 343, 1572–1576.

Heilbron, J. L., and Kevles, D. J. (1988). Finding a policy for mapping and sequencing the human genome: lessons from the history of particle physics. *Minerva* 26, 299–314. doi: 10.1007/BF01096399

Holland, H. D. (2002). Volcanic gases, black smokers, and the Great Oxidation Event. *Geochim. Cosmochim. Acta* 66, 3811–3826.

Holligan, P. M., Viollier, M., Harbour, D. S., Camus, P., and Champagne-Philippe, M. (1983). Satellite and ship studies of coccolithophore production along a continental-shelf edge. *Nature* 304, 339–342.

Husselstein, T., Schaller, H., Gachotte, D., and Benveniste, P. (1999). Delta7-sterol-C5-desaturase: molecular characterization and functional expression of wild-type and mutant alleles. *Plant Mol. Biol.* 39, 891–906. doi: 10.1023/a:1006113919172

Jaramillo-Madrid, A. C., Abbriano, R., Ashworth, J., Fabris, M., Pernice, M., and Ralph, P. J. (2020a). Overexpression of key sterol pathway enzymes in two model marine diatoms alters sterol profiles in *Phaeodactylum tricornutum*. *Pharmaceuticals* 13:481. doi: 10.3390/ph13120481

Jaramillo-Madrid, A. C., Ashworth, J., Fabris, M., and Ralph, P. J. (2020b). The unique sterol biosynthesis pathway of three model diatoms consists of a conserved core and diversified endpoints. *Algal Res.* 48:101902.

Jiao, C., Sorensen, I., Sun, X., Sun, H., Behar, H., Alseekh, S., et al. (2020). The *Penium margaritaceum* genome: hallmarks of the origins of land plants. *Cell* 181, 1097.e12–1111.e12. doi: 10.1016/j.cell.2020.04.019

Kaneko, T., Sato, S., Kotani, H., Tanaka, A., Asamizu, E., Nakamura, Y., et al. (1996). Sequence analysis of the genome of the unicellular cyanobacterium *Synechocystis* sp. strain PCC6803. II. Sequence determination of the entire genome and assignment of potential protein-coding regions. *DNA Res.* 3, 109–136.

Keeling, P. J., and Palmer, J. D. (2008). Horizontal gene transfer in eukaryotic evolution. *Nat. Rev. Genet.* 9, 605–618.

Kidambi, S., and Patel, S. B. (2008). Cholesterol and non-cholesterol sterol transporters: ABCG5, ABCG8 and NPC1L1: a review. *Xenobiotica* 38, 1119–1139. doi: 10.1080/00498250802007930

Knights, B. A. (1970). Sterols in *Ascophyllum nodosum*. *Phytochemistry* 9, 903–905.

Knoch, E., Sugawara, S., Mori, T., Poulsen, C., Fukushima, A., Harholt, J., et al. (2018). Third DWF1 paralog in Solanaceae, sterol Delta(24)-isomerase, branches withanolide biosynthesis from the general phytosterol pathway. *Proc. Natl. Acad. Sci. U.S.A.* 115, E8096–E8103. doi: 10.1073/pnas.1807482115

Kolesnikova, M. D., Xiong, Q., Lodeiro, S., Hua, L., and Matsuda, S. P. (2006). Lanosterol biosynthesis in plants. *Arch. Biochem. Biophys.* 447, 87–95.

Komura, T., Wada, S., and Nagayama, H. (2014). The Identification of fucosterol in the marine brown *AlgaeHizikia fusiformis*. *Agric. Biol. Chem.* 38, 2275–2276.

Kumari, P., Kumar, M., Reddy, C. R. K., and Jha, B. (2013). "Algal lipids, fatty acids and sterols," in *Functional Ingredients From Algae for Foods and Nutraceuticals*, ed. H. Domínguez (Amsterdam: Woodhead), 87–134.

Kushiro, T., and Ebizuka, Y. (2010). "Triterpenes," in *Comprehensive Natural Products II*, eds L. Hung-Wen and L. Mander (Amsterdam: Elsevier Science), 673–708.

Lamacka, M., and Sajbidor, J. (1997). Ergosterol determination in *Saccharomyces cerevisiae*. Comparison of different methods. *Biotechnol. Tech.* 11, 723–725.

Lamb, D. C., Jackson, C. J., Warrilow, A. G., Manning, N. J., Kelly, D. E., and Kelly, S. L. (2007). Lanosterol biosynthesis in the prokaryote *Methylococcus capsulatus*: insight into the evolution of sterol biosynthesis. *Mol. Biol. Evol.* 24, 1714–1721. doi: 10.1093/molbev/msm090

Leblond, J. D., Timofte, H. I., Roche, S. A., and Porter, N. M. (2011). Sterols of glaucocystophytes. *Phycol. Res.* 59, 129–134. doi: 10.1111/j.1472-4669.2008.00167.x

Lecain, E., Chenivesse, X., Spagnoli, R., and Pompon, D. (1996). Cloning by metabolic interference in yeast and enzymatic characterization of *Arabidopsis thaliana* sterol Δ^7-reductase. *J. Biol. Chem.* 271, 10866–10873. doi: 10.1074/jbc.271.18.10866

Lee, A. K., Banta, A. B., Wei, J. H., Kiemle, D. J., Feng, J., Giner, J. L., et al. (2018). C-4 sterol demethylation enzymes distinguish bacterial and eukaryotic

sterol synthesis. *Proc. Natl. Acad. Sci. U.S.A.* 115, 5884–5889. doi: 10.1073/pnas.1802930115

Lepesheva, G. I., Friggeri, L., and Waterman, M. R. (2018). CYP51 as drug targets for fungi and protozoan parasites: past, present and future. *Parasitology* 145, 1820–1836. doi: 10.1017/S0031182018000562

Lepesheva, G. I., Nes, W. D., Zhou, W., Hill, G. C., and Waterman, M. R. (2004). CYP51 from *Trypanosoma brucei* is obtusifoliol-specific. *Biochemistry* 43, 10789–10799. doi: 10.1021/bi048967t

Li, F. W., Brouwer, P., Carretero-Paulet, L., Cheng, S., De Vries, J., Delaux, P. M., et al. (2018). Fern genomes elucidate land plant evolution and cyanobacterial symbioses. *Nat. Plants* 4, 460–472. doi: 10.1038/s41477-018-0188-8

Li, J., Nagpal, P., Vitart, V., Mcmorris, T. C., and Chory, J. (1996). A role for brassinosteroids in light-dependent development of *Arabidopsis*. *Science* 272, 398–401. doi: 10.1126/science.272.5260.398

Lombard, J., and Moreira, D. (2011). Origins and early evolution of the mevalonate pathway of isoprenoid biosynthesis in the three domains of life. *Mol. Biol. Evol.* 28, 87–99.

Lommer, M., Specht, M., Roy, A. S., Kraemer, L., Andreson, R., Gutowska, M. A., et al. (2012). Genome and low-iron response of an oceanic diatom adapted to chronic iron limitation. *Genome Biol.* 13:R66.

Lovato, M. A., Hart, E. A., Segura, M. J., Giner, J. L., and Matsuda, S. P. (2000). Functional cloning of an *Arabidopsis thaliana* cDNA encoding cycloeucalenol cycloisomerase. *J. Biol. Chem.* 275, 13394–13397. doi: 10.1074/jbc.275.18.13394

Lu, Y., Jiang, J., Zhao, H., Han, X., Xiang, Y., and Zhou, W. (2020). Clade-specific sterol metabolites in dinoflagellate endosymbionts are associated with coral bleaching in response to environmental cues. *mSystems* 5:e00765-20. doi: 10.1128/mSystems.00765-20

Lu, Y., Zhou, W., Wei, L., Li, J., Jia, J., Li, F., et al. (2014). Regulation of the cholesterol biosynthetic pathway and its integration with fatty acid biosynthesis in the oleaginous microalga *Nannochloropsis oceanica*. *Biotechnol. Biofuels* 7:81. doi: 10.1186/1754-6834-7-81

Luo, X., Su, P., and Zhang, W. (2015). Advances in microalgae-derived phytosterols for functional food and pharmaceutical applications. *Mar. Drugs* 13, 4231–4254. doi: 10.3390/md13074231

Lupette, J., Jaussaud, A., Seddiki, K., Morabito, C., Brugiere, S., Schaller, H., et al. (2019). The architecture of lipid droplets in the diatom *Phaeodactylum tricornutum*. *Algal Res. Biomass Biofuels Bioprod.* 38:101415.

Mackenzie, A. S., Brassell, S. C., Eglinton, G., and Maxwell, J. R. (1982). Chemical fossils: the geological fate of steroids. *Science* 217, 491–504. doi: 10.1126/science.217.4559.491

Mangiarotti, A., Genovese, D. M., Naumann, C. A., Monti, M. R., and Wilke, N. (2019). Hopanoids, like sterols, modulate dynamics, compaction, phase segregation and permeability of membranes. *Biochim. Biophys. Acta Biomembr.* 1861:183060. doi: 10.1016/j.bbamem.2019.183060

Maniet, G., Jacquet, N., and Richel, A. (2019). Recovery of sterols from vegetable oil distillate by enzymatic and non-enzymatic processes. *Compt. Ren. Chim.* 22, 347–353.

Marechal, E., and Lupette, J. (2019). Relationship between acyl-lipid and sterol metabolisms in diatoms. *Biochimie* 169, 3–11. doi: 10.1016/j.biochi.2019.07.005

Marsan, M.-P., Muller, I., and Milon, A. (1996). Ability of clionasterol and poriferasterol (24-epimers of sitosterol and stigmasterol) to regulate membrane lipid dynamics. *Chem. Phys. Lipids* 84, 117–121.

Martin-Creuzburg, D., and Elert, E. V. (2009). "Ecological significance of sterols in aquatic food webs," in *Lipids in Aquatic Ecosystems*, eds M. T. Arts, M. T. Brett, and M. Kainz (Berlin: Springer Science & Business Media), 43–64.

Martin-Creuzburg, D., and Merkel, P. (2016). Sterols of freshwater microalgae: potential implications for zooplankton nutrition. *J. Plankton Res.* 38, 865–877.

McKean, M. L., and Nes, W. R. (1977). Evidence for separate intermediates in the biosynthesis of 24α- and 24β-alkylsterols in tracheophytes. *Phytochemistry* 16, 683–686.

Men, S., Boutte, Y., Ikeda, Y., Li, X., Palme, K., Stierhof, Y. D., et al. (2008). Sterol-dependent endocytosis mediates post-cytokinetic acquisition of PIN2 auxin efflux carrier polarity. *Nat. Cell Biol.* 10, 237–244. doi: 10.1038/ncb1686

Mercer, E. I., London, R. A., Kent, I. S. A., and Taylor, A. J. (1974). Sterols, sterol esters and fatty acids of *Botrydium granulatum, Tribonema aequale* and *Monodus subterraneus*. *Phytochemistry* 13, 845–852. doi: 10.1016/S0031-9422(00)91149-X

Meyer, M. M., Xu, R., and Matsuda, S. P. T. (2002). Directed evolution to generate cycloartenol synthase mutants that produce lanosterol. *Org. Lett.* 4, 1395–1398.

Mikami, K., Ito, M., Taya, K., Kishimoto, I., Kobayashi, T., Itabashi, Y., et al. (2018). Parthenosporophytes of the brown alga *Ectocarpus siliculosus* exhibit sex-dependent differences in thermotolerance as well as fatty acid and sterol composition. *Mar. Environ. Res.* 137, 188–195. doi: 10.1016/j.marenvres.2018.02.003

Miller, M. B., Haubrich, B. A., Wang, Q., Snell, W. J., and Nes, W. D. (2012). Evolutionarily conserved Delta(25(27))-olefin ergosterol biosynthesis pathway in the alga *Chlamydomonas reinhardtii*. *J. Lipid Res.* 53, 1636–1645. doi: 10.1194/jlr.M027482

Mitova, M. I., Usov, A. I., Bilan, M. I., Stefanov, K. L., Dimitrova-Konaklieva, S. D., Tonov, D. P., et al. (1999). Sterols and polysaccharides in freshwater algae *Spirogyra* and *Mougeotia*. *Z. Naturforsch. C* 54, 1016–1020.

Moreau, R. A., Nystrom, L., Whitaker, B. D., Winkler-Moser, J. K., Baer, D. J., Gebauer, S. K., et al. (2018). Phytosterols and their derivatives: structural diversity, distribution, metabolism, analysis, and health-promoting uses. *Prog. Lipid Res.* 70, 35–61. doi: 10.1016/j.plipres.2018.04.001

Morikawa, T., Mizutani, M., Aoki, N., Watanabe, B., Saga, H., Saito, S., et al. (2006). Cytochrome P450 CYP710A encodes the sterol C-22 desaturase in *Arabidopsis* and tomato. *Plant Cell* 18, 1008–1022. doi: 10.1105/tpc.105.036012

Morikawa, T., Saga, H., Hashizume, H., and Ohta, D. (2009). CYP710A genes encoding sterol C22-desaturase in Physcomitrella patens as molecular evidence for the evolutionary conservation of a sterol biosynthetic pathway in plants. *Planta* 229, 1311–1322. doi: 10.1007/s00425-009-0916-4

Moseley, K. R., and Thompson, G. A. (1980). Lipid composition and metabolism of *Volvox carteri*. *Plant Physiol.* 65, 260–265.

Moss, G. P. (1989). Nomenclature of steroids (Recommendations 1989). *Pure Appl. Chem.* 61, 1783–1822.

Najle, S. R., Hernandez, J., Ocana-Pallares, E., Garcia Siburu, N., Nusblat, A. D., Nudel, C. B., et al. (2020). Genome-wide transcriptional analysis of *Tetrahymena thermophila* response to exogenous cholesterol. *J. Eukaryot. Microbiol.* 67, 209–222. doi: 10.1111/jeu.12774

Najle, S. R., Nusblat, A. D., Nudel, C. B., and Uttaro, A. D. (2013). The Sterol-C7 desaturase from the ciliate *Tetrahymena thermophila* is a Rieske Oxygenase, which is highly conserved in animals. *Mol. Biol. Evol.* 30, 1630–1643. doi: 10.1093/molbev/mst076

Nakamoto, M., Schmit, A. C., Heintz, D., Schaller, H., and Ohta, D. (2015). Diversification of sterol methyltransferase enzymes in plants and a role for beta-sitosterol in oriented cell plate formation and polarized growth. *Plant J.* 84, 860–874. doi: 10.1111/tpj.13043

Nes, C. R., Singha, U. K., Liu, J., Ganapathy, K., Villalta, F., Waterman, M. R., et al. (2012). Novel sterol metabolic network of *Trypanosoma brucei* procyclic and bloodstream forms. *Biochem. J.* 443, 267–277. doi: 10.1042/BJ20111849

Nes, W. D. (2011). Biosynthesis of cholesterol and other sterols. *Chem. Rev.* 111, 6423–6451.

Newton, M. S., Arcus, V. L., Gerth, M. L., and Patrick, W. M. (2018). Enzyme evolution: innovation is easy, optimization is complicated. *Curr. Opin. Struct. Biol.* 48, 110–116.

Nguyen, H. M., Baudet, M., Cuine, S., Adriano, J. M., Barthe, D., Billon, E., et al. (2011). Proteomic profiling of oil bodies isolated from the unicellular green microalga *Chlamydomonas reinhardtii*: with focus on proteins involved in lipid metabolism. *Proteomics* 11, 4266–4273. doi: 10.1002/pmic.201100114

Nusblat, A. D., Munoz, L., Valcarce, G. A., and Nudel, C. B. (2005). Characterization and properties of cholesterol desaturases from the ciliate *Tetrahymena thermophila*. *J. Eukaryot. Microbiol.* 52, 61–67. doi: 10.1111/j.1550-7408.2005.3279rr.x

Nuzzo, G., Gallo, C., D'ippolito, G., Manzo, E., Ruocco, N., Russo, E., et al. (2018). UPLC(-)MS/MS identification of sterol sulfates in marine diatoms. *Mar. Drugs* 17:E10. doi: 10.3390/md17010010

Ohyama, K., Suzuki, M., Kikuchi, J., Saito, K., and Muranaka, T. (2009). Dual biosynthetic pathways to phytosterol via cycloartenol and lanosterol in *Arabidopsis*. *Proc. Natl. Acad. Sci. U.S.A.* 106, 725–730. doi: 10.1073/pnas.0807675106

Ourisson, G., Albrecht, P., and Rohmer, M. (1982). Predictive microbial biochemistry — from molecular fossils to procaryotic membranes. *Trends Biochem. Sci* 7, 236–239.

Ourisson, G., and Nakatani, Y. (1994). The terpenoid theory of the origin of cellular life: the evolution of terpenoids to cholesterol. *Chem. Biol.* 1, 11–23.

Patterson, G. W. (1971). The distribution of sterols in algae. *Lipids* 6, 120–127.

Patterson, G. W. (1974). Sterols of some green algae. *Comp. Biochem. Physiol. Part B Comp. Biochem.* 47, 453–457.

Patterson, G. W., and Nes, W. D. (1991). *Physiology and Biochemistry of Sterols*. Champaign: American Oil Chemists' Society.

Pearson, A., Flood Page, S. R., Jorgenson, T. L., Fischer, W. W., and Higgins, M. B. (2007). Novel hopanoid cyclases from the environment. *Environ. Microbiol.* 9, 2175–2188.

Pereira, A. L., and Vasconcelos, V. (2014). Classification and phylogeny of the cyanobiont *Anabaena azollae* strasburger: an answered question? *Int. J. Syst. Evol. Microbiol.* 64, 1830–1840. doi: 10.1099/ijs.0.059238-0

Piretti, M. V., Pagliuca, G., Boni, L., Pistocchi, R., Diamante, M., and Gazzotti, T. (1997). Investigation of 4-methyl sterols from cultured dinoflagellate algal strains. *J. Phycol.* 33, 61–67.

Poklepovich, T. J., Rinaldi, M. A., Tomazic, M. L., Favale, N. O., Turkewitz, A. P., Nudel, C. B., et al. (2012). The cytochrome b5 dependent C-5(6) sterol desaturase DES5A from the endoplasmic reticulum of *Tetrahymena thermophila* complements ergosterol biosynthesis mutants in *Saccharomyces cerevisiae*. *Steroids* 77, 1313–1320. doi: 10.1016/j.steroids.2012.08.015

Pollier, J., Vancaester, E., Kuzhiumparambil, U., Vickers, C. E., Vandepoele, K., Goossens, A., et al. (2019). A widespread alternative squalene epoxidase participates in eukaryote steroid biosynthesis. *Nat. Microbiol.* 4, 226–233. doi: 10.1038/s41564-018-0305-5

Raederstorff, D., and Rohmer, M. (1987). Sterol biosynthesis via cycloartenol and other biochemical features related to photosynthetic phyla in the amoeba *Naegleria lovaniensis* and *Naegleria gruberi*. *Eur. J. Biochem.* 164, 427–434. doi: 10.1111/j.1432-1033.1987.tb11075.x

Raederstorff, D., and Rohmer, M. (1988). Polyterpenoids as cholesterol and tetrahymanol surrogates in the ciliate *Tetrahymena*-pyriformis. *Biochim. Biophys. Acta* 960, 190–199. doi: 10.1016/0005-2760(88)90064-1

Rampen, S. W., Abbas, B. A., Schouten, S., and Sinninghe Damste, J. S. (2010). A comprehensive study of sterols in marine diatoms (Bacillariophyta): implications for their use as tracers for diatom productivity. *Limnol. Oceanogr.* 55, 91–105.

Rivero-Calle, S., Gnanadesikan, A., Del Castillo, C. E., Balch, W. M., and Guikema, S. D. (2015). Multidecadal increase in North Atlantic coccolithophores and the potential role of rising CO(2). *Science* 350, 1533–1537. doi: 10.1126/science.aaa8026

Roberts, C. W., Mcleod, R., Rice, D. W., Ginger, M., Chance, M. L., and Goad, L. J. (2003). Fatty acid and sterol metabolism: potential antimicrobial targets in apicomplexan and trypanosomatid parasitic protozoa. *Mol. Biochem. Parasitol.* 126, 129–142. doi: 10.1016/s0166-6851(02)00280-3

Rohmer, M. (1999). The discovery of a mevalonate-independent pathway for isoprenoid biosynthesis in bacteria, algae and higher plants. *Nat. Prod. Rep.* 16, 565–574. doi: 10.1039/a709175c

Rohmer, M., Bouvier, P., and Ourisson, G. (1979). Molecular evolution of biomembranes: structural equivalents and phylogenetic precursors of sterols. *Proc. Natl. Acad. Sci. U.S.A.* 76, 847–851. doi: 10.1073/pnas.76.2.847

Rosenwasser, S., Mausz, M. A., Schatz, D., Sheyn, U., Malitsky, S., Aharoni, A., et al. (2014). Rewiring host lipid metabolism by large viruses determines the fate of *Emiliania huxleyi*, a bloom-forming alga in the ocean. *Plant Cell* 26, 2689–2707. doi: 10.1105/tpc.114.125641

Rubinstein, I., Goad, L. J., Clague, A. D. H., and Mulheirn, L. J. (1976). The 220 MHz NMR spectra of phytosterols. *Phytochemistry* 15, 195–200.

Saar, J., Kader, J.-C., Poralla, K., and Ourisson, G. (1991). Purification and some properties of the squalene-tetrahymanol cyclase from *Tetrahymena thermophila*. *Biochim. Biophys. Acta Gen. Sub.* 1075, 93–101. doi: 10.1016/0304-4165(91)90080-z

Saenz, J. P., Sezgin, E., Schwille, P., and Simons, K. (2012). Functional convergence of hopanoids and sterols in membrane ordering. *Proc. Natl. Acad. Sci. U.S.A.* 109, 14236–14240.

Salvador-Castell, M., Tourte, M., and Oger, P. M. (2019). In search for the membrane regulators of *Archaea*. *Int. J. Mol. Sci.* 20:4434. doi: 10.3390/ijms20184434

Sawai, S., Ohyama, K., Yasumoto, S., Seki, H., Sakuma, T., Yamamoto, T., et al. (2014). Sterol side chain reductase 2 is a key enzyme in the biosynthesis of cholesterol, the common precursor of toxic steroidal glycoalkaloids in potato. *Plant Cell* 26, 3763–3774. doi: 10.1105/tpc.114.130096

Schaeffer, A., Bouvier-Navé, P., Benveniste, P., and Schaller H. (2000). Plant sterol-C24-methyl transferases: different profiles of tobacco transformed with SMT1 or SMT2. *Lipids* 35, 263–269. doi: 10.1007/s11745-000-0522-1

Schaeffer, A., Bronner, R., Benveniste, P., and Schaller, H. (2001). The ratio of campesterol to sitosterol that modulates growth in *Arabidopsis* is controlled by STEROL METHYLTRANSFERASE 2;1. *Plant J.* 25, 605–615. doi: 10.1046/j.1365-313x.2001.00994.x

Schaller, H. (2010). "Sterol and steroid biosynthesis and metabolism in plants and microorganisms," in *Comprehensive Natural Products II*, eds L. Hung-Wen and L. Mander (Amsterdam: Elsevier Science), 755–787.

Schaller, H., Bouvier-Navé, P., and Benveniste, P. (1998). Overexpression of an *Arabidopsis* cDNA encoding a Sterol-C241-methyltransferase in tobacco modifies the ratio of 24-Methyl cholesterol to sitosterol and is associated with growth reduction. *Plant Physiol.* 118, 461–469. doi: 10.1104/pp.118.2.461

Schonknecht, G., Chen, W. H., Ternes, C. M., Barbier, G. G., Shrestha, R. P., Stanke, M., et al. (2013). Gene transfer from bacteria and *Archaea* facilitated evolution of an extremophilic eukaryote. *Science* 339, 1207–1210. doi: 10.1126/science.1231707

Seckbach, J., Ikan, R., Ringelberg, D., and White, D. (1993). Sterols and phylogeny of the acidophilic hot springs algae *Cyanidium caldarium* and *Galdieria sulphuraria*. *Phytochemistry* 34, 1345–1349.

Shimizu, Y., Alam, M., and Kobayashi, A. (1976). Letter: dinosterol, the major sterol with a unique side chain ion the toxic dinoflagellate, *Gonyaulax tamarensis*. *J. Am. Chem. Soc.* 98, 1059–1060. doi: 10.1021/ja00420a054

Silipo, A., Vitiello, G., Gully, D., Sturiale, L., Chaintreuil, C., Fardoux, J., et al. (2014). Covalently linked hopanoid-lipid A improves outer-membrane resistance of a *Bradyrhizobium* symbiont of legumes. *Nat. Commun.* 5:5106. doi: 10.1038/ncomms6106

Singh, R., Parihar, P., Singh, M., Bajguz, A., Kumar, J., Singh, S., et al. (2017). Uncovering potential applications of cyanobacteria and algal metabolites in biology, agriculture and medicine: current status and future prospects. *Front. Microbiol.* 8:515. doi: 10.3389/fmicb.2017.00515

Sonawane, P. D., Pollier, J., Panda, S., Szymanski, J., Massalha, H., Yona, M., et al. (2016). Plant cholesterol biosynthetic pathway overlaps with phytosterol metabolism. *Nat. Plants* 3:16205.

Sperling, P., Ternes, P., Zank, T. K., and Heinz, E. (2003). The evolution of desaturases. *Prostaglandins Leukot. Essent. Fatty Acids* 68, 73–95.

Strauss, J. F. III, Liu, P., Christenson, L. K., and Watari, H. (2002). Sterols and intracellular vesicular trafficking: lessons from the study of NPC1. *Steroids* 67, 947–951. doi: 10.1016/s0039-128x(02)00042-9

Summons, R. E., Bradley, A. S., Jahnke, L. L., and Waldbauer, J. R. (2006). Steroids, triterpenoids and molecular oxygen. *Philos. Trans. R. Soc. Lond. B. Biol. Sci.* 361, 951–968.

Suzuki, M., Xiang, T., Ohyama, K., Seki, H., Saito, K., Muranaka, T., et al. (2006). Lanosterol synthase in dicotyledonous plants. *Plant Cell Physiol.* 47, 565–571.

Taipale, S. J., Hiltunen, M., Vuorio, K., and Peltomaa, E. (2016). Suitability of phytosterols alongside fatty acids as chemotaxonomic biomarkers for phytoplankton. *Front. Plant Sci.* 7:212. doi: 10.3389/fpls.2016.00212

Takishita, K., Takaki, Y., Chikaraishi, Y., Ikuta, T., Ozawa, G., Yoshida, T., et al. (2017). Genomic evidence that methanotrophic endosymbionts likely provide deep-sea bathymodiolus mussels with a sterol intermediate in cholesterol biosynthesis. *Genome Biol. Evol.* 9, 1148–1160. doi: 10.1093/gbe/evx082

Tasende, M. G. (2000). Fatty acid and sterol composition of gametophytes and sporophytes of *Chondrus crispus* (*Gigartinaceae*, *Rhodophyta*). *Sci. Mar.* 64, 421–426.

Tomazic, M. L., Najle, S. R., Nusblat, A. D., Uttaro, A. D., and Nudel, C. B. (2011). A novel sterol desaturase-like protein promoting dealkylation of phytosterols in *Tetrahymena thermophila*. *Eukaryot. Cell* 10, 423–434. doi: 10.1128/EC.00259-10

Tomazic, M. L., Poklepovich, T. J., Nudel, C. B., and Nusblat, A. D. (2014). Incomplete sterols and hopanoids pathways in ciliates: gene loss and acquisition during evolution as a source of biosynthetic genes. *Mol. Phylogenet. Evol.* 74, 122–134. doi: 10.1016/j.ympev.2014.01.026

Tsuda, K., Akagi, S., and Kishida, Y. (1957). Discovery of cholesterol in some red algae. *Science* 126, 927–928. doi: 10.1126/science.126.3279.927

Urbina, J. A., Concepcion, J. L., Rangel, S., Visbal, G., and Lira, R. (2002). Squalene synthase as a chemotherapeutic target in *Trypanosoma cruzi* and *Leishmania mexicana*. *Mol. Biochem. Parasitol.* 125, 35–45. doi: 10.1016/s0166-6851(02)00206-2

Veron, B., Billard, C., Dauguet, J. C., and Hartmann, M. A. (1996). Sterol composition of *Phaeodactylum tricornutum* as influenced by growth temperature and light spectral quality. *Lipids* 31, 989–994. doi: 10.1007/BF02522694

Volkman, J. K. (2003). Sterols in microorganisms. *Appl. Microbiol. Biotechnol.* 60, 495–506.

Volkman, J. K. (2016). "Sterols in microalgae," in *The Physiology of Microalgae*, eds M. Borowitzka, J. Beardall, and J. Raven (Berlin: Springer), 485–505.

Volkman, J. K., Smith, D. J., Eglinton, G., Forsberg, T. E. V., and Corner, E. D. S. (1981). Sterol and fatty acid composition of four marine haptophycean algae. *J. Mar. Biol. Assoc. U. K.* 61, 509–527.

Wang, S., Li, L., Li, H., Sahu, S. K., Wang, H., Xu, Y., et al. (2020). Genomes of early-diverging streptophyte algae shed light on plant terrestrialization. *Nat. Plants* 6, 95–106. doi: 10.1038/s41477-019-0560-3

Wei, J. H., Yin, X., and Welander, P. V. (2016). Sterol synthesis in diverse bacteria. *Front. Microbiol.* 7:990. doi: 10.3389/fmicb.2016.00990

Weng, J. K., and Noel, J. P. (2013). Chemodiversity in *Selaginella*: a reference system for parallel and convergent metabolic evolution in terrestrial plants. *Front. Plant Sci.* 4:119. doi: 10.3389/fpls.2013.00119

Wiersma, S. J., Mooiman, C., Giera, M., and Pronk, J. T. (2020). Squalene-tetrahymanol cyclase expression enables sterol-independent growth of *Saccharomyces cerevisiae*. *Appl. Environ. Microbiol.* 86:e00672-20. doi: 10.1128/AEM.00672-20

Wong, K. C. (2019). Big data challenges in genome informatics. *Biophys Rev* 11, 51–54.

Xu, R., Fazio, G. C., and Matsuda, S. P. (2004). On the origins of triterpenoid skeletal diversity. *Phytochemistry* 65, 261–291. doi: 10.1016/j.phytochem.2003.11.014

Yakobov, N., Fischer, F., Mahmoudi, N., Saga, Y., Grube, C. D., Roy, H., et al. (2020). RNA-dependent sterol aspartylation in fungi. *Proc. Natl. Acad. Sci. U.S.A.* 117, 14948–14957. doi: 10.1073/pnas.2003266117

Ye, N., Zhang, X., Miao, M., Fan, X., Zheng, Y., Xu, D., et al. (2015). Saccharina genomes provide novel insight into kelp biology. *Nat. Commun.* 6:6986. doi: 10.1038/ncomms7986

Zhang, X., Lin, K., and Li, Y. (2020). Highlights to phytosterols accumulation and equilibrium in plants: biosynthetic pathway and feedback regulation. *Plant Physiol. Biochem.* 155, 637–649. doi: 10.1016/j.plaphy.2020.08.021

Zhou, W., Debnath, A., Jennings, G., Hahn, H. J., Vanderloop, B. H., Chaudhuri, M., et al. (2018). Enzymatic chokepoints and synergistic drug targets in the sterol biosynthesis pathway of *Naegleria fowleri*. *PLoS Pathog.* 14:e1007245. doi: 10.1371/journal.ppat.1007245

Zhou, W., Fisher, P. M., Vanderloop, B. H., Shen, Y., Shi, H., Maldonado, A. J., et al. (2020). A nematode sterol C4alpha-methyltransferase catalyzes a new methylation reaction responsible for sterol diversity. *J. Lipid Res.* 61, 192–204. doi: 10.1194/jlr.RA119000317

Conflict of Interest: The authors declare that the research was conducted in the absence of any commercial or financial relationships that could be construed as a potential conflict of interest.

Copyright © 2021 Darnet, Blary, Chevalier and Schaller. This is an open-access article distributed under the terms of the Creative Commons Attribution License (CC BY). The use, distribution or reproduction in other forums is permitted, provided the original author(s) and the copyright owner(s) are credited and that the original publication in this journal is cited, in accordance with accepted academic practice. No use, distribution or reproduction is permitted which does not comply with these terms.

frontiers in Plant Science

ORIGINAL RESEARCH
published: 08 June 2021
doi: 10.3389/fpls.2021.648494

Functional and Predictive Structural Characterization of WRINKLED2, A Unique Oil Biosynthesis Regulator in Avocado

*Jyoti R. Behera[1], Md. Mahbubur Rahman[1,2†], Shina Bhatia[1†], Jay Shockey[3] and Aruna Kilaru[1]**

[1] Department of Biological Sciences, East Tennessee State University, Johnson City, TN, United States, [2] Department of Biological Systems Engineering, Virginia Tech, Blacksburg, VA, United States, [3] United States Department of Agriculture, Agricultural Research Service, New Orleans, LA, United States

OPEN ACCESS

Edited by:
Mie Shimojima, Tokyo Institute of Technology, Japan

Reviewed by:
Jin-Song Zhang, State Key Laboratory of Plant Genomics, Institute of Genetics and Developmental Biology (CAS), China
Koichi Kobayashi, Osaka Prefecture University, Japan

***Correspondence:**
Aruna Kilaru
kilaru@etsu.edu

† These authors have contributed equally to this work

Specialty section:
This article was submitted to Plant Physiology, a section of the journal Frontiers in Plant Science

Received: *31 December 2020*
Accepted: *03 May 2021*
Published: *08 June 2021*

Citation:
Behera JR, Rahman MM, Bhatia S, Shockey J and Kilaru A (2021) Functional and Predictive Structural Characterization of WRINKLED2, A Unique Oil Biosynthesis Regulator in Avocado. Front. Plant Sci. 12:648494. doi: 10.3389/fpls.2021.648494

WRINKLED1 (WRI1), a member of the APETALA2 (AP2) class of transcription factors regulates fatty acid biosynthesis and triacylglycerol (TAG) accumulation in plants. Among the four known *Arabidopsis WRI1* paralogs, only *WRI2* was unable to complement and restore fatty acid content in *wri1-1* mutant seeds. Avocado (*Persea americana*) mesocarp, which accumulates 60-70% dry weight oil content, showed high expression levels for orthologs of *WRI2*, along with *WRI1* and *WRI3*, during fruit development. While the role of WRI1 as a master regulator of oil biosynthesis is well-established, the function of WRI1 paralogs is poorly understood. Comprehensive and comparative *in silico* analyses of WRI1 paralogs from avocado (a basal angiosperm) with higher angiosperms *Arabidopsis* (dicot), maize (monocot) revealed distinct features. Predictive structural analyses of the WRI orthologs from these three species revealed the presence of AP2 domains and other highly conserved features, such as intrinsically disordered regions associated with predicted PEST motifs and phosphorylation sites. Additionally, avocado WRI proteins also contained distinct features that were absent in the nonfunctional *Arabidopsis* ortholog *At*WRI2. Through transient expression assays, we demonstrated that both avocado WRI1 and WRI2 are functional and drive TAG accumulation in *Nicotiana benthamiana* leaves. We predict that the unique features and activities of ancestral *PaWRI2* were likely lost in orthologous genes such as *AtWRI2* during evolution and speciation, leading to at least partial loss of function in some higher eudicots. This study provides us with new targets to enhance oil biosynthesis in plants.

Keywords: AP2 domain, *Arabidopsis thaliana,* fatty acids, mesocarp, *Persea americana,* transcription factor, triacylglycerol, WRINKLED1

INTRODUCTION

WRINKLED1 (WRI1) belongs to the APETALA2/ethylene-responsive element binding protein (AP2/EREBP) class of transcription factors that play a master role in the developmental regulation of oil biosynthesis in plants (Cernac and Benning, 2004). The WRI1 transcription factor was first identified in *Arabidopsis*, where mutant seeds showed 80% reduction in triacylglycerol (TAG)

content relative to wild-type (WT), 50% increase in sucrose levels, and a wrinkled seed coat phenotype. Subsequent studies revealed that WRI1 regulates a number of genes involved in controlling carbon allocation between sucrose and fatty acids in developing seeds (Focks and Benning, 1998). As such, *Arabidopsis wri1* mutant seeds were unable to efficiently convert carbon from sucrose and glucose into fatty acids during seed development. The genes regulated by WRI1 include *phosphoglycerate mutase, plastidial pyruvate kinase* β*-subunit 1 (PI-PK*β*1), pyruvate dehydrogenase 1*α *(PDHE1*α*), biotin carboxyl carrier protein 2 (BCCP2), acyl carrier protein 1 (ACP1),* and *keto-ACP synthase 1 (KAS1)* (Baud and Lepiniec, 2009; Maeo et al., 2009). Additionally, BIOTIN ATTACHMENT DOMAIN CONTAINING (BADC) proteins are conditional inhibitors of fatty acid biosynthesis; the genes encoding for *BADC1*, 2, and 3 were also positively regulated by WRI1 (Keereetaweep et al., 2018; Liu et al., 2019) Hence, fatty acid and storage lipid biosynthesis mediated through WRI1-induced genes is a complex and tightly regulated process.

DNA-binding studies and predictive structural analyses have shown that the regulation of glycolytic and fatty acid biosynthesis genes is achieved by the binding of AP2 domains in WRI1 with the AW-box, a 5′- upstream element ($[CnTnG](n)_7[CG]$) in the promoter region of the target genes (Ruuska et al., 2002; Cernac and Benning, 2004; Baud et al., 2007, 2009; Maeo et al., 2009; Fukuda et al., 2013; Kuczynski et al., 2020). Specifically, in *Arabidopsis* WRI1 (*At*WRI1), two AP2 domains (73 and 62 amino acid residues, respectively) are present in the *N*-terminal domain. A small exon coding for the predicted residues "VYL" (valine-tyrosine-leucine) is a functionally important element in the first AP2 domain and is widely conserved among many WRI1 orthologs. Mutation in any of these three residues rendered complementation constructs insufficient to rescue the low seed oil phenotype of retransformed *wri1-1* plants (Ma et al., 2013). Furthermore, three intrinsically disordered regions (IDRs) were identified in *At*WRI1, with one located near the *N*-terminus, preceding the first AP2 domain, and the other two towards the *C*-terminal region, after the second AP2 domain (Ma et al., 2015). While part of the *C*-terminal region from 307 to 397 in *At*WRI1 is implicated in positive regulation of transcriptional activity (Ma et al., 2015), the occurrence of a PEST motif in nearby IDR3 likely acts as a recognition site for proteolytic degradation. The disordered state of IDR3 likely favors kinase access to key residues in this region and PEST residue phosphorylation serves as a signature that is recognized by key enzymes in the degradation pathway (Belizario et al., 2008). Since the PEST motif does not overlap with the transactivation domain (TAD), deletion or mutation of this motif increased the stability of WRI1 (Ma et al., 2015).

Since the discovery and characterization of WRI1 as a master regulator of fatty acid biosynthesis in seed tissues, its homologs have been identified in diverse plant species (Tang et al., 2019). In *Arabidopsis*, four paralogs of WRI1 (WRI1, WRI2, WRI3, and WRI4) were identified, all of which belong to the AP2/EREBP family of transcription factors. These genes, except *AtWRI2*, were also shown to play functional roles in fatty acid biosynthesis in various tissues (To et al., 2012). WRI1 is the dominant isoform that largely controls fatty acid metabolic gene expression during seed development and maturation. A basal level of transcriptional activity is however, maintained in *wri1* mutant seeds, suggesting a redundant role played by functional paralogs (Baud et al., 2009). Both *WRI3* and *WRI4* are highly expressed in floral tissue and stems, and thus contribute to fatty acid production for sustained cutin synthesis (To et al., 2012). Conservation of functional homology of WRI1 genes from other species such as *Zea mays* (Pouvreau et al., 2011), *Brassica napus* (Liu et al., 2010), and *Camelina sativa* (An et al., 2017) was shown by the complementation of *Arabidopsis wri1* mutants. In maize, there are two alternate splice forms of a *WRI1* gene (*ZmWRI1a* and *ZmWRI1b*); *ZmWRI1a* is strongly expressed in endosperm and clearly regulates kernel oil accumulation. The tissue-specific and temporal regulation of *ZmWRI1b* expression is different and suggestive of an ongoing evolutionary functional specialization of these two isoforms (Pouvreau et al., 2011). Transgenic expression of two *WRI1* isoforms from *B. napus* (*BnWRI1-1* and *BnWRI1-2*) increased the seed oil content by 20% in *Arabidopsis* seeds (Liu et al., 2010). Similarly, *Cs*WRI1 from *Camelina sativa* also partially restored the seed fatty acid levels in *Arabidopsis wri1* mutants; its transient expression also increased the TAG content in tobacco leaves (An et al., 2017). More recently, various transcriptome studies have extended the role of WRI1 in regulation of oil biosynthesis beyond seed tissues. The function of WRI1 in regulation of fatty acid synthesis in oil palm (*Elaeis guineensis*) mesocarp, which accumulates about 90% oil by dry weight, was established unequivocally (Bourgis et al., 2011; Ma et al., 2013). Furthermore, *Eg*WRI1 was able to rescue the low oil content in *Atwri1-1* seeds suggesting that WRI1 is responsible for oil accumulation in both seed and non-seed tissues (Ma et al., 2013) in some plant species. Additional studies have identified high expression of tissue-specific *WRI1* paralogs in diverse non-seed tissues such as Chinese tallow (Divi et al., 2016), potato, oat, and mesocarp of avocado (Kilaru et al., 2015; Rahman et al., 2016).

Avocado (*Persea americana*) is a basal angiosperm and occupies a useful evolutionary niche as one of the earliest lineages near the origin of flowering plants (Chanderbali et al., 2008). Avocado is also an ideal plant system to study oil biosynthesis for various reasons. The mesocarp of avocado accumulates 60–70% of oil by dry weight, of which, more than 80% is composed of nutritionally desirable oleic acid (Kikuta and Erickson, 1968; Kilaru et al., 2015). Additionally, transcriptome studies of developing mesocarp revealed that its oil accumulation is strongly correlated with the expression of fatty acid biosynthetic genes and *WRI* orthologs (Kilaru et al., 2015). Orthologs of all four members of the *AtWRI* gene family are present in avocado, referred to as putative *PaWRI1* to *PaWRI4*, and all but the *PaWRI4* are highly expressed in avocado mesocarp in correlation with oil accumulation. Avocado is unique in that it is the first plant system with confirmed concomitant expression of multiple *WRI1* paralogs during oil accumulation, which has not been observed previously. *PaWRI3* and *PaWRI4* are likely the functionally diverged products of a relatively recent gene duplication event, given that *PaWRI4* is not expressed in the presence of highly expressed *PaWRI3* (Kilaru et al., 2015).

Since *AtWRI2* was unequivocally shown to lack any role in oil biosynthesis, high expression of its ortholog during non-seed oil accumulation in avocado was intriguing. Thus, we carried out comprehensive and comparative *in silico* analysis followed by transient expression studies to examine if *Pa*WRI2 was functional and associated with TAG accumulation.

MATERIALS AND METHODS

Predictive Structural Analyses

Sequences of the WRI homologs for different species were retrieved from the NCBI database based on the BLASTP search using corresponding WRI-paralogs from *Arabidopsis* as query. Putative transcript sequences of *PaWRI1, 2, 3*, and *4* were obtained from the previously published avocado transcriptome data (Ibarra-Laclette et al., 2015; Kilaru et al., 2015; Rendón-Anaya et al., 2019). Full-length sequences were subsequently confirmed by cDNA synthesis and PCR amplification using gene specific primers, and sequencing, and deposited in the GenBank. The accession numbers for all the sequences used in this study are provided in the Data Availability Statement. Various bioinformatics tools were utilized for the subsequent *in silico* analyses (**Supplementary Table 1**).

The predicted protein sequence of each avocado gene was generated with the ExPASy translation tool. Multiple Sequence Alignment was done using the PRALINE online tool (Simossis and Heringa, 2003; **Supplementary Table 1**). For sequence comparison, all three avocado WRI paralogs were compared to their orthologs from *Arabidopsis* and maize, with protein sequences in FASTA format was used as inputs. BLOSUM62 exchange weights matrix was used, with gap penalties value 12 for open and 1 for extension. Homology-extended alignment was performed keeping all other parameters at the default values provided by the software. The outputs were obtained in a color-coded conservation scoring format where the conservation at each position of amino acid was denoted by a score from 0 to 10; 0 being the least-conserved position and 10 (indicated by asterisk) being the highest. The information about the positioning of AP2 domains in each WRI protein sequence was obtained from the NCBI database.

The amino acid composition profile of each protein was determined using COMPOSITION PROFILER (Vacic et al., 2007; **Supplementary Table 1**). Each of the protein sequences was used as a query sample against the SwissProt 51 dataset. The graphical output was obtained in a bar chart format composed of twenty data points for each amino acid arranged in increasing order of hydrophobicity (Eisenberg), where bar heights indicate enrichment (upward) or depletion (downward). The software also performs statistical analyses to evaluate whether the enrichment and depletion of amino acids were significant at a (α) of 0.05. Only the significantly enriched amino acids are represented in green and the depleted amino acids in blue.

Composition of each of the secondary structures, such as α-helix, β-strand, β-turn, and random coil structures, were predicted using the Self-Optimized Prediction Method with Alignment (SOPMA) secondary structure prediction online tool (Combet et al., 2000; **Supplementary Table 1**) with default parameters. Percentages for each of the predicted secondary structure components are denoted in the tables and the respective positions of each are expressed in graphical format.

The prediction of IDRs was conducted using the Predictors of Natural Disordered Regions (PONDR-VL3) online tool (Peng et al., 2005; **Supplementary Table 1**). The disordered regions in the full-length protein sequences were identified and provided as graphic format outputs. A score above the threshold value of 0.5 indicates a propensity of that stretch of protein to be a part of an IDR. Only the stretches of >30 amino acid residues showing disordered tendency are considered as likely IDRs in the protein tertiary structure.

Kinase phosphorylation potential of each Ser (S), Thr (T), or Tyr (Y) residue was evaluated using the NetPhos 3.1 online tool (Blom et al., 1999). The likelihood threshold values were considered at 0.5. The positions of putative PEST motifs were predicted using the epestfind online tool (**Supplementary Table 1**).

Statistical Analysis

The transient expression assays were performed in triplicate and data were expressed as their mean value with standard deviation (SD). To test for significance amongst the dataset, one-way analysis of variance (ANOVA) followed by Tukey's post-test was performed using Minitab software (version 18) at *p*-level of 0.05 ($p < 0.05$).

cDNA Synthesis and Cloning

Total RNA extract from avocado mesocarp was available from the previous study (Kilaru et al., 2015). From the total RNA, cDNA was synthesized using oligo dT primer and superscript reverse transcriptase (Promega). Full-length coding sequences of putative *PaWRI1* and *PaWRI2* were amplified by PCR using specific primers (*PaWRI1-F*: 5′-GCTCCC**ATGG**ACACATCTTCTCCCCTCTCCAATT-3′ and *PaWRI1-R*: 5′-CTATCCGCGGCTAAGAACATATGCTGATGG GAAGCGGAT-3′ for *PaWRI1*; *PaWRI2-F* : 5′-GCTCCC **ATGG**CTTCTTCTCCTTCGTCGTCG-3′ and *PaWRI2-R*: 5′-GCGGTCCGCGGTTATTCTTGACGGAAGAAAGTATATG TTG-3′ for *PaWRI2*) containing *Nco*I and *Sac*II restriction sites (underlined) in their forward and reverse primers, respectively. Initiator methionine codons in the forward primers are shown in bold. The PCR products were digested with appropriate restriction endonucleases, and cloned into the corresponding sites in entry vector pK34 with a dual CaMV35S promoter and terminator (Shockey et al., 2015) using T4 DNA ligase (New England Biolabs). Ligation reactions were chemically transformed into Top10 *E. coli* competent cells, grown on solid media containing ampicillin, and insert-positive colonies were identified by colony PCR. Insert sequence accuracy was confirmed by sequencing. For expression in tobacco leaves, *Asc*I fragments representing the promoter:gene:terminator cassettes from the K34-based entry plasmids were cloned into the binary expression vector pB110 (Shockey et al., 2015), followed by another round of *E. coli* transformation and colony selection, this

time using kanamycin as the selective agent. The viral silencing suppressor protein gene P19 (Wood et al., 2009) was also cloned into pB110 behind the CaMV35S promoter using this strategy, and was later used for co-infiltration into *N. benthamiana* leaves.

Transient Expression

Wild type tobacco (*Nicotiana benthamiana*) was used for all transient expression experiments. All plants were grown in a growth chamber (Percival Scientific, Perry, IA, United States) under long day conditions (15 h L/9 h D) at 24°C and 60% relative humidity. Six weeks old plants were used for transient expression. For plant transformation, 100 μL of *Agrobacterium* LBA4404 competent cells were gently mixed with 100-1000 ng of binary plasmid DNA expressing the gene of interest, kept on ice for 5 min, then immediately transferred into liquid nitrogen. Subsequently, the flash-frozen mixture was incubated for 5 min at 37°C in a water bath and then transferred into 1 mL of LB media and incubated for 2-4 h at 28°C. After the incubation period, the bacterial cells were pelleted by gentle centrifugation and resuspended in 100 μl LB and immediately plated onto LB agar containing kanamycin (50 μg/mL) and rifampicin (50 μg/mL). Positive colonies were used for overnight culture in LB liquid media containing appropriate antibiotics at 28°C. The overnight culture was further supplemented with 100 μM acetosyringone and allowed to grow for additional 2 h. After incubation, the solution was centrifuged at 400 × *g* for 5 min at room temperature and the pellet was resuspended in infiltration buffer (5 mM $MgSO_4$, pH 5.7, 5 mM methyl ethanesulfonate, and 100 mM acetosyringone). Finally, *Agrobacterium* constructs with an O.D. of 0.3 at 600 nm were prepared and infiltrated into *N. benthamiana* leaves. After infiltration, plants were maintained under ambient conditions in the growth chamber, to avoid any external stressors. Plants were allowed to grow for 6-7 days to express the recombinant protein. Subsequently, inoculated areas of leaves were harvested and either processed immediately or stored at −80°C for further analyses.

Nile Red Staining

After *Agrobacterium* infiltration, *N. benthamiana* plant leaf discs were collected and fixed with paraformaldehyde in 1X phosphate-buffered saline (PBS). Nile Red (in dimethyl sulfoxide) was diluted in 1X PBS (final concentration 4 μg/mL) was used for lipid droplet staining; leaf discs were immediately observed using a Leica TCS SP8 confocal fluorescence microscope. The excitation and emission wavelength for Nile Red staining were 488 nm and 560-620 nm, respectively. Images were acquired as a z-stack of 10 optical sections. The dimensions of each panel were 161.7 × 161.7 μm and the total number of LDs per view were quantified using ImageJ software the count was normalized to LD /mm^2. Images were obtained from three biological replicates.

Extraction of Plant Lipids

Other infiltrated *N. benthamiana* leaf discs were collected at 6-7 days after *Agrobacterium* infiltration and used for total lipid extraction. Lipids were extracted using the hexane:isopropanol method (Hara and Radin, 1978). Briefly, 200 mg of plant tissue (fresh weight, FW) was ground in liquid nitrogen and 2 ml hot isopropanol was added, then heated to 70°C for 30 min in water to inactivate any internal lipase activity. After cooling to room temperature, one mL of chloroform and 250 μL water were added to achieve a final ratio of 2 mL isopropanol: 1 mL chloroform: 0.45 ml water. The samples were stored O/N at 4°C. The next day, the supernatant was collected from the sample after vortexing and centrifugation for 5 min at 5000 × *g*. One mL of chloroform and 2 mL of 1M KCl were added to the sample to achieve phase separation. After centrifugation, the upper aqueous phase and interphase were aspirated by using a Pasteur pipette. The sample was then washed twice with 2 mL of 1M KCl and the organic phase was collected and dried under nitrogen gas. Dried lipid samples were reconstituted in ∼1 mL of chloroform and transferred into a pre-weighed glass vial. After evaporating the chloroform in nitrogen gas, each glass vial was weighed again to obtain the total lipid weights. Before homogenization, an appropriate amount of heptadecanoic acid, 17:0 standard (100 μg; Sigma-Aldrich) was added to the plant tissue.

Fatty Acid Analysis by Gas Chromatography-Flame Ionization Detection (GC-FID)

Total lipids extracted from the infiltrated leaves were esterified to determine fatty acid composition. To perform fatty acid methyl esterification (FAME), HCl methanolic acid (1 N) was added to the samples and the mixture was heated for 2 h at 85°C in a water bath. After cooling to room temperature, 1 mL KCl and 1 mL hexane were added for phase separation. The hexane organic phase containing FAMEs was collected and dried under nitrogen gas at 40°C. Each FAME sample was resuspended in 1 μL of hexane and analyzed by gas chromatography coupled with a flame ionization detector (GC-FID, Varian). A capillary column (DB-23; 30 m × 0.32 mm I.D., 0.25 μm) with helium as carrier gas (flow rate of 1.5 mL/min) was used. The injection temperature was set at 150°C, which was ramped after 3 min to 240°C at 6°C/min; the detection temperature was 300°C. The retention time for each fatty was determined based on comparison to the Supelco FAME mix standards, and quantified relative to the C17:0 internal standards. Each sample was analyzed in triplicate.

RESULTS AND DISCUSSION

Primary Sequence Features of WRI Paralogs in Avocado Differ From Their Dicot and Monocot Orthologs

To identify distinct structural characteristics among the WRI orthologs, comprehensive *in silico* analyses were conducted. Initially, phylogenetic analyses of WRI orthologs from select basal angiosperms (avocado and *Amborella*), monocots (rice, maize, and oil palm) and dicots (*Arabidopsis*, rapeseed, castor, grape, and poplar) was carried out (**Supplementary Figure 1**). These analyses revealed that WRI2-orthologs evolved independently and earlier than their corresponding paralogs in the respective plant species (**Supplementary Figure 1**). Further comprehensive analyses of structural features of *Pa*WRI2, relative to its

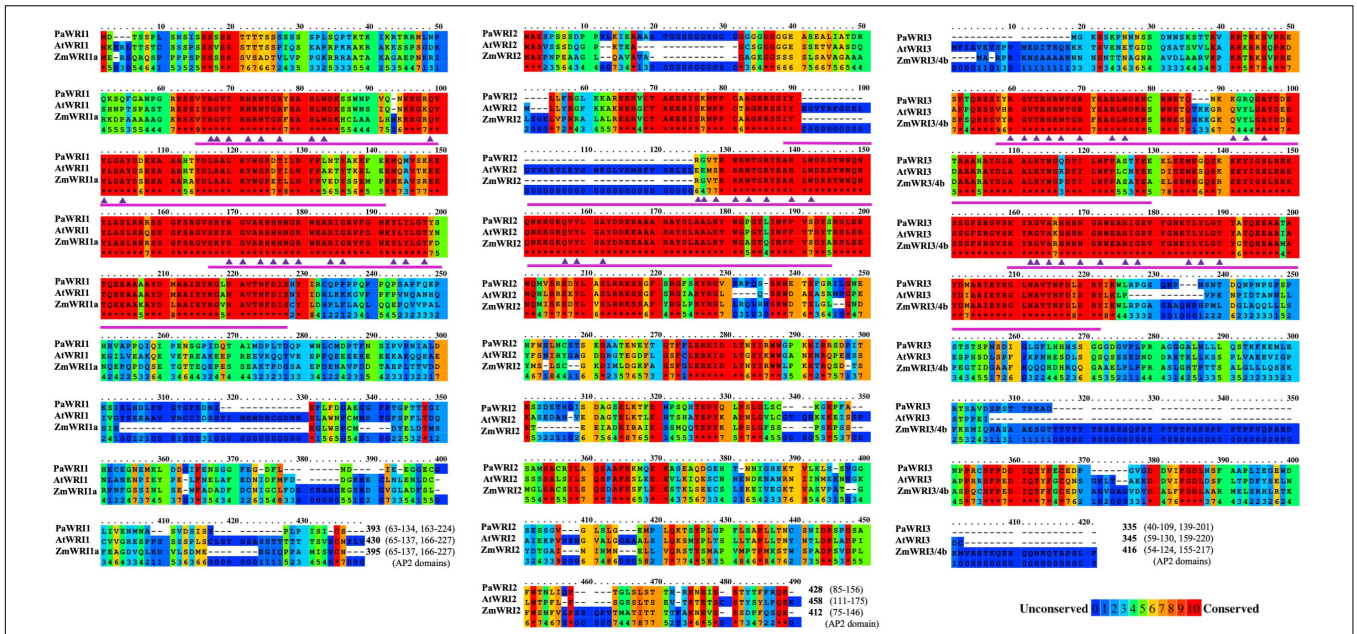

FIGURE 1 | Primary sequence features of WRI homologs. Multiple sequence alignment of primary sequences of WRI1, 2, and 3 from *P. americana* (Pa), *A. thaliana* (At), and *Z. mays* (Zm) in a color-coded format; red and blue colors represent the most (10, indicated by asterisk) and least (0) conserved regions, respectively, on a scale of 0 to 10. Position of the AP2 domains and sequence length are indicated at the end of the alignment. The amino acid residues in the AP2 domain important for DNA interaction are represented by (▲).

paralogs and orthologs specifically from maize and arabidopsis were determined by protein sequence comparison. Among the three species, the WRI1 protein sequences shared an overall identity of 50%, while WRI2, WRI3, and WRI4 showed 45, 57, and 59% identity, respectively (**Figure 1**). Additionally, phylogenetic analysis showed that avocado WRI3 and WRI4 share > 70% identity and are likely the result of a gene duplication event (**Supplementary Figure 1**). Duplicated genes may retain functional redundancy, but in some cases attain specialized temporal- or tissue-specific roles. *PaWRI3* transcripts were abundant and *PaWRI4* was poorly expressed in avocado mesocarp (Kilaru et al., 2015), suggestive of a larger role for *PaWRI3* in mesocarp lipid metabolism. Whether the functional role of WRI2 orthologs in oil biosynthesis is conserved in any of the plant species has not been elucidated, except for *At*WRI2, where it was shown to be non-functional based on its inability to complement *Atwri1-1* mutant (To et al., 2012). As such, only WRI1, WRI2, and WRI3 orthologs were included in the subsequent *in silico* comparisons.

Primary sequence comparisons revealed that avocado WRI1 and WRI3 proteins were generally shorter than their corresponding orthologs in *Arabidopsis* and maize (**Figure 1**) and also to some of other monocot and dicot orthologs examined (**Supplementary Figure 2**). Specifically, *Pa*WRI1 is shorter than *At*WRI1 and *Zm*WRI1a by 37 and 2 amino acids, respectively. *Pa*WRI3 is only 10 amino acids shorter than *At*WRI3, but 81 amino acid shorter than *Zm*WRI3/4b. *Pa*WRI2 is 30 amino acids shorter than *At*WRI2 and 16 amino acids longer than *Zm*WRI2. Interestingly, the relative position of the regions that contributed to shorter avocado WRI sequence among its paralogs varied. In the case of WRI1, both avocado and maize lacked several amino acids downstream of the second AP2 domain that are present in *At*WRI1, while for WRI2, several amino acids in both *N*-terminal and *C*-terminal regions were absent. However, for WRI3, *Pa*WRI3 and *At*WRI3 lacked several *N*- and *C*-terminal amino acids that are present in *Zm*WRI3/4b. More than 45% of the shared identity is found in the *N*-terminal AP2 domains, which is a distinct feature of the APETALA protein family. As a result, the *N*-terminal region of WRI1 orthologs in different plant species is highly conserved, whereas the *C*-terminal region that harbors the TAD is variable (Kong et al., 2019; Tang et al., 2019; Fei et al., 2020).

Among the two highly conserved *N*-terminal AP2 domains, the first domain is typically more conserved than the second (Cernac and Benning, 2004), although both were similarly, conserved across the orthologs of the three species examined in detail here. Also, while both AP2 domains are present in the WRI1, WRI3, and WRI4 orthologs, the WRI2s, including *Pa*WRI2, lacked the second AP2 domain (**Figure 1** and **Supplementary Figure 2**). Moreover, unlike *Pa*WRI2 or *Zm*WRI2, the single AP2 domain present in *At*WRI2 was interrupted by a stretch of 35 additional amino acids (**Figure 1** and **Supplementary Figure 2**). Plant AINTEGUMENTA transcription factors are able to bind DNA promoters despite having only a single AP2 domain (Krizek, 2003), but yeast-one hybrid studies have shown that *At*WRI2 was unable to bind to the promoter of the *BCCP2* gene (To et al., 2012), likely due to the interruption present in the AP2 domain. The need for an intact AP2 domain to bind DNA promoter motifs might explain the lack of

function for *At*WRI2; whether this function exists in *Zm*WRI2 remains unexplored.

The WRI AP2 domains interact with the DNA elements called the "AW-box" in target gene promoters (Cernac and Benning, 2004). While the identity of the protein residues that bind to the AW element is not yet known, based on the sequence and structural similarity to the GCC-box binding domain (GBD) of *At*ERF1 (1GCC; PDB database), 11 amino acid residues in the AP2 domain were predicted to interact with the target promoters (Okamuro et al., 1997; Allen et al., 1998). While these 11 amino acid residues are conserved among the WRI1 orthologs, *At*WRI2 showed mutation in the first three residues (R→E, G→E, & T→S) and *Pa*WRI3 had mutations in two residues (Q→K, Y→R) (**Figure 1** and **Supplementary Figure 2**). The evolution of these three residues could also contribute to the loss of function in *At*WRI2; DNA binding activity in *Pa*WRI3 is yet to be explored.

Although the larger *N*-terminal region is highly conserved overall, the sequence upstream of the AP2 domains is variable among the orthologs. Particularly, the presence of repeat regions of serine residues in *Pa*WRI1 and glycine in *Pa*WRI2 is similar to their respective orthologs in *Arabidopsis* but not in maize. The serine-rich region in the *N*-terminus is thought to have gradually evolved among vascular plants (Tang et al., 2019), which may play a role in functional regulation and subcellular localization (Casal et al., 2002; Ma et al., 2015), whereas the role of glycine repeats in *Pa*WRI2 is not known. The micro-exon encoding the "VYL" motif in the first AP2 domain is essential for *At*WRI1 function (Ma et al., 2013). This domain is present in all WRI proteins here, except for *Pa*WRI3 and *Pa*WRI4 (**Figure 1**). Previous studies showed that site-directed mutagenesis of the amino acids "VYL" in *At*WRI1 failed to complement *Atwri1-1* mutant but the WRI1 isoform in castor bean (*Rc*WRI1-B) and rice (*Os*WRI1-1) were functionally active despite lacking the motif (Ma et al., 2013; Ji et al., 2018; Mano et al., 2019). Thus, the mechanistic role of the "VYL" motif is not well-understood, and the functional importance appears to be species-dependent. High *PaWRI3* expression during oil accumulation suggests that this protein might be functional, even in the absence of the motif. Additionally, two KIN10-mediated phosphorylation target residues (T70 and S166) identified in *At*WRI1 are conserved in all the avocado paralogs, but S166 is absent in both *At*WRI2 and *Zm*WRI2 (**Supplementary Figure 3**). Phosphorylation of these two residues by KIN10 triggers WRI1 degradation as a response to elevated sugar levels in the cell (Zhai et al., 2017). This suggests a possible *Pa*WRI2-mediated, sugar-dependent regulation of avocado oil biosynthesis (that is likely aided by *Pa*WRI1 and *Pa*WRI3 as well), while such a mechanism is lost for WRI2 orthologs in at least some higher plants.

Additionally, other interesting protein structural variations were also observed. In general, the *C*-termini share very little sequence similarity. An acidic residue-rich region that overlaps with the putative TAD in *Arabidopsis* WRI1 was identified in monocots and other dicots (Ma et al., 2015; Tang et al., 2019). However, the TAD in *At*WRI1 (307-397) is not conserved in other orthologs and about twenty six amino acid deletions were identified in that region of *Pa*WRI1 (**Figure 1**). Among the three WRIs in avocado, *Pa*WRI2 has the longest *C*-terminal region (sequences downstream of AP2 domain; 272 residues, compared to 169 and 134 in *Pa*WRI1 and *Pa*WRI3, respectively) although the length variation is commonly observed in other plant species (Tang et al., 2019). Also, both *Pa*WRI3 and *At*WRI3 lack several amino acids in their *C*-terminal domains, compared to their maize ortholog with an extended *C*-terminus (**Figure 1**).

Avocado WRI Sequences Include the Signature of a Structurally Disordered Protein Fold

Amino acid composition biases are important for protein function and are prominent among eukaryotic transcription factors. Particularly, enrichment with hydrophilic or depletion of hydrophobic amino acids leads to generation of a disordered protein fold that is associated with proteostasis (Dyson and Wright, 2005; Gao and Xu, 2012). The locally present unstructured regions due to amino acid composition biases are referred to as intrinsically disordered regions (IDRs) and the proteins as intrinsically disordered proteins (IDPs; Liu et al., 2006). The disordered value of *At*WRI1 was ∼53% due to composition bias (Ma et al., 2015); similar analysis of other WRI homologs also revealed enriched polar amino acids and depleted hydrophobic amino acids (**Supplementary Figure 4**). Sequence alignment analysis has already indicated a great degree of dissimilarity in *N*- and *C*-terminal regions flanking the AP2 domains. To investigate compositional preference and to search for regions of significant enrichment, we used the SwissProt 51 database as a standard reference. The data showed that serine (S) is enriched in all the homologs, except *Zm*WRI3/4b. Hydrophobic amino acids like Ile (I), Val (V), and Leu (L) were significantly depleted in most of the WRI homologs (**Supplementary Figure 4**). For example, L and V were depleted in *Pa*WRI1 and *Pa*WRI2, respectively, while all the three residues (I, V, and L) were depleted in *Pa*WRI3. However, unlike the other orthologs, the polar amino acid Lys (K) was significantly depleted only in *Pa*WRI1 (**Supplementary Figure 4**). The tendency for enrichment of polar amino acids or depletion of hydrophobic amino acids was highest in *At*WRI1 and lowest in *Pa*WRI1, while the contrary was true for WRI3 orthologs. Among the WRI2 orthologs, however, the propensity was higher for *Zm*WRI2 followed by *Pa*WRI2 and then *At*WRI2. Overall, the degree of positive S bias and depletion of non-polar amino acids like I, V, and L suggests that WRI transcription factors in avocado have a characteristic feature of IDPs.

A disorder-promoting amino acid composition among the WRI homologs suggests that achieving secondary structure folds would be difficult. A hydrophobic core is important for nucleation of protein folding in an aqueous environment; depletion or low proportions of hydrophobic amino acids will typically lead to random coil (Eisenberg et al., 1986). Unstructured folds or random coil regions are common among eukaryotic proteins including transcription factors (Uversky and Dunker, 2010). Such features enable proteins to adopt different conformations to interact with multiple target partners

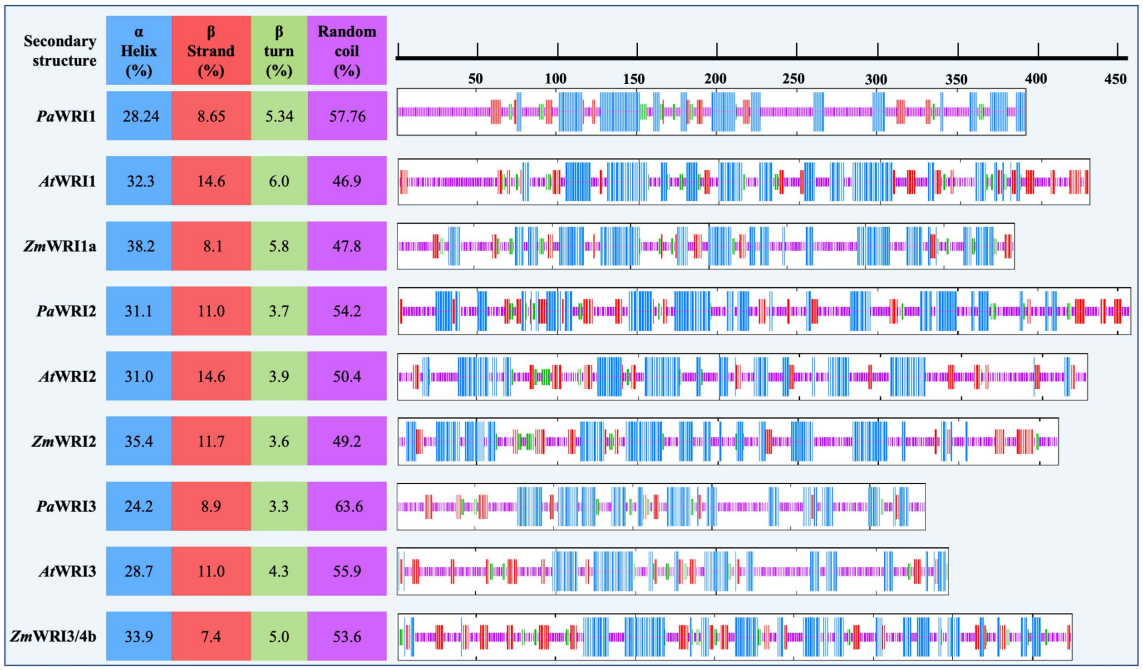

FIGURE 2 | Proportion of the predicted secondary structures in WRI homologs. Position of each of the secondary structures α helix (blue), β strand (red), β turn (green), and random coil (pink) among all the WRI1 homologs are schematically represented on the right. The color-coded regions represent the position of the corresponding secondary structures. Proportion of each of the secondary structures is represented as a percentage value on the left, for each homolog.

and other coregulatory proteins (Khan and Kumar, 2009). The composition analyses of WRI homologs were used to predict the degree of secondary structure (α-helix, β-sheet, β-turn, and random coil) for each protein. In all the homologs, random coil structure was the highest in proportion, followed by α-helix, β-strand, and β-turn (**Figure 2**). All the avocado WRI paralogs have > 50% random coil region, which is greater than in their respective orthologs in *Arabidopsis* and maize. The random coil regions are mostly present in the *N*- and *C*-terminal regions, while the AP2 domain regions contain abundant α- helix and β-sheet content and a low proportion of random coils (**Figure 2**). The crystal structure of the GCC-box binding domain (similar to AP2 domain) of EREBP protein also has the same feature, where the β-sheets were particularly responsible for DNA binding (Allen et al., 1998). Although the 3D structure of the AP2 domains is yet to be resolved, based on the sequence homology, it is expected that their promoter binding ability is also achieved in a similar manner. Additionally, extensive random coil structure flanking the WRI AP2 domains can also contribute to effective binding to different promoters. Such functionality is evident from the demonstrated ability of *At*WRI1 to bind to the promoter regions of various fatty acid synthesis genes (Baud and Lepiniec, 2009; Maeo et al., 2009). Overall, it can be inferred that a high proportion of random coil structure associated with WRI homologs, including those from avocado, contributes to high conformational flexibility to interact with their target genes resulting in a complex network of WRI-mediated regulation of oil biosynthesis. These findings support the possibility that *Pa*WRI1, *Pa*WRI2, and *Pa*WRI3 have retained relatively more flexible and dynamic structures that allow for greater conformational promiscuity to interact with numerous target proteins.

Avocado WRI2 Lacks the *C*-Terminal IDR3 Region

Intrinsically disordered regions in the protein structure can prevent the formation of a hydrophobic core and result in improper folding (Uversky et al., 2000; Romero et al., 2001). In all three WRI homologs, in addition to the local random coil structures, amino acid bias also contributed to IDRs. The propensity for disorderliness was about two-fold higher among WRI homologs analyzed, compared to the mean value of 23% observed in the general *Arabidopsis* proteome (Oldfield et al., 2005). The overall disorder percentage among WRI1 orthologs was as follows: *Zm*WRI1a > *At*WRI1 > *Pa*WRI1, whereas for WRI2 orthologs, *Pa*WRI2 > *Zm*WRI2 > *At*WRI2 and for WRI3, *Zm*WRI3/4b > *Pa*WRI3 > *At*WRI3 (**Table 1**). While a higher percentage of disorderliness promotes flexibility and protein interaction, accessibility to proteases and the likelihood of protein degradation also increases. So, the relatively higher disordered values associated with both *Pa*WRI2 and *Pa*WRI3 and lower values with *Pa*WRI1 might reflect a complex homeostasis, in which one protein could compensate for the degradation of the other to achieve sustained fatty acid biosynthesis during the prolonged period of TAG accumulation in avocado mesocarp.

TABLE 1 | Details of the disorder value and the position of various intrinsically disordered regions (IDRs) and PEST motifs in WRI homologs.

Proteins	% Disorder	IDR1	IDRIa	IDR2	IDR3	PEST motifs
PaWRIl	51.4	1-67	*	226-273	314-375	1-35,228-247
AtWRIl	52.5	1-71	*	249-313	368-430	3.34, 396-430
ZmWRIla	56.7	1-67	135-175	238-313	356-395	6-32,232-273,273-319
PaWRI2	54.2	1-85	171-201	266-381	*	*
AtWRI2	45.4	1-57	*	278-377	426-458	*
ZmWRI2	48.0	1-74	*	247-319	362-412	*
PaWRB	55.8	1-53	115-147	215-315	*	206-242, 277-295
AtWRB	52.7	1-70	137-168	236-314	*	*
ZmWRB/4b	57.9	1-63	131-164	246-362	*	302-344

**Indicates the absence of the corresponding IDR or PEST motif.*

The percentage disorder observed was reflected in the number of IDRs identified in each homolog. The protein sequences of *Pa*WRI1, *At*WRI1, and *Zm*WRI1 were predicted to contain three, three and four IDRs, respectively; all WRI2 and WRI3 proteins showed the presence of three IDRs (**Figure 3**). For further comparisons, the identified IDRs were named based on their position, similar to previously identified IDRs in *At*WRI1, i.e., IDR1, IDR2, and IDR3. While IDR1 and IDR2 were unanimously predicted in all homologs, avocado WRI2 and WRI3 paralogs lacked the IDR3 in their *C*-terminal region. An additional short IDR (30-40 aa), which we referred to as IDR1a, was predicted in the linker region connecting the two AP2 domains (*Zm*WRI1a and all the three WRI3) and following the single AP2 domain in *Pa*WRI2 proteins (**Figure 3**). Interestingly, the size of the IDRs was quite variable among the homologs (**Table 1**). Long IDRs (>30 aa) are common, comprising ∼33% of the eukaryotic proteome and affect transcription and translational activity, post-translational modifications, transportation and signal transduction activity, and also stability and degradation (Ward et al., 2004; Dyson and Wright, 2005; Van Der Lee et al., 2014). Shorter IDRs in the linker regions typically offer conformation flexibility that is needed for DNA-binding proteins (Tompa, 2005; Van Der Lee et al., 2014; Davey, 2019). The shorter IDR1a in the linker regions of some WRI orthologs, as well as the other longer IDRs around the AP2 domains are likely to provide conformational flexibility for an effective interaction with the target promoters while IDRs in the C-terminus might be associated with protein stability.

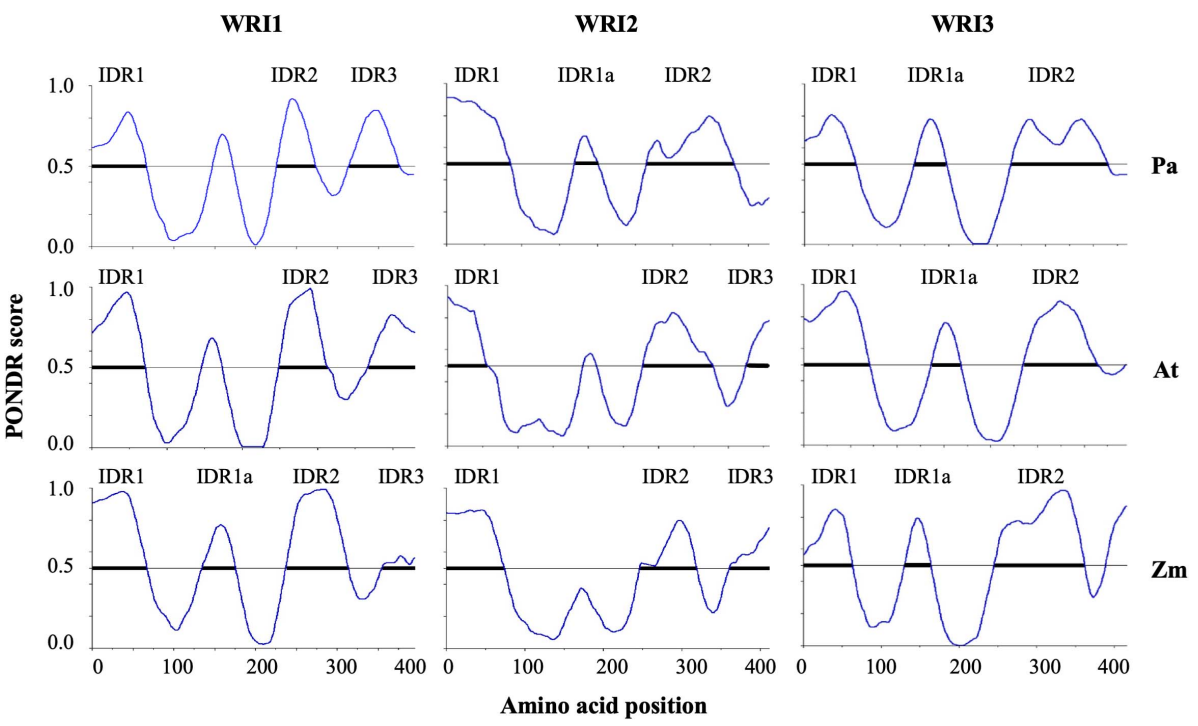

FIGURE 3 | Graphical representation of the predicted IDRs in the WRI homologs. The predicted IDRs in all the WRI homologs are graphically plotted with the amino acid position on the *x*-axis and the PONDR score on the *y*-axis. Regions showing PONDR score > 0.5 are considered as IDRs.

Disordered *N*- and *C*-terminal regions are common in DNA-binding proteins; *C*-terminal IDR is especially prevalent in transcription factors (Van Der Lee et al., 2014). Previously characterized *At*WRI1 IDR3 was shown to have a functional role in transactivation, although a three-fold increase in expression upon the truncation of IRD3 suggested that its presence likely also serves as a target for protein degradation pathways (Ma et al., 2015). IDR3 is absent in *Pa*WRI2 although the other analyzed WRI2 orthologs have an IDR in their *C*-terminus (**Figure 3** and **Supplementary Figure 5**). However, the *Pa*WRI2 contains relatively long IDR1 and IDR2 (85 and 116 residues) compared to the respective orthologs in *Arabidopsis* and maize (57 aa and 100 aa, and 74 and 73 aa, respectively). These IDRs likely provide the necessary degree of transactivation capacity, while such function was lost in *At*WRI2. The functional role of *Zm*WRI2 remains to be examined. Similarly, IDR3 is absent in yellow nutsedge (*Cyperus esculentus*) WRI1 (*Ce*WRI1), although it retained its functional role in oil biosynthesis (Grimberg et al., 2015) and showed autoregulatory effect on the *AtWRI1* promoter (Snell et al., 2019). Hence, it is possible that *Pa*WRI2 is still able to activate the target genes in a similar manner to the transactivation mechanism shown by *Ce*WRI1. On the other hand, long IDRs are also preferential targets for post-translational modification and protein binding that protect it from proteolytic cleavage (Dyson and Wright, 2005). The stability of *At*WRI1 is enhanced upon interaction with either BTB/POZMATH1 (BPM1) or 14-3-3 proteins (Chen et al., 2013; Ma et al., 2016), although the complete interaction network is currently unknown. Hence, it is possible that the difference in functionality between *Pa*WRI2 and *At*WRI2 could be the result of distinct post-translational modifications and/or protein interactions.

The *C*-Terminal Region of Avocado WRI2 Lacks a PEST Motif

Among the WRI homologs examined, the *C*-terminal region downstream of the AP2 domain is highly variable (**Figure 1**). Nevertheless, this region does harbor some conserved features, without any particular trend in amino acid properties that are likely responsible for the regulation of the protein. Specifically, a region of the protein sequence that is enriched in proline (P), glutamic acid (E), serine (S), and threonine (T), referred to as PEST motifs occur among WRI homologs and were mostly associated with the IDRs (Ma et al., 2015). These PEST motifs are typically involved in proteasome-mediated protein turnover (García-Alai et al., 2006; Belizario et al., 2008). They are abundant among many key metabolic enzymes, transcription factors, protein kinases, and phosphatases in the cell, and function as a tool to maintain cellular homeostasis (Rechsteiner and Rogers, 1996). PEST-containing proteins make up a prevalent portion (∼25%) of the eukaryotic proteome and are enriched with disorder-promoting amino acids. The PEST motif associated with IDRs promotes proteolysis through ubiquitin-proteasome degradation or calpain cleavage (Gregory and Hann, 2000; Bordone and Campbell, 2002; Singh et al., 2006).

While all three WRI1 orthologs contained one PEST motif in their *N*-termini, *At*WRI1 and *Pa*WRI1 had one each, and *Zm*WRI1a had two, PEST motifs predicted in their respective *C*-terminal IDRs (**Figure 4** and **Table 1**). However, the PEST motif in the *C*-terminal region of *Pa*WRI1 has no potential phosphorylation site (**Figure 4**), and thus is an unlikely protease target. Interestingly, all WRI2 orthologs (including *Pa*WRI2) and *At*WRI3 lacked PEST motifs. Maize and avocado WRI3 orthologs, although lacking *N*-terminal PEST motifs, contained one and two each, respectively, embedded in their *C*-terminal IDRs (**Figure 4** and **Table 1**). The association of PEST motifs with the IDR increases surface accessibility and favors it as a target for degradation signal attachment and phosphorylation (Singh et al., 2006). Additionally, while both *N*- and *C*-terminal PEST motifs are involved in proteolysis, a preference for *C*-terminal PEST motifs is noted in several proteins (Rechsteiner and Rogers, 1996; Singh et al., 2006). Among the WRI homologs, most PEST motifs were associated with the *C*-terminus and likely play a role in transcription factor stability control.

The PEST motif associated with *At*WRI1 IDR3 participates in phosphorylation-dependent protein degradation but was not critical for transactivation (Ma et al., 2015). Furthermore, transient expression of truncated *At*WRI1 (1-397) in *N. benthamiana* leaves increased oil accumulation suggesting that the PEST motif plays a role in protein accumulation without affecting basic function (Ma et al., 2015). Hence, the absence of a *C*-terminal IDR-associated PEST motif in *Pa*WRI2 might contribute to its increased stability and sustained activity, possibly contributing to high oil accumulation in avocado mesocarp. Although *PaWRI3* transcript levels were high in avocado mesocarp during the period of oil accumulation, any effects of PEST motifs on transcript accumulation are currently unknown (Kilaru et al., 2015). The role of *N*-terminal PEST motifs in WRI homologs also has not been studied but is predicted to maintain homeostasis and protein interaction. Overall, our analyses suggest that lack of a PEST motif in the *C*-terminal region of *Pa*WRI2, versus its presence in this region of *Pa*WRI1 and *Pa*WRI3, contributes to the mediation of the complex regulatory mechanism of homeostasis in avocado mesocarp tissue.

Both *Pa*WRI1 and *Pa*WRI2 Contain Phosphorylation Sites in the *C*-Terminal Region

Phosphorylation is among the major categories of post-translational modifications that control protein function. Phosphosites present in the long disordered regions in IDPs are preferentially phosphorylated by cellular kinases (Koike et al., 2020). To investigate the possible targets in our WRI protein set, we evaluated each of the putative residues Ser (S), Thr (T), and Tyr (Y) for phosphorylation modification potential using NetPhos 3.1 (Blom et al., 1999). The extensive S residues were most often identified as kinase target sites, followed by T and Y. Most of the identified phosphorylation sites overlapped with the predicted PEST motifs (**Figure 5**). Previous analysis of *At*WRI1 identified four S residues in the IDR3-PEST

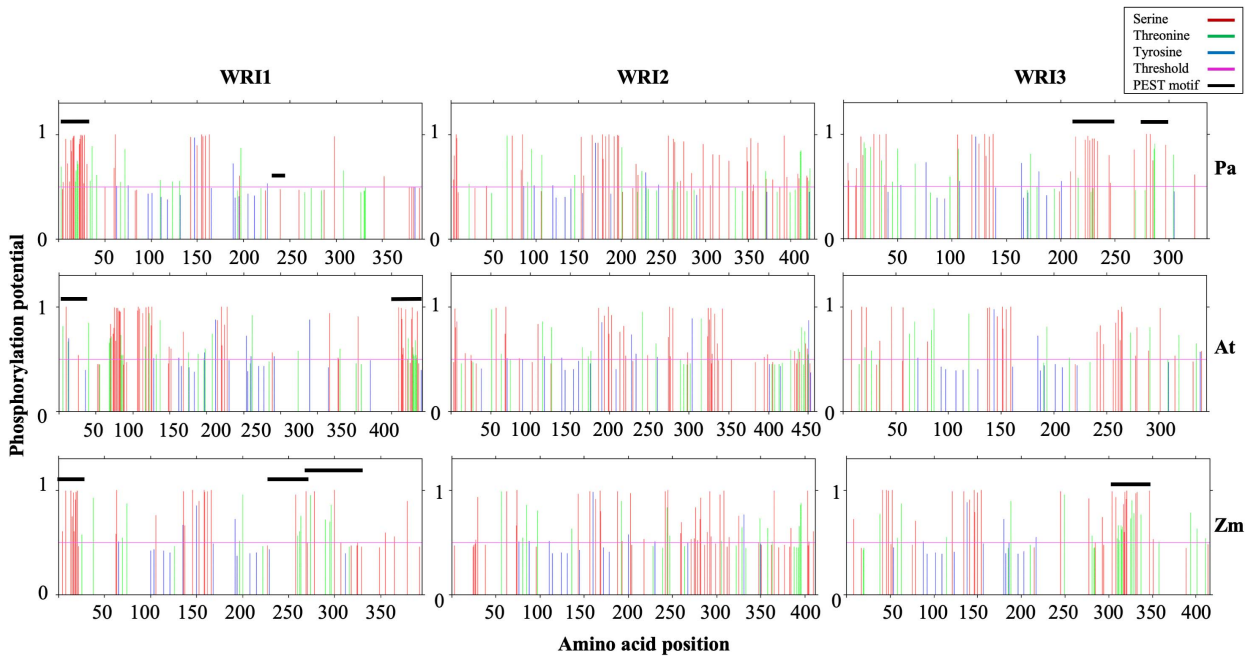

FIGURE 4 | Schematic presentation of potential phosphorylation sites in the WRI homologs. Predicted phosphorylation potential for S (Red), T (green), and Y (blue) residue and their amino acid position are shown in the plots. The residues with potential higher than threshold value of 0.5 have higher probability of being phosphorylated. Residues that correspond to PEST motifs are also indicated by a black line.

motif as potential phosphorylation targets, and mutation of all these residues to Ala (A) (*At*WRI1^{4SA}) resulted in increased stability and increased TAG accumulation in transiently expressed *N. benthamiana* leaves (Ma et al., 2015). Possibly, the Ser (S) residues are important and/or sufficient for the PEST motif recognition and phosphorylation by target enzymes to upregulate protein degradation. Since both *Pa*WRI1 and *Pa*WRI2 lack PEST motifs in their *C*-terminal ends, those regions did not show an enrichment of phosphorylation sites (**Figure 4**); these patterns thus differ significantly from those of *At*WRI1 and *At*WRI2. However, *Pa*WRI2 was enriched with potential phosphorylation sites after amino acid position 350, which were absent in *At*WRI2. Also, the region between the two AP2 domains in WRI1 and WRI3 orthologs and the region downstream of the AP2 domain in WRI2 orthologs were enriched with phosphorylation targets. Additionally, two KIN10-mediated phosphorylation target residues (T70 and S166, present in the first and second AP2 domains of *At*WRI1) were also conserved in all WRI homologs except *At*WRI2 and *Zm*WRI2 (Zhai et al., 2017). Although a large fraction of the identified phosphorylation sites remains unexplored, the high proportion of random coil structure and abundant IDR regions associated with each of the WRI proteins, including the avocado homologs, likely favor cellular protein kinase access, resulting in structural and/or functional modulation. Hence, phosphorylation, whether associated with residues in PEST domains or elsewhere, is also likely to play an important role in maintaining homeostasis of WRI paralogs in avocado mesocarp.

Distinct Features of *Pa*WRI2 Are Likely Associated With Its Function

Previous studies reported the differentiation of avocado WRI2 from the other gene family members, likely due to an ancient gene duplication event. The loss of function in WRI2 from more recently evolved plant families such as *Arabidopsis*, suggests loss of selective pressure and enzyme function during evolution (Kilaru et al., 2015). We identified characteristic features of avocado WRI2 that might explain the retention of its functional role, through *in silico* analyses. All the WRI2 orthologs share only one AP2 domain, suggesting that it is functionally very important. Previous studies (Ma et al., 2013) suggested that the presence of a micro-exon, encoding the three residues "VYL," is present in WRI1 orthologs from diverse plant species and is highly correlated with WRI protein functionality. *PaWRI2* retains this exon, while *AtWRI2* does not (**Figure 1**), suggesting that this element contributes to *Pa*WRI2 protein function. Another unique difference between *At*WRI2 and *Pa*WRI2 is the absence of IDR3 but presence of IDR1a in *Pa*WRI2 (**Figure 3**). Previous studies have reported that post-translational modifications in the *C*-terminal IDRs affect the stability of WRI1 proteins, for example, phosphorylation of the IDR3 PEST motif in *At*WRI1 enhances protein degradation (Ma et al., 2015). As such, IDR3 in *At*WRI2 might negatively affect its conformational flexibility and hence contribute to its loss of function. Conversely, in *Pa*WRI2, the presence of IDR1a adjacent to the single AP2 domain (**Figure 3**) might contribute to productive interaction with target promoters. Furthermore, retention of function in *Pa*WRI2

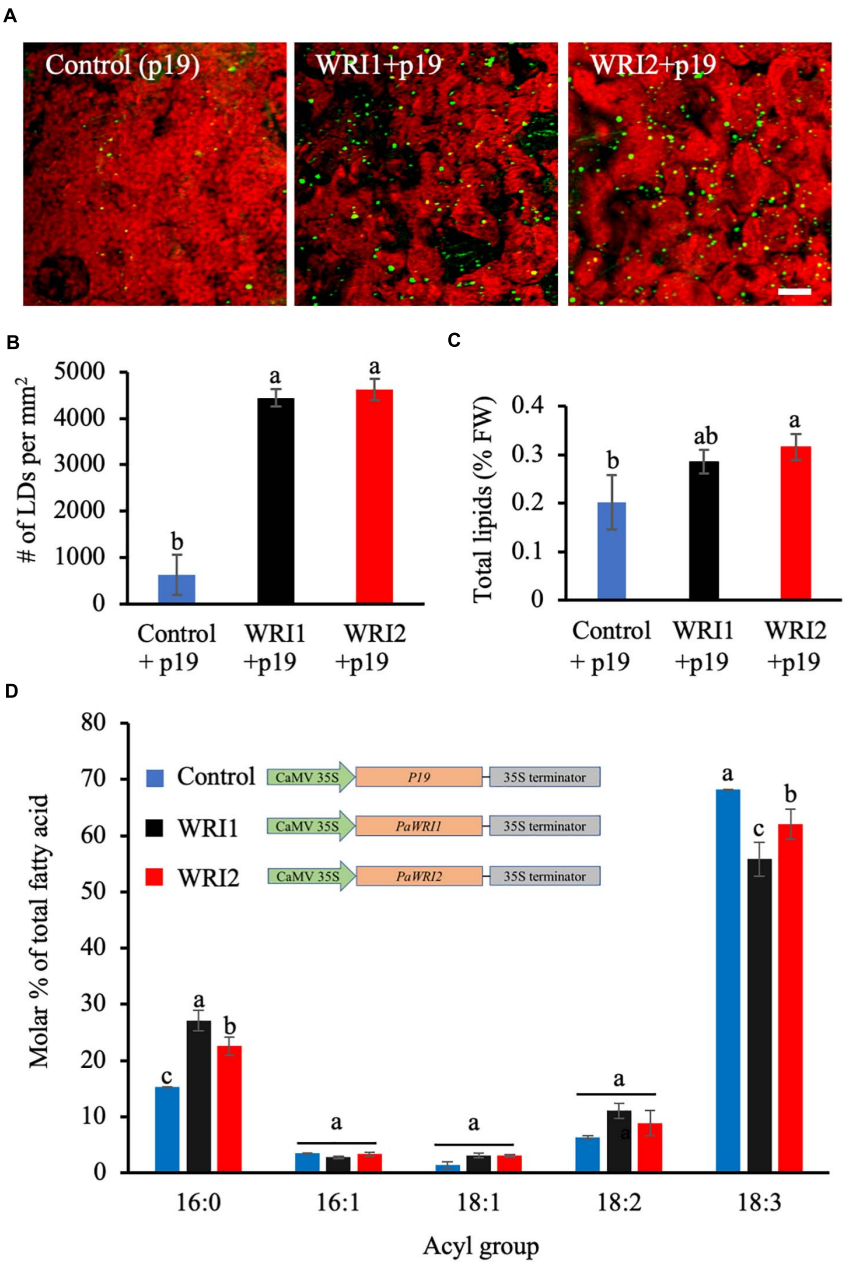

FIGURE 5 | Lipid content and fatty acid composition of *N. benthamiana* leaves expressing *PaWRI1* and *PaWRI2*. **(A)** Confocal images of accumulated lipid droplets (LDs) stained with Nile Red (green) in *N. benthamiana* leaves infected with *Agrobacterium* expressing control (*p19* alone), *PaWRI1* (+*p19*), and *PaWRI2* (+*p19*) constructs. Scale bar corresponds to 20 μm. **(B)** Quantification of accumulated LDs per unit surface area of the leaf tissue. **(C)** Quantification of total lipid (TL) content. **(D)** fatty acid profile of total lipids extracted from the infiltrated leaves. Data represent mean ± sd ($n = 3$; $p < 0.05$).

might be attained due to the presence of only one *C*-terminal IDR that does not contain PEST motifs (**Figure 3** and **Table 1**), likely reducing the number of phosphorylation targets (**Figure 4**) and positively contributing to PaWRI2 protein stability.

These *in silico* analyses suggested many intriguing features that differentiate *Pa*WRI2 from *At*WRI2. Therefore, to confirm functionality *in vivo*, we performed transient expression assays in *N. benthamiana* leaves.

Unlike *AtWRI2*, the Expression of *PaWRI2* Is Associated With Lipid Accumulation

Phylogenetic analyses of *WRI1* homologs indicate that *WRI2* has independently diverged from the remaining three orthologs, while *WRI3* and *WRI4* arose from a gene duplication event with *WRI1* and evolved independently (**Supplementary Figure 1**; Kilaru et al., 2015). Among the four *WRI1* orthologs in

Arabidopsis, both *AtWRI3* and *AtWRI4*, but not *AtWRI2*, shared functional similarity with *AtWRI1* and were able to complement the *wri1* mutant and restore seed oil biosynthesis to near-wild type levels (To et al., 2012). However, the uniquely high expression levels of *PaWRI2* in avocado mesocarp during oil accumulation and distinct evolutionary separation from the remaining orthologs was intriguing (Kilaru et al., 2015). As such, to compare the functional role of *PaWRI2* to that of *PaWRI1* in oil accumulation, both genes were transiently expressed in *N. benthamiana* leaves. After seven days of co-infiltration of *Agrobacterium* expressing *PaWRI1* or *PaWRI2* and *P19*, a silencing−suppressor protein that enhances transgene expression (Naim et al., 2016), the leaves were harvested and analyzed for lipid accumulation. Interestingly, transient expression of both *PaWRI1* and *PaWRI2* resulted in a 7-fold increase in the number of LDs in *N. benthamiana* leaves (**Figures 5A,B**).

We further examined if these transcription factors affected fatty acid biosynthesis and thus lipid content in the leaf. Co-expression of *PaWRI2*/*P19* generated a 1.5-fold increase in the total lipid content, relative to leaves expressing *P19* alone (**Figure 5C**). The *PaWRI2*-mediated increase in lipid content, which was about 44% was greater than the 17-41% oil enhancement shown by the three transiently expressed isoforms of camelina *CsWRI1* in *N. benthamiana* leaves (An et al., 2017). Typically, *N. benthamiana* leaves contain about 0.2 to 0.3% lipids by FW of which only 20-30% is TAG. Ectopic expression studies using WRI1 orthologs have reported increase in total lipids of which 80-90% was TAG (An et al., 2017). *PaWRI1* expression resulted in higher LD numbers but only a smaller and statistically insignificant increase in total lipid content (**Figure 5C**).

Analysis of leaf total lipid fatty acid profile from samples expressing *PaWRI1* or *PaWRI2* further revealed a significant increase in 16:0 and decrease in 18:3 content, relative to the wild type leaves (**Figure 5D**). Although the role of WRI1 in oil accumulation has been unequivocally established, its ability to regulate fatty acid composition is not clear and is presumed to depend on the species, tissue type and its origin. For example, when camelina *CsWRI1* was expressed in *N. benthamiana* leaves, the content of both 18:1 and 18:2 increased and 18:3 decreased, while in transgenic seeds of stably transformed *Arabidopsis wri1* mutant plants, 18:3 content was highest and 18:1 remained low (An et al., 2017). Also, transient expression of *WRI1* homologs from potato, poplar, nutsedge, oat, and *Arabidopsis* showed reduced 18:0 and higher proportions of 18:1, relative to the control leaves (Grimberg et al., 2015). Interestingly, although avocado mesocarp lipids are highly enriched in monounsaturated fatty acid (oleic acid, 18:1) (Kikuta and Erickson, 1968; Kilaru et al., 2015), transient expression of neither *PaWRI* nor *PaWRI2* affected the oleic acid content in *N. benthamiana* leaves. Nevertheless, leaves expressing either *PaWRI* or *PaWRI2* showed a ∼1.4 − 1.7-fold increase in 16:0 and a ∼0.8 − 0.9-fold decrease in 18:3 levels. With ∼20% reduction in 18:3, this effect was higher with *PaWRI1* expression than with *PaWRI2*, where the decrease accounted for ∼10% (**Figure 5D**). Previous studies showed that transient expression of *WRI1* homologs in *N. benthamiana* leaves led to downregulation of the transcripts encoding plastidial fatty acid desaturase 7 (FAD7) that is responsible for the desaturation of 18:2 to 18:3, and long chain acyl-CoA synthetase 1 and 2 (LACS 1, 2), which catalyze the synthesis of long chain acyl-CoA that serves as a substrate for TAG assembly (Lu et al., 2009; Zhang et al., 2012; Grimberg et al., 2015). Whether *PaWRI1* and *PaWRI2* transient expression caused increased 16:0 and decreased 18:3 content due to changes in *FAD7*, *LACS1* and/or *LACS2* expression remains to be examined. Together, the transient expression studies implicate that both *PaWRI1* and *PaWRI2* are functional and able to induce lipid accumulation in non-seed tissues and also affect fatty acid composition (**Figures 5B,C**). *PaWRI2* enhanced lipid content and altered fatty acid composition more effectively than *PaWRI1*. These properties of *Pa*WRI2 are functionally unique and contrast sharply to that of *At*WRI2, which lacked any significant role in fatty acid biosynthesis (To et al., 2012). Considering the evolutionary position of avocado as a basal angiosperm, it is possible that *Pa*WRI2 is structurally unique and evolved as an early regulator of fatty acid biosynthesis, while such ability was lost in *At*WRI2 but retained by its paralogs.

CONCLUSION

Avocado mesocarp is one of the most oleate-rich sources of oil in the plant kingdom. Detailed molecular knowledge of the regulatory machinery responsible for such sustained fatty acid biosynthetic and TAG assembly activity during the long fruit development period remains unresolved for non-seed tissues. Additionally, while the role for WRI1 as a master regulator of oil biosynthesis in oil-rich seed tissues in several species is well established, its significance in non-seed tissues remains unclear. Although the three WRI2 orthologs analyzed in this study contained only one AP2 domain, reflecting an ancestral feature, an interruption in the domain by a 35 amino acid stretch in *At*WRI2 was likely sufficient for loss of its function (**Figure 1**). Additionally, mutation in three amino acid residues in the AP2 domain of *At*WRI2 that are important for DNA binding might have also affected its function (**Figure 1**). In contrast, structurally unique characteristics of *Pa*WRI2, compared to its orthologs and paralogs, clarify its efficiency and functional novelty, despite containing only a single AP2 domain. *Pa*WRI2 lacked IDR3 (**Figure 4** and **Table 1**) and the *C*-terminal PEST motif (**Figure 4**), which is expected to increase protein stability and sustained activity. Additionally, while disorder-promoting amino acid composition bias resulting in random coil secondary structure was inherent in all the orthologs (**Supplementary Figure 4**), *Pa*WRI2 displayed the highest disorder (**Figure 2**), suggesting maximum flexibility in interacting with target genes. Additionally, some conserved structural features such as the "VYL" micro exon and the KIN10 target residues (T70 and S166 identified in *At*WRI1) suggest that *Pa*WRI2 is involved in the maintenance of sugar-dependent lipid homeostasis in avocado mesocarp. Also, distinct phosphorylation targets that were predicted in the *C*-terminal region (**Figure 4**) might play

a role in post-translational modifications, which can affect protein half-life, subcellular function, protein-protein interaction and homeostasis. Based on the previous RNA-seq analyses, it was clear that *Pa*WRI1, 2 and 3 are highly expressed during the extended period of oil accumulation. In our study, we show that *Pa*WRI2, unlike its ortholog *At*WRI2, was functional and induced oil accumulation in and altered the fatty acid profile of transiently infected leaf tissue more effectively than *Pa*WRI1 (**Figure 5**). Although the WRI2 orthologs formed a monophyletic clade as a result of independent divergence from their other paralogs, loss of function events among some orthologs were likely random. Bioinformatic analyses support the idea that all three mesocarp-expressed WRI paralogs, including *Pa*WRI2, are functional and likely contribute to coordinated and sustained oil biosynthesis. Further studies are pertinent to establish more details of the underlying regulatory network in oil biosynthesis in non-seed tissues in plants.

DATA AVAILABILITY STATEMENT

The original contributions presented in the study are available publicly at NCBI (https://www.ncbi.nlm.nih.gov/): *PaWRI* (MZ322905), *PaWRI2* (MZ322906), *PaWRI3* (MZ322907). The protein sequences used for data analyses are available publicly at NCBI (https://www.ncbi.nlm.nih.gov/): *At*WRI1 (NP_001030857.1), *At*WRI2 (NP_001189729.1), *At*WRI3 (NP_563990.1), *At*WRI4 (NP_178088.2), *Zm*WRI1a (NP_001137064.1), *Zm*WRI2 (NP_001145827.1), *Zm*WRI3/4b (XP_008651355.1), *Atr*WRI1 (XP_011620741.1), *Atr*WRI2 (XP_020526667.1), *Atr*WRI3 (XP_006845421.1), *Vv*WRI1 (XP_010659009.1), *Vv*WRI2 (XP_002284093.1), *Vv*WRI3 (XP_010652396.1), *Rc*WRI1 (NP_001310691.1), *Rc*WRI2 (XP_015581065.1), *Rc*WRI3 (NP_001310645.1), *Rc*WRI4 (XP_015573687.1), *Os*WRI1 (BAD68218.1), *Os*WRI2 (XP_015638088.1), *Os*WRI3 (XP_015617951.1), *Os*WRI4 (XP_015619972.1), *Br*WRI1 (XP_009116120.1), *Br*WRI2 (XP_009133508.1), *Br*WRI3 (XP_009149048.1), *Br*WRI4 (XP_009106692.1), *Eg*WRI1 (AHX71676.1), *Eg*WRI2 (XP_010938537.1), *Eg*WRI3 (XP_010912920.2), *Eg*WRI4 (XP_010914036.1), *Pt*WRI1 (XP_024465221.1), *Pt*WRI2 (XP_024458881.1), *Pt*WRI3 (XP_002297679.2), and *Pt*WRI4 (XP_024467077.1).

AUTHOR CONTRIBUTIONS

JB and SB conducted the bioinformatic analyses. SB and MR performed the cloning. MR conducted the transient expression assays. JB and MR performed the statistical analysis. JB, JS, and AK wrote the manuscript with assistance from MR and SB. All authors read and approved the final manuscript and contributed to the research design and data analyses.

FUNDING

This research was supported in part by minor and major grants from research and development committee, East Tennessee State University (ETSU) awarded to AK. Additionally, JB, MR, and SB received funds from School of Graduate Studies, ETSU. SB and MR received Sigma Xi GIAR Award. SB also received Fraley's Memorial Research Award from the Department of Biological Sciences, ETSU.

SUPPLEMENTARY MATERIAL

The Supplementary Material for this article can be found online at: https://www.frontiersin.org/articles/10.3389/fpls.2021.648494/full#supplementary-material

Supplementary Figure 1 | Phylogenetic analysis and percentage identity among WRI1 homologs**. (A)** Phylogenetic analysis of WRI1 homologs in *Arabidopsis thaliana (At)*, *Zea mays (Zm)*, *Amborella trichopoda (Atr)*, *Populus trichocarpa (Pt)*, *Ricinus communis (Rc)*, *Brassica rapa (Br)*, *Elaeis guineensis (Eg)*, *Vitis vinifera (Vv)*, *Oryza sativa (Os)* and *Persea americana (Pa)* was carried out using UPGMA method (see **Supplementary Table 1**). An AP2-domain transcription factor from *Chlamydomonas reinhardtii* (*Cr*AP2) was used as outgroup. Percentages indicate bootstrap values for 1000 replicates. The WRI-orthologs are shown in color; WRI1 (black), WRI2 (pink), WRI3 (orange), WRI4 (blue). **(B)** Percentage of amino acid sequence identity among the WRI1 homologs from avocado (*Pa*), Arabidopsis (*At*), and maize (*Zm*).

Supplementary Figure 2 | Sequence alignment of WRI1, WRI2, and WRI3 from various species showing conserved amino acids. Multiple sequence alignment of primary sequences of WRI1, 2, and 3 from species as described in **Supplementary Figure 1** are shown in a color-coded format; red and blue colors represent the most (10, indicated by asterisk) and least (0) conserved regions, respectively on a scale of 0 to 10. Positions of the AP2 domains are shown as pink color bars under the sequences and the amino acid residues in the AP2 domain important for DNA interaction are represented by (▲).

Supplementary Figure 3 | Multiple sequence alignment of WRI1 homologs from the select three species. The alignment shows KIN10 target sites (red box) in the WRI1 homologs with reference to T70 and S166 identified in *At*WRI1. The S166 residue is mutated in *At*WRI2 and *Zm*WRI2. The highlighted amino acid residues correspond to the PEST motifs.

Supplementary Figure 4 | Amino acid composition profile of WRI1 homologs. Amino acid composition profile of WRI1 homologs showing the enriched and depleted amino acids as compared to SwissProt51 database. The amino acids are arranged in the increasing order of hydrophobic character on the *x*-axis and the *y*-axis represents the composition profile. The values >0 represents an enrichment and <0 represents a depletion of corresponding amino acids in the protein sequence. The significantly ($p < 0.05$) enriched (green) and depleted (blue) residues are denoted in color.

Supplementary Figure 5 | Graphical representation of the predicted IDRs. The predicted IDRs in all the WRI homologs are graphically plotted with the amino acid position on the *x*-axis and the PONDR score on the *y*-axis. Regions showing PONDR score > 0.5 are considered as IDRs. For *Atr*WRI1 and *Atr*WRI2, although the figures are not showing the PONDR score, the predicted IDRs by the same software are as follows: 30-53, 137-160, 234-348 for WRI1 and 12-84, 168-190 for WRI2. Both of them have the *C*-terminal IDR.

Supplementary Table 1 | List of online tools used for various predictive structural analysis of WRI1 orthologs.

REFERENCES

Allen, M. D., Yamasaki, K., Ohme-takagi, M., Tateno, M., and Suzuki, M. (1998). A novel mode of DNA recognition by a β -sheet revealed by the solution structure of the GCC-box binding domain in complex with DNA. *EMBO J.* 17, 5484–5496. doi: 10.1093/emboj/17.18.5484

An, D., Kim, H., Ju, S., Go, Y. S., Kim, H. U., and Suh, M. C. (2017). Expression of camelina WRINKLED1 isoforms rescue the seed phenotype of the arabidopsis wri1 mutant and increase the triacylglycerol content in Tobacco leaves. *Front. Plant Sci.* 8, 1–13. doi: 10.3389/fpls.2017.00034

Baud, S., and Lepiniec, L. (2009). Regulation of de novo fatty acid synthesis in maturing oilseeds of Arabidopsis. *Plant Physiol. Biochem.* 47, 448–455. doi: 10.1016/j.plaphy.2008.12.006

Baud, S., Mendoza, M. S., To, A., Harscoët, E., Lepiniec, L., and Dubreucq, B. (2007). WRINKLED1 specifies the regulatory action of LEAFY COTYLEDON2 towards fatty acid metabolism during seed maturation in Arabidopsis. *Plant J.* 50, 825–838. doi: 10.1111/j.1365-313X.2007.03092.x

Baud, S., Wuillème, S., To, A., Rochat, C., and Lepiniec, L. (2009). Role of WRINKLED1 in the transcriptional regulation of glycolytic and fatty acid biosynthetic genes in Arabidopsis. *Plant J.* 60, 933–947. doi: 10.1111/j.1365-313X.2009.04011.x

Belizario, J., Alves, J., Garay-Malpartida, M., and Occhiucci, J. (2008). Coupling Caspase Cleavage and Proteasomal Degradation of Proteins Carrying PEST Motif. *Curr. Protein Pept. Sci.* 9, 210–220. doi: 10.2174/138920308784534023

Blom, N., Gammeltoft, S., and Brunak, S. (1999). Sequence and structure-based prediction of eukaryotic protein phosphorylation sites. *J. Mol. Biol.* 294, 1351–1362. doi: 10.1006/jmbi.1999.3310

Bordone, L., and Campbell, C. (2002). DNA ligase III is degraded by calpain during cell death induced by DNA-damaging agents. *J. Biol. Chem.* 277, 26673–26680. doi: 10.1074/jbc.M112037200

Bourgis, F., Kilaru, A., Cao, X., Ngando-Ebongue, G. F., Drira, N., Ohlrogge, J. B., et al. (2011). Comparative transcriptome and metabolite analysis of oil palm and date palm mesocarp that differ dramatically in carbon partitioning (Proceedings of the National Academy of Sciences of the United States of America (2011) 108, 30 (12527-12532) DOI. *Proc. Natl. Acad. Sci. U. S. A.* 108:18186. doi: 10.1073/pnas.1115243108

Casal, J. J., Davis, S. J., Kirchenbauer, D., Viczian, A., Yanovsky, M. J., Clough, R. C., et al. (2002). The serine-rich N-terminal domain of oat phytochrome a helps regulate light responses and subnuclear localization of the photoreceptor. *Plant Physiol.* 129, 1127–1137. doi: 10.1104/pp.010977

Cernac, A., and Benning, C. (2004). WRINKLED1 encodes an AP2/EREB domain protein involved in the control of storage compound biosynthesis in Arabidopsis. *Plant J.* 40, 575–585. doi: 10.1111/j.1365-313X.2004.02235.x

Chanderbali, A. S., Albert, V. A., Ashworth, V. E. T. M., Clegg, M. T., Litz, R. E., Soltis, D. E., et al. (2008). Persea americana (avocado): Bringing ancient flowers to fruit in the genomics era. *BioEssays* 30, 386–396. doi: 10.1002/bies.20721

Chen, L., Lee, J. H., Weber, H., Tohge, T., Witt, S., Roje, S., et al. (2013). Arabidopsis BPM proteins function as substrate adaptors to a CULLIN3-based E3 ligase to affect fatty acid metabolism in plants. *Plant Cell* 25, 2253–2264. doi: 10.1105/tpc.112.107292

Combet, C., Blanchet, C., Geourjon, C., and Deléage, G. (2000). NPS@: Network protein sequence analysis. *Trends Biochem. Sci.* 25, 147–150. doi: 10.1016/S0968-0004(99)01540-6

Davey, N. E. (2019). The functional importance of structure in unstructured protein regions. *Curr. Opin. Struct. Biol.* 56, 155–163. doi: 10.1016/j.sbi.2019.03.009

Divi, U. K., Zhou, X. R., Wang, P., Butlin, J., Zhang, D. M., Liu, Q., et al. (2016). Deep sequencing of the fruit transcriptome and lipid accumulation in a non-seed tissue of Chinese tallow, a potential biofuel crop. *Plant Cell Physiol.* 57, 125–137. doi: 10.1093/pcp/pcv181

Dyson, H. J., and Wright, P. E. (2005). Intrinsically unstructured proteins and their functions. *Nat. Rev. Mol. Cell Biol.* 6, 197–208. doi: 10.1038/nrm1589

Eisenberg, D., Wilcox, W., and McLachlan, A. D. (1986). Hydrophobicity and amphiphilicity in protein structure. *J. Cell. Biochem.* 31, 11–17. doi: 10.1002/jcb.240310103

Fei, W., Yang, S., Hu, J., Yang, F., Qu, G., Peng, D., et al. (2020). Research advances of WRINKLED1 (WRI1) in plants. *Funct. Plant Biol.* 47, 185–194. doi: 10.1071/FP19225

Focks, N., and Benning, C. (1998). wrinkled1: A Novel, Low-Seed-Oil Mutant of Arabidopsis with a Deficiency in the Seed-Specific Regulation of Carbohydrate Metabolism. *Plant Physiol.* 118, 91–101. doi: 10.1104/pp.118.1.91

Fukuda, N., Ikawa, Y., Aoyagi, T., and Kozaki, A. (2013). Expression of the genes coding for plastidic acetyl-CoA carboxylase subunits is regulated by a location-sensitive transcription factor binding site. *Plant Mol. Biol.* 82, 473–483. doi: 10.1007/s11103-013-0075-7

Gao, J., and Xu, D. (2012). Correlation Between Posttranslational Modification and Intrinsic Disorder in Protein. *Pac Symp Biocomput.* 2012, 94–103.

García-Alai, M. M., Gallo, M., Salame, M., Wetzler, D. E., McBride, A. A., Paci, M., et al. (2006). Molecular basis for phosphorylation-dependent, PEST-mediated protein turnover. *Structure* 14, 309–319. doi: 10.1016/j.str.2005.11.012

Gregory, M. A., and Hann, S. R. (2000). c-Myc Proteolysis by the Ubiquitin-Proteasome Pathway: Stabilization of c-Myc in Burkitt's Lymphoma Cells. *Mol. Cell. Biol.* 20, 2423–2435. doi: 10.1128/mcb.20.7.2423-2435.2000

Grimberg, Å, Carlsson, A. S., Marttila, S., Bhalerao, R., and Hofvander, P. (2015). Transcriptional transitions in Nicotiana benthamiana leaves upon induction of oil synthesis by WRINKLED1 homologs from diverse species and tissues. *BMC Plant Biol.* 15:579. doi: 10.1186/s12870-015-0579-1

Hara, A., and Radin, N. S. (1978). Lipid Extraction of Tissues with a Low-Toxicity Solvent. *Anal. Biochem.* 90, 420–426. doi: 10.1016/0003-2697(78)90046-5

Ibarra-Laclette, E., Méndez-Bravo, A., Pérez-Torres, C. A., Albert, V. A., Mockaitis, K., Kilaru, A., et al. (2015). Deep sequencing of the Mexican avocado transcriptome, an ancient angiosperm with a high content of fatty acids. *BMC Genomics* 16, 1–18. doi: 10.1186/s12864-015-1775-y

Ji, X., Mao, X., Hao, Q., Liu, B., Xue, J., and Li, R. (2018). Splice Variants of the Castor WRI1 Gene Upregulate Fatty Acid and Oil Biosynthesis When Expressed in Tobacco Leaves. *Int. J. Mol. Sci.* 19:46. doi: 10.3390/ijms19010146

Keereetaweep, J., Liu, H., Zhai, Z., and Shanklin, J. (2018). Biotin Attachment Domain-Containing Proteins Irreversibly Inhibit Acetyl CoA Carboxylase. *Plant Physiol.* 177, 208–215. doi: 10.1104/pp.18.00216

Khan, S. H., and Kumar, R. (2009). An Overview of the Importance of Conformational Flexibility in Gene Regulation by the Transcription Factors. *J. Biophys.* 2009:210485. doi: 10.1155/2009/210485

Kikuta, Y., and Erickson, L. C. (1968). Seasonal Changes of Avocado Lipids During Fruit Development and Storage. *Calif. Avocado Soc.* 52, 102–108.

Kilaru, A., Cao, X., Dabbs, P. B., Sung, H. J., Rahman, M. M., Thrower, N., et al. (2015). Oil biosynthesis in a basal angiosperm: Transcriptome analysis of Persea Americana mesocarp. *BMC Plant Biol.* 15:586. doi: 10.1186/s12870-015-0586-2

Koike, R., Amano, M., Kaibuchi, K., and Ota, M. (2020). Protein kinases phosphorylate long disordered regions in intrinsically disordered proteins. *Protein Sci.* 29, 564–571. doi: 10.1002/pro.3789

Kong, Q., Yuan, L., and Ma, W. (2019). WRINKLED1, a "Master Regulator" in Transcriptional Control of Plant Oil Biosynthesis. *Plants* 8:238. doi: 10.3390/plants8070238

Krizek, B. A. (2003). AINTEGUMENTA utilizes a mode of DNA recognition distinct from that used by proteins containing a single AP2 domain. *Nucleic Acids Res.* 31, 1859–1868. doi: 10.1093/nar/gkg292

Kuczynski, C., McCorkle, S., Keereetaweep, J., Shanklin, J., and Schwender, J. (2020). An Expanded Role for WRINKLED1 Metabolic Control Based on Combined Phylogenetic and Biochemical Analyses. *bioRxiv*, 2020.01.28.923292 [preprint] doi: 10.1101/2020.01.28.923292

Liu, H., Zhai, Z., Kuczynski, K., Keereetaweep, J., Schwender, J., and Shanklin, J. (2019). WRINKLED1 Regulates BIOTIN ATTACHMENT DOMAIN-CONTAINING Proteins that Inhibit Fatty Acid Synthesis. *Plant Physiol.* 181, 55–62. doi: 10.1104/pp.19.00587

Liu, J., Hua, W., Zhan, G., Wei, F., Wang, X., Liu, G., et al. (2010). Increasing seed mass and oil content in transgenic Arabidopsis by the overexpression of wri1-like gene from Brassica napus. *Plant Physiol. Biochem.* 48, 9–15. doi: 10.1016/j.plaphy.2009.09.007

Liu, J., Perumal, N. B., Oldfield, C. J., Su, E. W., Uversky, V. N., and Dunker, A. K. (2006). Intrinsic disorder in transcription factors. *Biochemistry* 45, 6873–6888. doi: 10.1021/bi0602718

Lu, S., Song, T., Kosma, D. K., Parsons, E. P., Rowland, O., and Jenks, M. A. (2009). Arabidopsis CER8 encodes LONG-CHAIN ACYL-COA SYNTHETASE 1 (LACS1) that has overlapping functions with LACS2 in plant wax

and cutin synthesis. *Plant J.* 59, 553–564. doi: 10.1111/j.1365-313X.2009.03892.x

Ma, W., Kong, Q., Arondel, V., Kilaru, A., Bates, P. D., Thrower, N. A., et al. (2013). WRINKLED1, A Ubiquitous Regulator in Oil Accumulating Tissues from Arabidopsis Embryos to Oil Palm Mesocarp. *PLoS One* 8, 1–13. doi: 10.1371/journal.pone.0068887

Ma, W., Kong, Q., Grix, M., Mantyla, J. J., Yang, Y., Benning, C., et al. (2015). Deletion of a C-terminal intrinsically disordered region of WRINKLED1 affects its stability and enhances oil accumulation in Arabidopsis. *Plant J.* 83, 864–874. doi: 10.1111/tpj.12933

Ma, W., Kong, Q., Mantyla, J. J., Yang, Y., Ohlrogge, J. B., and Benning, C. (2016). 14-3-3 protein mediates plant seed oil biosynthesis through interaction with AtWRI1. *Plant J.* 88, 228–235. doi: 10.1111/tpj.13244

Maeo, K., Tokuda, T., Ayame, A., Mitsui, N., Kawai, T., Tsukagoshi, H., et al. (2009). An AP2-type transcription factor, WRINKLED1, of Arabidopsis thaliana binds to the AW-box sequence conserved among proximal upstream regions of genes involved in fatty acid synthesis. *Plant J.* 60, 476–487. doi: 10.1111/j.1365-313X.2009.03967.x

Mano, F., Aoyanagi, T., and Kozaki, A. (2019). Atypical Splicing Accompanied by Skipping Conserved Micro-exons Produces Unique WRINKLED1, An AP2 Domain Transcription Factor in Rice Plants. *Plants* 8:207. doi: 10.3390/plants8070207

Naim, F., Shrestha, P., Singh, S. P., Waterhouse, P. M., and Wood, C. C. (2016). Stable expression of silencing-suppressor protein enhances the performance and longevity of an engineered metabolic pathway. *Plant Biotechnol. J.* 14, 1418–1426. doi: 10.1111/pbi.12506

Okamuro, J. K., Caster, B., Villarroel, R., Van Montagu, M., and Jofuku, K. D. (1997). The AP2 domain of APETALA2 defines a large new family of DNA binding proteins in Arabidopsis. *Proc. Natl. Acad. Sci. U. S. A.* 94, 7076–7081. doi: 10.1073/pnas.94.13.7076

Oldfield, C. J., Cheng, Y., Cortese, M. S., Brown, C. J., Uversky, V. N., and Bunker, A. K. (2005). Comparing and combining predictors of mostly disordered proteins. *Biochemistry* 44, 1989–2000. doi: 10.1021/bi047993o

Peng, K., Vucetic, S., Radivojac, P., Brown, C. J., Dunker, A., and Obradovic, Z. (2005). Optimizing Long Intrinsic Disorder Predictors With Protein Evolutionary Information. *J. Bioinform. Comput. Biol.* 3, 35–60. doi: 10.1142/s0219720005000886

Pouvreau, B., Baud, S., Vernoud, V., Morin, V., Py, C., Gendrot, G., et al. (2011). Duplicate Maize Wrinkled1 Transcription Factors Activate Target Genes Involved in Seed Oil Biosynthesis. *Plant Physiol.* 156, 674–686. doi: 10.1104/pp.111.173641

Rahman, M., Liu, Q., Zhou, X.-R., and Singh, S. P. (2016). Oil-rich nonseed tissues for enhancing plant oil production. *CAB Rev. Perspect. Agric. Vet. Sci. Nutr. Nat. Resour.* 11, 1–11. doi: 10.1079/PAVSNNR201611021

Rechsteiner, M., and Rogers, S. W. (1996). PEST sequences and regulation by proteolysis. *Trends Biochem. Sci.* 21, 267–271. doi: 10.1016/S0968-0004(96)10031-1

Rendón-Anaya, M., Ibarra-Laclette, E., Méndez-Bravo, A., Lan, T., Zheng, C., Carretero-Paulet, L., et al. (2019). The avocado genome informs deep angiosperm phylogeny, highlights introgressive hybridization, and reveals pathogen-influenced gene space adaptation. *Proc. Natl. Acad. Sci. U. S. A.* 116, 17081–17089. doi: 10.1073/pnas.1822129116

Romero, P., Obradovic, Z., Li, X., Garner, E. C., Brown, C. J., and Dunker, A. K. (2001). Sequence complexity of disordered protein. *Proteins* 42, 38–48. doi: 10.1002/1097-0134(20010101)42:1<38::aid-prot50>3.0.co;2-3

Ruuska, S. A., Girke, T., Benning, C., and Ohlrogge, J. B. (2002). Contrapuntal Networks of Gene Expression during Arabidopsis Seed Filling. *Plant Cell* 14, 1191–1206. doi: 10.1105/tpc.000877

Shockey, J., Mason, C., Gilbert, M., Cao, H., Li, X., Cahoon, E., et al. (2015). Development and analysis of a highly flexible multi-gene expression system for metabolic engineering in Arabidopsis seeds and other plant tissues. *Plant Mol. Biol.* 89, 113–126. doi: 10.1007/s11103-015-0355-5

Simossis, V. A., and Heringa, J. (2003). The PRALINE online server: Optimising progressive multiple alignment on the web. *Comput. Biol. Chem.* 27, 511–519. doi: 10.1016/j.compbiolchem.2003.09.002

Singh, G. P., Ganapathi, M., Sandhu, K. S., and Dash, D. (2006). Intrinsic unstructuredness and abundance of PEST motifs in eukaryotic proteomes. *Proteins Struct. Funct. Genet.* 62, 309–315. doi: 10.1002/prot.20746

Snell, P., Grimberg, Carlsson, A. S., and Hofvander, P. (2019). WRINKLED1 is subject to evolutionary conserved negative autoregulation. *Front. Plant Sci.* 10:387. doi: 10.3389/fpls.2019.00387

Tang, T., Du, C., Song, H., Aziz, U., Wang, L., Zhao, C., et al. (2019). Genome-wide analysis reveals the evolution and structural features of WRINKLED1 in plants. *Mol. Genet. Genomics* 294, 329–341. doi: 10.1007/s00438-018-1512-8

To, A., Joubès, J., Barthole, G., Lécureuil, A., Scagnelli, A., Jasinski, S., et al. (2012). WRINKLED Transcription Factors Orchestrate Tissue-Specific Regulation of Fatty Acid Biosynthesis in Arabidopsis. *Plant Cell* 24, 5007–5023. doi: 10.1105/tpc.112.106120

Tompa, P. (2005). The interplay between structure and function in intrinsically unstructured proteins. *FEBS Lett.* 579, 3346–3354. doi: 10.1016/j.febslet.2005.03.072

Uversky, V. N., and Dunker, A. K. (2010). Understanding protein non-folding. *Biochim. Biophys. Acta* 1804, 1231–1264. doi: 10.1016/j.bbapap.2010.01.017

Uversky, V. N., Gillespie, J. R., and Fink, A. L. (2000). Why are "natively unfolded" proteins unstructured under physiologic conditions? *Proteins Struct. Funct. Genet.* 41, 415–427. doi: 10.1002/1097-0134(20001115)41:3

Vacic, V., Uversky, V. N., Dunker, A. K., and Lonardi, S. (2007). Composition Profiler: A tool for discovery and visualization of amino acid composition differences. *BMC Bioinform.* 8, 1–7. doi: 10.1186/1471-2105-8-211

Van Der Lee, R., Buljan, M., Lang, B., Weatheritt, R. J., Daughdrill, G. W., Dunker, A. K., et al. (2014). Classification of intrinsically disordered regions and proteins. *Chem. Rev.* 114, 6589–6631. doi: 10.1021/cr400525m

Ward, J. J., Sodhi, J. S., McGuffin, L. J., Buxton, B. F., and Jones, D. T. (2004). Prediction and Functional Analysis of Native Disorder in Proteins from the Three Kingdoms of Life. *J. Mol. Biol.* 337, 635–645. doi: 10.1016/j.jmb.2004.02.002

Wood, C. C., Petrie, J. R., Shrestha, P., Mansour, M. P., Nichols, P. D., Green, A. G., et al. (2009). A leaf-based assay using interchangeable design principles to rapidly assemble multistep recombinant pathways. *Plant Biotechnol. J.* 7, 914–924. doi: 10.1111/j.1467-7652.2009.00453.x

Zhai, Z., Liu, H., and Shanklin, J. (2017). Phosphorylation of WRINKLED1 by KIN10 results in its proteasomal degradation, providing a link between energy homeostasis and lipid biosynthesis. *Plant Cell* 29, 871–889. doi: 10.1105/tpc.17.00019

Zhang, J., Liu, H., Sun, J., Li, B., Zhu, Q., Chen, S., et al. (2012). Arabidopsis Fatty Acid Desaturase FAD2 Is Required for Salt Tolerance during Seed Germination and Early Seedling Growth. *PLoS One* 7:e30355. doi: 10.1371/journal.pone.0030355

Disclaimer: Mention of trade names or commercial products in this publication is solely for the purpose of providing specific information and does not imply recommendation or endorsement from the United States Department of Agriculture. The USDA is an equal opportunity provider and employer.

Conflict of Interest: The authors declare that the research was conducted in the absence of any commercial or financial relationships that could be construed as a potential conflict of interest.

Copyright © 2021 Behera, Rahman, Bhatia, Shockey and Kilaru. This is an open-access article distributed under the terms of the Creative Commons Attribution License (CC BY). The use, distribution or reproduction in other forums is permitted, provided the original author(s) and the copyright owner(s) are credited and that the original publication in this journal is cited, in accordance with accepted academic practice. No use, distribution or reproduction is permitted which does not comply with these terms.

frontiers in Plant Science

ORIGINAL RESEARCH
published: 19 November 2021
doi: 10.3389/fpls.2021.763742

Haematococcus pluvialis Accumulated Lipid and Astaxanthin in a Moderate and Sustainable Way by the Self-Protection Mechanism of Salicylic Acid Under Sodium Acetate Stress

*Qunju Hu[1,2], Mingjian Song[1], Danqiong Huang[1], Zhangli Hu[1], Yan Wu[3] and Chaogang Wang[1]**

[1] Shenzhen Key Laboratory of Marine Bioresource and Eco-Environmental Science, Shenzhen Engineering Laboratory for Marine Algal Biotechnology, Guangdong Provincial Key Laboratory for Plant Epigenetics, College of Life Sciences and Oceanography, Shenzhen University, Shenzhen, China, [2] Marine Resources Big Data Center of South China Sea, Southern Marine Science and Engineering Guangdong Laboratory Zhanjiang, Zhanjiang, China, [3] Instrumental Analysis Center, Shenzhen University, Shenzhen, China

OPEN ACCESS

Edited by:
Eric Marechal,
UMR 5168 Laboratoire de Physiologie Cellulaire Végétale (LPCV), France

Reviewed by:
Regis Rene Le-Feuvre,
University of Concepción, Chile
Jianhua Fan,
East China University of Science and Technology, China

***Correspondence:**
Chaogang Wang
charlesw@szu.edu.cn

Specialty section:
This article was submitted to Marine and Freshwater Plants, a section of the journal Frontiers in Plant Science

Received: 01 September 2021
Accepted: 18 October 2021
Published: 19 November 2021

Citation:
Hu Q, Song M, Huang D, Hu Z, Wu Y and Wang C (2021) *Haematococcus pluvialis* Accumulated Lipid and Astaxanthin in a Moderate and Sustainable Way by the Self-Protection Mechanism of Salicylic Acid Under Sodium Acetate Stress. *Front. Plant Sci.* 12:763742. doi: 10.3389/fpls.2021.763742

To elucidate the mechanism underlying increased fatty acid and astaxanthin accumulation in *Haematococcus pluvialis*, transcriptome analysis was performed to gain insights into the multiple defensive systems elicited by salicylic acid combined with sodium acetate (SAHS) stresses with a time course. Totally, 112,886 unigenes and 61,323 non-repeat genes were identified, and genes involved in carbon metabolism, primary and secondary metabolism, and immune system responses were identified. The results revealed that SA and NaAC provide both energy and precursors to improve cell growth of *H. pluvialis* and enhance carbon assimilation, astaxanthin, and fatty acids production in this microalga with an effective mechanism. Interestingly, SA was considered to play an important role in lowering transcriptional activity of the fatty acid and astaxanthin biosynthesis genes through self-protection metabolism in *H. pluvialis*, leading to its adaption to HS stress and finally avoiding massive cell death. Moreover, positive correlations between 15 key genes involved in astaxanthin and fatty acid biosynthesis pathways were found, revealing cooperative relation between these pathways at the transcription level. These results not only enriched our knowledge of the astaxanthin accumulation mechanism in *H. pluvialis* but also provided a new view on increasing astaxanthin production in *H. pluvialis* by a moderate and sustainable way in the future.

Keywords: salicylic acid and sodium acetate stresses, *Haematococcus pluvialis*, transcriptomic analysis, metabolic coordination, astaxanthin biosynthesis, fatty acids biosynthesis

INTRODUCTION

Astaxanthin ($C_{40}H_{52}O_4$, 3, 3′-dihydroxy-β, β-carotene-4, 4′-dione) is a bright red secondary carotenoid from the xanthophylls group, which is considered to be the most potent antioxidant in nature, and an important pigment for industrial markets (Machado et al., 2016; Shah et al., 2016; Molino et al., 2018). Naturally, astaxanthin is obtained from aquatic and non-aquatic microorganisms, such as bacteria, yeasts, fungi, and microalgae (Silva et al., 2012; Molino et al., 2018; Wan et al., 2021). *Haematococcus pluvialis*, a unicellular microalga distributed in various habitats worldwide, is considered the best astaxanthin natural source (Ranga Rao et al., 2010). The life cycle of this microalga consists of four phases, including macrozooid (zoospore), microzooids, palmella, and aplanospore (Shah et al., 2016). Stress conditions, e.g., nutrition deficiency, ferrous ion addition, salinity, high light intensity, UV-B irradiation, and drought, induce astaxanthin biosynthesis in *H. pluvialis* cells from lower content, 0.1% on a dry basis, in the macrozooid phase until the range of 1.5–4% on a dry basis in the aplanospore phase (Fábregas et al., 2003; Cerón et al., 2007; Chen et al., 2015; Hong et al., 2015; Hu et al., 2020). Various plant hormones and their derivatives can also affect astaxanthin accumulation in *H. pluvialis* (Shah et al., 2016). Under stress conditions, *H. pluvialis* cells also accumulate large amounts of neutral lipids in the aplanospore phase. Approximately, 96% of astaxanthin molecules are predominantly esterified with fatty acids and deposited in triacylglycerols (TAG)-rich cytosolic lipid globules (LBs). Thus, the increased neutral lipids in the cells are hypothesized to be a matrix for solubilizing of the esterified astaxanthin, and the suitable profile of lipids indicates a possibility of biodiesel production from *H. pluvialis* (Holtin et al., 2009; Saha et al., 2013; Shah et al., 2016). Although *H. pluvialis* is the best natural source of astaxanthin known to date, its productivity still needs to be improved. Furthermore, the ability to produce additional high-value compounds in addition to astaxanthin will enhance economic value of *H. pluvialis* (Le-Feuvre et al., 2020).

Various carbon sources have been studied for mixotrophic or heterotrophic cultivation of *H. pluvialis*, including acetate, glucose, glycerol, rice straw hydrolyzates, and organic-rich wastewaters (Leite et al., 2015; Gupta et al., 2019). *H. pluvialis* can also utilize exogenous organic carbon substrates (Kobayashi et al., 1992), and sodium acetate (NaAC) was considered to significantly accelerate cell growth or astaxanthin accumulation (Kobayashi et al., 1993; Orosa et al., 2001; Tolga et al., 2010; Pang et al., 2019; Zhang et al., 2019; Cong et al., 2020). In *H. pluvialis*, exogenous NaAC increases respiratory rates and suppresses photosynthetic activity in the cells (Zhang et al., 2019). It can be used as an effective carbon source, providing energy for the biosynthesis of astaxanthin and fatty acids (Cong et al., 2020; Oslan et al., 2021; Wang et al., 2021; Zhao et al., 2021). NaAC can be utilized by the tricarboxylic acid cycle to control the flux of carbon. It is postulated that NaAC enhances astaxanthin accumulation in *H. pluvialis* cells in three ways, including, (i) Increased acetyl-CoA from the carbon flux directly enhances respiratory rates of the cells and provides both NAD(P)H and carbon skeletons for the biosynthesis of astaxanthin; (ii) Increased acetyl-CoA indirectly enhances biosynthesis of fatty acids and accelerates the accumulation of astaxanthin; (iii) Enhanced photoprotection capacity promotes the posttranslational activation of carotenoid biosynthesis and fatty acid elongation (Kobayashi et al., 1993; He et al., 2018; Zhang et al., 2019).

Li et al. (2020) indicated that the effective strategy to enhance astaxanthin production was to apply stress to induce astaxanthin production through directing the flow and partition of carbon toward lipids and astaxanthin biosynthesis while maintaining biomass growth by keeping carbon fixation and assimilation at the same time. Biomass growth rates of microalgae could be determined roughly by organic carbon uptake and photosynthesis rates (Li et al., 2020). Astaxanthin accumulated in *H. pluvialis* cells has been known to be deposited in cytoplasm lipid droplets (Pick et al., 2019). The increasing titer of lipids in the *Haematococcus* biomass was considered to increase the astaxanthin content simultaneously. Overexpression of the relevant genes that encode the esterifying enzymes might promote lipid and astaxanthin biosynthesis (Li et al., 2020). However, the effect of NaAC on the accumulation of astaxanthin is always integrated with the increase of biomass production (Göksan et al., 2010). Transcriptome analysis demonstrated that the addition of NaAC under high light condition upregulated several pathways of basal and secondary metabolism, including carbon fixation in photosynthetic organisms, fatty acid elongation, biosynthesis of unsaturated fatty acids, and carotenoid biosynthesis, resulting in enhanced astaxanthin accumulation (Hu et al., 2019). However, adding an excessively high concentration of NaAC (HS) has increased the damage to *H. pluvialis* cells in our pretest study.

In addition, chemicals are used as effective and economic stimulants to promote astaxanthin content in *H. pluvialis* cells (Yu et al., 2015; Cui D. et al., 2020; Li et al., 2020, 2021). Currently, small chemical regulators, especially phytohormones, have been intensively studied for their effects on the physiology and bioproduct biosynthesis in microalgae (Yu et al., 2015; Li et al., 2020). The phytohormones, such as abscisic acid, brassino steroids, diethyl aminoethyl hexanoate, fulvic acid, gibberellins, melatonin, methyl jasmonate, and salicylic acid, have been demonstrated to substantially affect the physiology, biomass growth, or astaxanthin accumulation of the *Haematococcus* cells (Lu et al., 2010; Raman and Ravi, 2011; Gao et al., 2012a,b, 2013a,b; Zhao Y. et al., 2015; Zhao et al., 2018, 2019; Ding et al., 2018a,b, 2019a; Hu et al., 2021). Salicylic acid (SA) is an important phenolic compound involved in regulating the growth and development of plants, and also regulating the responses of plants to biotic and abiotic stress factors (Raskin, 1992; Khan et al., 2010, 2012, 2013, 2014, 2015; Miura and Tada, 2014). SA is considered to significantly regulate some important plant physiological processes, for example, photosynthesis, nitrogen metabolism, proline metabolism, production of glycine betaine, plant water relations, and antioxidant defense system, under stress conditions and thereby protects plants against abiotic stresses (Khan et al., 2010, 2012, 2013, 2014, 2015; Nazar et al., 2015; Miura and Tada, 2014). Fu et al. (2021) revealed that SA, as a signaling molecule, accelerated growth and

proliferation of microalgal through exhibited positive impacts on DNA replication, carbon assimilation, and TCA cycle of the cells. SA stimulates astaxanthin accumulation at moderate levels (Lu et al., 2010) and inhibits astaxanthin biosynthesis at high concentrations in *H. pluvialis* (Raman and Ravi, 2011). It was indicated that SA enhanced the transcriptional expression of eight carotenogenic genes in *H. pluvialis*, although these genes exhibited different expression patterns (Gao et al., 2012b). Following supplementation of *H. pluvialis* cultures with SA, a time course-dependent changes in the transcriptome analysis identified several related genes coding for enzymes and transcription factors related to the carotenoid and astaxanthin metabolism (Gao et al., 2015). Gao et al. (2016) also indicated that the proteins enriched in lipid metabolism are regulated differently in SA and JA treatments with time, consistent with the genetictranscriptional expressions of genes involving in the fatty acid biosynthesis pathway.

Transcriptome analysis has become a preferred tool for gene transcription level studies (Cheng et al., 2017). Transcriptome data are valuable resources for investigating plants exposed to stress conditions. Because of the inaccessibility of a complete reference genome sequence to quantifying the transcriptome, global transcriptomic analysis of *H. pluvialis* was slowly investigated. And the potential mechanisms of SA on *H. pluvial is* combined with other environmental stresses in protecting *H. pluvialis* cells against these abiotic stresses, and improving the fatty acid and astaxanthin biosynthesis process is still under question. Thus, we chose SA and HS as variables in this study to explore the molecular mechanism of the *H. pluvialis* of astaxanthin and fatty acid biosynthesis by transcriptome analysis according to SAHS treatment time. Based on the genome database of *H. pluvialis* in our previous report (Luo et al., 2018), detailed genetic information revealed its resistance mechanism. The sequenced unigenes were assembled by the reported genome data and then annotated in various databases, including COG, GO, kyoto encyclopedia of genes and genomes (KEGG), NR, Swiss-Prot, and PFAM. The assembling and the annotation of the transcriptome sequences were considered to provide valuable genomic information for greater insight into the molecular mechanism of SA in *H. pluvialis* in response to HS concentration. The abovementioned results were further supported by the qRT-PCR results, changes in cell morphology and intracellular pigments, and fatty acids contents of *H. pluvialis* cells. In sum, this study provides a new practical method to increase astaxanthin and fatty acids accumulation in *H. pluvialis* and insights into the underlying mechanism promoting SA effect on industrial production of astaxanthin and biodiesel in *H. pluvialis*.

MATERIALS AND METHODS

Microalga Strains and Culturing Conditions

In this study, *Haematococcus pluvialis* 192.80 obtained from Sammlung von Algenkulturen Göttingen Culture Collection of Algae was cultured in Bold Basal Medium media in 250-ml Erlenmeyer flasks with permeable sealing membranes. Cells were cultured at 22°C under continuous fluorescent light (20 $\mu mol \cdot m^{-2} \cdot s^{-1}$) until the logarithmic phase (about 1×10^5 $cells \cdot ml^{-1}$). Then, the cells were collected together and evenly divided into 18 aliquots (300 ml algal culture in each 500 ml Erlenmeyer flasks) and used for salicylic acid (SA) and high concentration of sodium acetate (HS, 45 mM) treatments (SAHS). The SA dosages were at 25 $mg \cdot L^{-1}$ for the induction (Gao et al., 2012b, 2015), and cultures were sampled at 0, 1, 6, 12, 24, and 48 h, respectively. The sampled cells were centrifuged at 6,000 *g* for 5 min, harvested and immediately frozen in liquid nitrogen for 10 min, and stored at −80°C until further analysis. Each treatment consisted of three biological repeats.

Microalgal Morphology

The microalga cells were observed on an Olympus BX61 microscope with an Olympus DP10 digital camera (Olympus, Japan) at each sampling time to track the progress of morphology and color changes of *H. pluvialis* cells during the treatments.

Growth, Lipid, and Astaxanthin Analysis

Cell numbers were calculated by the Thoma counting method using an Olympus CX40 microscope (Olympus, Japan), and the biomass dry cell weight (DCW) was measured gravimetrically at each sampling time (Hu et al., 2015). Fatty acid methyl ester (FAME) analysis was determined using a method previously optimized by Ma et al. (2018), and astaxanthin yield was measured using spectrophotometry (Boussiba et al., 1992).

RNA Extraction and cDNA Library Construction

Haematococcus pluvialis cells sampled from control, and SAHS treatment at 1, 6, 12, 24, and 48 h (named SAHS_1, SAHS_6, SAHS_12, SAHS_24, and SAHS_48) at the same stages were merged together for the isolation of total RNA. RNA was extracted using TRIzol reagent (Invitrogen, United States) according to the manufacturer's protocols. The extracted quality of RNA was checked by agarose gel electrophoresis and the BioPhotometer Plus photometer (Eppendorf, Germany). RNA integrity was evaluated using the Agilent 2100 Bioanalyzer (Agilent Technologies, United States), and libraries with RNA integrity $\geq$5 were subsequently analyzed. Then, the construction, validation, and sequencing of the RNA libraries were conducted using the method mentioned in our previous report in cooperation with Majorbio Co. (Shanghai, China) (Hu et al., 2021).

Sequence Assembly and Annotation

Raw reads were processed using FASTX-Toolkit[1]. Reads containing more than 5% unknown nucleotides and the low-quality reads were removed using SeqPrep[2] and Sickle[3] to obtain clean reads, and further mapped to the reference genome using TopHat2[4]. Subsequently, the mapped reads were assembled using

[1]http://hannonlab.cshl.edu/fastx_toolkit
[2]https://github.com/jstjohn/SeqPrep
[3]https://github.com/najoshi/sickle
[4]http://tophat.cbcb.umd.edu/

the TopHat-Cufflinks platform[5], and extension of gene structure and identification of novel transcripts were performed through comparison with reference genome and known annotated genes using the Cuffcompare software (Trapnell et al., 2010). Following assembly of the reads, annotation of all these unigenes was processed using BLAST with a cutoff *E*-value of e^{-5} based on various protein databases, including COG (Clusters of Orthologous Groups of proteins), GO (Gene Ontology), KEGG, NR (NCBI non-redundant protein sequences), Swiss-Prot (A manually annotated and reviewed protein sequence database), and Pfam (protein family) for further analysis.

The Fragments Per Kilobase per Million mapped fragments (FPKM) value of each gene was calculated using Cufflinks (see text footnote 5), and the read counts of each gene were obtained by HTSeq package 2010[6]. Principal component analysis of the six RNA libraries was performed using the fast prcomp function (Molecular Devices, LLC, CA, United States), in which a score matrix was used to select probe sets that best fit the first principal component (PC1) and PC2. Differentially expressed genes (DEGs) were identified using the DEGSeq[7], and *p*-adjust <0.001 and | log2FC| > = 1 were set as the significant differential expression threshold. Based on hypergeometric test and Bonferroni adjustment [corrected *p*-value (FDR) ≤0.05], KEGG pathway enrichment of the DEGs was analyzed. Short Time-series Expression Miner (STEM) was used to analyze and cluster expression trends of DEGs in response to SAHS stresses, clustered the DEGs into 50 expression profiles. Profiles with $p < 0.01$ were further separately subjected to the KEGG database for pathway enrichment, in which pathways with $p < 0.01$ were focused as significantly enriched pathways. All the above bioinformatics analysis was based on the integrated cloud platform of I-Sanger[8], which was similar to that in our previous report (Hu et al., 2021). All sequence data from this study have been deposited in the public NCBI Sequence Read Archive (SRA) database under accession No. PRJNA675306.

RNA Isolation and Real-Time Quantitative Reverse Transcriptase PCR

According to the manufacturer's protocols, RNA of the *Haematococcus pluvialis* samples was isolated using an RNA fast 200 kit (Fastagen, Shanghai, China). Then, PrimeScript™ RT reagent Kits with gDNA Eraser (Perfect Real Time) (TaKaRa, Japan) were used to perform the first-strand complementary DNA (cDNA) synthesis. cDNA was synthesized using oligo(dT) primers through reverse transcription with a total of 0.5 μg RNA in a 20-μl reaction system. A total of 16 genes, including eight kinds of carotenoid biosynthesis-related genes, seven fatty acid biosynthesis-related genes, and the β-actin gene, were selected for real-time fluorescence quantitative PCR (qRT-PCR) to investigate their expression profiles in response to SAHS treatment. The expression level of these genes was normalized to β-actin as the reference gene, as in previous studies (Eom et al., 2006; Lei et al., 2012; Ma et al., 2018; Hu et al., 2021). For qRT-PCR, gene-specific primers and methods were consistent with that reported in our previous study (Hu et al., 2021). The tested gene expression levels were determined using $2^{-\Delta\Delta CT}$ values (Livak and Schmittgen, 2001).

Statistical Analysis

The experiments were conducted with biological triplicate from separate microalgal cultures except for the transcriptome analysis. Data in the figures and tables were shown as the average of triplicate, and error bars were standard errors. One-way ANOVA (SPSS 19.0) was performed for statistical analysis, and *P*-values of less than 0.05 were considered as statistically significant.

RESULTS

Microscopy and Growth Measurements

In this study, visual observations revealed that color of the *Haematococcus pluvialis* cultures changed from green to lime green during the SAHS treatment from Stage Control to Stage SAHS_48. Morphological changes of *H. pluvialis* cells at the different SAHS treatment stages were also observed, displaying that the orange-red partial of the cells increased with treatment time extension (Control, SAHS_1, SAHS_6, SAHS_12, SAHS_24, and SAHS_48) (**Figure 1**), which might indicate that the content of carotenoid or astaxanthin in *H. pluvialis* cells increased during the 2-day incubation. Interestingly, flagella loss of the *H. pluvialis* cells was not observed in this study.

The growth pattern of *H. pluvialis* under SAHS treatment was also measured and showed in **Table 1**. All the treatments were started with the same cell density (CD) ($9.92 \pm 1.12 \times 10^4$ cells·ml^{-1}) and displayed a fluctuation level during the treatment stages, indicating that SAHS stresses did not cause cell death during the 2-day incubation. As revealed in **Table 1**, DCW from the treatments gradually increased with the treatment time. DCW at the early treatment stage, e.g., control, was significantly lower than the later stages. While DCW at later treatment stages, including SAHS_24 and SAHS_48, was significantly higher than the early stages, demonstrating that biomass growth was improved during the 2-day incubation. Carotenoid content (CC) accumulated in *H. pluvialis* cells remained the same in the early treatment stages until SAHS_6 and significantly increased during stage transitions with the treatment time extension. Single-cell carotenoid content (SCCC) displayed a similar change pattern with CC, which was at a low level at the early treatment stages and significantly increased during the later stages. The highest SCCC was 11.82 ± 0.44 pg·cell^{-1} achieved during Stage SAHS_48, about 135.46% higher than Stage Control. Astaxanthin content (AC) under SAHS treatment was 0.77 ± 0.04, 0.76 ± 0.04, 0.79 ± 0.03, 0.93 ± 0.02, 0.88 ± 0.08, and 1.16 ± 0.01 mg·L^{-1} in Control, SAHS_1, SAHS_6, SAHS_12, SAHS_24, and SAHS_48, respectively. AC in *H. pluvialis* cells also showed a similar change pattern with SCCC, and the highest AC at Stage SAHS_48 was about 50.65% compared with Stage Control. A basal level of total fatty acids (TFA) of 154.56 ± 16.56 mg·g^{-1} by

[5]http://cole-trapnelllab.github.io/cufflinks/

[6]http://www-huber.embl.de/users/anders/HTSeq

[7]http://bioconductor.org/packages/stats/bioc/DEGSeq/

[8]https://www.i-sanger.com/

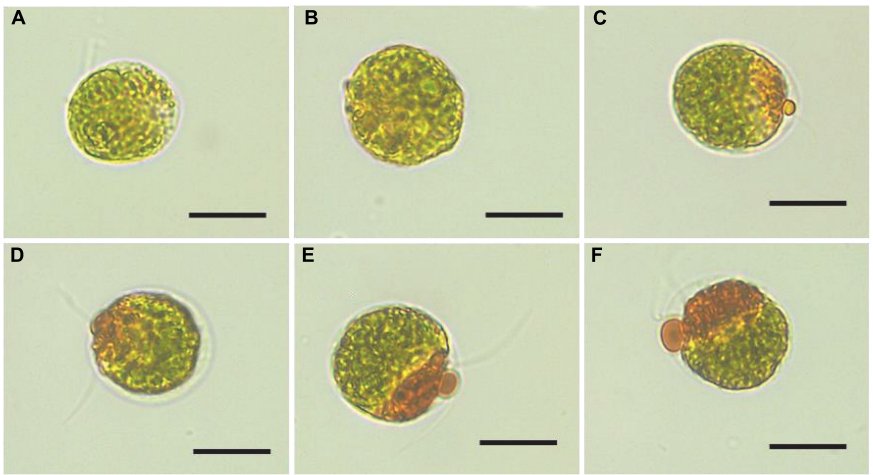

FIGURE 1 | Microscopic images of *Haematococcus pluvialis* cells at different SAHS treatment stages. **(A–F)** represent the samples of Control, SAHS_1, SAHS_6, SAHS_12, SAHS_24, and SAHS_48, respectively. Scale bar = 20 μm.

TABLE 1 | Effects of SAHS treatments on growth measurements of *Haematococcus pluvialis*.

Stages Measurements	Control	SAHS_1	SAHS_6	SAHS_12	SAHS_24	SAHS_48
CD	9.92 ± 1.12^{ab}	7.44 ± 0.86^{c}	11.31 ± 0.39^{a}	8.92 ± 0.24^{bc}	10.58 ± 0.68^{ab}	10.23 ± 0.67^{ab}
DCW	0.13 ± 0.01^{c}	0.16 ± 0.02^{bc}	0.20 ± 0.02^{ab}	0.20 ± 0.02^{ab}	0.22 ± 0.02^{a}	0.24 ± 0.02^{a}
CC	0.49 ± 0.01^{d}	0.43 ± 0.01^{d}	0.43 ± 0.07^{d}	0.67 ± 0.03^{c}	0.96 ± 0.06^{b}	1.21 ± 0.03^{a}
SCCC	5.02 ± 0.54^{d}	5.86 ± 0.67^{d}	3.81 ± 0.76^{e}	7.53 ± 0.40^{c}	9.05 ± 0.43^{b}	11.82 ± 0.44^{a}
AC	0.77 ± 0.04^{cd}	0.76 ± 0.04^{d}	0.79 ± 0.03^{cd}	0.93 ± 0.02^{b}	0.88 ± 0.08^{bc}	1.16 ± 0.01^{a}
TFAC	154.56 ± 16.56^{c}	165.30 ± 17.13^{c}	162.06 ± 6.25^{c}	186.74 ± 9.75^{bc}	223.69 ± 18.80^{a}	210.10 ± 15.8^{ab}

Data are given as means ± SD, n = 3. CD, cell density (× 10^4 cell·ml^{-1}); DCW, dry cell weight (mg·L^{-1}); CC, carotenoids content (mg·L^{-1}); SCCC, single cell carotenoids content (pg·cell^{-1}); AC, astaxanthin content (mg·L^{-1}); TFAC, total fatty acids content (mg·g^{-1}); Lowercase letters indicate significant differences ($p < 0.05$) among the treatments.

DCW was measured in this study that increased significantly with the treatment time extension. The high TFAC at Stage SAHS_48 (210.10 ± 15.8 mg·g^{-1} by DCW) was about 35.96% higher than the lowest (154.56 ± 16.56 mg·g^{-1} by DCW) at Stage Control.

Sequencing, *de novo* Transcriptome Assembly and Annotation

The molecular basis of the morphological and growth differences in *Haematococcus pluvialis* cells upon exposure to SAHS treatment was described based on a time course-dependent gene expression profiling, which was generated by RNA-Seq analyses performed on the alga samples. In total, six libraries were constructed and analyzed. The high throughput RNA sequencing obtained over 8.23 Gb clean data from each of the microalgal RNA libraries with Q20 all higher than 97.88% and a low-quality reads rate lower than 0.03% (**Table 2**). GC contents of the libraries ranged from 59.31 to 59.61%, and the mapping rate of all clean reads was higher than 91.46% (**Table 2**).

Assembly of the reads generated a total of 112,886 unigenes, whose size varied from 69 to 38,640 bp with an average length of 1,409 bp and N50 of 1,959 bp, and a total length of 86,419,450 bp. Generally, 93,942, 94,780, 93,220, 94,517, 93,946, and 95,137 transcripts were found transiently expressed and induced by SAHS at stages of Control, SAHS_1, SAHS_6, SAHS_12, SAHS_24, and SAHS_48, respectively. The transcripts numbers identified in each *H. pluvialis* RNA library, expressed in FPKMs, are shown in **Figure 2**. In general, approximately 55% of the transcripts were in the 0.5–5 FPKM range, and 28% in the range of 5–100 FPKM (**Figure 2A**). Principal component analysis revealed that the six libraries could be assigned to separated groups (**Figure 2B**), suggesting that the overall transcriptome profiling of *H. pluvialis* was different at each SAHS treatment stage. Thus, the result distinguished *H. pluvialis* with responding to SAHS stresses at different stages. According to the PC analysis, the six libraries were assigned to three groups, in which stages SAHS_1, SAHS_6, and SAHS_12 were clustered together, suggesting that their overall transcriptome profiling was similar. Stages SAHS_24 and SAHS_48 were clustered together, and Stage Control clustered separately. Overall, a total of 112,886 unigenes and 61,323 genes were annotated by BLAST in the six databases. Specifically, 25,758 (40.28%), 25,100 (39.25%), 17,459 (27.30%), 33,350 (52.15%), 20,205 (31.60%), and 24,942 (39.00%) genes were annotated in COG, GO, KEGG, NR, Swiss-Prot, and Pfam, respectively (**Table 3**).

TABLE 2 | RNA sequencing and mapping results.

Algal RNA libraries	Raw reads	Clean reads	Clean bases (nt)	Error rate (%)	Q20 (%)	GC content (%)	Mapping rate (%)
Control	51,078,628	50,323,266	7,453,145,620	0.02	98.03	59.41	93.87
SAHS_1	52,323,726	51,666,152	7,693,273,478	0.02	98.12	59.39	93.22
SAHS_6	49,328,446	48,739,818	7,254,036,353	0.02	98.15	59.61	93.59
SAHS_12	51,611,652	50,932,110	7,568,702,271	0.02	98.03	59.6	93.21
SAHS_24	51,642,478	50,784,936	7,538,385,545	0.03	97.88	58.98	91.88
SAHS_48	51,786,720	50,980,450	7,557,044,313	0.02	98.10	59.31	91.46

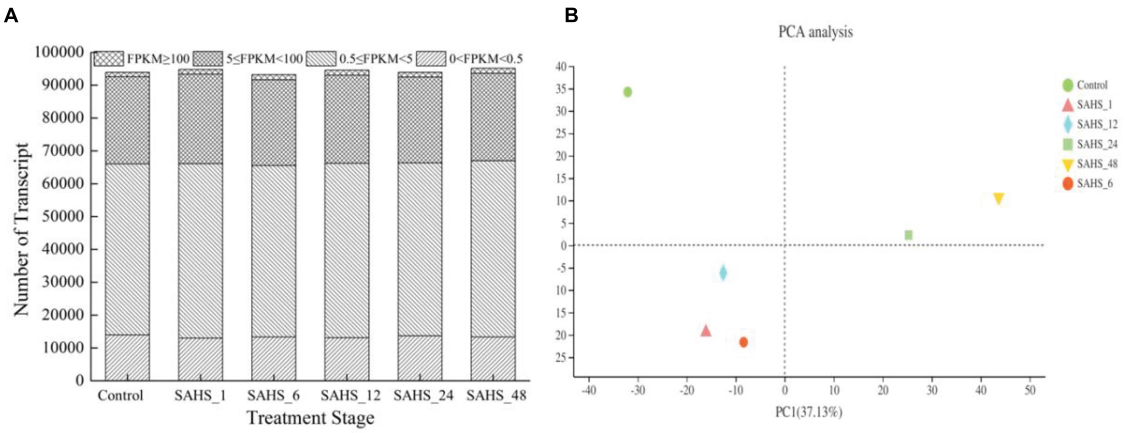

FIGURE 2 | Global expression profiling of *H. pluvialis* unigenes at different treatment stages. **(A)** Numbers of detected unigenes in each library. **(B)** Principal component analysis of the RNA-Seq libraries.

Differentially Expressed Genes

Cluster analysis of the differentially expressed genes (DEGs) was conducted to judge expression patterns of DEGs at different treatment stages. Pairwise comparisons were conducted among the six stages to identify DEGs correlating with SAHS, which revealed the expression changes of global genes during the 2-day incubation. As shown in **Table 4**, differential expression analysis revealed gene expression changes, and the numbers of upregulated or downregulated DEGs were displayed during the treatment stage transitions. For example, SAHS treatment stage transition from Control to SAHS_48 had the highest DEGs number (11,313) with 5,998 upregulated and 5,315 downregulated genes, while Stage SAHS_1 relative to SAHS_6 had the fewest DEGs (2,858), in which 2,051 genes were significantly downregulated, and 807 were upregulated. The stage transition from SAHS_24 to SAHS_48 also had a few DEGs numbers (3,350) with 2,374 upregulated and 976 downregulated genes. Stage Control relative to SAHS_1 had DEGs number of 6,411, in which 3,316 genes were significantly upregulated and 2,425 were downregulated. Stage transition of SAHS_6 to SAHS_12 had DEGs number of 3,822 with 2,565 significantly upregulated and 1,257 significantly downregulated genes. While stage SAHS_12 relative to SAHS_24 had a high DEGs number (6,941), in which 3,244 genes were significantly upregulated, and 3,697 were significantly downregulated.

TABLE 3 | The *de novo* transcriptome assembly and annotation results of unigenes in public protein databases.

Statistics	Results
Assembly	
Total unigenes	112,886
Total genes	61,323
Total length (bp)	86,419,450
Mean length (bp)	1,409
N50	1,959
Annotation	
Annotated in COG	25,758 (40.28%)
Annotated in GO	25,100 (39.25%)
Annotated in KEGG	17,459 (27.30%)
Annotated in NR	33,350 (52.15%)
Annotated in Swiss-Prot	20,205 (31.60%)
Annotated in PFAM	24,942 (39.00%)

Gene Expression Profiling and Kyoto Encyclopedia of Genes and Genomes Pathway Enrichments

Gene expression patterns throughout SAHS treatment were classified into 50 profiles, and STEM analysis demonstrated that 14 profiles, including Profiles 19, 49, 0, 35, 6, 40,

TABLE 4 | Numbers of DEGs involved in SAHS treatment stage transitions.

Stages	CN	SAHS_1	SAHS_6	SAHS_12	SAHS_24	SAHS_48
CN	–	3,985/2,425	3,316/4,011	3,395/2,052	5,281/5,145	5,998/5,315
SAHS_1	2,425/3,985	–	807/2,051	1,401/1,896	3,404/4,092	4,444/4,270
SAHS_6	4,011/3,316	2,051/807	–	2,565/1,257	3,047/1,538	4,665/2,322
SAHS_12	3,395/2,052	1,896/1,041	1,257/2,565	–	3,244/3,697	4,541/3,912
SAHS_24	5,145/5,281	4,092/3,404	1,538/3,047	3,697/3,244	–	2,374/976
SAHS_48	5,315/5,998	4,270/4,444	2,322/4,665	3,912/4,541	976/2,374	–

3, 43, 36, 14, 46, 33, 30, and 27, had *P*-values lower than 0.01 (**Figure 3**). The numbers of genes and significant enriched KEGG pathways of these profiles are shown in the **Supplementary Table 1**.

According to the results, the expression pattern of 2,062 genes in Profile 49 was upregulated during the treatment stages from Control to SAHS_48 in a row. The significantly enriched ($p < 0.01$) KEGG pathways were related to "fatty acid elongation," "fatty acid biosynthesis," "fatty acid degradation," "prodigiosin biosynthesis," "cutin, suberin, and wax biosynthesis," "amino sugar and nucleotide sugar metabolism," "fructose and mannose metabolism," "ascorbate and aldarate metabolism," "protein processing in the endoplasmic reticulum," "MAPK signaling pathway plant," "protein export," and "plant hormone signal transduction." And, in the profile, 35,954 genes were lowly expressed at early SAHS treatment stages, and highly expressed at Stage SAHS_48. The significantly enriched KEGG pathways were related to "fatty acid elongation," "photosynthesis," "cutin, suberin, and wax biosynthesis," and "thermogenesis." The 809 genes in Profile 46 were lowest at Stage Control, and then highly

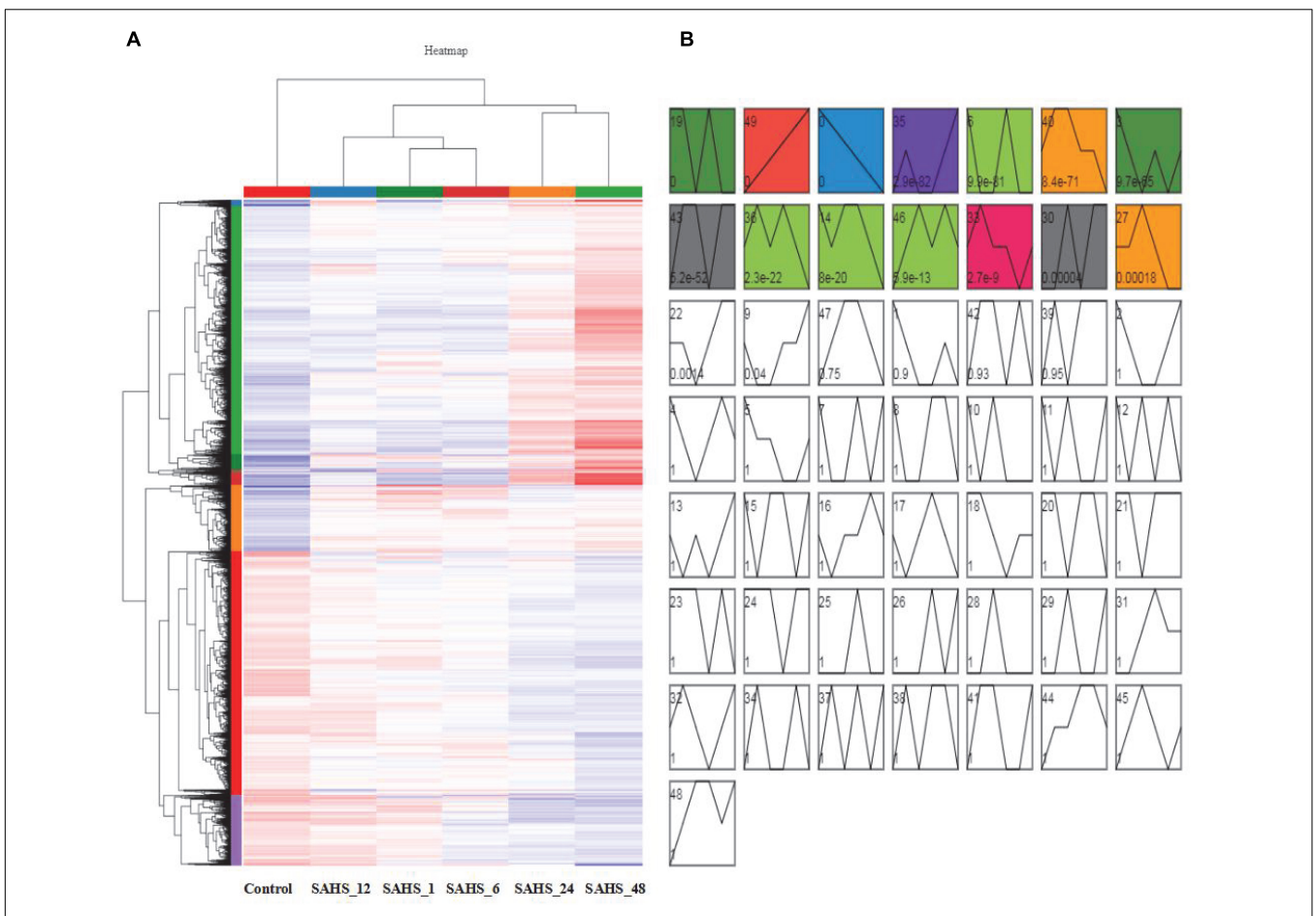

FIGURE 3 | Cluster analysis and gene expression profiling of DEGs. **(A)** Cluster analysis of the DEGs. The *X* axis indicates sample type, the *Y* axis represents relative expression levels, and the red and blue represent upregulation and downregulation. **(B)** Gene expression profiling of DEGs by STEM analysis. The 14 colored profiles are significant profiles ($p < 0.01$), and the *P*-values in each cluster is shown.

expressed in other stages. Two KEGG pathways were significantly enriched in this profile, which were "nitrogen metabolism" and "aminoacyl-tRNA biosynthesis." The significantly enriched KEGG pathways in these profiles were similar, to a certain extent. These pathways were mostly related to secondary metabolite metabolism, cell wall synthesis, and signal transduction, while the 1,717 genes downregulated during the treatment stages from Control to SAHS_48 in a row were classified in Profile 0. For the genes in other significantly classified profiles, including Profiles 40, 3, 36, 14, and 27, they were highly expressed in early treatment stages, and lowly expressed in late treatment stages. The significantly enriched KEGG pathways in these profiles were composed of "citrate cycle (TCA cycle)," "fatty acid biosynthesis," "phenylalanine, tyrosine, and tryptophan biosynthesis," "pantothenate and CoA biosynthesis," "other types of O-glycan biosynthesis," "biosynthesis of unsaturated fatty acids," "ribosome biogenesis in eukaryotes," "parathyroid hormone synthesis, secretion, and action," "tryptophan metabolism," "beta-alanine metabolism," "alanine, aspartate, and glutamate metabolism," "purine metabolism," "pyruvate metabolism," "propanoate metabolism," "glycine, serine, and threonine metabolism," "thiamine metabolism," "sphingolipid metabolism," "synthesis and degradation of ketone bodies," "valine, leucine, and isoleucine degradation," "lysine degradation," "ABC transporters," "peroxisome," "glycolysis/gluconeogenesis," "the AGE-RAGE signaling pathway in diabetic complications," "relaxin signaling pathway," "MAPK-signaling pathway plant," "phosphatidylinositol signaling system," "human cytomegalovirus infection," and "homologous recombination." These pathways were mostly related to the regulation of stress response and cellular proliferation, apoptotic regulation, membrane transport, and hormone biosynthesis.

There were 976 genes in Profile 43; they showed low-expression levels at Stage Control and SAHS_12 and high-expression levels at the other stages. The significantly enriched KEGG pathways in this profile were "biosynthesis of terpenoids and steroids," "selenocompound metabolism," "carotenoid biosynthesis," and "fatty acid elongation." These pathways were mostly related to secondary metabolites biosynthesis.

According to the above results, genes that highly expressed at early SAHS treatment stages and lowly expressed at late stages were classified in Profiles 49, 35, and 46, and they were significantly enriched into pathways involved in fatty acid biosynthesis, secondary metabolism biosynthesis, signaling pathway, and so on. While the genes lowly expressed at early SAHS treatment stages and highly expressed at late stages were classified in Profiles 0, 40, 3, 36, 14, and 27, which were significantly enriched into KEGG pathways involved in regulation of stress response and cellular proliferation, apoptotic regulation, membrane transport, and hormone biosynthesis. The biosynthesis pathways of secondary metabolites we are interested in, for example, terpenoids and carotenoid, were also enriched in Profile 43. Under SAHS stresses, our study focused on carbon fixation, carotenoid biosynthesis, and fatty acid biosynthesis pathways.

Effects of Salicylic Acid and High Concentration of Sodium Acetate Treatment on Specific Biological Pathways

In *Haematococcus pluvialis*, the maintenance of cellular homeostasis and biosynthesis of primary and secondary metabolites, e.g., fatty acids and astaxanthin, should generate a significant metabolic activity level and considerable demand for energy under stress conditions. Hence, our attention was focused on three specific pathways based on the analysis of DEGs in KEGG enrichment pathways, including "carbon fixation in photosynthetic organisms," "fatty acid biosynthesis," and "carotenoid biosynthesis" to explore the specific effects of the SAHS induction treatment stages (Control, SAHS_1, and SAHS_48) on *H. pluvialis*.

Transcriptome and Pathway Analysis in Carbon Fixation

"Carbon fixation in photosynthetic organisms" in the KEGG database was generated to construct the carbon metabolism pathway of *H. pluvialis*. The results of Stage transition of SAHS_1 vs. Control and SAHS_48 vs. SAHS_1 revealed that key enzymes belong to the Calvin—Benson cycle (C_3 pathway), C_4-Dicarboxylic acid cycle (C_4 pathway), and CAM pathway, e.g., phosphoenolpyruvate carboxylase (PEPC), pyruvate orthophosphate dikinase (PPDK), and malate dehydrogenase (MDH) were observed in *H. pluvialis*.

Further analysis determined the changes in carbon fixation pathways during Stage transition from Control to SAHS_1 and SAHS_1 to SAHS_48. During Stage transition of SAHS_1 vs. Control, four enzymes were upregulated, whereas two were downregulated in the C_4 pathway (**Table 5**). Expression levels of the phosphoenolpyruvate carboxylase (PPC, EC: 4.1.1.31), aspartate transaminase (AST, EC: 2.6.1.1), and phosphoenolpyruvate carboxykinase (ATP) (PEPCK, EC: 4.1.1.49) increased by 16.30-, 2.13-, and 19.95-fold, respectively, in the C_4 pathway. The expression level of malate dehydrogenase (oxaloacetate-decarboxylating) (NADP+) (MDH, EC: 1.1.1.40), which catalyzes the oxidative decarboxylation of (S)-malate in the presence of $NADP^+$ and divalent metal ions, and decarboxylation of oxaloacetate, decreased by 2.33-fold. Conversely, one enzyme was upregulated, and eight downregulated in the C_3 pathway, indicating that the key enzymes were downregulated. Expression levels of the downregulated genes decreased by 2.25- to 14.17-fold. Only the expression level of glyceraldehyde-3-phosphate dehydrogenase (GAPDH, EC: 1.2.1.12) increased in the C_3 pathway by 5.30-fold. According to the results, when the culture environment shifted from control to SAHS treatment, the genes involved in the C_3 pathway theoretically showed lower enzyme activity to help cells overcome the SAHS stresses. The downregulation of the expression levels of the genes might be due to high acetate concentrations. These enzymes created a counter-clockwise network, thereby reducing the content of 3-glycerol phosphate, starch, and sucrose in the cells. In addition, one enzyme was upregulated and one downregulated in the

TABLE 5 | The up and downregulated genes related to the carbon fixation pathways during SAHS Stage transitions.

KEGG Orthology Category Description	SAHS_1 vs. Control		SAHS_48 vs. SAHS_1	
	Regulate mode	FC	Regulate mode	FC
C4-Dicarboxylic acid cycle (C_4 pathway)				
PEPC; Phosphoenolpyruvate carboxylase [EC: 4.1.1.31]	Up	16.30	Up	2.09
PEPCK; Phosphoenolpyruvate carboxykinase (ATP) [EC: 4.1.1.49]	Up	19.95	Down	7.44
AST; Aspartate transaminase [EC: 2.6.1.1]	Up	2.13	Down	1.93
MDH; Malate Dehydrogenase (NADP+) [EC: 1.1.1.82]	Down	2.32	–	
ALT; Alanine Transaminase [EC: 2.6.1.2]	–		Up	2.53
MDH; Malate Dehydrogenase (oxaloacetate-decarboxylating) (NADP+) [EC: 1.1.1.40]	Down	2.33	Down	2.62
Calvin-Benson cycle (C_3 pathway)				
FBA; Fructose-bisphosphate aldolase [EC: 4.1.2.13]	Down	3.04	Up	2.02
FBPase; Fructose-bisphosphatase [3.1.3.11]	Up/down	–	Up	6.45
TK; Transketolase [EC: 2.2.1.1]	Down	2.25	–	
G3PDH; Glyceraldehyde-3-phosphate Dehydrogenase (NADP+) (phosphorylating) [EC: 1.2.1.13]	Down	14.17	Up	5.93
GAPDH; Glyceraldehyde-3-phosphate Dehydrogenase (phosphorylating) [EC: 1.2.1.12]	Up	5.30	Up/down	–
RPI; Ribulose-phosphate 3-epimerase [EC: 5.1.3.1]	Down	2.30	Down	2.07
PRK; Phosphoribulokinase [EC: 2.7.1.19]	Down	3.44	Up	2.49
PGK; Phosphoglycerate kinase [EC: 2.7.2.3]	Down	4.14	Up/down	–
Rubisco; Ribulose-bisphosphate carboxylase [EC: 4.1.1.39]	Up/down	–	Up	2.34
CAM pathway				
PEPC; Phosphoenolpyruvate carboxylase [EC: 4.1.1.31]	Up	16.30	Up	2.09
MDH; Malate Dehydrogenase (oxaloacetate-decarboxylating) (NADP+) [EC: 1.1.1.40]	Down	2.33	Down	2.62

FC, fold change.

CAM pathways. For example, the expression level of the PEPC (EC: 4.1.1.31)-encoding gene, which is specific to CO_2 fixation in algal cells, increased by 16.30-fold. However, the expression of MDH (EC: 1.1.1.40) decreased by 2.33-fold.

During Stage transition from SAHS_48 to SAHS_1, four enzyme-encoding genes were upregulated and two downregulated in the C_3 pathway. And there were two enzymes that were upregulated, and three were downregulated in the C_4 pathway. Additionally, one enzyme was upregulated, and one downregulated in the CAM pathway. As estimated, the concentrations of the two upregulated enzymes, including PEPC and alanine transaminase (ALT, EC: 2.6.1.2), increased by 2.09 and 2.53 folds, respectively, in the C_4 pathway. However, expression levels of three downregulated enzymes in this pathway, PEPCK, AST, and MDH, decreased by 7.44, 1.93, and 2.62-fold, respectively. The expression levels of fructose-bisphosphatase (FBPase, EC: 3.1.3.11) and glyceraldehyde-3-phosphate dehydrogenase (NADP+) (phosphorylating) (G3PDH, EC: 1.2.1.13) increased 6-fold in the C_3 pathway, and the only downregulated enzyme in this pathway, ribulose-phosphate 3-epimerase (RPI, EC: 5.1.3.1), decreased by 2.07-fold. In the CAM pathways, PEPC expression increased by 2.09-fold, and MDH expression levels decreased by 2.62-fold during the stage transition from SAHS_1 to SAHS_48.

Transcriptome and Pathway Analysis Involved in Carotenoid Biosynthesis

It was reported that the carotenoid biosynthesis-related genes were also upregulated with the increase in inorganic carbon (Wen et al., 2015). The universal isoprenoid precursor (IPP) and dimethylallyl pyrophosphate (DMAPP), the allylic isomer of IPP, were synthesized through the non-mevalonate pathway. The condensation reaction of IPP and DMAPP yields geranylgeranyl pyrophosphate (GGPP) for primary carotenoid biosynthesis (Lemoine and Schoefs, 2010).

According to the results, seven enzymes were upregulated, whereas three were downregulated in the carotenoid biosynthesis pathway during Stage transition of SAHS_1 vs. Control. Phytoene synthase (PSY, EC: 2.5.1.32) catalyzes the condensation of two GGPP molecules into one phytoene, which was

TABLE 6 | The up and downregulated genes related to the carotenoid biosynthesis pathway during SAHS stage transitions.

KEGG Orthology Category Description	SAHS_1 vs. Control		SAHS_48 vs. SAHS_1	
	Regulate mode	FC	Regulate mode	FC
PSY; 15-*cis*-phytoene synthase [EC: 2.5.1.32]	Up	5.05	Down	1.53
PDS; 15-*cis*-phytoene desaturase [EC: 1.3.5.5]	Up	3.09	Down	2.04
ZDS; 9,9′-*di-cis*-ζ-carotene desaturase [EC: 1.3.5.6]	Up	3.77	Down	4.17
CrtL-e; Lycopene ε-cyclase [EC: 5.5.1.18]	Down	7.67	Up	5.37
CrtL-b; Lycopene β-cyclase [EC: 5.5.1.19]	Up	2.10	–	
LUT5, CYP97A3; β-ring hydroxylase [EC: 1.14.-.-]	Down	2.52	–	
ZEP; zeaxanthin epoxidase [1.14.15.21]	Down	Inf	Up	Inf
CrtZ; β-carotene 3-hydroxylase [EC: 1.14.15.24]	Up	3.65	–	
CCD8; carlactone synthase [EC: 1.13.11.69]	Up	4.30	Up	3.08
CrtW; β-carotene 4-ketolase [1.14.99.63]	Up	4.24	–	

FC, fold change; Inf, infinity.

5.05-fold upregulated upon exposure to the SAHS stresses (**Table 6**). Phytoene is further converted to β-carotene by the successively catalyzing 15-*cis*-phytoene desaturase (PDS, EC: 1.3.5.5), 9,9′-*di*-*cis*-ζ-carotene desaturase (ZDS, EC: 1.3.5.6), and lycopene β-cyclase (CRTL-b, EC 5.5.1.19), which were upregulated by 3.09-, 3.77-, and 2.10-fold, respectively, under SAHS stresses. PDS is a rate-limiting enzyme of the carotenoid biosynthesis pathway, and the upregulation of its expression level may confer elevated astaxanthin biosynthesis capacity (Li et al., 2010). According to the results reported by Kobayashi (2003), astaxanthin is produced from β-carotene *via* two pathways, i.e., hydroxylation and oxidation of β-carotene catalyzed by β-carotene 3-hydroxylase (CrtZ, EC: 1.14.15.24) and β-carotene 4-ketolase (CrtW, EC: 1.14.99.63), which were upregulated by 3.65- and 4.24-fold, indicating enhanced astaxanthin production in *H. pluvialis* cells as a quick response to SAHS stresses.

During Stage transition from SAHS_1 to SAHS_48, three kinds of enzyme-encoding genes involved in the carotenoid biosynthesis pathway were downregulated, including PSY, PDS, and ZDS, by 1.53-, 2.04-, and 4.17-fold (**Table 6**). The other three enzyme-encoding genes, including lycopene ε-cyclase (CrtL-e, EC: 5.5.1.18), zeaxanthin epoxidase (ZEP, 1.14.15.21), and carlactone synthase (CCD8, EC: 1.13.11.69), were upregulated in this pathway by 5.37, Inf, and 3.08-fold. These results indicated the downregulation of β-carotene and astaxanthin biosynthesis and enhanced accumulation of ε-carotene and violaxanthin during this Stage transition.

Transcriptome and Pathway Analysis Involved in Fatty Acid Biosynthesis

It is well-known that astaxanthin is linearly correlated with the accumulation of fatty acids in *H. pluvialis* cells under environmental stresses, and over 96% astaxanthin is esterified by fatty acids to form astaxanthin ester and stored in triacylglycerol-rich cytoplasmic lipid droplets (Zhekisheva et al., 2002; Lei et al., 2012; Chen et al., 2015; Ma et al., 2018; Ding et al., 2019b; Pick et al., 2019; Cui J. et al., 2020). The increased production of neutral lipids is hypothesized to provide a solubility media for astaxanthin esters (Saha et al., 2013). Therefore, the formation of lipid droplets is a key factor driving and limiting astaxanthin accumulation in *H. pluvialis* (Cheng et al., 2017). As a result, any potential discrepancy of FAs upon exposure to SAHS stresses will be an important complement to the efficient astaxanthin accumulation knowledge of *H. pluvialis*.

During Stage transition from Control to SAHS_1, six enzyme-encoding genes involved in the fatty acid biosynthesis pathway were upregulated (**Table 7**). Acetyl-CoA carboxylase (ACC; EC: 6.4.1.2) and fatty acid synthase (FASN; EC: 2.3.1.85) begin the *de novo* fatty acid synthesis in eukaryotic algae (Harwood, 2019; Li-Beisson et al., 2019). ACC catalyzed the carboxylation of acetyl-CoA to generate malonyl-CoA (Hasan et al., 2018), which is the first committed and the rate-limiting step of fatty acid biosynthesis (Chen et al., 2019), and was upregulated by 2.45-fold. The sole enzyme, FASN, which is capable of the reductive *de novo* biosynthesis of long-chain fatty acids from nicotinamide adenine dinucleotide phosphate- NADPH-, malonyl-CoA, and acetyl-CoA (Ruth and Javier, 2006), was upregulated by 2.64-fold. Then, the enzyme [acyl-carrier-protein] *S*-malonyltransferase (FabD; EC: 2.3.1.39), which enhanced the production of malonyl-ACP from malonyl-CoA, was upregulated by 3.41-fold. Then, the acyl chain is elongated with the condensation reaction between malonyl-ACP and acyl-ACP in each turn until hexadecanoyl-ACP is finally formed (Sánchez and Harwood, 2002). Stearoyl-[acyl-carrier-protein] 9-desaturase (AAD; EC: 1.14.19.2) catalyzes the introduction of a double bond to the acyl group and esterifies to produce acyl-ACP (Rismani-Yazdi et al., 2011). The termination of the elongation of fatty acids is catalyzed by Oleoyl-[acyl-carrier-protein] hydrolase (OAH; EC: 3.1.2.14) *via* removing of an acyl group from acyl-ACP (Rismani-Yazdi et al., 2011). Long-chain-fatty-acid—CoA ligase (ACSL; EC: 6.2.1.3) activates the hexadecanoic acid through the esterification of hexadecanoyl-CoA and is further used in glycerolipid metabolism, glycerophospholipid metabolism, and fatty acid elongation. AAD, OAH, and ACSL were upregulated by 6.54-, 3.09-, and 2.85-fold, respectively. During Stage transition of SAHS_48 vs. SAHS_1, two kinds of enzymes were upregulated in the fatty acid biosynthesis pathway, including FASN and FabD, by 13.50- and 5.00-fold (**Table 7**). In addition, three enzymes (FabF, AAD, and OAH) were downregulated in this pathway by 2.75-, 3.35-, and 3.23-fold, respectively.

Analysis of the Expression Levels by Real-Time Quantitative PCR

In this study, expression levels of the key genes involved in carotenogenic and fatty acid biosynthesis pathways were determined during the SAHS treatment stages. The results demonstrated that expression levels of the studied genes varied among the stages (**Figures 4**, **5**). To study the relationship between the genes involved in carotenogenic and fatty acid

TABLE 7 | The up and downregulated genes related to the fatty acid biosynthesis pathway during SAHS Stage transitions.

KEGG Orthology Category Description	SAHS_1 vs. Control		SAHS_48 vs. SAHS_1	
	Regulate mode	FC	Regulate mode	FC
FASN; Fatty-acid synthase [EC: 2.3.1.85]	Up	2.64	Up	13.50
ACC; Acetyl-CoA carboxylase [6.4.1.2]	Up	2.45	Down/up	–
FabD; ACP *S* -malonyltransferase [EC: 2.3.1.39]	Up	3.41	Up	5.00
FabF; β-ketoacyl-ACP synthase II [EC: 2.3.1.179]	–		Down	2.75
AAD; Stearoyl-ACP 9-desaturase [EC: 1.14.19.2]	Up	6.54	Down	3.35
OAH; Oleoyl-ACP hydrolase [EC: 3.1.2.14]	Up	3.09	Down	3.23
Long-chain-fatty-acid—CoA ligase [ACSL; EC: 6.2.1.3]	Up	2.85	Down/up	–

FC, fold change.

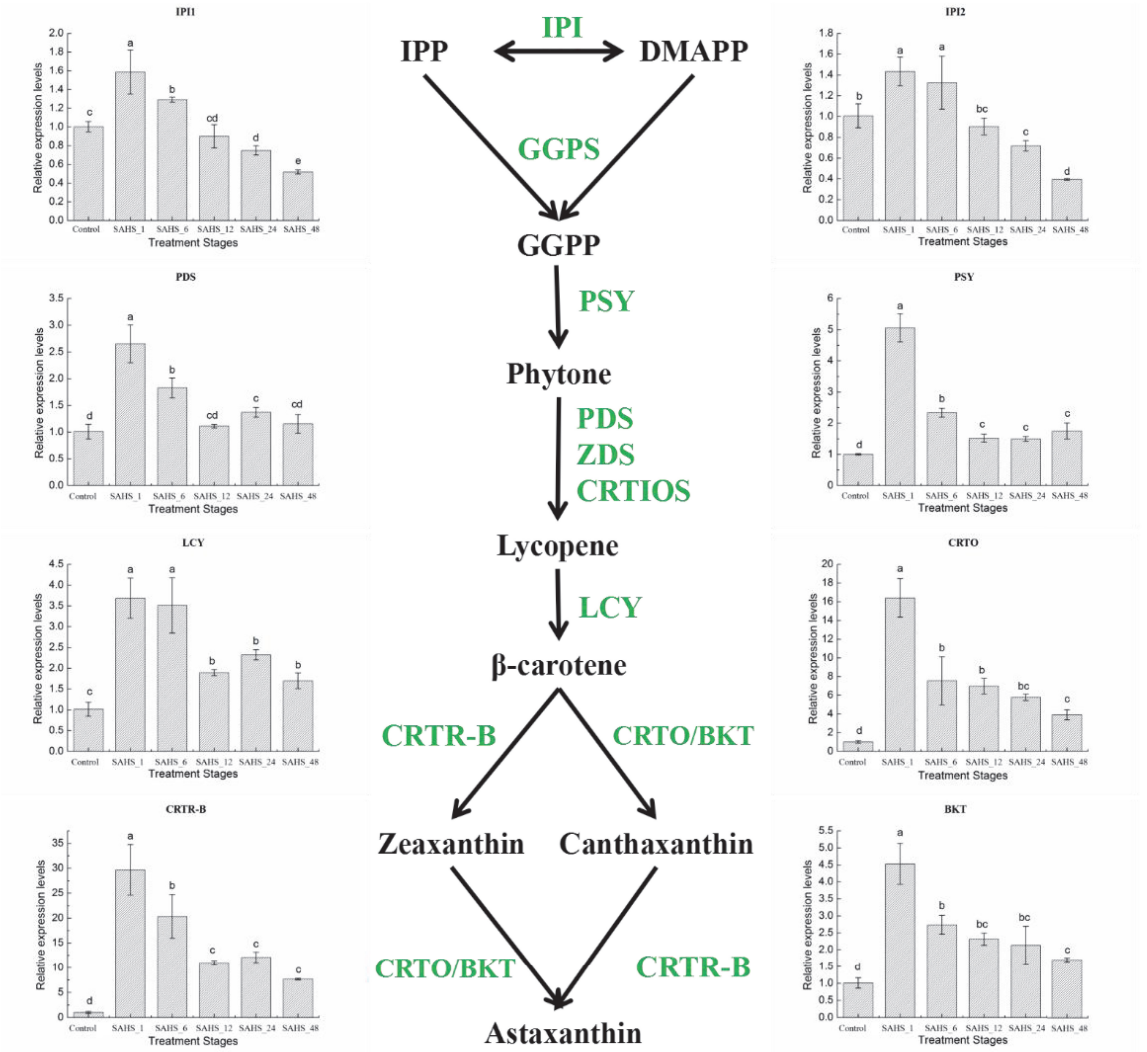

FIGURE 4 | Expression of genes in the *H. pluvialis* astaxanthin biosynthesis pathway under different treatment stages. Lower case letters indicate significant differences ($p < 0.05$) among the treatments.

biosynthesis pathways, the Pearson's correlation analysis (SPSS 19.0) was carried out, and the results are summarized in **Table 8**.

Transcript Expression of Carotenogenic Genes

Isopentenyl pyrophosphate isomerase (IPI) catalyzes the isomerization of IPP to DMAPP, and DMAPP is the precursor for the formation of the carotenoid backbone (Lee and Schmidt-Dannert, 2002). PDS catalyzes the first two dehydrogenation reactions to convert the pale yellow phytoene into ζ-carotene and phytofluene, which is one of the rate-limiting steps for carotenoid biosynthesis (Steinbrenner and Sandmann, 2006; Liu et al., 2013, 2014; Galarza et al., 2018). Then, phytoene, the first tetraterpene carotenoid in carotenoid biosynthesis pathway of *H. pluvialis*, is formed by PSY, a synthase catalyzing the head-to-tail condensation of two GGPP molecules (Gong and Bassi, 2016). The synthesis of phytoene is also a rate-limiting step for astaxanthin accumulation in *H. pluvialis* (Gong and Bassi, 2016). The flux of β-carotene from lycopene is catalyzed by lycopene β-cyclase (LCY; Gao et al., 2012a,b, 2013a; Galarza et al., 2018). Carotenoid oxygenase (CRTO) and carotenoid hydroxylase (BKT2) are two types of β-carotene ketolases/oxygenases that catalyze β-carotene to produce astaxanthin together with β-carotene hydroxylase (CRTR-B; Meng et al., 2005, 2006; Gao et al., 2010).

The expression levels of the eight carotenogenic genes varied among the stages (**Figure 4**). In this study, all of these genes were overexpressed at the transcript level during the 2-day cultivation. IPI1 and IPI2 had a similar expression pattern, both were over-expressed at a transcriptional level on Stage SAHS_1 and then significantly downregulated ($p < 0.05$) with treatment time extension. SAHS_48 showed the lowest expression level, which was significantly downregulated in comparison with the

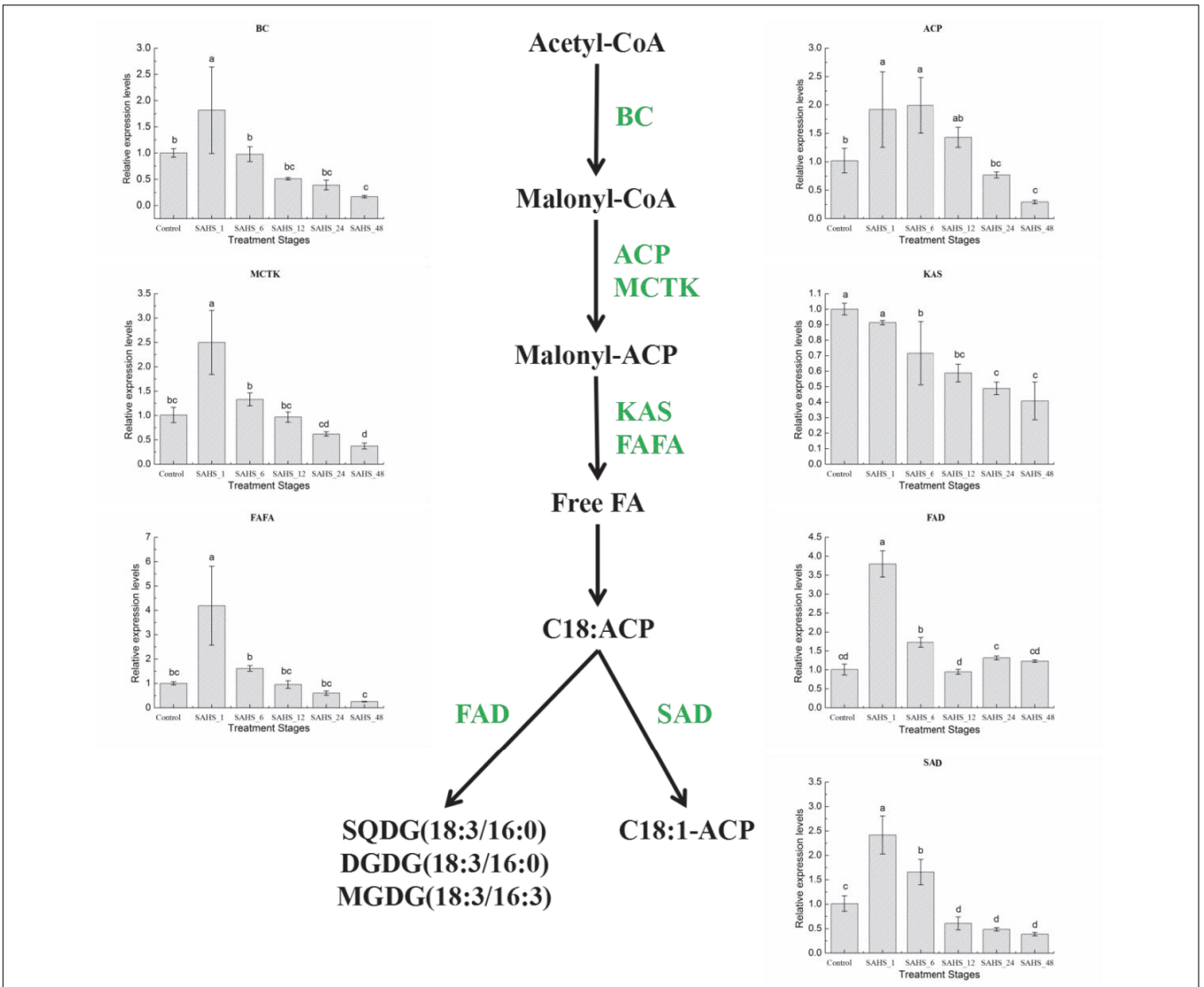

FIGURE 5 | Expression of genes in the *H. pluvialis* fatty acids biosynthesis pathway under different treatment stages. Lower case letters indicate significant differences ($p < 0.05$) among the treatments.

control. The highest expression levels of these genes were all achieved in Stage SAHS_1, which were significantly upregulated by 2.65 ± 0.35-, 5.06 ± 0.45-, 3.68 ± 0.48-, 16.41 ± 2.06-, 29.68 ± 5.06-, and 4.53 ± 0.60-fold in comparison with the Stage Control in PDS, PSY, LCY, CRTO, CRTR-B, and BKT, respectively. Moreover, expression levels of these genes were significantly downregulated along with the treatment time. According to the above results, the expression of the carotenogenic genes displayed a similar pattern. In general, expression of these genes was significantly upregulated after SAHS treatment for 1 h and then downregulated with treatment time extended. The expression levels of PDS, PSY, LCY, CRTO, CRTR-B, and BKT during all treatment stages were higher than that of control, resulting in continuous biosynthesis of carotene and astaxanthin. Posttranscriptional regulation of these genes was thought to play a role in astaxanthin accumulation.

Transcript Expression of Fatty Acid Biosynthesis Genes

Biotin carboxylase is a subunit of acetyl coenzyme A carboxylase-biotin carboxylase, which catalyzes the carboxylation of acetyl-CoA to form malonyl-CoA, and is the first rate-limiting step of fatty acid biosynthesis in *H. pluvialis*. Acyl carrier protein (ACP) catalyzes a growing chain bound to a thiol ester at the distal thiol of a 4′-phosphopantetheine moiety, which acts as a vital component in both polyketide and fatty acid biosynthesis processes. Malonyl-CoA: ACP transacylase (MCTK) catalyzes the transfer of malonyl moiety from malonyl-CoA onto ACP, which is the fatty acid elongation step through extending the growing the length of acyl chain by two carbons. Furthermore, the condensation reaction between acetyl CoA and malonyl ACP is catalyzed by 3-ketoacyl-ACP synthase (KAS). In the

TABLE 8 | Correlations between expression of carotenogenic and fatty acid biosynthesis genes (cofactors, Pearson correlation in SPSS 19).

Genes	IPI1	IPI2	PDS	PSY	LCY	CRTO	CRTR_B	BKT	BC	ACP	MCTK	KAS	FAFA	FAD	SAD
IPI1	1	0.927**	0.796**	0.769**	0.692**	0.684**	0.700**	0.704**	0.911**	0.755**	0.850**	0.657**	0.896**	0.784**	0.926**
IPI2	0.927**	1	0.705**	0.618**	0.699**	0.602**	0.664**	0.661**	0.792**	0.798**	0.844**	0.741**	0.732**	0.633**	0.874**
PDS	0.796**	0.705**	1	0.934**	0.853**	0.913**	0.932**	0.910**	0.734**	0.647**	0.873**	0.304	0.824**	0.934**	0.884**
PSY	0.769**	0.618**	0.934**	1	0.771**	0.915**	0.872**	0.909**	0.749**	0.503*	0.825**	0.317	0.903**	0.983**	0.845**
LCY	0.692**	0.699**	0.853**	0.771**	1	0.799**	0.925**	0.861**	0.530*	0.616**	0.691**	0.181	0.652**	0.739**	0.754**
CRTO	0.684**	0.602**	0.913**	0.915**	0.799**	1	0.952**	0.967**	0.597**	0.611**	0.836**	0.189	0.770**	0.881**	0.760**
CRTR_B	0.700**	0.664**	0.932**	0.872**	0.925**	0.952**	1	0.951**	0.556*	0.669**	0.806**	0.172	0.709**	0.841**	0.790**
BKT	0.704**	0.661**	0.910**	0.909**	0.861**	0.967**	0.951**	1	0.606**	0.639**	0.841**	0.234	0.767**	0.874**	0.774**
BC	0.911**	0.792**	0.734**	0.749**	0.530*	0.597**	0.556*	0.606**	1	0.535*	0.779**	0.678**	0.930**	0.792**	0.881**
ACP	0.755**	0.798**	0.647**	0.503*	0.616**	0.611**	0.669**	0.639**	0.535*	1	0.788**	0.424	0.514*	0.483*	0.708**
MCTK	0.850**	0.844**	0.873**	0.825**	0.691**	0.836**	0.806**	0.841**	0.779**	0.788**	1	0.629**	0.798**	0.828**	0.913**
KAS	0.657**	0.741**	0.304	0.317	0.181	0.189	0.172	0.234	0.678**	0.424	0.629**	1	0.531*	0.389	0.644**
FAFA	0.896**	0.732**	0.824**	0.903**	0.652**	0.770**	0.709**	0.767**	0.930**	0.514*	0.798**	0.531*	1	0.916**	0.878**
FAD	0.784**	0.633**	0.934**	0.983**	0.739**	0.881**	0.841**	0.874**	0.792**	0.483*	0.828**	0.389	0.916**	1	0.856**
SAD	0.926**	0.874**	0.884**	0.845**	0.754**	0.760**	0.790**	0.774**	0.881**	0.708**	0.913**	0.644**	0.878**	0.856**	1

**Indicated that there was a significant correlation between the expression genes at the $p < 0.05$ level; **Indicated that there was a significant correlation between the expression genes at the $p < 0.01$ level.*

fatty acid biosynthesis pathway, the chain-length-determining enzyme, Acyl-ACP thioesterase (FATA), catalyzes the hydrolysis of the thioester bond of acyl-ACP, releasing ACP and free fatty acid. Stearoyl-ACP-desaturase (SAD) plays an essential role in determining the ratio of saturated to unsaturated fatty acids by catalyzing the conversion of 18:0 to C18:1n9. And the conversion of C18:3n3 from C18:2n6 is catalyzed by ω-3 fatty acid desaturase (FAD; Zhao N. et al., 2015; Ma et al., 2018).

As shown in **Figure 5**, mRNA expression of most fatty acid biosynthesis genes, except for KAS, was significantly upregulated after SAHS treatment for 1 h and then downregulated according to the time extension. The highest expression level of these six genes was achieved during Stage SAHS_1, which were upregulated by 1.82 ± 0.82-, 1.92 ± 0.67-, 2.50 ± 0.66-, 4.19 ± 1.62-, 3.80 ± 0.35-, and 2.41 ± 0.39-fold in comparison with that of Stage Control in BC, ACP, MCTK, FAFA, FAD, and SAD, respectively. KAS was downregulated with the extension of SAHS treatment time in the 2-day incubation period. The lowest expression level for all these genes was achieved in Stage_48, downregulated by 0.17 ± 0.02-, 0.29 ± 0.03-, 0.37 ± 0.06-, 0.41 ± 0.12-, and 0.39 ± 0.03-fold in comparison with the Stage Controls BC, ACP, MCTK, KAS, FAFA, and SAD, respectively.

Correlations Between the Expression of Carotenogenic and Fatty Acid Biosynthesis Genes

Pearson's correlation analysis (SPSS 19.0) was carried out to study the relationship of gene expressions between the key genes involved in two important biosynthesis pathways, including carotenogenic and fatty acid, in *H. pluvialis*, and the results are summarized in **Table 8**.

According to the results in **Table 8**, the correlations between these genes were different, and no gene expression demonstrated a negative correlation with the others in this study. Expression levels of almost all these genes showed a significant or very significant correlation with that of the other genes, except KAS. The expression of KAS shared very significant correlations with IPI1 and IPI2 genes involved in the carotenogenic biosynthesis pathway and BC, MCTK, and SAD genes involved in the fatty acid biosynthesis pathway. The expression of KAS displayed a significant correlation with FAFA.

DISCUSSION

In this study, a time course-dependent gene expression profiling and carotenoid and fatty acid biosynthesis under SAHS stresses were studied. Astaxanthin accumulated in *H. pluvialis* cells is known to be deposited in cytoplasm lipid droplets (Pick et al., 2019). According to the growth pattern of this microalga, cell growth was improved during the incubation period, and the induced accumulation of carotenoid/astaxanthin and fatty acids in the single cells under SAHS treatment corresponded with the increased orange-red partial of the microalga cells (**Figure 1** and **Table 1**). The results displayed that SAHS stresses not only enhanced carotenoid/astaxanthin and fatty acids production in *H. pluvialis* but also maintained its biomass growth, which might provide foundation to optimize the astaxanthin production efficiency in large scale *H. pluvialis* cultivation with commercial applications. Meanwhile, the accumulation of fatty acids during incubation indicated that SAHS stresses might be a suitable treatment condition for biodiesel production in *H. pluvialis*.

High-quality sequencing and assembly data were obtained for exploration of molecular processes or pathways involved in adaptation and pressure response of *H. pluvialis* to SAHS stresses in this study (**Tables 2**, **3**). The results provided a

comprehensive achievement of all functionally characterized genes involved in SAHS-responding determination, and several genes involved in carbon metabolism, primary and secondary metabolism, and immune system responses were identified. It was displayed that the numbers of DEGs decreased along with the sequential transition of the SAHS treatment stages. More DEGs were upregulated for most of the Stage transitions, suggesting that there were greater differences in global gene expression and functions in *H. pluvialis* during earlier response stages (**Table 4**). Higher transcriptional activity was observed during the immediate response of *H. pluvialis* to SAHS stresses, and its adaption to the stress conditions resulted in lower transcriptional activity. This result was similar to the PC analysis, indicating that the six libraries were assigned to three separated groups. STEM analysis displayed the 14 significant gene expression profiles under SAHS stresses. It is conceivable that a significant level of metabolic activity and considerable demand for energy should be generated to maintain the cellular homeostasis and biosynthesis of astaxanthin and lipids in *H. pluvialis* cells in response to stressful conditions.

How Salicylic Acid and High Concentration of Sodium Acetate Treatment Affected the Specific Biological Pathways?

Analysis of the specific biological pathways showed that the main metabolic pathway in *H. pluvialis* under the SAHS stresses is the C_3 pathway. *H. pluvialis* cells were induced to employ the CO_2-concentrating mechanism (CCM) to adapt to the altered environmental conditions. After 1 h of SAHS stresses exposure, enzymes of the C_4 pathway were upregulated immediately to produce CO_2, which finally entered the C_3 pathway. Under prolonged treatment, enzymes of the C_4 pathway were upregulated to decompose malic acid into pyruvate, whereas pyruvate was an intermediate metabolite with important functions, taking part in the metabolism of three major nutrients (i.e., proteins, carbohydrates, and lipids). The enzymes of the C_3 pathway were also upregulated during Stage transition from SAHS_1 to SAHS_48, indicating higher process efficiency of the C_3 cycle. The enzymes in the CAM pathway displayed the same change pattern, which was upregulated to malic acid and then to pyruvate *via* decomposition. SA was thought to play a role in the adaption of *H. pluvialis* cells to HS stress, leading more carbon to flux into the synthesis of pigments, which can offer more help for the cells to adapt to low light conditions under the consistent HS stress. The biosynthesis of fatty acids in *H. pluvialis* cells was upregulated in response to SAHS stresses throughout the cultivation period. However, the biosynthesis of unsaturated fatty acids and long-chain fatty acids was upregulated initially and inhibited with time extension.

It was previously reported that intensive production of carbohydrates is the first response of *H. pluvialis* to abiotic stresses, which were then partially degraded to support fatty acid synthesis (Recht et al., 2012; Cheng et al., 2016; Li et al., 2017). In this study, the increased production of CO_2 and pyruvate in the carbon fixation pathway enhanced the production of proteins, carbohydrates, and lipids. The increased expression of genes related to the carbon fixation pathway indicated that both SA and NaAC improved energy production of the microalgal cells, which means enhanced carbon assimilation and cell division (Sun et al., 2018; Fu et al., 2021), and meanwhile, increased production of astaxanthin and fatty acids in this study. The upregulation of genes involved in the carotenoid biosynthesis pathway enhanced the biosynthesis of astaxanthin and associated pigments. The upregulation of the expression levels of FASN, ACC, and FabD genes enhanced fatty acid biosynthesis, and, thus, promoted both the astaxanthin esterification and deposition pathways in *H. pluvialis* cells. SA was reported to downregulate the responsible genes for fatty acids biosynthesis, except for the SA24 group by RNA-Seq analysis (Gao et al., 2016). In this study, majority of the genes related to fatty acid biosynthesis in *H. pluvialis* were upregulated during the 1st-h SAHS treatment, and the genes involved in free fatty acid biosynthesis were upregulated during the 48-h cultivation. In contrast, the genes involved in unsaturated fatty acid biosynthesis were downregulated at 48 h in comparison with the SAHS_1 stage. Therefore, the induced fatty acid production during 48-h SAHS treatment was likely to provide astaxanthin storage capacity within *H. pluvialis* cells. Fatty acid biosynthesis was induced immediately after addition of high concentration NaAC in the *H. pluvialis* culture medium, which might be owing to NaAC provided both energy and carbon skeleton for the biosynthesis of fatty acid. The downregulation of unsaturated fatty acid biosynthesis genes in Stage SAHS_48 in comparison with Stage SAHS_1 was speculated to be caused by exogenous SA, which provided the protection mechanism of the microalga cells against the abiotic stress caused by high NaAC, for the unsaturated fatty acid could prevent *H. pluvialis* cells from damage by a reactive oxygen species.

In conclusion, our study speculated that SA and excessive NaAC provide both energy and precursors for astaxanthin and fatty acid biosynthesis with an effective mechanism in *H. pluvialis*. SA might act as a signaling molecule to improve cell growth of *H. pluvialis* and promote and drive the above physiological properties in the cells to provide self-protection metabolism for this microalga at the same time. This may be a matter of gene expression, and further attention is required to draw the conclusion.

How Salicylic Acid and High Concentration of Sodium Acetate Treatment Affected the Expression Levels of Carotenoid and Fatty Acid Biosynthesis Genes?

Gao et al. (2015) revealed that the expression pattern of the five genes involved in the carotenoid biosynthesis pathway in *H. pluvialis*, including PDS, ZDS, CRTZ, CRTB, and ZEP, differed between salicylic acid and jasmonic acid inductions. Expression levels of the PSY, PDS, ZDS, and CRTR-B genes were upregulated, correlating with excessive accumulation of astaxanthin in *H. pluvialis* cells. They showed variable upregulated patterns under the stress of the same level of jasmonic acid or SA

inductions. The downregulation of PSY, PDS, and LCYB during the first 2 days was considered to be caused by environmental changes and may exhibit certain synergy among the expression of these carotenogenic genes. They also demonstrated in another study that the transcriptional expression levels of eight carotenoid genes in *H. pluvialis* were all downregulated in the first 12 h (except BKT and PDS genes), follow SA25 treatment, and were less than 2.5-fold in comparison with Control follow SA25 treatment in 2-day cultivation (except PDS gene) (Gao et al., 2012b). The phytoene and astaxanthin biosynthesis-related genes were studied at the transcript level under NaAC stress by Cong et al. (2020), who reported that CrtW and CrtZ, the two key enzymes involved in astaxanthin biosynthesis, were continuously upregulated since the 1st day of induction, while expression levels of PSY, PDS, and LCYB genes were continuously upregulated ever since the 3rd day of induction. He et al. (2018) conducted systemic transcriptome analysis about three variables, including light, acetate, and Fe^{2+}, to explore the molecular mechanism of astaxanthin accumulation in the red-cell stage of *H. pluvialis*. It was demonstrated that the expression of CRTZ gene was significantly promoted by acetate induction; acetate was further revealed to promote astaxanthin biosynthesis in *H. pluvialis* by enhancing the expression of CRTZ gene, and meanwhile, inhibiting the expression of LCYE gene. Based on the mode of β-actin gene of *H. pluvialis* under nitrogen starvation, Zhao et al. (2020) revealed that expression of the astaxanthin biosynthesis-related genes was significantly promoted to distribute carbon flow through the MEP pathway to the astaxanthin biosynthesis pathway permanently to defend the nitrogen starvation stress. In particular, expression levels of the most astaxanthin biosynthesis-related genes, including IPI, PSY, ZDS, CHYB, and BKT, all increased by more than 5-fold.

With regard to lipids, Gao et al. (2016) displayed that transcriptional expression of the fatty acid biosynthesis genes, including BC, MCTK, ACP, KAS, FAFA, FAD, and SAD, was in line with the RNA-Seq transcriptomic analysis. Expression levels of the seven genes were all decreased after SA treatment for 6 h, and the transcriptional levels of SA1 were similar to that of SA24, except for FAD gene, which was significantly higher in SA24 than SA1. It was found that the synthesis of storage lipid was stimulated substantially by high irradiance induction conditions and regulated by expression of *de novo* genes involved in the fatty acid biosynthesis pathway (Gwak et al., 2014). He et al. (2018) demonstrated that the genes involved in fatty acid-related pathways, especially the fatty acid elongation pathway, were significantly affected by acetate induction conditions and acetate-promoted expression of the lipid pathway-related genes in *H. pluvialis*. Addition of acetate in cultivation system of *H. pluvialis* further enhanced expression levels of the KCS and MECR genes. Zhao et al. (2020) revealed that all the transcripts associated with the *de novo* biosynthesis of fatty acids showed a higher expression level with nitrogen starvation.

In this study, the q-RT-PCR results indicated that most of the genes involved in our interested pathways revealed a similar expression pattern, which was upregulated immediately from Stage control to SAHS_1 and then decreased with the treatment time extension. Meanwhile, expression of the KAS gene showed a consistently decreasing trend with the time extension. However, expression of the IPI genes achieved the highest levels at Stage SAHS_48, while expression of PDS, PSY, LCY, CRTO, CRTR-B, and BKT genes displayed a similar or a higher level at Stage SAHS_48 compared with the control. The majority of the genes involved in the fatty acid biosynthesis pathway, including BC, ACP, MCTK, FAFA, FAD, and SAD, displayed the same expression pattern, which was significantly upregulated after SAHS treatment for 1 h and then downregulated with the treatment time extension (except KAS), and the transcriptional levels of Stage SAHS_48 were significantly lower than that of Stage Control, except for FAD, which was similar to Control. The above results were consistent with the RNA-Seq transcriptomic analysis, which revealed that addition of high concentration of NaAC immediately induced fatty acid and astaxanthin biosynthesis in *H. pluvialis* cells. And the upregulation of carotenoid biosynthesis genes resulted in continuous accumulation of astaxanthin in the microalga cells, which was observed. The downregulation of fatty acid biosynthesis-related genes, especially the unsaturated fatty acid biosynthesis genes, from Stage SAHS_1 to SAHS_48 demonstrated that exogenous SA played a role in providing a protection mechanism for *H. pluvialis* cells against the abiotic stress caused by high NaAC. These results were consistent with the astaxanthin, and fatty acid accumulation speculated to stimulate the self-protective metabolism as a defense against the high concentration sodium acetate stress (Cong et al., 2020).

The correlations between these genes were all positively correlated. The gene clusters involved in either carotenoid or fatty acid biosynthesis pathways significantly positively correlated, which might indicate that these two pathways were stoichiometrically coordinated at the transcript level. Our detailed correlation analysis between genes involved in these two pathways provided some interesting hints for the molecular mechanism involved in coordination between astaxanthin and fatty acid biosynthesis (**Table 8**). The correlation analysis between gene expressions in the two pathways might detect some new vital genes and provide insight into the coordination between them. SA was thought to act as a signaling molecule and play a role in inhibiting the upregulation of the fatty acid and astaxanthin biosynthesis genes through self-protection metabolism in *H. pluvialis*, leading to its adaption to HS stress and finally avoid the massive cell death, which was caused by excessive NaAC condition. These results were consistent with the previous study reported by Ma et al. (2018), which revealed that nitrogen starvation-induced gene expressions of astaxanthin and fatty acid-related genes (except for IPI1 and IPI2) corresponded to the accumulation of total astaxanthin and fatty acid content in *H. pluvialis*. It was deduced in this study that SA and NaAC provide both energy and precursors for astaxanthin and fatty acid biosynthesis with an effective mechanism in *H. pluvialis*. SA played a role in improving cell growth of *H. pluvialis*, promoting and driving physiological properties to provide self-protection metabolism in the microalga cells against the abiotic stress caused by excessive NaAC.

Hence, the results of this study provided the foundation to optimize the induction conditions leading to improving

astaxanthin production efficiency in large-scale cultivation. Further studies on the molecular mechanism for lipid and astaxanthin accumulation *via* salicylic acid combined with sodium acetate are required.

DATA AVAILABILITY STATEMENT

The datasets presented in this study can be found in online repositories. The names of the repository/repositories and accession number(s) can be found below: https://www.ncbi.nlm.nih.gov/, PRJNA675306.

AUTHOR CONTRIBUTIONS

QH performed the experiments, analyzed the data, supervised the experimental work, and wrote the manuscript. MS performed the additional experiments. CW designed the study and formulated the manuscript. DH, ZH, and YW provided additional supervision and contributed to the final manuscript. All authors contributed to the article and approved the submitted version.

FUNDING

This work was supported financially by the National Key Research and Development Plan Special Project for Synthetic Biology (2018YFA0902500), National Natural Science Foundation of China (31970366 and 31470389), China Postdoctoral Science Foundation (2019M663042), Natural Science Foundation of Guangdong Province (2019A1515011701), and Shenzhen Scientific Project (JCYJ20190808114216058).

SUPPLEMENTARY MATERIAL

The Supplementary Material for this article can be found online at: https://www.frontiersin.org/articles/10.3389/fpls.2021.763742/full#supplementary-material

REFERENCES

Boussiba, S., Fan, L., and Vonshak, A. (1992). Enhancement and determination of astaxanthin accumulation in green alga *Haematococcus pluvialis*. *Method Enzymol.* 213, 386–391.

Cerón, M. C., García-Malea, M. C., Rivas, J., Acien, F. G., Fernandez, J. M., Guerrero, M. G., et al. (2007). Antioxidant activity of *Haematococcus pluvialis* cellsgrown in continuous culture as a function of their carotenoid and fatty acid content. *Appl. Microbiol. Biotech.* 74, 1112–1119. doi: 10.1007/s00253-006-0743-5

Chen, D. C., Yuan, X., Liang, L. M., Liu, K., Ye, H. Y., Liu, Z. Y., et al. (2019). Overexpression of acetyl-CoA carboxylase increases fatty acid production in the green alga *Chlamydomonas reinhardtii*. *Biotechnol. Lett.* 41, 1133–1145. doi: 10.1007/s10529-019-02715-0

Chen, G., Wang, B., Han, D., Sommerfeld, M., Lu, Y., Chen, F., et al. (2015). Molecular mechanisms of the coordination between astaxanthin and fatty acid biosynthesis in *Haematococcus pluvialis* (Chlorophyceae). *Plant J. Cell Mol. Biol.* 81, 95–107. doi: 10.1111/tpj.12713

Cheng, J., Li, K., Yang, Z. B., Zhou, J. H., and Cen, K. F. (2016). Enhancing the growth rate and astaxanthin yield of *Haematococcus pluvialis* by nuclear irradiation and high concentration of carbon dioxide stress. *Bioresource Technol.* 204, 49–54. doi: 10.1016/j.biortech.2015.12.076

Cheng, J., Li, K., Zhu, Y. X., Zhou, J. H., and Cen, K. F. (2017). Transcriptome sequencing and metabolic pathways of astaxanthin accumulated in *Haematococcus pluvialis* mutant under 15% CO_2. *Bioresource Technol.* 228, 99–105. doi: 10.1016/j.biortech.2016.12.084

Cong, X. M., Zang, X. N., Dong, M. M., Wang, Z. D., He, B. X., Hou, L. L., et al. (2020). Accumulation of phytoene and astaxanthin and related genes expression in *Haematococcus pluvialis* under sodium acetate stress. *Aquat. Biol.* 29, 155–164.

Cui, D., Hu, C. C., Zou, Z., Sun, X., Shi, J., and Xu, N. (2020). Comparative transcriptome analysisunveils mechanisms underlying the promoting effect of potassium iodide onastaxanthin accumulation in *Haematococcus pluvialis* under high light stress. *Aquaculture* 525, 1–13.

Cui, J., Yu, C., Zhong, D. B., Zhao, Y., and Yu, X. (2020). Melatonin and calcium actsynergistically to enhance the coproduction of astaxanthin and lipids in*Haematococcus pluvialis* under nitrogen deficiency and high light conditions. *Bioresource Technol.* 305, 1–11. doi: 10.1016/j.biortech.2020.123069

Ding, W., Peng, J., Zhao, Y., Zhao, P., Xu, J. W., Li, T., et al. (2019a). A strategy forboosting astaxanthin accumulation in green microalga *Haematococcus pluvialis* byusing combined diethyl aminoethyl hexanoate and high light. *J. Appl. Phycol.* 31, 171–181.

Ding, W., Li, Q., Han, B., Zhao, Y., Geng, S., Ning, D., et al. (2019b). Comparativephysiological and metabolomic analyses of the hyper-accumulation of astaxanthinand lipids in *Haematococcus pluvialis* upon treatment with butylated hydroxyanisole. *Bioresource Technol.* 292, 1–10.

Ding, W., Zhao, Y., Xu, J. W., Zhao, P., Li, T., Ma, H., et al. (2018a). Melatonin: a multifunctional molecule that triggers defense responses against highlight and nitrogen starvation stress in *Haematococcus pluvialis*. *J. Agric. Food Chem.* 66, 7701–7711. doi: 10.1021/acs.jafc.8b02178

Ding, W., Zhao, P., Peng, J., Zhao, Y., Xu, J. W., Li, T., et al. (2018b). Melatonin enhances astaxanthin accumulation in the green microalga *Haematococcuspluvialis* by mechanisms possibly related to abiotic stress tolerance. *Algal Res.* 33, 256–265.

Eom, H., Lee, C. G., and Jin, E. (2006). Gene expression profile analysis in astaxanthin-induced *Haematococcus pluvialis* using a cDNA microarray. *Planta* 223, 1231–1242. doi: 10.1007/s00425-005-0171-2

Fábregas, J., Domínguez, A., Maseda, A., and Otero, A. (2003). Interactions between irradianceand nutrient availability during astaxanthin accumulation and degradation inHaematococcus pluvialis. *Appl. Microbiol. Biotechnol.* 61, 545–551. doi: 10.1007/s00253-002-1204-4

Fu, L., Li, Q. C., Chen, C. L., Zhang, Y. J., Liu, Y. L., Xu, L., et al. (2021). Benzoic and salicylic acid are the signaling molecules of Chlorella cellsfor improving cell growth. *Chemosphere* 265, 1–9.

Galarza, J. I., Gimpel, J. A., Rojas, V., Arredondo-Vega, B. O., and Henríquez, V. (2018). Over-accumulation of astaxanthin in *Haematococcus pluvialis* through chloroplast genetic engineering. *Algal Res.* 31, 291–297.

Gao, Z. Q., Li, Y., Wu, G. X., Li, G. Q., Sun, H. F., Deng, S. Z., et al. (2015). Transcriptome analysis in *Haematococcus pluvialis*: astaxanthin induction by Salicylic Acid (SA) and Jasmonic Acid (JA). *PLoS One* 10:e0140609. doi: 10.1371/journal.pone.0140609

Gao, Z. Q., Meng, C. X., and Ye, N. H. (2010). Three 5-flanking regions of crtO encoding - carotene oxygenase in *Haematococcus pluvialis*. *Mar. Sci. B* 12, 59–64.

Gao, Z. Q., Meng, C. X., Gao, H. Z., Li, Y., Zhang, X. W., Xu, D., et al. (2013a). Carotenoid genes transcriptional regulation for astaxanthin accumulation in fresh water unicellular alga *Haematococcus pluvialis* by gibberellin A3 (GA3).*Indian J. Biochem. Bio.* 50, 548–553.

Gao, Z. Q., Meng, C. X., Gao, H. Z., Li, Y., Zhang, X. W., Xu, D., et al. (2013b). Analysis of mRNA expression profiles of carotenogenesis andastaxanthin production of *Haematococcus pluvialis* under exogenous2, 4-epibrassinolide

(EBR). *Biol. Res.* 46, 201–206. doi: 10.4067/S0716-97602013000200012

Gao, Z. Q., Meng, C. X., Zhang, X. W., Xu, D., Zhao, Y. F., Wang, Y. T., et al. (2012a). Differential expression of carotenogenic genes, associated changes on astaxanthin production and photosynthesis features induced by JA in *Haematococcus pluvialis*. *PLoS One* 7:e42243. doi: 10.1371/journal.pone.0042243

Gao, Z. Q., Meng, C. X., Zhang, X. W., Xu, D., Miao, X. X., Wang, Y. T., et al. (2012b). Induction of salicylic acid (SA) on transcriptional expression of eight carotenoid genes and astaxanthin accumulation in *Haematococcus pluvialis*. *Enzyme Micro. Technol.* 51, 225–230. doi: 10.1016/j.enzmictec.2012.07.001

Gao, Z. Q., Miao, X. X., Zhang, X. W., Wu, G. X., Guo, Y. Y., Wang, M. M., et al. (2016). Comparative fatty acid transcriptomic test and iTRAQ-based proteomic analysis in *Haematococcus pluvialis* upon salicylic acid (SA) and jasmonic acid (JA) inductions. *Algal Res.* 17, 277–284.

Göksan, T., Iknur, A. K., and Gökpnar, S. (2010). An alternative approach to the traditional mixotrophic cultures of *Haematococcus pluvialis* Flotow (Chlorophyceae). *J. Microbiol. Biotechnol.* 20, 1276–1282.

Gong, M. Y., and Bassi, A. (2016). Carotenoids from microalgae: a review of recent developments. *Biotechnol. Adv.* 34, 1396–1412. doi: 10.1016/j.biotechadv.2016.10.005

Gupta, S., Pawar, S. B., and Pandey, R. A. (2019). Current practices and challenges in using microalgae for treatment ofnutrient rich wastewater from agro-based industries. *SciTotal Environ.* 687, 1107–1126. doi: 10.1016/j.scitotenv.2019.06.115

Gwak, Y., Hwang, Y. S., Wang, B. B., Kim, M., Jeong, J., Lee, C. G., et al. (2014). Comparative analyses of lipidomes and transcriptomes reveal a concerted action of multiple defensive systems against photooxidative stress in *Haematococcus pluvialis*. *J. Exp. Bot.* 65, 4317–4334. doi: 10.1093/jxb/eru206

Harwood, J. L. (2019). Algae: critical sources of very long-chain polyunsaturated fatty acids. *Biomolecules* 9, 1–14. doi: 10.3390/biom9110708

Hasan, H., Abd-Rahim, M. H., Campbell, L., Carter, D., Abbas, A., and Montoya, A. (2018). Overexpression of acetyl-COA carboxylase in, aspergillus terreus, to increase lovastatin production. *New Biotechnol.* 44, 1–8.

He, B. G., Hou, L. L., Dong, M. M., Shi, J. W., Huang, X. Y., Ding, Y. T., et al. (2018). Transcriptome analysis in *Haematococcus pluvialis*: astaxanthin induction by high light with acetate and Fe^{2+}. *Int. J. Mol. Sci.* 19, 1–18. doi: 10.3390/ijms19010175

Holtin, K., Kuehnle, M., Rehbein, J., Schuler, P., Nicholson, G., and Albert, K. (2009). Determinationof astaxanthin and astaxanthin esters in the microalgae *Haematococcus pluvialis* by LC-(APCI)MS and characterization of predominant carotenoid isomers by NMR spectroscopy. *Anal. Bioanal. Chem.* 395, 1613–1622. doi: 10.1007/s00216-009-2837-2

Hong, M. E., Hwang, S. K., Chang, W. S., Kim, B. W., Lee, J., and Sang, J. S. (2015). Enhanced autotrophic astaxanthin production from *Haematococcus pluvialis* under high temperature via heat stress-driven Haber–Weiss reaction. *Appl. Microbiol. Biotech.* 99, 5203–5215. doi: 10.1007/s00253-015-6440-5

Hu, C. Y., Cui, D. D., Sun, X., Shi, J. X., and Xu, N. J. (2020). Primary metabolism is associated with the astaxanthin biosynthesis in the green algae *Haematococcus pluvialis* under light stress. *Algal Res.* 46, 1–14.

Hu, C. Y., Cui, D. D., Sun, X., Shi, J. X., Song, L. L., Li, Y. H., et al. (2019). Transcriptomic analysis unveils survival strategies of autotrophic *Haematococcus pluvialis* against high light stress. *Aquaculture* 513, 1–13.

Hu, Q. J., Huang, D. Q., Li, A. G., Hu, Z. L., Gao, Z. Q., Yang, Y. L., et al. (2021). Transcriptome-based analysisof the effects of salicylic acid and high lighton lipid and astaxanthin accumulationin *Haematococcus pluvialis*. *Biotechnol. Biofuels* 14, 1–20.

Hu, Q. J., Xiang, W. Z., Dai, S. K., Li, T., Yang, F. F., Jia, Q. K., et al. (2015). The influence of cultivation period on growth and biodiesel properties of microalga *Nannochloropsis gaditana* 1049. *Bioresource Technol.* 192, 157–164. doi: 10.1016/j.biortech.2015.04.106

Khan, M. I. R., Asgher, M., and Khan, N. A. (2014). Alleviation of salt-inducedphotosynthesis and growth inhibition by salicylic acid involves glycinebetaineand ethylene in mungbean (*Vigna radiata* L.). *Plant Physiol. Biochem.* 80, 67–74.

Khan, M. I. R., Fatma, M., Per, T. S., Anjum, N. A., and Khan, N. A. (2015). Salicylic acid-induced abiotic stresstolerance and underlyingmechanisms in plants. *Front. Plant Sci.* 6, 1–17. doi: 10.3389/fpls.2015.00462

Khan, M. I. R., Iqbal, N., Masood, A., Per, T. S., and Khan, N. A. (2013). Salicylicacid alleviates adverse effects of heat stress on photosynthesis through changesin proline production and ethylene formation. *Plant Signal. Behav.* 8:e26374. doi: 10.4161/psb.26374

Khan, N. A., Nazar, R., Iqbal, N., and Anjum, N. A. (2012). *Phytohormones andabiotic stress tolerance in plants*. Berlin: Springer, 1–311.

Khan, N., Syeed, S., Masood, A., Nazar, R., and Iqbal, N. (2010). Application ofsalicylic acid increases contents of nutrients and antioxidative metabolism inmungbean and alleviates adverse effects of salinity stress. *Intl. J. Plant. Biol.* 1, 1–8.

Kobayashi, M. (2003). Astaxanthin biosynthesis enhanced by reactive oxygen speciesin the green alga *Haematococcus pluvialis*. *Biotechnol. Bioproc. E* 8, 322–330.

Kobayashi, M., Kakizono, T., and Nagai, S. (1993). Enhanced carotenoid biosynthesis by oxidative stressin acetateinduced cyst cells of a green unicellular alga, *Haematococcus pluvialis*. *Appl. Environ.Microbiol.* 59, 867–873. doi: 10.1128/aem.59.3.867-873.1993

Kobayashi, M., Kakizono, T., Yamaguchi, K., Nishio, N., and Nagai, S. (1992). Growth and astaxanthin formation of *Haematococcus pluvialis*inheterotrophic and mixotrophic conditions. *J. Ferment. Bioeng.* 74, 17–20.

Lee, P. C., and Schmidt-Dannert, C. (2002). Metabolic engineering towards biotechnological production of carotenoids in microorganisms. *Appl. Microbiol. Biotechnol.* 60, 1–11. doi: 10.1007/s00253-002-1101-x

Le-Feuvre, R., Moraga-Suazo, P., Gonzalez, J., Martin, S. S., Henríquez, V., Donoso, A., et al. (2020). Biotechnology applied to *Haematococcus pluvialis* Fotow:challenges and prospects for the enhancementof astaxanthin accumulation. *J. Appl. Phycol.* 32, 3831–3852.

Lei, A. P., Chen, H., Shen, G. M., Hu, Z. L., Chen, L., and Wang, J. X. (2012). Expression of fatty acid synthesis genes and fatty acid accumulation in *Haematococcus pluvialis* under different stressors. *Biotechnol. Biofuels* 5, 1–11. doi: 10.1186/1754-6834-5-18

Leite, G. B., Paranjape, K., Abdelaziz, A. E. M., and Hallenbeck, P. C. (2015). Utilization of biodiesel-derived glycerol or xylose for increased growth and lipid production by indigenous microalgae. *Bioresource Technol.* 184, 123–130.

Lemoine, Y., and Schoefs, B. (2010). Secondary ketocarotenoid astaxanthin biosynthesisin algae: a multifunctional response to stress. *Photosynth. Res.* 106, 155–177. doi: 10.1007/s11120-010-9583-3

Li, K., Cheng, J., Lu, H. X., Yang, W. J., Zhou, J. H., and Cen, K. F. (2017). Transcriptome-based analysis on carbon metabolism of *Haematococcus pluvialis* mutant under 15% CO2. *Bioresource Technol.* 233, 313–321. doi: 10.1016/j.biortech.2017.02.121

Li, Q. Q., Zhao, Y. T., Ding, W., Han, B. Y., Geng, S. X., Ning, D. L., et al. (2021). Gamma-aminobutyricacid facilitates the simultaneous production of biomass, astaxanthin and lipids in *Haematococcus pluvialis* under salinity and high-light stress conditions. *Bioresource Technol.* 320, 1–11. doi: 10.1016/j.biortech.2020.124418

Li, X., Wang, X. Q., Duan, C. L., Yi, S. S., Gao, Z. Q., Xiao, C. W., et al. (2020). Biotechnological production of astaxanthin from the microalga *Haematococcus pluvialis*. *Biotechnol. Adv.* 43:107602. doi: 10.1016/j.biotechadv.2020.107602

Li, Y., Sommerfeld, M., Chen, F., and Hu, Q. (2010). Effect of photon flux densities onregulation of carotenogenesis and cell viability of *Haematococcuspluvialis*(Chlorophyceae). *J. Appl. Phycol.* 22, 253–263.

Li-Beisson, Y., Thelen, J. J., Fedosejevs, E., and Harwood, J. L. (2019). The lipid biochemistry of eukaryotic algae. *Prog. Lipid Res.* 74, 31–68. doi: 10.1016/j.plipres.2019.01.003

Liu, J., Sun, Z., Gerken, H., Huang, J., Jiang, Y., and Chen, F. (2014). Genetic engineering of the green alga *Chlorella zofingiensis*: a modified norflurazon-resistant phytoene desaturase gene as a dominant selectable marker. *Appl. Microbiol. Biotechnol.* 98, 5069–5079. doi: 10.1007/s00253-014-5593-y

Liu, L., Gerken, H., Huang, J., and Chen, F. (2013). Engineering of an endogenous phytoene desaturase gene as a dominant selectable marker for *Chlamydomonas reinhardtii* transformation and enhanced biosynthesis of carotenoids. *Process Biochem.* 48, 788–795.

Livak, K. J., and Schmittgen, T. D. (2001). Analysis of relative gene expression data using real time quantitative PCR and the $2^{-\Delta\Delta Ct}$ method. *Methods* 25, 402–408.

Lu, Y., Jiang, P., Liu, S., Gan, Q., Cui, H., and Qin, S. (2010). Methyl jasmonate-orgibberellins A3-induced astaxanthin accumulation is associated withup-regulation of transcription of β-carotene ketolase genes (bkts) inmicroalga *Haematococcus pluvialis*. *Bioresource Technol.* 101, 6468–6474. doi: 10.1016/j.biortech.2010.03.072

Luo, Q. L., Bian, C., Tao, M., Huang, Y., Zheng, Y. H., Lv, Y. Y., et al. (2018). Genome and transcriptome sequencing of the astaxanthin-producing green microalga, *Haematococcus pluvialis*. *Genome Biol. Evol.* 11, 166–173. doi: 10.1093/gbe/evy263

Ma, R. J., Thomas-Hall, S. R., Chua, E. T., Alsenani, F., Eltanahy, E., Netzel, M. E., et al. (2018). Gene expression profiling of astaxanthin and fatty acid pathways in *Haematococcus pluvialis* in response to different LED lighting conditions. *Bioresource Technol.* 250, 591–602. doi: 10.1016/j.biortech.2017.11.094

Machado, F. R. S. Jr., Trevisol, T. C., Boschetto, D. L., Burkert, J. F. M., Ferreira, S. R. S., Oliveira, J. V., et al. (2016). Technological process for cell disruption, extraction and encapsulation of astaxanthin from *Haematococcus pluvialis*. *J. Biotechnol.* 218, 108–114. doi: 10.1016/j.jbiotec.2015.12.004

Meng, C. X., Liang, C. W., Su, Z. L., Qin, S., and Tseng, C. K. (2006). There are two 5-flanking regions of bkt encoding beta-carotene ketolase in the *Haematococcus pluvialis*. *Phycologia* 45, 218–224.

Meng, C. X., Teng, C. Y., Jiang, P., Qin, S., and Tseng, C. K. (2005). Cloning and characterization of -carotene ketolase gene promoter in *Haematococcus pluvialis*. *Acta Bioch. Bioph. Sin.* 37, 270–275.

Miura, K., and Tada, Y. (2014). Regulation of water, salinity, and cold stressresponses by salicylic acid. *Front. Plant Sci.* 5:4. doi: 10.3389/fpls.2014.00004

Molino, A., Rimauro, J., Casella, P., Cerbone, A., Chianese, S., Karatza, D., et al. (2018). Extraction of astaxanthin from microalga *Haematococcus pluvialis* in red phase by using generally recognized as safe solvents and accelerated extraction. *J. Biotechnol.* 283, 51–61. doi: 10.1016/j.jbiotec.2018.07.010

Nazar, R., Umar, S., and Khan, N. A. (2015). Exogenous salicylic acidimproves photosynthesis and growth through increase in ascorbate-glutathionemetabolism and S assimilation in mustard under salt stress.*Plant Signal. Behav.* 10:e1003751. doi: 10.1080/15592324.2014.1003751

Orosa, M., Franqueira, D., Cid, A., and Albade, J. (2001). Carotenoid accumulationin *Haematococcus pluvialis*in mixotrophic growth. *Biotechnol. Lett.* 23, 373–378.

Oslan, S. N. H., Shoparwe, N. F., Yusoff, A. H., Rahim, A. A., Chang, C. S., Tan, J. S., et al. (2021). A review on *Haematococcus Pluvialis* bioprocess optimization of green and red stage culture conditions for the production of natural astaxanthin. *Biomolecules* 11:10.3390. doi: 10.3390/biom11020256

Pang, N., Fu, X., Martinez Fernandez, J. S., and Chen, S. (2019). Multilevel heuristic LED regime for stimulating lipid and bioproductsbiosynthesis in *Haematococcus pluvialis*under mixotrophic conditions. *Bioresource Technol.* 288, 1–8. doi: 10.1016/j.biortech.2019.121525

Pick, U., Zarka, A., Boussiba, S., and Davidi, L. (2019). A hypothesis about the origin of carotenoid lipid droplets in the green algae *Dunaliella* and *Haematococcus*. *Planta* 249, 31–47. doi: 10.1007/s00425-018-3050-3

Raman, V., and Ravi, S. (2011). Effect of salicylic acid and methyl jasmonate on antioxidant systems of *Haematococcus pluvialis*. *Acta Physiol. Plant* 33, 1043–1049.

Ranga Rao, A., Raghunath Reddy, R. L., Baskaran, V., Sarada, R., and Ravishankar, G. A. (2010). Characterization of microalgal carotenoids by mass spectrometry and their bioavailability andantioxidant properties elucidated in rat model. *J. Agr. Food Chem.* 58, 8553–8559. doi: 10.1021/jf101187k

Raskin, I. (1992). Role of salicylic acid in plants. *Annu. Rev. PlantPhysiol.* 43, 438–463.

Recht, L., Zarka, A., and Boussiba, S. (2012). Patterns of carbohydrate and fatty acid changesunder nitrogen starvation in the microalgae *Haematococcus pluvialis*and*Nannochloropsis* sp. *Appl. Microbiol. Biotechnol.* 94, 1495–1503. doi: 10.1007/s00253-012-3940-4

Rismani-Yazdi, H., Haznedaroglu, B. Z., Bibby, K., and Peccia, J. (2011). Transcriptome sequencing and annotation of the microalgae *Dunaliella tertiolecta*: Pathway description and gene discovery for production of next-generation biofuels. *BMC Genomics* 12:148. doi: 10.1186/1471-2164-12-148

Ruth, L., and Javier, A. M. (2006). pharmacological inhibitors of fatty acid synthase (fasn)-catalyzed endogenous fatty acid biogenesis: a new family of anti-cancer agents? *Curr. Pharm. Biotechnol.* 7, 483–494. doi: 10.2174/138920106779116928

Saha, S. K., McHugh, E., Hayes, J., Moane, S., Walsh, D., and Murray, P. (2013). Effect of variousstress-regulatory factors on biomass and lipid production in microalga*Haematococcus pluvialis*. *Bioresource Technol.* 128, 118–124. doi: 10.1016/j.biortech.2012.10.049

Sánchez, J., and Harwood, J. L. (2002). Biosynthesis of triacylglycerols and volatiles in olives. *Eur. J. Lipid Sci. Tech.* 104, 564–573.

Shah, M. M. R., Liang, Y., Cheng, J. J., and Daroch, M. (2016). Astaxanthin-producing green microalga *Haematococcus pluvialis*: from single cell to high value commercial products. *Front. Plant Sci.* 7, 1–28. doi: 10.3389/fpls.2016.00531

Silva, C. M., Borba, T. M., Burkert, C. A. V., and Burkert, J. F. M. (2012). Carotenoid production by *Phaffia rhodozyma* using raw glycerol as an additional carbon source. *Int. J. Food Eng.* 8, 1–16.

Steinbrenner, J., and Sandmann, G. (2006). Transformation of the green alga *Haematococcus pluvialis* with a phytoene desaturase for accelerated astaxanthin biosynthesis. *Appl. Environ. Microbiol.* 72, 7477–7484. doi: 10.1128/AEM.01461-06

Sun, H., Zhao, W., Mao, X., Li, Y., Wu, T., and Chen, F. (2018). High-value biomass frommicroalgae production platforms: strategies and progress based on carbonmetabolism and energy conversion. *Biotechnol. Biofuels* 11, 1–23.

Tolga, G., Ak, I., and Gökpinar, S. (2010). An Alternative Approach to the Traditional Mixotrophic Cultures of*Haematococcus pluvialis*Flotow (Chlorophyceae). *J. Microbiol. Biotechnol.* 20, 1276–1282.

Trapnell, C., Williams, B. A., Pertea, G., Mortazavi, A., Kwan, G., van Beren, M. J., et al. (2010). Transcript assembly and quantification by RNA-seqreveals unannotated transcripts and isoform switchingduring cell differentiation. *Nat. Biotechnol.* 28, 511–515. doi: 10.1038/nbt.1621

Wan, X., Zhou, X. R., Moncalian, G., Su, L., Chen, W. C., Zhu, H. Z., et al. (2021). Reprogramming microorganisms for the biosynthesis of astaxanthin via metabolic engineering. *Prog. Lipid Res.* 81, 1–19. doi: 10.1016/j.plipres.2020.101083

Wang, X. D., Miao, X. X., Chen, G., Cui, Y. L., Sun, F. J., Fan, J. H., et al. (2021). Identification of microRNAs involved in astaxanthin accumulation responding to high light and high sodium acetate (NaAC) stresses in *Haematococcus pluvialis*. *Algal Res.* 2021:102179.

Wen, Z., Liu, Z., Hou, Y., Liu, C., Gao, F., Zheng, Y., et al. (2015). Ethanol induced astaxanthin accumulation and transcriptional expression of carotenogenic genes in *Haematococcus pluvialis*. *Enzyme Microb. Technol.* 78, 10–17. doi: 10.1016/j.enzmictec.2015.06.010

Yu, X., Chen, L., and Zhang, W. (2015). Chemicals to enhance microalgal growth and accumulation ofhigh-value bioproducts. *Front. Microbiol.* 6:56. doi: 10.3389/fmicb.2015.00056

Zhang, C. H., Zhang, L. T., and Liu, J. G. (2019). Exogenous sodium acetate enhances astaxanthin accumulationand photoprotection in *Haematococcus pluvialis*at the non-motilestage. *J. Appl. Phycol.* 31, 1001–1008.

Zhao, N., Zhang, Y., Li, Q. Q., Li, R. F., Xia, X. L., Qin, X. W., et al. (2015). Identification and expression of a stearoyl-ACP desaturase gene responsible for oleic acid accumulation in *Xanthoceras sorbifolia* seeds. *Plant Physiol. Biochem.* 87, 9–16. doi: 10.1016/j.plaphy.2014.12.009

Zhao, Y. T., Wang, H. P., Han, B. Y., and Yu, X. Y. (2019). Coupling of abiotic stresses and phytohormones for the production of lipidsand high-value by-products by microalgae: A review. *Bioresource Technol.* 274, 549–556. doi: 10.1016/j.biortech.2018.12.030

Zhao, Y. T., Wang, H. P., Yu, C. L., Ding, W., Han, B. Y., Geng, S. X., et al. (2021). Integration of physiological and metabolomic profiles to elucidate the regulatory mechanisms underlying the stimulatory effect of melatonin on astaxanthin and lipidscoproduction in *Haematococcus pluvialis* under inductive stress conditions. *Bioresource Technol.* 319:124150. doi: 10.1016/j.biortech.2020.124150

Zhao, Y., Hou, Y. Y., Chai, W. J., Liu, Z. Y., Wang, X., He, C. Q., et al. (2020). Transcriptome analysis of *Haematococcus pluvialis* of multiple defensive systems against nitrogen starvation. *Enzyme Microb. Tech.* 134:109487. doi: 10.1016/j.enzmictec.2019.109487

Zhao, Y., Shang, M., Xu, J. W., Zhao, P., Li, T., and Yu, X. (2015). Enhanced astaxanthinproduction from a novel strain of *Haematococcus pluvialis* using fulvic acid. *ProcessBiochem.* 50, 2072–2077.

Zhao, Y., Yue, C., Ding, W., Li, T., Xu, J. W., Zhao, P., et al. (2018). Butylatedydroxytoluene induces astaxanthin and lipid production in *Haematococcus pluvialis*under high-light and nitrogen-deficiency conditions. *Bioresource Technol.* 266, 315–321. doi: 10.1016/j.biortech.2018.06.111

Zhekisheva, M., Boussiba, S., Khozin-Goldberg, I., Zarka, A., and Cohen, Z. (2002). Accumulation of oleic acid in *Haematococcus pluvialis* (Chlorophyceae) undernitrogen starvation or high light is correlated with that of astaxanthin esters. *J.Phycol.* 38, 325–331.

Conflict of Interest: The authors declare that the research was conducted in the absence of any commercial or financial relationships that could be construed as a potential conflict of interest.

Publisher's Note: All claims expressed in this article are solely those of the authors and do not necessarily represent those of their affiliated organizations, or those of the publisher, the editors and the reviewers. Any product that may be evaluated in this article, or claim that may be made by its manufacturer, is not guaranteed or endorsed by the publisher.

Copyright © 2021 Hu, Song, Huang, Hu, Wu and Wang. This is an open-access article distributed under the terms of the Creative Commons Attribution License (CC BY). The use, distribution or reproduction in other forums is permitted, provided the original author(s) and the copyright owner(s) are credited and that the original publication in this journal is cited, in accordance with accepted academic practice. No use, distribution or reproduction is permitted which does not comply with these terms.

Advantages of publishing in Frontiers

OPEN ACCESS
Articles are free to read for greatest visibility and readership

FAST PUBLICATION
Around 90 days from submission to decision

HIGH QUALITY PEER-REVIEW
Rigorous, collaborative, and constructive peer-review

TRANSPARENT PEER-REVIEW
Editors and reviewers acknowledged by name on published articles

Frontiers
Avenue du Tribunal-Fédéral 34
1005 Lausanne | Switzerland

Visit us: www.frontiersin.org
Contact us: frontiersin.org/about/contact

REPRODUCIBILITY OF RESEARCH
Support open data and methods to enhance research reproducibility

DIGITAL PUBLISHING
Articles designed for optimal readership across devices

FOLLOW US
@frontiersin

IMPACT METRICS
Advanced article metrics track visibility across digital media

EXTENSIVE PROMOTION
Marketing and promotion of impactful research

LOOP RESEARCH NETWORK
Our network increases your article's readership